BNL-96453-2011

Interim Design Report

The IDS-NF Collaboration

R. J. Abrams, S. K. Agarwalla, A. Alekou, C. Andreopoulos, C. M. Ankenbrandt, S. Antusch, M. Apollonio, M. Aslaninejad, J. Back, P. Ballett, G. Barker, S. Bhattacharya, K. B. Beard, E. Benedetto, J. R. J. Bennett, J. S. Berg, M. Blennow, V.Blackmore, A. Blondel, A. Bogacz, M. Bonesini, C. Bontoiu, C. Bromberg, S. Brooks, C. Booth, A. Bross, O. Caretta, A. Cervera-Villaneuva, S. Choubey, D. Cline, J. Cobb, P. Coloma, L. Coney, M.A.C. Cummings, T. Davenne, A. de Gouvea, C. Densham, X. Ding, A. Donini, P. Dornan, M. Dracos, F. Dufour, R. Eccleston, R. Edgecock, I. Efthymiopoulos, M. Ellis, E. Fernandez-Martinez, R. Fernow, G. Flanagan, J. C. Gallardo, R. Garoby, R. Gandhi, B. Gavela, S. Geer, S. Gilardoni, J. J. Gomez-Cadenas, S. Goswami, V. B. Graves, R. Gupta, G. Hanson, P. Harrison, P. Hernandez, P. Huber, D. Indumathi, R.P. Johnson, C. Johnstone, T. Hart, Y. Karadzhov, D. Kelliher, H. Kirk, J. Kopp, P. Kyberd, Y. Kudenko, Y. Kuno, A. Kurup, A. Laing, T. Li, M. Lindner, K. Long, J. Lopez Pavon, P. Loveridge, S. Machida, D. Majumdar, M. Maltoni, J. Martin-Albo, M. Martini, R. Matev, K. T. McDonald, A. McFarland, D. Meloni, M. Mezzetto, P. Migliozzi, S. R. Mishra, N. Mokhov, N. Mondal, J. Morfin, Y. Mori, V. Morozov, D. Neuffer, T. Ota, V. Palladino, S. Parke, S. Pascoli, J. Pasternak, J. Peltoniemi, R. Petti, T. Planche, M. Popovic, J. Pozimski, C. Prior, G. Prior, G. Rees, S. Rigolin, T. J. Roberts, Y. Roblin, C. Rogers, R. Samulyak, T. Schwetz, N. Simos, N. Sinha, P. Snopok, G. Skoro, F. J. P. Soler, N. Souchlas, J. Strait, D. Stratakis, S. Striganov, J. Tang, J. W. G. Thomason, L. Tortora, R. Tsenov, W. Winter, H. Witte, O. Yasuda, C. Y. Yoshikawa, M. Zisman,

November 2011

Physics Department

Brookhaven National Laboratory

U.S. Department of Energy
Office of Science

DISCLAIMER

International Design Study for the Neutrino Factory

IDS-NF-020
BNL-96453-2011
CERN-ATS-2011-216
EUROnu-WP1-05
FERMILAB-PUB-11-581-APC
RAL-TR-2011-018

Interim Design Report

The IDS-NF collaboration

November 7, 2011

S. Choubey, R. Gandhi, S. Goswami
Harish-Chandra Research Institute, Chhatnag Road, Jhunsi, Allahabad, 211019, India
J.S. Berg, R. Fernow, J.C. Gallardo, R. Gupta, H. Kirk, N. Simos, N. Souchlas
Brookhaven National Lab, P.O. Box 5000, Upton, NY 11973-5000, USA
M. Ellis[1], P. Kyberd
Brunel University West London, Uxbridge, Middlesex UB8 3PH, UK
E. Benedetto, E. Fernandez-Martinez, I. Efthymiopoulos, R. Garoby, S. Gilardoni, M. Martini, G. Prior
European Organization for Nuclear Research, CERN CH-1211, Geneva 23, Switzerland
D. Indumathi, N. Sinha
The Institute of Mathematical Sciences, IV Cross Road, CIT Campus, Taramani, Chennai 600 113, Tamil Nadu, India
P. Ballett, S. Pascoli
Institute for Particle Physics Phenomenology, Department of Physics, University of Durham, Science Laboratories, South Rd, Durham, DH1 3LE, UK
A. Bross, S. Geer, C. Johnstone, J. Kopp, N. Mokhov, J. Morfin, D. Neuffer, S. Parke, M. Popovic, J. Strait, S. Striganov
Fermilab, P.O. Box 500, Batavia, IL 60510-5011, USA
A. Blondel, F. Dufour
University de Geneve, 24, Quai Ernest-Ansermet, 1211 Geneva 4, Suisse
A. Laing, F.J.P. Soler
School of Physics and Astronomy, Kelvin Building, University of Glasgow, Glasgow G12 8QQ, Scotland, UK
M. Lindner, T. Schwetz
Max Planck Institut für Kernphysik, PO Box 103980, 69029 Heidelberg, Germany
A. Alekou, M. Apollonio, M. Aslaninejad, C. Bontoiu, P. Dornan, R. Eccleston, A. Kurup, K. Long, J. Pasternak, J. Pozimski
Physics Department, Blackett Laboratory, Imperial College London, Exhibition Road, London, SW7 2AZ, UK
A. Bogacz, V. Morozov, Y. Roblin
Jefferson Laboratory, 12000 Jefferson Avenue, Newport News, VA 23606, USA
S. Bhattacharya, D. Majumdar
Saha Institute of Nuclear Physics, Sector-I, Block-AF, Bidhannagar, Kolkata 700064, India
Y. Mori, T. Planche
Kyoto University, Research Reactor Institute, 2,Asashiro-Nishi, Kumatori-cho, Sennan-gun, Osaka 590-0494 Japan
M. Zisman
Lawrence Berkeley National Laboratory, 1 Cyclotron Road, Berkeley, CA 94720, USA
D. Cline, D. Stratakis, X. Ding
Department of Physics and Astronomy, University of California, Los Angeles, CA 90095, USA

[1] Now at Westpac Institutional Bank, Sydney, NSW, Australia

P. Coloma, A. Donini[2], B. Gavela, J. Lopez Pavon, M. Maltoni
Universidad Autonoma de Madrid and Instituto de Fisica Teorica, UAM/CSIC, Cantoblanco, E-28049, Madrid, Spain;
C. Bromberg
Michigan State University, 150 Administration Building, East Lansing, Michigan 48824, USA
M. Bonesini
Sezione INFN Milano Bicocca, Dipartimento di Fisica G. Occhialini, Piazza Scienza 3, 20126 Milano, Italy
T. Hart
The University of Mississippi, Department of Physics and Astronomy, 108 Lewis Hall, PO Box 1848, Oxford, Mississippi 38677-1848, USA
Y. Kudenko
Institute for Nuclear Research of Russian, Academy of Sciences, 7a, 60th October Anniversary prospect, Moscow 117312, Russia
N. Mondal
Tata Institute of Fundamental Research, School of Natural Sciences, Homi Bhabha Rd., Mumbai 400005, India
S. Antusch, M. Blennow, T. Ota
Max Planck Institut für Physik, Werner Heisenberg Institut für Physik, Fohringer Ring 6, D-80805 Munich, Germany
R.J. Abrams, C.M. Ankenbrandt, K.B. Beard, M.A.C. Cummings, G. Flanagan, R.P. Johnson, T.J. Roberts, C.Y. Yoshikawa
Muons Inc., 552 N. Batavia Avenue, Batavia, IL 60510, USA
P. Migliozzi, V. Palladino
Universita di Napoli Federico II, Dipartimento di Scienze Fisiche, Complesso Universitario di Monte S. Angelo, via Cintia, I-80126 Napoli, Italy
A. de Gouvea
Northwestern University, Dept. of Physics and Astronomy, 2145 Sheridan Road, Evanston, Illinois 60208-3112 USA
V.B. Graves
Oak Ridge National Laboratory, P.O. Box 2008, Oak Ridge, TN 37831, USA
Y. Kuno
Osaka University, Graduate School, School of Science, 1-1 Machikaneyama-cho, Toyonaka, Osaka 560-0043, Japan
J. Peltoniemi
Puulinnankatu 12 F 50, FI-90570 Oulu, Finland
V. Blackmore, J. Cobb, H. Witte
Particle Physics Department, The Denys Wilkinson Building, Keble Road, Oxford, OX1 3RH, UK

[2] Also at Universidad de Valencia and Instituto de Fisica Corpuscular, UV/CSIC, Apart. 22085, E-46071, Valencia, Spain

M. Mezzetto, S. Rigolin
Dipartimento di Fisica, Universita di Padova and INFN Padova, Via Marzolo 8, I-35131, Padova, Italy
K.T. McDonald
Princeton University, Princeton, NJ, 08544, USA
L. Coney, G. Hanson, P. Snopok
Department of Physics and Astronomy, University of California, Riverside, CA 92521, USA
L. Tortora
Sezione INFN Roma Tre, Dipartimento di Fisica E. Amaldi, Via della Vasca Navale 84, 00146 Roma, Italy
C. Andreopoulos, J.R.J. Bennett, S. Brooks, O. Caretta, T. Davenne, C. Densham, R. Edgecock[3], D. Kelliher, P. Loveridge, A. McFarland, S. Machida, C. Prior, G. Rees, C. Rogers, J.W.G. Thomason
STFC Rutherford Appleton Laboratory, Chilton, Didcot, Oxfordshire, OX11 0QX, UK
C. Booth, G. Skoro
University of Sheffield, Dept. of Physics and Astronomy, Hicks Bldg., Sheffield S3 7RH, UK
Y. Karadzhov, R. Matev, R. Tsenov
Department of Atomic Physics, St. Kliment Ohridski University of Sofia, 5 James Bourchier Boulevard, BG-1164 Sofia, Bulgaria
R. Samulyak
Physics and Astronomy Department, Stony Brook University, Stony Brook, NY 11794-3800, USA
S.R. Mishra, R. Petti
Department of Physics and Astronomy, University of South Carolina, Columbia SC 29208, USA
M. Dracos
IPHC, Université de Strasbourg, CNRS/IN2P3, F-67037 Strasbourg, France
O. Yasuda
Department of Physics, Toyko Metropolitan University, 1-1 Minami-Osawa, Hachioji-shi, Toyko, Japan 192-0397
S.K. Agarwalla, A. Cervera-Villanueva, J.J. Gomez-Cadenas, P. Hernandez, T. Li, J. Martin-Albo
Instituto de Fisica Corpuscular (IFIC), Centro Mixto CSIC-UVEG, Edificio Investigacion Paterna, Apartado 22085, 46071 Valencia, Spain
P. Huber
Virginia Polytechnic Inst. and State Univ., Physics Dept., Blacksburg, VA 24061-0435
J. Back, G. Barker, P. Harrison
Department of Physics, University of Warwick, Coventry, CV4 7AL, UK
D. Meloni, J. Tang, W. Winter
Fakultät für Physik und Astronomie, Am Hubland, 97074 Würzburg, Germany

[3] also at University of Huddersfield, Queensgate, Huddersfield, HD1 3DH, UK

Foreword

The International Design Study for the Neutrino Factory (the IDS-NF) [1] was established by the community at the ninth "International Workshop on Neutrino Factories, super-beams, and beta-beams" which was held in Okayama in August 2007 [2]. The IDS-NF mandate is to deliver the Reference Design Report (RDR) for the facility on the timescale of 2012/13 [3]. The RDR is conceived as the document upon which requests for the resources to carry out the first phase of the Neutrino Factory project can be made. The RDR will include: the physics performance of the Neutrino Factory and the specification of each of the accelerator, diagnostic, and detector systems; an estimate of the cost of the facility; and an estimate of the schedule for its implementation. The RDR will also include a discussion of the remaining technical risks and an appropriate risk-mitigation plan.

The mandate for the study [3] requires an Interim Design Report to be delivered midway through the project as a step on the way to the RDR. This document, the IDR, has two functions: it marks the point in the IDS-NF at which the emphasis turns to the engineering studies required to deliver the RDR and it documents baseline concepts for the accelerator complex, the neutrino detectors, and the instrumentation systems. The IDS-NF is, in essence, a site-independent study. Example sites, CERN, FNAL, and RAL, have been identified to allow site-specific issues to be addressed in the cost analysis that will be presented in the RDR. The choice of example sites should not be interpreted as implying a preferred choice of site for the facility.

This document is organised as follows. The physics case for the Neutrino Factory is reviewed and the performance of the IDS-NF baseline for the facility are presented in section 1. The baseline concepts for the accelerator facility and the neutrino detectors are reviewed in sections 2 and 3 respectively. The steps that the IDS-NF collaboration plans to take to prepare the RDR are presented in section 4 together with a summary of the accelerator and detector R&D programmes that are required to complete the detailed specification of the facility and to mitigate technical risks that have been identified.

Contents

Executive summary

Introduction

The starting point for the International Design Study for the Neutrino Factory (the IDS-NF [1]) was the output of the earlier International Scoping Study for a future Neutrino Factory and super-beam facility (the ISS) [4–6]. The accelerator facility described in section 2 incorporates the improvements that have been derived from the substantial amount of work carried out within the Accelerator Working Group. Highlights of these improvements include:

- Initial concepts for the implementation of the proton driver at each of the three example sites, CERN, FNAL, and RAL;
- Detailed studies of the energy deposition in the target area;
- A reduction in the length of the muon beam phase-rotation and bunching systems;
- Detailed analyses of the impact of the risk that stray magnetic field in the accelerating cavities in the ionisation cooling channel will reduce the maximum operating gradient. Several alternative ionisation-cooling lattices have been developed as fallback options to mitigate this technical risk;
- Studies of particle loss in the muon front-end and the development of strategies to mitigate the deleterious effects of such losses;
- The development of more complete designs for the muon linac and re-circulating linacs;
- The development of a design for the muon FFAG that incorporates insertions for injection and extraction; and
- Detailed studies of diagnostics in the decay ring.

Other sub-systems have undergone a more "incremental" evolution; an indication that the design of the Neutrino Factory has achieved a degree of maturity. The design of the neutrino detectors described in section 3 has been optimised and the Detector Working Group has made substantial improvements to the simulation and analysis of the Magnetised Iron Neutrino Detector (MIND) resulting in an improvement in the overall neutrino-detection efficiency and a reduction in the neutrino-energy threshold. In addition, initial consideration of the engineering of the MIND has generated a design that is feasible and a finite element analysis of the toroidal magnetic field to produce a realistic field map has been carried out. Section 3 also contains, for the first time, a specification for the near-detector systems and a demonstration that the neutrino flux can be determined with a precision of 1% through measurements of inverse muon decay at the near detector.

The performance of the facility, the work of the Physics and Performance Evaluation Group, is described in section 1. The effect of the improved MIND performance is to deliver a discovery reach for CP-invariance violation in the lepton sector, the determination of the mass hierarchy, and of θ_{13} that extends down to values of $\sin^2 2\theta_{13} \sim 5 \times 10^{-5}$ and is robust against systematic uncertainties. In addition, the improved neutrino-energy threshold has allowed an indicative analysis of the kind of re-optimisation of the facility that could be carried out should θ_{13} be found close to the current upper bound. The results presented in section 1 demonstrate that the discovery reach as well as the precision with which the oscillation parameters can be measured at the baseline Neutrino Factory is superior to that of other proposed facilities for all possible values of $\sin^2 2\theta_{13}$.

Motivation

The phenomenon of neutrino oscillations, arguably the most significant advance in particle physics over the past decade, has been established through measurements on neutrinos and anti-neutrinos produced in the sun, by cosmic-ray interactions in the atmosphere, nuclear reactors, and beams produced by high-energy particle accelerators [7]. In consequence, we know that the Standard Model is incomplete and must be extended to include neutrino mass, mixing among the three neutrino flavours, and therefore lepton-flavour non conservation. These observations have profound implications for the ultimate theory of particle interactions and for the description of the structure and evolution of the Universe. In particular:

- Mixing among the three massive neutrinos admits the possibility that the matter-antimatter (CP) symmetry is violated via the neutrino-mixing matrix. Such an additional source of CP-invariance violation may hold the key to explaining how the antimatter created in the Big Bang was removed from the early Universe;
- If a neutrino is to be distinguished from its antineutrino counterpart it is necessary to assign a conserved lepton number to the neutrino. At present there is no theoretical justification for such a conserved quantum number. If lepton number is not conserved, then a neutrino is indistinguishable from an antineutrino, i.e. the neutrino is a Majorana particle; a completely new state of matter. If this is so, then it is conceivable that the "see-saw" mechanism may give an explanation of why the neutrino mass is tiny compared to the other matter fermions and may help to explain why the neutrino mixing angles are so large compared to those of the quarks; and
- The neutrino abundance in the Universe is second only to that of the photon and so, even with a tiny mass, the neutrino may make a significant contribution to the dark matter which is known to exist. Therefore, the neutrino may play an important role in determining the structure of the Universe.

These exciting possibilities justify an energetic and far reaching programme.

An essential part of such a programme is to make precision measurements of the oscillation parameters. Assuming the three flavours and the unitary neutrino-mixing matrix that is presently favoured, oscillation measurements can be used to determine the three mixing angles and the phase parameter that can provide a new source of CP-invariance violation. Neutrino-oscillation measurements can also be used to determine the two (signed) mass differences. This programme is similar to the long-standing investigations of quark mixing via the CKM matrix and it would now seem to be clear that an understanding of the flavour problem will definitely necessitate precision measurements in both quark and lepton sectors.

Not all the properties of the neutrino can be determined by oscillation experiments. Equally important is the determination of the Majorana or Dirac nature of the neutrino which requires a totally different experiment. Currently, the search for neutrinoless double beta decay is the most promising. In addition, although oscillation measurements determine the mass differences, they are insensitive to the absolute mass, m_1, of the lightest mass state. The determination of m_1 requires a very precise measurement of the end-point of the electron spectrum in beta decay. The mass would also follow from the observation of neutrinoless double beta decay.

The Neutrino Factory, described in this report, is capable of generating the intense, high-energy neutrino and anti-neutrino beams which are required to make the exquisitely sensitive oscillation measurements:

- The deviation of θ_{23} from $\pi/4$;
- The deviation of θ_{13} from 0;

and, for $\sin^2 2\theta_{13} \gtrsim 5 \times 10^{-5}$:

- The degree to which CP-invariance is violated in the (Dirac) lepton sector; and
- The neutrino mass hierarchy.

The intense beams will be equally valuable should there be either an extended neutrino sector that includes, for example, a fourth generation or sterile-neutrino state or new non-standard interactions. The large data sets that will be collected will have a unique potential to throw light on the physics of flavour and hence the ultimate theory of particle physics.

Neutrino oscillations and the Neutrino Factory

Neutrino oscillations are described by a unitary "mixing matrix" that rotates the mass basis into the flavour basis. The mixing matrix is parametrised by three mixing angles (θ_{12}, θ_{23}, and θ_{13}) and one phase parameter (δ) [8–11]. If δ is non-zero (and not equal to π), then CP-invariance violation in the neutrino sector will occur so long as $\theta_{13} > 0$. Measurements of neutrino oscillations in vacuum can be used to determine the moduli of the mass-squared differences $\Delta m^2_{31} = m^2_3 - m^2_1$ and $\Delta m^2_{21} = m^2_2 - m^2_1$ (where the m_i are the masses of the neutrino mass eigenstates) and, with the aid of interactions with matter, also the sign. The bulk of the measurements of neutrino oscillations to date have been collected using the dominant, "disappearance", channels $\nu_e \to \nu_e$ and $\nu_\mu \to \nu_\mu$. These data have yielded values for two of the three mixing angles (θ_{12} and θ_{23}), the magnitude of the mass-squared differences Δm^2_{31} and Δm^2_{21}, and that $m_2 > m_1$ (i.e. that $\Delta m^2_{21} > 0$). The challenge to the neutrino community, therefore, is to determine the sign of Δm^2_{31} (the "mass hierarchy"), to measure θ_{13} and δ, and to improve the accuracy with which θ_{23} is known.

Over the next few years, the T2K, NOνA, Double Chooz, Daya Bay, and RENO experiments will exploit the sub-leading, $\nu_\mu \to \nu_e$ and $\bar{\nu}_e \to \bar{\nu}_x$ channels to improve significantly the precision with which θ_{13} is known. The NOνA long-baseline experiment may also be able to determine the mass hierarchy if θ_{13} is close to the present upper limit. However, it is very unlikely that either T2K or NOνA will be able to discover CP-invariance violation, i.e. that $\delta \neq 0, \pi$.

The most effective channel for a precision measurement of θ_{13} and the search for CP-invariance violation is the sub-leading $\nu_e \to \nu_\mu$ oscillation. The determination of the mass hierarchy relies on the measurement of the oscillation frequency of neutrinos passing through the earth, hence the sensitivity increases as the distance the neutrino beam propagates through the earth increases. The best sensitivity to CP-invariance violation is also found at large source-detector distances as long as the neutrinos have a sufficiently large energy, E_ν. Therefore, optimum sensitivity to the parameters of the Standard Neutrino Model (SνM) can be achieved at a facility that provides intense, high-energy ν_e and $\bar{\nu}_e$ beams.

In the Neutrino Factory, beams of ν_e and $\bar{\nu}_\mu$ ($\bar{\nu}_e$, ν_μ) are produced from the decays of μ^+ (μ^-) circulating in a storage ring. As the muon charge-to-mass ratio is large the neutrinos carry away a substantial fraction of the energy of the parent muon, hence, high neutrino energies can readily be

achieved. Time-dilation is also beneficial, allowing sufficient time to produce a pure, collimated beam. Charged-current interactions induced by "golden channel", $\nu_e \to \nu_\mu$, oscillations produce muons of charge opposite to those produced by the $\bar{\nu}_\mu$ in the beam and thus a magnetised detector is required. The additional capability to investigate the "silver" ($\nu_e \to \nu_\tau$) and "platinum" ($\overline{\nu}_\mu \to \bar{\nu}_e$) channels makes the Neutrino Factory the ideal place to look for oscillation phenomena that are outside the standard, three-neutrino-mixing paradigm. It is thus the ideal facility to serve the precision era of neutrino oscillation measurements. The performance of the Neutrino Factory is described in detail in section 1.

The IDS-NF baseline

The optimisation of the Neutrino Factory baseline to maximise the performance of the facility for the discovery of CP-invariance violation, the mass hierarchy, and the determination of θ_{13} is described in section 1. The optimum requires two distant detectors. One at the "magic baseline", 7 000–8 000 km from the source, will have excellent sensitivity to the mass hierarchy and $\sin^2 2\theta_{13}$. The second source-detector distance in the range 2 500–5 000 km will give the best sensitivity to CP-invariance violation but requires a stored-muon energy in excess of 20 GeV. The sensitivity to non-standard interactions at the Neutrino Factory improves as the stored-muon energy is increased, reaching a plateau at around ~ 25 GeV [12]. A baseline stored muon energy of 25 GeV has therefore been adopted.

The baseline accelerator facility described in section 2 provides a total of 10^{21} muon decays per year split between the two distant neutrino detectors. The process of creating the muon beam begins with the bombardment of a pion-production target with a 4 MW, pulsed proton beam. The target must be sufficiently heavy to produce pions copiously, yet not so large as to cause a significant rate of interaction of the secondary pions within the target material. In addition, the target must withstand the substantial beam-induced shock. The IDS-NF baseline calls for a free-flowing, liquid-mercury-jet target operating in a solenoid-focusing, pion-capture channel. This is followed by a solenoidal transport channel in which the pions decay to muons. The emerging muon beam is then bunched and rotated in phase space to produce a beam with small energy spread. At this point, the muon beam occupies a large volume of phase space which must be reduced, "cooled", before it can be injected into the acceleration sections. As a consequence of the short muon lifetime, traditional cooling techniques are inappropriate, so the required phase-space reduction is achieved by means of ionisation cooling. This involves passing the muon beam through a material in which it loses energy through ionisation and then re-accelerating the beam in the longitudinal direction to replace the lost energy. The IDS-NF baseline calls for lithium-hydride absorbers embedded in a solenoidal transport channel with re-acceleration achieved using 201 MHz cavities at a gradient of 16 MV/m. Subsequent muon acceleration must be rapid, especially at low muon energy. For the baseline, muons are accelerated to 0.9 GeV in a superconducting linac and then to 12.6 GeV in a sequence of two re-circulating linear accelerators (RLAs). The final stage of acceleration, from 12.6 GeV to the stored-muon energy of 25 GeV, is provided by a fixed-field alternating-gradient (FFAG) accelerator.

The baseline neutrino detector described in 3 is a revision of the Magnetised Iron Neutrino Detector (MIND) developed within the ISS [6]. MIND is a MINOS-like iron-scintillator sandwich calorimeter with a sampling fraction optimised for the Neutrino Factory beam [13]. The baseline calls for a fiducial mass of 100 kTon to be placed at the intermediate baseline and a 50 kTon detector at the magic baseline.

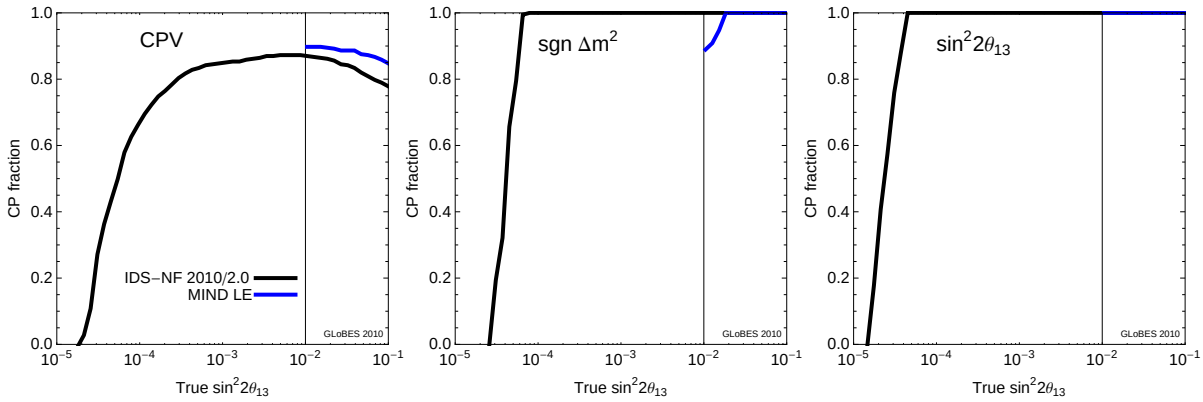

Figure 1. The discovery potential at 3σ for CP violation (left panel), the mass hierarchy (central panel), and $\sin^2 2\theta_{13}$ (right panel). The discovery reach is plotted in terms of the CP fraction as a function of $\sin^2 2\theta_{13}$. The performance of the IDS-NF baseline Neutrino Factory is shown as the black solid line. The Neutrino Factory re-optimised for large $\sin^2 2\theta_{13}$ is shown as the blue solid line.

The performance of the IDS-NF baseline Neutrino Factory in terms of the 3σ discovery reach for CP violation, the mass hierarchy, and θ_{13} is shown in figure 1. The discovery reach is presented in terms of the fraction of all possible values of δ (the "CP fraction") and plotted as a function of $\sin^2 2\theta_{13}$. As described in detail in section 1, the discovery reach of the Neutrino Factory is significantly better than the realistic alternative facilities, particularly for small values of θ_{13}. Should θ_{13} be discovered to be large, i.e. close to the present upper bound, a re-optimisation of the baseline Neutrino Factory will still yield superior performance.

The Neutrino Factory as part of the muon-physics programme

The properties of the muon make it a unique tool for particle physics. In addition to the decays that provide intense, high-energy ν_e and $\bar{\nu}_e$ beams, the great precision with which properties such as $g-2$ can be calculated using the Standard Model makes it an ideal tool in the search for new phenomena. Furthermore, the observation of charged lepton flavour violation (cLFV) in muon decay, predicted in many models, would revolutionise current theories, whilst the muon's comparatively large mass and point-like nature make it an appealing candidate to provide multi-TeV lepton-antilepton collisions at a Muon Collider.

Neutrino oscillations involve processes in which lepton flavour is not conserved. Therefore, processes such as $\mu \to e\gamma$, $\mu \to eee$, and muon to electron conversion in the field of the nucleus ($\mu N \to eN$) will occur. Rates for such cLFV processes can be calculated in the Standard Model extended to take into account neutrino oscillations but they are minuscule (of the order of 10^{-54}) and so the observation of such processes would be a clear signal of new physics. To achieve the requisite sensitivities, intense muon beams are required and the techniques proposed for the Neutrino Factory, such as high power, pulsed proton beams with short ($\lesssim 10\,\text{ns}$) bunches, pion capture in solenoidal fields, the manipulation of muon beams of large emittance, and FFAG acceleration are of great relevance.

A Muon Collider [14] offers crucial advantages over an e^+e^- collider of the same centre-of-mass energy and luminosity because the muon mass is roughly 200 times that of the electron. The large muon mass leads to a relatively low rate of synchrotron radiation, making it possible to design a circular machine in which 100% of multi-TeV $\mu^+\mu^-$ collisions occur within $\sim 0.1\%$ of the nominal centre-of-mass energy of the collider. In addition, should the Higgs boson be discovered and have the expected coupling proportional to mass, the Muon Collider could be used as a "Higgs Factory" at which detailed studies of its properties may be carried out.

A conceptual design for the Muon Collider has been proposed [15] in which the systems that make up the Neutrino Factory form the "front-end" of the Muon Collider. Indeed, should the techniques required to realise the Neutrino Factory be demonstrated, the principal accelerator-system challenge that would remain for the Muon Collider would be the development of an ionisation-cooling system that could reduce all six phase-space dimensions of the muon beams such that a luminosity in excess of $10^{34}\,\mathrm{cm}^{-2}$ could be achieved. Therefore, the implementation of the Neutrino Factory is desirable to mitigate the technical risks presented by the Muon Collider.

The Neutrino Factory is the facility of choice for the study of neutrino oscillations: it has excellent discovery reach and offers the best precision on the mixing parameters, particularly in the difficult region of small θ_{13}. The ability to vary the stored-muon energy and perhaps the detector technology can provide the flexibility to respond to developments in our understanding and the discovery of new phenomena. The R&D programme required to make the Neutrino Factory a reality will directly benefit the development of the Muon Collider and experiments that seek to discover cLFV. A comprehensive muon-physics programme is compelling indeed.

1. Physics at the Neutrino Factory

1.1. The physics case for advanced neutrino experiments

The unambiguous observation of neutrino oscillations is arguably the most significant development in particle physics of the past two decades [16]. It revealed, beyond reasonable doubt, that neutrinos have mass and that leptons mix. Neutrino masses are not accounted for in the Standard Model of particle physics. It is not hard to modify the Standard Model Lagrangian to accommodate neutrino masses [17]. Indeed, one can write down several different "Standard Neutrino Model" (SνM) Lagrangians that render neutrinos massive that are consistent with the available data. The candidates for the SνM introduce various new degrees of freedom at a variety of energy scales (from below the electron-Volt scale all the way to the Grand Unification scale). Part of the mission of particle-physics experiments in the next few decades will be to elucidate the mechanism by which neutrino mass is generated. The next generation of neutrino experiments will represent a moderate extension of existing techniques. This makes them technologically attractive, since the technical risks are relatively low, but also limits their physics sensitivity. To exploit to the full the discoveries made to date in neutrino physics, advanced neutrino experiments, based on novel technologies, are required. The Neutrino Factory is the ultimate advanced neutrino oscillation facility. In this section, the scientific case for advanced neutrino oscillation experiments in general and of the Neutrino Factory in particular is reviewed.

While the mechanism behind neutrino-mass generation remains unknown, a very successful phenomenological description exists. It considers the existence of three massive neutrinos ν_1, ν_2, and ν_3 with masses m_1, m_2, and m_3, respectively. These mass eigenstates are linear combinations of the "active" neutrino flavours, ν_e, ν_μ, and ν_τ, labelled according to the way they interact with the W-boson and the charged-leptons, e, μ, and τ. One can pick a weak-basis in which neutrinos with a well-defined flavour are related to neutrinos with a well-defined mass via the unitary lepton mixing matrix U: $\nu_\alpha = U_{\alpha i}\nu_i$ ($\alpha = e, \mu, \tau,\ i = 1, 2, 3$). It is customary to define the neutrino masses as follows: $m_1 < m_2$ while m_3 is either the heaviest or the lightest neutrino. To identify m_3, $|m_3^2 - m_1^2|$ and $|m_3^2 - m_2^2|$ are evaluated and the smaller combination is chosen such that it is larger than $m_2^2 - m_1^2$. With the masses labelled in this way, $m_3 > m_2$ if $m_3^2 - m_1^2$ is positive and $m_3 < m_1$ if $m_3^2 - m_1^2$ is negative. Note that $\Delta m^2_{21} = m_2^2 - m_1^2$ is a positive-definite quantity, while $\Delta m^2_{31} = m_3^2 - m_1^2$ is allowed to have either sign. It is also customary to refer to the spectrum $m_3 > m_2 > m_1$ as "normal", in which case $\Delta m^2_{31} > 0$, while the $m_2 > m_1 > m_3$ spectrum is referred to as "inverted," in which case $\Delta m^2_{31} < 0$. Once the neutrino mass eigenstates are properly defined, it is also customary to parametrise U as prescribed in the Particle Data Book [18]. The neutrino mixing angles (θ_{ij}) are related to the mixing-matrix elements by:

$$\frac{|U_{e2}|^2}{|U_{e1}|^2} \equiv \tan^2\theta_{12}; \qquad \frac{|U_{\mu 3}|^2}{|U_{\tau 3}|^2} \equiv \tan^2\theta_{23}; \text{ and} \qquad U_{e3} \equiv \sin\theta_{13} e^{-i\delta}; \tag{1}$$

where δ is the CP-odd, "Dirac", phase. Two other CP-odd phases might be required to complete the parametrisation of U if the neutrinos are Majorana fermions. However, these "Majorana" phases can not be observed in neutrino oscillations and will henceforth be ignored. Neutrino-oscillation data are sensitive to the neutrino mass-squared differences, the values of the mixing angles θ_{12}, θ_{13}, θ_{23}, and δ. Two of the three mixing angles are large, in stark contrast to the quark-mixing matrix, in which

all mixing parameters are either small ($\sin\theta_c \sim 0.23$, where θ_c is the Cabibbo angle) or very small ($|V_{ub}| \sim 0.004$). In the neutrino sector, three parameters remain unknown or only poorly constrained: the sign of Δm^2_{31}; δ; and the mixing angle θ_{13}. The remaining parameters are known at the $\sim$ 5–10% level [19, 20].

If θ_{13} is "large", the current generation of experiments (which includes Double Chooz [21], RENO [22], Daya Bay [23], T2K [24] and Noνa [25]) may determine that θ_{13} is not zero and Noνa may provide a non-trivial hint regarding the sign of Δm^2_{31}. It is also expected that the precision with which $|\Delta m^2_{31}|$ and $\sin^2 2\theta_{23}$ are known will improve significantly. Even under these conditions, it is widely anticipated that by the end of the current decade we shall not know the sign of Δm^2_{31} and will have no information regarding whether CP-invariance is violated in neutrino interactions ($\delta \neq 0, \pi$). On the other hand, if θ_{13} is "small", not withstanding a measurement of $|\Delta m^2_{31}|$ with significantly improved precision, a more precise measurement of $\sin^2 2\theta_{23}$, and a more stringent bound on θ_{13}, our understanding of the neutrino-oscillation parameters might not be too different from what it is today.

To complete our knowledge of the parameters that describe neutrino oscillations, the goals of advanced experiments must be:

- To search for CP-invariance violation in neutrino oscillations by seeking to measure the CP-odd phase δ;
- To establish whether the neutrino-mass spectrum is normal or inverted by determining the sign of Δm^2_{31};
- To determine θ_{13} with good precision (or constrain it to be very small indeed); and
- To measure as precisely as possible all the oscillation parameters.

The search for CP-invariance violation in neutrino oscillations provides a unique opportunity to further our understanding of CP-invariance. Experiments have demonstrated that the CP-odd phase of the quark mixing matrix, $\delta_{\rm CKM}$, controls all CP-invariance violation in the quark sector. The past generation of neutrino-oscillation experiments has revealed that there is at least one more CP-violating parameter in the lepton mixing matrix, δ. In practise, δ can only be observed in neutrino oscillation experiments and an advanced neutrino experiment is required to explore this new window into CP-invariance violation.

To determine how precisely the oscillation parameters must be measured, it is important to assess the precision at which our understanding would change qualitatively. Attempts to understand the underlying physics behind the pattern of lepton mixing provide some guidance [17, 26, 27]). Such attempts often make predictions regarding the specific values for the different parameters or, perhaps more generically, make predictions regarding relations among different oscillation parameters. One guiding principle for precision measurements of neutrino oscillations should be the ability to provide unambiguous tests of these relations. An example is given by the tri-bimaximal mixing pattern ($\sin^2\theta_{23} = 1/2$, $\sin^2\theta_{12} = 1/3$, and $\sin^2\theta_{13} = 0$) [28]; a popular, zeroth-order ansatz that guides theoretical research in neutrino flavour. Different models make different predictions regarding deviations from this ansatz, which are usually small and proportional to some other small parameters in flavour physics. Neutrino physics offers one known small (but non-zero) parameter: the ratio of the two mass-squared differences, $\Delta m^2_{12}/|\Delta m^2_{31}| \equiv \epsilon \sim 0.03$ [29]. Current data constrain $\sin^2\theta_{13} \lesssim \epsilon$, $\sin^2\theta_{12} - 1/3 \lesssim \epsilon$, while $\sin^2\theta_{23} - 1/2 \lesssim \sqrt{\epsilon}$. An important next-to-next-generation goal would be to test whether $\sin^2\theta_{13} \lesssim \epsilon^2$, $\sin^2\theta_{12} - 1/3 \lesssim \epsilon^2$, and $\sin^2\theta_{23} - 1/2 \lesssim \epsilon$ (or better).

High-precision measurements of neutrino oscillations are required to test whether the origin of

neutrino mass is also the origin of the baryon asymmetry of the Universe, through leptogenesis [30, 31]. Several indirect generic predictions of leptogenesis can be verified with neutrino experiments: neutrinos are expected to be Majorana fermions, and it is expected, quite generically, that neutrino oscillations violate CP-invariance, even if no model independent relation between "high-energy" and "low-energy" CP-invariance violation exists. Quantitative tests are all model dependent and will rely on very precise measurements in neutrino oscillations and elsewhere. For example, precise measurements of oscillation parameters could validate a specific flavour model, which allows one to relate "high-energy" and "low-energy" parameters. Furthermore, discoveries at collider experiments and searches for charged-lepton flavour violation may provide other hints that render leptogenesis either "very likely" or "most improbable" [32]. We are very far from testing leptogenesis conclusively, but precise measurements of all neutrino oscillation parameters – far beyond where we are now – are a *conditio sine qua non*.

Precision measurements of the oscillation parameters are also required to confirm or refute with confidence the current three-active-neutrino formalism. Ultimately, one aims not only at constraining the mixing-parameter space, but also at *over-constraining* it. Several important questions need to be addressed:

- Are there really only three light neutrinos and is U a unitary matrix?
- Are there other neutrino interactions? And,
- Is there only one source of CP-invariance violation in the neutrino sector?

While our understanding of the neutrino has increased tremendously over the past decade, we are far from providing a satisfactory answer to any of these questions. In this respect, our understanding of the lepton-flavour sector is far behind our understanding of the quark-flavour sector.

Some manifestations of new physics are best investigated with neutrino oscillation experiments. For example, the search for light sterile neutrinos which may be related to the origin of neutrino masses. Sterile neutrinos can be detected via the observation of new oscillation frequencies and mixing angles. Tests of the unitarity of the lepton-mixing matrix may also point to new "neutrino" degrees of freedom that are too heavy to be seen in oscillation experiments. Neither of these phenomena can be studied outside of neutrino oscillation experiments. Other new-physics ideas to which measurements of neutrino oscillation are uniquely sensitive are related to physics at the electroweak scale, including new four-fermion neutrino interactions (of the current–current type, $\propto (\bar{\nu}_\alpha \Gamma \nu_\beta)(\bar{f}\Gamma' f)$, where f is a charged fermion). Some of these possibilities will be discussed in more detail later in this section. Indeed, non-standard neutrino interactions are often used as proxies for the discussion of the sensitivity of neutrino-oscillation experiments to new physics.

In many candidate new-physics scenarios, a combination of different experimental probes will be required in order to piece together a more fundamental description of how nature works at the smallest distance scales. In addition to studies of neutrino flavour-change, these include collider experiments (for example, the LHC and a next-generation lepton collider), searches for charged-lepton flavour violation in the muon and tau sectors, searches for the permanent electric dipole moments of fundamental particles, including the electron and the muon, searches for lepton-number violation, especially searches for neutrinoless double-beta decay, and direct and indirect searches for dark matter. In many new-physics scenarios, in particular when it comes to identifying the physics responsible for neutrino masses, advanced neutrino oscillation experiments are guaranteed to play a leading role.

Neutrino experiments have proved, over the past few decades, that our ability to predict what will be detected, and to identify what are the important questions, is limited at best. It is safe to

state, however, that a Neutrino Factory, combined with a multi-kTon detector at an underground facility, offers a unique and powerful tool for the study of fundamental physics. In order to prepare for the unexpected, it is vital that advanced set-ups be versatile and multifaceted. The Neutrino Factory fits the bill. In addition to providing the neutrino beams required for the definitive, precision neutrino-oscillation programme, the Neutrino Factory also provides an ideal environment in which to study a variety of other phenomena. The well-characterised neutrino beam from the muon storage ring allows a programme of extremely precise neutrino scattering measurements to be carried out at a near detector, including studies of neutrino flavour-change at very short baselines and precision measurements of neutrino scattering on nucleons [33] and electrons [34]. The latter allow for uniquely sensitive tests of the electroweak theory.

Activities not directly related to neutrino physics can also be addressed at a Neutrino Factory complex. The availability of a large number of muons allows one to consider new set-ups for searching for rare muon processes [35], especially $\mu \to e$ conversion in nuclei, and for measurements of the electroweak properties of the muon, including the muon electric and magnetic dipole moments. The availability of a large number of protons—used to make the muons for the storage ring—allows one to consider a suite of hadronic experiments including, for example, those required to study very rare kaon phenomena ($K \to \pi\bar{\nu}\nu$, $K \to \pi\mu^{\pm}e^{\mp}$, $K^+ \to \pi^-\ell^+\ell'^+$, etc). At the opposite end of the neutrino beam, the very large detector complex also serves many purposes. Depending on the location and composition, very large detectors can be used to study naturally occurring neutrinos—especially the atmospheric neutrinos and, perhaps, neutrinos from Supernova explosions. Finally, the large instrumented volumes can be used for searching for proton decay. Indeed, the Kamiokande and IMB experiments were originally constructed to look for proton decay, stumbled upon atmospheric neutrino oscillations, and observed neutrinos produced in super-novæalong the way.

1.2. Neutrino oscillation update

A reasonable understanding of the parameters describing three–flavour neutrino oscillations has been developed from the results of a variety of experiments involving solar and atmospheric neutrinos, as well as man-made neutrinos from nuclear power plants and accelerators. Table I summarises the results of two recent global fits to world neutrino data from [19] and [36], both updated as of November 2010. Details of another recent analysis can be found in [37, 38].

Spectral information from the KamLAND reactor experiment [39, 40] leads to an accurate determination of Δm^2_{21} with the remarkable precision of 7% at 3σ. The sign of Δm^2_{21} being determined using solar neutrino data from SNO (see for example [41]). KamLAND data also start to contribute to the lower bound on $\sin^2\theta_{12}$, whereas the upper bound is dominated by solar data. From the Sudbury Neutrino Observatory (SNO) we use the data of its final phase, where the neutrons produced in the neutrino neutral current (NC) interaction with deuterium are detected mainly by an array of ^{3}He NC detectors (NCD) [42], as well as the recent joint re-analysis of data from Phase I and Phase II (the pure D_2O and salt phases) [43]. In this analysis, an effective electron kinetic energy threshold of 3.5 MeV has been used (Low Energy Threshold Analysis, LETA), and the determination of the total neutrino flux has been improved by about a factor two. These improvements have been possible thanks mainly to the increased statistics, in particular the NC event sample in the LETA is increased by about 70% as a result of the decrease of the thresholds of 5 MeV and 5.5 MeV used in the Phase I

Table I. Determination of three–neutrino oscillation parameters from 2010 global data [19, 36]. For Δm^2_{31} and $\sin^2\theta_{13}$ the upper (lower) row corresponds to inverted (normal) neutrino mass hierarchy.

	Ref. [19] (updated)		Ref. [36] (updated)	
parameter	best fit$\pm 1\sigma$	3σ interval	best fit$\pm 1\sigma$	3σ interval
Δm^2_{21} [10^{-5} eV^2]	7.60 ± 0.20	6.98–8.18	$7.59^{+0.20}_{-0.17}$	7.09–8.19
Δm^2_{31} [10^{-3} eV^2]	-2.35 ± 0.09	$-(2.07$–$2.65)$	$-(2.34^{+0.10}_{-0.09})$	$-(2.08 - 2.64)$
	$+2.44 \pm 0.09$	$+(2.17$–$2.74)$	$+2.45 \pm 0.09$	$+(2.18 - 2.73)$
$\sin^2\theta_{12}$	$0.317^{+0.017}_{-0.016}$	0.27–0.37	$0.318^{+0.019}_{-0.016}$	0.27–0.38
$\sin^2\theta_{23}$	$0.45^{+0.09}_{-0.05}$	0.34–0.65	0.51 ± 0.06	0.39–0.64
$\sin^2\theta_{13}$	$0.009^{+0.015}_{-0.008}$	≤ 0.048	0.017 ± 0.010	≤ 0.048
			$0.012^{+0.010}_{-0.007}$	≤ 0.042

in Phase II analyses respectively. Furthermore, energy resolution, background suppression, and systematic uncertainties have been improved. Data from SNO are combined with the global data on solar neutrinos [44–46] including updates on Gallium experiments [47, 48] as well as results from Borexino [49] on ^{7}Be neutrinos yielding an improved determination of the atmospheric parameters.

The MINOS experiment [50] is searching for ν_μ disappearance with a baseline of 735 km. The latest data were presented at the Neutrino 2010 Conference [51] for the neutrino (7.2×10^{20} p.o.t.) and the anti-neutrino (1.71×10^{20} p.o.t.) running modes. The data confirm the energy-dependent disappearance of ν_μ, showing significantly fewer events than expected in the case of no oscillations in the energy range $\lesssim 6$ GeV, whereas above $\sim 6\,\mathrm{GeV}$ the spectrum is consistent with the no-oscillation expectation.

Figure 2 shows a re-analysis of MINOS neutrino and anti-neutrino data. One can see that there is a slight tension between the neutrino and anti-neutrino results: there is no overlap of the allowed regions at less than 90% CL. However, at 3σ the results are fully consistent. We find the following χ^2 minima and goodness-of-fit (GOF) values:

$$\begin{aligned} \nu: &\quad \chi^2_{\mathrm{min},\nu} = 24.4/(27-2) \quad \mathrm{GOF} = 49.6\%; \\ \bar{\nu}: &\quad \chi^2_{\mathrm{min},\bar{\nu}} = 15.0/(13-2) \quad \mathrm{GOF} = 18.4\%; \\ \nu+\bar{\nu}: &\quad \chi^2_{\mathrm{min,tot}} = 46.1/(40-2) \quad \mathrm{GOF} = 17.3\%. \end{aligned} \tag{2}$$

Hence the combined neutrino and anti-neutrino fit still provides a very good GOF. Using the consistency test from reference [52] yields $\chi^2_{\mathrm{PG}} = \chi^2_{\mathrm{min,tot}} - \chi^2_{\mathrm{min},\nu} - \chi^2_{\mathrm{min},\bar{\nu}} = 6.6$. The value of χ^2_{PG} has to be evaluated for 2 degrees of freedom, which implies that neutrino and anti-neutrino data are consistent with a probability of 3.7%. This number indicates a slight tension between the sets, at the level of about 2.1σ. In the global analysis [36] only neutrino data are used from MINOS, whereas in the analysis in [19] both neutrino and anti-neutrino data are included. It is clear from figure 2 that the improvement in the quality of the fit when the anti-neutrino data are added is negligible.

We combine the long-baseline accelerator data from MINOS as well as from K2K [53] with atmospheric neutrino measurements from Super-Kamiokande I+II+III [54]. The determination of $|\Delta m^2_{31}|$ is dominated by spectral data from the MINOS experiment, where the sign of Δm^2_{31} (*i.e.*, the neutrino mass hierarchy) is undetermined by present data. The measurement of the mixing angle θ_{23} is still largely dominated by atmospheric neutrino data from Super-Kamiokande with a best-fit point close

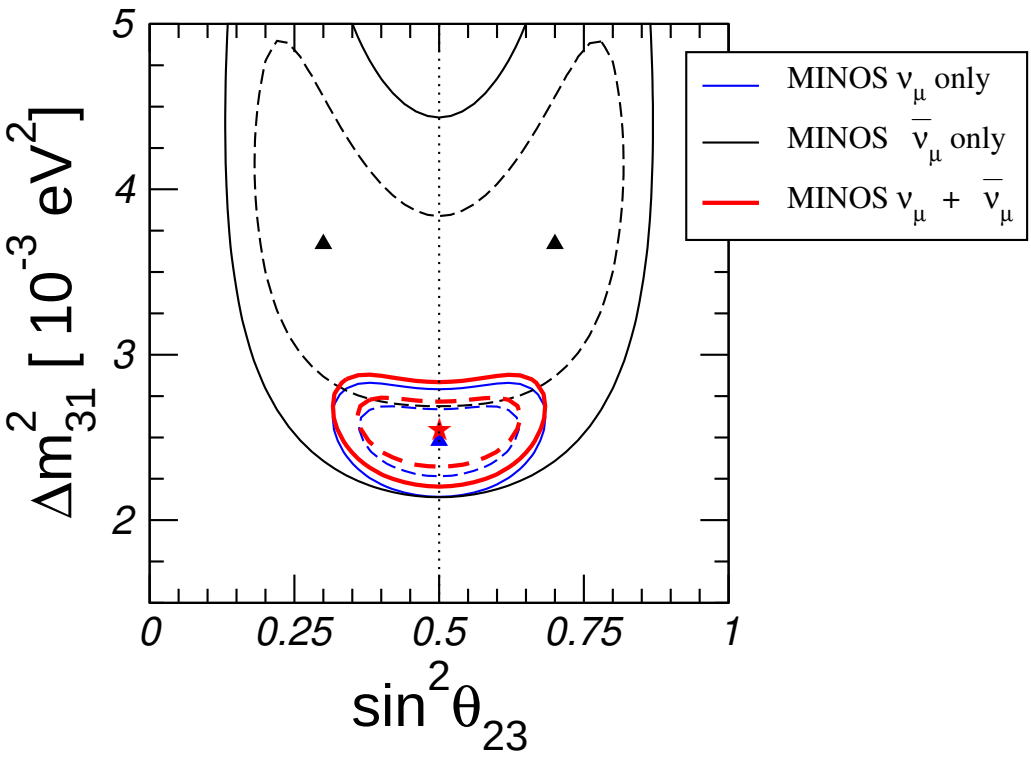

Figure 2. Allowed regions from recent MINOS data, using neutrinos-only, anti-neutrinos-only, and in combination.

to maximal mixing. Small deviations from maximal mixing due to sub-leading, three-flavour effects (not included in the analysis of [36]) have been found in references [16, 19, 55], see table I. A comparison of these subtle effects can be found in reference [56]. While an excess of sub-GeV e-like data provides an explanation for the deviations from maximality obtained in [19, 55], these results are not statistically significant, and are not confirmed by a recent analysis including Δm^2_{21} effects from the Super-Kamiokande collaboration [54].

The third mixing angle θ_{13} is of crucial importance for future oscillation experiments. Figure 3 summarises the information on θ_{13} from present data, which emerges from an interplay of different data sets. An important contribution to the bound comes from the CHOOZ reactor experiment [57] combined with the determination of $|\Delta m^2_{31}|$ from atmospheric and long-baseline experiments. Using this set of data, a possible hint for a non-zero θ_{13} from atmospheric data has been found in references [55, 58]. The origin of such a hint has been investigated in some detail in reference [59], and more recently in [19, 38]. From these results one may conclude that the statistical relevance of the hint for non-zero θ_{13} from atmospheric data depends strongly on the details of the rate calculations and of the χ^2 analysis. Furthermore, the origin of this effect might be traced back to a small excess (at the 1σ level) in the multi-GeV electron-like (e-like) data sample in SK-I, which however is no longer present in the combined SK-I + SK-II data and is extremely weak in the combined SK-I + SK-II + SK-III data set.

A recent analysis (neglecting sub-leading Δm^2_{21} effects) from the Super-Kamiokande collaboration

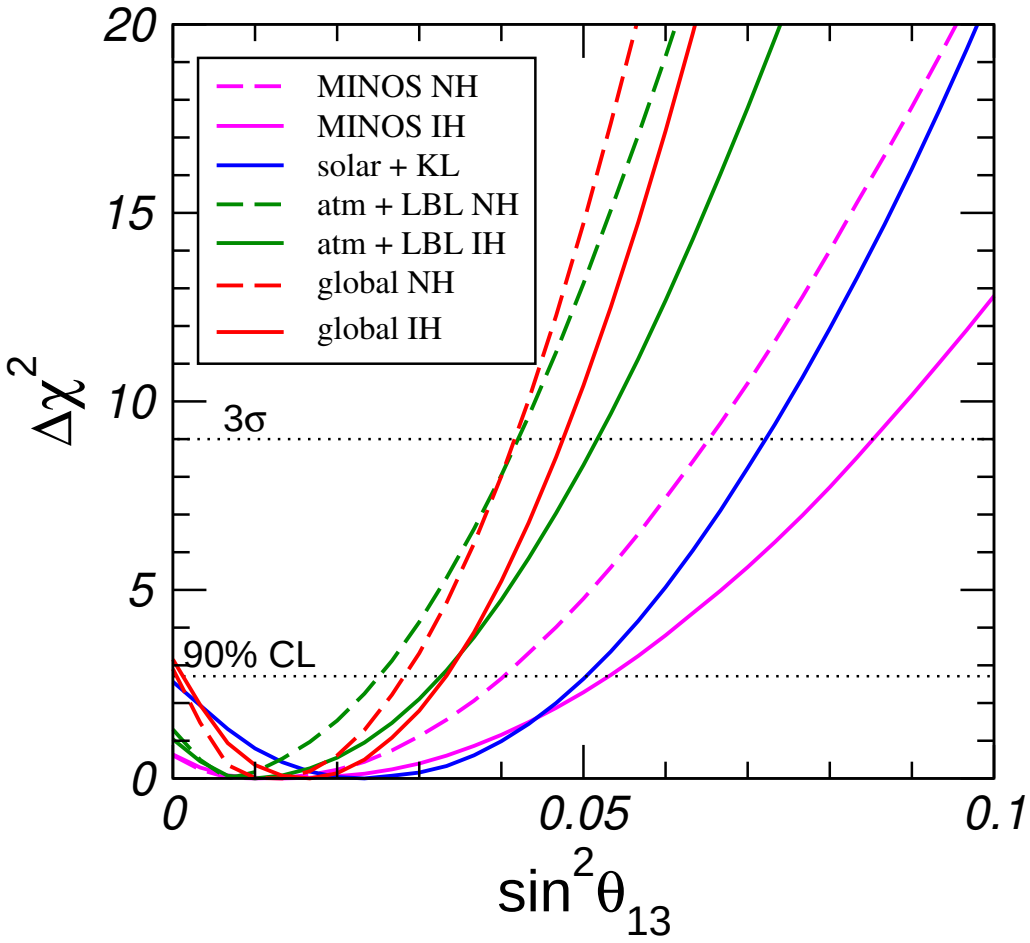

Figure 3. Dependence of $\Delta\chi^2$ on $\sin^2\theta_{13}$ from various data sets, shown for NH (solid) and IH (dashed). The curves labelled "MINOS" include disappearance and appearance data, and the curves labelled "atm + LBL" include Super-K atmospheric data + MINOS (disappearance and appearance) + K2K + CHOOZ.

finds no evidence of such a hint [54]. The results of this analysis have also been used in the global fit of [36]. However, in the combination of these data with MINOS disappearance and appearance data a slight preference for $\theta_{13} > 0$, with $\Delta\chi^2 = 1.6(1.9)$ at $\theta_{13} = 0$ for normal hierarchy (inverted hierarchy). This happens due to a small mismatch of the best fit values for $|\Delta m^2_{31}|$ at $\theta_{13} = 0$, which can be resolved by allowing for non-zero values of θ_{13}.

The MINOS Collaboration has recently reported new data from the search of $\nu_\mu \to \nu_e$ transitions in the Fermilab NuMI beam [60]. The new data are based on a total exposure of $7{\times}10^{20}$ protons-on-target, more than twice the size of the previous data release [61]. The new MINOS far detector data consists of 54 electron-neutrino events, while, according to the measurements in the MINOS Near Detector, $49.1 \pm 7.0(stat) \pm 2.7(syst)$ background events were expected. Hence the observed number of events is in agreement with background expectations within 0.7σ and the hint for a non-zero value of θ_{13} present in previous data has largely disappeared.

An important piece of information on θ_{13} comes from solar and KamLAND data. The relevant

survival probabilities are given by:

$$P_{ee} \approx \begin{cases} \cos^4\theta_{13}\left(1-\sin^2 2\theta_{12}\langle\sin^2\phi\rangle\right) & \text{solar, low energies / KamLAND} \\ \cos^4\theta_{13}\,\sin^2\theta_{12} & \text{solar, high energies} \end{cases}; \tag{3}$$

where $\phi = \Delta m^2_{21} L/4E$ and $\langle\sin^2\phi\rangle \approx 1/2$ for solar neutrinos. Equation (3) implies an anti-correlation of $\sin^2\theta_{13}$ and $\sin^2\theta_{12}$ for KamLAND and low-energy solar neutrinos. In contrast, for the high-energy part of the spectrum, which undergoes the adiabatic MSW conversion inside the sun and which is constrained by the SNO CC/NC measurement, a positive correlation of $\sin^2\theta_{13}$ and $\sin^2\theta_{12}$ emerges. As discussed in [62, 63], this complementarity leads to a non-trivial constraint on θ_{13} and allows the hint for a non-zero value of θ_{13} to be understood, which helps to reconcile the slightly different best fit points for θ_{12} as well as for Δm^2_{21} for solar data and data from KamLAND separately [16, 58, 63–65]. We found that the inclusion of the new solar data, and in particular of the SNO-LETA results, tends to lower the statistical significance of $\theta_{13} \neq 0$ from this data set. There is a minor dependence of the hint for θ_{13} on the solar model, as discussed for example in [19].

From the global data a significance for $\theta_{13} > 0$ of 1.8σ for the inverted hierarchy and 1.7σ for the normal hierarchy (NH) is obtained in [36] and 1.3σ in [19]. We find that the inverted hierarchy (IH) gives a slightly better fit, however, with only $\Delta\chi^2 = 0.7$ [36] with respect to the best fit in normal hierarchy and even less ($\Delta\chi^2 = 0.1$) in [19].

Recently the MiniBooNE collaboration announced updated results of their search for $\bar\nu_\mu \to \bar\nu_e$ transitions [66]. In the full energy range from 200 MeV to 3 GeV they find an excess of 43.2 ± 22.5 events over the expected background (the error includes statistical and systematic uncertainties). In the oscillation-sensitive region of 475 MeV to 1250 MeV the background-only hypothesis has a probability of only 0.5% [66]. This result is consistent with the evidence for $\bar\nu_\mu \to \bar\nu_e$ transitions reported by LSND [67] if interpreted in terms of neutrino oscillations, see figure 4. Any explanation of these hints for $\bar\nu_\mu \to \bar\nu_e$ transitions at the scale of $E/L \sim 1$ eV^2 has to satisfy strong constraints from various experiments. First, no evidence for transitions has been found in MiniBooNE neutrino data above 475 MeV [68]. This suggests that CP (or even CPT) violation has to be invoked to reconcile neutrino and anti-neutrino data. Second, severe constraints exist for $\bar\nu_e$ [57, 69] and $\nu_\mu, \bar\nu_\mu$ [70–73] disappearance at this scale, which have to be respected by any explanation of the $\bar\nu_\mu \to \bar\nu_e$ excesses.

The standard approach to the LSND problem is to introduce one or more sterile neutrinos at the eV scale. Adding one sterile neutrino one obtains the so-called (3+1) mass scheme. In this framework there is no CP violation at short baselines, and disappearance experiments strongly disfavour an explanation of the appearance signals, see for example [74]. The latest situation is summarised in figure 4 (taken from [75]), which shows the well known tension in the (3+1) oscillation fit: the region indicated from LSND combined with MiniBooNE anti-neutrino data (shaded region) and the constraint from all other experiments seeing no positive signal (blue curves) touch each other at $\Delta\chi^2 = 12.7$, which corresponds to 99.8% CL for 2 degrees of freedom. If two neutrino mass states at the eV scale are present [76, 77] ((3+2) scheme), the possibility of CP violation opens up [78], which allows the LSND and MiniBooNE neutrino data to be reconciled [79]. However, constraints from disappearance data still impose a challenge to the fit, and the overall improvement with respect to the (3+1) case is not significant [79, 80], see [75] for updated (3+2) results.

Apart from sterile-neutrino oscillations, various more exotic explanations of the LSND signal have been proposed, among them, sterile-neutrino decay [81–83], CPT violation [84–87], violation of Lorentz

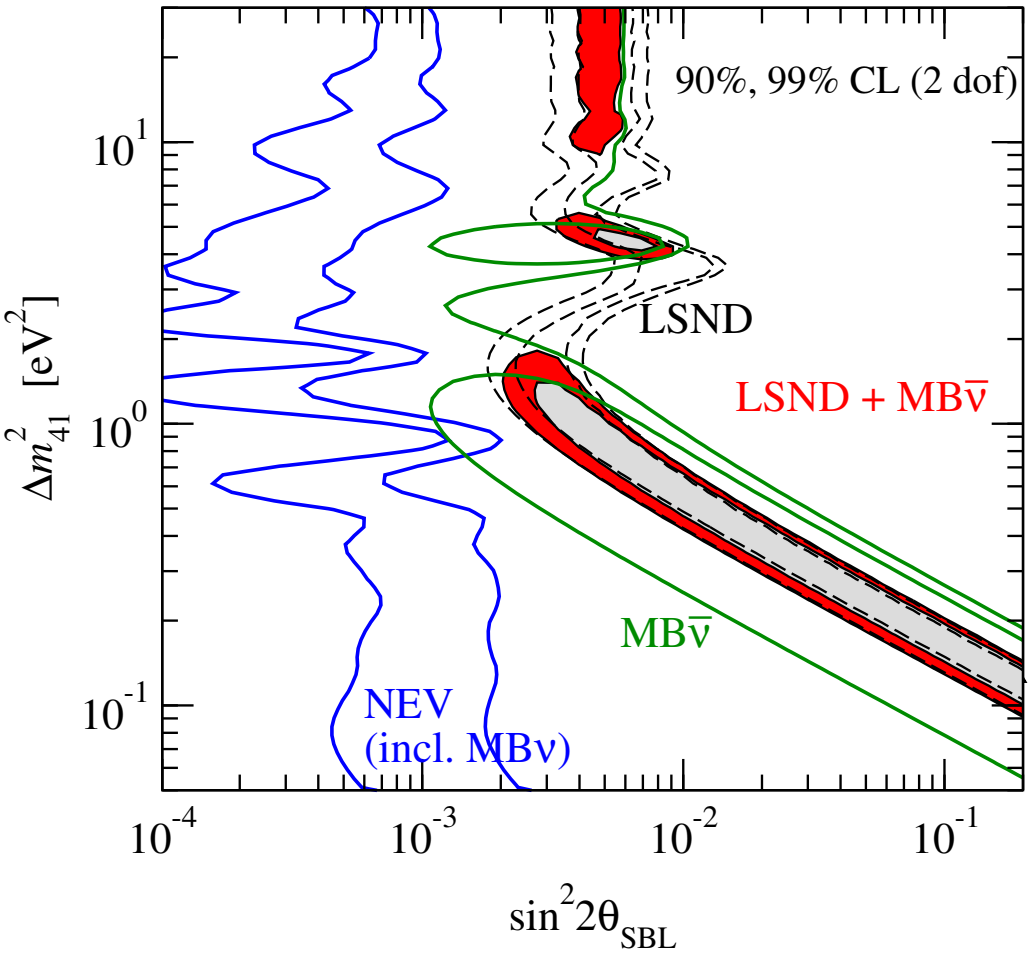

Figure 4. Constraint from no-evidence data (NEV) compared to the combined allowed regions from LSND and MiniBooNE $\bar{\nu}$ data (shaded) at 90% and 99% CL for (3+1) oscillations. We also show the individual regions from LSND and MiniBooNE $\bar{\nu}$ data.

symmetry [88–90], quantum decoherence [91, 92], mass-varying neutrinos [93, 94], shortcuts of sterile neutrinos in extra dimensions [95], sterile neutrino oscillations with a non-standard energy dependence [96], and sterile neutrinos plus non-standard interactions [75, 97]. Some of these proposals involve very speculative physics, and many of them fail to describe all data consistently.

Unfortunately the LSND puzzle is far from solved. The statistical significance of MiniBooNE data is not high enough to settle this issue unambiguously, and recent anti-neutrino data added more confusion to the topic. Moreover, the event excess in the low energy region observed at about 3σ in MiniBooNE neutrino data [68] provides another puzzle, which might or might not be related to the LSND one. Currently only global analyses relying on various different data sets can address the LSND issue, with disappearance experiments playing a crucial role. In view of future high precision oscillation experiments it would be highly desirable to understand better whether there is interesting neutrino physics happening at the scale $E_\nu/L \sim 1$ eV^2.

1.3. Expectations ahead of the Neutrino Factory

If a decision were to be taken after the completion of the Reference Design Report (RDR), say, in 2013, it would be necessary to evaluate the knowledge of the parameters that govern neutrino oscillations at this time and to assess the scientific risks for the Neutrino Factory. In anticipation, therefore, we describe the expectations for the status of measurements of θ_{13}, leptonic CP violation, and the mass hierarchy that will pertain after the Interim Design Report (IDR), but ahead of any decision to initiate the Neutrino Factory project.

1.3.1. Between IDR and RDR

Here we discuss the likely evolution of measurements of neutrino oscillations in the period between the completion of the IDR and the RDR, i.e., the time from now until the end of 2012. The most important question is whether $\theta_{13} > 0$ will have been discovered over this period. To address this question, we show in figure 5 the discovery potential as a function of $\theta_{13} > 0$ for those experiments in operation or under construction during 2009 which may provide useful information before the time that the RDR will be prepared (marked by the arrow). It may be seen from the figure that the key player is expected to be the Daya Bay experiment, which has a θ_{13} discovery reach of $\sin^2 2\theta_{13} \gtrsim 0.02$ at the 3σ CL ($\sin^2 2\theta_{13} \gtrsim 0.01$ at the 90% CL). Even if the anticipated timescale is not met, it is clear from the figure that T2K and NOνA will discover θ_{13} for the median δ within a few years of the publication of the RDR. Therefore, we assume that around the time of the RDR, we will know whether $\sin^2 2\theta_{13} \gtrsim 0.01$ ("θ_{13} discovered") or $\sin^2 2\theta_{13} \lesssim 0.01$ ("θ_{13} not discovered").

The most interesting question is whether CP violation and the mass hierarchy can be measured by the time the RDR is finished. We show in figure 6 the potential for the discovery of CP violation (left panel) and the mass hierarchy (right panel) as a function of $\sin^2 2\theta_{13}$ and the fraction of true δ at the 90% CL from T2K, NOνA and including data from reactor experiments (Double Chooz and Daya Bay) to improve the constraint on θ_{13}. The figure shows that even under optimistic conditions, such as at the 90% CL, for very large $\sin^2 2\theta_{13}$ close to the current bound, and for the inverted mass ordering (for which the combined performance is better), there cannot be any information on these performance indicators before the RDR even from a combined fit to all data. Since no next generation experiment beyond the ones discussed here are under construction at the moment, we do not expect any information on CP violation and the mass hierarchy from measurements of neutrino oscillations before the RDR is prepared.

1.3.2. Between RDR and data taking at the Neutrino Factory

After the RDR has been delivered, the precision with which $\sin^2 2\theta_{13}$ is known will improve rather slowly. Indeed, the ultimate precision will only be a factor of two or so better than the precision achieved at the time of the RDR since there is no experiment under construction which could improve this bound significantly (see figure 5). However, at the time the RDR is prepared, there may be a decision in favour of an alternative next-generation experiment, such as a super-beam upgrade, which may start data taking earlier or on a timescale similar to that of the Neutrino Factory. Therefore,

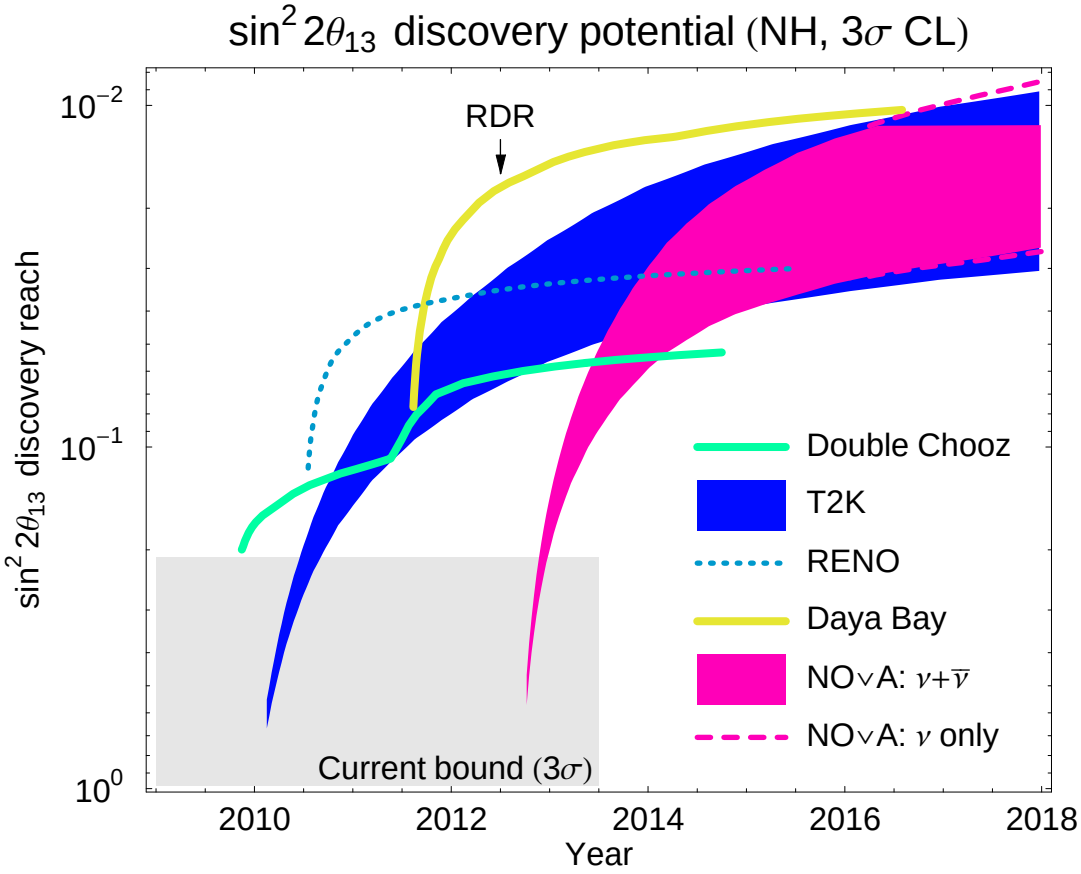

Figure 5. Evolution of the θ_{13} discovery potential as a function of time (3σ CL), i.e., the smallest value of θ_{13} that can be distinguished from zero at 3σ. The bands reflect the (unknown) true value of δ. Normal hierarchy assumed. Figure taken from reference [98].

we discuss the results to be expected from the experiments that will be in operation at the time the RDR is prepared and the results from potential upgrades separately. We assume that data taking at the Neutrino Factory may start as early as 2020

If $\sin^2 2\theta_{13} \gtrsim 0.01$ is discovered before the RDR is delivered, there is a chance that CP violation may be observed and the mass hierarchy determined. This chance is quantified in figure 6. If one believes the hint for $\sin^2 2\theta_{13} \simeq 0.06$ in reference [58], CP violation and the mass hierarchy might be discovered for about 30% of all values of δ at the 90% CL for the inverted hierarchy. Therefore, it is clear that a high-confidence-level discovery in advance of the start of data taking at the Neutrino Factory is extremely unlikely and could only come from a combination of different data [98]. The next generation of experiments will be needed to confirm this result and to determine the oscillation parameters with greater precision.

In summary, if $\theta_{13} > 0$ has not been discovered before the RDR is prepared, it is quite unlikely to be discovered until data from the experiments that are now under construction becomes available. Further, the experiments that are either operating or being constructed now will not be able to access

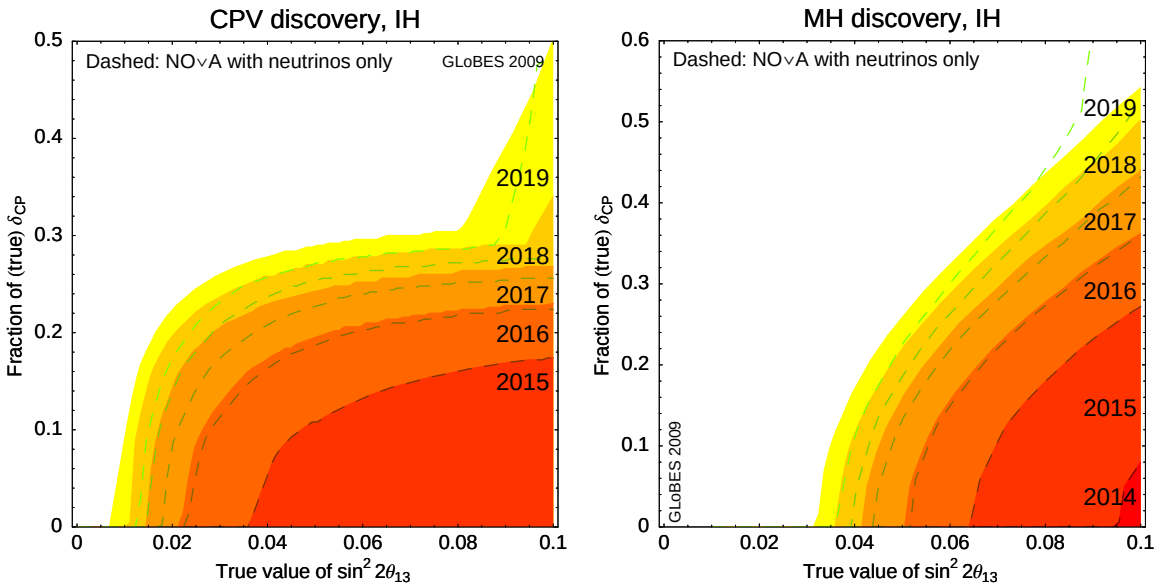

Figure 6. CP violation (left panel) and mass hierarchy (right panel) discovery potentials as a function of true $\sin^2 2\theta_{13}$ and fraction of true δ at the 90% CL from T2K, NOνA (reactor experiments, Double Chooz and Daya Bay, are included in the evaluation to constrain θ_{13}). The dashed curves refer to NOνA with neutrino running only, whereas the shaded contours refer to the nominal NOνA neutrino-anti-neutrino plan. If no contour is shown for a specific year, there is no sensitivity. Note the different scales on the vertical axes. Inverted hierarchy assumed. Figure taken from reference [98].

CP violation or the mass hierarchy for $\sin^2 2\theta_{13} \lesssim 0.01$ (see figure 6). Therefore, an advanced, high-sensitivity experiment will be needed.

1.4. The baseline configuration

Here we describe the optimisation and performance of the Neutrino Factory baseline setup. Two different optimisation strategies are possible depending on the available information on $\sin^2 2\theta_{13}$: if $\sin^2 2\theta_{13}$ is not discovered prior to the start of the Neutrino Factory project, then the prime goal of a Neutrino Factory would be to determine $\sin^2 2\theta_{13}$ *and* to be able to address the mass hierarchy and CP violation for the largest range of $\sin^2 2\theta_{13}$ feasible. We will refer to this as the "small $\sin^2 2\theta_{13}$" case. On the other hand, if $\sin^2 2\theta_{13}$ has been measured prior to the start of the Neutrino Factory project, then the goal is to obtain the most definitive measurements of the CP phase and the atmospheric parameters. We will refer to this as the "large $\sin^2 2\theta_{13}$" case. Note that, for large $\sin^2 2\theta_{13}$, the mass hierarchy would be measured by NOνA at less than $3\,\sigma$ for the vast majority of CP phases and that the precision on $\sin^2 2\theta_{13}$ obtained by Daya Bay would not be likely to be improved by any accelerator-based experiment. For practical purposes, the limiting value of $\sin^2 2\theta_{13}$ that separates the large and small $\sin^2 2\theta_{13}$ regimes is given by the sensitivity of Daya Bay which will eventually reach $\sin^2 2\theta_{13} \simeq 0.01$ at the $3\,\sigma$ level [98]. The Long Baseline Neutrino Experiment (LBNE) [99] at FNAL has the potential to improve upon the sensitivity of Daya Bay by a factor of between 1

and 5. However, this limit would be approached only towards the end of the 10 years of LBNE running and thus would be too late to inform the Neutrino Factory optimisation process. For a more detailed discussion of these possible optimisation strategies see reference [100]. The optimisation of the Neutrino Factory has been studied in great detail, for instance, in references [101–110]. Here we will give a brief summary of the considerations which led to the IDS-NF baseline setup. All results in this section have been computed using the General Long Baseline Experiment Simulator (GLoBES) software package [111, 112].

1.4.1. Optimisation of a single baseline Neutrino Factory

In figure 7 we show the sensitivity reach in $\sin^2 2\theta_{13}$ and δ as a function of the baseline, L, and stored-muon energy, E_μ. The left panel shows the $\sin^2 2\theta_{13}$ sensitivity (exclusion limit) including correlations and degeneracies while the right panel shows the CP violation discovery reach for one particular value of maximal CP violation. The results shown in figure 7 have been used to optimise the facility for the largest possible reach in $\sin^2 2\theta_{13}$, in other words, for the small $\sin^2 2\theta_{13}$ case. The optimum discovery reach in $\sin^2 2\theta_{13}$ is for the L and E_μ combinations in the white regions of the plots; for details, see reference [107]. The excellent sensitivity to $\sin^2 2\theta_{13}$ at about 7 500 km can be easily understood in terms of the magic baseline [105, 113]. At this baseline, which only depends on the matter-density profile, the effect of the CP phase vanishes, which results in a clean signal for $\sin^2 2\theta_{13}$ and the mass hierarchy. The optimum baseline for the measurement of CP-violation is found for L, E_μ combinations in the white region of the right panel. It turns out that, in terms of the $\sin^2 2\theta_{13}$ reach, a baseline between 2 500 km and 5 000 km is close to optimal. Therefore, the IDS-NF baseline setup specifies two long-baseline detectors, one between 2 500 km to 5 000 km and the second at between 7 000 km and 8 000 km.

As far as the muon energy dependence is concerned, there are two competing factors. The oscillation maximum is at relatively low energies in the Neutrino Factory spectrum, therefore a low energy threshold, has been identified as the main priority for the optimisation of the Magnetised Iron Emulsion Detector (MIND) [107]. The low energy threshold provided by the MIND (see section 3) allows for a reduction of E_μ to values as low as about $\sim$ 20 GeV without significant loss of sensitivity [107]. Therefore, the IDS-NF baseline setup with a MIND detector uses $E_\mu = 25$ GeV. On the other hand, matter effects play an important role, such as in the determination of the mass hierarchy. Assuming an averaged matter density $\rho = 3.4\,\mathrm{g/cm^3}$, the matter-resonance energy for a baseline of 4 000 km is at 9.3 GeV. One can already see from the left panel in figure 7 that this leads to the requirement that the peak of the neutrino flux exceeds this energy, which is equivalent to $E_\mu \gtrsim 15$ GeV for optimal performance at the very long baseline. Therefore, for the baseline Neutrino Factory, E_μ between about 15 GeV and 25 GeV can be considered optimal, where the lower end of this range is determined by Earth matter effects, and the upper end by detector performance and cost. These results, which are valid for the small $\sin^2 2\theta_{13}$ case, are fully confirmed by a recent analysis [110] based on the updated MIND performance as described in section 3.2.1.

On the one hand, the results on the optimisation of a single baseline serve as a starting point for the optimisation of the two baseline setup. As we will discuss later, two baselines are essential to ensure uniformly robust performance throughout the parameter space. On the other hand, a single baseline Neutrino Factory may be feasible, or even appropriate, under certain conditions, for example large

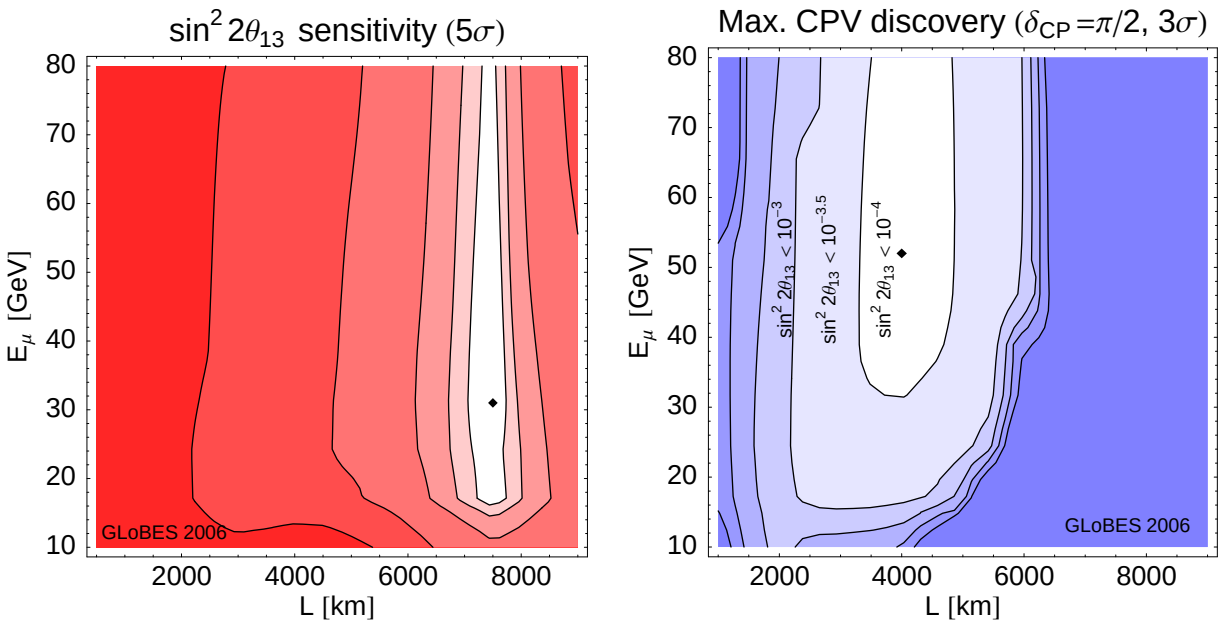

Figure 7. Optimisation of a single baseline Neutrino Factory as a function of baseline L and muon energy E_μ. The left panel shows the $\sin^2 2\theta_{13}$ sensitivity (exclusion limit) with the optimum sensitivity $\sin^2 2\theta_{13} \simeq 5.0 \times 10^{-4}$ (diamond). The contours show the regions within a factor of 0.5, 1, 2, 5, and 10 of the optimal sensitivity. The right panels shows the discovery reach for maximal CP violation, $\delta = \pi/2$, in terms of $\sin^2 2\theta_{13}$. Figure taken from reference [107].

θ_{13}.

A Neutrino Factory with a single baseline of $\sim 1\,000$ km was first proposed in references [114, 115] and was termed the "low-energy Neutrino Factory" (LENF), since the associated muon beam energies were much lower than the usual 25 GeV. At the LENF baseline, the oscillation spectrum at energies below 5 GeV is very rich, potentially allowing for very precise measurements of the unknown oscillation parameters θ_{13}, δ and the mass hierarchy. Since the initial studies [114, 115], developments of the accelerator and detector designs have enabled the experimental simulations to be refined and more detailed optimisation studies to be performed [116, 117]. The key finding of these studies is that, given sufficiently high statistics and a detector with excellent detection efficiency at low neutrino energy ($\lesssim 1$ GeV), an optimised LENF can have excellent sensitivity to the standard oscillation parameters, competitive with the usual two baseline, high energy setup for $\sin^2 2\theta_{13} \gtrsim 10^{-2}$.

In order to exploit the rich signatures at low energies, alternative detector types with a lower neutrino energy threshold and a better energy resolution compared to the MIND are necessary. Two possible alternative detector technologies have been considered: either a 20 kTon totally active scintillating detector (TASD) [118] or a 100 kTon liquid argon (LAr) detector [119], both of which would need to be magnetised; a challenging requirement. These detectors would be capable of detecting and identifying the charges of both electrons and muons, providing access to multiple oscillation channels: the ν_μ ($\bar{\nu}_\mu$) disappearance channels, as well as the golden ($\nu_e \to \nu_\mu$ and $\bar{\nu}_e \to \bar{\nu}_\mu$) [102] and platinum channels ($\nu_\mu \to \nu_e$ and $\bar{\nu}_\mu \to \bar{\nu}_e$). A detailed description of the assumptions used to simulate the

detectors is given in reference [116]. The main features of the TASD that were assumed were an energy threshold of 0.5 GeV with a detection efficiency of 94% above 1 GeV and 74% below 1 GeV for ν_μ and $\bar{\nu}_\mu$ with a background of 10^{-3}. For ν_e and $\bar{\nu}_e$ an efficiency of 47% above 1 GeV and 37% below 1 GeV with a background of 10^{-2} were assumed. The main sources of background were assumed to arise from charge mis-identification and neutral current events. The energy resolution was assumed to be 10% for all channels. The possibility of using non-magnetised TASD or LAr detectors was explored in reference [120]; however the reference LENF setup assumes that magnetisation will be possible. Recent interest in the LENF has also prompted the authors of reference [121] to study a setup with a 50 kTon liquid-scintillator detector. Each of the alternative detector technologies considered in the LENF studies is essentially fully active throughout its volume and therefore offers, for the first time, the possibility of observing the *platinum* channels in addition to the golden channels. Indeed, there were early indications that such detector technologies might be capable of detecting and distinguishing between e^- and e^+ as well as μ^- and μ^+. It is found that the complementarity between the platinum and golden channels can be of great benefit if statistics are limited, improving the sensitivity to the standard oscillation parameters. The inclusion of the platinum channels also turns out to be crucial for resolving degeneracies between the oscillation parameters and non-standard effects [117, 122] in the absence of a second baseline.

In previous work [123, 124], the LENF was configured with a stored muon energy of between 4 GeV and 5 GeV and a baseline of around 1 300 to 1 500 km, with 1 480 km corresponding to the configuration Fermilab to Henderson mine and 1300 km to the combination Fermilab to Homestake mine[4]. Here we focus on optimising a LENF for the purpose of measuring CP-violation. To this end, we compute the ability, under a range of experimental scenarios, of ruling out all CP-conserving values of δ. For each detector, a CP-violation discovery-potential-plot was first produced for each baseline and muon energy combination. Using a Poissonian χ^2 function and marginalising over all parameters except δ, plots showing the range of values of "true" θ_{13} and δ for which CP-violation could be detected at the 3σ significance were produced. The simulations assumed a normal mass hierarchy and the hierarchy degeneracy was taken into account during the marginalisation. The simulated oscillation parameters were chosen to be $\sin^2 2\theta_{12} = 0.3$, $\theta_{23} = \pi/4$, $\Delta m^2_{12} = 8.0 \times 10^{-5}\,\mathrm{eV}^2$ and $|\Delta m^2_{13}| = 2.5 \times 10^{-3}\,\mathrm{eV}^2$ with an uncertainty of 4 % and 10 % on the solar and atmospheric parameters respectively. For a few illustrative values of true θ_{13}, the CP fraction was then calculated for each choice of energy and baseline. The CP fraction is defined for each true θ_{13} as the fraction of true δ values which fall inside the CP discovery potential curve. Using these values, a contour plot was then produced of how the CP fraction varies as a function of baseline and muon energy for a given true θ_{13}, as shown in figure 8.

From figure 8, we see that for large values of θ_{13}, around $\sin^2 2\theta_{13} \gtrsim 10^{-2}$, CP fractions of 70 % to 90 % for most energies and baselines can be obtained. The only deviation from this is in the region of the lowest energies but longest baselines where we see a worse performance at around 40 % to 80 %. This poor performance may partially be explained by considering the uncertainty in θ_{13}: as this parameter is being marginalised over, the ability to measure the CP phase is diminished if θ_{13} cannot be constrained. The best constraints on θ_{13} are found near the first oscillation maximum; in the poor-performance region, the majority of neutrinos have baseline-energy ratios not matching this

[4] Homestake is the host site the proposed Deep Underground Science and Engineering Laboratory (DUSEL).

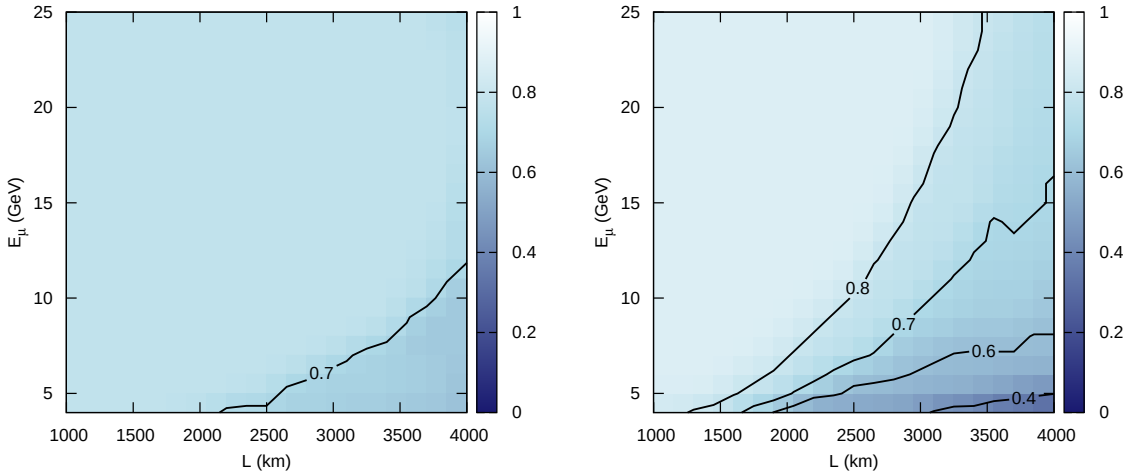

(a)$\sin^2 2\theta_{13} = 10^{-1}$ (b)$\sin^2 2\theta_{13} = 10^{-2}$

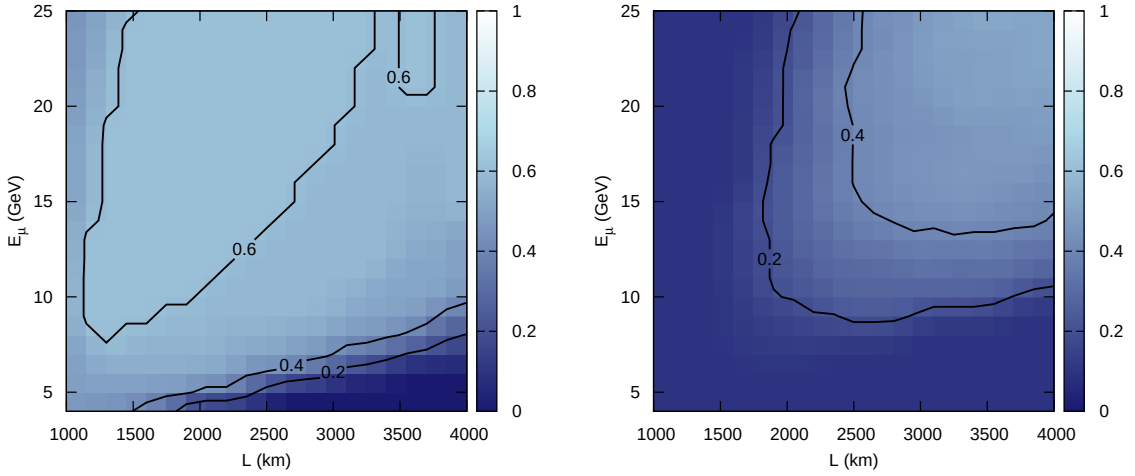

(c)$\sin^2 2\theta_{13} = 10^{-3}$ (d)$\sin^2 2\theta_{13} = 10^{-4}$

Figure 8. CP fraction as a function of baseline, L, and stored muon energy, E_μ. Results are shown for a 20 kTon TASD using the default muon intensity of 5×10^{21} μ^+ and 5×10^{21} μ^- for four different values of θ_{13}: (a) $\sin^2 2\theta_{13} = 10^{-1}$; (b) $\sin^2 2\theta_{13} = 10^{-2}$; (c) $\sin^2 2\theta_{13} = 10^{-3}$; and (d) $\sin^2 2\theta_{13} = 10^{-4}$.

condition. This region is also affected by the decrease of the neutrino flux at large baselines which compounds the poor performance.

Looking at smaller values of θ_{13}, around $\sin^2 2\theta_{13} \approx 10^{-3}$ we see a general decrease in CP fraction to a range of 50 % to 60 % and the region of poor performance which was mentioned earlier worsens to 0 % to 40 %. We also see another region in which the performance is significantly reduced; the region of highest-energies but shortest-baselines. This drop in performance is attributed to a decrease

in statistics: this region has the smallest baseline-energy ratio which means it is the furthest away from the oscillation maxima. When these effects are combined with the drop in statistics that arises from the lowering of θ_{13}, experiments in this region start to be severely compromised by the number of events. The same behaviour is seen for the updated MIND detector [110] and in figure 9.

As the true value of θ_{13} drops to $\sin^2 2\theta_{13} \lesssim 10^{-4}$, the performance decreases rapidly and we generally see CP fractions in the range of 0 % to 50 %. The two poorly performing regions continue to worsen and are mostly in the range 0 % to 30 %. Eventually, only the regions of $E \gtrsim 10\,\text{GeV}$ and $L \gtrsim 2\,000\,\text{km}$ have any appreciable CP fractions.

The high-energy regions of our CP fraction plots overlap with part of a previous optimisation study that considered the baseline Neutrino Factory [107, 110]. In figure 9 we show the same type of result as in figure 8, but now for a 50 kTon MIND detector corresponding to the one described in 3.2.1. Qualitatively the results in figures 8 and 9 are very similar and demonstrate that the decision between shorter baseline and lower energy versus longer baseline and higher energy is more driven by the magnitude of $\sin^2 2\theta_{13}$ than by the detector technology alone. Although the two experimental simulations have many differences, we see similar generic features: higher energies require longer baselines and as θ_{13} decreases the low energy, short baseline setups become increasingly disfavoured. Also, not surprisingly, when using a MIND somewhat larger energies at large $\sin^2 2\theta_{13}$ are favoured in order to avoid the effects from the energy threshold of the detector. For large θ_{13}, the baseline Neutrino Factory has a CP fraction around 80 % (see figure 13) and the LENF has CP fractions of 70 % to 80 % over a comparable region. But also, a MIND detector with 10 GeV muon energy has a similar performance of 80%, see figure 9. Thus, low energy setups are preferable at large $\sin^2 2\theta_{13} > 0.01$ for *both* MIND and TASD detectors. Any perceived performance advantage of one detector type with respect to the other strongly depends on the relative detector sizes and assumed beam luminosities.

The platinum channel

The most significant addition relative to the initial LENF studies would be the inclusion of the platinum channels, $\nu_\mu \to \nu_e$ and $\bar{\nu}_\mu \to \bar{\nu}_e$. We find that, if backgrounds are at a negligibly low level, the platinum channels always give a significant improvement to the setup. However, once realistic background levels of at least $\sim 10^{-2}$ on the platinum channels are included, much of this benefit is lost. There is still some improvement if statistics are limited to below the 5.0×10^{20} decays per year per polarity assumed in references [114, 115], but virtually nothing is gained in the case of higher statistics. This is illustrated in figure 10 where the 68%, 90% and 95% contours in the $\theta_{13} - \delta$ plane are shown for a true simulated value of $\theta_{13} = 1^\circ$ and $\delta = 0$, $\pm 90^\circ$ and $\pm 180^\circ$, comparing the results from a setup without the platinum channel ('Scenario 1' - blue dashed lines) and a setup which does include the platinum channel with a background of 10^{-2} ('Scenario 2' - solid red lines). Figure 10a shows the results in the low statistics case and figure 10b the high statistics case.

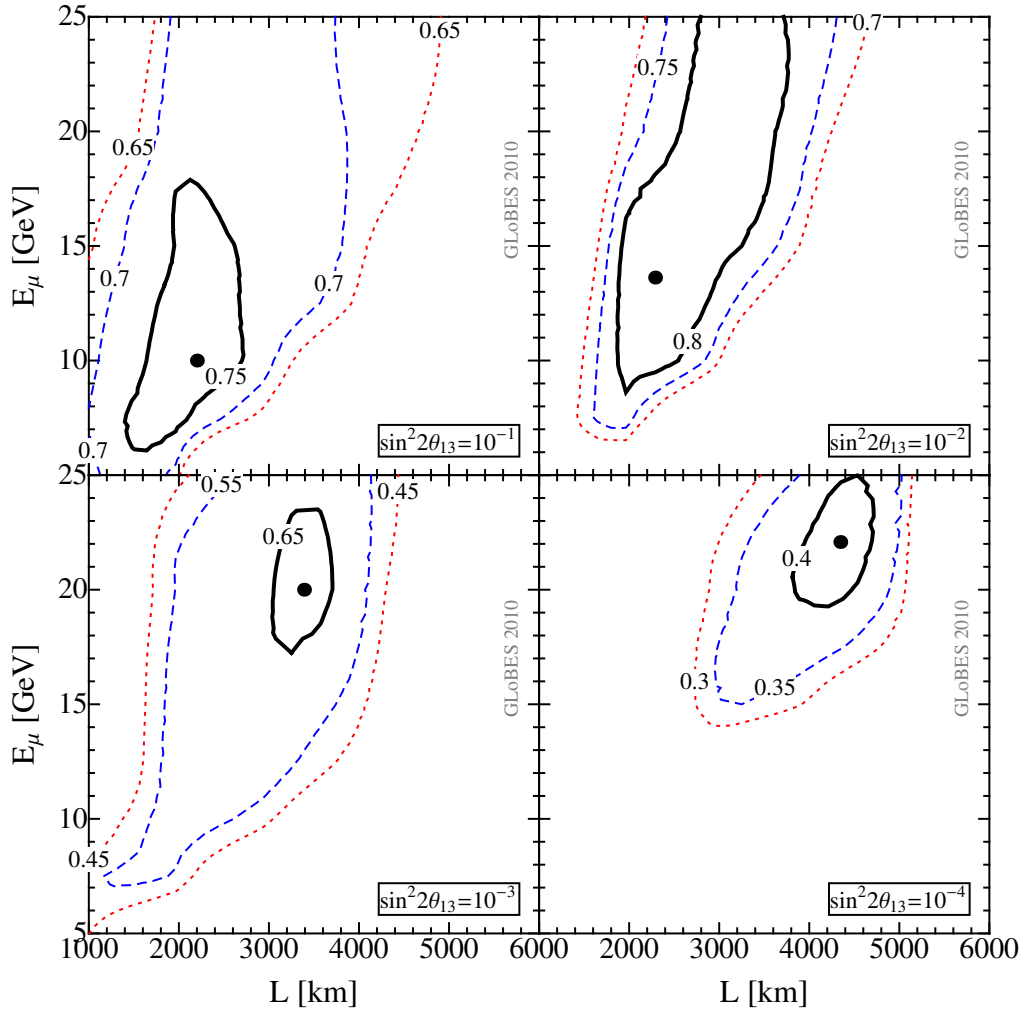

Figure 9. Fraction of δ for which CPV will be discovered (3σ CL) as a function of L and E_μ for the single baseline Neutrino Factory. The different panels correspond to different true values of $\sin^2 2\theta_{13}$, as given there. Here SF=1 (2.5×10^{20} muons per year and polarity) is used with a 50 kt detector. The optimal performance is marked by a dot: (2200,10.00), (2288,13.62), (3390,20.00) and (4345,22.08). Figure and caption taken from reference [110].

1.4.2. Optimisation of a two baseline Neutrino Factory

The simultaneous optimisation of two Neutrino Factory baselines has been studied in reference [109], see figure 11 (shaded regions). One easily recovers the behaviour discussed above: $\sin^2 2\theta_{13}$ (upper left panel) and mass hierarchy (upper right panel) sensitivity prefer a long baseline, but the combination with a shorter baseline is not significantly worse. For CP violation (lower left panel), however, one baseline has to be considerably shorter. If all performance indicators are combined (lower right panel), the optimum at 4 000 km plus 7 500 km is obtained. A very interesting study is performed in the dashed curves: these curves illustrate the effect of a potential non-standard interaction $\epsilon_{e\tau}$, which is known to harm especially the appearance channels. While the absolute performance for all perfor-

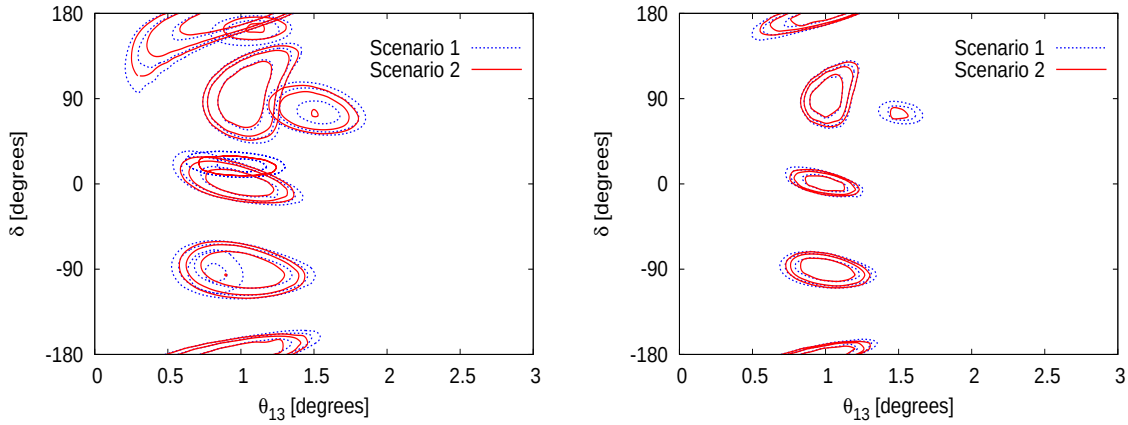

(a) 5.0×10^{20} decays per year.

(b) 1.4×10^{21} decays per year.

Figure 10. Sensitivity to θ_{13} and δ without the platinum channel (Scenario 1 - dashed blue lines) and with the platinum channel with a 10^{-2} background (Scenario 2 - solid red lines), in the case of a) low statistics (5.0×10^{20} decays per year and b) high statistics (1.4×10^{21} decays per year, significantly larger than the present IDS-NF baseline), for $\theta_{13} = 1°$. From reference [116].

mance indicators decreases, the position of the optimum in two baseline space remains qualitatively unchanged. Therefore, the two baseline setup is not only optimal for standard physics, but also robust with respect to unknown effects (see also reference [125]).

All this optimisation is based on the assumption that the experiment is optimised in the $\sin^2 2\theta_{13}$ direction. On the other hand, it has been demonstrated in the literature that intermediate values of $\sin^2 2\theta_{13}$ require the magic baseline as a degeneracy resolver (see reference [126] for degeneracy issues). Therefore, the optimisation of the Neutrino Factory does change qualitatively. However, note that for larger values of $\sin^2 2\theta_{13}$, which may be found in a first low energy phase of the Neutrino Factory, somewhat shorter baselines than 3000 km can be used; cf., figure 8 in reference [100].

Robustness of performance

Given the excellent performance of single baseline configurations over a wide range of $\sin^2 2\theta_{13}$ values, the question arises whether a second baseline is strictly required. The answer is a resounding yes, as the results shown in figure 12 decisively demonstrate. In this figure, we show the sensitivity reach for CP violation as a function of $\sin^2 2\theta_{13}$ in the left hand panel for three different configurations. "IDS-NF 2010/2.0" refers to a the reference setup defined in section 1.4.3, it employs two baselines of 4 000 km with a 100 kTon MIND and 7 500 km with a 50 kTon MIND. The muon energy is 25 GeV. "MIND LE" uses a single baseline of 2 000 km with a 100 kTon MIND and a muon energy of 10 GeV. "TASD LE" uses a single baseline of 1 300 km with a 20 kTon TASD and a muon energy of 5 GeV. The MIND performance is described in section 3.2.1 and the TASD performance is taken from reference [116]. All setups are assumed to run for 10 years with 10^{21} useful muon decays per year summed over both polarities. For a two baseline setup, this means that each detector receives only one half of this

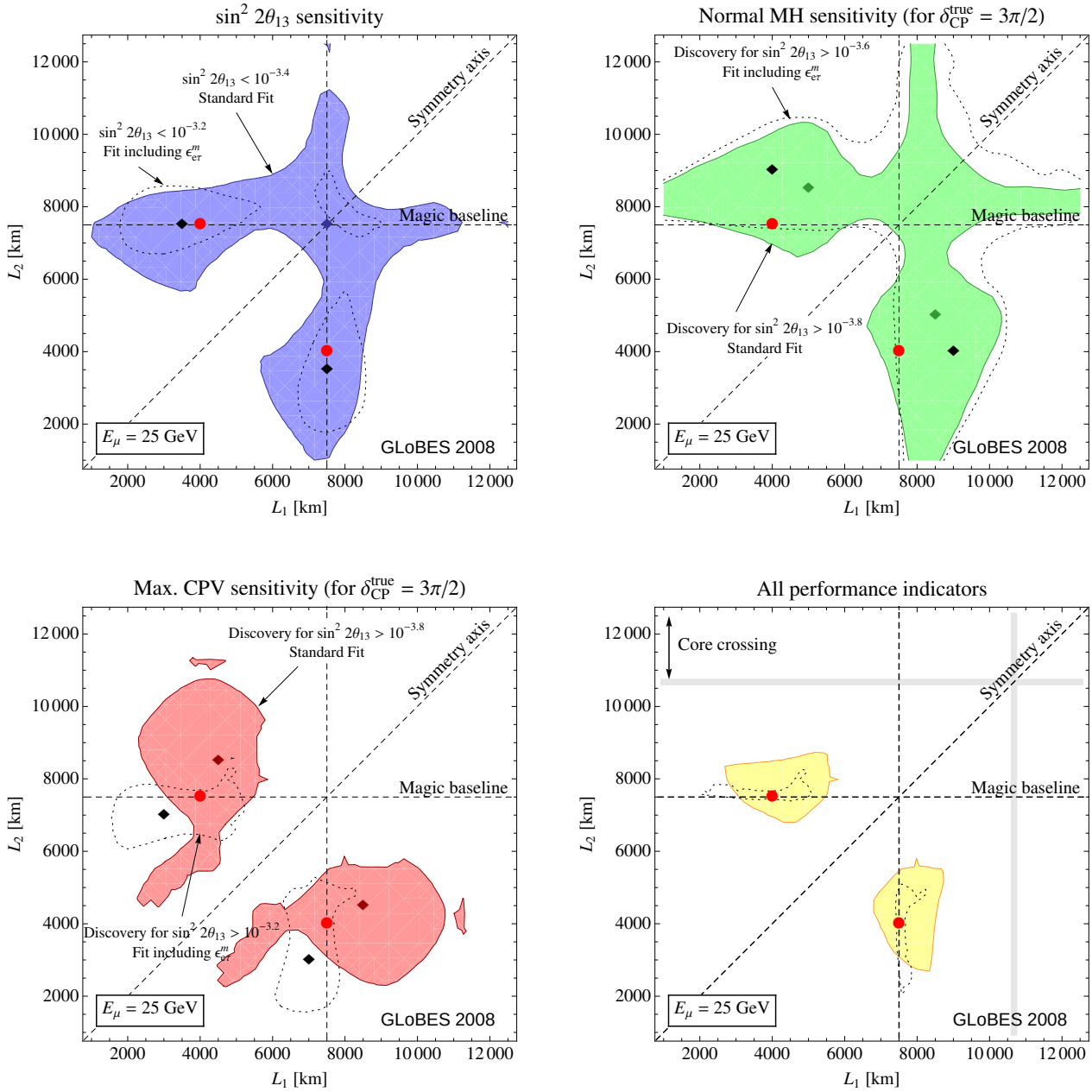

Figure 11. Two-baseline optimisation of the Neutrino Factory for the standard oscillation performance indicators. The upper left panel shows the (shaded) region where the sensitivity to $\sin^2 2\theta_{13}$ better than $10^{-3.4}$ (5σ), the upper right panel shows the (shaded) region where the sensitivity to the normal mass hierarchy (MH) is given for all $\sin^2 2\theta_{13} \geq 10^{-3.8}$ (5σ, $\delta_{\rm CP}^{\rm true} = 3\pi/2$), the lower left panel shows the (shaded) region where the sensitivity to maximal CP violation (CPV) is given for all $\sin^2 2\theta_{13} \geq 10^{-3.8}$ (5σ, $\delta_{\rm CP}^{\rm true} = 3\pi/2$), and the lower right panel shows the intersection of the three regions as the shaded region. The dotted curves have been obtained from a fit including a non-standard interaction parameter $\epsilon_{e\tau}$ marginalised (for the $\sin^2 2\theta_{13}$ ranges given in the plots). The diamonds show the setups with optimal sensitivities (coloured/grey for the shaded contours, black for the dotted contours), whereas the circles correspond to the IDS-NF standard choices $L_1 = 4\,000$ km and $L_2 = 7\,500$ km. Figure taken from reference [109].

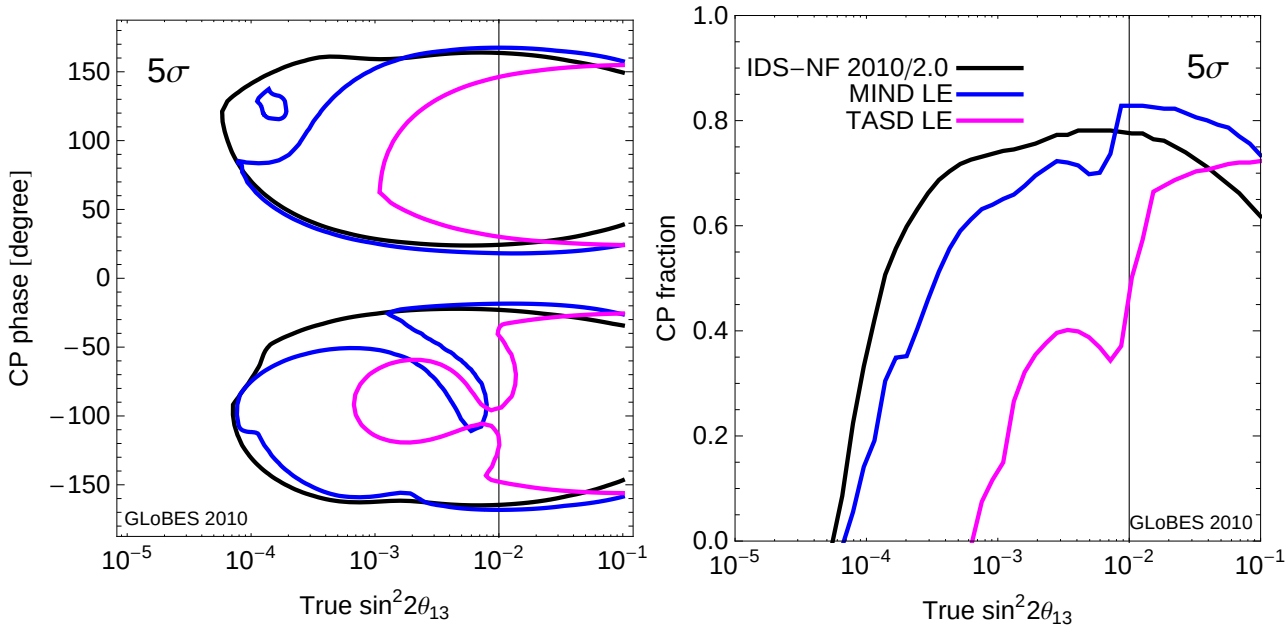

Figure 12. CP violation discovery reach (left hand panel) and CP fraction (right hand panel) comparing possible single-baseline setups with the two-baseline default configuration (IDS-NF 2010/2.0) TASD LE stands for a 20 kTon TASD detector at 1 300 km baseline with $E_\mu = 5$ GeV and MIND LE stands for a 100 kTon MIND at 2 000 km with $E_\mu = 10$ GeV. Note, that the results are shown at the $5\,\sigma$ confidence level.

flux. The systematics for all setups is the same: 1% on signal and 20% on background. The results are shown at the $5\,\sigma$ level, which helps to emphasise the crucial difference. For values of $\sin^2 2\theta_{13} > 0.01$ (thin vertical line) all three setups show a qualitatively very similar behaviour, but nonetheless there is a distinct differences in performance; the single-baseline setups perform better at very large values of $\sin^2 2\theta_{13}$. For values of $\sin^2 2\theta_{13} < 0.01$ the picture changes dramatically and the single-baseline setups suffer from a phenomenon called π-transit resulting in large regions of parameter space where sensitivity is lost. The reason for the occurrence of the π-transit was described in reference [127]: for certain combinations of the true values of the CP phase and $\sin^2 2\theta_{13}$, a CP violating true solution can be fitted with the wrong mass hierarchy and $\delta = \pi$. The location of the π-transit depends sensitively on the baseline and energy, and therefore MIND LE and TASD LE show this effect for slightly different values of $\sin^2 2\theta_{13}$, whereas IDS-NF 2010/2.0, the two baseline setup, is immune against this effect due the ability of the magic baseline to identify unambiguously the mass hierarchy. This is a rather general conclusion: all single-baseline setups we have studied suffer from the π-transit problem due to their relatively weak ability to determine the mass hierarchy.

We conclude that single-baseline setups, whether they use a MIND or TASD, all suffer from problems with degeneracies, also, in the context of new physics as will be discussed later in this section, for values of $\sin^2 2\theta_{13} \lesssim 0.01$. The actual extent of the problem and the precise boundary in $\sin^2 2\theta_{13}$ depend crucially on the detector performance and available statistics. However, once these factors

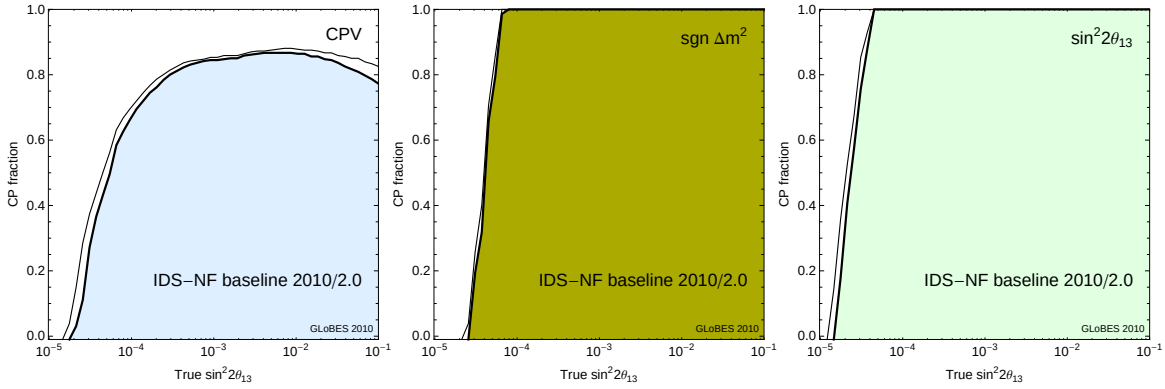

Figure 13. Performance of the baseline Neutrino Factory (100 kt at 4 000 km plus 50 kt at 7 500 km, updated MIND) in terms of the θ_{13}, CP violation, and mass hierarchy discovery reach at 3σ CL. The thick black line assumes default systematics, whereas the thin black line is for the case with no beam or detector systematics.

are known it is straightforward to derive the limiting values of $\sin^2 2\theta_{13}$ above which a given single baseline setup is safe from degeneracies. In those cases, single baseline setups typically achieve a higher precision for the CP phase than our standard two baseline configuration. Hence, for sufficiently large values of $\sin^2 2\theta_{13}$, a single baseline configuration offers a cost-effective way to improve the ability to measure the leptonic CP phase. Fortunately, the typical magnitude of the delimiting value of $\sin^2 2\theta_{13}$ is within the sensitivity reach of Daya Bay and therefore, sufficient data for a informed decision will be available.

1.4.3. Performance of the Neutrino Factory

Here we discuss the performance of the high energy Neutrino Factory for standard oscillation physics. We show in figure 13 the performance of the high energy Neutrino Factory (100 kt at 4000 km plus 50 kt at 7500 km) in terms of the θ_{13}, CP violation, and mass hierarchy discovery reach at 3σ CL using the updated MIND performance. The figure shows that for all performance indicators discovery reaches for $\sin^2 2\theta_{13}$ between 10^{-5} and 10^{-4} can be achieved, which corresponds to oscillation amplitudes about four orders of magnitude smaller than the current bounds. Non-zero θ_{13} and the mass hierarchy are discovered almost independently of the true value of δ. The CP-violation discovery reach is very stable over about two orders of magnitude $10^{-3.5} \lesssim \sin^2 2\theta_{13} \lesssim 10^{-1.5}$. Only for large values of $\sin^2 2\theta_{13}$, the fraction of δ (leftmost panel) decreases. This effect comes from correlations among matter density uncertainty (see references [128]), oscillation parameters (see, e.g., reference [127]), and other systematics. In addition, the explicit treatment of near detectors affects this range [129]. To illustrate the effect of beam and detector systematics we show the thin black line, which is computed for zero beam and detectors systematics. Even with the updated MIND the baseline setup is still found to be optimal for $\sin^2 2\theta_{13} < 0.01$ and the impact of tau contamination on the standard performance indicators is found to be negligible [110]. This issue is discussed in detail in section 1.4.4.

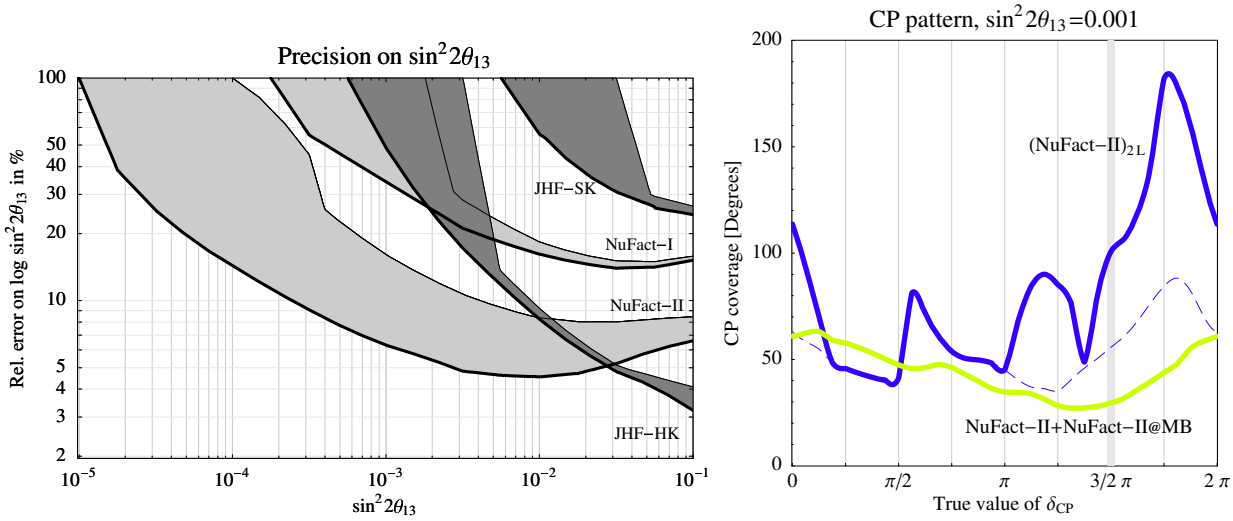

Figure 14. Performance indicators for the precision of θ_{13} (left panel) and δ (right panel) measurement at the Neutrino Factory. The precision of θ_{13} is shown as a function of the true $\sin^2 2\theta_{13}$ for a single baseline Neutrino Factory (90% CL); taken from reference [127]. The bands reflect the unknown true value of δ. The precision of δ ("CP coverage") is shown as a function of the true δ for a true $\sin^2 2\theta_{13} = 0.001$ (3σ CL); taken from reference [130]. The different curves correspond to a single baseline version with all muons in one storage ring (dark/blue solid curve) and a two baseline version (light/yellow solid curve). The dashed curve corresponds to not taking degeneracies into account.

Apart from the discovery reaches, for which canonical performance indicators representing the whole parameter space exist, the precision measurements of θ_{13} or δ strongly depend on the true values of θ_{13} and δ themselves. This is illustrated in figure 14 for two performance indicators. In the left panel, the precision of θ_{13} is shown as a function of the true $\sin^2 2\theta_{13}$ for a single baseline Neutrino Factory "NuFact-II". The bands reflect the unknown true value of δ. One can easily see from figure 14 that different experiments can be compared in this representation. In the right panel, the precision of δ ("CP coverage") is shown as a function of the true δ. Note that a CP coverage of 360° means that all values of δ fit the chosen true value, i.e., no information on δ can be obtained (for details, see reference [130]). The maximum in the figure of 180° means that about 50% of all values of δ can be excluded. Comparing the two solid curves, one can easily see that the magic baseline combination acts as a risk minimiser: the curve becomes relatively flat with a 3σ (full width) error of 30° to 60°, corresponding to a 1σ (half width) error of 5° to 10°. This corresponds to a precision similar to the quark sector. Note that the right panel is shown for a particular true value of $\sin^2 2\theta_{13}$. Another performance indicator that is often used is obtained by fitting for θ_{13} and δ simultaneously at several selected sets of true $\{\theta_{13}, \delta\}$. While this result corresponds most closely with what would be expected from the Neutrino Factory, the analysis has yet to be repeated for the revised Neutrino Factory baseline presented here. Figure 14 is therefore included to provide examples of the precision with which θ_{13} and δ would be measured at representative facilities.

There are other measurements in standard oscillation physics which can be performed at the Neutrino Factory and which are not related to the performance indicators discussed above. For example,

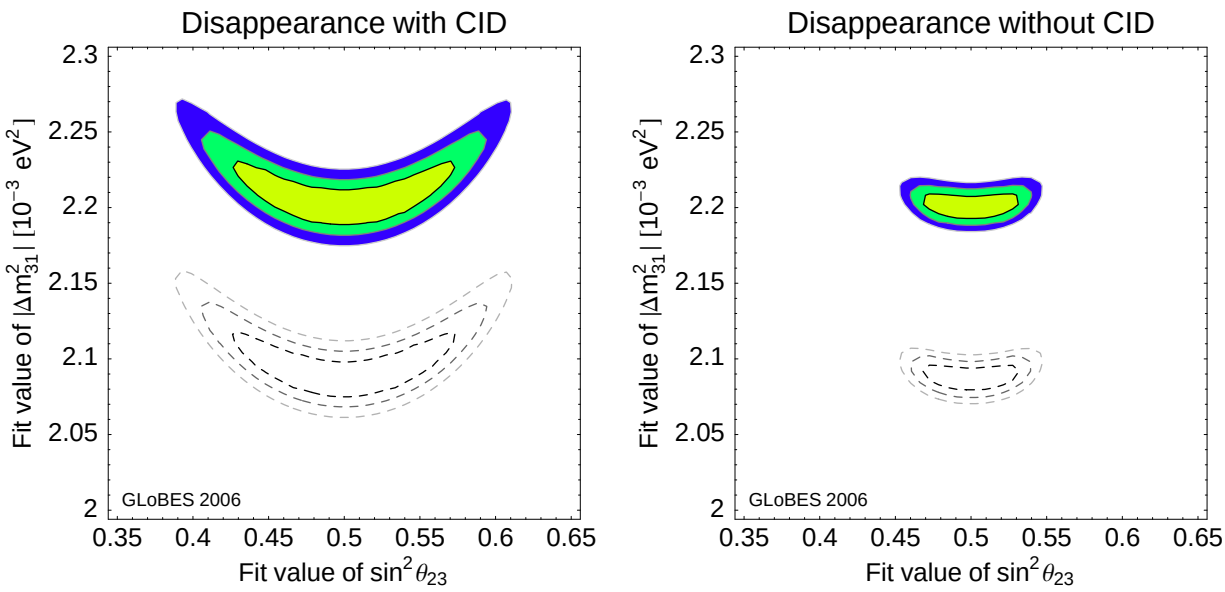

Figure 15. Comparison of Δm^2_{31}-θ_{23}-precision in an analysis with charge identification (CID, left panel) and without CID (right panel) in the disappearance channel including all correlations (1σ, 2σ, 3σ, 2 d.o.f., $\sin^2 2\theta_{13} = 0$). The appearance information is added as usual with CID. Dashed curves correspond to the inverted hierarchy solution. Figure taken from reference [107].

we show in figure 15 the combined precision in Δm^2_{31} and θ_{23} for maximal atmospheric mixing. The different shaded and dashed regions correspond to the normal and inverted hierarchy fit (for the true normal hierarchy), which are separated by $2 \cdot \Delta m^2_{21} \cdot \cos^2\theta_{12}$ (see, e.g., reference [131]). Obviously, one can measure Δm^2_{31} with a precision better than Δm^2_{21}. The splitting of the measured region is a relic of choosing Δm^2_{31} instead of an appropriate intermediate value between Δm^2_{31} and Δm^2_{32}, which results in a different mass-squared splitting for normal and inverted hierarchy for fixed $|\Delta m^2_{31}|$. It does not mean that one can measure the mass hierarchy using this effect [131]. By comparing the left and right panels, it can be seen that it is important to use a data sample without charge identification (CID) for the analysis of the disappearance channels, because the overall efficiency and threshold are much better and the CID background is comparatively small [107]. In reference [107] it also has been demonstrated that the very long baseline clearly helps to constrain θ_{23} even further.

Other potential measurements within the SνM framework at the Neutrino Factory include deviations from maximal mixings [132], the high-confidence check of the MSW effect in Earth matter, even for $\sin^2 2\theta_{13} = 0$, by the solar term of the appearance channel [133], the percent-level determination of the average matter density along the baseline [108, 134, 135], and the mass hierarchy determination if $\sin^2 2\theta_{13} = 0$ [131, 136]. For these measurements, a very long baseline is typically the key ingredient.

1.4.4. The problem of τ-contamination

The problem of τ-contamination was first studied in reference [137] in the context of precision measurements of the atmospheric parameters $(\Delta m^2_{32}, \theta_{23})$ using the $\nu_\mu \to \nu_\mu$ channel at a Neutrino Factory. It was shown in section 1.4.3, figure 15, that it is useful to add all muons in the final state without CID. The improved efficiency in the low-energy part of the neutrino spectrum, however, has the drawback that a previously irrelevant background now becomes potentially harmful. Oscillations into ν_τ, unless suppressed by low efficiency at low energy, enhance both the right- and wrong-sign muon samples. In previous analyses, the poor efficiency of the detector below 10 GeV allowed τ-contamination to be neglected [102, 138]. In the case of the detection of the platinum channel, τ-contamination also affects the electron sample. However, detectors capable of measuring the platinum channel are usually assumed to be capable of distinguishing the electron from tau decay from the true platinum-electron sample. Oscillations of $\nu_e, \nu_\mu \to \nu_\tau$ will produce τs through $\nu_\tau N$ CC interactions within the detector that will, eventually, decay into muons (approximately 17% of them). These muons from taus will, therefore, "contaminate" the "direct" muon samples (coming from $\nu_e, \nu_\mu \to \nu_\mu$ oscillations). Notice that muons from taus are not background but as good a signal as the direct muons. Muons from τ-decay accumulate in low-energy muon bins, since the associated neutrinos produced in τ-decay result in a "secondary" muon which has, on average, 1/3 of the τ energy [137].

It is very hard to remove the muons from tau decay using kinematic cuts in a MIND-like detector. Any cuts that attempt to do so drastically reduce the direct muon events as well and hence worsen the sensitivity to the oscillation parameters. They escape essentially all filters designed to kill the dominant backgrounds and directly add to the direct muon sample, see reference [137]. On the other hand, neglect of the tau contribution will lead to an incorrect conclusion about the precision achievable at the Neutrino Factory on a given observable. The "τ-contamination" must be added to the signal and it must be studied together with it.

1.4.4.1. Impact on the atmospheric parameters measurement

The fit of the atmospheric parameters for a typical sample set of inputs ($\Delta m^2 = \Delta m^2_{31} = 2.4 \times 10^{-3}$ eV^2, $\theta_{23} = 41.9°; \theta_{13} = 1°; \delta = 0$) is shown in figure 16 (left), from reference [137]. The contours represent the allowed region in Δm^2–θ_{23} parameter space at 99% CL ($\Delta\chi^2 = 9.21$). The solid line corresponds to direct muon events alone and the dashed line to the total right-sign muon sample, including those from tau decay. It can be seen that the allowed region is much more constrained with direct muons only than when including muons from taus. In particular, the inclusion of the tau contribution worsens the precision with which θ_{23} and its deviation from maximality can be measured: a spread of $\sim 2°$ if tau events are removed turns into $\sim 4.5°$ when they are included. The reason is the following: since the θ_{23}-dependent terms come with opposite sign in $P_{\mu\mu}$ and $P_{\mu\tau}$, and the statistics of τ-events is significant, the combination of muons from direct production and from tau decays marginally decreases the sensitivity of the event rates to this angle. On the other hand, the τ-contamination does not affect the determination of (the modulus of) Δm^2. The largest true value of θ_{23} that can be discriminated at 99% CL from maximal θ_{23} is shown in figure 16 (right) as a function of Δm^2. While there is a distinct but mild dependence on Δm^2, it is seen that τ-contamination worsens the ability to discriminate θ_{23} from maximality, thus making this measurement harder than originally

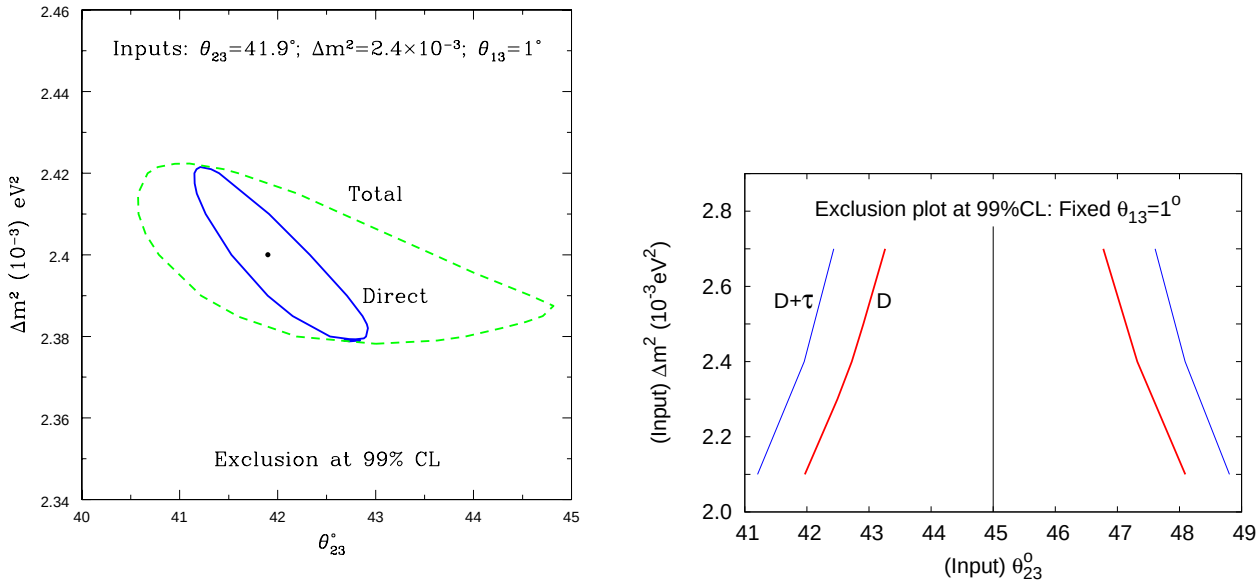

Figure 16. Left: 99% CL contours in Δm^2–θ_{23} from CC events directly producing muons (solid line) and with the inclusion of muons from tau decay as well (dashed line). The input parameters are: $\Delta m^2 = \Delta m^2_{31} = 2.4 \times 10^{-3}$ eV^2, $\theta_{23} = 41.9°$. From reference [137]. Right: The largest (smallest) true value of θ_{23} in the first (second) octant that can be discriminated at 99% CL from $\theta_{23} = \pi/4$ as a function of Δm^2 when only Direct (D) and total ($D + \tau$) events are considered. In both panels, θ_{13} has been fixed to 1° and $\delta = 0$. From reference [137].

expected.

1.4.4.2. Impact on the θ_{13} and δ measurement

The problem of τ-contamination of the $\nu_e \to \nu_\mu$ channel was studied in detail in reference [139]. A good signal-to-background ratio is crucial to determine simultaneously, and with good precision, θ_{13} and δ, since in this channel we have a sample of tens of events at most. In order to separate high-energy charged currents from the low-energy dominant neutral current background good energy reconstruction is crucial. For this reason, in the standard MIND analysis at the Neutrino Factory, the neutrino energy is reconstructed by adding the energy of the muon and that of the hadronic jet. This operation, however, yields a biased result when the muon comes from a tau decay and it is detected in an iron calorimeter such as MIND, since no additional information regarding the missing energy arising from the neutrinos in the $\tau \to \nu_\tau \bar{\nu}_\mu \mu^-$ decay can be provided. This would not be the case in an emulsion cloud chamber or liquid-argon detector capable of separating the $\nu_e \to \nu_\tau$ signal from $\nu_e \to \nu_\mu$ and of measuring precisely the kinematics of the process under study. In this case the neutrino energy could also be reconstructed for $\nu_e \to \nu_\tau \to \tau \to \mu$ transitions. The sample of wrong-sign muons from the decay of wrong-sign taus will be distributed erroneously in neutrino energy bins, thus contaminating the wrong-sign muon sample by events in which the parent neutrino

energy reconstruction is biased.

Consider a ν_τ of energy E_{ν_τ}, interacting in MIND and producing a wrong-sign τ of energy E_τ together with a hadronic jet of energy E_h. After τ-decay, $E_{\nu_\tau} = E_\tau + E_h = (E_\mu + E_{miss}) + E_h$, where E_{miss} is the missing energy carried away by the two neutrinos in the τ-decay. Experimentally, we observe the secondary muon and a hadronic jet, a signal essentially indistinguishable from that of a wrong-sign muon from CC ν_μ interactions. However, in the latter case, the addition of the (primary) muon energy E_μ and of the hadronic jet energy E_h results in the correct parent ν_μ energy, $E_{\nu_\mu} = E_\mu + E_h$. On the other hand, in the former case the addition of the (secondary) muon energy E_μ and of the hadronic jet energy E_h results in the wrongly reconstructed fake neutrino energy $E_{fake} = E_\mu + E_h = E_{\nu_\tau} - E_{miss}$. If we divide the τ three-body decay energy distribution in discrete fake neutrino energy bins, we find that for a monochromatic ν_τ beam of energy E_{ν_τ}, the final muon will be assigned to a given fake neutrino energy bin of energy $E_{\mu,j}$ with probability $V_j(E_{\nu_\tau})$, where $j = 1, \ldots, N^\mu_{bin}$. We can compute the distribution of ν_τ of a given energy E_{ν_τ} and divide them into ν_τ energy bins of energy $E_{\tau,i}$, where $i = 1, \ldots, N^\tau_{bin}$. The ensemble of the probability vectors $V_j(E_{\tau.i})$, for i and j running over all the ν_μ and ν_τ energy bins, is represented by the migration matrix M_{ij}. After having computed M_{ij}, the number of total wrong-sign muons in a given neutrino energy bin is given by:

$$N_i(\theta_{13}, \delta) = \sum_{i=1,N_{bin}} \left[N^\mu_i(\theta_{13}, \delta) + \sum_{j=1,N_{bin}} M_{ij} N^\tau_j(\theta_{13}, \delta) \right] . \tag{4}$$

The resulting fraction of wrong sign muons which stem from τ-decay is found to be as large as 60% in the energy range from $5 - 10\,\mathrm{GeV}$ but only a few percent for higher energies.

If not properly treated, the τ-contamination introduces an intolerable systematic error, in particular for large θ_{13}. Figure 17 (left), from reference [139], shows that the test of the hypothesis that simulated data including the τ-contamination, $N_i(\theta_{13}, \delta)$, can be fitted using the direct wrong-sign muon distribution, $N^\mu_i(\theta_{13}, \delta)$, fails at more than 3σ for $\theta_{13} \geq 5^\circ$. For $\theta_{13} \in [1^\circ, 5^\circ]$, even if $N^\mu_i(\theta_{13}, \delta)$ can fit the τ-contaminated data (albeit with a relatively poor χ^2), the error in the joint measurement of θ_{13} and δ can be so large that it could actually obviate the use of the Neutrino Factory as a precision facility (see, again, reference [139] for a detailed analysis of the errors introduced by a wrong treatment of the τ-contamination). On the other hand, once M_{ij} has been statistically computed, experimental data distributed in reconstructed neutrino energy bins, can be fitted using the complete wrong-sign muons distribution $N_i(\theta_{13}, \delta)$, properly taking into account the τ-contamination of the golden-muon sample. Using this procedure, the systematic error introduced by the muons from taus is completely removed. The remaining error is the statistical error of the migration matrix elements, which is under control.

It is worth noting that the τ-contamination of the wrong-sign muon sample, once properly treated, does not worsen the measurement of θ_{13} and δ, as was the case for the measurement of the atmospheric parameters. This is illustrated in figure 17 (right) where the CP fraction achieved using the golden-muon sample only and the total wrong-sign muon sample are compared. It can be seen that the only difference between the two lines is a slight displacement of the wiggles at $\sin^2 2\theta_{13} \sim 10^{-3}$ ($\theta_{13} \sim 1^\circ$). The wiggles are a consequence of the loss of sensitivity to CP violation introduced by the so-called "sign clones" for negative δ (a phenomenon known as π-transit, [127]). Since the location of the clones in the two samples differs, a small difference in the location of the wiggles is found when the two lines are compared. We can see, however, that once the τ-contamination is properly treated, no (significant)

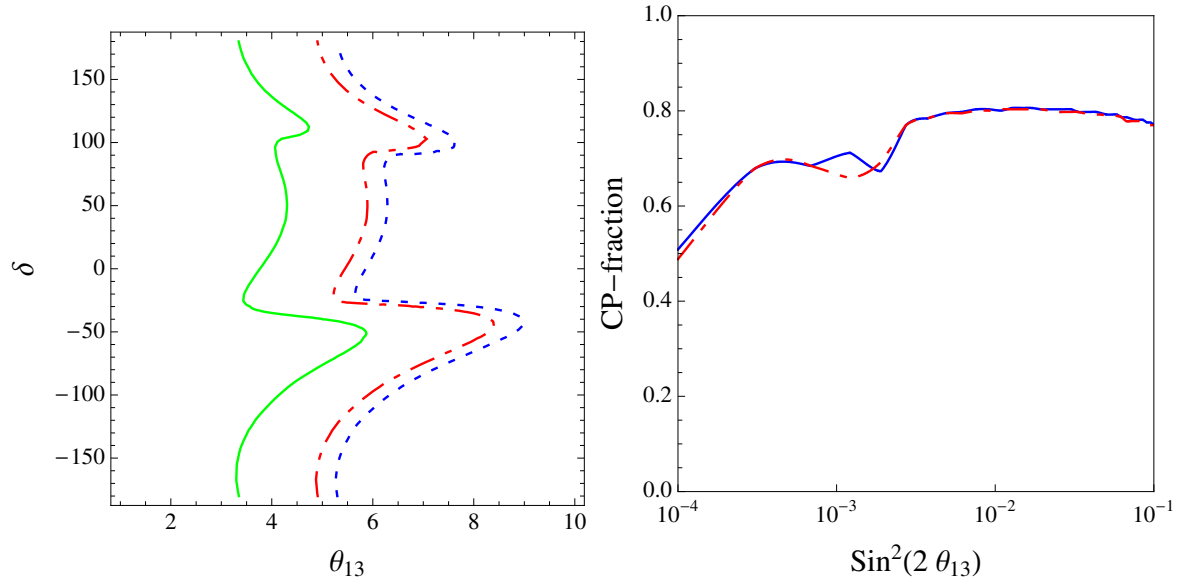

Figure 17. Left: Test of the hypothesis that a simulation of the data that includes the effect of the τ-contamination at $L = 4\,000$ km can be fitted with the golden muon theoretical distribution. In the regions to the right of the contour lines, the hypothesis can be rejected at 1, 2 or 3σ (from left to right), assuming the goodness-of-fit statistics follows the χ^2 distribution with $n = 8$ dof. From reference [139]. Right: Comparison of the CP-fraction achievable at the IDS-NF baseline Neutrino Factory when the τ-contamination is correctly taken into account (dashed red line) with respect to the ideal one in which no muons from taus are considered (solid blue line).

loss in the CP-fraction is found anywhere else. This result differs from that shown in section 1.4.4.1. The main difference between the two channels is the statistical weight of the two signals. In the case of the θ_{23}-measurement through $\nu_\mu \to \nu_\mu$ disappearance, the right-sign muon direct sample is represented by tens of thousands of events, and the corresponding τ-contamination by $\sim 10\%$ of the signal. This is still a huge number of events, and it affects the precision with which we are able to measure θ_{23} and its deviation from maximality. On the other hand, when dealing with the golden channel measurement of θ_{13} and δ, the signal is represented by tens of events. Once the problem of the wrong assignment of muons from taus into reconstructed energy bin is solved by means of the migration matrix approach, the residual statistical impact of the τ-contamination for $\theta_{13} \leq 10^\circ$ is small.

1.5. Comparison with the physics performance of alternative experiments

A Neutrino Factory is not the only facility that has been proposed for the study of neutrino oscillations with great accuracy. Several other approaches, in particular beta-beams and super-beams, are currently being examined. Given the existence of several options, each of which comes with its own advantages and disadvantages, a critical comparison of the various facilities is called for. However, this report is about the feasibility and physics reach of the Neutrino Factory and, therefore, we feel that we have neither the space, the expertise, nor a mandate to provide an in-depth critical comparison. At the same time, it would be a disservice to the reader to shun the comparison altogether and thus,

we will present a comparison of the physics sensitivities only, which in turn are based on the outcome of studies of the facilities that are presently under way. All results in this section have been computed using the GLoBES software [111, 112].

1.5.1. Super-Beams

There are two large super-beam studies under way, one is for the SPL at CERN as part of EUROnu and the other is in the context of LBNE in the US. Both experiments will employ a horn-focused pion beam as the neutrino source and use baselines of 130 km (SPL) and 1 300 km (LBNE). In both experiments the primary proton-beam power will be at the MW level, however the proton energies will be very different, 4 GeV for the SPL and 120 GeV for LBNE. The SPL will use a water Cherenkov detector, with 440 kTon fiducial volume [140]; the detector performance is taken from references [141, 142]. Note that the SPL beam has been studied in quite some detail as part of EUROnu and there it was found that the neutrino fluxes can be optimised by changing the target and horn configuration [140], which improves the anticipated performance compared with that obtained in earlier studies.

LBNE will use either a water Cherenkov detector or a liquid-Argon detector with a 6-times smaller mass. It has been shown [99, 143] that physics-wise the two detector configurations are equivalent and therefore we will consider only the water-Cherenkov option. The default fiducial volume for the water Cherenkov detector in LBNE is 200 kTon and the baseline is from Fermilab to DUSEL, which is 1 300 km. The implementation of both the beam spectrum and detector performance follows reference [99]. We also consider a possible luminosity upgrade as provided by Project X.

1.5.2. Beta-beams

Beta-beams have been proposed in reference [144] and the idea is to exploit the β-decay of relatively short-lived radio-isotopes with half-lives of around 1 s which are ionised, accelerated to relativistic speeds and put into a storage ring, where they eventually decay. As a result of the high Lorenz $\gamma \simeq 50 - 500$, the (anti-)neutrino emission will be directed in the forward direction with an opening angle of $1/\gamma$. Neutrino beams can be produced using β^+ emitters. The maximum neutrino energy that is available, $E_{\rm max}$, is given by the end-point of the β-spectrum, Q_β, and the Lorenz boost, $E_{\rm max} = \gamma Q_\beta$. Given the fact that $2Q_\beta$ lies in the range of $1 - 10\,{\rm MeV}$, it follows that neutrino beam energies in the range from $0.1 - 5\,{\rm GeV}$ are possible. Currently, four isotopes are being studied: ^{18}Ne and ^{8}B for neutrino production and ^{6}He and ^{8}Li for anti-neutrino production; their properties are listed in table II. Clearly, the ions with a large Q_β will yield higher neutrino energies for a given Lorenz γ, but for a given energy they will yield less flux since the flux is proportional to γ^{-2}. All of these isotopes are too short-lived to have significant natural abundance and thus they need to be produced artificially. It turns out that the achievable production rates ultimately limit the luminosity of these kinds of neutrino beams. The intensities considered to be the goals are 1.1×10^{18} ions per year for ^{18}Ne and 2.9×10^{18} ions per year for ^{6}He [145]. For some time it was not quite clear whether these ion intensities are feasible, but recent developments within EUROnu indicate that, for ^{18}Ne, the required intensity can be achieved [146].

In the phenomenological literature it has been pointed out that large Lorenz boosts, around 350,

Table II. A/Z, half-life and end-point energies for two β^+-emitters (^{18}Ne and ^{8}B) and two β^--emitters (^{6}He and ^{8}Li).Table adapted from [147].

Element	A/Z	$T_{1/2}$ (s)	Q_β [MeV]	Decay Fraction
^{18}Ne	1.8	1.67	3.41	92.1%
^{8}B	1.6	0.77	13.92	100%
^{6}He	3.0	0.81	3.51	100%
^{8}Li	2.7	0.83	12.96	100%

possibly combining data from all four ion species, can lead to physics sensitivities which are on par with that of the Neutrino Factory [148–156]. However, there are currently no attempts to perform a feasibility study of any of these so called "high-γ" beta-beams. As a consequence, it it is not possible to assess the cost and technological risks associated with the high-γ options. Therefore, we will not consider them here and instead will focus on those options which are currently studied, at a machine level, within the EUROnu Beta-Beam work package; i.e., only the $\gamma = 100$ option will be considered. For this reason, we also do not consider ^{8}Li or ^{8}B because they require higher values of γ to be useful, see, for example, [156].

1.5.3. Comparison

It is possible that a next-generation super-beam (or combined super-beam/beta-beam) experiment could be constructed on the same timescale as the Neutrino Factory, or might even start earlier. Possible candidates are the LBNE and SPL experiments shown in figure 18 with their θ_{13}, CP violation, and mass hierarchy discovery potentials.

If $\sin^2 2\theta_{13} \gtrsim 0.01$ is discovered before the RDR is prepared, CP violation can be measured at the 3σ CL, depending on the option and exact value of $\sin^2 2\theta_{13}$, for between 60% and 75% of all values of δ. For the current hint $\sin^2 2\theta_{13} = 0.06$, a discovery can be made for up to 70% of all possible values of δ. The mass hierarchy discovery is, in this case, guaranteed by the LBNE option; for the alternatives the discovery reach strongly depends on $\sin^2 2\theta_{13}$ in this range. For comparison, in figure 18 the 3σ curves from the existing experiments in 2025 are also shown (curves "2025"). As we have demonstrated, the Neutrino Factory can do significantly better for the CP violation discovery, and, of course, also measure the mass hierarchy in that range. Very importantly, the CP fraction in figure 18 can be related to the precision measurement of δ for the CP conserving values. Therefore, the higher the CP fraction, the higher the precision. In either case, a Neutrino Factory will provide a more precise measurement than any other experiment, especially if a single baseline configuration, optimised for the, by then known, value of $\sin^2 2\theta_{13}$ were employed.

If the data indicate that $\sin^2 2\theta_{13} \lesssim 0.01$ at the time the RDR is in preparation, alternatives to the Neutrino Factory have a discovery potential for $\sin^2 2\theta_{13}$ significantly exceeding the existing experiments, in some cases by up to an order of magnitude. Depending on $\sin^2 2\theta_{13}$, CP violation may be discovered for up to 65% of possible values of δ (SPL & LBNE). The mass hierarchy can only be

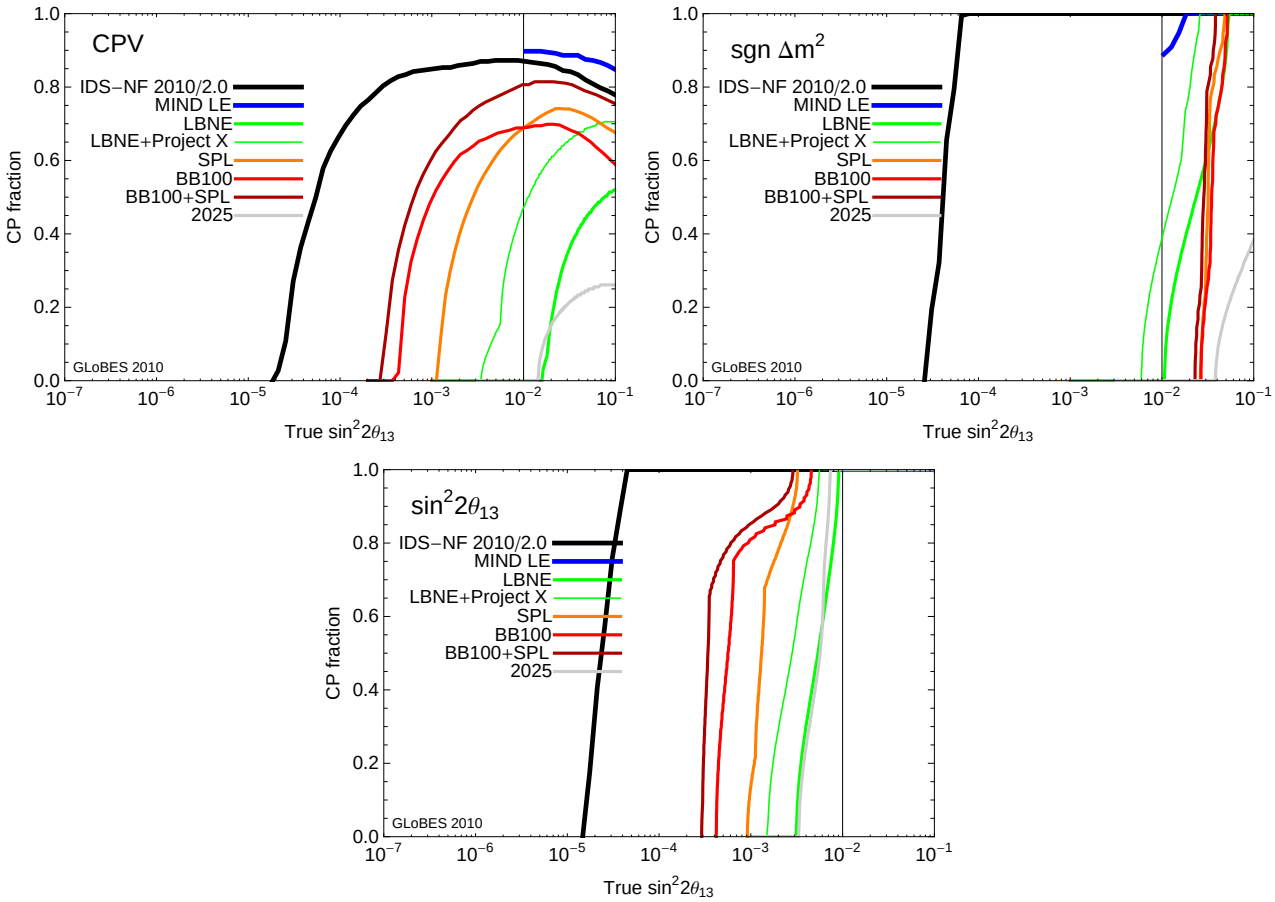

Figure 18. Comparison of the physics reach of different future facilities for the discovery of CP violation (top left panel), the mass hierarchy (top right panel), and $\sin^2 2\theta_{13}$ bottom panel. The sensitivities of the SPL super-beam are taken from [142]. The beta-beam curves are also taken from [142], however with the ion intensities reduced to the EURISOL values [145]. Curves for LBNE are taken from [143] and correspond to the results in [99]. The θ_{13} sensitivities expected from current experiments are shown as vertical lines [98]. MIND LE is a single-baseline Neutrino Factory optimised for large $\sin^2 2\theta_{13} > 0.01$, see also section 1.4.1.

accessed by LBNE in a small fraction of the parameter space. The CP violation plot demonstrates that these experiments have limited potential for $\sin^2 2\theta_{13} \lesssim 0.01$, since the small data samples that can be expected will cut off the sensitivity at some value of $\sin^2 2\theta_{13}$. Figure 18 shows that the Neutrino Factory can do significantly better. It is also interesting from figure 18 that the alternatives are either optimised for the CP violation (SPL/BB100) or the mass hierarchy discovery (LBNE). No option other than the Neutrino Factory can do all these measurements equally well.

In summary, even if $\theta_{13} > 0$ is discovered by the generation of experiments currently under construction, it is likely that the discovery of CP violation and precision measurement of the CP phase require data from advanced experiments, like the Neutrino Factory. If θ_{13} is not discovered by the generation of experiments presently under construction, there will be no further information on CP

violation and mass hierarchy from these experiments, and an advanced experiment is mandatory to make further progress. In this case, the super-beam and beta-beam based alternatives will be strongly limited by the size of the data sample that can be collected and only the Neutrino Factory provides a robust sensitivity to all observables throughout the accessible parameter space.

1.6. Non-standard neutrino interactions

Since the Neutrino Factory is the most ambitious concept available for advancing our knowledge of lepton flavour physics, the search for new and exotic phenomena in the lepton sector will be an important part of its physics program. In this section, we will outline the results that can be obtained on non-standard neutrino interactions, non-unitarity in the lepton mixing matrix, and sterile-neutrino scenarios.

1.6.1. Effective theory of new physics in the neutrino sector

Without any knowledge of possible high-energy extensions of the Standard Model, an effective theory approach is well-suited to parameterising the effects of such extensions on neutrino-oscillation experiments. Non-standard interactions (NSI) mediated by effective higher-dimensional operators can lead to additional, possibly flavour-violating, contributions to the MSW potential that neutrinos experience when travelling through matter, and they can affect the neutrino production and detection processes [157, 158]. The neutrino oscillation probability in the presence of NSI can be written:

$$P(\nu_\alpha^s \to \nu_\beta^d) = \left| \left[\left(1+\varepsilon^d\right)^T \, e^{-iH_{\rm NSI}L} \, \left(1+\varepsilon^s\right)^T \right]_{\beta\alpha} \right|^2 , \tag{5}$$

with the Hamiltonian:

$$H_{\rm NSI} = U \begin{pmatrix} 0 & & \\ & \Delta m^2_{21}/2E & \\ & & \Delta m^2_{31}/2E \end{pmatrix} U^\dagger + V_{\rm MSW}(\mathbb{1}+\varepsilon^m) \, . \tag{6}$$

Here, U is the lepton-mixing matrix, $V_{\rm MSW}$ is the Mikheyev-Smirnov-Wolfenstein (MSW) potential corresponding to the matter traversed by the neutrinos, and ε^d, ε^s, and ε^m are complex 3×3 matrices parameterising the relative strength of the non-standard effects compared to Standard Model weak interactions. If $\varepsilon^s_{\alpha\beta}$ is non-zero, neutrinos produced in interactions with charged leptons of flavour α will have a non-standard component of flavour β. If $\varepsilon^d_{\beta\alpha} \neq 0$, neutrinos of flavour β can produce a charged lepton of flavour α in the detector. The Hermitian matrix ε^m is responsible for non-standard matter effects. Note that in most concrete models, the elements of ε^d, ε^s, and ε^m are not all independent.

Model-independent experimental constraints on the $\varepsilon^{s,d,m}_{\alpha\beta}$ range from 10^{-4} to $\mathcal{O}(1)$ [16, 159–162], while model-dependent limits are often much tighter [163, 164] since, in concrete models, NSI in the neutrino sector are usually accompanied by non-standard effects in the charged-lepton sector that are constrained, for example, by rare decay searches or measurements of the weak mixing angle.

If NSI are induced by dimension-6 operators that arise when heavy mediator fields are integrated out, we expect $\varepsilon^{s,d,m}_{\alpha\beta} \sim g^2 M_W^2 / g^2_{\rm NSI} M^2_{\rm NSI}$, where g is the weak gauge coupling, $g_{\rm NSI}$ is the coupling

constant of the heavy mediators, and $M_{\rm NSI}$ is their mass. If $g_{\rm NSI} \sim g$ and $M_{\rm NSI} \sim$ few $\times$ 100 GeV, we naively expect $\varepsilon^{s,d,m}_{\alpha\beta} \sim 0.01$. Most dimension-6 operators of this magnitude are, however, already ruled out by several orders of magnitude by constraints from the charged-lepton sector.

Such constraints are avoided if NSI are generated by dimension-8 operators such as:

$$(\bar{L}_\alpha H)\gamma^\rho(\bar{H}^\dagger L_\beta)(\bar{E}_\gamma\gamma_\rho E_\delta)\,, \tag{7}$$

where L, H, and E are a left-handed lepton field, the Standard Model Higgs field, and a right-handed charged-lepton field, respectively, and α, β, γ, δ are flavour indices. When H acquires a non-zero vacuum expectation value v, this operator leads to $SU(2)$-violating four-fermion contact interactions, so that NSI in the neutrino sector can be generated without inducing phenomenologically-problematic four-charged-lepton couplings or other harmful effects. On the other hand, this procedure leads to an additional suppression of order $v2/M2$ and requires some cancellation conditions at tree level [164]. Larger non-standard effects could be generated in theories involving *light* mediators ($\ll M_W$) with very small couplings. Models containing light new particles have recently received a lot of interest in the context of Dark Matter searches (see for example references [165–170]), but possible effects in the neutrino sector are less well explored in the literature. For very light mediators, processes with small or no momentum transfer, such as coherent forward scattering leading to non-standard neutrino matter effects, will be enhanced compared to processes with large momentum transfer from which most NSI constraints are derived.

Finally, there are more exotic scenarios of new interactions in the neutrino sector that could be tested at the Neutrino Factory. One example for such a scenario is long-range leptonic forces [171–176], which are phenomenologically equivalent to NSI even though the theoretical motivation is very different.

1.6.2. Neutrino Factory sensitivities to non-standard interactions

The far detectors of the Neutrino Factory will offer a unique opportunity to constrain or measure the elements of ε^m, corresponding to non-standard matter effects. This is shown in figure 19 under the assumption that only one of the $\varepsilon^m_{\alpha\beta}$ is non-zero at a time. We see that existing model-independent constraints can be significantly improved, and that the Neutrino Factory would begin to probe the parameter region $\varepsilon^m_{\alpha\beta} \lesssim 0.01$ that is most interesting from the model-building point of view. We also compare the sensitivity to standard oscillation observables (θ_{13}, CP violation, MH) in a conventional fit to the sensitivities that may be achieved if one NSI parameter ($\epsilon^m_{e\tau}$) is allowed to be non-zero. It turns out that allowing for the possibility of non-standard effects reduces the sensitivity to standard oscillation observables.

For NSI affecting the neutrino production and detection mechanisms, even tighter constraints can often be obtained from the Neutrino Factory *near* detector. To demonstrate this, we consider non-standard contributions to the charged-current neutrino production and detection processes [158]. New contributions to ν_e and ν_μ production or detection are difficult to observe because they are degenerate with systematic biases in the neutrino cross section calculations or in the normalisation of the beam flux. A near detector with charge identification capabilities, however, would be sensitive to flavour-violating processes such as $\mu \to e\nu_e\nu_e$, $\mu \to e\nu_\mu\nu_\mu$, $\nu_e + N \to \mu + X$, and $\nu_\mu + N \to e + X$ [129].

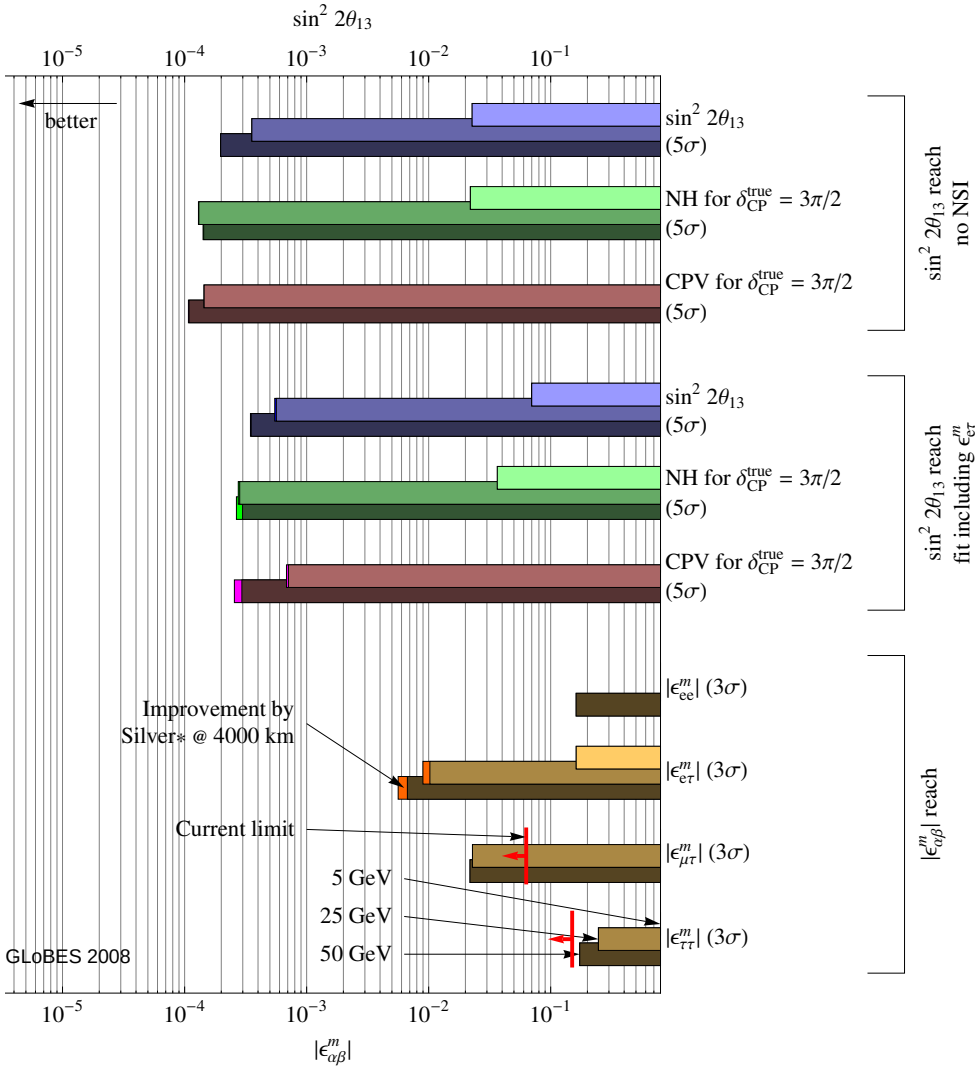

Figure 19. Summary of the Neutrino Factory performance with and without the presence of non-standard interactions. The IDS-NF setup with two 50 kTon magnetised iron detectors (MIND) at baselines of 4 000 km and 7 500 km was used, and the "true" parameter values $\sin^2 2\theta_{13} = 0.001$ and $\delta_{\rm CP} = 3\pi/2$ were assumed (the detector mass used differs from the present IDS-NF baseline). The plot shows that sensitivities are poor at $E_\mu = 5$ GeV (light bars) due to the high energy threshold of the MIND detector, but increase dramatically at $E_\mu = 25$ GeV (medium light bars). The benefit from increasing E_μ further to 50 GeV (dark bars) is only marginal, as is the benefit from including a silver channel ν_τ detector at 4 000 km ("Silver*"). Current model-independent limits on NSI are taken from [16, 160, 162]. No strong limits exist for ϵ^m_{ee} and $\epsilon^m_{e\tau}$. Figure taken from reference [109].

Another interesting possibility is the construction of a detector sensitive to ν_τ to look for processes such as $\mu \to e\nu_\alpha\nu_\tau$ or $\nu_\alpha + N \to \tau + X$ for $\alpha = e, \mu$. This possibility has been considered in references [129, 177–179]. In table III, we summarise some expected bounds on CC NSI operators for the Neutrino Factory with and without a near detector capable of ν_τ detection. We see that some bounds can be improved by almost two orders of magnitude compared to their current values, and that the Neutrino

Table III. Expected sensitivities and current bounds for the coupling constants (relative to Standard Model weak interactions) of some NSI operators relevant to the Neutrino Factory experiment. Numbers in parenthesis are for a model with charged-singlet scalar mediation, while numbers without parenthesis are model-independent.

	Sensitivity w/o ν_τ ND	Sensitivity w/ ν_τ ND	Current bound [129, 163]
$\epsilon^s_{e\tau}$ $(\mu \to e\nu_\mu\nu_\tau)$	$4 \cdot 10^{-3}$	$7 \cdot 10^{-4}$	$3.2 \cdot 10^{-2}$ $(1.8 \cdot 10^{-3})$
$\epsilon^s_{\mu\tau}$ $(\mu \to e\nu_e\nu_\tau)$	$4 \cdot 10^{-1}$ $(3 \cdot 10^{-3})$	$6 \cdot 10^{-4}$ $(6 \cdot 10^{-4})$	$3.2 \cdot 10^{-2}$ $(1.9 \cdot 10^{-3})$

Factory would probe the parameter region expected if NSI are induced by $\mathcal{O}$(TeV) mediators.

1.6.3. Non-standard interactions in a low-energy Neutrino Factory

Let us now comment on the NSI sensitivity of a low-energy Neutrino Factory (LENF). We have analysed the LENF setup defined in [180], using the MonteCUBES (Monte Carlo Utility Based Experiment Simulator) software package [181, 182]. The LENF has leading order sensitivity to $\varepsilon^m_{e\mu}$ and $\varepsilon^m_{e\tau}$ from the golden and platinum channels. We have found that the sensitivity is limited by the correlations between the standard oscillation and non-standard parameters, and thus that increasing statistics does *not* increase the sensitivity of the setup, in direct contrast to standard oscillation measurements. Instead, it is necessary to include information from a second baseline, or from a complementary channel such as the platinum channel. With the performance of the platinum channel as assumed in [180] (47% efficiency, 10^{-2} background), the platinum channel has the greatest impact for *large* values of θ_{13}. However, we have found that a platinum channel with hypothetically perfect performance ($\sim 100\%$ efficiency, negligible background) has an effect even for small values of θ_{13}, indicating that there is a critical signal-to-background threshold that must be overcome in order for it to become effective.

In figure 20 we show how the platinum channel helps to maintain sensitivity to the standard oscillation parameters, when marginalisation over all NSI parameters, as well as the oscillation parameters is performed: we show the 68%, 90% and 95% regions obtained in the $\theta_{13} - \delta$ plane when only the golden channel and $\nu_\mu/\bar{\nu}_\mu$ disappearance channels are used ('Scenario 1' - dotted blue lines), and when combined with the platinum channel ('Scenario 2' - solid red lines). The left-hand figure shows the results when *only* the standard oscillation parameters are marginalised over, and the right-hand figure the results when all oscillation *and* NSI parameters are taken into account. This shows that the sensitivity of Scenario 1 to θ_{13} and δ is diminished by taking into account the possibility of non-zero NSIs, but that Scenario 2 is almost unaffected—the addition of the platinum channel makes the setup more robust.

For measuring the NSI parameters themselves, the LENF running for 5 years per polarity (i.e., 10 years running are assumed, the same assumption that has been made in evaluating the performance of the other long-baseline experiments) has sensitivity to $\varepsilon^m_{e\mu}$ and $\varepsilon^m_{e\tau}$ down to $\sim 10^{-2}$ (figure 21). If the running time is doubled, no significant improvement is gained, indicating that the limiting factor is not statistics. These bounds are a significant improvement upon the current bounds [161, 162], but

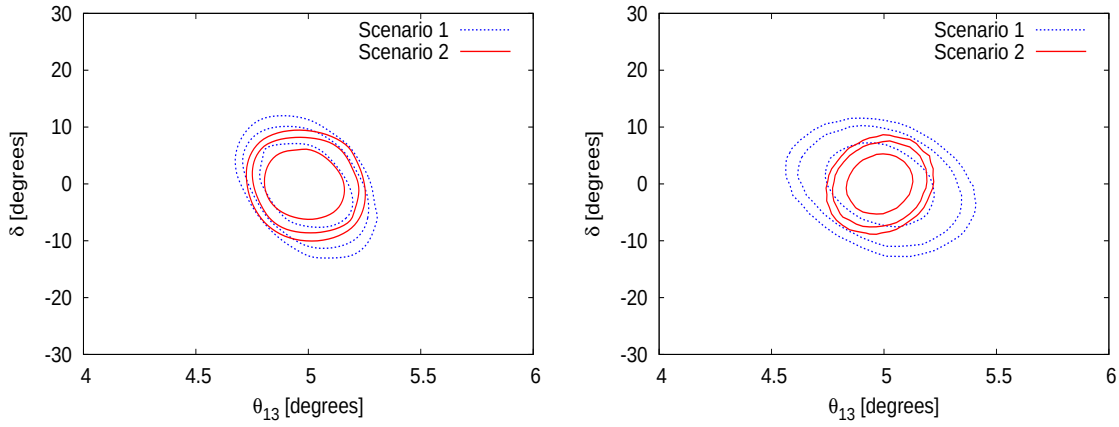

Figure 20. 68%, 90% and 95% regions in the $\theta_{13} - \delta$ plane when marginalising over standard oscillation parameters only (left) and when marginalising over all standard oscillation and NSI parameters (right), for true values of $\theta_{13} = 5°$, $\delta = 0$ and $\varepsilon^m_{e\mu} = \varepsilon^m_{e\tau} = 0$. Scenario 1 is a LENF setup without platinum channel; Scenario 2 is the LENF with platinum channel. Figure taken from reference [180].

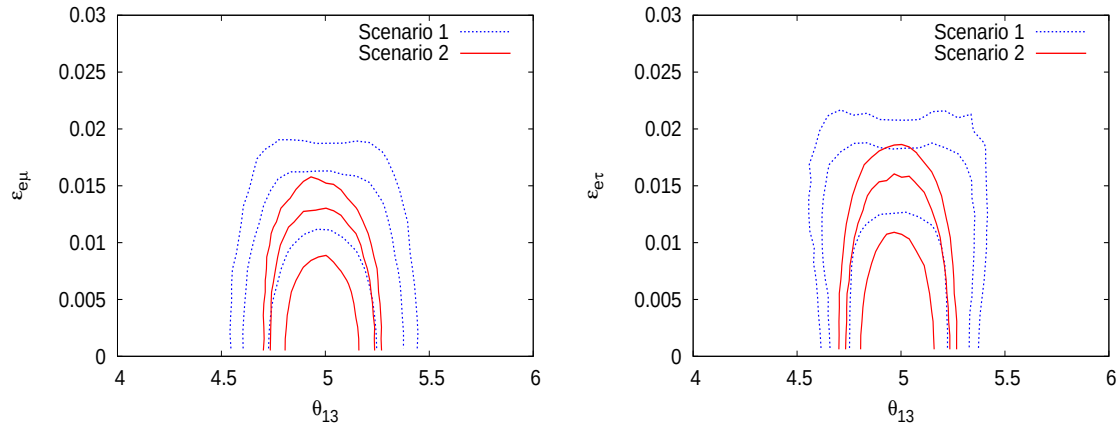

Figure 21. 68%, 90% and 95% regions in the $\theta_{13} - \varepsilon^m_{e\mu}$ (left) and $\theta_{13} - \varepsilon^m_{e\tau}$ (right) plane for $\theta_{13} = 5°$, $\delta = 0$, and $\varepsilon^m_{e\mu} = \varepsilon^m_{e\tau} = 0$. Figure taken from reference [180].

not as strong as those which the Neutrino Factory can obtain.

1.6.4. Non-unitarity of the leptonic mixing matrix

A non-unitary mixing matrix in the charged-current coupling of neutrinos and charged leptons is a general prediction of extensions of the Standard Model (SM) that include new fermion degrees of freedom that can mix with the SM leptons [183]. Indeed, the full mixing matrix including the extra degrees of freedom would thus be larger than the standard three-by-three matrix. While the full mixing matrix should be unitary, such a constraint does not apply to the 3×3 sub-matrix accessible

at low energies. In particular, many extensions of the SM that try to accommodate the evidence for neutrino masses and mixings from neutrino-oscillation experiments introduce such extra leptonic degrees of freedom. This is the case for example of the type-I and type-III seesaw models. The study of deviations from unitarity of the leptonic mixing matrix can therefore provide a tool to explore the origin of neutrino masses beyond the SM [184–188].

In a completely general way, the non-unitary leptonic mixing matrix N can be parametrised as the product of a Hermitian matrix, $1+\eta$, times a unitary matrix U [189]:

$$N = (1+\eta)U \ . \tag{8}$$

Such a modification of the SM charged-current interactions would affect lepton universality tests, the measurement of G_F from muon decay compared to other measurements, rare lepton decays and the invisible width of the Z, and strong constraints can be derived on the allowed size of η [163, 183, 190–192]: $\eta_{ee} < 2.0 \times 10^{-3}$, $\eta_{e\mu} < 5.9 \times 10^{-5}$, $\eta_{e\tau} < 1.6 \times 10^{-3}$, $\eta_{\mu\mu} < 8.2 \times 10^{-4}$, $\eta_{\mu\tau} < 1.0 \times 10^{-3}$ and $\eta_{\tau\tau} < 2.6 \times 10^{-3}$, at the 90 % CL. Up to order η effects, the matrix U can be identified with the PMNS matrix as extracted from experimental data without taking non-unitarity into account. Since η is much smaller than the experimental uncertainties on the PMNS matrix elements, the corrections are negligible.

The effects of a non-unitary mixing at the Neutrino Factory have been studied in references [177, 178, 189, 193, 194]. In particular, in [177] this study was performed in detail for a setup very similar to the IDS-NF baseline Neutrino Factory (muon energy 25 GeV, two 50 kt magnetised iron detectors at baselines of 4 000 km and 7 500 km) and considering simultaneously the effect of all extra non-unitarity parameters in the fit. To perform a fit in this high-dimensional parameter space, the Markov Chain Monte Carlo tool MonteCUBES, a plug-in for the widely used GLoBES software [111, 112], has been used. It was found that, given the very stringent present limits on the allowed deviations from unitarity, the Neutrino Factory could only improve constraints on the $\eta_{e\tau}$ and $\eta_{\mu\tau}$ elements of the matrix η. Indeed, it is easier to search for off diagonal elements since they imply lepton flavour violation and the present bounds on $\eta_{e\mu}$ from $\mu \to e\gamma$ are too strong to improve through measurements of neutrino oscillations. The sensitivity of the Neutrino Factory to these parameters could be significantly improved if a near detector capable of τ detection is included, since the zero-distance effects caused by the unitarity deviations could be tested.

In figure 22 the sensitivity limits on the parameters $\eta_{\tau\mu} = |\varepsilon_{\tau\mu}|e^{i\phi_{\tau\mu}}$ and $\eta_{\tau e} = |\varepsilon_{\tau e}|e^{i\phi_{\tau e}}$ are depicted. The different curves correspond to different sizes of the τ detector close to the muon storage ring; from left to right, 10 kTon, 1 kTon, 100 ton, no near detector. As can be seen, the sensitivity to the real part of $\eta_{\mu\tau}$ is remarkable, down to $\sim 5 \times 10^{-4}$ without the inclusion of any near detector. This stems from the fact that matter effects in the ν_μ disappearance channel depend linearly on this parameter. The inclusion of near detectors able to detect ν_τ appearance with increasing size improves also the sensitivity to the imaginary part of $\eta_{\mu\tau}$, since the zero-distance effect only depends on the modulus, but the sensitivity is not as good, reaching $\sim 10^{-3}$ for a 1 kTon detector, since the effect is second order. A larger detector would thus be required to improve over present limits. Regarding $\eta_{e\tau}$, the sensitivity of the Neutrino Factory in the absence of a near detector sensitive to τ production is much poorer, down to $\sim 2 \times 10^{-3}$ for some values of the phase. This mainly stems from second-order terms in the ν_μ appearance channel. The inclusion of near detectors to search for τ appearance again improves the sensitivity. However, as for the $\eta_{\mu\tau}$ element, detectors larger than 1 kTon would be needed to

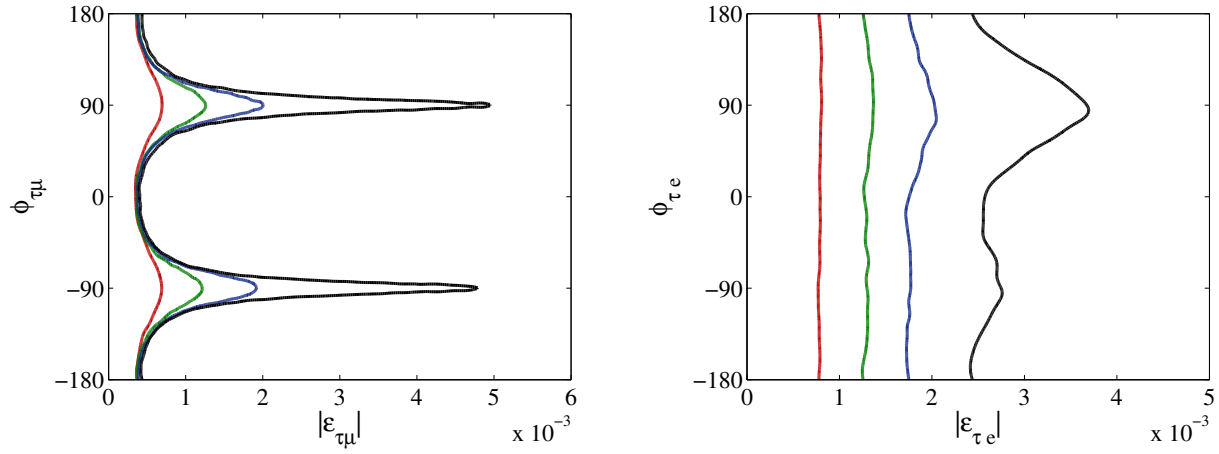

Figure 22. The 90 % confidence level sensitivity of the IDS Neutrino Factory to the unitarity violating parameters $\eta_{\tau\mu} = |\varepsilon_{\tau\mu}|e^{i\phi_{\tau\mu}}$ (left) and $\eta_{\tau e} = |\varepsilon_{\tau e}|e^{i\phi_{\tau e}}$ (right). The different curves correspond to different sizes of the near τ detector, from left to right, 10 kTon, 1 kTon, 100 ton, no near detector. Figure taken from reference [177].

improve over present bounds.

1.6.5. Discovery reach for sterile neutrinos

Sterile neutrinos (Standard Model singlet fermions) are a very common prediction in many models of new physics and, if they are light and mix with the three standard neutrinos, it is possible to search for them at neutrino oscillation experiments. Sterile neutrinos have received a lot of attention in the context of seemingly anomalous results from the LSND and MiniBooNE experiments [66, 67]. Here, we will discuss the discovery reach for sterile neutrinos at the Neutrino Factory. We consider the simplest scenario in which only one sterile neutrino is added to the three active neutrinos of the Standard Model in the so-called 3+1 scheme, which recovers the standard picture in the case of small active-sterile mixings. For the sake of simplicity, we focus only on the scheme where the fourth state is the heaviest and the normal hierarchy is assumed in the standard sector.

1.6.5.1. Theoretical formalism/notation

The numerical results on the discovery reach can be understood from the analytical expressions of the transition probabilities. Instead of using a parametrisation-independent approach, where all the probabilities are directly expressed in terms of matrix elements of the 4×4 unitary mixing matrix U, we rely on a particular parametrisation which allows the standard PMNS matrix to be recovered for small "new" mixing angles:

$$U = R_{34}(\theta_{34},\, 0)\; R_{24}(\theta_{24},\, 0)\; R_{14}(\theta_{14},\, 0)\; R_{23}(\theta_{23},\, \delta_3)\; R_{13}(\theta_{13},\, \delta_2)\; R_{12}(\theta_{12},\, \delta_1)\,, \tag{9}$$

where $R_{ij}(\theta_{ij},\ \delta_l)$ are the complex rotation matrices in the ij-plane. In the short-baseline limit $|\Delta_{41}| = \Delta m^2_{41} L/4E \sim \mathcal{O}(1) \gg |\Delta_{31}|$, the matter effects can be safely ignored, and the relevant probabilities read:

$$\mathcal{P}_{e\mu} = \mathcal{P}_{\mu e} = 4c^2_{14}s^2_{14}s^2_{24}\sin^2\Delta_{41}\,; \tag{10}$$

$$\mathcal{P}_{ee} = 1 - \sin^2(2\theta_{14})\sin^2\Delta_{41}\,; \tag{11}$$

$$\mathcal{P}_{\mu\tau} = 4c^4_{14}c^2_{24}s^2_{24}s^2_{34}\sin^2\Delta_{41}\,; \text{and} \tag{12}$$

$$\mathcal{P}_{\mu\mu} = 1 - c^2_{14}s^2_{24}\left[3 + 2c^2_{14}\cos(2\theta_{24}) - \cos(2\theta_{14})\right]\sin^2\Delta_{41}\,; \tag{13}$$

where we used the short-hand notation $\Delta_{ij} = \Delta m^2_{ij} L/4E$. From these probabilities we can see that θ_{24} can be measured by $\mathcal{P}_{\mu\mu}$ and θ_{14} by $\mathcal{P}_{ee}$. On the other hand, θ_{34} only shows up in combination with the other small mixing angles. For long baselines, some of the relevant features of the probability transitions can be well understood using simple perturbative expansions: for $\Delta_{31} = \mathcal{O}(1) \ll \Delta_{41}$ and up to the second order in $s_{13}, s_{14}, s_{24}, s_{34}, \hat{s}_{23} = \sin\theta_{23} - \frac{1}{\sqrt{2}}$, and considering Δ_{21} as small as s^2_{ij}, we obtain:

$$\begin{aligned}
\mathcal{P}_{\mu\mu} \;=\;& \cos^2(\Delta_{31})(1 - 2s^2_{24}) + 8\hat{s}^2_{23}\sin^2(\Delta_{31}) + c^2_{12}\Delta_{12}\sin(2\Delta_{31}) + \\
& 2s_{24}s_{34}\cos\delta_3\Delta_n\sin(2\Delta_{31}) - \\
& 2s^2_{13}\Delta_{31}\cos(\Delta_{31})\,\frac{(\Delta_{31}-\Delta_e)\Delta_e\sin(\Delta_{31}) - \Delta_{31}\sin(\Delta_{31}-\Delta_e)\sin(\Delta_e)}{(\Delta_{31}-\Delta_e)^2}\,; \textit{and}
\end{aligned} \tag{14}$$

$$\begin{aligned}
\mathcal{P}_{\mu\tau} \;=\;& \sin^2(\Delta_{31})(1 - 8\hat{s}^2_{23} - s^2_{24} - s^2_{34}) - c^2_{12}\Delta_{12}\sin(2\Delta_{31}) - \\
& s_{24}s_{34}\sin(2\Delta_{31})\left[2\Delta_n\cos\delta_3 - \sin\delta_3\right] - \\
& s^2_{13}\Delta_{31}\sin\Delta_{31}\,\frac{\Delta_{31}\left\{\sin(\Delta_{31}-\Delta_e) + \sin(\Delta_e)\right\} - 2(\Delta_{31}-\Delta_e)\Delta_e\cos(\Delta_{31})}{(\Delta_{31}-\Delta_e)^2}\,;
\end{aligned} \tag{15}$$

from which we learn that with long baselines, θ_{24} is best accessed via $\mathcal{P}_{\mu\mu}$ with the first term proportional to $\cos^2(\Delta_{13})$. The leading sensitivity to θ_{34} can be expected from $\mathcal{P}_{\mu\tau}$ (the *discovery channel* as introduced in [195]). Notice also the dependence on the phase δ_3 in both probabilities, which makes them useful to check whether other sources of CP violation beside the standard one (δ_2 in our parametrisation) can be tested at the Neutrino Factory.

1.6.5.2. Results for the IDS-NF baseline

We first discuss general constraints on the new mixing angles θ_{14}, θ_{24}, and θ_{34}, and on the additional mass squared difference Δm^2_{41} without any additional assumptions [196]. The oscillation channels considered, simulated with a modified version of the GLoBES software, are electron-to-muon neutrino oscillations (appearance channels) and muon-to-muon neutrino oscillations (disappearance channels) (see [196] for all details of the simulations). In addition to the IDS-NF baseline setup, we have also considered near detectors with a fiducial mass of 32 Ton and a distance of $d = 2$ km from the end of the decay straight, which corresponds to an effective baseline of 2.28 km. We show the resulting exclusion limits in the θ_{i4}—Δm^2_{41} planes in figure 23.

The main sensitivity is obtained at about $\Delta m^2_{41} \simeq 10\,\mathrm{eV}^2$, which comes from the distance chosen for the near detectors. Since the efficiencies for muon-neutrino detection are typically better than

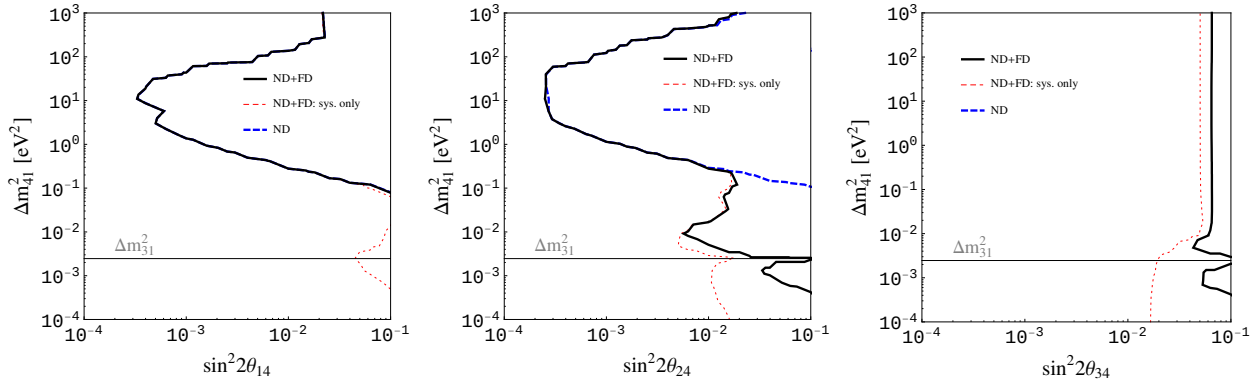

Figure 23. The exclusion limit at 90% CL (2 d.o.f) for $\sin^2 2\theta_{i4}$–$\Delta m^2_{41} (i = 1, 2, 3)$ (region on r.h.s. of curves excluded). We have assumed a Neutrino Factory with two 50 kTon magnetised iron far detectors (FD) at 4 000 km and 7 500 km, and with 32 Ton near detectors (ND) at ~ 2 km. The thick solid black curve is for the full ND + FD setup, while the dashed blue curve shows the impact of the near detectors separately. The thin red dotted curve illustrates how the sensitivity would improve if parameter correlations and degeneracies were absent, so that only statistical and systematical uncertainties would contribute. Figure taken from reference [196].

those for ν_e, the sensitivity to θ_{24} is slightly better than that to θ_{14} for our assumptions. As expected, there is no sensitivity to θ_{34} coming from the near detectors, because the ν_τ disappearance channel does not exist. For the effect at long baselines, it is useful to consider first the thin dashed curves in figure 23, which correspond to a simulation including only statistical and systematic errors, but no parameter correlations. In all three panels, the sensitivity changes as a function of Δm^2_{41} in the region where $\Delta m^2_{41} \sim \Delta m^2_{31}$. This is due to the fact that the Neutrino Factory is sensitive to the atmospheric oscillation frequency, whereas for $\Delta m^2_{41} \sim \Delta m^2_{21}$, no particular additional effects from the solar frequency can be found. As expected (see equation (14)), the main sensitivity is found for θ_{24}. However, there is also some sensitivity to θ_{14}, which vanishes after the marginalisation, and some sensitivity to θ_{34}, which is even present for $\Delta m^2_{41} = 0$ for systematics only. After we include parameter correlations by marginalising over all free oscillation parameters (thick solid curves), only the sensitivities to θ_{24} and θ_{34} remain in the Δm^2_{41} regions close to the atmospheric Δm^2_{31} and above, where the effects of Δm^2_{41} average out. Very interestingly, note that mixing-angle correlations destroy the sensitivities for $\Delta m^2_{41} = \Delta m^2_{31}$, where $m_4 = m_3$ and no additional Δm^2_{41} is observable, leading to small gaps (see horizontal lines). We have tested that the sensitivity to θ_{34} is a matter-potential-driven, statistics-limited, higher-order effect present in the muon-neutrino disappearance channels. We see from the three panels of figure 23 that it is not easy to disentangle the parameters for arbitrarily-massive sterile neutrinos. Parameter correlations lead to a pollution of the exclusion limit of a particular mixing angle with Δm^2_{41}. In addition, there is a competition between Δm^2_{41} and Δm^2_{31} at the long baseline. Near detectors, on the other hand, have very good sensitivities to θ_{14} and θ_{24} but cannot measure θ_{34}. Nevertheless, the absolute values of the sensitivities are quite impressive. Especially, θ_{24} can be very well constrained close to the atmospheric mass squared difference range. This indicates that sterile neutrino bounds in that range should be also obtainable from current

atmospheric neutrino oscillation experiments. Note that while one may expect some effect from $\mathcal{P}_{\mu\tau}$, we have tested the impact of ν_τ detectors at all baselines, and we have not found any improvement of the sensitivities. The reason is that the θ_{34} effect at the long baseline comes with the same energy dependence as the θ_{24} effect, which means that one cannot disentangle these, as discussed in section 1.6.5.1.

1.6.5.3. Optimisation issues and sensitivity of alternative setups

Although a similar analysis for CP-violating signals has not been carried out, the authors of reference [195] have presented a first analysis of the precision achievable in the simultaneous measurement of mixing angles and CP-violating phases (but see [194, 195, 197–203] for preliminary analyses). The experimental setup adopted there is a Neutrino Factory with 50 GeV stored muons, with two detectors of the hybrid-MIND type (a magnetised emulsion cloud chamber followed by a magnetised iron tracking calorimeter), located at $L = 3\,000$ km and 7 500 km. The ν_τ identification turns out to be of primary importance for the study of CP violation. As an example, for the simultaneous measurement of θ_{34} and δ_3 it has been shown that, using the ν_μ disappearance channel only, we are able to measure a non-vanishing δ_3 for values of θ_{34} above $\sin^2 2\theta_{34} \geq 0.4$ ($\theta_{34} \geq 18°$), and that the detector at $L = 3\,000$ km has no δ_3-sensitivity whatsoever. Adding the $\nu_\mu \to \nu_\tau$ discovery channel data, the $L = 3000$ km detector is no longer useless for the measurement of δ_3: spikes of δ_3-sensitivity for particular values of δ_3 can be observed, in some cases outperforming the far-detector results. However, it is in the combination of the two baselines that a dramatic improvement in the δ_3-discovery potential is achieved. When the $\nu_\mu \to \nu_\tau$ data are included, a non-vanishing δ_3 can be measured for values of θ_{34} as small as $\sin^2 2\theta_{34} = 0.06$ ($\theta_{34} = 7°$) for $\theta_{24} = 5°$ and $\sin^2 2\theta_{34} = 0.10$ ($\theta_{34} = 9°$) for $\theta_{24} = 3°$.

1.6.6. New physics summary

We have shown that, in addition to its unique capability of clarifying the flavour structure of neutrinos in the standard framework, the Neutrino Factory is also able to probe possible modifications of the oscillation pattern due to new physics. For example, it is very sensitive to non-standard matter effects, non-standard charged current interactions, non-unitarity in the leptonic mixing matrix, and sterile neutrinos. Especially for non-standard effects modifying the neutrino-production and detection processes and, for short-baseline oscillations into sterile neutrinos, a crucial role is played by the near detector. A very important aspect of new physics searches at a Neutrino Factory is the possibility to identify new sources of CP violation by studying their effect on the oscillation pattern. Many other electroweak precision experiments do not rely on interference phenomena and are therefore insensitive to CP-violating phase factors.

Quantitatively, we have shown that the constraints the Neutrino Factory can set on non-unitarity in the mixing matrix and on active-sterile neutrino mixing are comparable to or slightly better than the existing ones, while current model-independent bounds on non-standard neutrino interactions can be significantly improved. The Neutrino Factory could probe interactions 100 times weaker than Standard Model weak interactions, and the low energy option, though less sensitive, would still allow for improvements compared to existing bounds.

The NSI sensitivity of the Neutrino Factory naively translates into sensitivity to new physics scales of several 100 GeV, implying that the Neutrino Factory could provide measurements complementary to those expected from the LHC. On the other hand, in many concrete models, non-standard neutrino interactions large enough to be seen at the Neutrino Factory are already ruled out by other experiments probing correlated effects in the charged-lepton sector. Therefore, from a model-builder's point of view the new physics discovery reach of the Neutrino Factory is limited. However, as neutrinos have proved theoretical prejudices to be wrong in the past, the versatility and precision of a Neutrino Factory will still make new physics searches a worthwhile and integral part of its physics program.

1.7. Physics Summary

Neutrino oscillations and the associated large leptonic family mixing are arguably the first clear-cut discovery of physics beyond the Standard Model that is not obtained from cosmology. Large mixing angles came as a surprise and, while we have been able to formulate a plethora of theories which can accommodate these results, we are far from an actual understanding of mixing in particular and flavour in general. This lack of understanding is also exemplified by the non-observation of new physics in B-factories. In some models of neutrino mass generation, there is a connection between neutrinos and Grand Unification. In this class, called see-saw models, neutrinos can be ultimately responsible for the observed matter-antimatter asymmetry of the Universe. In the first place, this requires neutrinos themselves to violate matter-antimatter symmetry. The origin of flavour is one of the profound open questions in particle physics and studies of neutrino oscillations will play a crucial part in providing the data, which is necessary to make progress towards an answer.

The Neutrino Factory will be the ultimate neutrino physics facility and provides a superior performance for CP violation, the mass hierarchy and θ_{13}, see figure 18. At the same time, it provides the necessary precision to test rigorously the three-flavour oscillation framework and thus, also has the potential to discover new physics. The IDS-NF baseline configuration for the Neutrino Factory consists of one 100 kTon MIND at a baseline of between 2 500 km and 5 000 km, to determine the CP phase, and one 50 kTon MIND at a baseline of between 7 000 km and 8 000 km to determine θ_{13} and the mass hierarchy. The stored muon energy is 25 GeV and 10^{21} useful muon decays per year are available. This baseline configuration has been derived under the assumption that $\sin^2 2\theta_{13} < 0.01$, i.e., $\theta_{13} \neq 0$ has not been discovered prior to the start of the Neutrino Factory project. In this case, the second, longer baseline is necessary to ensure a robust physics performance throughout the parameter space, see figure 12, and to provide the best possible sensitivity to new physics. On the other hand, if $\sin^2 2\theta_{13} > 0.01$, then it is very likely that $\sin^2 2\theta_{13}$ will be measured before we embark onto the Neutrino Factory project and hence we would use this information to optimise the design of the facility. Thus, in this case, we would use a single baseline between 1 500—2 500 km and a stored muon energy around 10 GeV, see top left panel of figure 7. The detector can still be a 100 kTon MIND, since recent updates of the MIND analysis, in particular the inclusion of quasi-elastic events, have improved the low-energy performance significantly as explained in detail in section 3.2.1.

In terms of new physics sensitivities, we have studied sterile neutrinos and non-standard interactions as generic examples and find the Neutrino Factory, in its baseline configuration, provides good sensitivity to physics that cannot be studied at the LHC or elsewhere. In addition, a Neutrino Factory, in most cases, would be able to disentangle a new physics contribution from the usual oscillations.

We, as a community, have been searching for new physics for many decades in vain. The discovery of neutrino mass is the first tangible sign for physics beyond the Standard Model. It seems therefore, natural and compelling to follow up on this initial discovery by a dedicated, long term science program with the goal to establish the flavour physics of neutrinos at a level of precision comparable to that at which we have tested the CKM description of quark flavour. The results presented in this section are supported by a large body of literature and demonstrate clearly that a Neutrino Factory is the ultimate tool to study neutrinos and their flavour transitions with the highest precision.

2. The Neutrino Factory accelerator complex

2.1. Overview

The Neutrino Factory accelerator systems are required to produce a high-intensity, high-energy neutrino beam with a very well-known energy spectrum and without the contamination of unwanted neutrino flavours. The energy spectrum is well-defined since it arises from the decay of muons confined within a storage ring with a relatively small energy spread. The muon beam is accelerated to high energy thereby creating a high-energy neutrino spectrum. The accelerator facility (shown schematically in figure 24 produces a high-intensity neutrino beam by creating large numbers of muons, capturing as many of them as possible, and minimising the loss of these muons before they can be directed toward the detector. Table IV quantifies these characteristics: it gives the muon beam energy and the number of muon decays in the direction of the neutrino detector. The uncertainty in the neutrino flux is limited by the angular divergence of the stored muon beam [204]. Table IV, therefore, also specifies the maximum angular divergence of the muon beam. Two storage rings are required to serve simultaneously both the detector at the intermediate baseline and that at the long baseline. The decay rings have straight sections inclined so that the straight sections point at the distant detectors. The lengths of the straight sections form a significant fraction of the decay ring circumference so that the fraction of the stored muons decaying in the direction of the detectors is maximised.

Table IV. Parameters characterising the muon beam produced by the accelerator facility. Muon decays are a total for all signs and detector baselines.

Parameter	**Value**
Muon total energy	25 GeV
Production straight muon decays in 10^7 s	10^{21}
Maximum RMS angular divergence of muons in production straight	$0.1/\gamma$
Distance to intermediate baseline detector	2 500–5 000 km
Distance to long baseline detector	7 000–8 000 km

2.1.1. Principal subsystems

Muon beams at the Neutrino Factory are produced from the decays in flight of pions produced by the bombardment of a target by a high-power, pulsed proton beam. The muons produced in this way must be captured and manipulated in 6-D phase space such that the maximum number are transported into the phase-space region that is required for acceleration and storage in the decay ring. After the phase-space manipulation, the muon beam energy is increased to 25 GeV in a number of acceleration stages. Finally, the beam is injected into the storage ring, where it circulates as the muons decay into neutrinos.

The number of muons created is approximately proportional to the power in the proton beam, defined as the product of the number of protons per bunch, the energy of each proton, and the rate at which bunches hit the target. The power of the proton beam is chosen to be sufficient to produce the

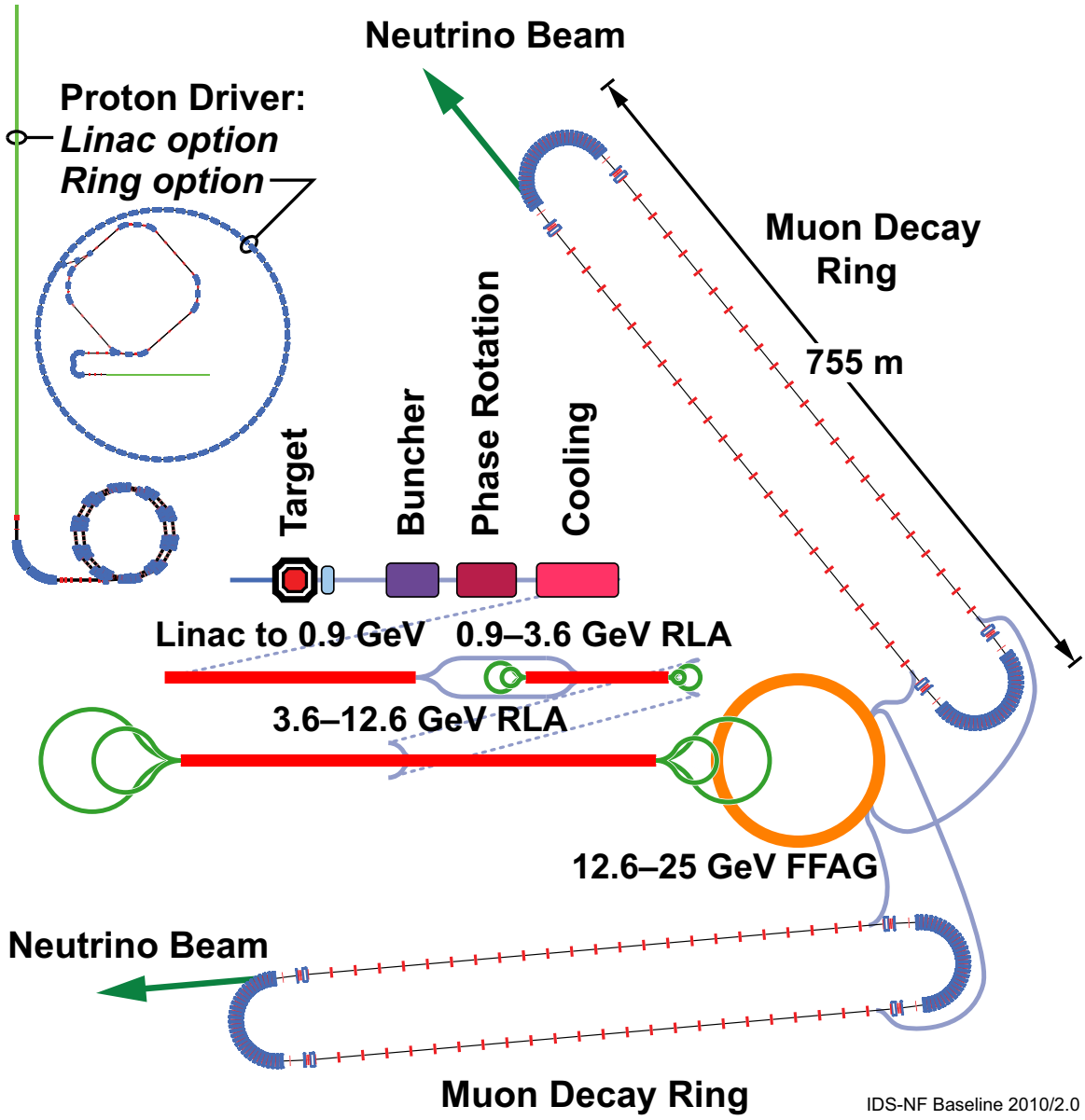

Figure 24. Schematic drawing of the IDS-NF accelerator complex.

desired number of muons (see table IV). Other parameters are chosen such that the number of muons produced per unit power is nearly optimal (see table V) given the method we are using to capture the muons. This report will not define a specific proton driver for the Neutrino Factory. Rather, we describe three designs that could be implemented by appropriately developing infrastructure at three of the world's proton-accelerator laboratories (CERN, FNAL, and RAL). These laboratories have been chosen as example sites to allow practical considerations to be evaluated. The range of proton-driver technologies being studied is matched to the constraints of the example sites and covers the technologies most likely to be employed. We believe that this strategy will allow us to demonstrate that it is feasible to deliver the required beam parameters from a number of possible sites and using

a variety of technologies.

The target that the proton beam hits is a liquid mercury jet. The liquid jet avoids issues of structural damage from the beam that a solid target faces. The proton beam hits the target inside a 20 T solenoid, which tapers down to 1.5 T in a distance of 15 m. The high field and the taper give a large angular acceptance for the pions at the target. The solenoid channel allows both muon signs to be captured.

The pion beam from the target decays into muons in a long decay channel, and the resulting muon beam has a large energy spread as well as an energy-time correlation, the latter arising because the pions are not highly relativistic. A sequence of RF cavities, the frequency of which decreases with distance, then turns this distribution into a train of bunches. A subsequent sequence of cavities, with frequency decreasing down the channel, then changes the energies of the individual bunches so that all the bunches have the same energy. These "bunching" and "phase-rotation" sections are followed by an ionisation-cooling channel, which reduces the transverse emittance of the bunches, thereby increasing the number of muons that can be transmitted into the acceptance of the acceleration systems that follow.

Acceleration of the muon beam occurs in a number of stages. The first stage is a linac, which accelerates the beam to 0.9 GeV total energy. This is followed by two recirculating linear accelerators (RLAs), taking the beam to 3.6 GeV and 12.6 GeV, respectively. RLAs are preferable to a series of single-pass linacs since the beam makes multiple passes through the RF cavities (4.5 passes in our design), consequently reducing the cost of the acceleration system. The RLA technique cannot be applied at lower energies, however, since the beam has a low velocity which, combined with its large relative-energy spread and large geometric emittance, would make a linac phased for a higher energy inefficient at the lower, initial energy. The final stage of acceleration is performed in a fixed-field alternating-gradient (FFAG) accelerator, which permits even more passes (11) through the RF cavities. The switchyard in an RLA will not permit such a large number of passes, while the FFAG cannot achieve this large number number of turns at lower energies. Each acceleration stage is thus chosen to use the most efficient acceleration technique for its energy range.

The full-energy beam is next injected into two racetrack-shaped decay rings. Each decay ring points toward one of the far detectors (the "intermediate" baseline or the "long" baseline). Each decay ring is capable of storing both muon signs simultaneously.

2.1.2. Progress within the IDS-NF accelerator study to date

The IDS-NF adopted, with slight modifications, the specification for the Neutrino Factory accelerator complex developed by the Accelerator Working Group of the International Scoping Study of a future Neutrino Factory and super-beam facility (the ISS) [5]. The initial baseline (referred to as 2007/1.0) is defined in [205]. The specification of the accelerator facility presented below (referred to as 2010/1.0) is the result of a substantial amount of work and constitutes a revision of the initial baseline [206]. The principal developments that have resulted from the work of the Accelerator Working Group of the IDS-NF or that have informed the choice of baseline are summarised below.

The MERIT experiment, a test of a liquid-mercury-jet target, has been completed, and the data have been analysed [207]. The mercury jet was in a high-field solenoid and was hit by a proton beam from the CERN PS. The experiment demonstrated that such a target is able to withstand the high power-density that will be present at the Neutrino Factory. MERIT also showed that if two bunches

hit the target in rapid succession, the disruption of the mercury jet caused by the first bunch does not reduce the number of pions produced by the second bunch unless the bunches are separated by more than 350 μs (because the disruption increases with time). This result is important for the specification of the time structure of the bunches coming from the proton driver when beam loading in the RF cavities in the muon acceleration system is considered. In addition, the observed disruption length combined with the speed of the jet allow operation at repetition rates of up to 70 Hz.

The geometry of the proton beam and mercury jet has been optimised as a function of energy [208, 209]. The performance of the target was improved as a result, and the energy dependence of the pion-production rate was computed more precisely. The effect of a non-zero beam divergence was computed. As a result of this calculation, a requirement for the proton-beam emittance was determined (see table V). Comparisons were made between MARS [210–214] (version 1507 is used throughout this document) and FLUKA [215, 216] simulations for this target system [217].

Very detailed studies were made of the energy deposition in the target region [209, 218]. The studies indicate that the energy deposition in the superconducting solenoids in the target region is too large, so the solenoids in the target region will be redesigned to allow more room for shielding.

In the muon front-end, the bunching and phase-rotation sections have been shortened, creating a system that produces the same number of muons in a shorter bunch train [219, 220]. Studies of the performance of RF cavities in magnetic fields have continued [221] and the MICE experiment continues to make progress towards a demonstration of the ionisation cooling technique [222]. Indications that the maximum cavity-gradient may be reduced in magnetic fields have led to the consideration of front-end lattices that give adequate performance should the RF cavities not reach the gradients specified for the magnetic field configuration of the baseline lattice for the IDS-NF muon front end. The performance of the baseline lattices, along with that of the modified lattices, has been computed [220, 223–227]. Particle losses and energy deposition in the front end have been computed, and methods to reduce their impact are beginning to be studied.

Tracking studies with more realistic fields have been done on the first acceleration linac, resulting in slight modifications to the lattice design. The RLA designs have been improved by modifying the quadrupole gradient profile in the linacs to increase performance [228]. A chicane has been designed for the locations where the arcs cross each other [219]. In the arc-crossing and injection chicanes, chromatic corrections have been incorporated and preliminary tracking results have indicated that chromatic correction in these regions alone is sufficient to achieve acceptable performance.

A new FFAG design has been developed that has a high average RF gradient to reduce the effect of non-linear coupling of transverse into longitudinal motion [229]. Injection and extraction schemes have been developed for the FFAG ring [230] and we have begun to study the designs of the injection and extraction kickers and septa. These preliminary studies indicated that longer drifts were necessary, and as a result the FFAG design was modified. Chromaticity correction in the FFAG has been studied more extensively [229].

We have begun studies of diagnostics in the decay ring. We have a preliminary design for a polarimeter to be used for beam-energy measurement [231]. In addition, a helium gas Cherenkov detector has been considered for angular divergence measurement [232]. Other methods of beam-divergence measurement are now being studied as the Cherenkov solution proved difficult.

Table V. Proton driver requirements. A proton kinetic energy in the range 5 GeV to 15 GeV has been shown to provide adequate performance. The number of protons, beam radius, β^*, and geometric emittance (see section 2.3) correspond to the values for an 8 GeV proton beam.

Parameter	**Value**
Kinetic energy	5–15 GeV
Average beam power	4 MW
	(3.125×10^{15} protons/s)
Repetition rate	50 Hz
Bunches per train	3
Total time for bunches	240 μs
Bunch length (rms)	1–3 ns
Beam radius	1.2 mm (rms)
Rms geometric emittance	< 5 μm
β^* at target	≥ 30 cm

2.2. Proton driver

The proton driver at the Neutrino Factory is required to deliver a proton-beam of 4 MW at a repetition rate of 50 Hz to the pion-production target. The proton-beam energy must be in the multi-GeV range in order to maximise the pion yield. In addition, the Neutrino Factory specifies a particular time structure consisting of three very short bunches separated by about 120 μs. To allow the muon beam to be captured efficiently, short, 1–3 ns rms, bunches are required. Each bunch from the proton driver will become a separate muon bunch train. The bunch separation is constrained by beam loading in the downstream muon accelerator systems and by the time scale for disruption of the mercury-jet target. The proton beam parameters necessary to produce the desired number of muons in the storage rings of the Neutrino Factory are listed in table V. In order to achieve such short bunches, a dedicated bunch compression system must be designed to deal with the very strong space-charge forces. Several proton-driver schemes fulfilling these requirements have been proposed (see below and appendices). Typically they consist of an H^--ion source followed by a radio-frequency quadrupole (RFQ), a chopper, and a linear accelerator. In some cases the final energy of the proton driver is delivered by the linac. In these linac-based scenarios, the beam time structure must be obtained with the help of charge-exchange injection into an accumulator ring followed by fast phase rotation in a dedicated compressor ring.

Such a linac-based solution was adopted for the CERN Neutrino Factory scenario, which would be based on the proposed 5 GeV, high-power version of the Superconducting Proton Linac (SPL) [233], which can deliver 10^{14} protons at the repetition rate of 50 Hz [234]. In the recent past, the Superconducting Proton Linac study evolved into an international collaboration whose aim is the optimisation of the architecture of a pulsed superconducting high-power proton linac. The most recent design of the SPL and the description of the goals of the collaboration, can be found in [235]. In the CERN scenario, the chopped beam from the SPL would be injected into an isochronous accumulator ring in which 120 ns long bunches are formed without the need for an RF system. The absence of synchrotron motion in the accumulator ring makes it important to study the stability of the beam in the presence of space-charge. As presented in [236], transverse stability can be obtained with a suitable choice of

Table VI. Parameters of the accumulator and compressor rings for the CERN proton driver scenario.

Parameter	**Value**
Accumulator ring	
Circumference	185 m
No. of turns for accumulation	640
Working point (H/V)	7.37/5.77
Total bunch length	120 ns
RMS momentum spread	0.863×10^{-3}
Compressor ring	
Circumference	200 m
No. of turns for compression	86
RF voltage	1.7 MV
Gamma transition	2.83
Working point	4.21/2.74

chromaticity as shown in figure 25 (left panel) and longitudinal stability can be achieved by limiting the longitudinal broad-band impedance to a few ohms as shown in figure 25 (right panel) [236]. Two-dimensional phase-space painting is used in the stripping injection into the accumulator ring, allowing the temperature of the stripping foil to be kept below 2000 K. The beam parameters after accumulation are obtained as a compromise between the competing requirements of minimising the heating of the injection foil, maximising the aperture, and adequate compensation of the space-charge forces and are set to allow for RF phase-rotation in the downstream compressor ring. The size of the two rings is determined by the requirement that successive bunches must arrive at the correct location in the compressor ring. The compressor ring has a large phase slip factor, which is needed for the fast phase rotation. Tracking simulations in the compressor ring have been performed using the ORBIT code [237]. The good performance of the compressor ring is demonstrated in figure 26 (left panel). The simulations have also been used to investigate the transverse phase space. Figure 26 (right panel) shows that the transverse space charge can be tolerated due to the limited number of turns of the beam in the compressor ring and the relatively large dispersion, which effectively lowers the tune shift by enlarging the beam size. The parameters of the accumulator and compressor rings are listed in table VI. More details of the CERN proton driver scenario can be found in [238]. The low energy normal-conducting part of the SPL is currently under construction and should become operational in the following few years as part of the LHC injector chain. The existing proton linac, the Linac2, will be replaced soon by the more modern Linac4 [239] that will accelerate H- up to 160 MeV, before injecting them in the PSB. The linac performances will match the requirements of the program of increasing the LHC luminosity. The status of the construction of the Linac4 in 2010 can be found in [240]; in particular, the construction of the new Linac building was recently concluded. Figure 27 shows an overview of the Linac integration with respect to the existing accelerator complex.

A proton driver for a Neutrino Factory situated at Fermilab would be based upon an upgrade of the proposed Project X linac, as described in Appendix A. Fermilab is currently designing a high-intensity proton source that will deliver beam at 3 GeV and 8 GeV. As presently conceived, the Project X linac will deliver only $\approx 10\%$ of the proton-beam power needed for the Neutrino Factory at 8 GeV. However, Project X is designed such that it can be upgraded to deliver the full beam

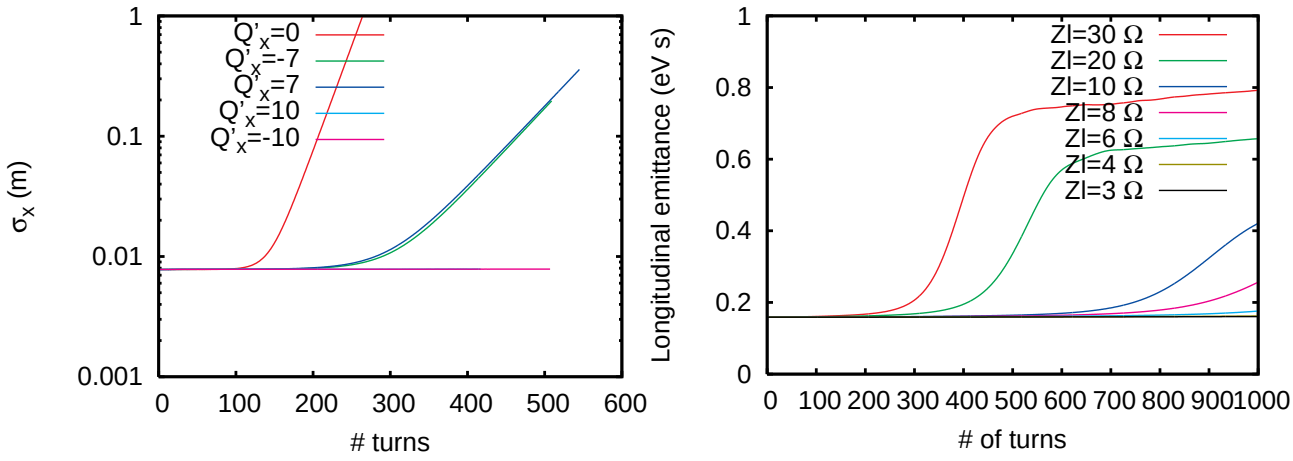

Figure 25. Horizontal beam size evolution, for various values of chromaticity, assuming a transverse impedance of 1 MΩ/m, Q_R=1, f_R=1 GHz (left). Longitudinal emittance evolution for different values of $Z_\parallel/n$ (right). The lines for 3 and 4 Ω lie on top of each other in the figure.

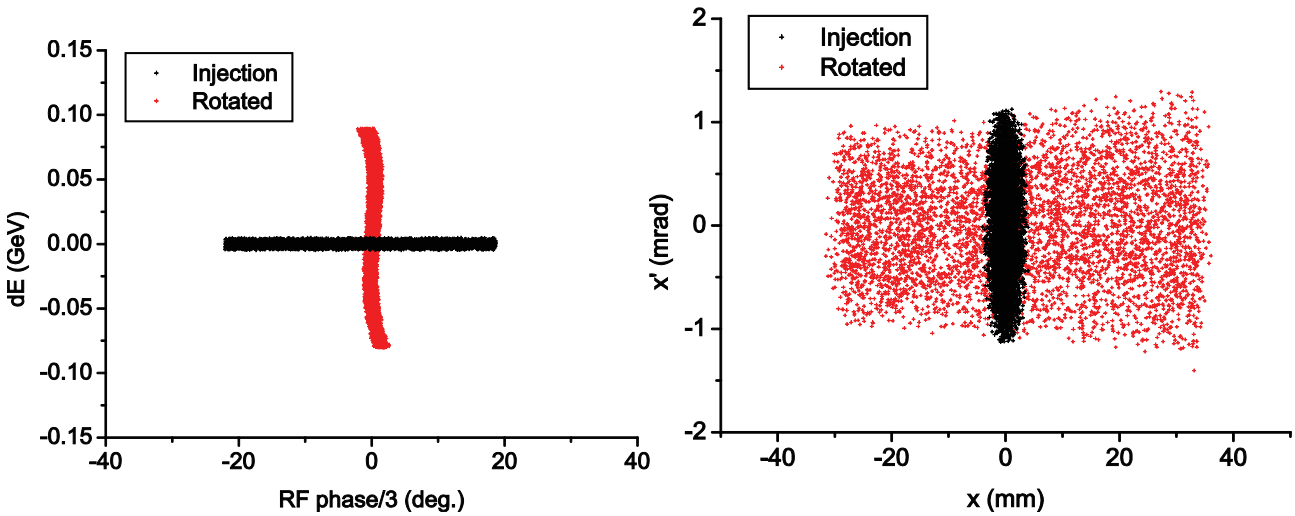

Figure 26. Phase space plots before and after bunch rotation.

power (4 MW at 8 GeV) required for the Neutrino Factory. Just as in the CERN scheme, additional accumulator and compressor rings will be needed to provide the correct time structure.

Project X will accelerate H^--ions in two superconducting linacs. A CW linac will accelerate beam to 3 GeV, where the majority of the beam will be used for experiments. A small portion of the beam will be directed into a pulsed linac to be further accelerated to 8 GeV. At 8 GeV, the beam will be accumulated in the Recycler ring before being transferred to the Main Injector. The proton beam will then be accelerated to higher energy for the long-baseline neutrino program.

The CW linac will be operated with an average current of 1 mA. Less than 5% of the CW-linac beam will be directed to the pulsed linac. Initially, the pulsed-linac beam will provide ≈ 350 kW of

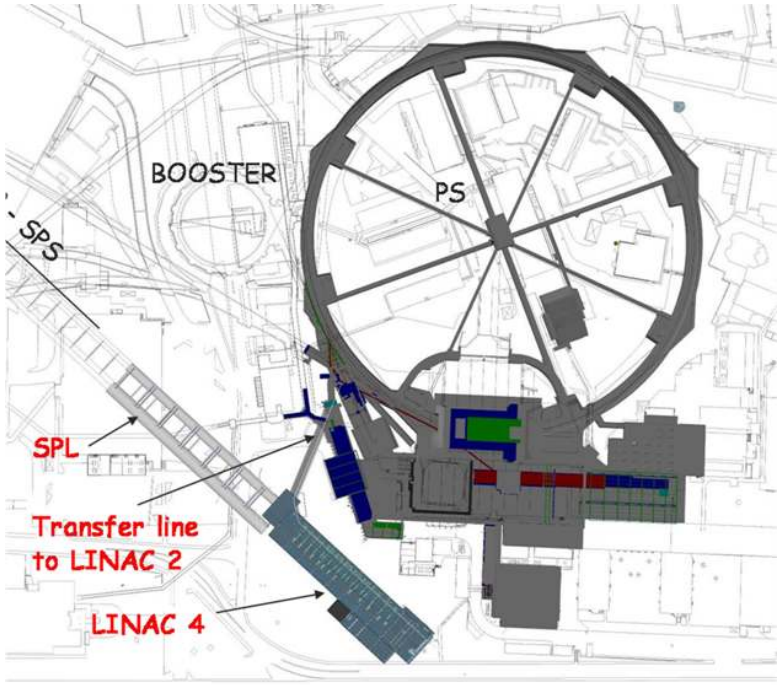

Figure 27. The CERN Linac4 with respect to the rest of the site.

beam power at 8 GeV. If the pulsed linac is capable of operating 50% of the time, then the required beam power of 4 MW could be reached. The option of converting the pulsed linac into a CW linac is not being considered. Instead, the average current of the CW linac can be raised to 4-5 mA. While designing Project X, provision is being made to allow the CW linac to be upgraded to accelerate the increased beam current that will be required to serve the Neutrino Factory.

For Project X to serve the Neutrino Factory, an accumulation ring will be put at the end of the second linac. At injection into the accumulation ring there will be a stripping system, foil or laser based, to convert the H^--ions to protons. The front-end of Project X will have a programmable chopper so that beam will be injected into three RF buckets in the accumulation ring. After injection is complete, the RF bucket voltage will be increased to shorten the bunches. The accumulated protons will then be transferred to a separate bunch-shortening (compressor) ring. Bunch rotation will be used to achieve the final bunch length (2 ns). The three bunches will be extracted with the proper spacing (120 μs) to the target station. The accumulation, bunch shortening, and targeting will be done at 50 Hz, as required for the Neutrino Factory.

Project X will be located within the Tevatron ring at Fermilab. The accumulation ring will be situated near the end of the pulsed linac. Once the beam has been converted from H^--ions to protons, the beam can be transported some distance to the bunch-shortening ring. Extraction from the bunch shortening ring to the target sets the orientation of the ensuing muon collection and acceleration. All components of the Neutrino Factory, including a decay ring, fit within the Tevatron ring footprint.

A Neutrino Factory sited at the Rutherford Appleton Laboratory (RAL) would be served by a proton driver based on an upgrade to the ISIS pulsed-proton source. In this scenario, a chain of

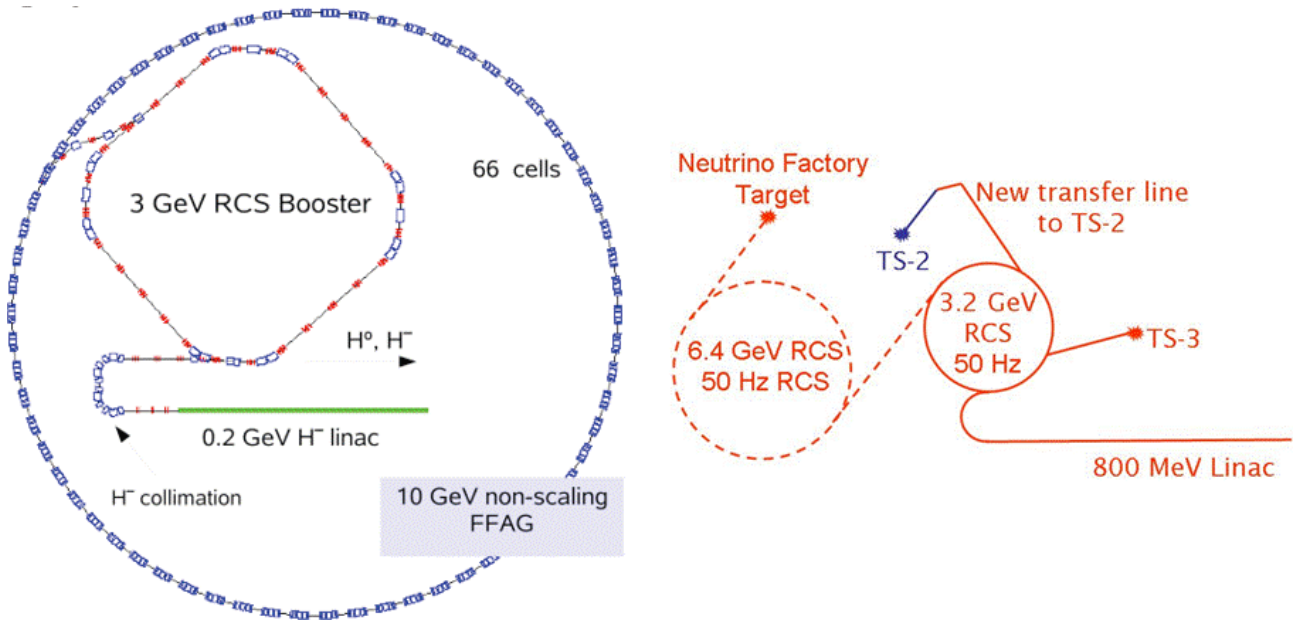

Figure 28. Left panel: Layout of the ISS proton driver based on an RCS and an FFAG. Right panel: Layout of the common proton driver for ISIS and the Neutrino Factory at RAL.

circular accelerators, typically Rapid Cycling Synchrotrons (RCSs), provides an alternative to the linac-based options outlined above. Here, bunch compression is accomplished adiabatically in the RCS or, alternatively, in an FFAG ring as proposed in the ISS study [5]. Recently the attractive idea of a common proton driver for the spallation neutron source and the Neutrino Factory was proposed in the framework of the ongoing ISIS megawatt-upgrade programme. In such a scenario, the proton drivers for both facilities would share the same source, chopper, linac, accumulator, and acceleration up to 3.2 GeV. After extraction, a number of bunches would be sent directly to the neutron-spallation target while three others would be injected into a second RCS or FFAG where, after acceleration to somewhere between 6.4 and 10.3 GeV followed by bunch compression, the beam would be extracted towards the Neutrino Factory pion-production target. The layout of the proton drivers using the RCS machines can be seen in figure 28. The left panel shows the solution based on an RCS booster and FFAG ring developed during the ISS [5]. The right panel shows the layout of the common proton driver for the spallation-neutron source and the Neutrino Factory that is presently under development. For the ISIS megawatt upgrade to be compatible with the Neutrino Factory, an 800 MeV H^- linac has been designed, candidate lattices for the 3.2 GeV booster RCS have been identified, and preliminary parameters for the final RCS ring have been proposed. More details of the Neutrino Factory proton driver option based on an upgrade of facilities at RAL are presented in Appendix B.

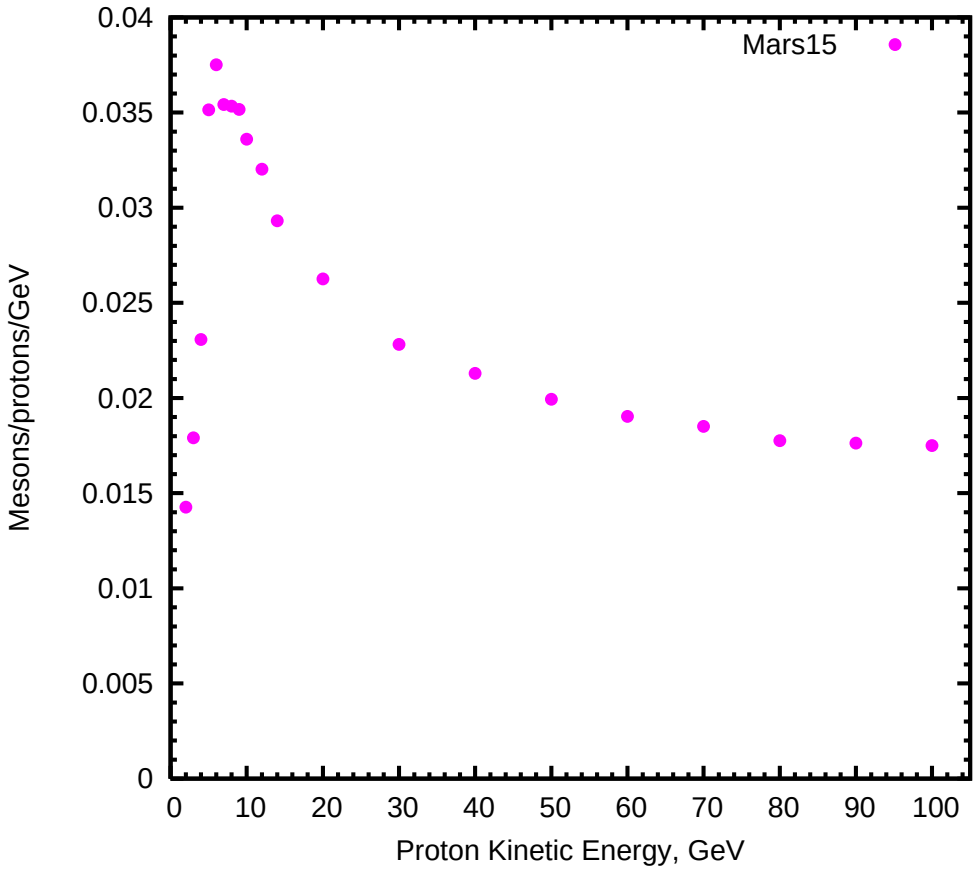

Figure 29. The meson production efficiency, normalised to the beam power, as a function of incoming proton beam [208]. Production efficiency is the number of mesons 50 m downstream from the target with kinetic energy in the range of 40–180 MeV. This criterion has been found to have a good correlation with the muons that are transmitted through the front end.

2.3. Target

2.3.1. Introduction to the target system

The requirements for the proton driver at the Neutrino Factory [14] (summarised in table V) call for a target capable of intercepting and surviving a 4 MW pulsed proton beam with a repetition rate of 50 Hz. The assumption of 8 GeV for the proton-beam energy arises from an optimisation study (performed with MARS [210–214]) in which the target parameters were evaluated as a function of the kinetic energy of the incoming proton beam. The resulting meson ("meson" in this document denotes muons, charged pions, and charged kaons) production-efficiency is shown in figure 29. The peak production-efficiency occurs for proton kinetic energies of 6–8 GeV. The β^* requirement (at the centre of the beam-target crossing) was determined by studying the production efficiency for the target geometry defined in table VII for a proton beam of 8 GeV and 1.2 mm rms radius as a function of β^*. The result, shown in figure 30, lead to the requirement that β^* should be at least 30 cm.

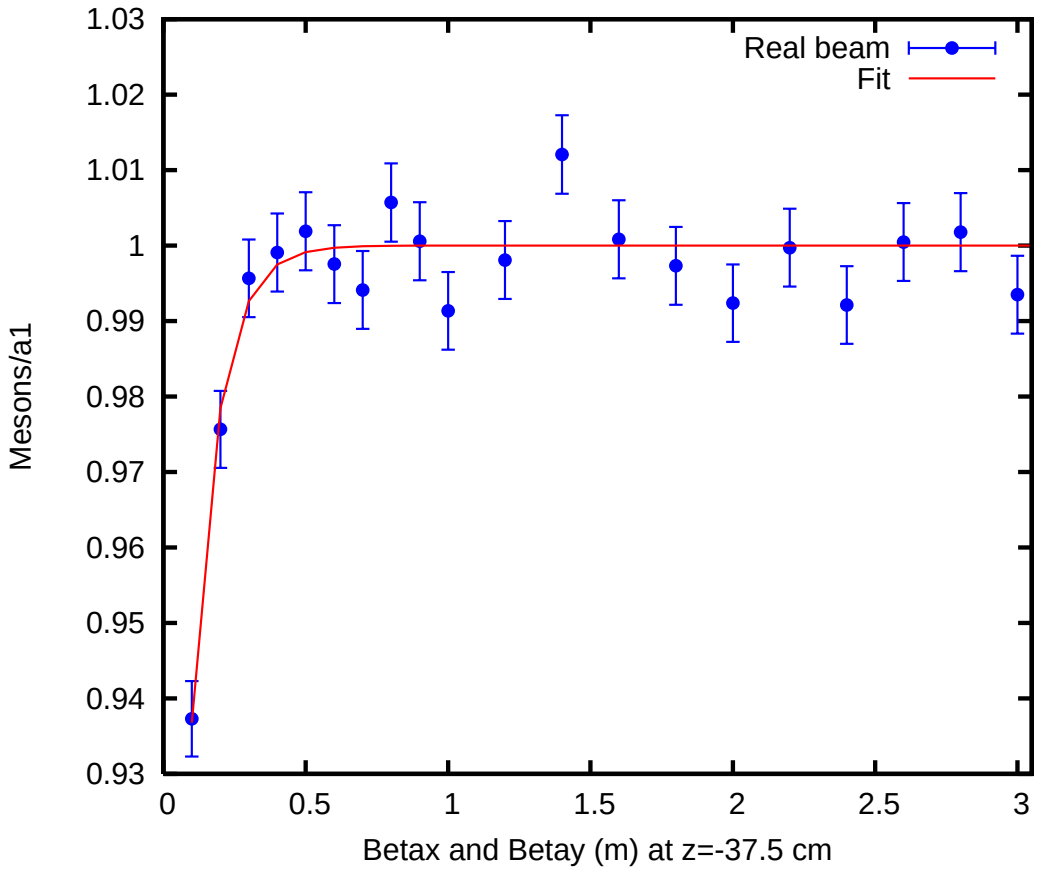

Figure 30. The meson production efficiency as a function of the β^* of the incoming proton beam [209]. The data are fit to the function $y = a_1 - a_2 e^{-kx}$, with x being the beta function of the beam distribution at $z = -37.5$ cm (the centre of the beam-target crossing) and y being the production efficiency. The results are scaled to a_1, the limit of the fit as the beta function goes to infinity.

The proton-beam bunch-length requirement is derived from a calculation in which the front end of a Neutrino Factory complex is simulated with the code ICOOL [241]. The muon throughput is obtained as a function of the mesons produced at the target for proton beams with various bunch lengths [242]. The results are shown in figure 31.

The proposed target system simultaneously captures charged pions of both signs, hence the use of solenoid magnets in the target system (rather than toroidal magnets that primarily capture particles of only one sign, as is typical in target systems for "conventional" neutrino beams).

The target, the proton beam dump, and a shield/heat exchanger are to be located inside a channel of superconducting solenoid magnets that capture, confine and transport secondary pions and their decay muons to the muon front-end (see section 2.4). In the present baseline configuration, most of the 4 MW beam power is dissipated within a few meters of the target, inside the solenoid channel, which presents severe engineering challenges.

Maximal production of low-energy pions is obtained with a proton beam of 1–1.5 mm (RMS) radius and a target of radius three times this. The target parameters have been determined by extensive simulations using the MARS modelling code [209].

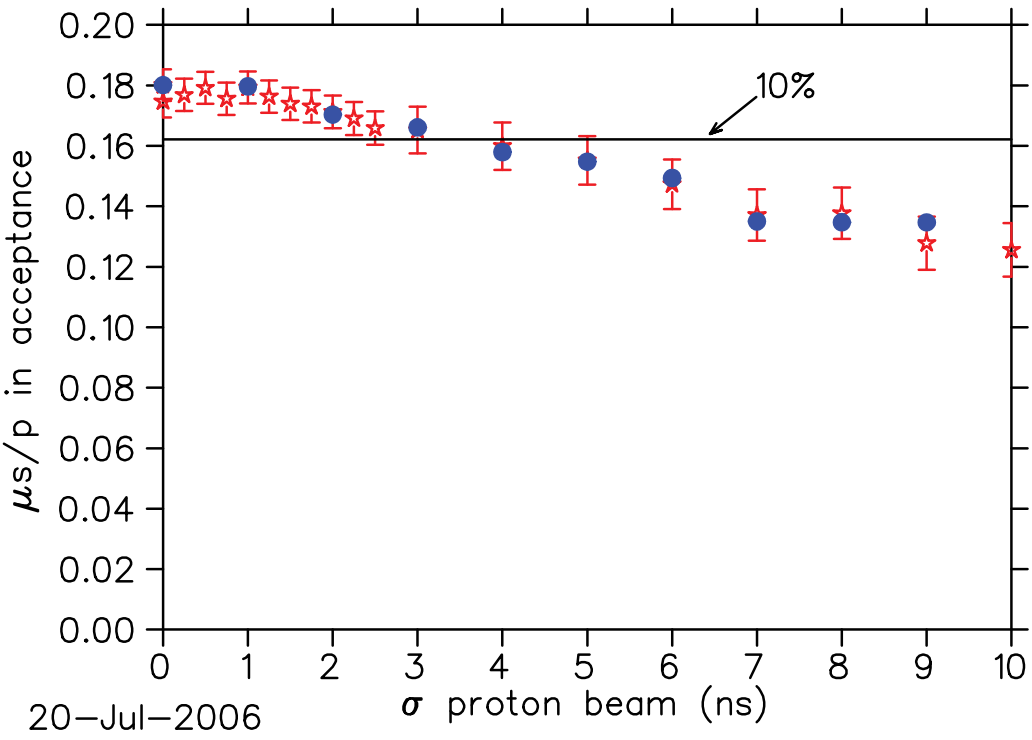

Figure 31. The final muon throughput of the front end as a function of the incoming proton beam bunch length [242]. Solid blue dots and red stars are data for two equivalent methods of creating the beam distribution in time.

The effect of beam-induced shock in solid targets has been studied using a high-current pulse with a rapid rise time to deliver a high power-density in tungsten and tantalum wires [243]. The results indicate that a system in which tungsten bars are exchanged between beam pulses can withstand the beam-induced shock. However, schemes for a set of moving solid targets have yet to be shown to be compatible with the confined environment provided by the solenoid magnets that form the pion-capture system. Hence, the baseline target concept is for a free liquid-mercury jet. A free-flowing jet is chosen because the intense beam-induced pressure waves in the liquid target would damage or lead to the failure of any pipe containing the liquid in the interaction region. The parameters of the present target-system baseline are summarised in table VII.

The concept of a mercury jet target within a high-field solenoid has been validated by R&D over the past decade, culminating in the MERIT experiment [244] that ran in the fall of 2007 at the CERN PS. The experiment benefited from the intensity of the beam pulses (up to 30×10^{12} protons per pulse) and the flexible beam structure available for the extracted PS proton beam. Key experimental results include the demonstration that [207]:

- The magnetic field of the solenoid greatly mitigates both the extent of the disruption of the mercury and the velocity of the mercury ejected after interception of the proton beam. The disruption of a 20 m/s mercury jet in a 20 T field is sufficiently limited that a repetition rate as high as 70 Hz is feasible without loss of secondary particle production;
- Individual beam pulses with energies up to 115 kJ can safely be accommodated;

Table VII. Baseline target system parameters.

Parameter	Value
Target type	Free mercury jet
Jet diameter	8 mm
Jet velocity	20 m/s
Jet/solenoid axis angle	96 mrad
Proton beam/solenoid axis angle	96 mrad
Proton beam/jet angle	27 mrad
Capture solenoid (SC-1) field strength	20 T
Front-end π/μ transport channel field strength	1.5 T
Length of transition between 20 T and 1.5 T	15 m

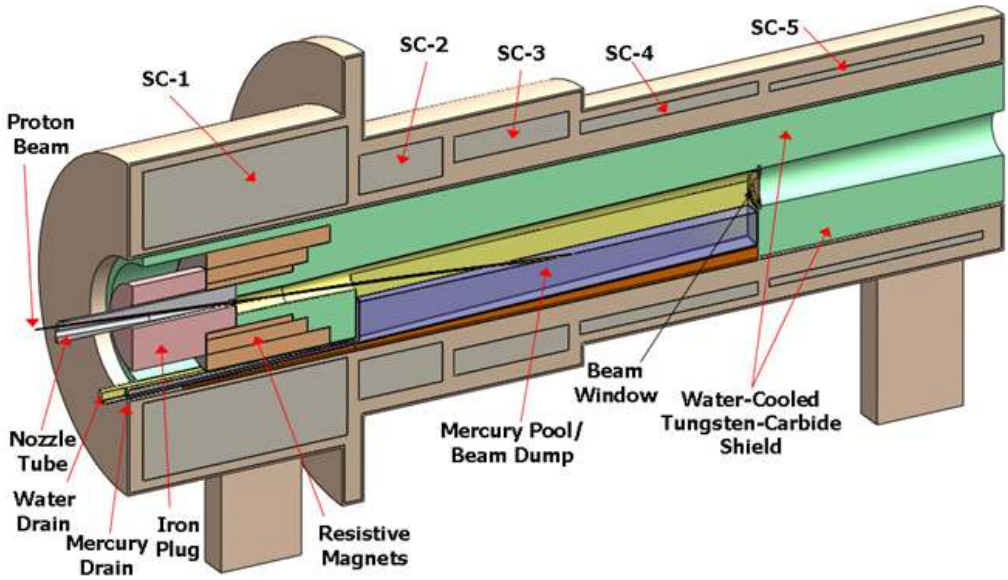

Figure 32. Baseline target system concept, with small changes from Neutrino Factory Study II [245]. SC-n are the superconducting magnets.

- Subsequent proton-beam pulses separated by up to 350 μs have the same efficiency for secondary particle production as does the initial pulse; and
- The disruption of the mercury jet caused by the second of two beam pulses separated by more than 6 μs is unaffected by the presence of the first beam pulse.

In the Neutrino Factory target system, the mercury jet is collected in a pool, inside the solenoid magnet channel, that also serves as the proton beam-dump, as sketched in figure 32. Disruption of this pool by the mercury jet (equivalent to a mechanical power of 3 kW) and by the non-interacting part of the proton beam is nontrivial, and needs further study.

The superconducting magnets of the target system must be shielded against the heat and radiation damage caused by secondary particles issuing from the target (and beam dump). A high-density shield is favoured to minimise the inner radii of the magnets.

The baseline shield concept is a stainless-steel vessel of complex shape (see figure 32) containing

water-cooled tungsten-carbide beads. Calculations using MARS in an MCNP mode (MCNP mode gives more accurate treatment of low-energy neutrons) show that for an 8 GeV, 4 MW incoming proton beam, the radiation penetrating the shielding (as configured in Study II [245]) results in 50 kW of power being deposited in the superconducting coils that surround the target [246]. This would present a severe operational burden on the cryo-system and hence is not considered practical. Effort to produce a new baseline for the shielding is under way.

The solenoid magnets of the target system vary in strength from 20 T (SC-1 in figure 32) down to 1.5 T in the subsequent constant-field transport channel. Table VIII gives the solenoid parameters as established in Study II [245]. The interface between the target station and the muon front-end is taken to be the point at which the constant-field capture channel begins, 15 m downstream of magnet SC-1 in the present baseline. The initial superconducting coil (SC-1), which is responsible for generating a 14 T field at the site of the target, has the most challenging mechanical requirements. The stored energy of this magnet is 600 MJ, and the radial and hoop stresses are 110 MPa and 180 MPa, respectively [247].

Table VIII. Solenoid coil and iron plug geometric parameters. The centre of the beam-target crossing is at −37.5 cm.

	z (m)	**Δz** (m)	**R_i** (m)	**ΔR** (m)	**I/A** (A/mm^2)	**nI** (A)	**nIl** (A-m)
Fe	0.980	0.108	0.000	0.313	0.00	0.00	0.00
	1.088	0.312	0.000	0.168	0.00	0.00	0.00
Cu coils	1.288	0.749	0.178	0.054	24.37	0.98	1.26
	1.288	0.877	0.231	0.122	19.07	2.04	3.74
	1.288	1.073	0.353	0.137	14.87	2.18	5.78
SC coils	0.747	1.781	0.636	0.642	23.39	26.77	160.95
	2.628	0.729	0.686	0.325	25.48	6.04	32.23
	3.457	0.999	0.776	0.212	29.73	6.29	34.86
	4.556	1.550	0.776	0.107	38.26	6.36	33.15
	6.206	1.859	0.776	0.066	49.39	6.02	30.59
	8.000	0.103	0.416	0.051	68.32	0.36	1.00
	8.275	2.728	0.422	0.029	69.27	5.42	14.88
	11.053	1.749	0.422	0.023	75.62	3.00	8.18
	12.852	1.750	0.422	0.019	77.37	2.61	7.09
	14.652	1.749	0.422	0.017	78.78	2.30	6.22
	16.451	1.750	0.422	0.015	79.90	2.07	5.59
	18.251	2.366	0.422	0.013	-0.85	2.53	6.80

A 20 T field is beyond the capability of Nb_3Sn, and magnet SC-1 is proposed as a hybrid of a 14 T superconducting coil with a 6 T hollow-core copper solenoid insert. A 45 T solenoid with this type of construction (but a significantly smaller bore of 32 mm diameter) has been operational since 2000 at the National High Magnetic Field Laboratory (Florida, USA) [248]. A 19 T resistive magnet with a 16 cm bore at the Grenoble High Magnetic Field Laboratory [249] was used in an earlier phase [250] of the Neutrino Factory R&D program. A topic for further study is possible fabrication of SC-1 as a high-T_C magnet with no copper-solenoid insert, which could provide more space for internal shielding of

SC-1 and/or permit operation at a higher field for a potential increase in the meson-capture efficiency.

The target system (and also the subsequent π/μ solenoid transport channel) will be subjected to considerable activation, such that once beam has arrived on target all subsequent maintenance must be performed by remote-handling equipment. The infrastructure associated with the target hall, with its remote-handling equipment, and hot-cells for eventual processing of activated materials, may be the dominant cost of the target system.

2.3.2. Sub-systems

2.3.2.1. Target

2.3.2.1.1. Baseline Concept

The target itself is a free liquid mercury jet ($Z = 80$, $A = 200.6$, density $\rho = 13.5$ g/cm^3, nuclear interaction length $\lambda_I \approx 15$ cm) of diameter $d = 8$ mm, flowing at $v = 20$ m/s. The volume-flow rate is 1.0 L/s and the mechanical power in the flowing jet is 2.7 kW. The flow speed of 20 m/s ensures that the gravitational curvature of the jet over the two nuclear interaction lengths (30 cm) through which the proton beam passes is negligible compared to its diameter and that more than two nuclear interaction lengths of new target material are presented to the beam every 20 ms, the time between beam pulses at a repetition rate of 50 Hz.

According to a MARS15 simulation [209, 251], $\sim 11\%$ of the beam energy is deposited in the target, corresponding to 9 kJ/pulse at 50 Hz. This energy is deposited over two nuclear interaction lengths along the jet (30 cm, 15 cm^3), so, noting that the specific heat of mercury is ~ 4.7 J/cm^3/K, the temperature rise of the mercury during a beam pulse is about 130 K. The boiling point of mercury is 357 °C, so the mercury jet, which enters the target volume at room temperature, is not vaporised at 50-Hz operation.

Although the mercury jet is not vaporised, it will be disrupted and dispersed by the pressure waves induced by the pulsed energy deposition. The MERIT experiment [252] showed that for pulses equivalent to 50 Hz operation at 4 MW beam power, this disruption results in droplets with peak velocity of ~ 50 m/s in a 15 T field. Extrapolating these results to 20 T field at the Neutrino Factory target yields a maximum droplet-velocity of ~ 30 m/s.

The optimal production of pions in the acceptance of the muon front-end is achieved by appropriate tilts of the mercury jet and proton beam with respect to the magnetic axis. These tilts depend slowly on the proton-beam energy (as does the optimum radius of the jet), and the current best values are based on MARS15 simulations and are given in table VII.

The Reynolds number of the mercury flow in the jet is $R = \rho v d/\eta \approx 1400$. Noting that the viscosity of mercury is $\eta = 1.5$ mPa·s, the flow can be turbulent. Hence, the quality of the jet is an issue, although operation in a high magnetic field damps surface perturbations [250]. The nozzle will need to be as close as feasible to the interaction region. High velocity mercury may generate erosion of the nozzle, e.g., by erosion-corrosion or by cavitation; this part of the system would need to be carefully designed but may be studied off-line using a suitable mercury flow loop. Detailed design work of the nozzle is under way.

2.3.2.1.2. Possible Target Alternatives

Alternatives to the liquid-mercury jet target that are under consideration are: a liquid-metal jet using a metal that is solid at room temperature; a helium-cooled metallic low-Z static packed bed; a metal-powder-jet; and a system of solid tungsten bars that are exchanged between beam pulses.

A eutectic alloy of lead and bismuth (melting point 124 °C) would have similar performance to a mercury target, with the challenge of operating the target flow-loop at temperatures above the boiling point of water, with that flow-loop in thermal contact with the water-cooled shield of the superconducting magnets. The activation products from a lead-bismuth target are more troublesome than those of a mercury target. A helium cooled low-Z static packed bed of beryllium (or possibly titanium) would give a low-Z (the advantages of which are described below) alternative to graphite that is considerably more tolerant to radiation damage and therefore would have a greater lifetime than the graphite, provided that sufficient cooling can be achieved. The powder-jet and solid alternatives are discussion in Appendices 1 and 2.

2.3.2.2. Proton Beam Dump

The target system requires the proton beam dump to be inside the superconducting magnet channel, only ≈ 1 m from the target. The baseline design is to use the pool that collects the mercury from the target jet as the beam dump. The mercury is to be drained from the upstream end of the pool, in a passage that is a sector of the annular space between the resistive magnet and superconducting magnet SC-1.

The dump must dissipate the ~ 3 kW of mechanical power in the mercury jet, as well as ~ 20 kW of power in the attenuated proton beam. The beam dump must also be able to withstand one or two full intensity beam pulses before the beam can be tripped in the event that the mercury jet fails, or the beam misses the jet. The vessel that contains the mercury pool will be subject to substantial radiation damage and heating by the secondary particles from the target, and must be replaced periodically.

2.3.2.3. Beam Windows

The volume that contains the target and mercury pool beam dump is the primary containment vessel for the mercury. This containment vessel includes a small window upstream through which the proton beam enters and a larger window on the downstream face of the vessel, currently specified to be at the boundary between superconducting magnets SC-4 and SC-5, through which the desired secondary pions and muons (as well as other particles) pass. The containment vessel is to be operated with helium gas (plus mercury vapour) at atmospheric pressure.

The upstream proton-beam window has yet to be specified, either as to design or location. The larger exit window is specified to be made of beryllium. It will be a double window, such that the volume between the two windows can support a flow of helium gas to cool the window, and which can be monitored for indications of window failure. The complexity of such a window system is indicated in figure 33 which shows the beam window in use on the T2K target at J-PARC [253]. The window

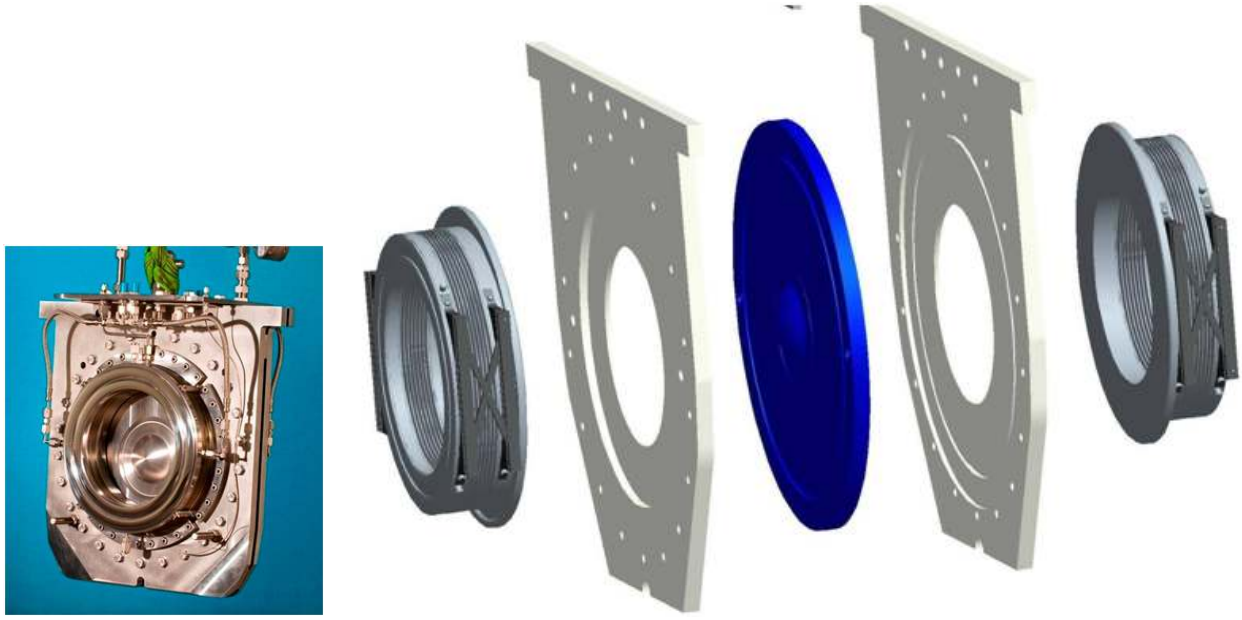

Figure 33. Photograph and schematic of the T2K beam window [253], which was designed for a 0.75 MW beam.

system is a replaceable item, and will be sealed to the downstream face of the primary containment vessel and to the upstream face of the pion-decay-channel vessel via inflatable "pillow" seals.

2.3.2.4. The Internal Shield

A major challenge of the target system is the dissipation of the 4 MW of beam power inside the superconducting magnet string without quenching the magnets or extreme shortening of their operational lifetime due to radiation damage. Most of the beam power will be dissipated in an internal shield composed of a high-Z material, which will have to extend well beyond the downstream end of the target system into the muon front-end.

The baseline scenario is for a shield of tungsten-carbide beads cooled by water. Pure tungsten beads would provide better shielding, but tungsten corrodes in water in a high radiation environment (see, for example, [254]). Random packing of spherical beads of a single radius will result in a configuration with about 63% by volume of tungsten-carbide, and 37% water [255]. The flow path of the coolant is not presently specified; multiple inlets and outlets will be appropriate for a shield of total length 30 m—50 m. One inlet is required at the very upstream end of the shield where the heat load is the largest.

All high-Z target systems proposed so far rely on recirculating target material from the target interaction region to be externally cooled. This requires either a radial or longitudinal gap to be engineered between the solenoid coils and shielding.

The outer radius of the shield was specified to be 63 cm in Feasibility Study II [245], but subsequent MARS15 simulations indicate that this would imply a load of ~ 25 kW in magnet SC-1 [209]. A low-Z target material would considerably reduce neutron production compared with a high-Z material,

which could potentially reduce this energy deposition. Interim values of up to 75 cm for the outer radius of the shield are being considered. Studies are under way to determine acceptable criteria for the total power deposition and the peak local power deposition for the various magnets to be stable against quenching and radiation damage. The details of the present baseline concept should therefore be regarded as preliminary.

2.3.2.5. The solenoid magnets

An early concept [256] for a muon collider assumed separate targets for production/collection of positive and negative particles. It was soon realised that the use of solenoid magnets would permit a single channel to operate with both signs [257], and that the initial capture in a high-field solenoid followed by a series of solenoids each of slightly lower field than the last exchanges transverse for longitudinal momentum [258]. Another advantage is that the solenoid-magnet coils would be farther from the high radiation due to secondary particles from the target than would toroidal coils [259].

The design of the first magnet, with baseline field of 20 T is challenging. The use of a 6 T water-cooled, hollow-core-copper solenoid insert is required if the superconducting outsert is made from Nb_3Sn. This copper magnet receives a very high radiation dose (while acting as a partial shield for the superconducting outsert) and is anticipated to be a replaceable component with a lifetime of 4 years or less. If the presence of this copper magnet leads to a requirement for thicker shielding and consequently larger inner diameter for the superconducting outsert, such that the latter is untenable, we must consider the option of only a 14 T Nb_3Sn magnet, or development of a large-bore high-T_C magnet (or more simply, a high-T_C-Nb_3Sn hybrid [260]; tests of YBCO indicate that it has good resistance to radiation damage [261]). The impact on muon yield of any such revision will also need to be addressed.

Another issue is the very large axial forces between the various magnets of the target system. A further complication is the requirement that the axial field profile in the beam-jet interaction region be smooth, such that the mercury jet is minimally perturbed as it enters this field. The baseline scenario calls for an iron plug at the upstream end of the first magnet, through which the proton beam and mercury jet enter. The presence of this plug adds considerable complexity to the mechanical design of the system and is an important technical issue.

2.3.3. Particle Production Simulations

Many of the studies above were performed using the MARS simulation code. It is essential to understand the dependence of particle production on target parameters (geometry, proton energy, material, etc.), and to have the proper values for the production rates. This is necessary both for particles giving the desired muons and for particles that lead to undesired energy deposition in the surrounding system.

Computations of particle production by both MARS and FLUKA [215, 216, 218] have been performed. Summaries of some simulations comparing results from different codes and lattices are shown in figure 34. A study [262] of the dependence of muon yield on target material has been performed using G4beamline [263] for different hadronic models. The results from this study give a flat distri-

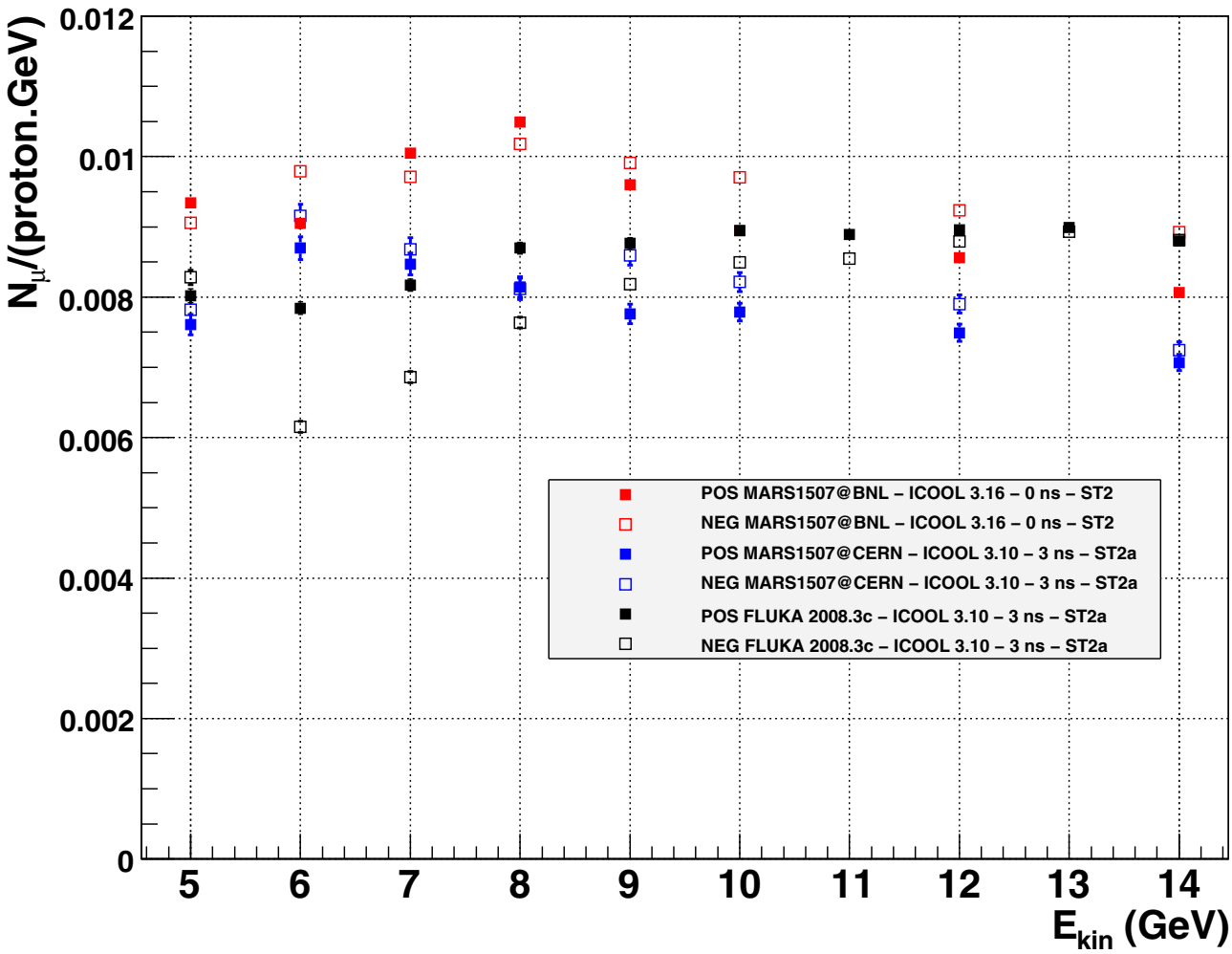

Figure 34. The muon yield, normalised to the beam power. An initial beam is generated by MARS as installed at BNL (red) and CERN (blue), and FLUKA 2008.3c (black), with an effective bunch length of 0 ns (red), 3 ns (blue and black). Mesons are then tracked through the front end using ICOOL 3.10 (blue) and ICOOL 3.16 (red). For the black points, an acceptance map approximating the effect of passing the particle through ICOOL 3.10 has been applied. After this, an acceptance cut is performed for a longitudinal momentum range of 100–400 MeV/c, normalised longitudinal acceptance of 150 mm, and normalised transverse acceptance of 30 mm using ECALC9F [264]. ST2 and ST2a denote different field tapering parameters, with the field going from 20 T to 1.25 T and 1.75 T respectively.

bution for high-Z materials for a beam energy between 5 and 8 GeV, whereas low-Z materials give a strong dependence of the muon yield on beam energy, favouring low energy.

A recent study [265] has been made, using HARP data [266, 267] convolved with the acceptance of the front-end channel of the Neutrino Factory and correcting for the phase space not covered as well as for thick-target effects not accounted for in the cross-section data. The simulations were performed with a more recent version (1509) of the MARS code. Results from this study show that the dependence of the muon yield on proton beam energy is relatively flat, with the yield being within 10% of the maximum value (at 7 GeV) in an energy range of 4 GeV—11 GeV. These results are in

basic agreement with those from figure 34, but show a somewhat flatter distribution than those of the pure simulation studies. It will be important to cross-validate these simulations against newer versions of the simulation codes as they become available.

2.4. Muon front-end

The Neutrino Factory muon front-end consists of a pion decay channel and longitudinal drift, followed by an adiabatic buncher, phase-rotation system, and ionisation-cooling channel.

The present design is based on the lattice presented in the Neutrino Factory Study 2A report [268] and subsequently developed in the ISS [5] with several modifications: the taper from the target solenoid has been adjusted; the solenoid-field strength in the drift, buncher, and phase rotation sections has been reduced from 1.75 T to 1.5 T; the whole system has been shortened; and the thickness of the lithium hydride absorbers in the cooling section has been increased. These changes result in the same muon-capture performance in a shorter bunch train, reducing requirements on some systems downstream of the muon front-end.

2.4.1. Decay and longitudinal drift

Downstream of the target solenoid, the magnetic field is adiabatically reduced from 20 T to 1.5 T over a distance of 15 m. Over the same distance, the beam pipe radius increases from 0.075 m to 0.3 m. This arrangement captures within the 1.5 T decay channel a secondary-pion beam with a large energy spread.

The initial proton bunch is relatively short (between 1 ns and 3 ns rms, see section 2.2) resulting in a short pion bunch. As the secondary pions travel from the target they drift longitudinally, following $ct = s/\beta_z + ct_0$, where s is distance along the transport line and $\beta_z = v_z/c$ is the relativistic longitudinal velocity. Hence, downstream of the target, the pions and their daughter muons develop a position-energy correlation in this RF-free decay channel. In the present baseline, the longitudinal drift length $L_D = 57.7$ m, and at the end of the decay channel there are about 0.4 muons of each sign per incident 8 GeV proton.

2.4.2. Buncher

The drift channel is followed by a buncher section that uses RF cavities to form the muon beam into a train of bunches and a phase-energy rotating section that decelerates the leading high-energy bunches and accelerates the late low energy bunches, so that each bunch has the same mean energy. The baseline design delivers a bunch train that is less than 80 m long. This is an improvement over the version of the design developed for the ISS [5] which delivered a 120 m long bunch train containing the same number of muons.

A shorter bunch train makes some downstream systems easier to design. For example, one of the constraints on the minimum length of the decay rings is the total length of the bunch train. By making the bunch train shorter, it may be possible to make the decay rings shorter. Also, the FFAG ring has a rather demanding kicker system, mostly driven by the total circumference of the ring but also

Table IX. Summary of front-end RF requirements. The total installed RF voltage is 1184 MV.

	Length [m]	**Number of cavities**	**Frequencies [MHz]**	**Number of frequencies**	**Peak gradient [MV/m]**	**Peak power requirements**
Buncher	33.0	37	319.6 to 233.6	13	3 to 9.71	1–3.5 MW/freq.
Rotator	42.0	56	230.2 to 202.3	15	13	2.5 MW/cavity
Cooler	97.5	130	201.25	1	15	4 MW/cavity
Total	172.5	219	319.6 to 201.25	29		562 MW

influenced by the length of the bunch train. A shorter bunch train makes these kickers slightly easier to construct.

To determine the required buncher parameters, we consider reference particles $(0,\ N_B)$ at $p_0 = 233$ MeV/c and $p_{N_B} = 154$ MeV/c, with the intent of capturing muons from an initial kinetic energy range of 50 to 400 MeV. The RF cavity frequency, f_{RF}, and phase are set to place these particles at the centre of bunches while the RF voltage increases along the channel. These conditions can be maintained if the RF wavelength, λ_{RF}, increases along the buncher, following:

$$N_B \lambda_{RF}(s) = N_B \frac{c}{f_{RF}(s)} = s\left(\frac{1}{\beta_{N_B}} - \frac{1}{\beta_0}\right); \tag{16}$$

where s is the total distance from the target, β_0 and β_{N_B} are the velocities of the reference particles, and N_B is an integer. For the present design, N_B is chosen to be 10, and the buncher length is 31.5 m. With these parameters, the RF cavities decrease in frequency from 320 MHz ($\lambda_{RF} = 0.94$ m) to 230 MHz ($\lambda_{RF} = 1.3$ m) over the length of the buncher.

The initial geometry for the placement of the RF cavities uses $0.4 - 0.5$ m long cavities placed within 0.75 m long cells. The 1.5 T solenoid focusing of the decay region is continued through the buncher and the rotator section which follows. The RF gradient is increased from cell to cell along the buncher, and the beam is captured into a string of bunches, each of which is centred about a test particle position, with energies determined by the spacing from the initial test particle such that the i^{th} reference particle has velocity:

$$1/\beta_i = 1/\beta_0 + \frac{i}{N_B}\left(\frac{1}{\beta_{N_B}} - \frac{1}{\beta_0}\right). \tag{17}$$

In the initial design, the cavity gradients, V_{RF}, follow a linear increase along the buncher:

$$V_{RF}(z) \approx 9\frac{z}{L_B} MV/m\,; \tag{18}$$

where z is distance along the buncher and L_B is the length of the buncher. The gradient at the end of the buncher is 9 MV/m. This gradual increase of the bunching voltage enables a somewhat adiabatic capture of the muons into separated bunches, which minimises phase-space dilution.

In the practical implementation of the buncher concept, this linear ramp of cavity frequency is approximated by a sequence of RF cavities that decrease in frequency along the 33 m beam transport allotted to the buncher. The number of different RF frequencies is limited to a more manageable 13 (1–4 RF cavities per frequency). The linear ramp in gradient described by equation 18 is approximated by the placement and gradient of the cavities in the buncher. Table IX shows a summary of the RF cavities that are needed in the buncher, rotator, and cooling sections.

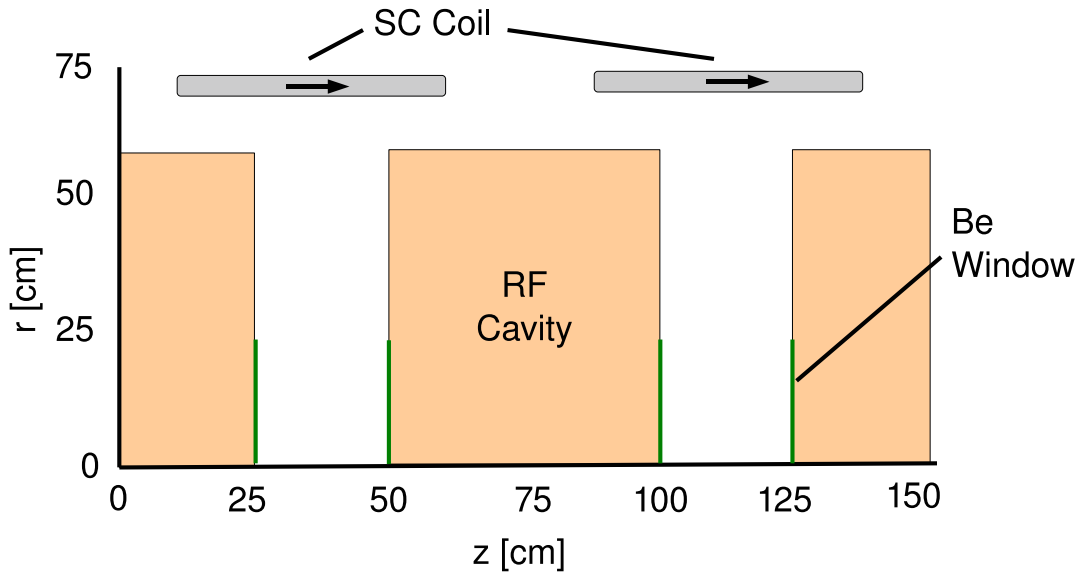

Figure 35. Schematic radial cross section of a rotator cell.

2.4.3. Rotator

In the rotator section, the RF bunch-spacing between the reference particles is shifted away from the integer, N_B, by an increment, δN_B, and phased so that the high-energy reference particle is stationary and the low-energy one is uniformly accelerated to arrive at the same energy as the first reference particle at the end of the rotator. For the baseline, $\delta N_B = 0.05$ and the bunch spacing between the reference particles is $N_B + \delta N_B = 10.05$. This is accomplished using an RF gradient of 12 MV/m in 0.5 m long RF cavities within 0.75 m long cells. The RF frequency decreases from 230.2 MHz to 202.3 MHz along the length of the 42 m long rotator region. A schematic of a rotator cell is shown in figure 35.

The RF frequency is set by requiring that the trajectories of the reference particles be spaced in ct by $(N_B + \delta N_B)$ wavelengths. In a practical implementation, a continuous change in frequency from cavity to cavity is replaced by grouping adjacent sets of cavities into the same RF frequency. The 42 m long RF rotator, then contains 56 RF cavities grouped into 15 frequencies.

Within the rotator, as the reference particles are accelerated to the central energy (at $p = 233$ MeV/c) at the end of the channel, the beam bunches formed before and after the central bunch are decelerated and accelerated respectively, obtaining at the end of the rotator a string of bunches of equal energy for both muon species. At the end of the rotator the RF frequency matches into the RF frequency of the ionisation cooling channel (201.25 MHz). The average momentum at the rotator is 230 MeV/c. The performance of the bunching and phase rotation channel, along with the subsequent cooling channel, is displayed in figure 36, which shows, as a function of the distance down the channel, the number of muons within a reference acceptance. The phase rotation increases the "accepted" muons by a factor of four.

A critical feature of the muon production, collection, bunching, and phase rotation system is that

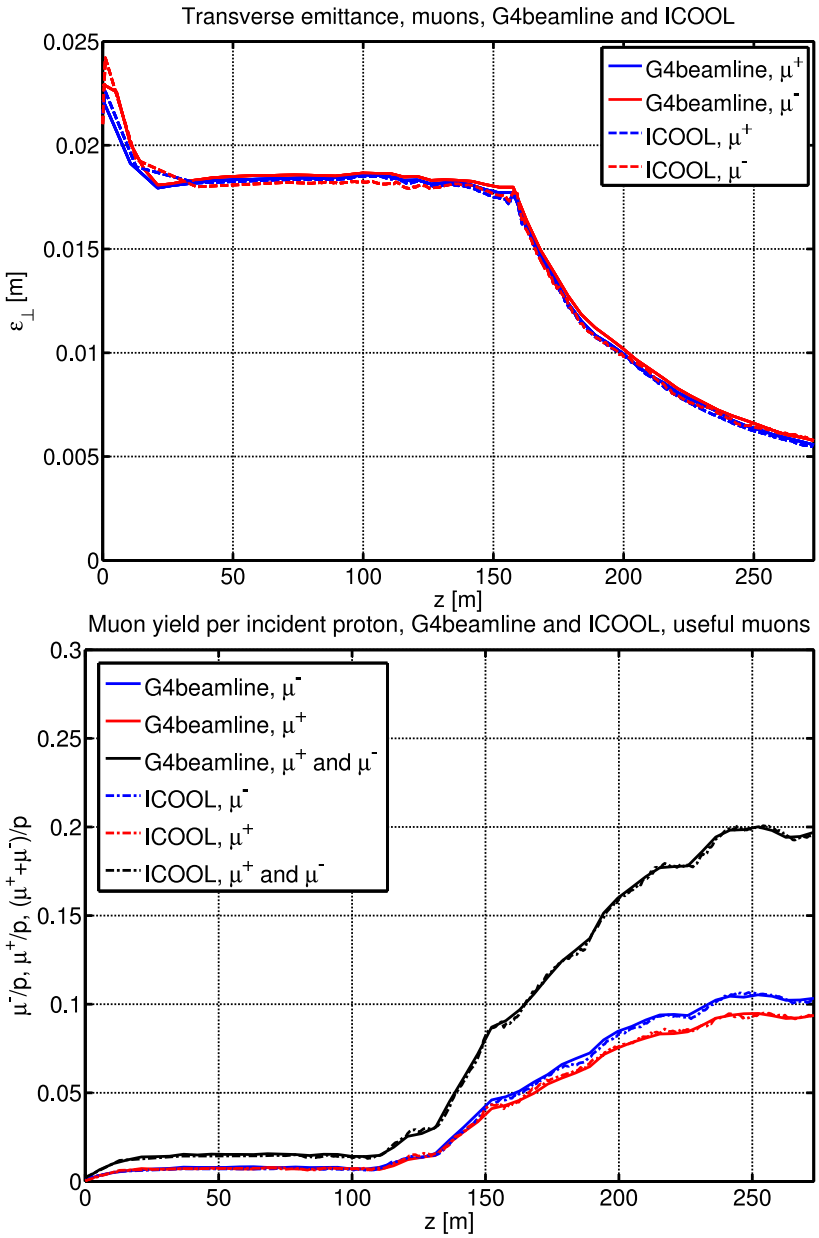

Figure 36. Performance of the bunching and cooling channel as a function of distance along the channel, as simulated using the ICOOL code [241] and the G4beamline code [263]. (top) The evolution of the rms transverse emittance (computed over all bunches). (bottom) The evolution of the number of muons within a reference acceptance (muons within 201.25 MHz RF bunches with momentum in the range 100–300 MeV/c, transverse amplitude squared less than 0.03 m and longitudinal amplitude squared less than 0.15 m). The cooling section starts at $s = 155$ m, where the rms transverse emittance is 0.018 m and 0.08 μ per proton are in the reference acceptance. The capture performance is shown for a cooling channel extending to $s = 270$ m although in this design the cooling channel extends only to 230 m. Acceptance is maximal at 0.20 μ per initial 8 GeV proton at $s = 240$ m (85 m of cooling) and the RMS transverse emittance is 7 mm. At $s = 230$ m (75 m of cooling) the number of μ per proton is 0.19 and the transverse emittance is 7.5 mm.

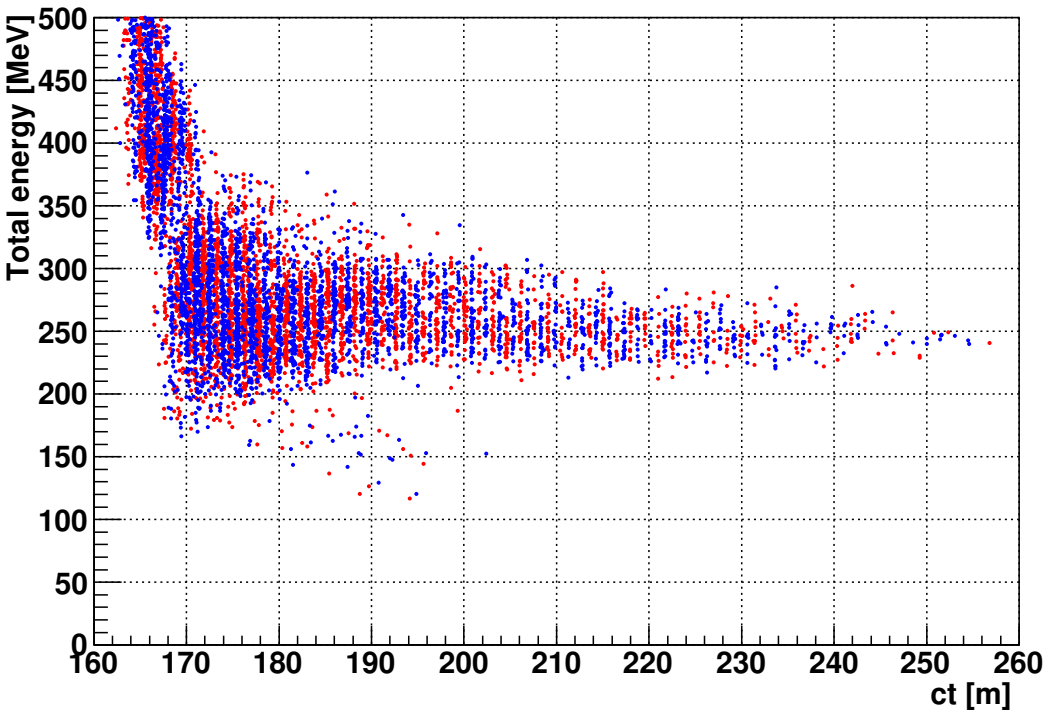

Figure 37. Distribution of particles in longitudinal phase-space at the phase rotation end. $\mu+$ are shown in red and $\mu-$ are shown in blue.

it produces bunches of both signs (μ^+ and μ^-) at roughly equal intensities. This occurs because the focusing systems are solenoids which focus both signs, and the RF systems have stable acceleration for both signs, separated by a phase difference of π. The distribution of muons in longitudinal phase space for particles of both signs at the end of the rotator is shown in figure 37.

2.4.4. Cooling channel

The baseline cooling-channel design consists of a sequence of identical 1.5 m long cells (figure 38). Each cell contains two 0.5 m-long RF cavities, with 1.1 cm thick LiH discs at the ends of each cavity (4 per cell) and a 0.25 m spacing between cavities. The LiH discs provide the energy-loss material for ionisation cooling. The cells contain two solenoid coils with opposite polarity. The coils produce an approximately sinusoidal variation of the magnetic field in the channel with a peak value on-axis of 2.8 T, providing transverse focusing with $\beta_\perp = 0.8$ m. The currents in the first two cells are perturbed from the reference values to provide matching from the constant-field solenoid in the buncher and rotator sections. The total length of the cooling section is 75 m (50 cells). Based on the simulation results shown in figure 36, the cooling channel is expected to reduce the rms transverse normalised emittance from $\epsilon_N = 0.018$ m to $\epsilon_N = 0.0075$ m. The rms longitudinal emittance is $\epsilon_L = 0.07$ m/bunch.

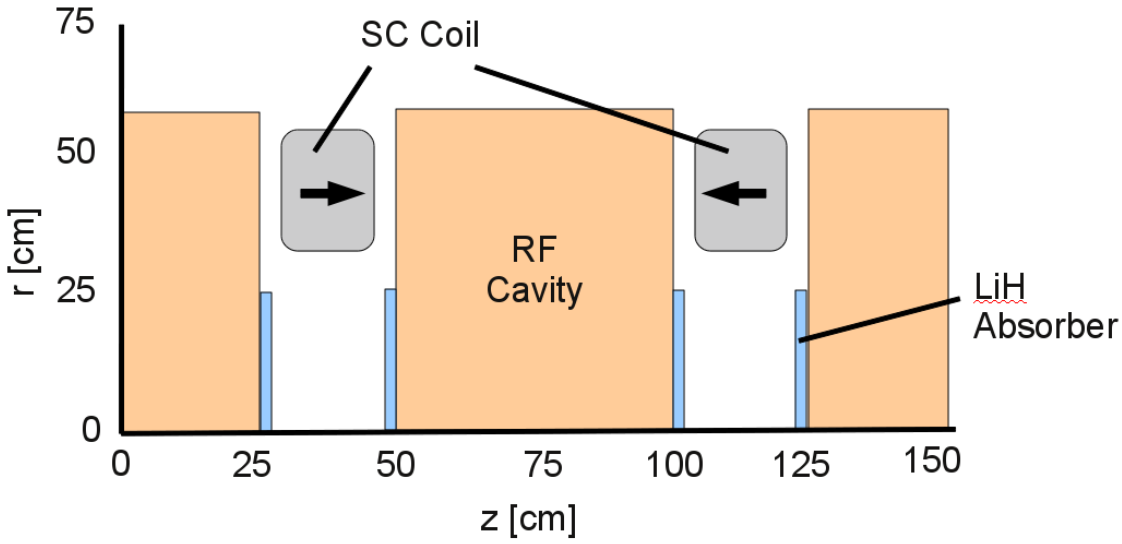

Figure 38. Schematic radial cross section of a cooling cell.

The effect of the cooling can be measured by counting the number of simulated particles that fall within a reference acceptance that approximates the expected acceptance of the downstream accelerator.

The squared amplitude $A_\perp^2$ is given by:

$$A_\perp^2 = p_z/m\left[\beta_\perp(x'^2+y'^2)+\gamma_\perp(x^2+y^2)+2\alpha_\perp(xx'+yy')+2(\beta_\perp\kappa-\mathcal{L})(xy'-yx')\right]; \tag{19}$$

where $\beta_\perp$, $\alpha_\perp$, $\gamma_\perp$ are solenoidal equivalents of the Twiss parameters, κ is the solenoidal focusing strength, and $\mathcal{L}$ is the dimensionless kinetic angular momentum [264, 269].

For longitudinal motion, the variables $t_c = ct$ (phase lag in periods within a bunch multiplied by RF wavelength) and ΔE (energy difference from centroid) are used rather than (z, z'). The longitudinal squared amplitude is given by:

$$A_L^2 = \frac{c}{m_\mu}\left[\frac{t_c^2}{\delta}+\delta\left(\Delta E-\frac{\alpha_L t_c}{\delta}\right)^2\right]; \tag{20}$$

where δ is defined by:

$$\delta = \frac{c\left\langle t_c^2\right\rangle}{m_\mu\epsilon_L}; \tag{21}$$

ϵ_L is a normalised longitudinal emittance:

$$\epsilon_L = \frac{c}{m_\mu}\sqrt{\left\langle t_c^2\right\rangle\left\langle\Delta E^2\right\rangle-\left\langle t_c\Delta E\right\rangle^2}; \tag{22}$$

and α_L is a correlation factor:

$$\alpha_L = \frac{c}{m_\mu\epsilon_L}\left\langle t_c\Delta E\right\rangle . \tag{23}$$

Following criteria developed using the ECALC9F program (distributed with ICOOL), a particle is considered to be within the acceptance of the machine if the transverse amplitude squared $A_\perp^2$ is less than 0.03 m and the longitudinal amplitude squared is less than 0.15 m. Note that the transverse and longitudinal notations are not the same and transverse-longitudinal amplitude correlations are not included. This is a crude first approximation to the muon accelerator acceptance, but is used in the present tables for consistent comparison of simulations.

Using the output from our re-optimised buncher and rotator, we have tracked particles through the cooling channel, and obtain, within the reference acceptances, 0.19 μ per 8 GeV incident proton. The acceptance criteria remove larger amplitude particles from the distribution and the rms emittance of the accepted beam is therefore much less than that of the entire beam. The rms transverse emittance, $\epsilon_\perp$, of the accepted beam is 0.004 m and the rms longitudinal emittance is 0.036 m.

At the end of the cooling channel, there are interlaced trains of positive and negative muon bunches. The trains of usable muon bunches are 80 m long (50 bunches), with 70% of the muons in the leading 20 bunches (30 m). The bunch length is 0.16 m in ct for each bunch, with a mean momentum of 230 MeV/c and an rms width δp of 28 MeV/c. For the accepted beam, the rms bunch width is 3.8 cm and the rms transverse momentum is 10 MeV/c.

2.4.5. Simulation codes

Two independently-developed codes have been used for tracking simulations of the muon front-end by the Monte Carlo method: ICOOL version 3.20 [241]; and G4beamline version 2.06 [263].

ICOOL is under active development at the Brookhaven National Laboratory. It is a 3-dimensional tracking program that was originally written to study ionisation cooling of muon beams. The program simulates particle-by-particle propagation through materials and electromagnetic fields. The physics model is most accurate for muons in the kinetic energy range of 50 MeV to 1 GeV, but tracking of electrons, pions, kaons, and protons is also possible. ICOOL includes a number of custom models for particle decay, delta-ray production, multiple Coulomb scattering, ionisation energy loss, and energy straggling.

G4beamline is a particle tracking and simulation program under active development by Muons, Inc. Physics processes are modelled using the Geant4 toolkit with the QGSP_BERT physics package [270] and it is specifically designed to simulate beam lines, and other systems using single-particle tracking.

Both codes use semi-analytic procedures to compute electromagnetic fields. Solenoid fields are generated as a sum of elliptic integrals calculated using the solenoid-coil geometry [271]. RF cavities are modelled using a Bessel function radially and a sinusoid in time for the ideal field produced by a cylindrical pillbox cavity.

Good agreement is shown in the muon yield and the yield of other particle species from the two codes (see figures 36 and 40). Note that different versions of ICOOL have been shown to disagree at the level of a few percent [272].

Analysis of results is performed using ECALC9F version 2.07 in addition to custom scripts written in Python and MATLAB. The beam has been generated using MARS 15.07. We expect a significant systematic error on the overall rate owing to uncertainty in the models used to generate the input beam.

Table X. Front-end RF requirements for the buncher system.

Frequency [MHz]	V_{Tot} (per frequency) [MV]	Number of cavities	Length [m]	Gradient [MV/m]	Peak RF Power (per frequency) [MW]
319.63	1.37	1	0.4	3.42	0.2
305.56	3.92	2	0.4	4.894	0.6
293.93	3.34	2	0.45	4.17	0.5
285.46	4.8	2	0.45	5.34	1
278.59	5.72	2	0.45	6.36	1.25
272.05	6.66	3	0.45	4.94	1.5
265.8	7.57	3	0.45	5.61	1.5
259.83	8.48	3	0.45	6.3	2
254.13	9.41	3	0.45	6.97	2.3
248.67	10.33	4	0.45	7.65	2.3
243.44	11.23	4	0.45	8.31	2.5
238.42	12.16	4	0.45	9.01	3
233.61	13.11	4	0.45	9.71	3.5
Total	98.1	37			22

2.4.6. RF Requirements and Design

The RF cavities in this design are all normal conducting cavities having 29 frequencies in the range 201.25 MHz to 320 MHz. The cavities are 50 cm long with peak field gradients in the range 4 MV/m to 15 MV/m, with the highest voltage required for the 201 MHz cavities. The power consumption of these cavities has been estimated semi-analytically using standard formulæ, and the results are listed in tables X and XI, together with the RF cavities required. The position and phase of every cavity is listed in Table XII.

Several RF cavities have been constructed to support the muon accelerator design effort [221]. A 43 cm long, 201 MHz RF cavity has been constructed and operated at peak gradients up to 21 MV/m and 10 more RF cavities are under construction as part of the international Muon Ionisation Cooling Experiment (MICE) [222]. Additionally, several 805 MHz cavities have been constructed and operated at gradients up to 40 MV/m. Design and construction of cavities with intermediate frequencies is not expected to present any additional difficulties.

2.4.7. Effect of magnetic field on RF gradient

There is empirical evidence that magnetic fields overlapping RF cavities, as present in the muon front-end, may induce breakdown in the cavities [273, 274]. The performance of the muon front-end using a reduced field has been explored using ICOOL. In figure 39, the muon transmission is shown as a function of fractional change in RF gradient in the buncher, rotator, and cooling channel. The simulations indicate that around the nominal gradient, muon transmission is rather insensitive to the peak gradients. If the achievable RF gradient falls dramatically below the nominal value, there is a significant effect on muon transmission. In order to mitigate this technical risk, several alternative

Table XI. Front-end RF requirements for the rotator and cooler systems. f_{RF} is the RF frequency, V_{tot} is the total voltage required at that frequency, n_{cav} is the number of cavities at that frequency, E_{peak} is the peak gradient in each cavity, and P_{peak} is the peak RF power required per cavity.

f_{RF} [MHz]	V_{tot} [MV]	n_{cav}	E_{peak} [MV/m]	P_{peak} [MW]
Rotator				
230.19	19.5	3	13.0	2.2
226.13	19.5	3	13.0	2.2
222.59	19.5	3	13.0	2.3
219.48	19.5	3	13.0	2.4
216.76	19.5	3	13.0	2.4
214.37	19.5	3	13.0	2.5
212.48	19.5	3	13.0	2.5
210.46	19.5	3	13.0	2.6
208.64	26.0	4	13.0	2.6
206.9	26.0	4	13.0	2.7
205.49	26.0	4	13.0	2.7
204.25	32.5	5	13.0	2.7
203.26	32.5	5	13.0	2.8
202.63	32.5	5	13.0	2.8
202.33	32.5	5	13.0	2.8
Total	364.0	56		144.8
Cooler				
201.25	880	130	16	4.3

lattices have been developed and are described briefly in Appendix D.

2.4.8. Magnet requirements and design

Pion capture in the target system is achieved using a series of solenoids in which the field tapers from 20 T to 1.5 T over 15 m (see section 2.3). Here we describe solenoids in the drift, buncher, and rotator that produce a constant magnetic field of 1.5 T and solenoids in the cooler that produce the alternating solenoid field configuration. These coils are summarised in table XIII.

The 1.5 T solenoids must accommodate the beam pipe, with a 30 cm radius. Within the buncher and rotator, they must also accommodate RF cavities with radii of 60 cm. This can be achieved using coils with an inner radius of 68 cm and a conductor radial thickness of 4 cm, so that the cavities fit entirely within the coils. A coil length of 50 cm spaced at 75 cm intervals leaves a gap of 25 cm between coils, matching the periodicity of the cooling channel and enabling access for room temperature services such as vacuum and RF power feeds. The required current for these coils is 47.5 A/mm^2 to give a total current of 0.95 MA-turns. The coils are therefore large enough to accommodate the beam pipe, RF and diagnostics, and added shielding. A smaller radius could be used in the first 60 m, which has no RF. The 135 m transport requires 180 such magnets.

The cooling system requires strong alternating-sign coils that are placed between RF cavities, fitting

Table XII. Full list of RF cavities. Cavities are grouped by frequency. Position is the position of the upstream edge of the first cavity in the group. z-Separation is the distance between the centres of each cavity in the group. 0° is bunching mode while 5° and 35° are partially accelerating modes.

z **Position** [m]	**Phase** [deg.]	**Peak gradient** [MV/m]	**Frequency** [MHz]	**Length** [m]	**Number**	z**-Separation** [m]
81.27	0.0	3.42	319.63	0.40	1	
85.02	0.0	4.894	305.56	0.40	2	0.40
88.77	0.0	4.17	293.93	0.40	2	0.40
91.77	0.0	5.34	285.46	0.45	2	0.45
94.02	0.0	6.36	278.59	0.45	2	0.45
96.27	0.0	4.94	272.05	0.45	3	0.45
98.52	0.0	5.61	265.8	0.45	3	0.45
100.77	0.0	6.3	259.83	0.45	3	0.45
103.02	0.0	6.97	254.13	0.45	3	0.45
105.27	0.0	7.65	248.67	0.45	3	0.45
107.52	0.0	8.31	243.44	0.45	3	0.45
109.77	0.0	9.01	238.42	0.45	3	0.45
112.02	0.0	9.71	233.61	0.45	3	0.45
114.27	5.0	13.0	230.19	0.5	3	0.75
116.52	5.0	13.0	226.13	0.5	3	0.75
118.77	5.0	13.0	222.59	0.5	3	0.75
121.02	5.0	13.0	219.48	0.5	3	0.75
123.27	5.0	13.0	216.76	0.5	3	0.75
125.52	5.0	13.0	214.37	0.5	3	0.75
127.77	5.0	13.0	212.48	0.5	3	0.75
130.02	5.0	13.0	210.46	0.5	3	0.75
132.27	5.0	13.0	208.64	0.5	4	0.75
135.27	5.0	13.0	206.90	0.5	4	0.75
138.27	5.0	13.0	205.49	0.5	4	0.75
141.27	5.0	13.0	204.25	0.5	5	0.75
145.02	5.0	13.0	203.26	0.5	5	0.75
148.77	5.0	13.0	202.63	0.5	5	0.75
152.52	5.0	13.0	202.33	0.5	5	0.75
154.6	35.0	16.0	201.25	0.5	130	0.75

Table XIII. Summary of front-end magnet requirements.

	Length [m]	**Inner radius** [m]	**Radial thickness** [m]	**Current density** [A/mm^2]	**Number**
Initial transport	0.5	0.68	0.04	47.5	180
Cooling channel	0.15	0.35	0.15	±107	130

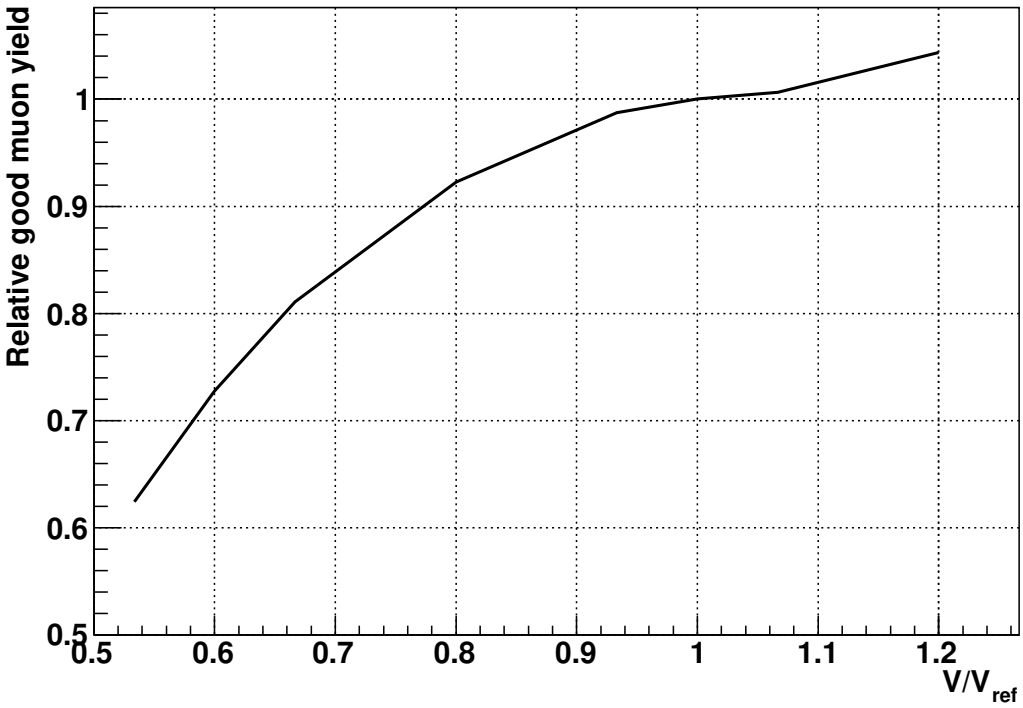

Figure 39. Relative (good) muon yield within the nominal acceptance as a function of the peak field gradient, simulated in ICOOL. $V_{\rm ref}$ is the baseline gradient; all cavities were scaled by the constant $V/V_{\rm ref}$.

within the 25 cm inter-cavity spaces (figure 38). The coils are 15 cm long with inner radius 35 cm, radial thickness 15 cm and current density of ± 107 A/mm^2 to give a total current of 2.4 MA-turns. The coil currents alternate in direction from coil to coil. These coils produce an on-axis solenoid field that varies from +2.8 T to −2.8 T over a 1.5 m period, following an approximately sinusoidal dependence. Maximum fields in the cooling cell volume are 5 T near the coil surfaces. 100 such coils are needed in a 75 m cooling system.

2.4.9. Beam Losses

There are significant particle losses along the beam line and these will result in a large energy deposition in superconducting magnets and other equipment. Two main risks have been identified: energy deposition by all particles may cause superconducting equipment to quench; and energy deposition by hadrons and other particles may activate equipment preventing hands-on maintenance.

In figure 40, the power deposited by transmission losses per unit length from various particle species is shown as a function of distance along the channel. Note that energy deposition in RF windows and absorbers is not included in this calculation. It is expected that this equipment will absorb several

kilowatts of beam power from each particle species.

In currently operating accelerators, uncontrolled hadronic losses must be less than ≈1 W/m to enable "hands-on" maintenance without additional time, distance, or shielding constraints. Magnets are expected to quench with beam losses above a few tens of W/cm^3. Several schemes are envisaged to control the beam losses and reduce them below these values.

Three devices are under study for reducing the transmission losses in the front-end:

- Low momentum protons may be removed by passing the bean through a low-Z "proton absorber" . This device takes advantage of the different stopping distance of protons compared with other particles in material;
- Particles with a high momentum, outside of the acceptance of the front-end, may be removed using a pair of chicanes. Dispersion is induced in the beam by means of bending magnets or tilted solenoids in a chicane arrangement and high-momentum particles are passed onto a beam dump. A design for the chicane is being developed that can accommodate the large momentum spread. In order to retain both muon species, one chicane is required for each sign; and
- Particles with transverse amplitude outside of the acceptance of the front-end may be removed using transverse collimators.

2.4.10. Summary

The Neutrino Factory muon front-end captures a substantial proportion of the muons produced by the Neutrino Factory target. Longitudinal capture is achieved using a buncher and energy-time phase-rotation system while transverse capture is achieved using a high field solenoid adiabatically tapered to 1.5 T and enhanced by ionisation cooling. Technical risks to the muon front-end are presented by the requirement for high peak RF fields in the presence of intense magnetic fields and irradiation of the accelerator hardware due to uncontrolled particle losses. Strategies have been outlined by which these risks can be mitigated. Overall, the muon front-end increases the capture rate of muons in the nominal accelerator acceptance by a factor 10.

2.5. Linac and RLA

The muon acceleration process involves a complex chain of accelerators including a (single-pass) linac, two recirculating linacs (RLAs) and an FFAG ring [275]. This section will discuss the linac, the two RLAs and the chicanes, shown schematically in figure 41.

Acceleration starts after ionisation cooling at 230 MeV/c and proceeds to 12.6 GeV. The pre-accelerator captures a large muon phase space and accelerates muons to relativistic energies, while adiabatically decreasing the phase-space volume so that effective acceleration in the RLA is possible. The RLA further compresses and shapes the longitudinal and transverse phase spaces, while increasing the energy. An appropriate choice of multi-pass linac optics based on FODO focusing assures a large number of passes in the RLA. The proposed "dog-bone" configuration facilitates simultaneous acceleration of both μ^+ and μ^- species through the requirement of mirror-symmetric optics in the return "droplet" arcs.

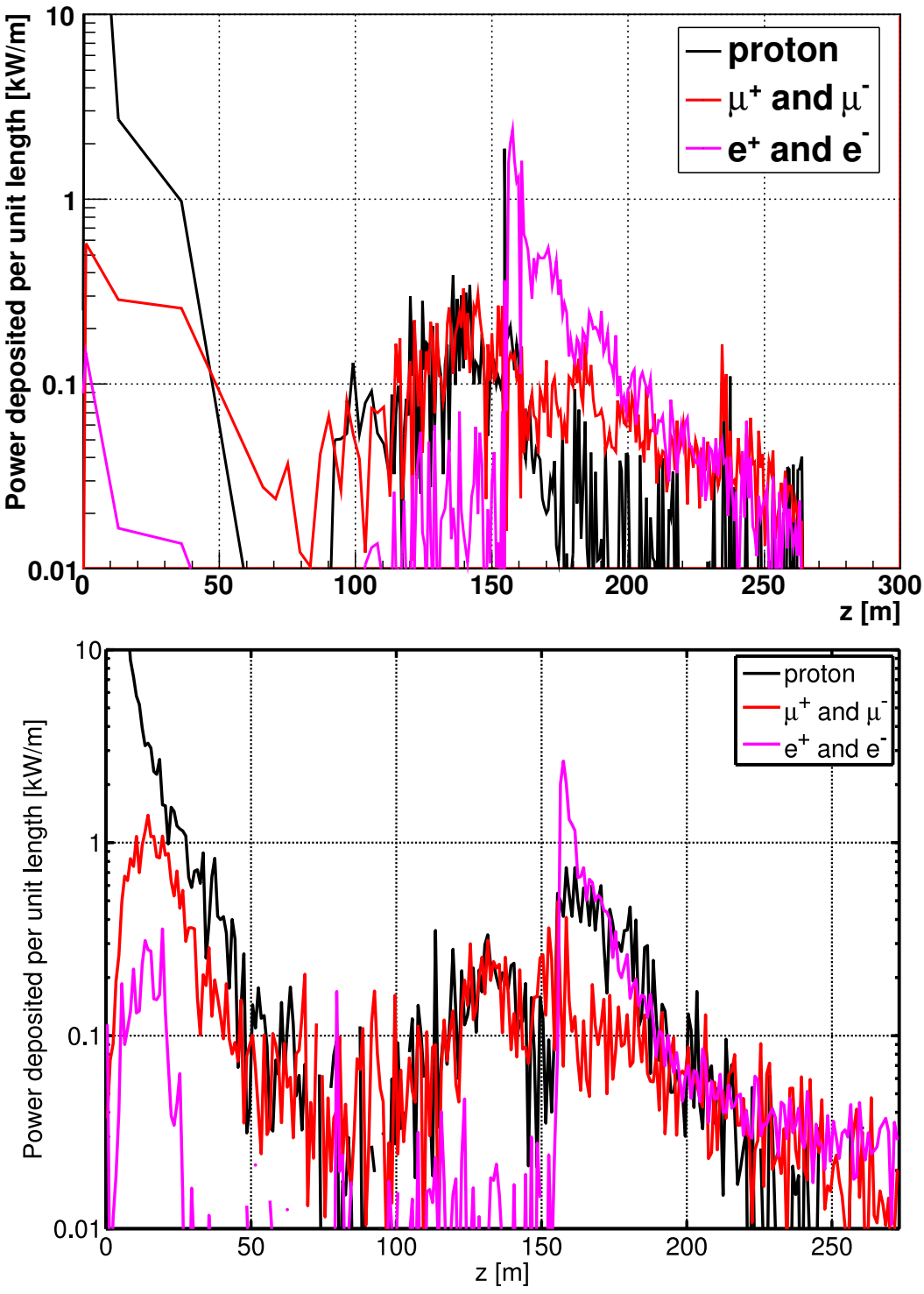

Figure 40. Power deposited by transmission losses of various particle species in the surrounding equipment simulated in (top) ICOOL and (bottom) G4Beamline.

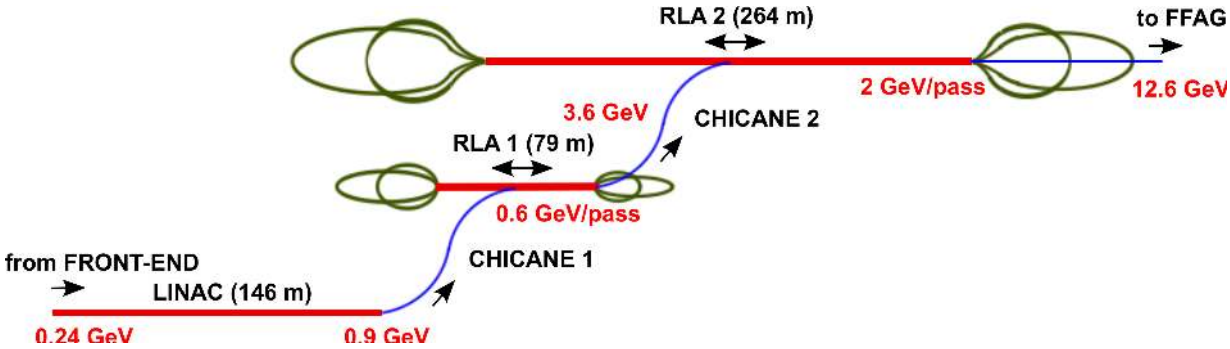

Figure 41. Layout of the linac and recirculating linacs connected by chicanes.

The linac consists of superconducting RF cavities and iron-shielded solenoids grouped in cryomodules [276], while the recirculating linacs RLA I and RLA II consist of superconducting RF cavities and quadrupoles. The linac is required to accelerate 0.22 GeV/c muons coming from the muon front-end to 0.9 GeV/c and, given these relatively low energies, solenoidal transverse focusing has been chosen so that the beam preserves its initial horizontal-vertical phase-space coupling. The transfer to RLA I is performed through the double chicane, "chicane 1", which consists of a vertical dipole spreader (at the beginning), horizontal bending magnets, a vertical dipole combiner (at the end), and quadrupoles for transverse focusing [228]. In this manner both positive and negative muons can be transferred, while keeping RLA I at the same height as the linac, a decision taken to simplify the civil engineering. With the beam now being relativistic, quadrupole focusing in a FODO-lattice is preferred for chicane 1. In addition, a number of sextupoles must be inserted at positions where the dispersion caused by bending has a maximum. Entering RLA I, the beam performs 4.5 passes at an average gain of 0.6 GeV/pass with an excursion along the return arcs after each pass. Single-cell, superconducting cavities provide acceleration along RLA I while transverse focusing is achieved by quadrupoles in a FODO arrangement along RLA I and its arcs. Similarly, through another double chicane, "chicane 2", the 3.6 GeV beam is transferred to RLA II where it again performs 4.5 passes but now at an average gain of 2 GeV/pass. Eventually, the beam is extracted and injected into the FFAG at 12.6 GeV. Section 2.5.4 reports the latest results of muon-beam tracking and the work which has been performed to allow tracking using realistic field maps for both RF cavities and solenoids.

2.5.1. Overall lattice description

2.5.1.1. Linear Pre-Accelerator

A single-pass linac raises the total energy from 0.244 GeV to 0.9 GeV. This makes the muons sufficiently relativistic to facilitate further acceleration in the RLA. The initial phase-space of the beam, as delivered by the muon front-end, is characterised by significant energy spread; the linac has been designed so that it first confines the muon bunches in longitudinal phase-space, then adiabatically super-imposes acceleration over the confinement motion, and finally boosts the confined bunches to 0.9 GeV. To achieve a manageable beam-size in the front-end of the linac, short focusing cells are

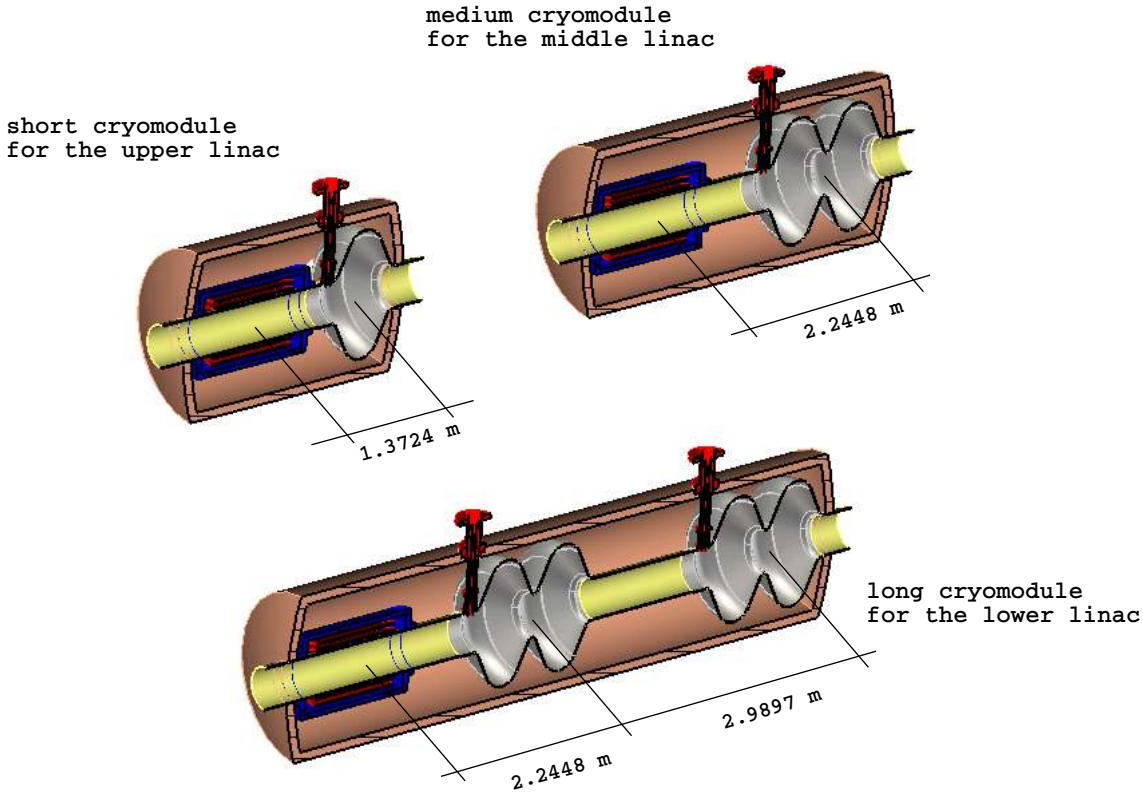

Figure 42. Layout of the three cryo-module types. The modules share the same solenoid and cavity type throughout in this study.

used for the first six cryo-modules [277]. The beam size is adiabatically damped with acceleration, allowing the short cryo-modules to be replaced with intermediate length cryo-modules, and then with 11 long cryo-modules. Consequently, the linac was split into three consecutive sections (referred as: the "upper", "middle" and "lower" linac sections) each section being built of a particular type of cryo-module as shown in figure 42. The important parameters for each section are summarised in table XIV. Each linac section is configured with periodic FOFO cells, matched at the section junctions, as illustrated in figure 43 [278]. Periodicity within each section is maintained by scaling the solenoid fields in consecutive cryo-modules linearly with increasing momentum as summarised in table XV.

One of the main requirements of the single-pass pre-accelerator linac is to compress adiabatically the longitudinal phase-space volume in the course of acceleration. The initial longitudinal acceptance of the linac (chosen to be 2.5 σ) calls for "full bucket acceleration"; with an initial momentum acceptance of $\Delta p/p = \pm 17\%$ and a bunch length of $\Delta\phi = \pm 102^\circ$ (in RF phase). To perform adiabatic bunching one needs to drive rather strong synchrotron motion along the linac. The profile of the RF-cavity phases is organised so that the phase of the first cavity is shifted by 73° (off crest) and then the cavity phase is gradually changed to zero by the end of the linac, see table XV and figure 44a. In the initial part of the linac, when the beam is still not relativistic, the far-off-crest acceleration induces rapid synchrotron motion (one full period, see figure 44b), which allows bunch compression in both

Table XIV. Summary of important linac parameters. Energy gain per cavity indicates which (half-)cavity in table XXII is being used.

Linac section	**upper**	**middle**	**lower**
Cell length (m)	3	5	8
Cryo-modules	6	8	11
Maximum β function (m)	2.90	4.93	8.25
RF cavities/lattice cell	1	1	2
RF cells/cavity	1	2	2
Maximum energy gain/cavity (MeV)	11.25	25.5	25.5

Table XV. For each cryo module, the kinetic energy at the exit of the module, the solenoid field (for a 1 m solenoid), and the RF phase (zero is on-crest). Taken from the OptiM model.

Short cryo-modules

Kin. energy (MeV)	141.6	145.1	149.0	153.1	157.6	162.4
Field (T)	−1.04	1.06	−1.07	1.09	−1.12	0.89
RF phase (deg.)	−73.3	−71.6	−69.8	−68.1	−66.4	−64.6

Medium cryo-modules

Kin. energy (MeV)	174.3	187.3	201.3	216.5	232.6	249.7	267.7	286.6
Field (T)	−0.99	0.98	−1.03	1.08	−1.14	1.21	−1.28	1.03
RF phase (deg.)	−62.11	−59.13	−56.22	−53.31	−50.40	−47.52	−44.67	−41.85

Long cryo-modules

Kin. energy (MeV)	326.4	368.6	412.6	458.3	505.5	553.7	602.8	652.6	702.8	753.3	803.9
Field (T)	−1.13	1.17	−1.29	1.41	−1.54	1.68	−1.81	1.95	−2.09	2.23	−2.37
RF phase (deg.)	−38.1	−33.8	−29.5	−25.5	−21.5	−17.8	−14.2	−10.8	−7.6	−4.5	−1.7

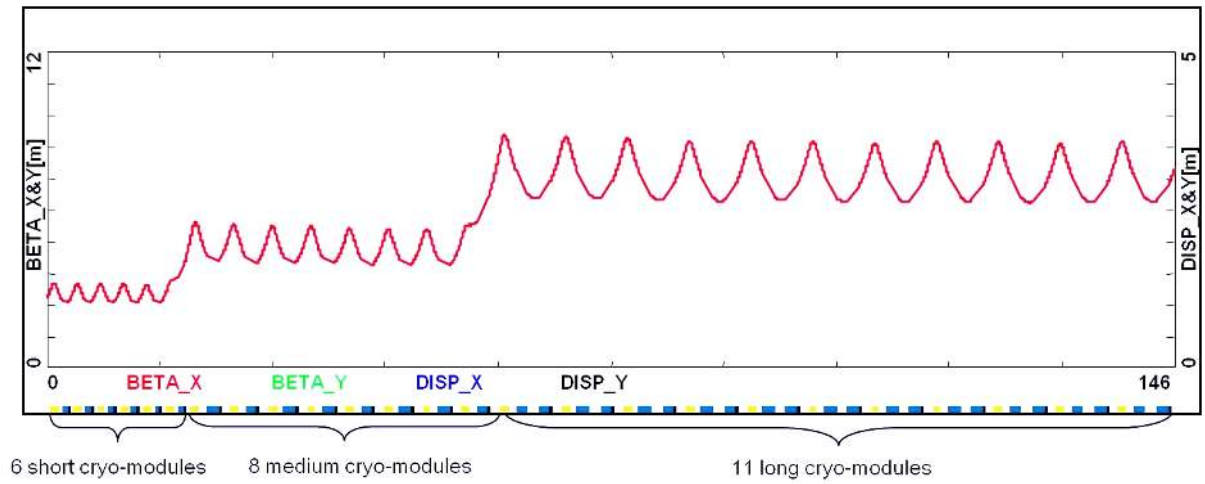

Figure 43. Transverse FOFO optics of the entire linac; the upper, middle and lower periodic sections uniformly matched at the junctions.

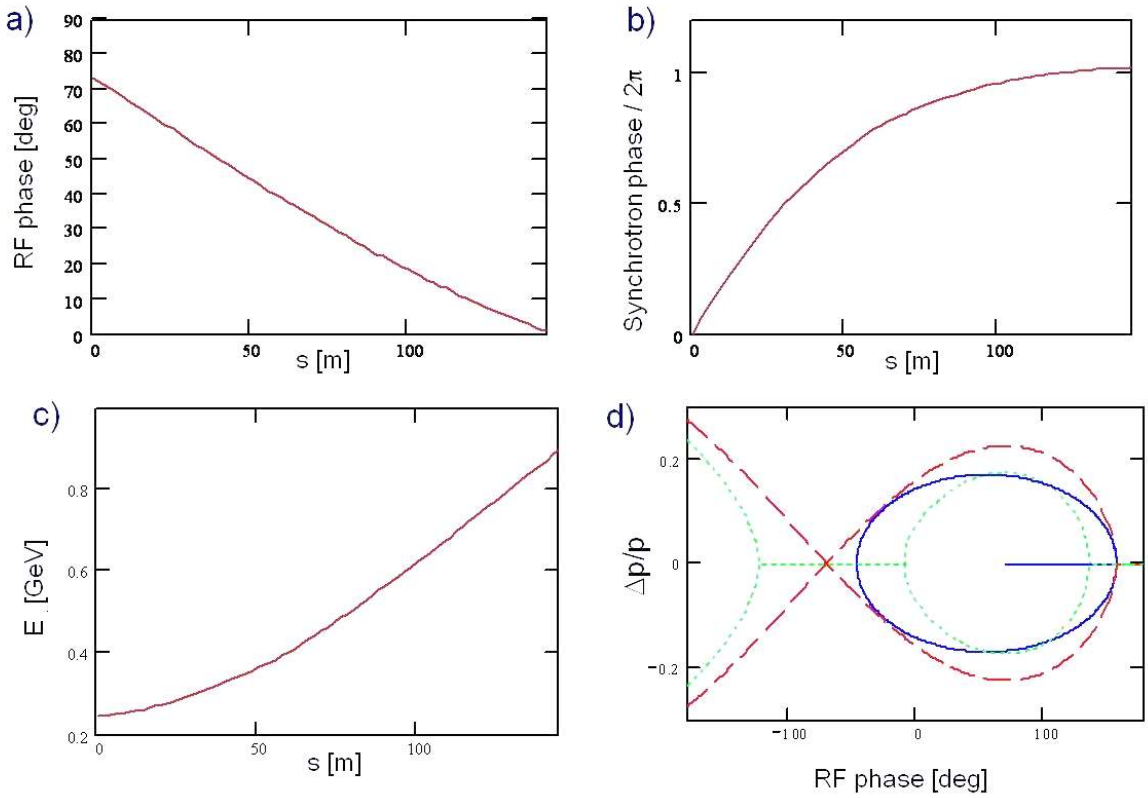

Figure 44. Longitudinal matching of a single-pass linac: a) the bunch starts far off-crest to capture the beam at low energy and then moves to the crest as the energy increases and the longitudinal acceptance improves; b) the synchrotron phase advances by a full period from the beginning to the end of the linac; c) the rate of energy gain increases as the bunch moves closer to crest. d) Longitudinal acceptance matched inside the separatrix and optimised for 'full bucket' acceleration.

bunch-length and momentum spread as illustrated in figure 44.

To maximise the longitudinal acceptance, the initial position of the bunch is shifted relative to the centre of the bucket, to keep the beam boundary inside the separatrix [276], as illustrated in figure 44d. The synchrotron motion also suppresses the sag in acceleration for the bunch head and tail. In our tracking simulation we have assumed a particle distribution that is Gaussian in 6D phase space with the tails of the distribution truncated at 2.5 σ, which corresponds to the beam acceptance. Despite the large initial energy spread, the particle tracking simulation through the linac does not predict any significant emittance growth [228]. Results of the simulation are illustrated in figure 45 which shows the longitudinal phase-space at the end of the linac as simulated by ELEGANT [279, 280]; tracking through the individual field maps of the linac's RF cavities and solenoids (figure 45a) and by a simple matrix based code OptiM [281] (figure 45b).

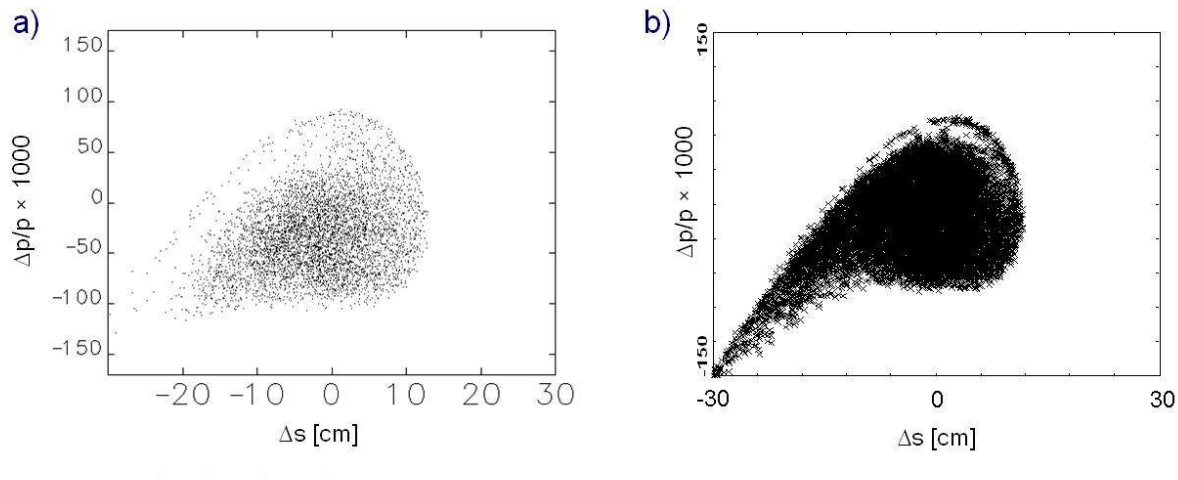

Figure 45. Longitudinal phase-space compression at the linac end as simulated by ELEGANT [279, 280] (left) and OptiM [281] (right).

Table XVI. Gradient, cryo-module by cryo-module along the 0.6 GeV linac. The quadrupole centres start at longitudinal position 46 cm with a spacing between quadrupole centres of 3 m. The FODO lattice starts at one end of the linac with the first F quad in the table, and is reflection symmetric about the centre of the last D quad shown in the table. There are RF cavities between each of the quadrupoles, except there are no cavities between the central D magnet and its adjacent F quadrupoles. In the first full pass, each cavity causes the beam to gain 25 MeV, starting with a kinetic energy of 1103.9 MeV at the beginning of that pass.

F Gradient (kG/cm)	0.402	0.385	0.368	0.352	0.335	0.318	0.301
D Gradient (kG/cm)	−0.394	−0.377	−0.360	−0.343	−0.325	−0.308	−0.301

2.5.1.2. RLA I

The dog-bone RLA I is designed to accelerate simultaneously the μ^+ and μ^- beams from 0.9 GeV to 3.6 GeV. The injection energy into the RLA and the energy gain per RLA linac (0.6 GeV) were chosen so that a tolerable level of RF phase slippage along the linac could be maintained ($\sim 20°$ in RF phase). To suppress chromatic effects, 90° FODO optics was used as a building block for both the linac and the return arcs. The layout and optics of the linac's periodic cell is shown in figure 46. The cavity from table XXII with the higher energy gain is used for the linac.

The focusing profile along the linac was chosen so that beams with a large energy spread could be transported within the given aperture. Since the beam is traversing the linac in both directions, a 'bisected' focusing profile [219] was chosen for the multi-pass linac. Here, the quadrupole gradients scale up with momentum to maintain 90° phase advance per cell for the first half of the linac (figure 47a), and then are mirror reflected in the second half, as illustrated in figure 47b. The complete focusing profile along the entire linac is summarised in table XVI.

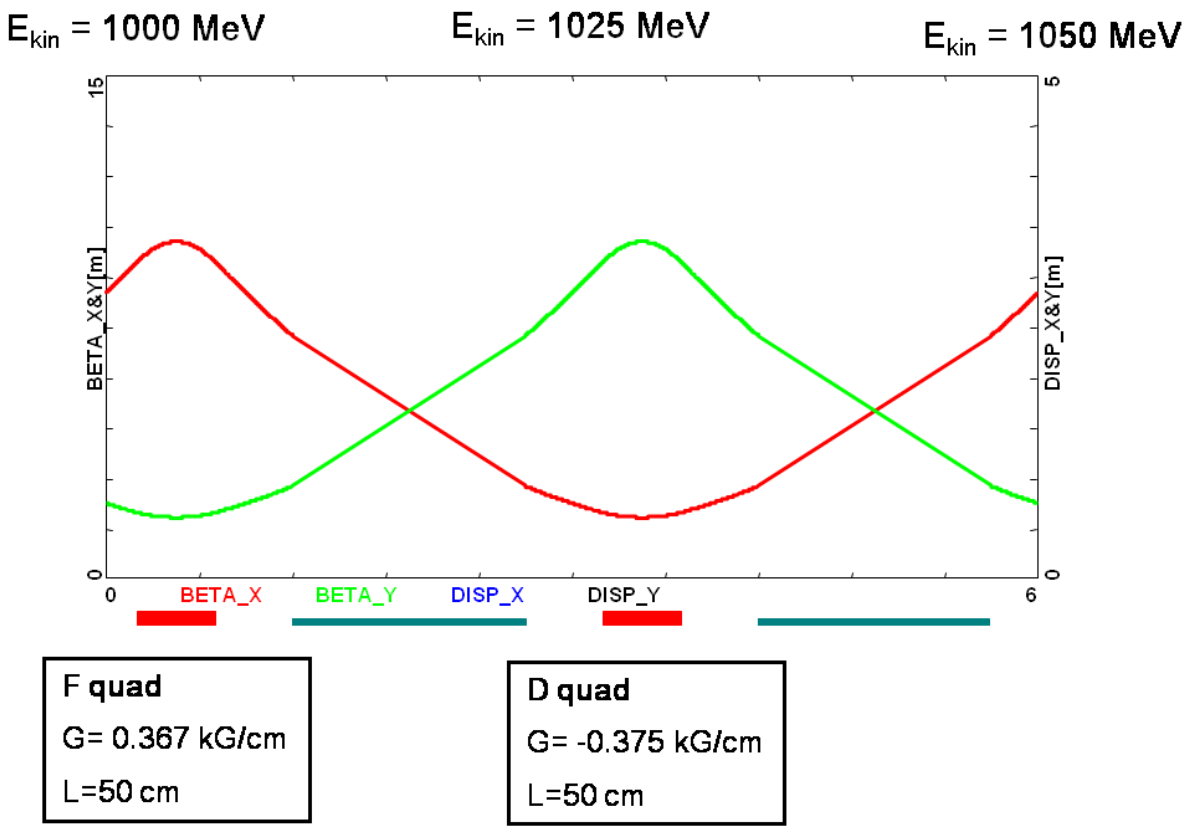

Figure 46. Periodic 90° FODO 6 m linac cell. A pair of 2-cell cavities is interleaved between quadrupoles. The cavity length is 1 RF wavelength and the elements are equally spaced.

At the ends of the RLA linacs, the beams need to be directed into the appropriate energy-dependent (pass-dependent) droplet arc for recirculation [277]. The entire droplet-arc architecture is based on 90° phase-advance cells with periodic beta functions, as shown in figure 48.

For practical reasons, horizontal rather than vertical beam separation has been chosen. Rather than suppressing the horizontal dispersion created by the spreader, it has been matched to that of the outward 60° arc. This is partially accomplished by removing one dipole (the one furthest from the spreader) from each of the two cells following the spreader. To switch from outward to inward bending, three transition cells are used, wherein the four central dipoles are removed. The two remaining dipoles at the ends bend the same direction as the dipoles to which they are closest. To facilitate simultaneous acceleration of both μ^+ and μ^- bunches, a mirror symmetry is imposed on the droplet-arc optics (oppositely charged bunches move in opposite directions through the arcs) [275]. This puts a constraint on the exit/entrance Twiss functions for two consecutive linac passes, namely $\beta^n_{out} = \beta^{n+1}_{in}$ and $\alpha^n_{out} = -\alpha^{n+1}_{in}$, where $n = 0, 1, 2...$ is the pass index. Complete droplet arc optics for the lowest energy arc (1.2 GeV) are shown in figure 49.

The momentum compaction is relatively large (6.5 m), which guarantees significant rotation in longitudinal phase-space as the beam passes through the arc. This effect, combined with off-crest

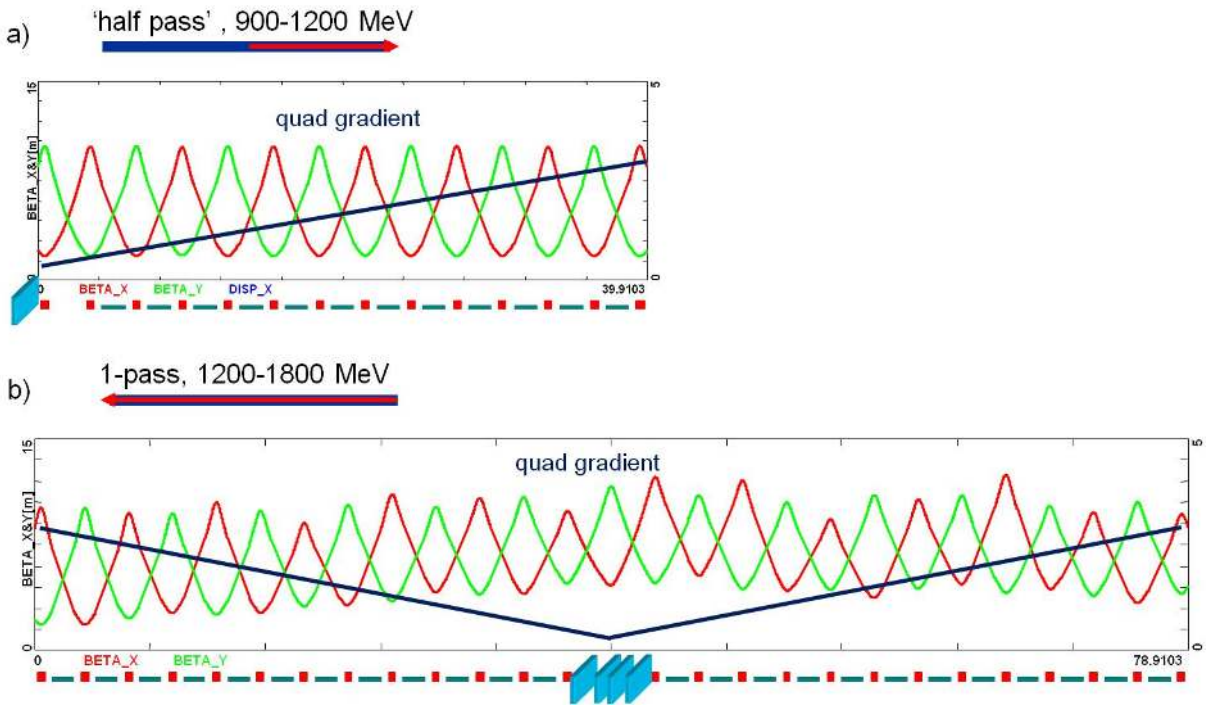

Figure 47. FODO-based multi-pass linac optics. The quadrupole gradients are scaled up with momentum for the first half of the linac, then they are mirror reflected in the second half. The injection chicane magnets are located at the middle of the linac (marked in blue).

acceleration in the subsequent linac, yields further compression of the longitudinal phase-space as the beam is accelerated [228].

All higher arcs are based on the same bends (1 m, 1.1 T dipoles) and they are configured via extending Arc 1 by additional inward and outward cells as summarised in table XVII. The transition regions always to have three cells. The quadrupole strengths in the arcs are scaled up linearly with momentum to preserve the 90° FODO lattice, as summarised in table XVII. Since the linac does not have a 90° phase advance per cell for later passes, the quadrupoles near the spreader must be modified to achieve matching, as described in Table XVIII. The matching designs will need to be slightly modified in future work to ensure that common magnets (namely the F magnet at the end of the linac and the ends of all the arcs) all have the same parameters.

2.5.1.3. RLA II

RLA II is designed to accelerate the μ^+ and μ^- beams from 3.6 GeV to 12.6 GeV. The injection energy and the energy gain per linac (2 GeV) were chosen so that a tolerable level of RF-phase slippage along the linac could be maintained. The optics configuration is almost identical to that of RLA I. It is again based on a 90° FODO lattice and a bisected multi-pass linac. The main difference is that the fundamental cell-length was extended to 12 m (cf. 6 m for RLA I). The layout and optics of the linac's

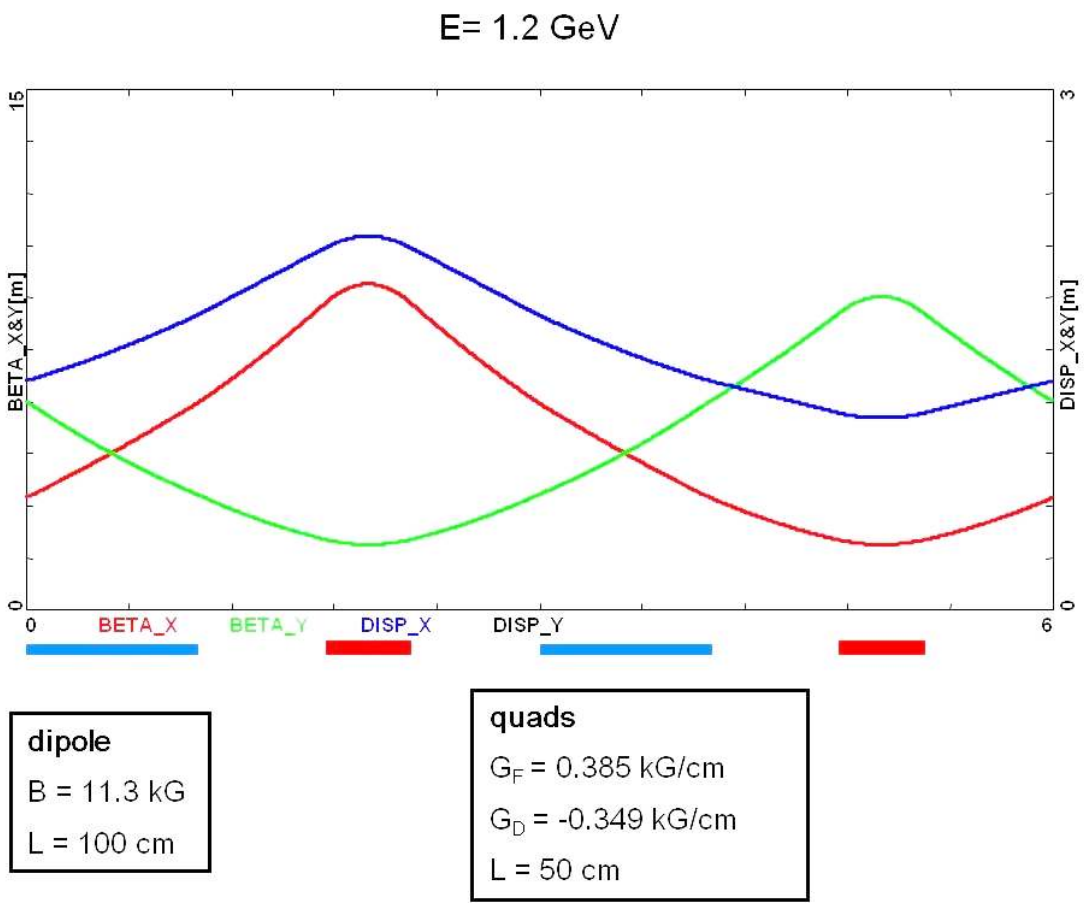

Figure 48. Periodic 90° FODO 6 m inward-bending cell, including a pair of rectangular bends interleaved between quads. All elements are equally spaced.

Table XVII. Higher arcs optics architecture; arc circumference and quadrupole strength scaled up with momentum. E is the arc energy, p/p_1 is the ratio of the momentum to the first arc momentum, $n_{\rm out}$ is the number of outward bending cells in each outward bend (the total is twice this), $n_{\rm in}$ is the number of inward bending cells, L is the arc length, and G_F and G_D are the focusing and defocusing quadrupole gradients, respectively.

E (GeV)	p/p_1	$n_{\rm out}$	$n_{\rm in}$	L (m)	G_F (kG/cm)	G_D (kG/cm)
1.2	1	2	10	130	0.385	−0.349
1.8	3/2	3	15	172	0.578	−0.524
2.4	2	4	20	214	0.770	−0.698
3.0	5/2	5	25	256	0.962	−0.873

Table XVIII. Strengths of matching quadrupoles in arc 2 of RLA I. Values for other arcs have not yet been computed.

Gradient (kG/cm)	0.5248	−0.5260	0.6321	−0.6878	0.6151	−0.5463

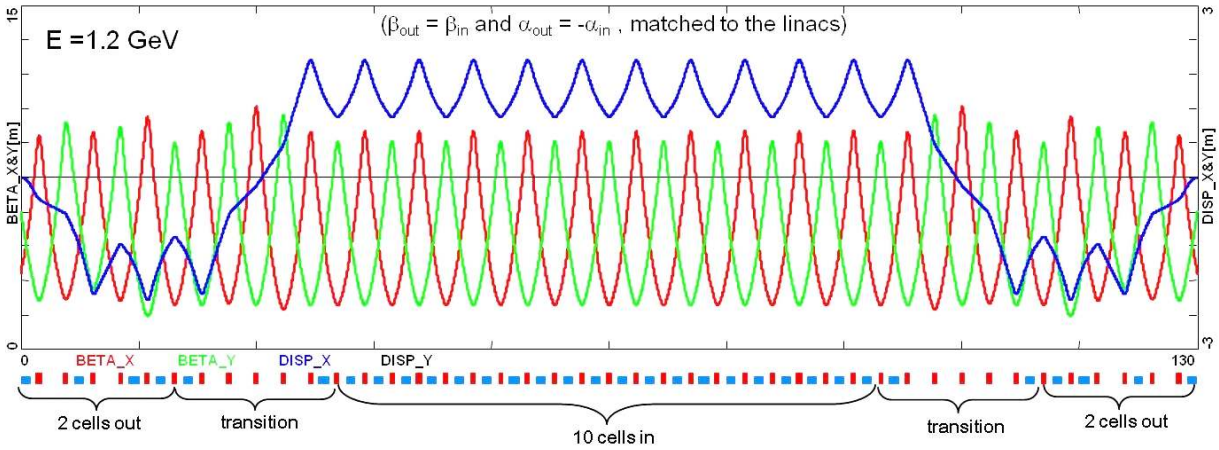

Figure 49. Compact droplet arc optics, featuring uniform periodicity of beta functions and dispersion, which is suppressed geometrically via 'missing dipoles' at the arc ends.

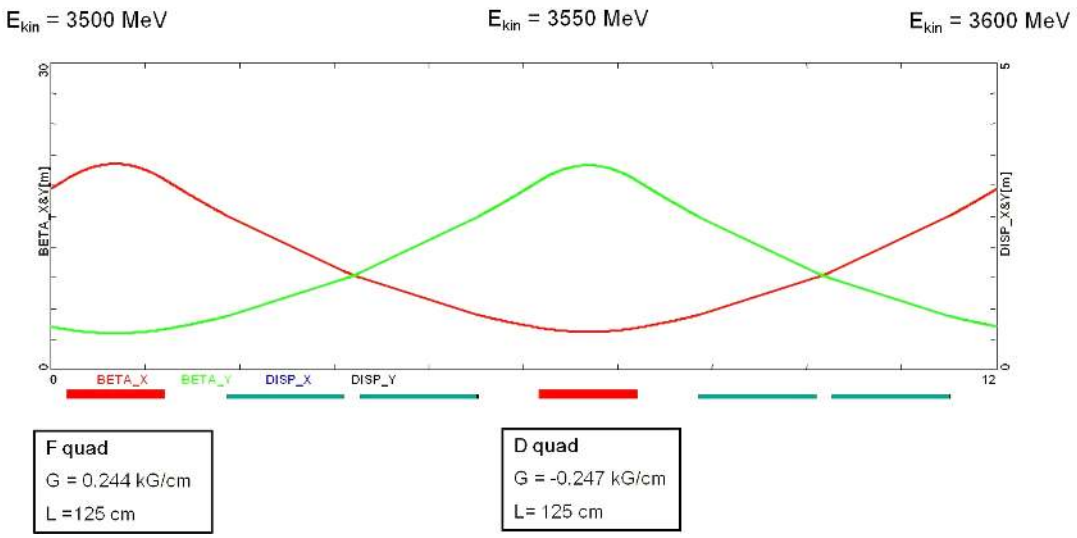

Figure 50. Periodic 90° FODO linac cell (12 m), including two pairs of 2-cell cavities interleaved between quadrupoles.

periodic cell is shown in figure 50. The cavity from table XXII with the higher energy gain is used for the linac.

As for RLA I, a bisected focusing profile was chosen for the multi-pass linac in RLA II, with the quadrupole gradients scaled up with momentum in the first half of the linac and mirror reflected in the second half, as illustrated in figure 51. The complete focusing profile along the entire linac is summarised in table XIX.

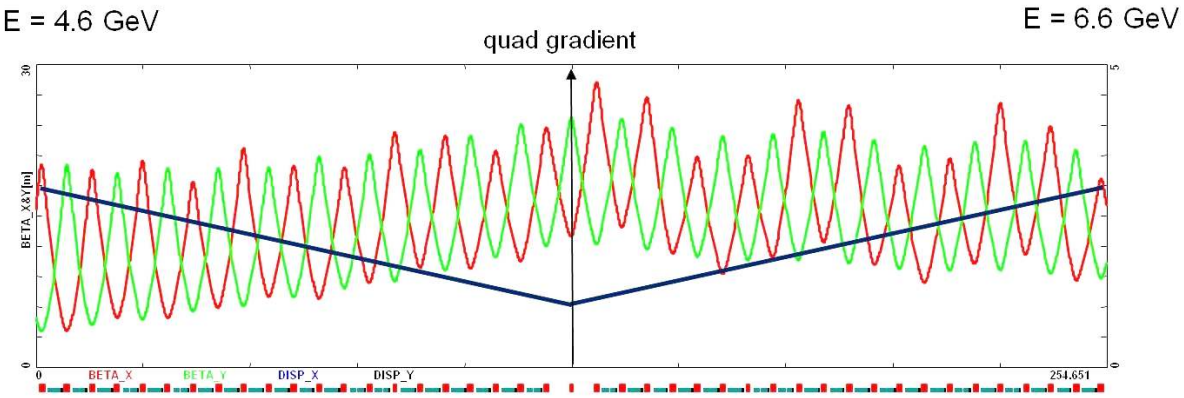

Figure 51. Bisected multi-pass linac optics. The quadrupole gradients are scaled up with momentum for the first half of the linac and mirror reflected in the second half.

Table XIX. Gradient and energy profile, cryo-module by cryo-module along the 2 GeV linac. As in table XVI, except that the spacing between quadrupole centres is 6 m, the first quad centre is at 133 cm, the energy gain between quadrupoles is 50 MeV, and the kinetic energy is 2894 MeV at the beginning of the first full pass.

Sequence	1	2	3	4	5	6
F grad. (kG/cm)	0.308	0.305	0.298	0.291	0.285	0.278
D grad. (kG/cm)	−0.313	−0.306	−0.299	−0.292	−0.285	−0.278
Sequence	7	8	9	10	11	
F grad. (kG/cm)	0.271	0.264	0.257	0.251	0.244	
D grad. (kG/cm)	−0.271	−0.264	−0.257	−0.250	−0.244	

All higher arcs are based on the same bends (2 m, 2.1 T dipoles) and they are configured via extending Arc 1 by additional inward and outward cells as summarised in table XX. Magnets to achieve these dipole fields will likely need to be superconducting. The quadrupole strengths in the arcs are scaled up linearly with momentum to preserve the 90° FODO lattice, as summarised in table XX.

Table XX. As in table XVII, but for arcs in RLA II. B is field for the dipoles.

E (GeV)	p/p_1	$n_{\mathbf{out}}$	$n_{\mathbf{in}}$	L (m)	G_F (kG/cm)	G_D (kG/cm)	B (T)
4.6	1	2	10	260	1.45	−1.42	2.10
6.6	1.43	3	15	344	2.08	−2.04	2.01
8.6	1.87	4	20	428	2.71	−2.66	1.96
10.6	2.30	5	25	512	3.34	−3.27	1.94

Table XXI. Lattice of injection chicane into RLA I. The left hand table gives the dipole parameters, the right hand table gives the quadrupole parameters. The dipoles are 60 cm long, the quadrupoles are 50 cm long. The chicane is 30 m long and designed for a kinetic energy of 803.877 MeV. s is the longitudinal position of the end of the magnet, B is the magnetic field of the dipole (H for horizontal, V for vertical), θ is the bend angle of the dipole, G is the quadrupole gradient, and ε_{in} and ε_{out} are the entrance and exit angles, respectively. Zero entrance and exit angles would correspond to a sector bend; an edge angle with the same sign as the bend angle rotates the edge such that a vector perpendicular to the edge and pointing out of the magnet rotates away from the centre of curvature (MAD convention).

Type	s (cm)	B (kG)	θ (deg.)	ε_{in} (deg.)	ε_{out} (deg.)
H	120	7.024468	8.01381	0	9
H	290	−7.024468	−8.01381	−9	0
V	504	−4.682978	−5.34254	0	−6
V	2306	4.682978	5.34254	6	0
H	2520	−7.024468	−8.01381	−9	0
H	2690	7.024468	8.01381	0	9

s (cm)	G (kG/cm)
50	−0.3682620
350	0.3090135
650	−0.3623229
950	0.3121510
1250	−0.3641247
1550	0.3121510
1850	−0.3641247
2150	0.3090135
2450	−0.3623229
2750	0.3172734

2.5.1.4. Injection double chicane

To transfer both μ^+ and μ^- bunches from one accelerator to the next, which is located at a different vertical elevation, we use a compact double chicane [275]. A FODO lattice is used with a 90° phase advance horizontally and a 120° phase advance vertically. Each "leg" of the chicane involves four horizontal and two vertical bending magnets, forming a double achromat in the horizontal and vertical planes, while preserving periodicity of the beta functions [228]. The lattice for RLA I is described in table XXI and figure 52. The injection chicane for RLA II will be similar, but has yet to be completed. The chicanes will have sextupoles to correct vertical emittance dilution, located at the peaks of the vertical dispersion (see figure 52). Their integrated strengths (in the first injection chicane) will be approximately 0.01 kG/cm.

The chicane and RLA lattices have not yet been simulated with realistic field maps but only with usual beam optics codes such as MADX [282], and OptiM [281]. As an example, the horizontal and vertical betatron functions of chicane 1 are shown in figure 53.

2.5.1.5. Arc crossings

One unfortunate feature of the dogbone lattice is that the arcs will cross each other. To address this, the arcs will have a vertical bypass in the region of the crossing, one arc going up and the other down, as shown in figure 54.

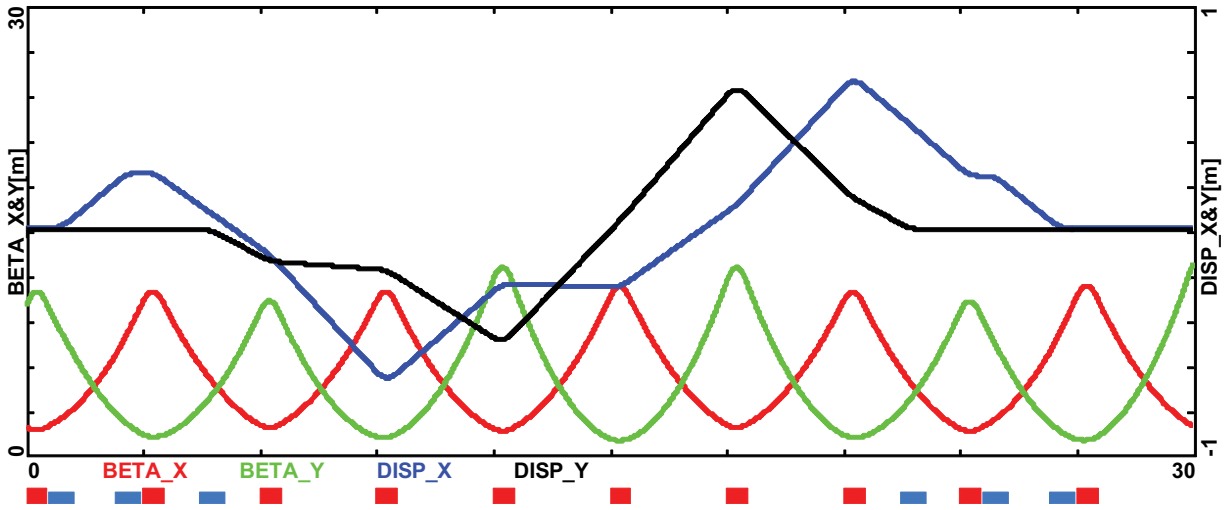

Figure 52. Diagram of the injection chicane lattice.

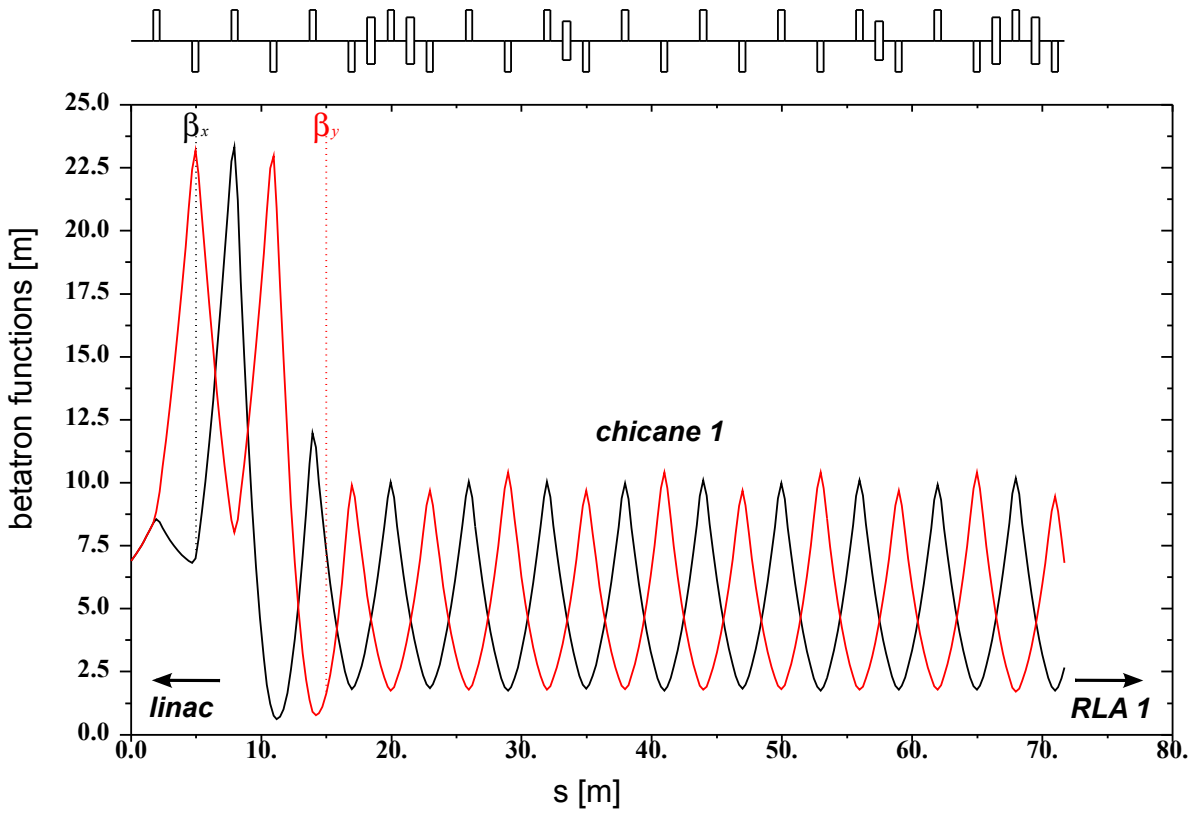

Figure 53. Horizontal and vertical betatron functions as the beam passes through chicane 1, calculated with MADX.

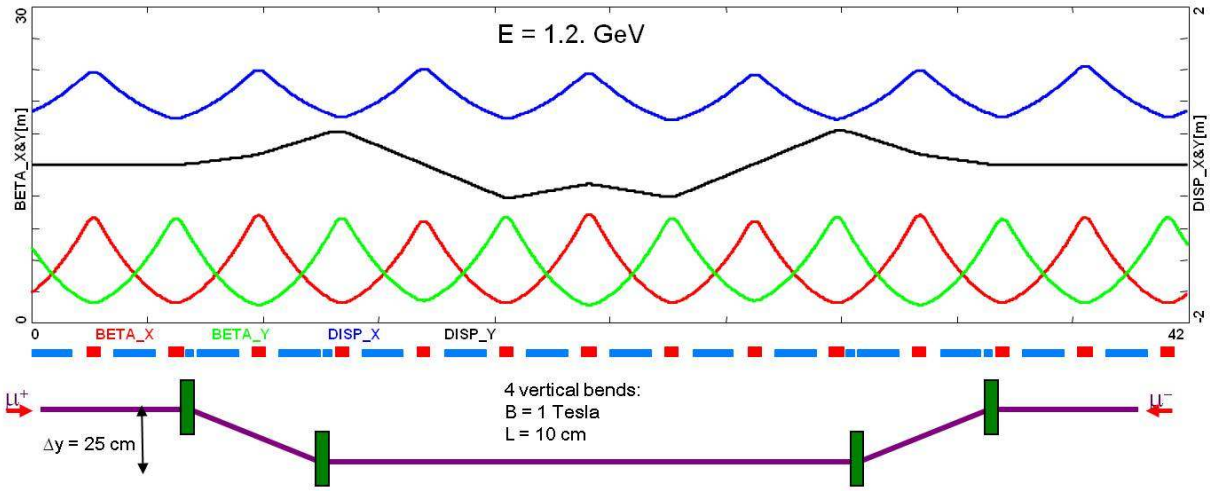

Figure 54. Diagram of the arc bypass lattice. The vertical dipoles are 10 cm long, centred in the gap between the adjacent dipole and quadrupole.

2.5.2. Magnets

The most important magnet types of the linac and RLA sections are: superconducting solenoids (linac) and normal conducting dipoles, combined dipole/sextupoles and quadrupoles (RLAs and chicanes). A detailed numerical simulation has been performed for the superconducting solenoids, while the design of normal conducting magnets is in progress. As shown in figure 55, a configuration of two superconducting coils with opposite currents shielded by a 5 cm thick iron wall is good enough to prevent longitudinal field leakage which may cause quenching of the neighbouring superconducting cavities. Also, it has been shown that the coils are far from the quench limit and may be made thinner.

2.5.3. RF system

The lattice designs for the acceleration systems are based on the Study II RF-cavity designs [245], the parameters of which are summarised in table XXII.

We have studied the optimisation of the cavity design. The layout of the standing wave superconducting RF cell has been optimised for a number of parameters. The target energy gain over the whole 66 cells of the linac is ~ 665 MeV, or a little more than 10 MeV/cell as shown in figure 56. Both single-cell and double-cell (π-mode) cavities have been simulated with specialised codes including Superfish [283, 284], CST-MWS [285] and Comsol [286] in order to obtain the electric- and magnetic-field maps necessary for particle tracking.

The peak electric fields are 23.09 MV/m in the upper linac and 26.17 MV/m the middle and lower linacs. In previous work [245], the references to 15 MV/m, 17 MV/m, and 17 MV/m cavities included the transit time factor for a $\beta = 1$ particle (26.17 MV/m $\times$ 0.65 = 17 MV/m, 0.65 is the transit time

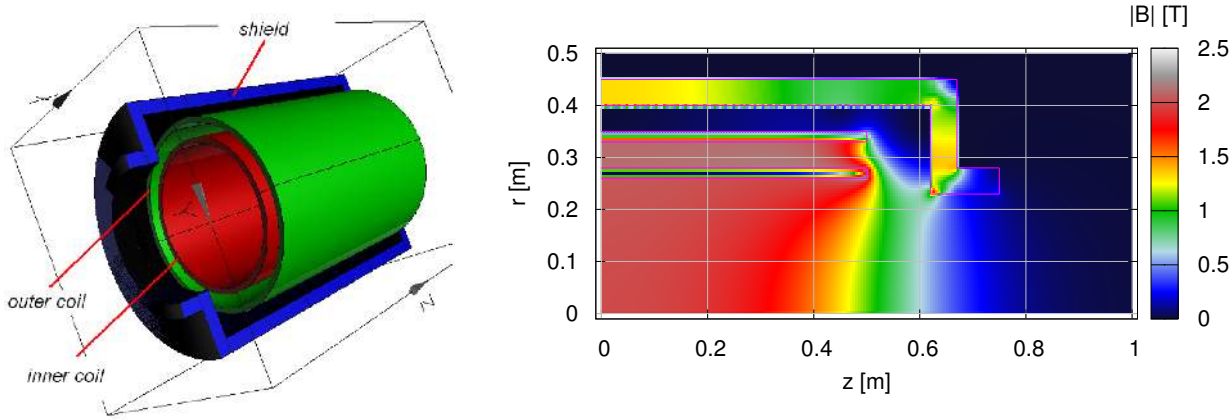

Figure 55. Layout of the shielded superconducting solenoid (left) and its 2D magnetic field map across the axial plane (right) for a peak magnetic field of 2 T.

Table XXII. Important parameters for the Study II superconducting RF cavity designs [245]. When single-cell cavities are used, appropriate parameters are cut in half.

RF frequency (MHz)	201.25	201.25
Cells per cavity	2	2
Aperture diameter (mm)	300	460
Energy gain/cavity (MeV)	25.5	22.5
Stored energy/cavity (J)	2008	1932
Input power/cavity (kW)	1016	980
RF on time (ms)	3	3
Loaded Q	10^6	10^6

factor). Here $0.90 \leq \beta \leq 0.99$ and the cavity phases were offset to introduce ~ 1 synchrotron period over the whole linac.

2.5.4. Beam tracking

First, using only solenoid field maps (no-acceleration), Gaussian muon bunches with very large emittances have been tracked through many cells of the three linac cell types in order to obtain the transverse acceptances. A significant number of muons are lost in the early part of the linac. Later in the linac, the beam is transported without additional loss making it possible to determine the rms transverse emittances shown in figure 57.

End-to-end, particle-tracking studies are in progress for the linac using the codes GPT [287], G4beamline [263], OptiM and ELEGANT. As an example, figure 58 shows the longitudinal and transverse phase-space evolution for the upper linac while figure 59 shows the particle trajectories and kinetic-energy increase along the entire linac.

length = 0.7448 m
radius = 0.6854 m
resonance freq. = 201.247 MHz
quality fact. = 24.67×10^9
transit time factor = 0.650 - 0.690
peak $\hat{E}$ = 26.17 MV/m
$|E|^{max}_{surf}$ = 21.70 MV/m
$|H|^{max}_{surf}$ = 48.06 kA/m
stored energy = 712 J

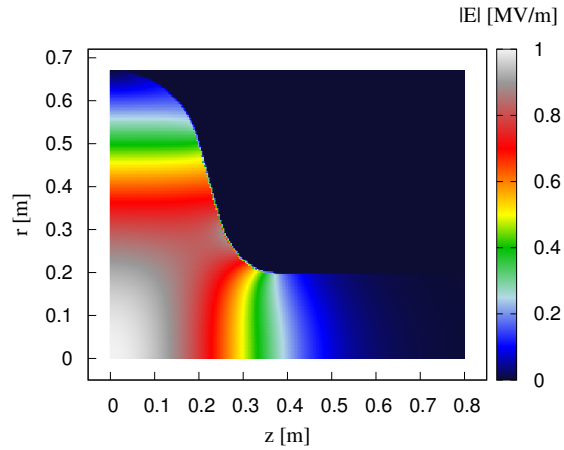

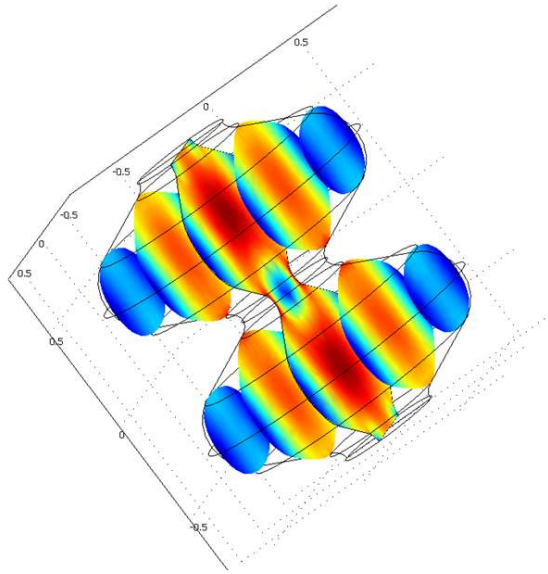

Figure 56. Main parameters of the superconducting RF cell and its electric field maps.

As figure 58 shows, there is noticeable (adiabatic) reduction of the transverse beam-size as the beam undergoes acceleration, although the phasing of the RF cavities is not yet fully optimised. Future studies will focus on the longitudinal phase space and on controlling the longitudinal-transverse phase-space coupling with the aim of transporting the beam along the whole linac with minimum losses.

2.6. Linear non-scaling FFAG

In the linac and RLAs described above, the cost of the RF systems dominates the cost of the beam lines that accelerate the beam. A better balance between magnet and RF costs would result by making more passes through the RF cavities. Unfortunately, the switchyard precludes one from making a large number of passes in the RLA linac. It would thus be advantageous to eliminate the switchyard and use a single arc for all energies. This could be accomplished by using a machine that allows a large energy range within a single fixed-field arc, i.e., a fixed field alternating gradient (FFAG) accelerator.

To keep the machine cost low and to allow the use of 201.25 MHz RF cavities, we use a design that differs from the original type of FFAG (referred to as a "scaling" FFAG). This new type of machine is called a linear "non-scaling" FFAG. Its important features are that it is isochronous near the middle

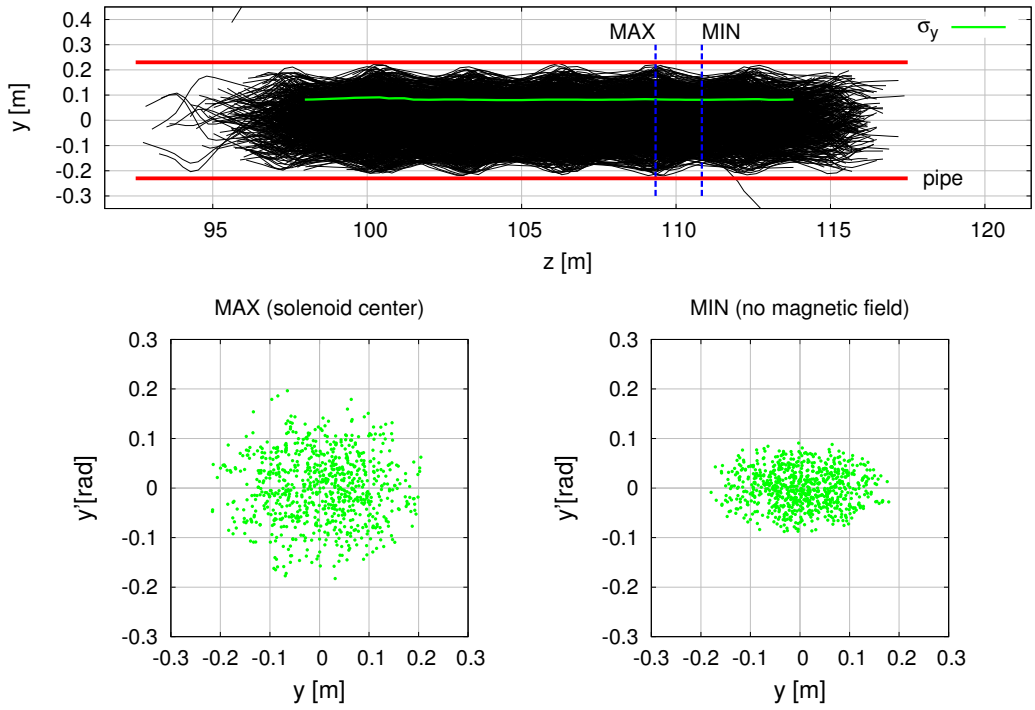

linac section		$\bar{\varepsilon}_x$ [mm rad]	σ_x [mm]	$\sigma_{x'}$ [mrad]	$\bar{\varepsilon}_y$ [mm rad]	σ_y [mm]	$\sigma_{y'}$ [mrad]
upper	MIN	5.7	78	43	5.7	82	40
middle	MIN	3.4	79	26	3.3	79	25
lower	MIN	2.2	87	15	2.1	88	16

Figure 57. Stable trajectories in the upper linac 36 cells downstream from the injection point (top), the y-phase space at the two positions indicated (middle) and values of the normalised transverse emittances and standard deviations (bottom).

of the energy range, limiting the phase slippage and thus permitting the use of high RF frequencies, and that its magnets are more compact than those of a comparable scaling FFAG.

We have optimised the design of a linear non-scaling FFAG [288], and the resulting parameters are given in tables XXIII–XXV. The important criteria for this optimisation were that the long drift length would be 5.0 m (to accommodate the septum, see below) and that the time-of-flight be a half integer number of RF periods per cell. With the exception of the lattice cells containing the injection and extraction insertions, the ring consists of identical cells, each containing an FDF triplet. Most cells contain a superconducting cavity, the parameters of which are given in table XXV. The magnet aperture is increased by 30% from what is required for the beam to ensure that the beam is in a region of the magnet with good field quality. The magnet angle and shift are defined as follows (see figure 60): upon entering the magnet, the coordinate axis bends toward the centre of the ring by half the given angle. The centre of the magnet is then shifted away from the centre of the ring by the shift value. Upon exiting the magnet, the coordinate axis bends toward the centre of the ring by the second

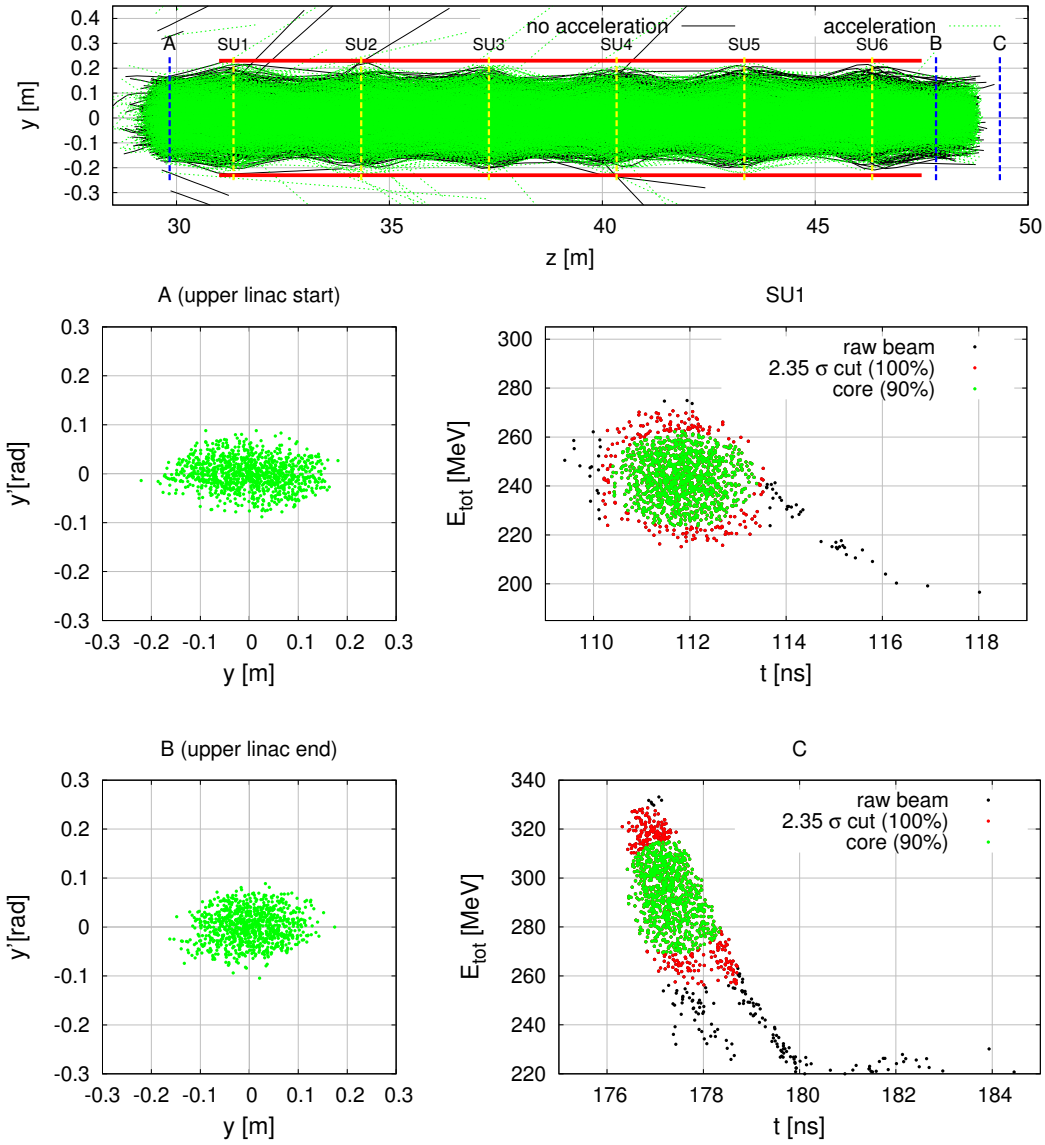

phase space		$\bar{\varepsilon}_x$ [mm rad]	σ_x [mm]	$\sigma_{x'}$ [mrad]	$\bar{\varepsilon}_y$ [mm rad]	σ_y [mm]	$\sigma_{y'}$ [mrad]
transverse	A	4.9	81	34	5.0	87	31
	B	4.5	61	33	4.6	62	36
		$(1/\beta\gamma)\times\ \bar{\varepsilon}_{\|\|}$ [ms eV]		σ_t [ns]		$\sigma_{E_{tot}}$ [MeV]	
longitudinal	SU1	2.7		0.72		13	
	C	1.7		0.55		15	

Figure 58. GPT particle trajectories through the upper linac (top), the y-phase space at its beginning/end (middle) and figures of the normalised emittances and standard deviations (bottom).

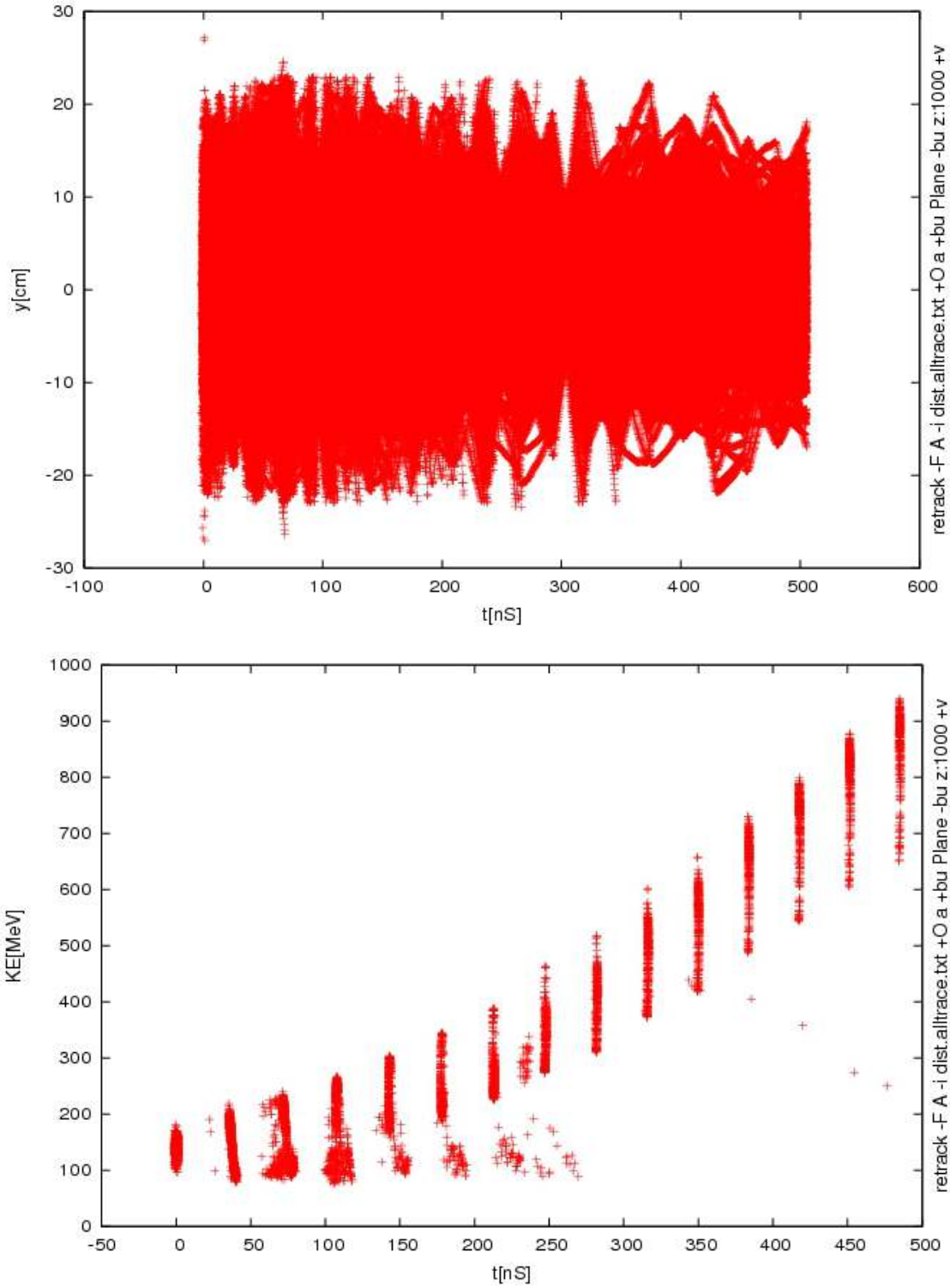

Figure 59. G4beamline particle tracking showing vertical projections of the trajectories (top) and kinetic energy (bottom) along the entire linac.

Table XXIII. Design requirements for the FFAG accelerator. Energies are total energy. Transverse acceptance is defined as $a^2p/(\beta_\perp mc)$, where a is the maximum beam radial displacement, $\beta_\perp$ is the Courant-Snyder beta function, p is the total momentum, m is the muon mass, and c is the speed of light. Longitudinal acceptance is $\Delta E \Delta t/mc$, where ΔE is the maximum energy half-width and Δt is the maximum half-width in time (assuming an upright longitudinal ellipse).

Injection energy	12.6 GeV	Transverse acceptance	30 mm
Extraction energy	25.0 GeV	Longitudinal acceptance	150 mm
Muons per train	2.4×10^{12}	Muon trains	3
Time between trains	120 μs	Repetition rate	150 Hz

Table XXIV. Magnetic lattice parameters of the linear non-scaling FFAG. The short drift is between each D and F in the triplet, the long drift is between the F magnets. The angle and shift are described in the text. The maximum magnet field is at the magnet aperture.

Cells	64
Long drift	5.0 m
Short drift	0.5 m
Circumference	667 m

	D	F
Length (m)	2.251117	1.086572
Angle (mrad)	156.837	-29.331
Shift (mm)	41.003	13.907
Field (T)	4.20784	-1.39381
Gradient (T/m)	-13.55592	18.04570
Aperture radius (mm)	137	163
Maximum field (T)	6.1	4.3

half of the bend angle.

2.6.1. Injection and Extraction

Injection and extraction occur at opposite sides of the ring. Each system will have reflection symmetry to accommodate both positively and negatively charged muons. There will be two septa in each system with kicker magnets between them. All the kickers in each system have the same strength. The septum and kicker magnets have length 4.4 m, i.e., there is 30 cm separation between each of these elements and the adjacent main magnets. Parameters for the injection/extraction magnets are given in table XXVI.

Table XXV. RF parameters and derived performance of the linear non-scaling FFAG. Cavity voltage is the maximum energy gain of a speed of light muon passing through the cavity [245].

RF frequency	201.25 MHz	Cavity voltage	25.5 MV
Aperture diameter	30 mm	Cells per cavity	2
Input power	1 MW	RF pulse length	3 ms
Stored energy	2008 J		
Cavities	48	Total voltage	1214 MV
Turns	11.6	Decay loss	6.7%

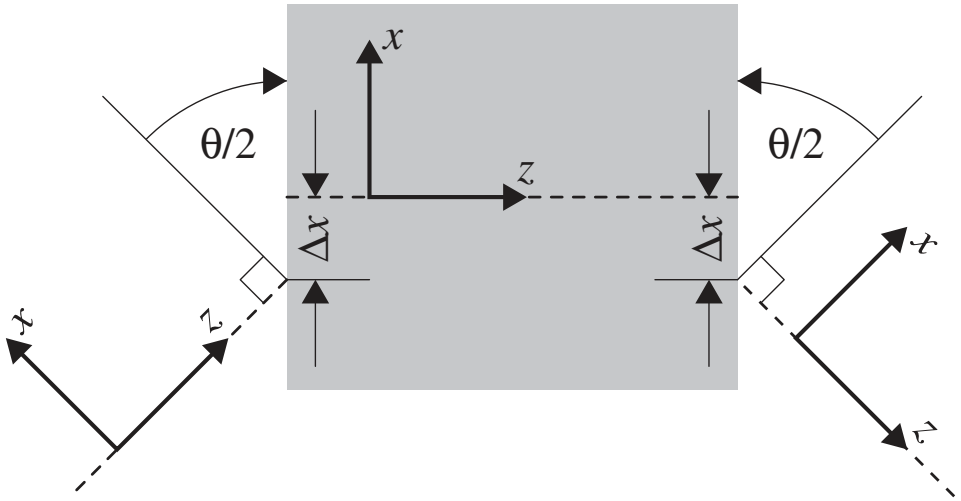

Figure 60. Geometry at a magnet. θ is the angle given in table XXIV, and Δx is the shift given in that same table.

Table XXVI. Injection/Extraction system parameters. Pattern contains a + for an outward kick, - for an inward kick, and a 0 for an empty drift. A septum is located at both ends of the kicker system.

	Injection	Extraction
Kickers	2	4
Pattern	-0-	++00++
Kicker field (T)	0.089	0.067
Septum field (T)	0.92	1.76
Kicker/septum length (m)	4.4	4.4

A septum field below 2 T is chosen in order to minimise the effect of the septum stray-field on the circulating beam. In order to estimate the clearance needed so that the extracted or injected beam avoids the magnet immediately following the septum, the dimensions of the superconducting combined-function magnet (SCFM) in the J-PARC neutrino beam line is used. The width of the J-PARC SCFM from the inner radius of the coils to the outer radius of the cold mass is 19.8 cm [289]. This distance is used, together with the size of the muon beam, in calculating the required septum bending angle. Taken together, these constraints require the long drift in the triplet to be at least 5 m in length.

In order to be feasible from an engineering perspective, the kicker-magnet peak fields are constrained to be less than 0.1 T. The separation between the kicked and circulating beams at the entrance of the septum is 2 cm. Two kicker magnets are required for injection. Due to the relatively high horizontal phase advance at this energy and the requirement of mirror symmetry, the kickers need to be separated by a single cell, resulting in an empty long drift at the centre of the injection system. At extraction four kickers are required, i.e., two pairs separated by two empty long drifts. Tracking results of the muon beam through the injection and extraction systems are shown in figure 61. As can be seen from the figure, injection is into the inside of the ring whereas the beam is extracted to the outside.

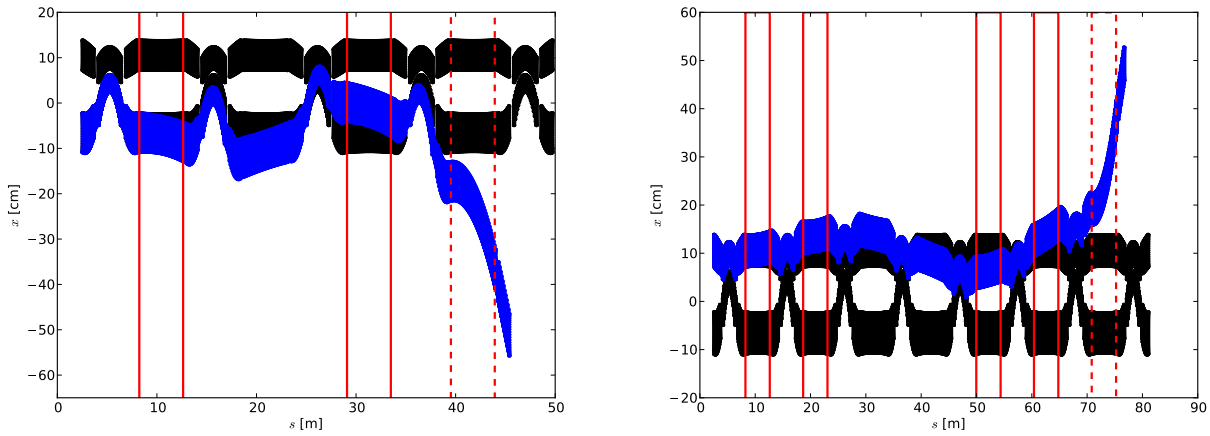

Figure 61. Injection scheme (left) and extraction scheme (right) for the FFAG ring. The full-acceptance circulating beam at injection and extraction momenta are shown in black and the injected and extracted beams in blue. The red vertical lines represent the location of the kicker magnets (solid) and septum (dashed).

Table XXVII. Magnet apertures (i.e., inner radius of magnet) in the Injection/Extraction system. In the rest of the ring, the magnet apertures are 16.3 cm and 13.7 cm for the F and D magnets, respectively.

	Magnet	Number	Aperture (cm)
Injection	F	4	20.8
	D	4	16.1
Extraction	F	8	19.8
	D	2	15.5

The distribution of kickers over several cells means that a number of large-aperture main magnets are required. The apertures are calculated by finding the smallest circle that encloses the kicked and circulating beam and adding an additional 1 cm clearance (for example see figure 62). The number of these magnets and their apertures are listed in table XXVII.

2.6.2. Kickers and Septa for the FFAG

Travelling-wave kicker magnets are proposed both for injection and extraction. The kicker system consists of a power supply charging pulse forming networks (PFNs), which are connected via fast thyratron switches and coaxial cables to the kicker magnet and terminated via a matching resistor. A CX1925X [290] thyratron switch and RG192 coaxial cables connected in parallel could be used. A current of about 30 kA is necessary to produce the required 0.1 T magnetic field in an aperture of about 0.3 m $\times$ 0.3 m. The same design is proposed for injection and extraction, as the requirements

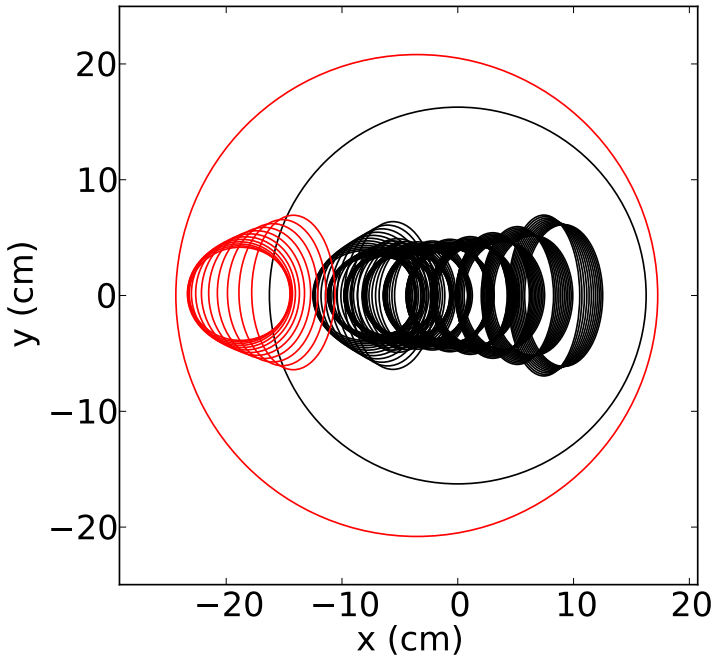

Figure 62. The circulating beam (black ellipses) enclosed by the normal F magnet aperture (black circle) and the additional aperture (red circle) required to accommodate the kicked beam (red ellipses, shown just before the septum at injection.

with respect to rise/fall time are very similar. This dictates the need for careful impedance matching to avoid any reflections, which is essential, especially for the injection case. In order to keep the rise- and fall-times low, the kicker magnet must be sub-divided into four or five separate units. The kicker uses a window-frame geometry, with the yoke made of ferrite to enhance the field level, limit the field leakage and improve the field quality. The ferrite Ferroxcube 8C11 [291] could be used for the kicker core. The detailed design of the kicker, including the matching capacitance scheme to minimise reflections, remains to be addressed in future studies. A voltage of 60 kV is assumed, which is compatible with existing fast thyratron switches and sets the impedance for the magnet and termination resistor at 1 Ω. The thyratron CX 1925X is limited to 10 kA peak current, which dictates the use of three 3 Ω PFNs connected in parallel for each sub-kicker. As the baseline muon pulse consists of three muon bunch-trains separated by 120 μs, a total of 9 PFNs for each sub-kicker is needed to avoid requiring an extremely demanding power supply to recharge the PFNs between the individual bunch trains. The total number of PFNs and switches per kicker unit installed in a single drift is thus 36 (assuming that the kicker is subdivided into four sub-kickers). Power supplies of $\approx$ 2.5 MW peak power are needed for every kicker and although it is expected that the majority of the power will be dumped into the termination resistor, thermal issues for the kicker magnet remain to be studied. A schematic of the kicker system is shown in figure 63 and some of its parameters are collected in table XXVIII.

Kicker magnets are used to suppress (create) the separation between the injected (extracted) and the

Table XXVIII. Parameters of the kicker system

Kicker total aperture (h×v)	0.3×0.3 m
Kicker length	4.4 m
Rise/fall time (5-95%)	1.9 μs
Kicker max field	≈0.1 T
Kicker pulse duration at the top	0.3 μs
Charging voltage	60 kV
Peak current in the magnet	30 kA
Kicker inductance	5.1 μH
Kicker impedance	1 Ω
Peak current at switch	10 kA
Repetition rate	50 Hz
Number of sub-kickers	4-5
Number of PFNs per micro-pulse per sub-kicker	3
Total number of PFNs	36 (for 4 sub-kickers)
Total averaged power per kicker	≈1.25 MW
Total peak power per kicker	≈2.5 MW

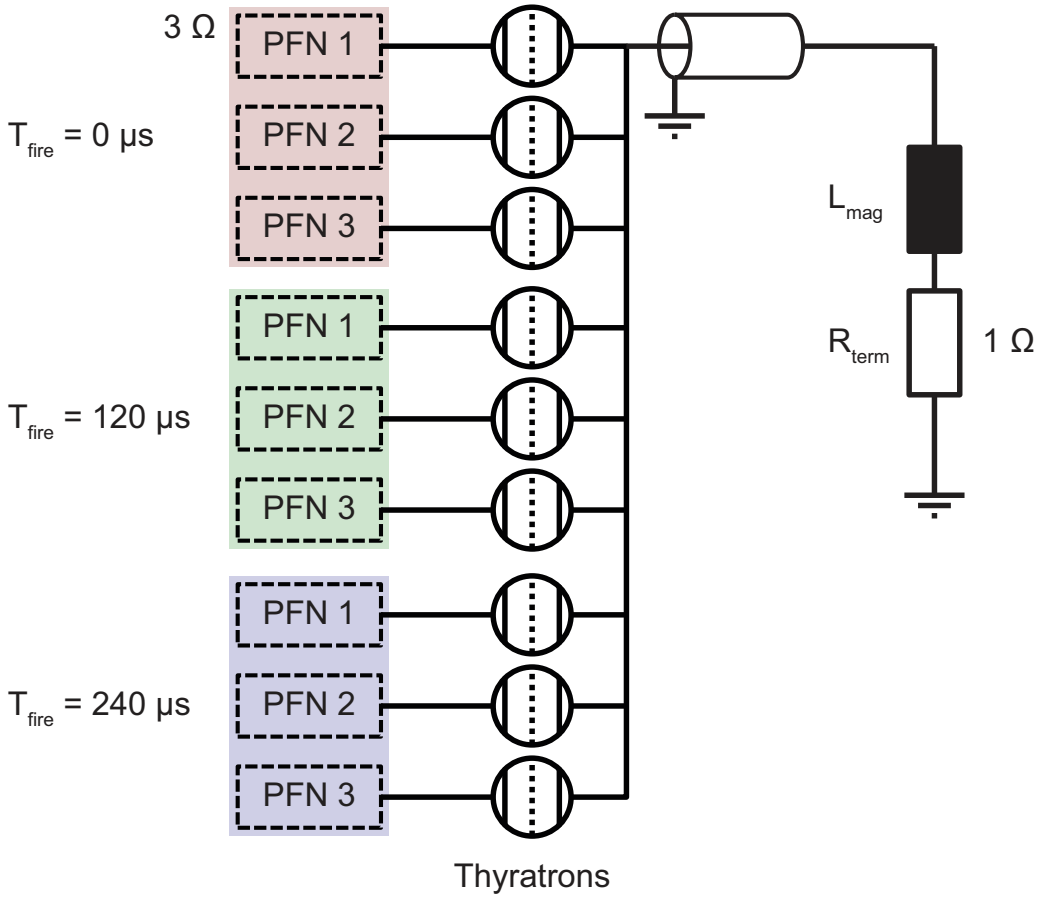

Figure 63. Schematic of the FFAG injection/extraction kicker system operating with 3 muon bunch trains. The above system is needed for every sub-kicker unit.

circulating beam, but in order for the beam to clear the external aperture of the main magnets, septa are required. The magnetic fields of septa for both injection and extraction are shown in table XXVI. As their aperture is large (≈0.3×0.3 m total), a rather high current-turn product of 450 kA-turns is required. Although the septum design could be based on normal conducting technology, a DC solution would be rather challenging due to problems with cooling the coils. This cooling problem could be reduced by pulsing the septum, but that would introduce eddy currents and variable stray fields in close proximity to the main superconducting magnets. Moreover, a rather substantial power supply would be needed. To avoid these challenges we propose to use superconducting technology for the septa, both for injection and extraction. As the extraction septum is the more challenging, design work has focused on this case. An identical device could also be used for injection. By using superconducting technology, high magnetic fields can easily be obtained using very thin conductor (8 mm) with a modest current density of 200 A/mm^2. The most challenging issue is the shielding of the circulating beam region from stray fields. In order to reduce the field leakage, COMSOL 4.0 [286] simulations have been performed using various yoke geometries. The current design is based on a window frame magnet with the yoke extending all around both extracted and circulating beam areas. The septum itself, which is 2 cm thick, is subdivided into the conductor part and the yoke part. Two yoke magnetic materials have been studied: a "standard" soft iron and the soft magnetic cobalt-iron alloy VACOFLUX 50 [292]. In addition, a chamfer was introduced on the side facing the circulating beam in order to further limit the field leakage. Figure 64 shows the simulations of the stray fields using different yoke materials and with and without the chamfer. The leakage field at the boundary of the septum on the side of the circulating beam is shown and was used to evaluate various designs. The 2D design of the extraction septum is shown in figure 65. Based on the electromagnetic simulations, the septum field will be held to less than 2 T, which dictates the length of the septum necessary to permit the beam to clear the adjacent main magnets. This turns out to be an important constraint in the FFAG lattice definition. The detailed cryogenic design and quench limit of the superconducting septum remain to be addressed.

2.6.3. Main Ring Magnets

The preliminary design of the main superconducting combined-function magnets for the linear non-scaling FFAG has been performed using the CERN ROXIE code [293]. As the design of the focusing (F) magnet is more advanced, we present only this element. The design uses the well-established technology of Nb-Ti superconducting magnets fabricated using Rutherford cable. In order to simplify the geometry and allow for flexible beam optics tuning, the magnet design is based on separate coils for dipole and quadrupole field components, which are assembled according to the conventional "$\cos\theta$" geometry. The inner layer creates a dipole field using 3 conductor blocks, and the outer layer creates a quadrupole field with 2 conductor blocks. For the needs of the current design the dipole and quadrupole cables have been generated in ROXIE based on the standard Large Hadron Collider (LHC) main dipole inner cable [294] at CERN. The cables consist of 28 strands and have a trapezoidal geometry. They would be constructed using the same filaments as the LHC magnet. An iron yoke made of soft magnetic steel is placed beyond the quadrupole layer. The magnet is closed with a clamp in order to limit field leakage in the long straight section, where it could affect hardware components like superconducting RF cavities or kickers. The geometry of coils and yoke for half of the F magnet is

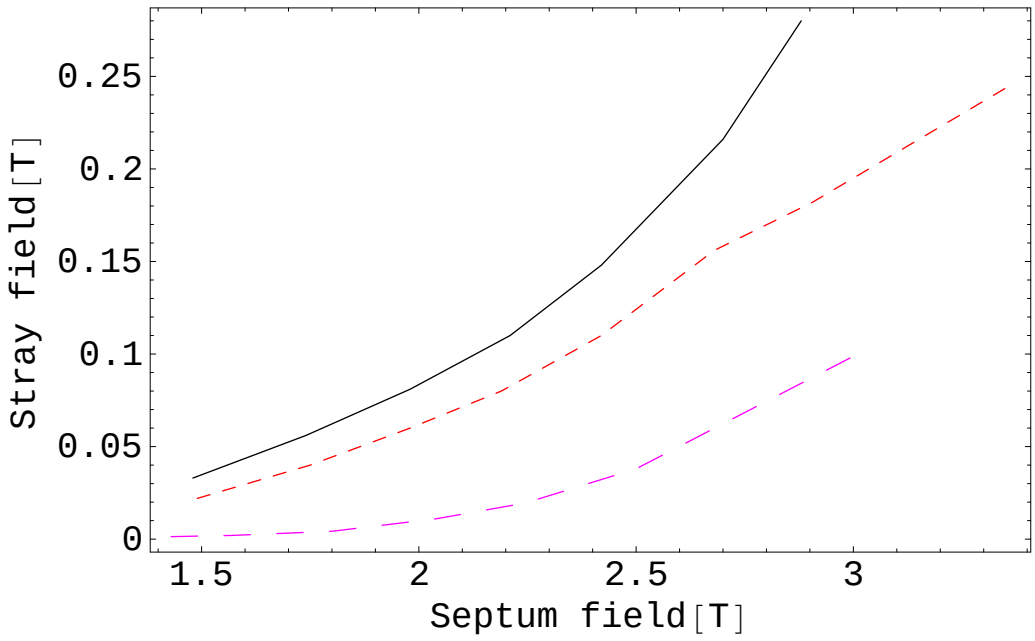

Figure 64. Stray fields in the superconducting septum using standard soft iron (black, solid line), using advanced material-VACOFLUX 50 (red line, short dash) and introducing a chamfer (magenta, long dash). The simulations were performed using the COMSOL 4.0 package.

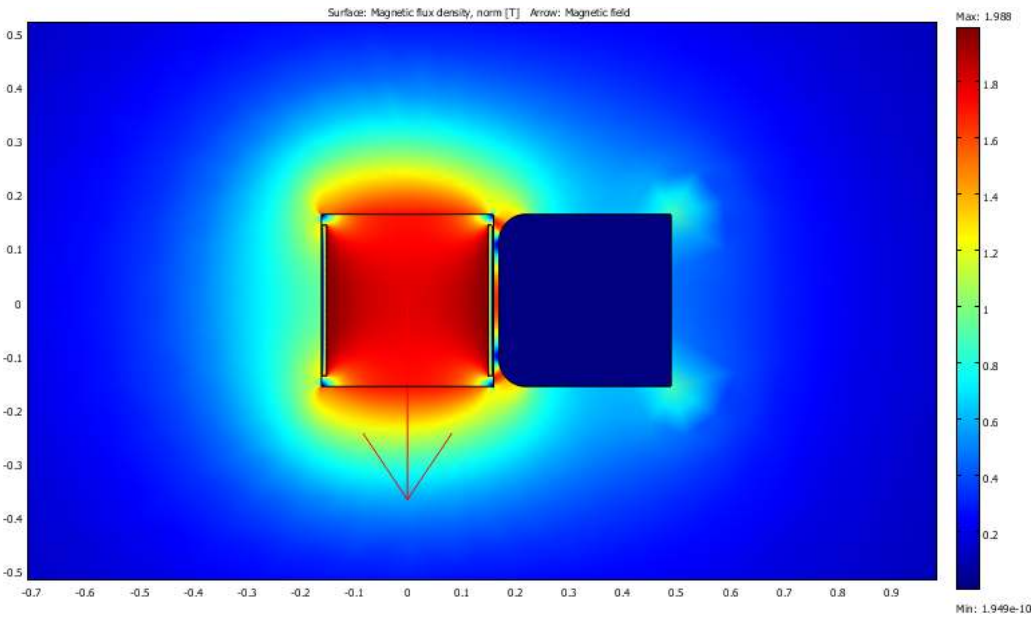

Figure 65. 2D section of the superconducting septum for a muon FFAG.

Table XXIX. Parameters of the main focusing FFAG magnet.

Strand diameter	1.065 mm
Number of strands per cable (dipole and quadrupole)	28
Cable height (dipole and quadrupole)	15 mm
Dipole cable inner/outer width	1.58/1.75 mm
Quadrupole cable inner/outer width	1.83/1.98 mm
Number of conductors in dipole blocks	52, 25, 13
Number of conductors in quadrupole blocks	41, 10
Inner radius of dipole blocks	163 mm
Inner radius of quadrupole blocks	179 mm
Inner radius of the yoke	300 mm
Yoke thickness	100 mm
Half of the yoke length (with clamp)	840 mm
Dipole current	3190 A
Quadrupole current	8490 A
Dipole current density	332 A/mm^2
Quadrupole current density	885 A/mm^2
Peak field in the conductors	5.75 T
Minimal temperature margin to quench at 2.2 K	3.84 K

shown in figure 66. The dipole field and gradient on axis have been reproduced according to the lattice design specifications with an accuracy of $\sim 10^{-4}$. The vertical field component on the median plane of the F magnet is shown in figure 67. The field quality off-axis still needs to be improved, which will require an update of the magnet geometry. A quench analysis has been performed using ROXIE, and calculations of the temperature margins suggest stable magnet operation. The principal parameters of the focusing (F) FFAG magnet are collected in table XXIX. Future studies will address the field quality, the possible addition of higher multipoles (mainly sextupole) for chromaticity correction, and the cryogenic design.

2.6.4. Beam loading

Beam loading will cause the different bunches to gain different amounts of energy. There are two time scales to consider: different energy gains within a train, and different energy gains for different trains.

On each pass, a bunch train extracts 9.7 J from a cavity. The last bunch will therefore gain 62 keV less energy per cavity pass than the first bunch. Through the entire acceleration cycle, this amounts to an energy difference from head to tail of 30 MV. This is small compared to the energy spread expected in the bunches.

Each proton driver cycle accelerates three bunches, which will hit the target in relatively rapid succession. Each proton driver bunch creates a separate bunch train in the muon accelerator. After a bunch train has completed its acceleration cycle, it has extracted 116 J from the cavities. If no power is added to the cavities, then the next bunch train will gain 360 MV less energy, which is too big a difference. To replace the extracted energy with an input power limitation of 1 MW per cavity requires 120 μs between bunch trains and therefore between proton driver bunches.

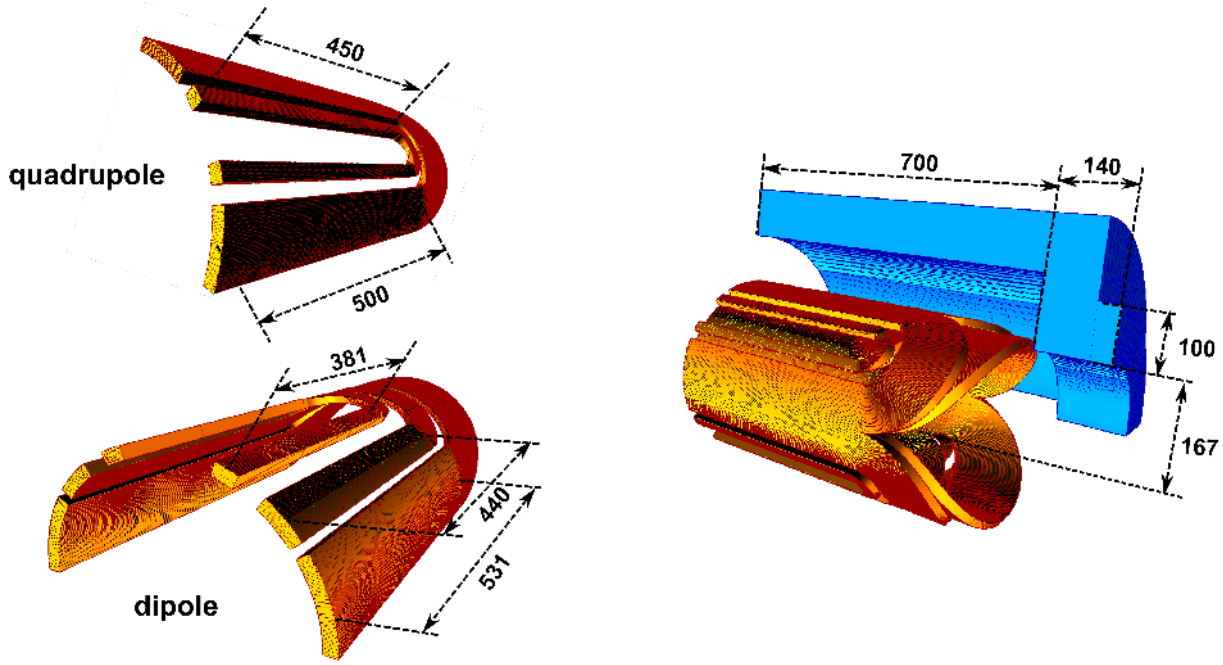

Figure 66. Geometry of the design of half of the F magnet for the FFAG ring.

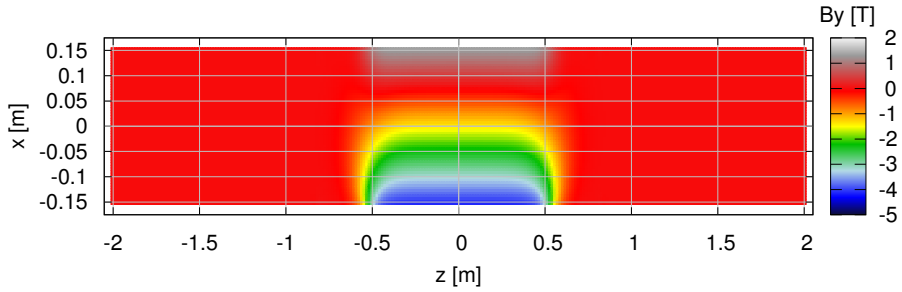

Figure 67. Vertical component of the magnetic field on the median plane of the F magnet obtained with the ROXIE code.

2.6.5. Risk Mitigation

The use of a linear non-scaling FFAG is expected to be a more cost-effective alternative to acceleration with an RLA. There are potential issues with this design, however. It is known that the large transverse emittance can lead to an effective longitudinal emittance growth in such a design [295]. If necessary, this effect could be reduced by increasing the average RF gradient and/or correcting the chromaticity, even partially [296]. The former can be accomplished by increasing the drift length to 5.5 m and putting a second RF cavity in each drift, but this would increase the machine cost by around 25%. Chromaticity correction is briefly discussed in Appendix F.

One could eliminate the FFAG, and extend the energy range of the linac and the RLAs so as to

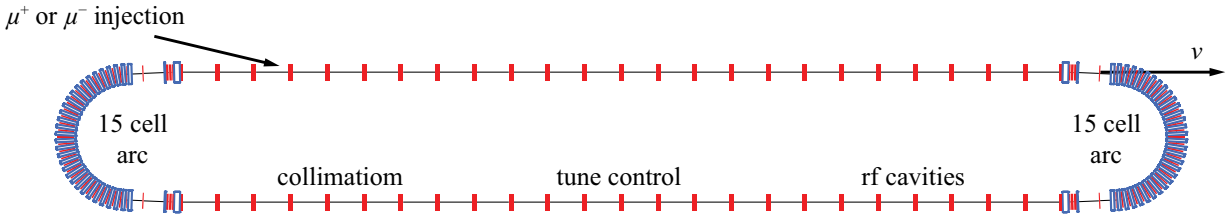

Figure 68. Racetrack design for the Neutrino Factory storage rings.

accelerate to 25 GeV. While early estimates led us to believe this is significantly more costly than accelerating with an FFAG, it remains to be demonstrated in detail. Furthermore, the injection and extraction hardware is technologically challenging, and likely very costly. Should the FFAG not be found to give a significant cost benefit, this alternative acceleration scenario without an FFAG could be used.

2.7. Decay ring

In the Neutrino Factory [5] neutrinos are generated from muon decays according to:

$$\mu^- \to e^- \bar{\nu}_e \nu_\mu \,; \text{ and } \mu^+ \to e^+ \nu_e \bar{\nu}_\mu \,. \tag{24}$$

Neutrinos are aimed at far detectors by collecting muons in storage rings with long straight sections pointing at the distant experimental facilities. The storage rings dip into the ground with angles of 18° and 36°, for baselines of 4000 and 7500 km, respectively.

Two geometries of ring have been considered. The geometry shown in figure 68 is designed to store either μ^+ or μ^- with a single straight pointing into the ground. The return straight is used for collimation, RF and tune control. A development of this concept can accommodate counter-rotating muons of both signs. An alternative is a triangular lattice (figure 69) with two production straights pointing in different directions sending neutrinos to combination of detectors dictated by the apex angle [297]. Since the beam must travel in a unique direction, two triangular rings would be built side by side in the same tunnel, one containing μ^+ and the other μ^-.

Some parameters driving the choice of the muon storage-ring geometry are the efficiency, defined as the ratio of the total length of neutrino production straights to the total circumference, and the depth of the tunnel, which implies geological and cost considerations. There will be at most three μ^+ and three μ^- bunch trains in the ring. Based on the proton driver described in section 2.2, a decay ring of 1.6 km in circumference can accommodate the equally-spaced, 250 ns long bunch trains and can allow time intervals of at least 100 ns between the neutrino bursts arising from the μ^+ and the μ^- bunches. The maximal tunnel depths for rings of this size are 444 m for the racetrack and 493 m for the triangle.

The optical properties of these rings are challenging. In order to keep the divergence of the neutrino beam sufficiently small, the rms divergence of the muon beam in the production straight section must not exceed 10% of the natural angular divergence of $1/\gamma$ that arises from the kinematics of muon decay. This requirement translates into high values for the β-functions in the production straights

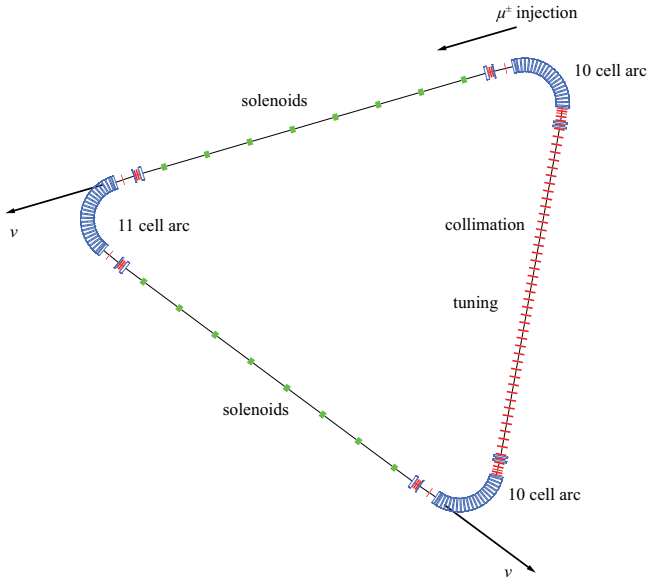

Figure 69. A triangular muon storage ring able to send neutrinos to detectors in two different directions.

($\sim$ 150 m) which need to be matched into the low values of $\sim$ 14 m in the arcs. At the ends of each straight, small bending magnets are included to ensure that neutrinos created in the matching section (where the muon beam still has a large divergence angle) cannot be seen by the detector. The production straights for the racetrack design are 599.4 m long, providing an efficiency of 37.2% for single-sign muon beams. The corresponding figures for the triangle lattice is 398.5 m (2 straights, 24.8% efficiency each).

The racetrack design has been chosen as the baseline. It is the most flexible possibility for directing neutrinos to any combination of far detector locations, and can direct neutrinos resulting from the decays of both muon charges to the same far detector if desired. In the following paragraphs we focus on the performances of the race-track rings and on the issue of muon-beam monitoring.

2.7.1. Performance

Starting from the initial design described in [297], MAD-X [282] has been used to determine the basic machine properties: Twiss parameters, working point, and dynamic aperture (DA). The structure of the ring is illustrated in figure 70, which shows the three main elements of the optics: straight sections; arcs; and matching sections. The central momentum is 25 GeV/c and the total length of this machine is 1608.8 m. Figure 71 (left) shows the optics of the decay-ring lattice, while the lattice, subdivided into its three main parts (straights, arcs, and matching sections), is described in tables XXX–XXXIII.

Beta functions are kept low in the arcs to reduce the size of the beam and maximise transmission. Conversely the beam envelope is increased in the straight sections, where keeping a small divergence is the primary requirement. The merging of these two opposite criteria is accomplished by the matching

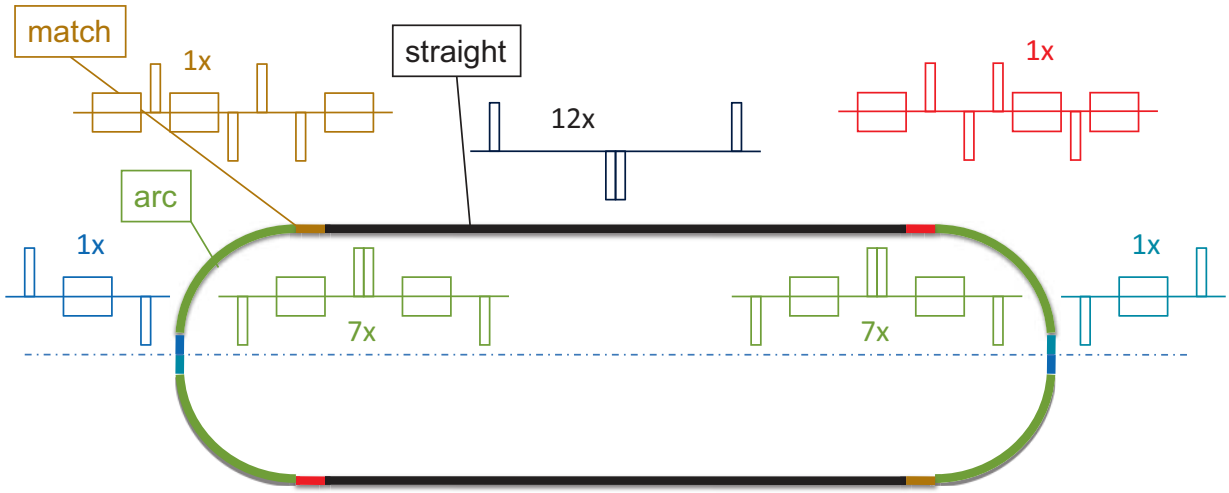

Figure 70. Schematic diagram of the racetrack decay ring illustrating its linear optics elements: (black) decay straights, (green/blue/cyan) arc sections, (red/brown) matching sections.

Table XXX. Sequence of regions and their lengths for the decay ring.

Section	**Length** (m)
1/2 straight	299.7
Matching cell	36.5
Arc	132.0
Matching cell	36.5
1/2 straight	299.7
1/2 straight	299.7
Matching cell	36.5
Arc	132.0
Matching cell	36.5
1/2 straight	299.7
Total length	1608.8

Table XXXI. Lattice for straight cell. There are 12 such cells in each of the two straights. The magnet type (superconducting, SC, or normal, NC) is given in the column headed "Type".

Element	**Length** (m)	**Field/Gradient** (T/Tm^{-1})	**Type**
QF	1.500	0.462	NC
Drift	21.975		
QD	1.500	−0.462	NC
QD	1.500	−0.462	NC
Drift	21.975		
QF	1.500	0.462	NC
Cell length	49.950		
Straight length	599.400		
Total length	1198.800		

Table XXXII. Lattice for matching cell. There is one such cell in each of the four matching sections. The magnet type (superconducting, SC, or normal, NC) is given in the column headed "Type".

Element	**Length** (m)	**Field/Gradient** (T/Tm^{-1})	**Type**
Drift	0.41		
Dipole	4.00	−0.64	NC
Drift	0.41		
QD	0.80	−9.17	SC
Drift	0.50		
QF	1.60	11.5	SC
Drift	0.45		
QD	1.60	−7.62	SC
Drift	0.50		
Dipole	0.60	−1.9	SC
Drift	14.25		
QF	0.80	4.00	SC
Drift	7.28		
Dipole	2.40	0.35	NC
Drift	0.90		
Cell length	36.50		
Total length	146.00		

Table XXXIII. Lattice for arc cell. There are 15 such cells in each of two arcs. The magnet type (superconducting, SC, or normal, NC) is given in the column headed "Type".

Element	**Length** (mm)	**Field/Gradient** (T/Tm^{-1})	**Type**
QD	0.5	−23.64	SC
Drift	0.7		
Dipole	2.0	−4.27	SC
Drift	0.7		
QF	0.5	24.05	SC
QF	0.5	24.05	SC
Drift	0.7		
Dipole	2.0	−4.27	SC
Drift	0.7		
QD	0.5	−23.64	SC
Cell length	8.8		
Arc length	132.0		
Total length	264.0		

sections, which also eliminate the high dispersion in the arcs.

Figure 71 (right) illustrates the phase advance along the ring: the working point is ($Q_x = 8.5229$, $Q_y = 8.2127$). Without sextupoles, a ±10% change in momentum causes the working point to move substantially in the (Q_x, Q_y) plane, crossing resonances that could be detrimental for the stability of the beam. To mitigate this effect, sextupoles can be introduced in the dispersive arcs. Chromaticity correction could be motivated by the desire for large momentum acceptance, the need for which is not

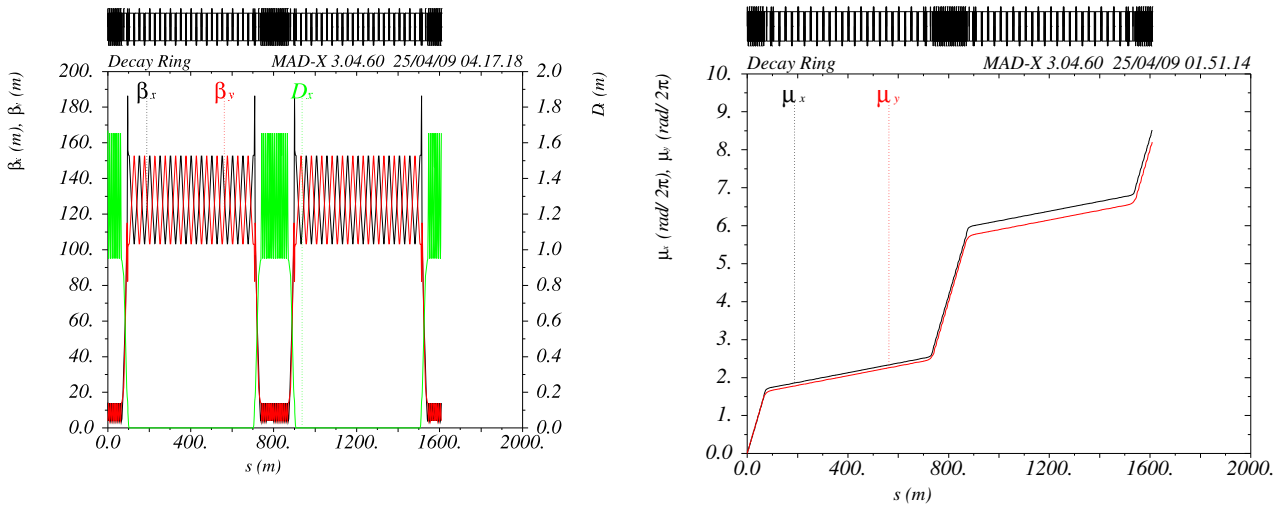

Figure 71. (Left): β_x (black) and β_y (red) functions for the decay rings. Their values are deliberately chosen high in the straight sections to reduce the divergence of the beam. Dispersion in the arcs is also shown (green). (Right): phase advance over one period in the decay ring with a fast increase in the arcs due the small beta functions and a slow increase in the straights where $\beta_{x,y}$ are large.

yet fully known due to concerns about longitudinal emittance growth in the FFAG, which is presently under study [229]. A visual summary of these results is shown in figure 72 where resonance diagrams and chromaticity plots are displayed.

2.7.1.1. Particle tracking and dynamic aperture

The introduction of non-linear elements along the ring is advocated to mitigate resonance-crossing effects, potentially catastrophic for a storage ring. However, two things should be stressed in the case of a muon ring: (a) at 25 GeV/c the average muon-lifetime corresponds to fewer than 100 turns in the 1608.8 m long ring, (b) the sextupoles introduced in the optics create coupling between the transverse planes and reduce the dynamic aperture of the beam. Concerning point (a), the question naturally arises whether it is important to avoid resonance crossing, given the relatively short beam-lifetime required. The second aspect has been investigated to produce a more quantitative answer and a summary of the dynamic aperture calculations is shown in figure 73. In the absence of errors, the dynamic aperture comfortably accommodates the nominal 30 mm rad acceptance. Studies of the dynamic aperture in the presence of errors will be carried out.

2.7.2. Decay ring instrumentation

In order to ensure the precise determination of the neutrino flux and momentum spectrum, continuous measurements of a number of the muon beam parameters are required. The critical parameters are: the muon energy (and polarisation), the beam divergence, and the beam current. Efforts are presently

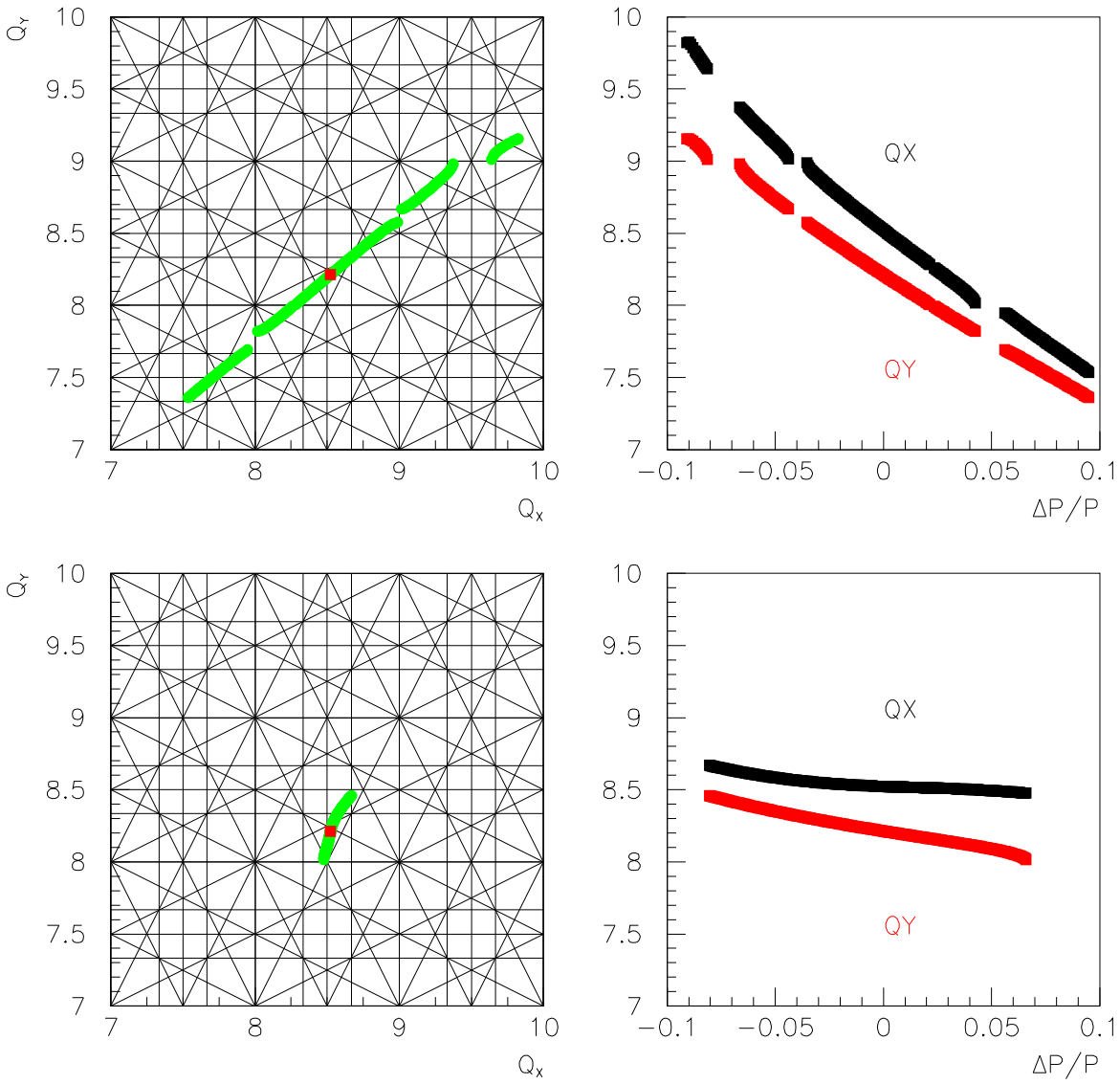

Figure 72. Upper section: linear optics configuration, showing the crossing of resonances (left) as a function of momentum spread (green line): the red dot shows the working point. The natural chromaticity of the beam is shown on the right for both the transverse planes. Lower section: the effect of sextupoles is shown. Chromaticity is strongly reduced (right) and so is the crossing of potentially dangerous resonances.

focused on the measurement of the first two parameters which are considered the more challenging. The beam current can be measured with sufficient precision using standard beam-current monitors. The following sections outline the principles of operation of the devices being considered to measure the beam energy (and polarisation) and the beam divergence.

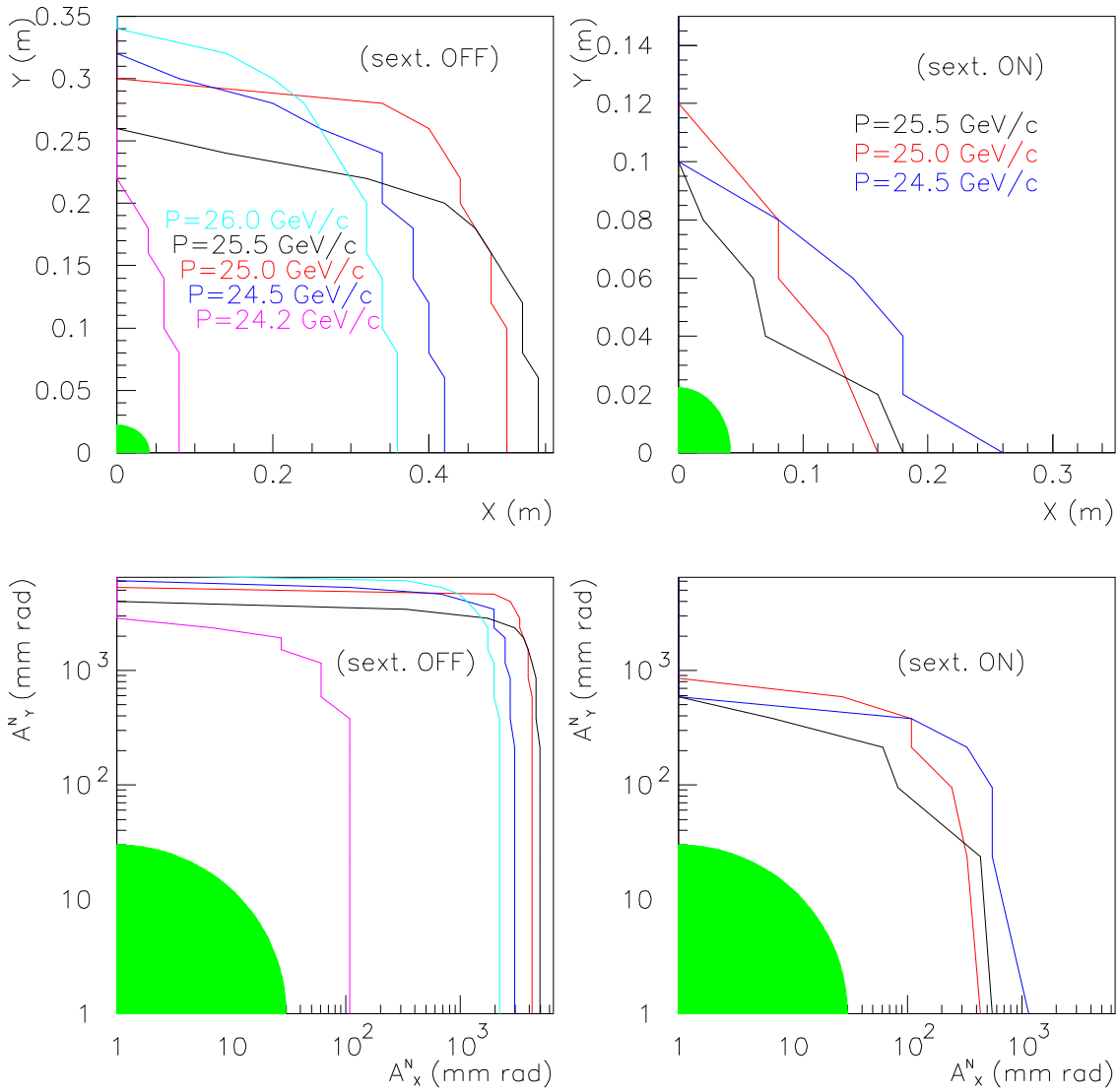

Figure 73. Dynamic aperture for the decay ring: (left column) linear optics, (right column) sextupoles introduced in the lattice. (Top) contour plots defining the maximal radius for a particle injected at the midpoint of an arc before being lost in the lattice. In off-momentum cases this radius is generally reduced. The green area represents the beam size corresponding to the nominal acceptance (30 mm rad). Points on the contour plots (R_x, R_y) are used to define the amplitudes in the two transverse planes (A_x^N, A_y^N), where $(A_i^N = \frac{p}{m_\mu} R_i^2/\beta_i)_{i=x,y}$ (bottom). In this case the green area marks the 30 mm rad fiducial acceptance.

2.7.2.1. Muon beam energy determination using spin polarisation measurements

Muons from pion decay are produced with a longitudinal polarisation of -100% in the decay rest frame. In the laboratory frame this number is expected to become -18% for pions between 200 MeV/c and

300 MeV/c [298]. This residual beam-polarisation can be used to determine the central energy of the beam [299]. Electrons from muon decays can be collected at the end of a straight section, exploiting the bending power of the dipoles (e.g., in the matching sections or in the arcs) and channelling the spectral components to counting devices [300]. Only part of the electron spectrum can be sampled (since electrons at high energy travel nearly parallel to the muon beam), however a general expression for the expected signal can be written as [300]:

$$\mathcal{E}(t) = \mathcal{E}_0 e^{-\alpha t}\left[1 + \frac{\beta}{7} e^{-\frac{1}{2}\left(\omega \frac{\Delta E}{E} t\right)^2} \cdot \mathcal{P} cos(\phi + \omega t)\right]; \tag{25}$$

where $\mathcal{E}_0$ is the total energy of the electrons at turn 0 and the Gaussian term parametrises the beam energy spread. If it is assumed that all the decay electrons can be collected, then $\mathcal{P}$ is the polarisation of the beam. If this is not the case, the $\mathcal{P}$ is a free parameter that can be related to the beam polarisation with further study. A fit to $\mathcal{E}(t)$ allows both the beam energy and the energy spread to be determined. An example of such a fit is shown in figure 74 for two energy bins, [0,5] GeV and [15,18] GeV. The precision with which E_μ and $\Delta E_\mu / E_\mu$ can be measured is a function of the number of captured electrons and of the number of sampled turns. With $\sim 3 \times 10^5$ electrons per turn reaching the device and 50 turns sampled, we expect a statistical precision 0.2% on the central muon energy and 4% on the energy spread for each machine fill. Since the physics requires only that the average energy distribution be known over significant periods of running, with 50 fills of the ring per second, the statistical uncertainties on the flux will be negligible. The systematic uncertainties of this method are also expected to be small. The central energy measurement affects the flux as E^3, but the precision achievable will be sufficient to make this source of flux uncertainty negligible. The measurement of the polarisation itself is more difficult, because it relies on knowing the collection efficiency of the decay electrons, which in turn requires detailed knowledge of the geometry of both the ring and the polarimeter. In a ring geometry, however, the polarisation precesses and thus its effect on the flux averages to zero with sufficient precision [298]. These preliminary numbers need a more realistic study of the systematics of the measurement, but they give an idea of the limits of the method. The relation between the oscillation excursions in the total recorded energy and the polarisation provides a measure of the latter.

Once the storage-ring lattice has been designed, a suitable location for the electron calorimeter can be determined. In the studies presented here, the electron calorimeter is taken to refer to a "generic" device that will eventually be designed to measure the electron energy. Figure 75 shows some of the possible locations for electron monitors, together with the main features of the dipole magnets used as spectrometers to separate electrons of different energies. When choosing a particular location, one must consider both the spectral power and the purity of the signal. Ideally, the device should collect electrons produced in the proximity of the spectrometer in order to avoid spurious effects from other magnets. With this in mind, we focused on two main cases:

- (A): a monitor placed downstream of the second bending magnet in the matching section, just before a quadrupole and orthogonal to the direction of the beam; and
- (B): a monitor placed in the third bending element of the arc section, parallel to the beam direction.

In case (A) the device sits transversely to the nominal beam orbit at a distance of about 13 m from a dipole (B = 1.9 T, L_{eff} = 0.6 m) with the long drift allowing a good spectral power despite the

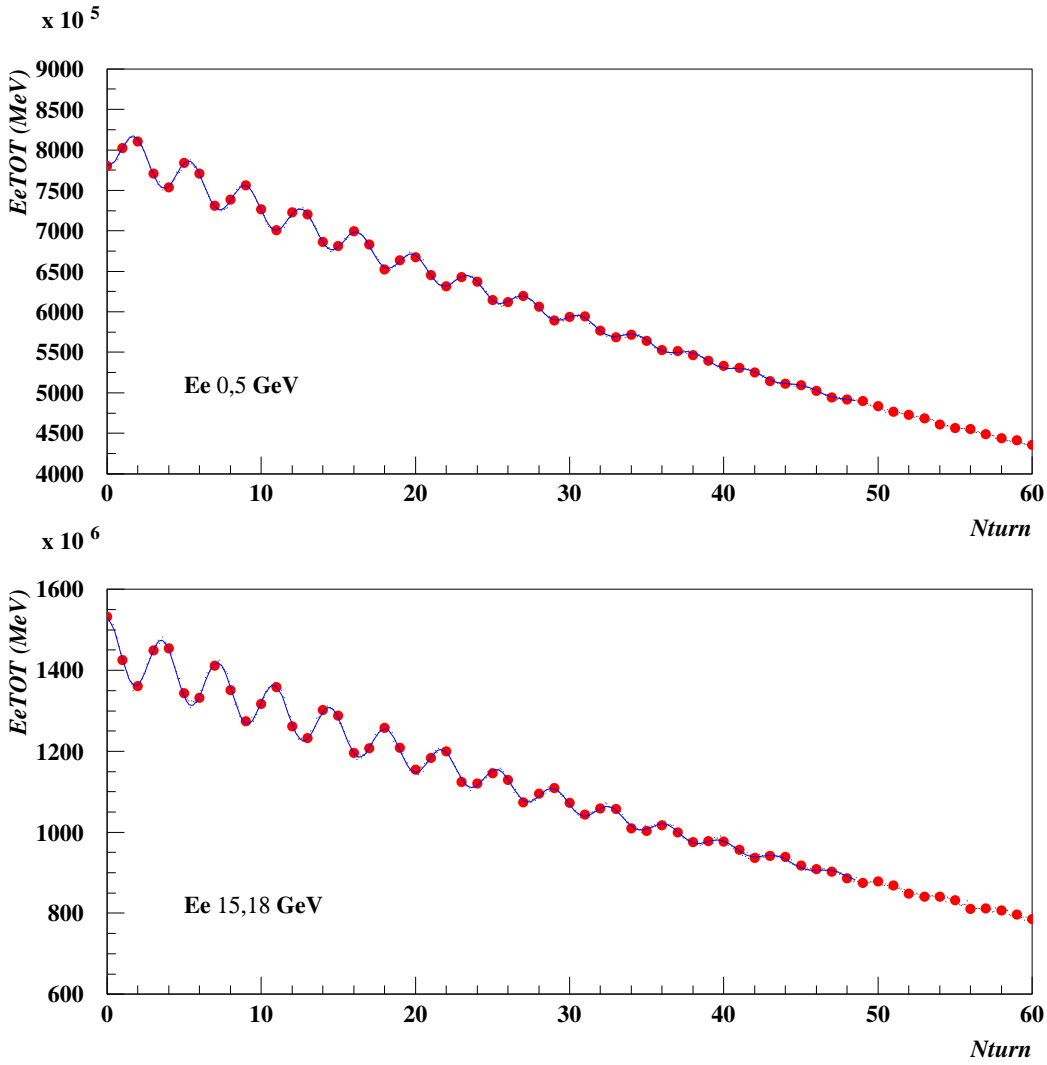

Figure 74. Total energy from electrons belonging to the [0,5] GeV (top) and [15,18] GeV (bottom) GeV intervals of the spectrum as a function of the number of turns. The red dots are samples taken at every turn, the superimposed curve is a fit to the function defined in equation 25.

relatively low magnetic field. The advantage of this location is that no special magnet is needed, which simplifies the engineering. Figure 75 (Case A) shows that at this location a device placed at >10 cm from the beam axis can intercept a fraction of the spectrum between 0 GeV and 18 GeV without disrupting the muon beam. In this case we simulated muon decays along the whole 13 m of drift to check the uniformity of the signal. Case (B) is similar to the idea for the polarimeter proposed in [300]. The advantage here is the good spectral power of the bending magnet due to its effective length and high field ($B = 4.3$ T, $L_{\text{eff}} = 2$ m). However, the requirement to modify the shape of the magnet, introducing apertures through the superconducting element, would pose engineering challenges. The

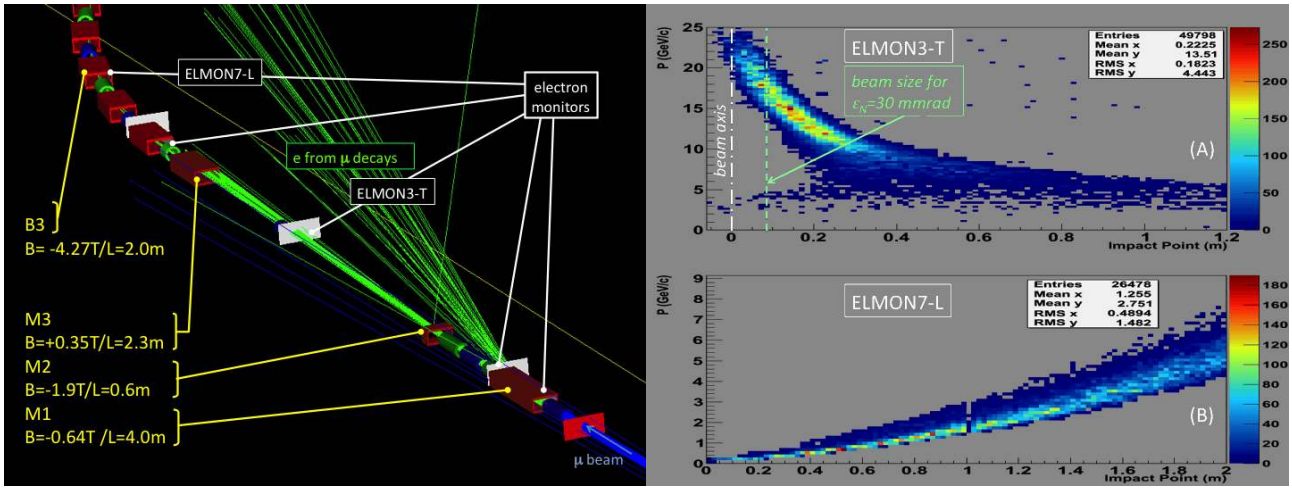

Figure 75. (Left): G4Beamline rendering of the region at the end of a straight section and beginning of the arc-section. In the middle the magnets of a matching section are visible. Locations for electron monitors are suggested. Blue tracks represent muons, green tracks the electrons from decays. (Right) Momentum as a function of the impact point position for: (A) a monitor placed transversely to the beam after a drift of 13 m past a dipole in the matching section. (B) a monitor parallel to the beam trajectory. In case (A) the position of the beam and its maximum width (for a normalised emittance of 30 mm rad) are shown.

graph shown in figure 75 is a superposition of decays that occur in the 2.4 m path between dipole B2 and dipole B3 (where the electron monitor is located). As in case (A), a good signal uniformity is found.

2.7.2.2. Muon beam divergence

The decay rings have been designed in order to keep a low rms divergence in the straight sections. This should be of the order of 10% of the natural divergence originating from muon decays into neutrinos ($1/\gamma = 4.0$ mrad). In order to measure this quantity, a device has to be inserted into the beam. The material budget of the device needs to be small so as to reduce the effects of multiple scattering and energy straggling. The original idea of a Cherenkov detector has been re-analysed in a critical way, while a new concept based on optical transition radiation is under study.

Cherenkov Radiator

This concept dates back to the first proposals for a Neutrino Factory and consists of a tank with thin walls containing He at high pressure (> 10 atm). Photons from Cherenkov radiation reach a mirror telescope located at about 20 m from the source and bounce back to a collector with sensors. The device is sensitive to the beam divergence, such that an inclination of the beam translates into a change in the image point. According to [232] this device should be very precise (0.04 mrad resolution),

however a review of this proposal makes it impractical for a number of reasons. The geometry and size of the device is related to the Cherenkov angle, which is a function of the helium-gas pressure. A pressure of the order of 15 atm is needed in order to fulfil the geometrical constraints of the telescope. This implies the use of a thick transparent window to contain the gas and to let the light travel towards the optical system. A thickness of 200 μm, which may be optimistically thin, causes the initial divergence of the beam of 0.4 mrad to grow to 0.46 mrad after 200 turns. The Cherenkov telescope is not particularly compact, due to the requirement to exploit a long lever arm. It should be noted that any layer of material placed across the beam will heat up due to energy loss, reaching more than 100 °C in $\sim$ 10 seconds. A heat-dissipation system is therefore needed to maintain an appropriate working temperature.

Optical transition radiation device

In order to overcome some of the aforementioned issues, alternative solutions have been examined that rely on the principle of optical transition radiation (OTR) [301]. When a charged particle crosses the boundary between vacuum and conductor (dielectric), electromagnetic radiation is produced both in the forward and backward directions (generated by the image charge within the conductor). A particular configuration is obtained when the conductor forms an angle of 45° with respect to the incident beam. In this case the "backward" radiation is orthogonal to the incident beam and can be collected out of the beam pipe. The shape of this radiation shows a typical two-lobed distribution with an opening angle of $1/\gamma$. Depending on the optics chosen, one can infer the beam divergence in two ways: a) by collecting the OTR pattern in the focal plane with one foil; or b) by reconstructing the beam in the image plane with three stations and then infer the divergence of the beam by means of the usual transport-matrix techniques. In case (a) the OTR pattern definition is a function of the beam divergence, so the divergence can be found by studying the ratio between minimum and maximum intensities of the OTR figure. From the literature [302, 303], we learn that in our case a resolution of 0.5 mrad should be achievable. This is not ideal, though further studies should be done in order to understand the real potential of this technique with a realistic muon beam, an optical system and the best sensors available today. Case (b) relies on the reconstruction of beam size at three different points. The spatial resolution is dominated by the optical system and the sensors used. At CEBAF a beam spot of 100 μm can be resolved [304], which makes this method interesting for our case, even if the uncertainty of the divergence measurement still has to be evaluated. The proposed OTR devices all rely on very thin (order of 50 μm) metal foils, which makes the technique interesting as it has the potential to offer a low material budget and has the capability of dissipating heat.

In conclusion, we identified three possible ways of measuring the divergence, one based on Cherenkov radiation and the other two relying on OTR techniques. The first one seems impractical, while the OTR techniques necessitate further studies to understand the level of precision reachable in our case.

3. Neutrino Detectors for the Neutrino Factory

3.1. Introduction

3.1.1. Baseline description for the far detectors

The IDS-NF baseline for the Neutrino Factory has been optimised as described in section 1. The optimum strategy to measure δ, θ_{31}, and the mass hierarchy (the sign of Δm^2_{13}) includes having two Magnetised Iron Neutrino Detectors (MIND), one with a fiducial mass of 100 kTon at $\sim 4\,000$ km and another with a fiducial mass 50 kTon at $\sim 7\,500$ km. The latter has been termed the "magic baseline", since matter effects cancel the effect of CP violation at this distance. The detector is optimised to carry out the detection of the "golden channel" ($\nu_e \to \nu_\mu$) through the wrong-sign muon signature. This strategy is more efficient for resolving degeneracies in the neutrino-oscillation formulæand provides better sensitivity than, for example, measuring the golden and the "silver" channel ($\nu_e \to \nu_\tau$) simultaneously.

The original golden channel at a Neutrino Factory analysis [102] assumed a cylindrical geometry with a cross-sectional radius of 10 m, with iron plates 6 cm thick, scintillator planes 2 cm thick and a 1 T solenoidal field operating at a 50 GeV Neutrino Factory. The International Scoping Study (ISS) [6, 305] assumed a cuboidal geometry of 14×14 m^2 with 4 cm thick iron and 1 cm thick scintillator and a 1 T dipole field, while operating at a 25 GeV Neutrino Factory.

For the most recent studies we have adopted a baseline cuboidal geometry with a cross-sectional area of 15×15 m^2 and length of either 63 m or 125 m, depending on the mass of the detector. The thickness of each plane of iron is 3 cm, followed by two planes of scintillator, each with 1 cm thickness. The three planes form a module of thickness 5 cm. The lateral resolution requirement is 1 cm, which is provided by having co-extruded scintillator bars 15 m long and 3.5 cm wide, read out using optical fibres and silicon photo-multipliers (SiPMT). The magnetic field assumed for this baseline is a 1 T dipole field. Table XXXIV lists the key parameters of the two far detectors. The purpose of studying this geometry was to perform a direct comparison with previous results and to determine the influence of a full reconstruction in conjunction with a modern likelihood analysis to eliminate background.

While we adopted this simplifying geometry and magnetic field to compare with previous simulations, we are aware that a 1 T dipole field is not practical from an engineering point of view. However, as described in section 3.2.2 we have now studied a more realistic octagonal geometry (14 m octagonal iron plates as shown in figure 76), with a toroidal field between 1 T and 2.2 T over the whole fiducial area. These parameters can be achieved with a 100 kA/turn current traversing the centre of the MIND plates and are shown to be feasible to manufacture. This more realistic geometry has not been simulated yet but we do not expect that the performance will differ greatly from what has been achieved, and will be described in section 3.2.1.

3.1.2. Baseline description for the near detectors

The baseline for the Neutrino Factory includes one or more near detectors. It is necessary to have one near detector for each of the straight sections of the storage ring at each of the two polarities, so four

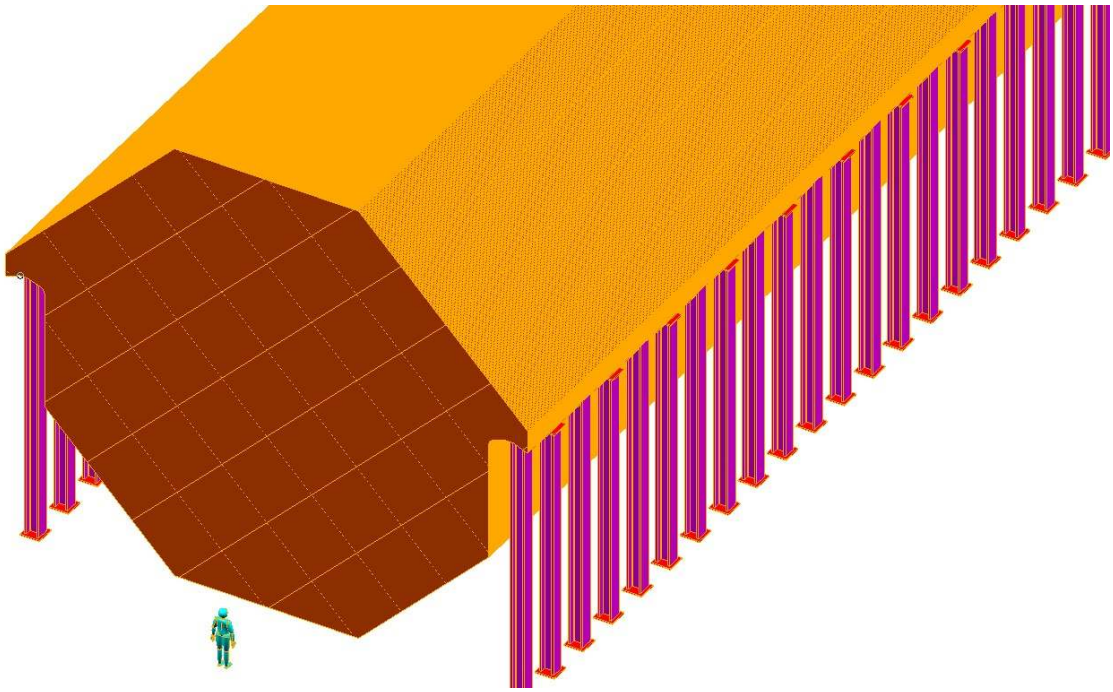

Figure 76. Schematic drawing of the Magnetised Iron Neutrino Detector (MIND).

Table XXXIV. Baseline parameters for the Magnetised Iron Neutrino Detectors at a Neutrino Factory. MIND 1 refers to the detector at $\sim 4\,000$ km and MIND 2 refers to the detector at $\sim 7\,500$ km.

Parameter	**MIND 1**	**MIND 2**
Distance (km)	3000-5000	7000-8000
Fiducial mass (kT)	100	50
Size iron plates (cm^3)	1500×1500×3	1500×1500×3
Length detector (m)	125	62.5
Number iron plates	2500	1250
Dimensions scintillator bars (cm^3)	1500×3.5×1	1500×3.5×1
Number scintillator bars per plane	429	429
Total number of scintillator bars	2.14×10^6	1.07×10^6
Total number of readout channels	4.28×10^6	2.14×10^6
Photon detector	SiPMT	SiPMT
Magnetic field (T)	> 1	> 1

near detectors designed to carry out measurements essential to the oscillation-physics programme are required. The near-detector measurements that are essential for the neutrino oscillation analysis are:

- Determination of the neutrino flux through the measurement of neutrino-electron scattering;
- Measurement of the neutrino-beam properties that are required for the flux to be extrapolated with accuracy to the far detectors;

- Measurement of the charm production cross sections (charm production in far detectors is one of the principal backgrounds to the oscillation signal); and
- Measurement of the neutrino-nucleon deep inelastic, quasi-elastic, and resonant-scattering cross sections.

The intense neutrino beam delivered by the Neutrino Factory makes it possible to carry out a unique neutrino-physics programme at the near detectors. This programme includes fundamental electroweak and QCD physics, such as measurements of parton distribution functions as a function of Q^2 and Bjorken x, QCD sum rules, nuclear re-interaction effects, strange particle production, a precise measurement of $\sin^2\theta_W$. The near detector must also be capable of searching for new physics, for example by detecting tau-leptons which are particularly sensitive probes of non-standard interactions at source and at detection. Tau neutrino detection is also important in the search for sterile neutrinos.

Here we itemise the general design features of the near detector:

- A detector with micron-scale resolution for charm and tau identification (either a silicon vertex or an emulsion-based detector);
- A low-Z, high-resolution target for flux and ν_μ- and ν_e-leptonic cross-section measurements (i.e., a scintillating-fibre tracker or a straw-tube tracker);
- A magnetic field for charged particle momentum measurement (with $\delta p/p \sim 1\%$ (for $p \sim 2 - 3\,\mathrm{GeV}$);
- A muon catcher for muon identification;
- Electron identification capabilities;
- Excellent energy resolution for flux extrapolation: this needs to be better than for the far detector, so the goal is to achieve $\delta E/E \sim 1\%$; and
- A variety of nuclear targets to measure cross-sections in iron and as a function of the nuclear target mass number A.

There are two options currently being considered: one which includes a high resolution scintillating fibre tracker and the other includes a transition-radiation straw-tube tracker. Both of these options will be studied to determine their capabilities.

3.2. Far Detectors

3.2.1. Magnetised Iron Neutrino Detector Performance

3.2.1.1. Introduction

Early papers on the physics outcomes of a Neutrino Factory concentrated on the sub-dominant $\nu_e \to \nu_\mu$ oscillation [306] in which a muon of opposite charge to that stored in the storage ring (wrong-sign muon) would be produced in a far detector by the charge current (CC) interactions of the oscillated ν_μ. The first analysis of the capabilities of a large Magnetised Iron Neutrino Detector to detect the wrong-sign muon signature (the golden channel) was discussed in [102], where it was demonstrated that this combination was capable of extracting the remaining unknown parameters in the three-by-three neutrino mixing matrix. This analysis was carried out assuming a Neutrino Factory with 50 GeV muons, and was optimised for high energy using a detector with 4 cm thick iron plates and

1 cm scintillator planes. Hence, the ability to reconstruct low energy muons was not part of the optimisation.

The International Scoping Study for a future Neutrino Factory and super-beam facility (the ISS) [4–6, 305] adopted a muon energy of 25 GeV, so the analysis was re-optimised for low-energy neutrino interactions. This study focused on the topology and kinematics of neutrino events in the detector, assuming perfect pattern recognition and smearing of the kinematic variables of the scattered muon and hadronic shower. Using a combination of cuts on the relative length of the two longest particles in the event and the momentum and isolation of this candidate, it was demonstrated that high signal-identification efficiency and background suppression could be achieved.

The work that has been carried out since the ISS, and is included in this Interim Design Report, has focused on testing these assumptions, by performing a full simulation and reconstruction of the candidate neutrino events, allowing a full characterisation of the detector response. Incorrect charge assignment (charge mis-identification) of non-oscillated $\overline{\nu}_\mu$ CC interactions, background from meson decays in the hadronic shower, and misidentification of neutral current (NC) and ν_e CC events present the most significant background for the Neutrino Factory beam.

The present study first focused on demonstrating the performance of reconstruction algorithms using deep inelastic scattering (DIS) neutrino events generated using LEPTO61 [307] and simulated using GEANT3 [308], as in the study performed for the ISS. Pattern recognition and reconstruction of candidate muons were carried out using a Kalman filter (RecPack [309]) and a Cellular Automaton algorithm, particularly useful in extracting low energy neutrino events [310]. Preliminary results were shown in [311] and were further developed in [13].

In conjunction with the development of reconstruction algorithms for MIND, an entirely new simulation was developed based on the NUANCE event generator [312] and GEANT4 [313]. This simulation, named G4MIND, will ultimately allow for a full optimisation of MIND in terms of segmentation, technology options and analysis algorithms. The work undertaken to develop the simulation and digitisation as well as the application and re-optimisation of the reconstruction algorithm introduced in [13] is described in this report. These results were used to determine the response matrices for this detector system (presented in Appendix H), which has been used to deduce the expected sensitivity of the combination of the MIND and a 25 GeV Neutrino Factory to key oscillation parameters.

3.2.1.2. Simulation using NUANCE and GEANT4

In previous studies, only deep inelastic scattering (DIS) events generated with LEPTO61 were considered. However, at energies below 5 GeV there are large contributions from quasi-elastic (QE), single pion production (1π) and other resonant production (DIS) events (see figure 77). A QE event may be accurately described by considering the interaction of the neutrino to take place with a nucleon as a whole ($\nu_\mu + n \rightarrow \mu^- + p$). The energy of such an event may readily be reconstructed from the momentum of the muon and the angle it makes with the beam direction. In addition, the low multiplicity of the event makes muon reconstruction simpler. 1π events should also improve the purity of the low-energy event sample due to their low multiplicity, although there may be increased background from pion decay. Other nuclear resonant events, producing 2 or 3 pions, as well as diffractive and coherent production, have much smaller contributions.

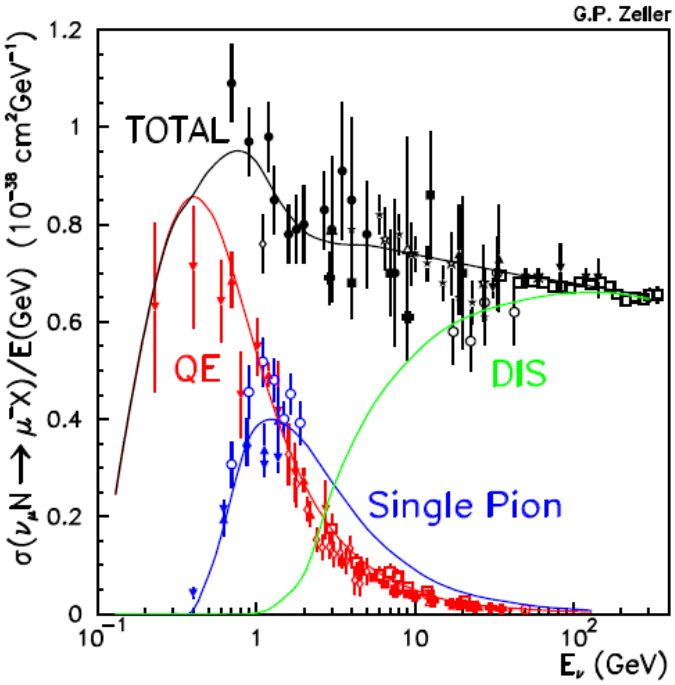

Figure 77. Experimentally measured cross-sections for quasi-elastic, single pion and deep inelastic ν_μ CC interactions with the predictions made by NUANCE [314].

Generation of all types of interaction was performed using the NUANCE framework [312]. The relative proportions of the interaction types generated by NUANCE are shown in figure 78 where 'other' interactions include the resonant, coherent and diffractive processes. NUANCE also includes a treatment to simulate the effect of re-interaction within the participant nucleon, which is particularly important for low energy interactions in high-Z targets such as iron.

From the flux spectrum used to generate the events and the resultant interaction spectrum, the cross section as a function of energy can be estimated by normalising the highest energy bin to the high-energy limit: 0.67×10^{-38} cm^2 GeV^{-1} for ν_μ and 0.34×10^{-38} cm^2 GeV^{-1} for $\overline{\nu}_\mu$ [315].

A new simulation of MIND using the GEANT4 toolkit G4MIND was developed to give as much flexibility to the geometry as possible so that an optimisation of all aspects of the detector could be carried out. The dimensions and spacing of all scintillator and iron pieces, as well as all external dimensions of the detector, can be controlled. This will allow for easy comparison of the simulation itself and the subsequent analyses to other potential Neutrino Factory detectors.

The detector transverse dimensions (x and y axes) and length in the beam direction (z axis), transverse to the detector face, are controlled from a parameter file. A fiducial cross section of 14 m×14 m, including 3 cm of iron for every 2 cm of polystyrene extruded plastic scintillator (1 cm of scintillator per view), was assumed. A constant magnetic field of 1 T is oriented in the positive y direction throughout the detector volume. Events generated using NUANCE in iron nuclei and scintillator (polystyrene) are selected in the relative proportion of the two materials. An event vertex

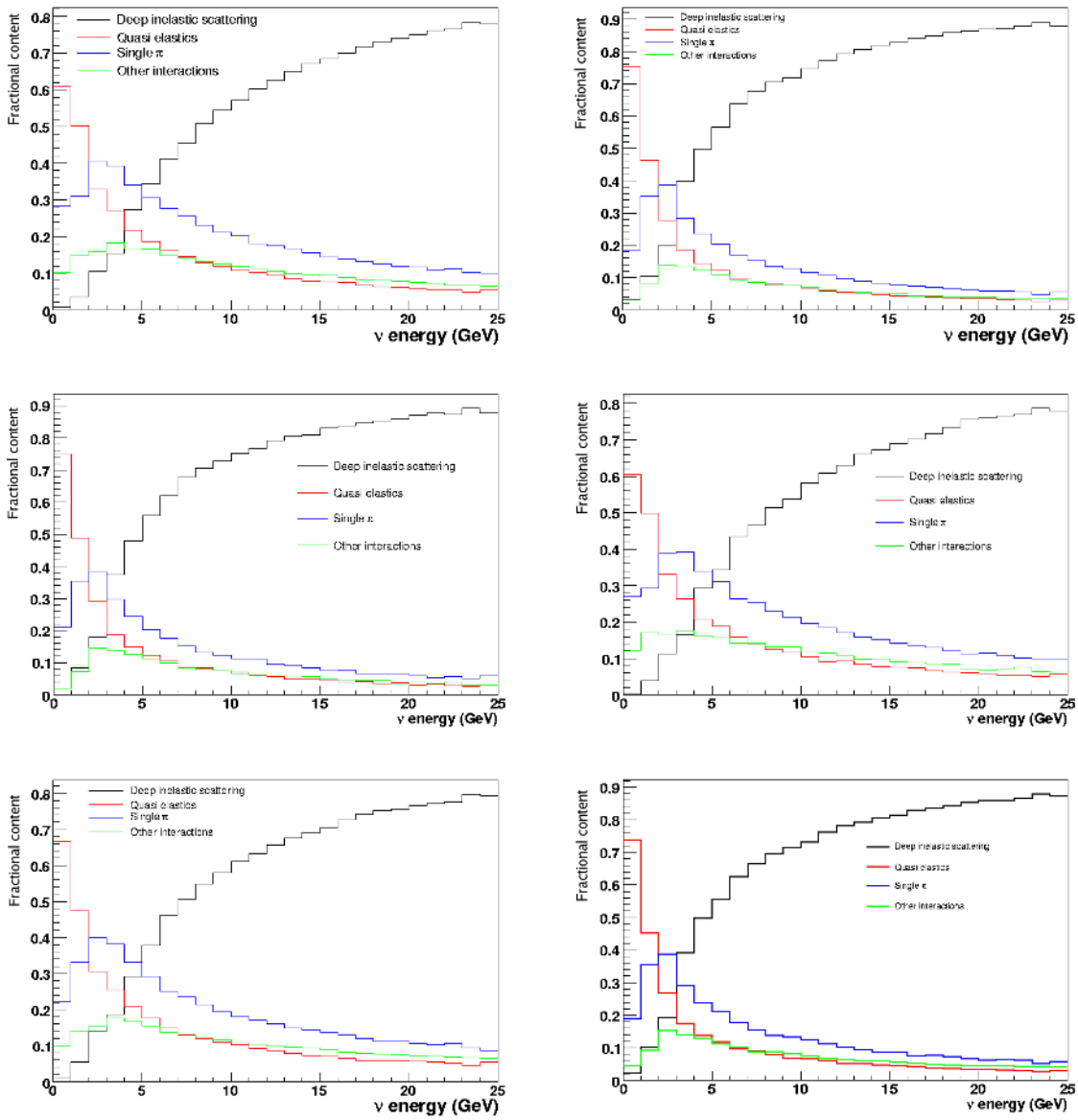

Figure 78. Proportion of total number of interactions of different ν interaction processes for events generated using NUANCE and passed to the G4MIND simulation. (top) $\overline{\nu}_\mu$ (left) and ν_e CC (right), (middle) ν_μ (left) and $\overline{\nu}_e$ CC (right) and (bottom) NC from anti-neutrinos (left) and neutrinos (right).

is then generated within one of the slabs of the appropriate material randomly positioned in three dimensions. Physics processes are modelled using the QGSP_BERT physics lists provided by GEANT4 [316].

Secondary particles are required to travel at least 30 mm from their production point or to cross a material boundary between the detector sub-volumes to have their trajectory fully tracked. Generally, particles are only tracked down to a kinetic energy of 100 MeV. However, gammas and muons are

excluded from this cut. The end-point of a muon track is important for muon pattern recognition.

A simplified digitisation model was considered for this simulation. Two-dimensional boxes – termed voxels – represent view-matched x and y readout positions. Any deposit which falls within a voxel has its energy deposit added to the voxel total raw energy deposit. The thickness of two centimetres of scintillator per plane assumes 1 cm per view.

Voxels with edge lengths of 3.5 cm were chosen, which results in a position resolution of $3.5/\sqrt{12} \cong$ 1 cm. The response of the scintillator bars is derived from the raw energy deposit in each voxel, read out using wavelength shifting (WLS) fibres with attenuation length $\lambda = 5$ m, as reported by the MINERvA collaboration [317]. Assuming that approximately half of the energy will come from each view, the deposit is halved and the remaining energy at each edge in x and y is calculated. This energy is then smeared according to a Gaussian with $\sigma/E = 6\%$ to represent the response of the electronics and then recombined into x, y and total $= x + y$ energy deposit per voxel. Assuming an output wavelength of 525 nm, a photo-detector quantum efficiency of ∼30% can be achieved (see figure 116 in section 3.2.2). A threshold of 4.7 photo electrons (pe) per view, as in MINOS [318], was assumed. Any voxel in which the two views do not make this threshold is cut. If only one view is above threshold, then only the view below the cut is excluded (see section 3.2.1.3). The digitisation of an example event is shown in figure 79.

3.2.1.3. Reconstruction of events

The reconstruction and analysis packages are described in detail in a previous publication [13]. We present here an update of the analysis based on the MIND simulation generated using NUANCE and GEANT4. The optimisation of cuts and the extraction of efficiencies were performed using a flux profile designed to maximise statistics in all energy bins of interest.

Many traversing particles, particularly hadrons, deposit energy in more than one voxel. Forming clusters of adjacent voxels reduces event complexity and can improve pattern recognition in the region of the hadron shower. The clustering algorithm is invoked at the start of each event. The voxels of every plane in which energy has been deposited are considered in sequence. Where an active voxel is in contact with no other active voxel, this voxel becomes a measurement point. If there are adjacent voxels, the voxel with the largest total deposit (at scintillator edge) is sought and all active voxels in the surrounding 3×3 area are considered to be part of the cluster. Adjacent deposits which do not fall into this area are considered separate. The cluster position is calculated independently in the x and y views as the energy-weighted sum of the individual voxels.

The clusters formed from the hit voxels of an event are then passed to the reconstruction algorithm. The separation of candidate muons from hadronic activity is achieved using two methods: a Kalman filter algorithm provided by RecPack [309] and a cellular automaton method (based on [310]).

The Kalman filter propagates the track parameters back through the planes using a helix model which takes into account multiple scattering and energy loss. Since, in general, a muon is a minimum ionising particle (MIP) and will travel further in the detector than hadronic particles, those hits furthest downstream are assumed to be muon hits and used as a seed for the Kalman filter. The seed "state vector" is then propagated back to each plane with multiple hits and the matching χ^2 to each of the hits is computed. Hits with matching χ^2 below 20 are considered and in each plane the one with the best matching among these is added to the trajectory and filtered (i.e. the track parameters

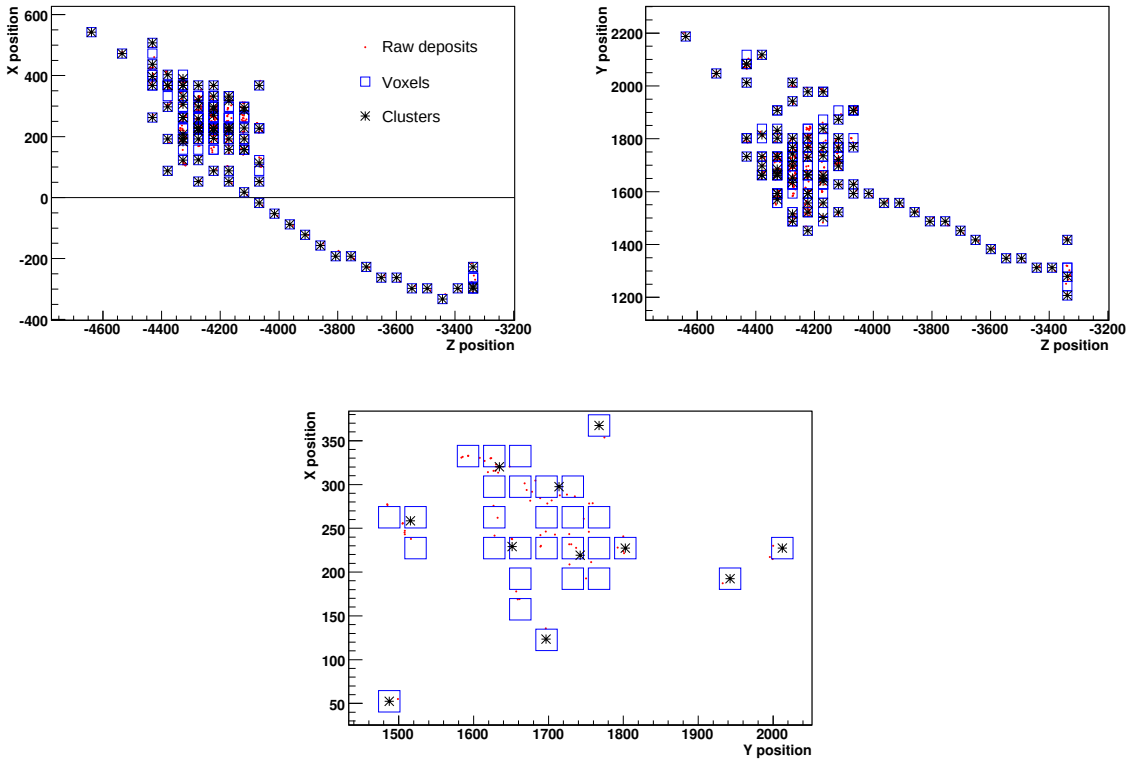

Figure 79. The digitisation and voxel clustering of an example event: (top left) bending plane view, (top right) non-bending plane, (bottom) an individual scintillator plane. The individual hits are small dots (in red), the blue squares are the voxels and the black asterisks represent the centroid positions of the clusters.

are updated with the new information). All accepted hits constitute the candidate muon and are presented for fitting with the remaining hits being considered as hadronic activity.

Events with high Q^2 or low neutrino energy can be rejected by the first method, since in general the muon will not escape the region of hadronic activity. The cellular automaton method uses a neighbourhood function first to rank all the hits and then to form all viable combinations into possible trajectories. A "neighbour" is defined as a hit in an adjacent plane within a pre-defined transverse distance of the projection into that plane of the straight line connecting hits in the previous two planes. Starting from the plane with lowest z position, hits are given incremental ranks higher than neighbours in the previous plane. Trajectories are then formed from every possible combination of one hit per plane starting with those of highest rank using the neighbourhood function.

Those trajectories formed using this method are then categorised according to length and χ^2. The candidate muon is then selected as the longest remaining trajectory with the lowest χ^2. All other hits in the event are considered to be from hadronic activity. Even if three planes in a row have no associated candidate hits, the event can still be accepted if 70% of the planes are considered to belong to the candidate-muon trajectory. This algorithm improves the efficiency and purity of muon candidates close the hadronic jet, since it ranks the likelihood that a given hit belongs to the muon

candidate or the hadronic jet.

An additional step was added to take into account that fully-contained muons (particularly μ^-) can have additional deposits at their endpoint due to captures on nuclei or due to decays. Long, well defined tracks can be rejected if there is additional energy deposited at the muon end point, since the cellular automaton interprets this as hadronic activity or a decay. Once the cellular automaton has completed the pattern recognition, a Kalman fit is used to estimate the track parameters. Additional energy deposits at the end of the muon track may cause confusion in determining the seed of the Kalman filter. Therefore, after sorting clusters into increasing z position, a pattern-recognition algorithm is used to identify the section of the track associated with the long muon section, used for momentum measurement via the Kalman filter, and the endpoint.

The complete pattern-recognition chain using these algorithms leads to candidate purity (fraction of candidate hits of muon origin) for ν_μ ($\overline{\nu}_\mu$) CC events as shown in figure 80. A cluster is considered to be of muon origin if greater than 80% of the raw deposits contained within the cluster were recorded as muon deposits. Overall, the candidate purity is in excess of 90% for true muon energies larger than $\sim 2\,\mathrm{GeV}$.

Fitting of the candidates proceeds using a Kalman filter to fit a helix to the candidate, using an initial seed estimated by a quartic fit, and then refitting any successes. Projecting successful trajectories back to the true vertex z position, the quality of the fitter can be estimated using the pulls of the different parameters in the fit vector (see figure 81).

The pulls on the position and direction exhibit a larger sigma than expected indicating that the position resolution is underestimated (i.e. that the resolution assumed in the fit is a little too small). This is attributed to clusters being made up of many particles in the high-occupancy vertex region. This effect will be better understood as the digitisation algorithms are improved. The momentum pull, however, behaves as expected but for a slight bias due to the fact that the energy loss is not updated along the track in the version of RecPack used for the study. In this version the energy loss is not changed as the filter progresses along the track and can result in a bias. The muon-momentum resolution is slightly improved from previous studies, particularly at low energies, and its resolution is parametrised as follows:

$$\frac{\sigma_{1/p}}{1/p} = 0.18 + \frac{0.28}{p} - 1.17 \times 10^{-3} p. \tag{26}$$

Hadronic reconstruction is predominantly performed using a smear on the true quantities as described in [13]. However, the presence of QE interactions in the sample allows for the reconstruction of certain events using the formula:

$$E_\nu = \frac{m_N E_\mu + \frac{m_{N_X}^2 - m_\mu^2 - m_N^2}{2}}{m_N - E_\mu + |p_\mu| \cos\vartheta}\,; \tag{27}$$

where ϑ is the angle between the muon momentum vector and the beam direction, m_N is the mass of the initial state nucleon, and m_{N_X} is the mass of the outgoing nucleon for the interactions $\nu_\mu + n \to \mu^- + p$ and $\overline{\nu}_\mu + p \to \mu^+ + n$ [319]. QE interactions can be selected using their distribution in ϑ and their event-plane occupancy among other parameters. Should the use of equation 27 result in a negative value for the energy, it is recalculated as the total energy of a muon using the reconstructed momentum.

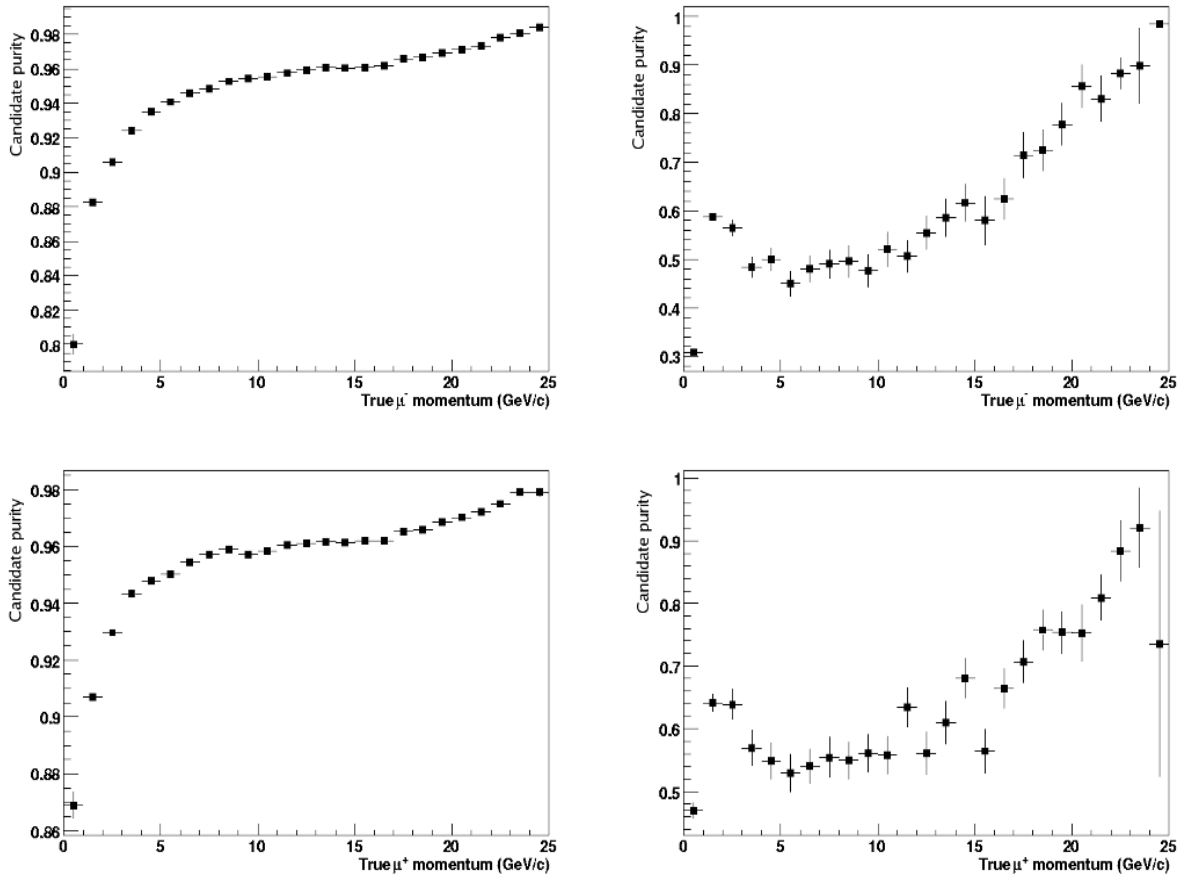

Figure 80. Muon candidate hit purity for ν_μ CC (top) and $\overline{\nu}_\mu$ CC (bottom) interactions extracted using (left) Kalman filter method and (right) cellular automaton method.

3.2.1.4. Analysis of potential signal and background

There are four principal sources of background to the wrong sign muon search: incorrect charge assignment (charge misidentification), wrong sign muons from hadron decay in $\overline{\nu}_\mu$ charged current (CC), neutral current (NC) and ν_e CC events wrongly identified as ν_μ CC. In order to reduce these backgrounds while maintaining good efficiency a number of offline cuts were employed. They can be organised in four categories: 1) ν_μ CC selection cuts; 2) NC rejection cuts; 3) kinematic cuts; and 4) muon quality cuts. Cut levels and likelihood distributions have been defined using a test statistic of ν_μ and $\overline{\nu}_\mu$ CC and NC events.

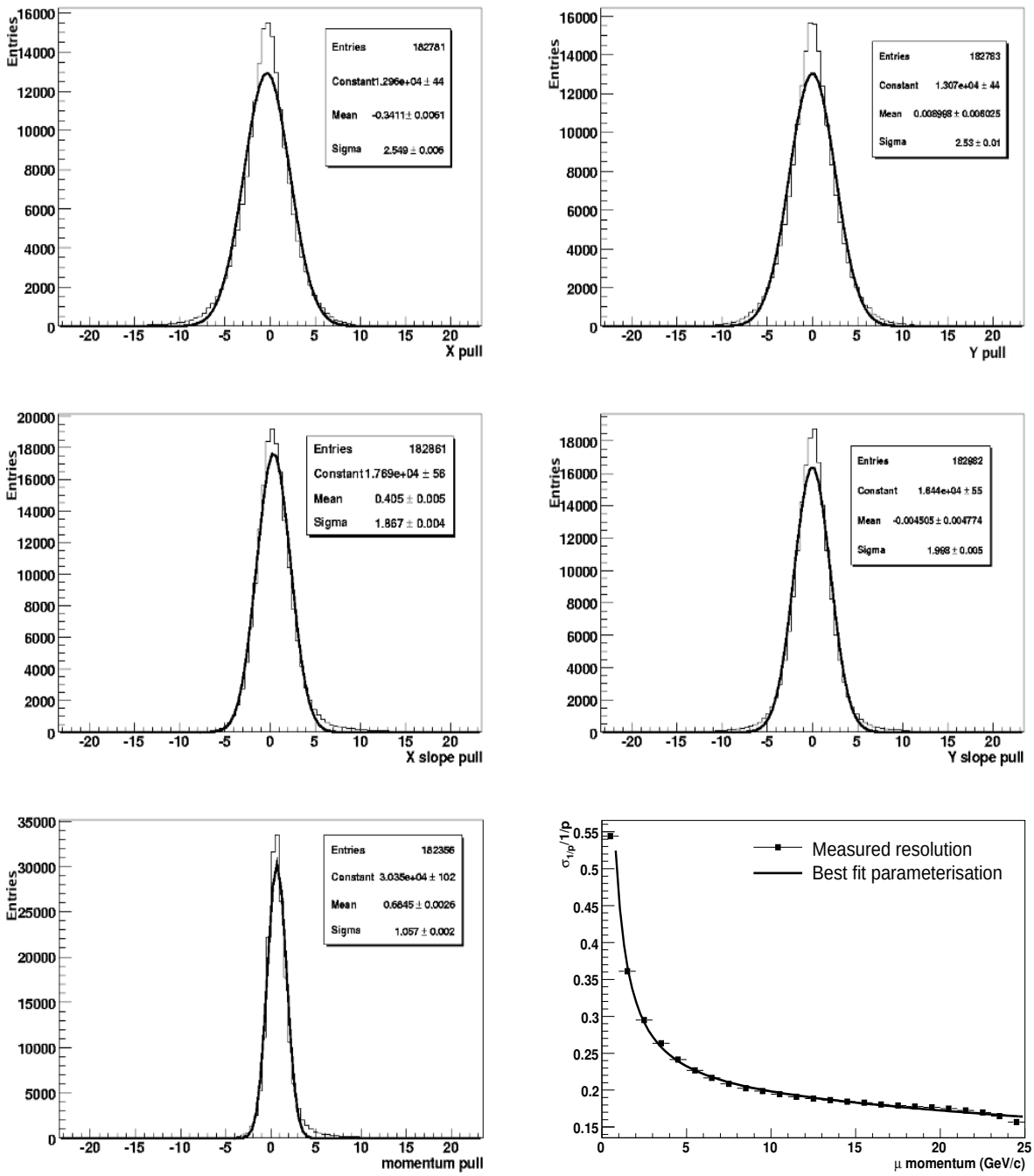

Figure 81. Pulls on the five Kalman filter vector parameters and the reconstructed momentum resolution: (top) X (left) and Y (right) position, (middle) X (left) and Y (right) slopes and (bottom) momentum pull (left) and momentum resolution (right).

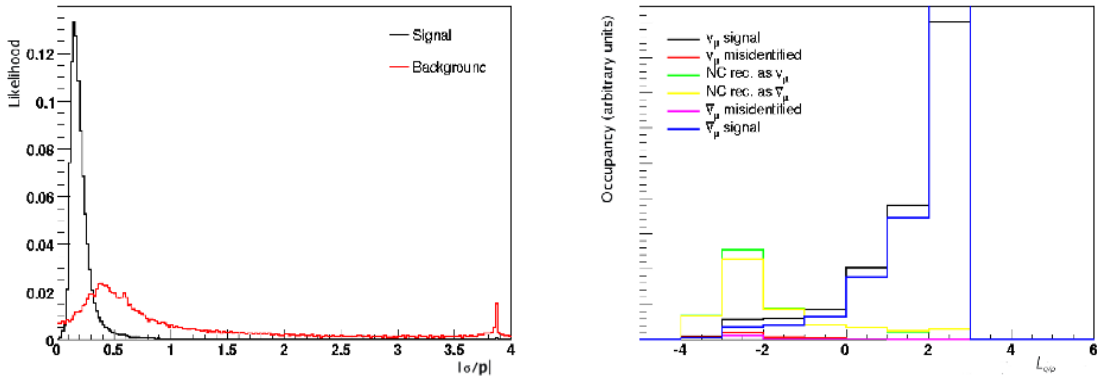

Figure 82. PDF of $\frac{\sigma_{q/p}}{q/p}$ (left) and the resulting log likelihood distribution ($\mathcal{L}_{q/p}$) for a test statistic (right).

q/p relative error

The error on the momentum parameter (charge divided by momentum, q/p) of the Kalman filter is a powerful handle in the rejection of background. The likelihood distributions for the combination of the two signals and of the neutral current and charged-current backgrounds (re-normalising in the latter case to take account of the different data-set sizes) are used to assess events as signal or background (shown in figure 82-left). Signal events are selected as those with a log-likelihood parameter $\mathcal{L}_{q/p} > -0.5$. As can be seen from figure 82-right this cut-level effectively rejects much of the background.

Neutral current rejection

Rejection of neutral current events is most efficiently performed using a likelihood analysis of trajectory quantities, as was carried out in MINOS. The three parameters used by MINOS were: number of hits in the candidate, fraction of the total visible energy in the candidate and the mean deposit per plane of the candidate. No improved background rejection was observed by using the latter two parameters, probably due to correlations between them. Only the number of hits, l_{hit}, was used to generate particle distribution functions (PDFs) for charged and neutral current events (see figure 83). Candidates with greater than 150 clusters are considered signal and for those with less than or equal 150 clusters, a log likelihood rejection parameter:

$$\mathcal{L}_1 = \log\left(\frac{l_{hit}^{CC}}{l_{hit}^{NC}}\right) ; \tag{28}$$

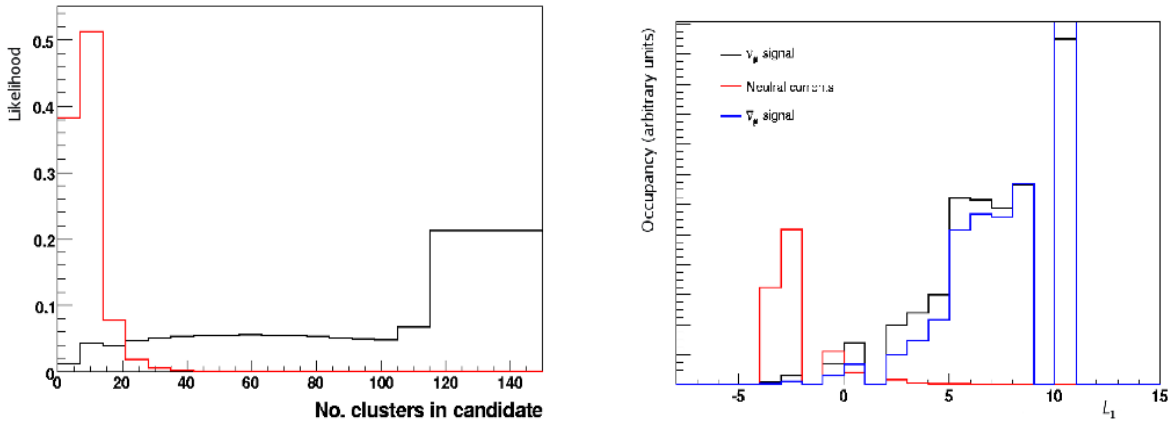

Figure 83. Number of clusters likelihood distribution function (left) and log-likelihood ratio (right) used to reject NC background. CC in black and NC in red.

is used, which is also shown in figure 83. Allowing only those candidates where the log parameter is $\mathcal{L}_1 > 1.0$ to remain in the sample ensures that the sample is pure.

Kinematic cuts

Kinematic cuts based on the momentum and isolation of the candidate, as related to the reconstructed energy of the event E_{rec}, can be used to reduce backgrounds from decays. The main isolation variable is defined as $Q_t = p_\mu \sin^2\theta$, where θ is the angle between the muon candidate and the hadronic-jet vector. Cuts based on these variables are an effective way to reduce all of the relevant beam related backgrounds:

$$E_{rec} \leq 5 \text{ GeV or } Q_t > 0.25 \text{ GeV/c}\,; \text{and} \tag{29}$$

$$E_{rec} \leq 7 \text{ GeV or } p_\mu \geq 0.3 \cdot E_{rec}\,. \tag{30}$$

The distributions after the application of the preceding cuts are those shown in figure 84.

The acceptance level is described in equations 29 and 30. With the exception of those events for which the energy is reconstructed using the quasi-elastic formula and hence do not have a hadronic shower the separation of which can be calculated, events are subject to the Q_t cut if their reconstructed energy is greater than 5 GeV. Those events fulfilling the condition of equation 29 and those reconstructed using the quasi-elastic formula are then subject to the second cut if they have $E_{rec} > 7$ GeV. All remaining events which fulfil the conditions of equation 30 (those above and to the left of the red lines in figure 84) are kept in the data set for the next series of cuts.

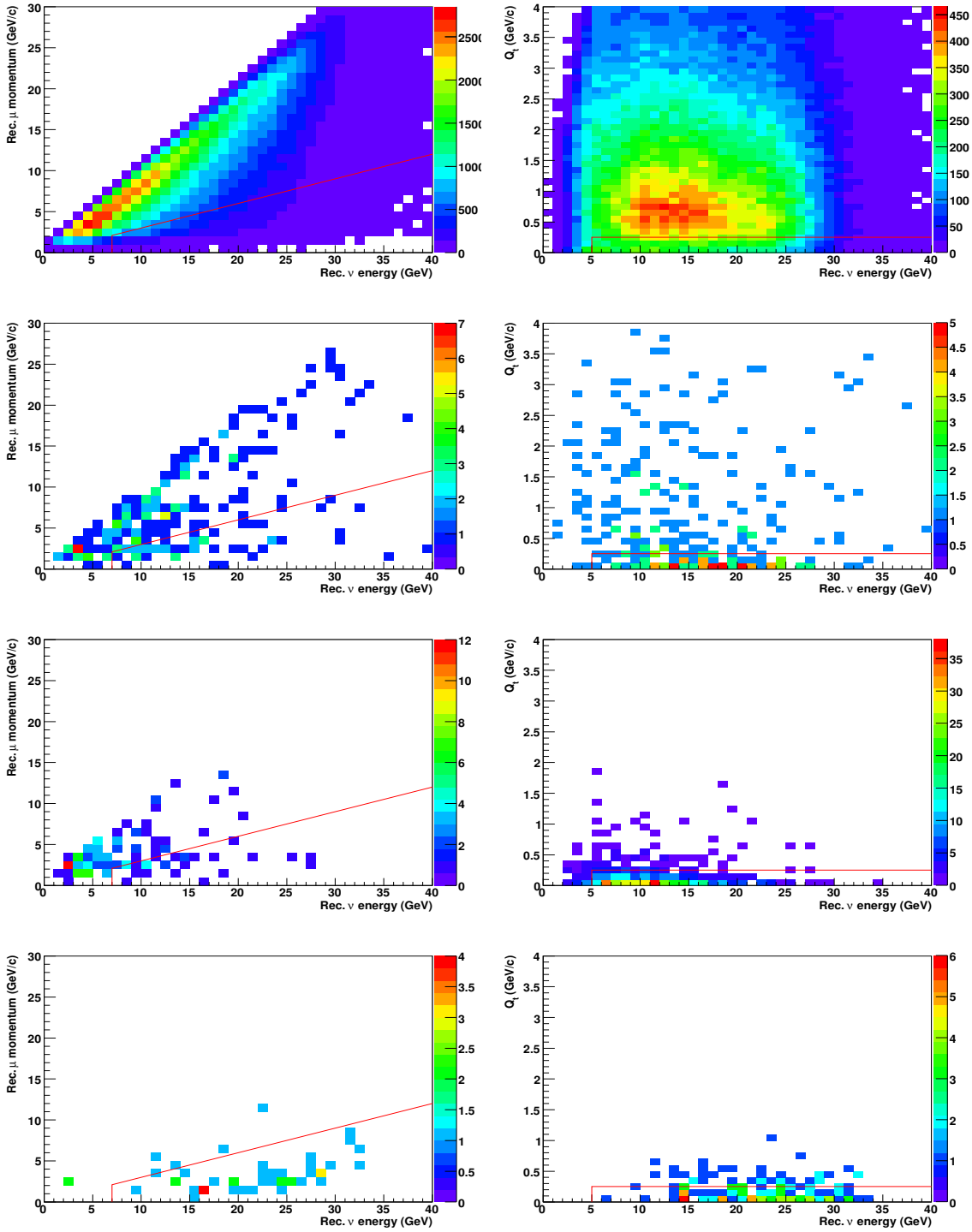

Figure 84. Distributions of kinematic variables: (left) Reconstructed muon momentum with reconstructed neutrino energy for (top→bottom) ν_μ ($\overline{\nu}_\mu$) signal, ν_μ ($\overline{\nu}_\mu$) CC background, NC background, ν_e ($\overline{\nu}_e$) CC background and (right) Q_t variable (in the same order).

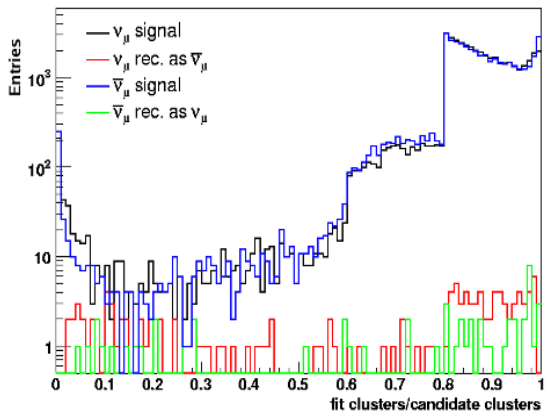

Figure 85. Distribution of the proportion of clusters fitted in the trajectory.

Additional quality cuts

A number of additional cuts have been developed to reduce the background from opposite sign ν_μ ($\overline{\nu}_\mu$) CC events at high neutrino energy. A set of new cuts in two categories are used: 1) Those related to the range in z, displacement in the bending plane, and reconstructed momentum of the candidate; and 2) a cut using the results of a re-fit of the remaining events to a quadratic.

Additionally, a fiducial cut requiring that the first cluster in a candidate be at least 2 m from the end of the detector is employed to reduce the misidentification of candidates originating at high z. Moreover, a high proportion of the misidentified candidates are not fully fitted. The distribution of the ratio of the candidate clusters which are fitted with respect to the total number of candidate clusters for signal and background is shown in figure 85. Accepting only those events with a candidate with 60% of its clusters fitted further reduces the background levels.

The momentum of the muon candidate can be badly reconstructed due to multiple scattering, badly assigned hits, and other effects. These badly reconstructed events contribute significantly to the overall background. In order to reduce this effect, three separate, but related cuts are employed. Firstly, a maximum reconstructed momentum, due to the finite resolution of the detector, is enforced at 40 GeV. Plotting the reconstructed momentum against the displacement in the longitudinal direction $dispZ$ of the candidate allows the candidate to be separated from the background (see figure 86). Additionally, the ratio between the lateral displacement in the bending plane $dispX$ and $dispZ$ against the number of hits in the candidate (see figure 86) provides further separation. The background events tend to be concentrated at low relative displacement and low number of hits. Events are accepted if they meet the conditions described in equation 31 and illustrated by the red lines in figure 86:

$$\frac{dispX}{dispZ} > 0.18 - 0.0026 \cdot N_h \,; \text{and} \tag{31}$$

$$dispZ > 6000 \text{ mm} \quad \text{or} \quad p_\mu \leq 3 \cdot dispZ \,; \tag{32}$$

where N_h is the number of clusters in the candidate, $dispZ$ is in units of mm, and p_μ in units of

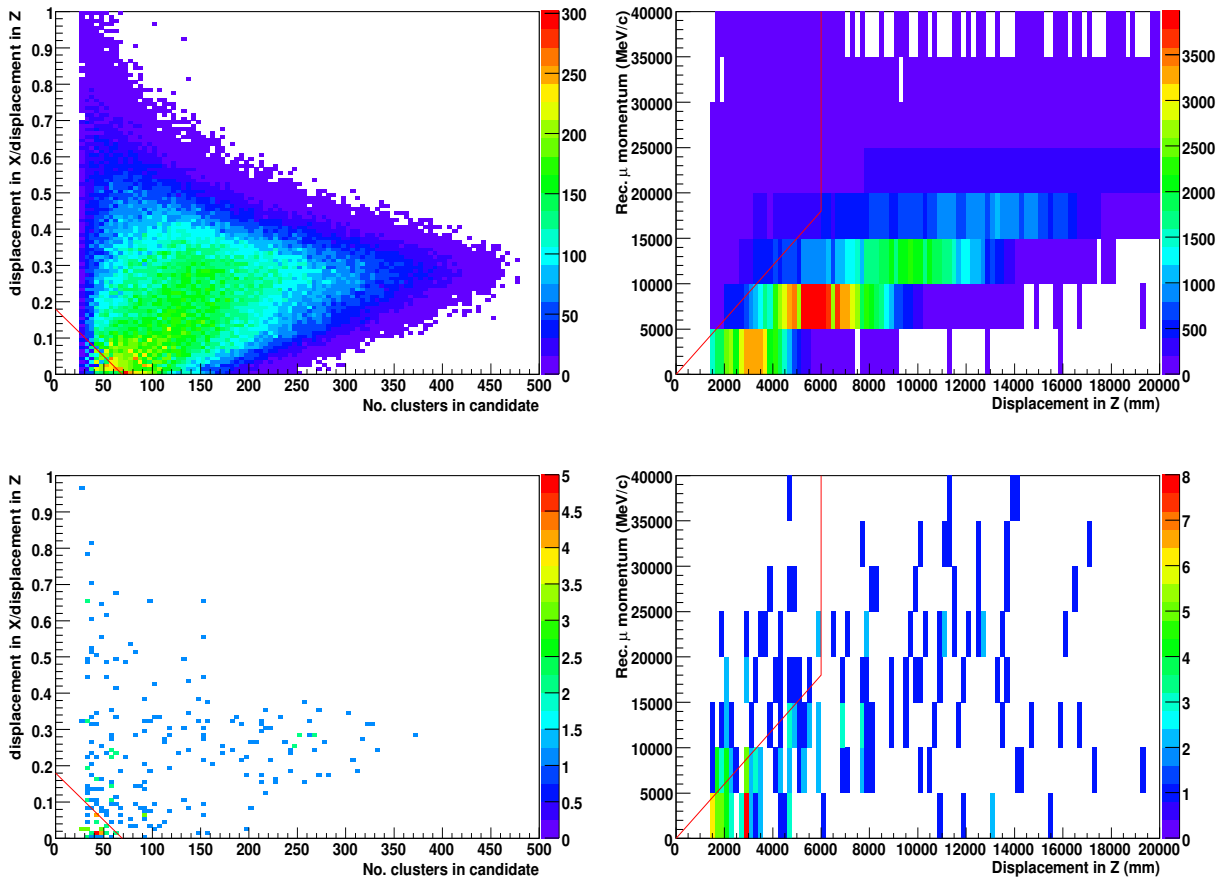

Figure 86. Distributions of momentum and displacement with cut levels: (top left) relative displacement in the bending plane to the z direction against candidate hits for signal events, (top right) reconstructed momentum against displacement in z for signal events and (bottom) as top for ν_μ ($\overline{\nu}_\mu$) CC backgrounds.

MeV/c.

The final cut involves fitting the candidate's projection onto the bending plane to a parabola. If the charge fitted is opposite to that found by the Kalman filter (in the current simulation a negatively-charged muon bends upwards so that for a parabola defined as $a + bz + cz^2$ the parameter c would be positive and the charge of the muon is $Q_{par} = -sign(c)$) the quality of the fit is assessed using the variable:

$$qp_{par} = \begin{cases} \left|\frac{\sigma_c}{c}\right|, \text{ if } Q_{par} = Q_{kal}\,; \\ -\left|\frac{\sigma_c}{c}\right|, \text{ if } Q_{par} = -Q_{kal}\,; \end{cases} \tag{33}$$

where Q_{kal} is the charge fitted by the Kalman filter fit. Defining the parameter in this way ensures that the cut is independent of the initial fitted charge. There are two types of events that are accepted:

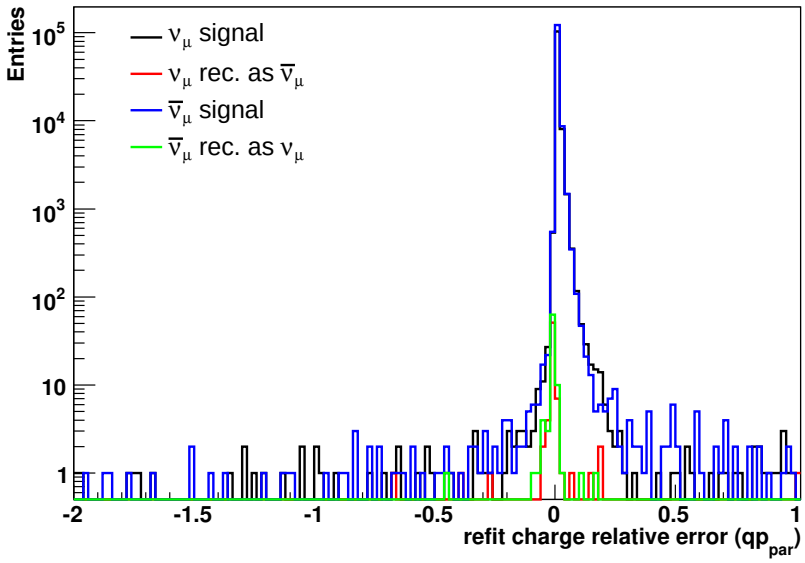

Figure 87. Distribution of the qp_{par} variable with the region where the parameter is < 0 representing those candidates fitted with charge opposite to the initial Kalman filter (region of highest occupancy shown).

those with $qp_{par} > 0.0$, in which there is no change in charge, and those candidates with $qp_{par} < -1.0$, in which there is a change in charge but the quality of the fit is poor, so the fit cannot be trusted. This qp_{par} cut effectively reduces the background level from CC mis-identification, as can be seen in figure 87.

Cut summary

In summary, the test statistic leads to the chain of cuts described above and in table XXXV. Application of this analysis and the resulting efficiencies and background suppression are described in the following section.

3.2.1.5. MIND response to the golden channel

Using a large data set of 3×10^6 events each of ν_μ CC, $\overline{\nu}_\mu$ CC, ν_e CC, $\overline{\nu}_e$ CC and 7×10^6 NC interactions from neutrinos and anti-neutrinos generated using NUANCE and tracked through the GEANT4 representation of MIND, the expected efficiency and background suppression for the reconstruction and analysis of the golden-channel appearance for both polarities of stored muons has been carried out. In addition, an estimate of the likely systematic error of the analysis has been made.

Table XXXV. Summary of cuts applied to select the golden channel appearance signals. The level of absolute efficiency and the main background level (with the dominant neutrino species) after each cut are also shown.

Cut	**Acceptance level**	**Eff. after cut**		**Main back** ($\times 10^{-3}$)	
		ν_μ	$\overline{\nu}_\mu$	ν_μ	$\overline{\nu}_\mu$
Fiducial	$z1 \leq 18000$ mm where *z1* is the lowest z cluster in the candidate	0.85	0.91	$120(\nu_e)$	$100(\overline{\nu}_e)$
Track quality	$\mathcal{L}_{q/p} > -0.5$	0.76	0.85	$20(\nu_e)$	$20(\overline{\nu}_e)$
Max. momentum	$P_\mu \leq 40$ GeV	0.76	0.84	$20(\nu_e)$	$20(\overline{\nu}_e)$
CC selection	$\mathcal{L}_1 > 1.0$	0.74	0.83	$0.49(\nu_e)$	$1.6(\nu_\mu)$
Fitted proportion	$N_{fit}/N_h \geq 0.6$	0.73	0.83	$0.46(\nu_e)$	$1.2(\nu_\mu)$
Kinematic	$E_{rec} \leq 5\ GeV$ or $Q_t > 0.25$ $E_{rec} \leq 7\ GeV$ or $P_\mu \geq 0.3E_{rec}$	0.63	0.77	$0.65(\overline{\nu}_\mu)$	$0.59(\nu_\mu)$
Displacement	$dispX/dispZ > 0.18 - 0.0026N_h$ $dispZ > 6000\ mm$ or $P_\mu \leq 3dispZ$	0.59	0.72	$0.38(\overline{\nu}_\mu)$	$0.38(\nu_\mu)$
Quadratic fit	$qp_{par} < -1.0$ or $qp_{par} > 0.0$	0.58	0.71	$0.07(\overline{\nu}_\mu)$	$0.07(\nu_\mu)$

Analysis efficiency

The resultant efficiencies for both polarities and the corresponding background levels expected for the appearance channels are summarised in Figs. 88 – 91. Numeric response matrices for each of the channels may be found in Appendix H. As can be seen in figure 88, the expected level of background from CC misidentification is significantly below 10^{-3} at all energies for the new simulation and re-optimised analysis.

The background from neutral current interactions also lies at or below the 10^{-4} level, with the high-energy region exhibiting a higher level than the low-energy region due to the dominance of DIS interactions because of increased visible energy and particle multiplicity. As expected, the NC background tends to be reconstructed at low energy due to the missing energy.

The background from ν_e ($\overline{\nu}_e$) CC interactions is once again expected to constitute a very low level addition to the observed signal. This background is particularly well suppressed due to the thickness of the iron plates and the tendency for the electron shower to overlap with any hadronic activity.

The efficiency of detection of the two ν_μ polarities was expected to have a threshold lower than that seen in previous studies due to the presence of non-DIS interactions in the data sample. The efficiencies expected for the current analysis are shown in figure 91.

Figure 92 shows a comparison of the resultant $\overline{\nu}_\mu$ efficiency with that extracted in previous studies. In the studies described in [102, 305, 320], the improvement in threshold with the development of the analysis and the introduction of the full spectrum of interactions is clear. The thresholds of the newest results, between 2 GeV and 3 GeV, correspond well with the expected saturation point of sensitivity to the extraction of the oscillation parameters. The inclusion of non-DIS events is responsible for reducing the threshold, manifested by comparing the black and blue curves (G4 efficiency) with the

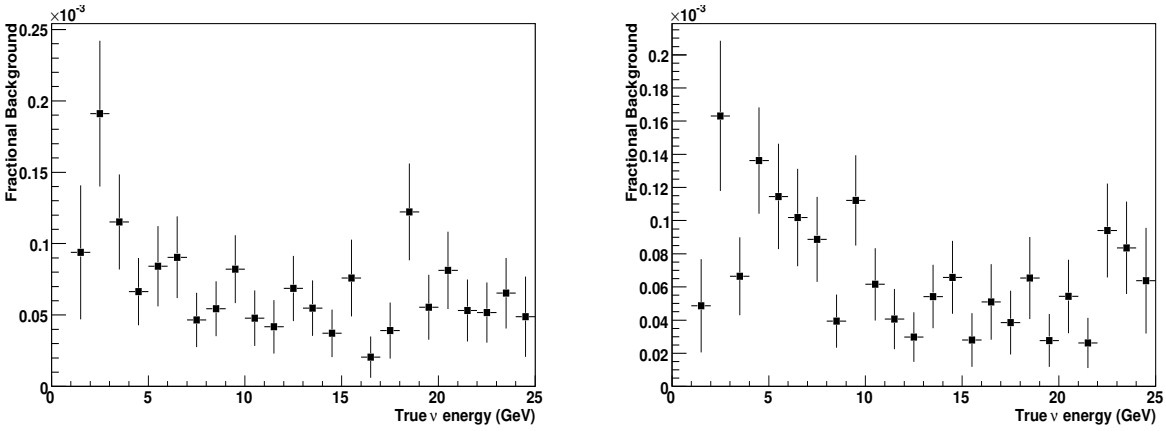

Figure 88. Background from mis-identification of ν_μ ($\overline{\nu}_\mu$) CC interactions as the opposite polarity. (left) $\overline{\nu}_\mu$ CC reconstructed as ν_μ CC, (right) ν_μ CC reconstructed as $\overline{\nu}_\mu$ CC as a function of true energy.

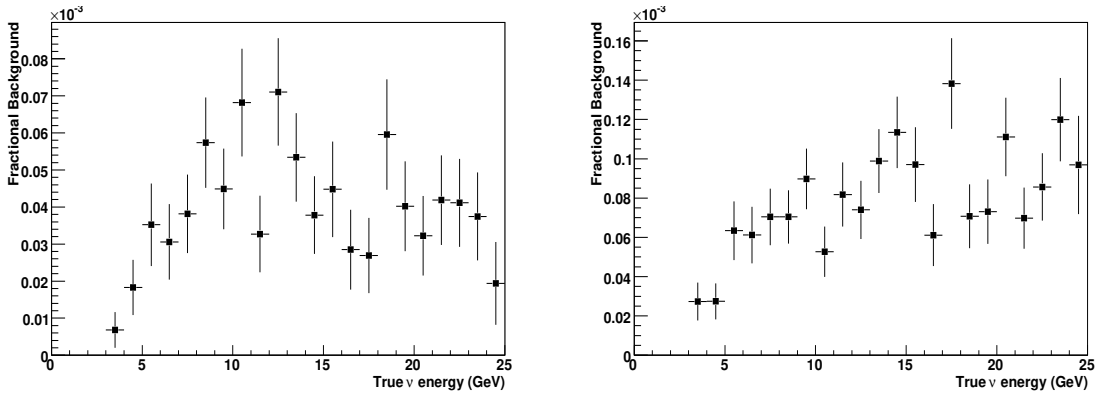

Figure 89. Background from mis-identification of NC interactions as ν_μ ($\overline{\nu}_\mu$) CC interactions. (left) NC reconstructed as ν_μ CC, (right) NC reconstructed as $\overline{\nu}_\mu$ CC. (top) as a function of true energy.

green curve (G3 efficiency) in figure 92 that only included DIS events.

The difference in efficiency between the two appearance channels is effectively described by the difference in the inelasticity of neutrino and anti-neutrino CC interactions. Neutrino DIS interactions with quarks have a flat distribution in the Bjorken variable:

$$y = \frac{E_\nu - E_l}{E_\nu}\,; \tag{34}$$

with E_l being the scattered-lepton energy. However, anti-neutrinos interacting with quarks follow a distribution $\propto\ (1-y)^2$ [321]. For this reason, neutrino interactions generally involve a greater energy

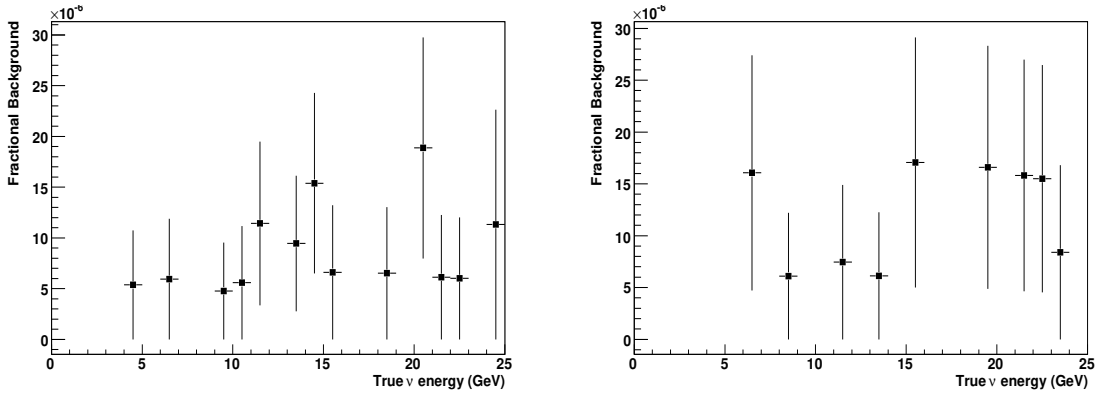

Figure 90. Background from mis-identification of ν_e ($\overline{\nu}_e$) CC interactions as ν_μ ($\overline{\nu}_\mu$) CC interactions. (left) ν_e CC reconstructed as ν_μ CC, (right) $\overline{\nu}_e$ CC reconstructed as $\overline{\nu}_\mu$ CC as a function of true energy.

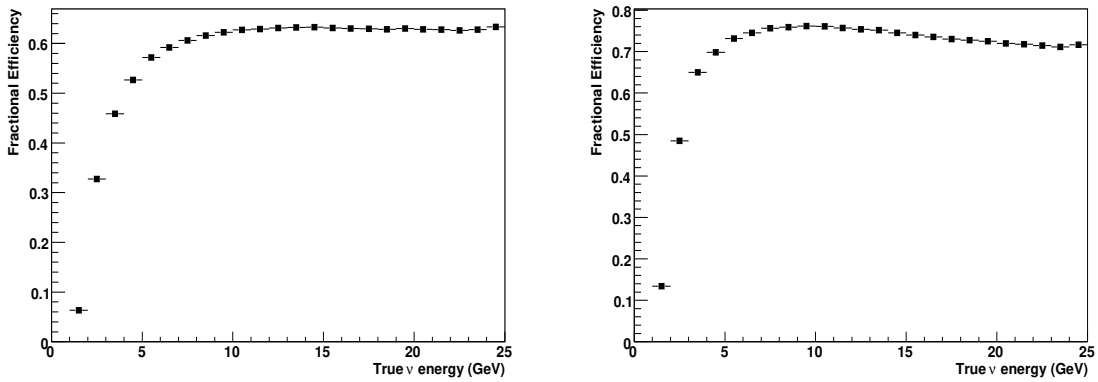

Figure 91. Efficiency of reconstruction of ν_μ ($\overline{\nu}_\mu$) CC interactions. (left) ν_μ CC efficiency, (right) $\overline{\nu}_\mu$ CC efficiency as a function of true energy.

transfer to the target. As can be seen from figure 93-(top left), the efficiencies for the two species, as a function of y after all cuts, are the same to within the uncertainties over the full y range. Hence, the difference in neutrino and anti-neutrino efficiencies, when translated into true neutrino-energy, can be explained by the greater abundance of neutrino events at high y. However, since the cross section for the interaction of neutrinos is approximately twice that for anti-neutrinos it is not expected that this reduced efficiency will affect the fit to the observed spectrum significantly.

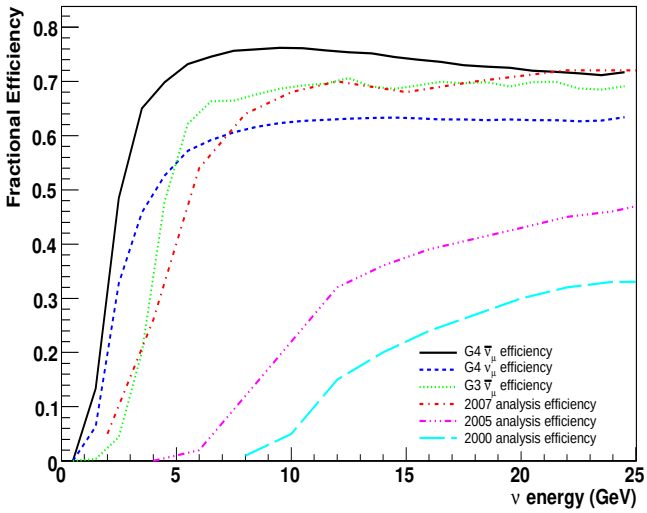

Figure 92. Evolution of the MIND $\overline{\nu}_\mu$ CC detection efficiency. For the 2000 analysis see [102], for 2005 see [320] and for 2007 see [305].

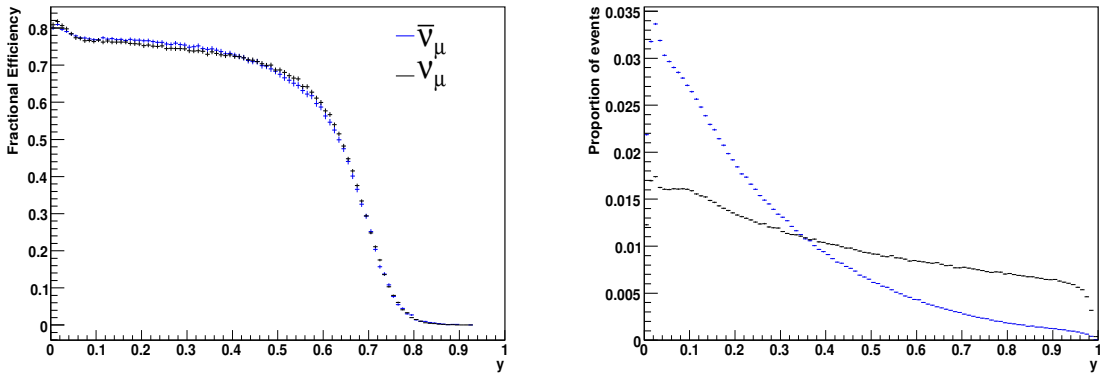

Figure 93. ν_μ CC and $\overline{\nu}_\mu$ CC signal detection efficiency as a function of y (left) and the normalised distribution of all events considered in each polarity as a function of y (right).

Study of systematic uncertainties

The efficiencies described above will be affected by several systematic effects. There will be many contributing factors including uncertainty in the determination of the parameters used to form the cuts in the analysis, uncertainty in the determination of the hadronic shower energy and direction resolution, uncertainty in the relative proportions of the different interaction types and any assump-

tions in the representation of the detector and electronics. While exact determination of the overall systematic error in the efficiencies is complicated, an estimate of the contribution of different factors can be obtained by setting certain variables to the extremes of their errors.

Since the neutrino energy is reconstructed generally from the sum of the hadron shower and primary muon energies, and this reconstructed quantity is used in the kinematic cuts, uncertainty in the energy and direction resolution of the detector could contribute significantly to the systematic error in the efficiencies. Taking a 6% error as quoted for the energy scale uncertainty assumed by the MINOS collaboration [318] and varying the constants of the energy and direction smears by this amount, it can be seen (figure 94) that, to this level, the hadronic resolutions have little effect on the true neutrino-energy efficiencies. However, the hadronic direction resolution is likely to have far greater uncertainty and would be very sensitive to noise in the electronics. Also shown in figure 94 are the efficiencies when the hadronic energy resolution parameters are 6% larger but with a 50% increase in the angular resolution parameters. Even at this level the observed difference in efficiency is only at the level of 1%.

The relative proportions of QE, DIS and other types of interaction in the data sample could have a significant effect on the signal efficiencies and backgrounds. The change in efficiency if the data sample were purely DIS is shown in figure 95. Although experimental data are available confirming the presence of non-DIS interactions in the energy region of interest, there are significant errors in the transition regions (see for example [322, 323]). These errors lead to an uncertainty in the proportion of the different types of interaction that can affect the efficiencies. In order to study the systematic error associated with this effect, many runs over the data-set were performed using different random seeds to exclude events of a particular type from the data-set or alternatively to exclude an equivalent proportion of the "rest". As an illustration of the method, consider the contribution from QE interactions. Taking the binned errors on the cross-section measurements from [322, 323], a run to reduce the QE content would exclude a proportion of events in a bin so that instead of contributing a proportion:

$$\frac{N_{QE}}{N_{tot}}\,; \tag{35}$$

where N_{QE} is the total number of QE interactions in the bin of interest and N_{tot} is the total number of interactions in the bin, it would instead contribute:

$$\frac{N_{QE} - \sigma_{QE} N_{QE}}{N_{tot} - \sigma_{QE} N_{QE}}\,; \tag{36}$$

where σ_{QE} is the proportional error on the QE cross section for the bin. The equivalent run to increase the QE contribution reduces the contribution of the "rest" by an amount calculated to give the corresponding proportional increase in QE interactions:

$$\frac{N_{QE} + \sigma_{QE} N_{QE}}{N_{tot} + \sigma_{QE} N_{QE}} = \frac{N_{QE}}{N_{tot} - \epsilon N_{rest}}\,; \tag{37}$$

where N_{rest} is the total number of non-QE interactions in the bin and ϵ is the required proportional reduction in the 'rest'. Solving for ϵ yields the required reduction:

$$\epsilon = \frac{\sigma_{QE}}{1 + \sigma_{QE}}\,. \tag{38}$$

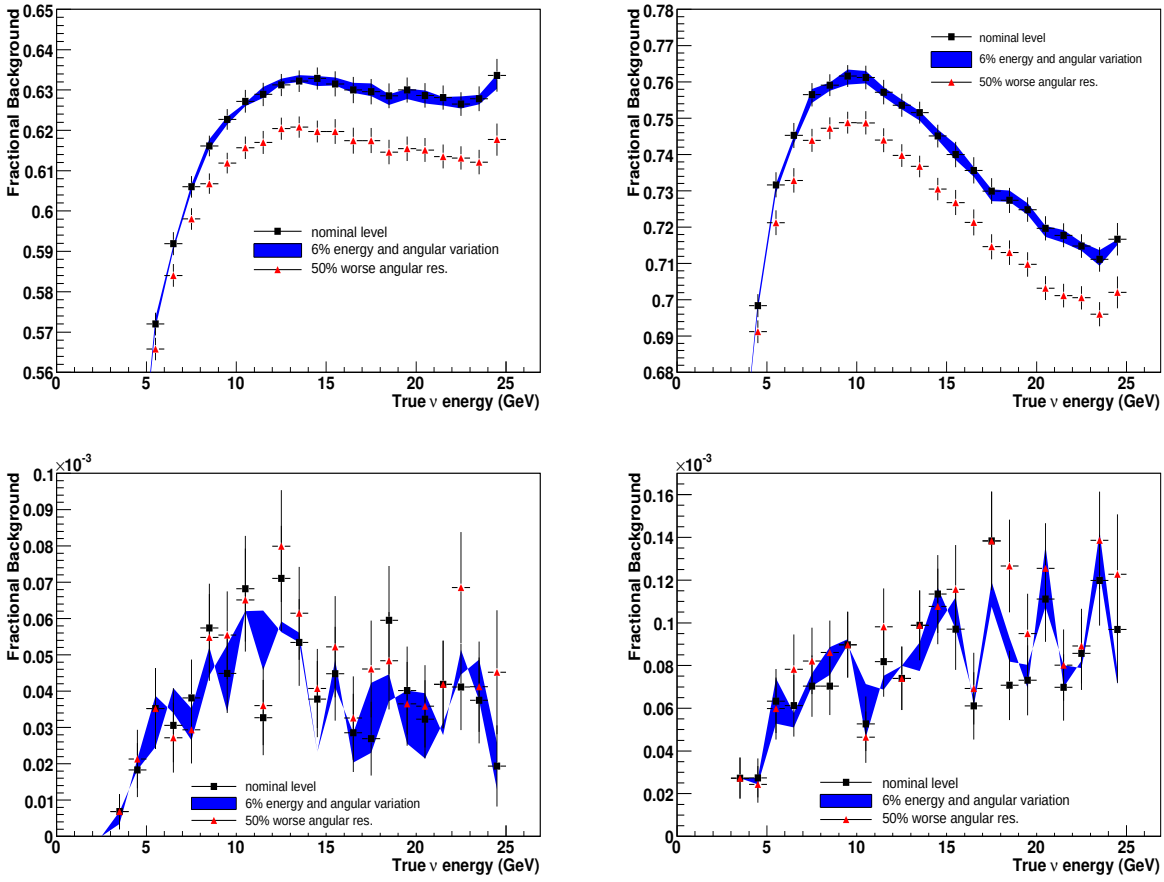

Figure 94. Variation of signal efficiency (top) and NC backgrounds (bottom) due to a 6% variation in the hadron shower energy and direction resolution and a more pessimistic 50% reduction in angular resolution (focused on region of greatest variation).

Sampling randomly and repeating runs ensures that any observed change in efficiency is not solely due to the particular events excluded. The 1σ systematic error can be estimated as the mean difference between the nominal efficiency and the increase due to a higher QE proportion or decrease due to exclusion. The errors in the true ν_μ and $\overline{\nu}_\mu$ efficiencies extracted using this method to vary the contribution of QE, single pion (1π) and other non-DIS interactions are shown in figure 96. Errors for 1π resonant reactions are estimated to be $\sim$20% below 5 GeV (as measured by the K2K near detector [324]) and at 30% above. Due to the large uncertainty, both theoretically and experimentally, on the models describing other resonances, coherent, diffractive and elastic processes, a very conservative error of 50% is taken when varying the contribution of the "others". As can be seen, the systematic effect is at the level of 1% in the efficiency threshold region with increased QE and 1π interactions generally increasing the efficiency and increased contribution of the "other" interactions having the possibility to decrease efficiency. This last effect is likely to be predominantly due to resonances producing multiple tracks. The effect on backgrounds, while expected to be minimal, has not yet been

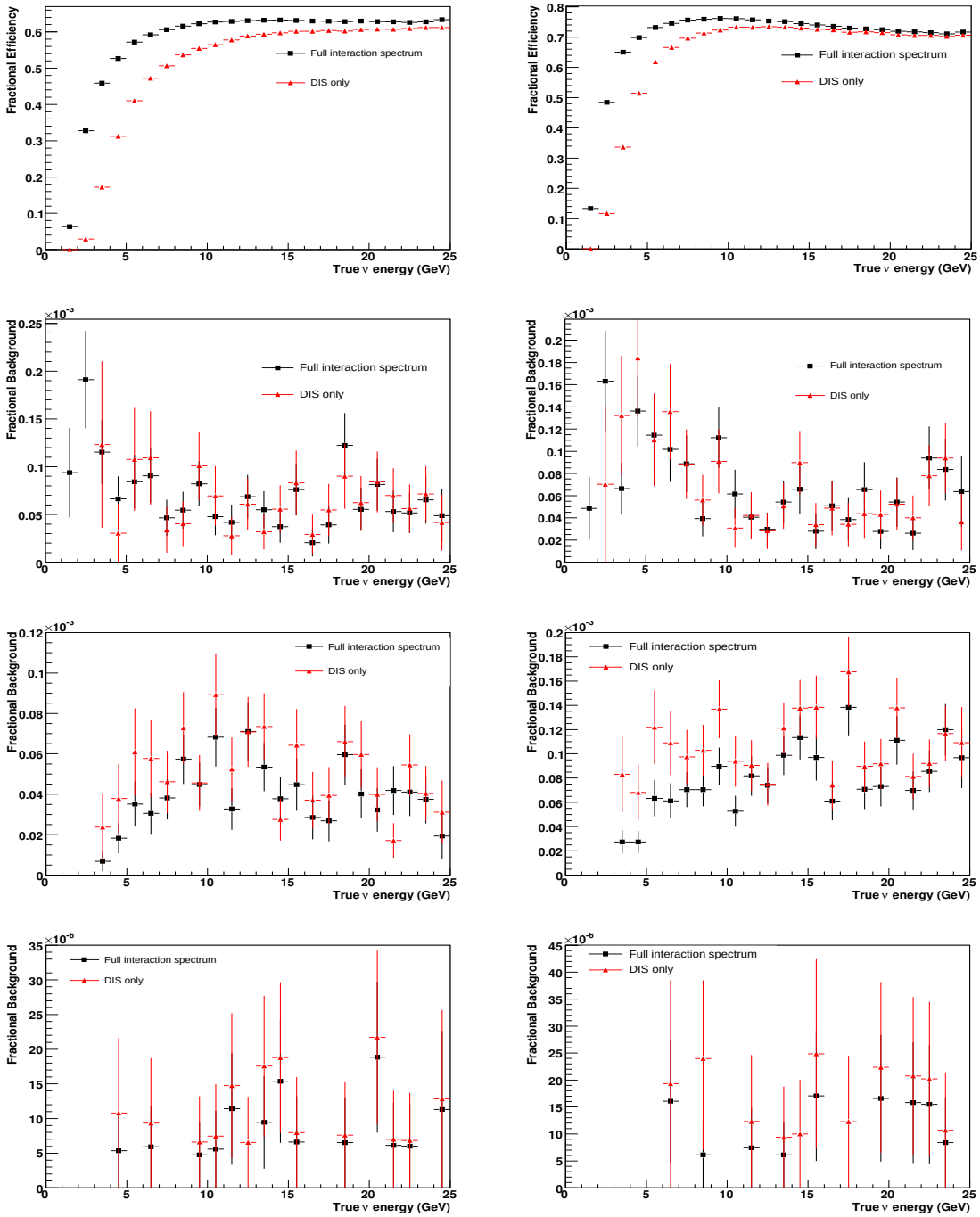

Figure 95. Efficiencies for a pure DIS sample compared to the nominal case. (top) Signal efficiency, (second line) ν_μ ($\overline{\nu}_\mu$) CC background, (third line) NC background and (bottom) ν_e ($\overline{\nu}_e$) CC background. ν_μ appearance on the left and $\overline{\nu}_\mu$ appearance on the right.

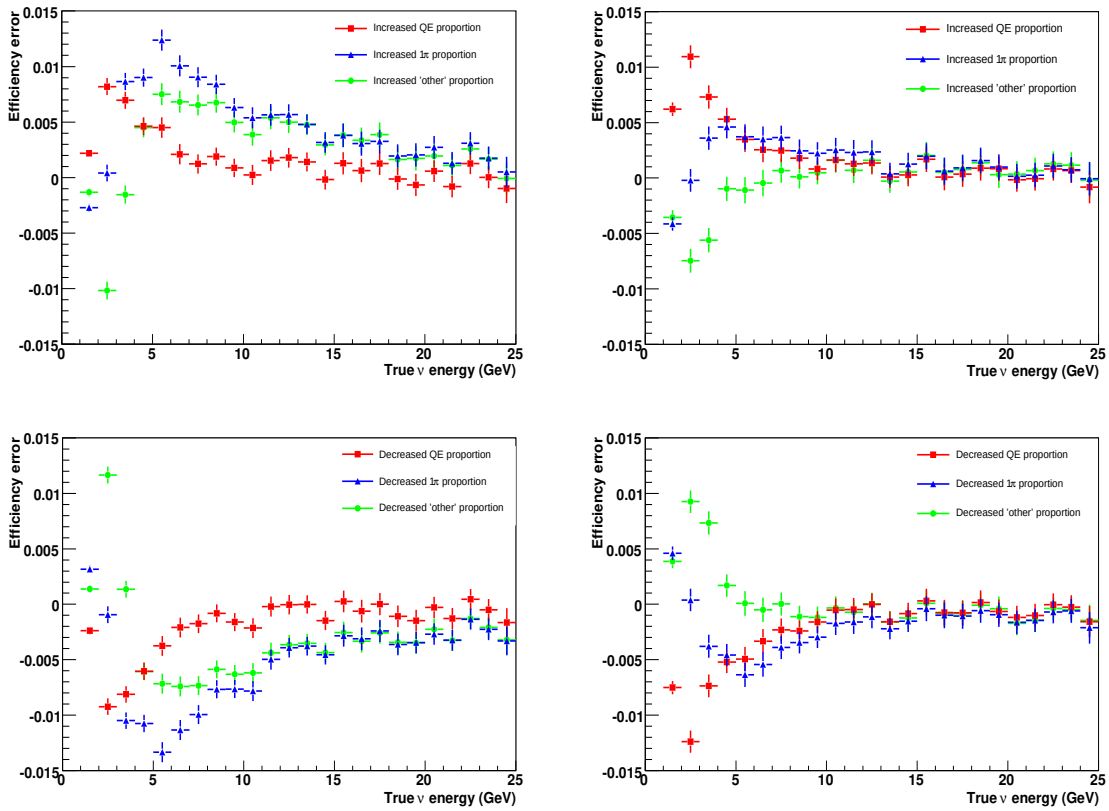

Figure 96. Calculated error on signal efficiencies on increasing (top) and decreasing (bottom) the proportion of non-DIS interactions in the data-set. (left) Errors on true energy ν_μ CC efficiency and (right) errors on true energy $\overline{\nu}_\mu$ CC efficiency

studied due to the statistical limitations in the data sample, making any calculation using this method unreliable.

3.2.2. MIND conceptual design

The Magnetised Iron Neutrino Detector (MIND) is an iron and scintillator sampling calorimeter which is essentially a larger version of the MINOS detector [325]. We have chosen a cross section of 14 m × 14 m in order to maximise the ratio of the fiducial mass to the total mass. The magnetic field will be toroidal as in MINOS and MIND will also use extruded scintillator for the readout material. Details on the iron plates, magnetisation, scintillator, photo-detector and electronics are given below.

3.2.2.1. Iron plates

For the iron plates in MIND, we are following the design strategy that was used for MINOS. The plates are octagons with overall dimension of 14 m × 14 m and 3.0 cm thick. They are fabricated from strips that are 1.5 cm thick, 2 m (or 3 m) wide and up to 14 m long. Two layers of crossed strips are plug welded together to form the full plate. MINOS used 2 m wide strips and we know that fabrication of iron components of this width and with lengths of up to 14 m is possible. Depending on the final plate fabricator, strip widths greater than 2 m are likely to be possible, so both 2 m and 3 m strip-width models were investigated. Initially it was thought that the much larger weight of the MIND plates (40 T versus 10 T for MINOS) would preclude the concept of hanging the plates on a rail system due to excessive stress in the ears. However, our analysis of the expected stress (see section 3.2.2.2 below) has shown that this is not the case. Essentially, no R&D on the MIND iron plates is needed. Final specification of the plate mosaic structure will be determined once a plate fabricator is chosen.

For the 2 m strip model, seven 2 m strips will be required to make up a whole layer. The layout of the top layer will be perpendicular to the bottom layer in each plane. For the 3 m strip model, the 14 m long strips will be both 3 m wide and 2 m wide. Four 3 m strips and one 2 m strip will be required to make up a whole layer. The layout of the top layer and the bottom layer remains perpendicular to one-another in each plane. The individual plates will be held together by plug welding the top layer to the bottom layer. Each ear of the plane is supported by a structural-steel rail which is in turn supported by structural-steel columns. The section of the MIND detector plane and the support structures are shown in figure 97 and figure 98.

A 'book-end' will be used to provide lateral support for the planes as the MIND detector is constructed. The plane will be attached to the book-end at the minimum of each vertex point in the octagon and each midpoint between the vertexes. This book-end will consist of a framework of structural-steel members and will be vertically supported by the floor slab and horizontally supported by the wall of the enclosure.

3.2.2.2. The finite-element model

Two finite-element models of the detector plane were created using higher order solid elements. The 2 m strip model is shown in figure 99 and the 3 m strip model is shown in figure 100. Loading was simulated by the gravity load of the plane. The plane was fixed at the bottom of the ears and the two top vertexes are fixed in the z direction to resist plane buckling. The linear buckling of the plane was also investigated. The total deformed shape of the 2 m strip plane is shown in figure 101. The directional deformations are shown in figures 102, 103 and 104 respectively. The maximum deflections occur at the ear and the bottom of the plane.

The stresses in the 2 m strip plane are shown in figure 105. The maximum von Mises stress is 6.8 ksi at the ear. In the regions away from that, all stresses are below the 12 ksi limit for AISI 1006 low carbon steel. The welded connections were examined by extracting nodal forces and moments from the 2 m strip plane model at 45 locations. The maximum load in the plane is in the ear area and is approximately 15 000 pounds per inch. In the linear buckling analysis of the 2 m strip plane, the

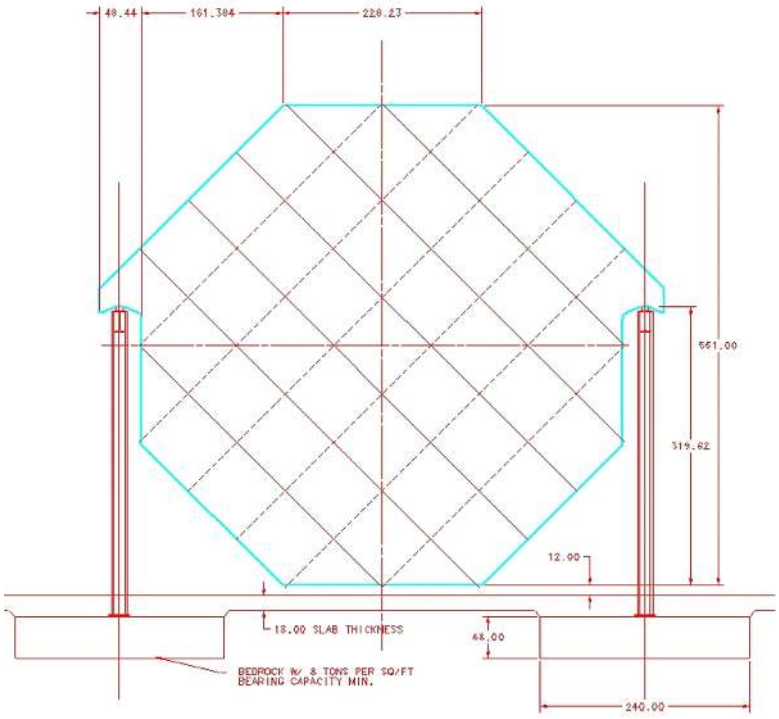

Figure 97. 2D diagram of MIND plate.

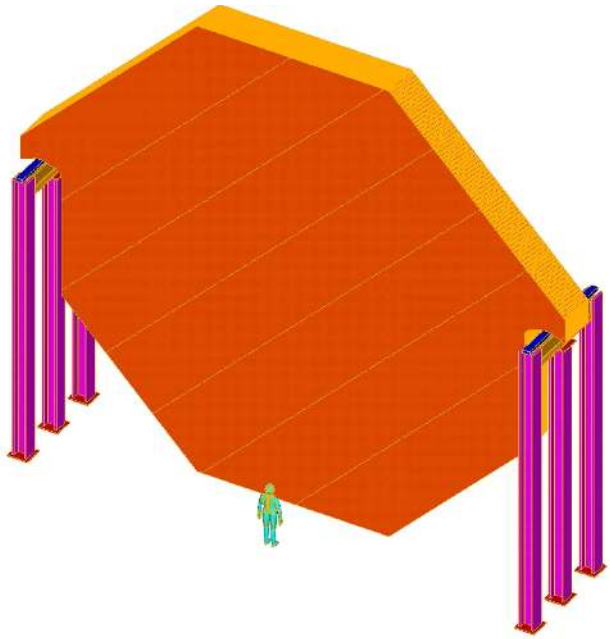

Figure 98. 3D diagram of MIND plate.

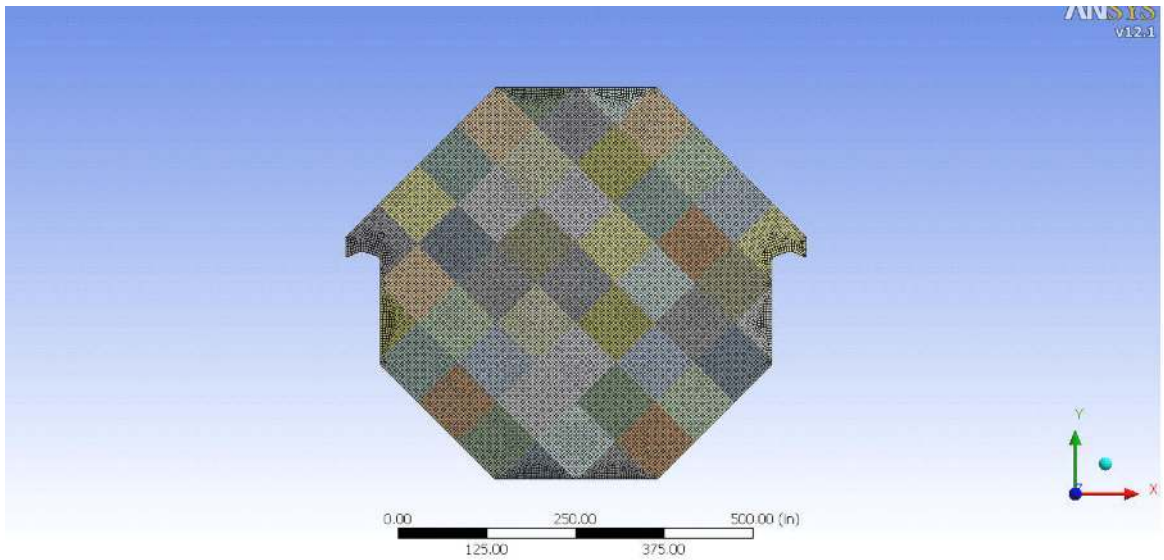

Figure 99. Finite-element model of plate with 2 m strips.

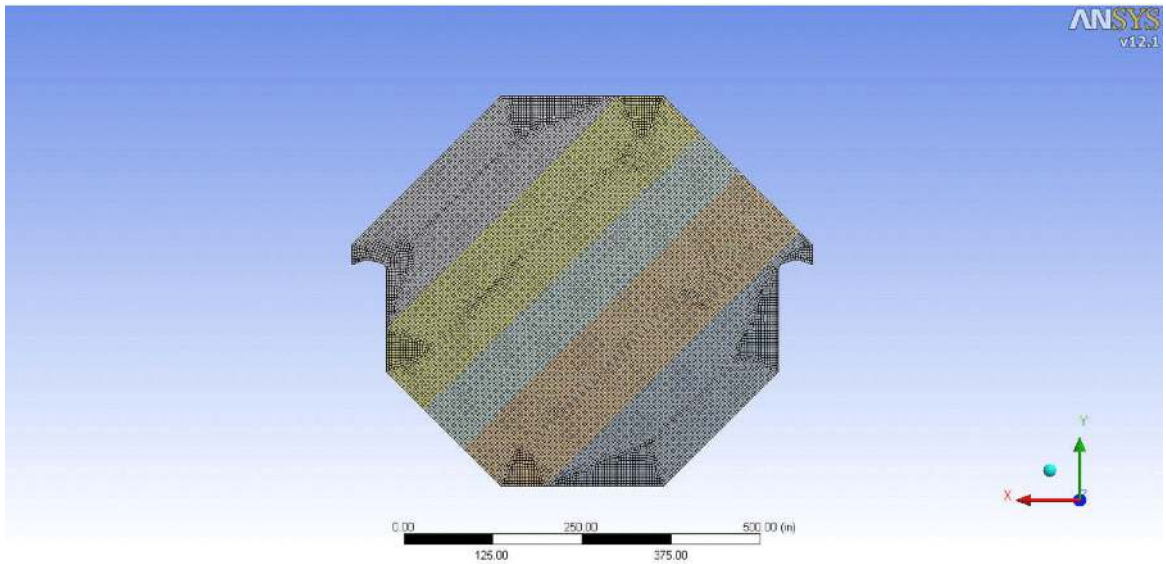

Figure 100. Finite-element model of plate that utilises both 3 m and 2 m strips.

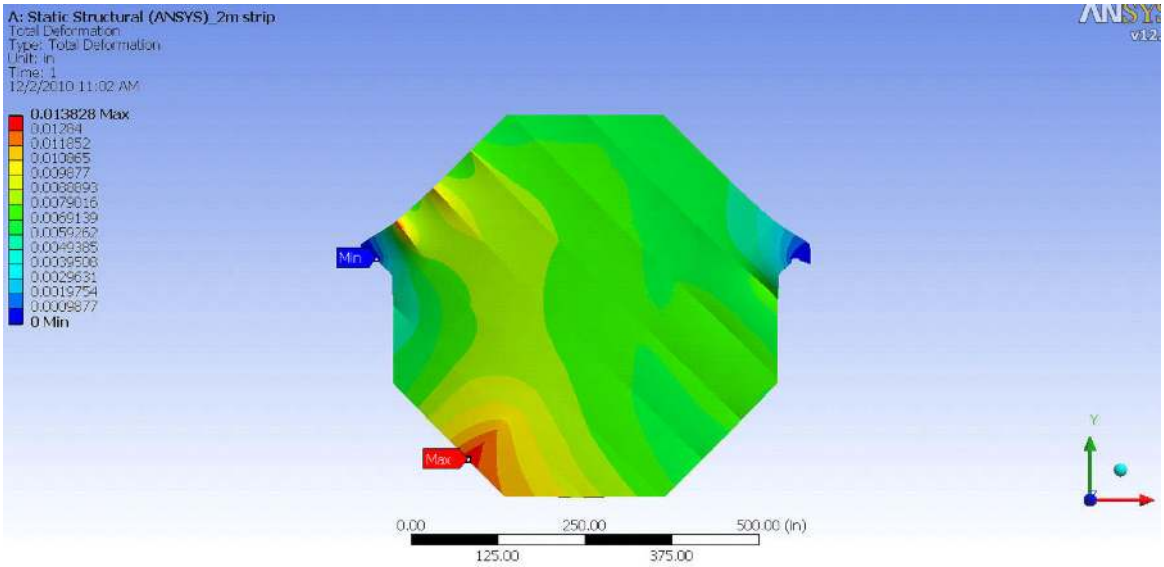

Figure 101. Total deformed shape of plate fabricated with 2 m strips

results show the first buckling mode has a load safety factor of 4.7.

For comparison, the total deformed shape of the 3 m strip plane is shown in figure 106. Again, the maximum deflections occur at the ear and the bottom of the plane. The stresses in the 3 m strip plane are shown in figure 107. The maximum von Mises stress is 22 ksi at the ear. In the regions away from the concentration, all stresses are below the 12 ksi limit for AISI 1006 low carbon steel. In the linear buckling analysis of the 3 m strip plane, the results show the first buckling mode has a load safety factor of 4.5, somewhat worse than in the case of the 2 m wide strip case.

3.2.2.3. Magnetisation

As mentioned above, MIND will have a toroidal magnetic field like that of MINOS. For excitation, however, we plan to use the concept of the superconducting transmission line (STL) developed for the Design Study for a staged Very Large Hadron Collider (VLHC) [326]. In order to obtain good field uniformity in a 14 m × 14 m plate, MIND requires a much larger excitation current-turn than the 15 kA-turn that is used in the MINOS room temperature Cu coils. 100 kA-turn is possible using the STL. The STL consists of a cylindrical superconducting braid inside a pipe cooled by super-critical helium. The superconductor and cryo-pipe are co-axial to a cylindrical cryostat/vacuum vessel, figure 108. Figure 108 shows the constructions details for the STL that was prototyped and tested for the VLHC study and consisted of: 1) a perforated Invar flow liner and support; 2) a copper stabiliser braid; 3) superconductor cable braid; 4) an Invar pipe that contains the helium; 5) the cold-pipe support; 6) cryo-shield; 7) super-insulation; and 8) the vacuum jacket/pipe.

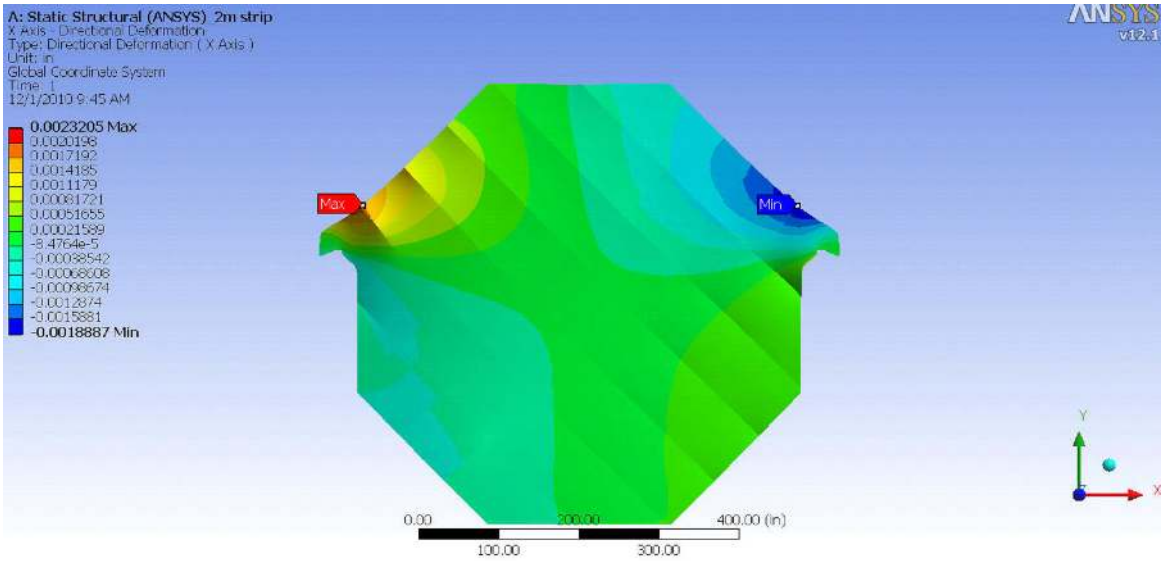

Figure 102. Deformation in x for plate using 2 m strips

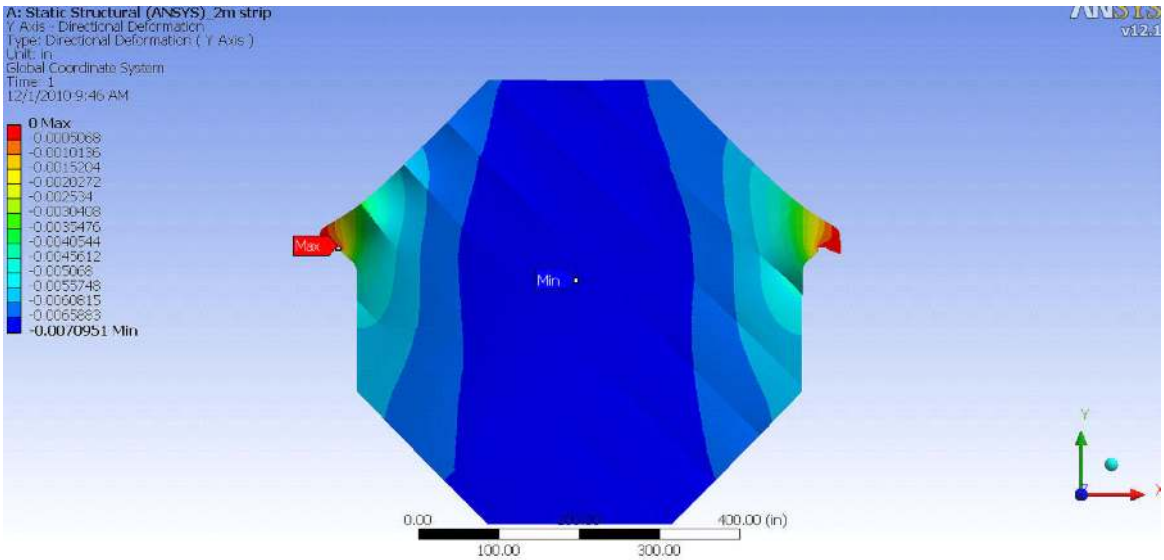

Figure 103. Deformation in y for plate using 2 m strips

Field Map

Using the MIND plate geometry shown in figure 97, a 2D magnetic analysis of the plate was performed. Figure 109 shows the model (1/8th) that was used in the analysis. A 100 cm diameter hole for the STL was assumed and the MINOS steel [318] BH curve was assumed. For this analysis, an excitation

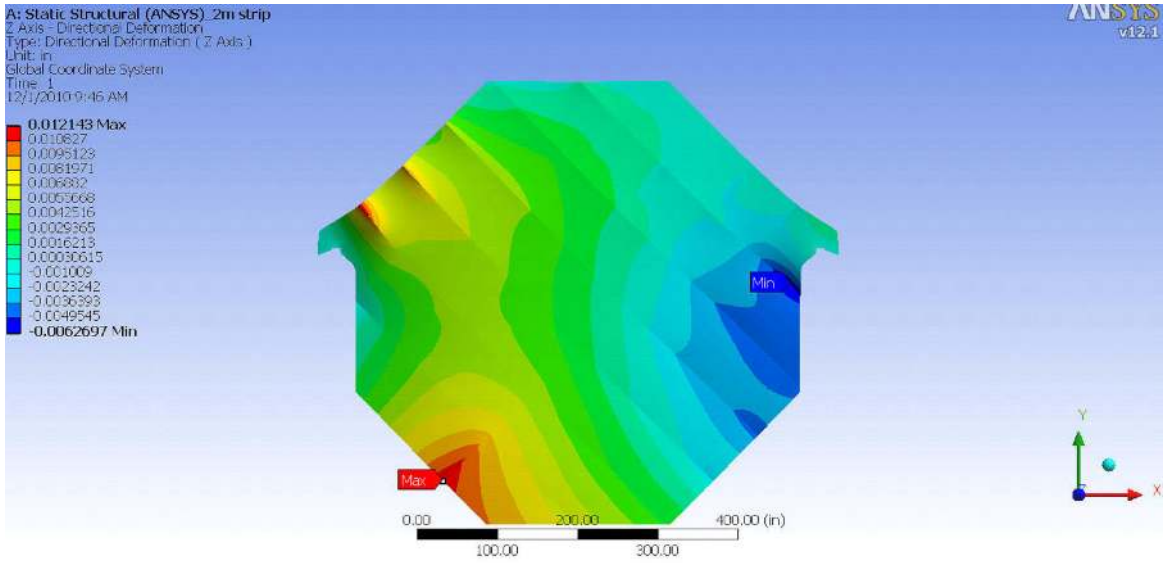

Figure 104. Deformation in z for plate using 2 m strips

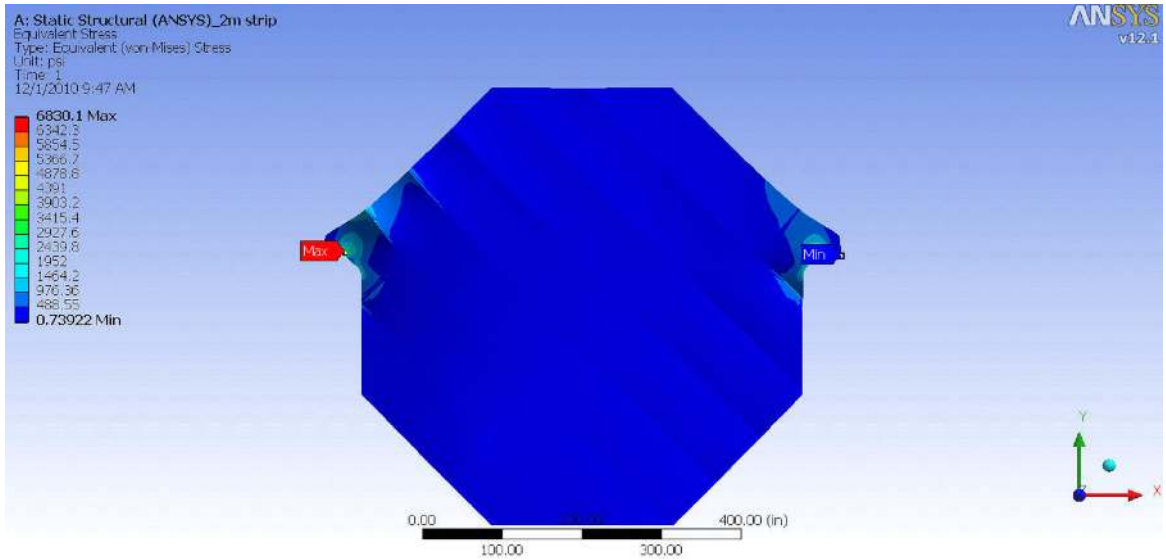

Figure 105. von Mises stress in plate using 2 m strips

current of 100 kA was used. This was the critical current achieved at 6.5 K in the STL test stand assembled for the VLHC proof-of-principle. In figure 110 we give the azimuthal B field along the two lines (A-B and A-C) shown in figure 109. Figure 111 gives the 2D contour lines of constant B.

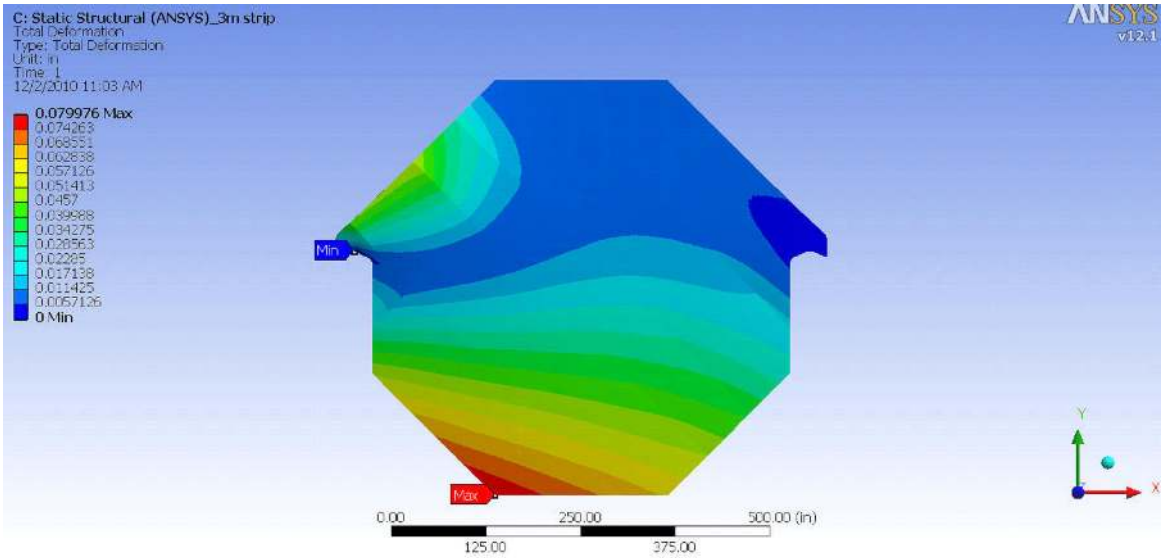

Figure 106. Total deformation for plate using 3 m and 2 m strips

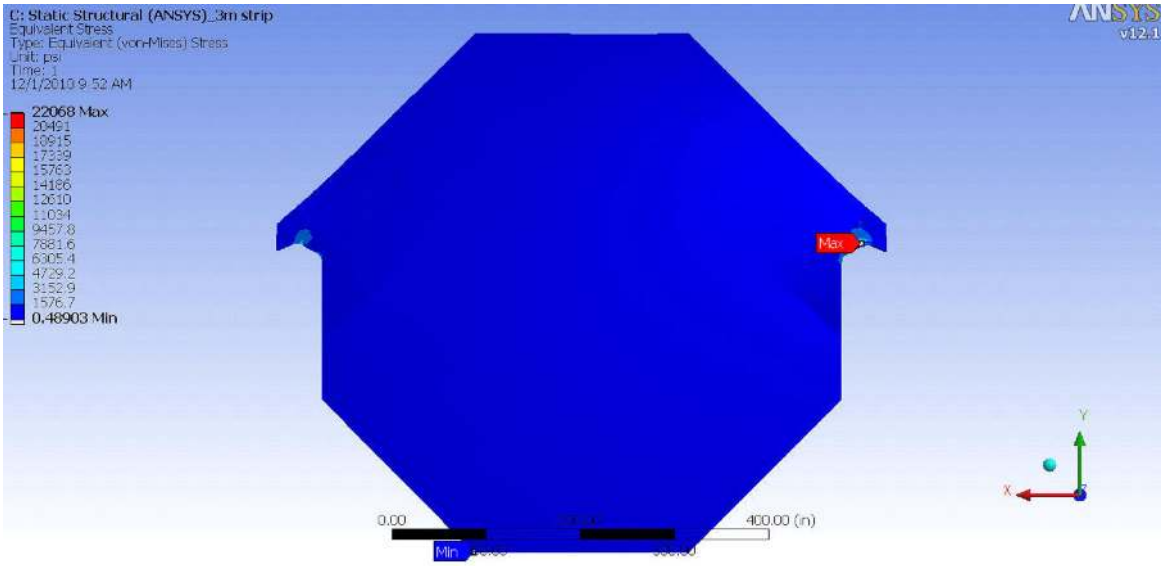

Figure 107. von Mises stress in plate using 3 m and 2 m strips

3.2.2.4. R&D Requirements

The STL described above was optimised for the 37 km radius of the VLHC. The loop length needed for MIND is quite a bit shorter than the 233 km needed for the VLHC. The optimised design of an STL for MIND is therefore likely to be different. The 2.5 cm He-flow region can most likely be reduced, for

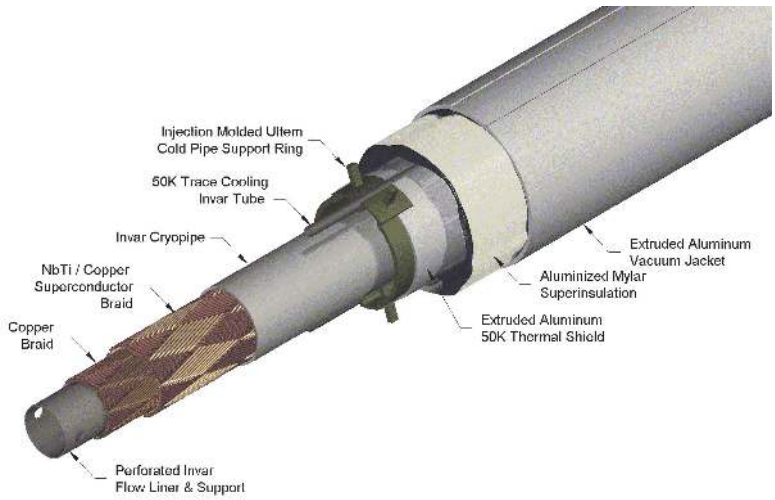

Figure 108. Schematic of superconducting transmission line showing construction details.

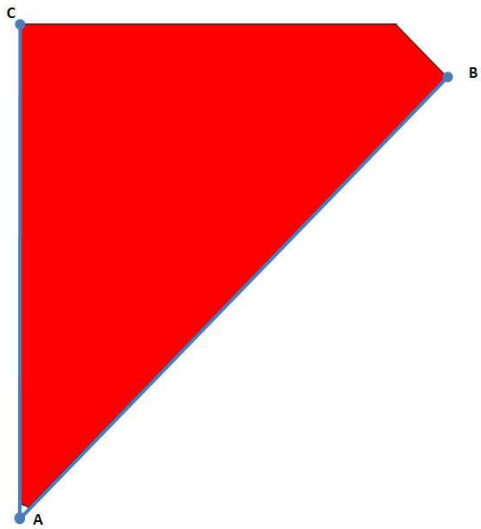

Figure 109. 1/8th model used for magnetic analysis.

example. In addition, we would like to consider an STL with multiple internal current loops so that a 100 kA room temperature driving source is not needed. The total amount of superconductor would be roughly the same; 5-10 turns with a current of 20-10 kA each would be more manageable from the viewpoint of the power source.

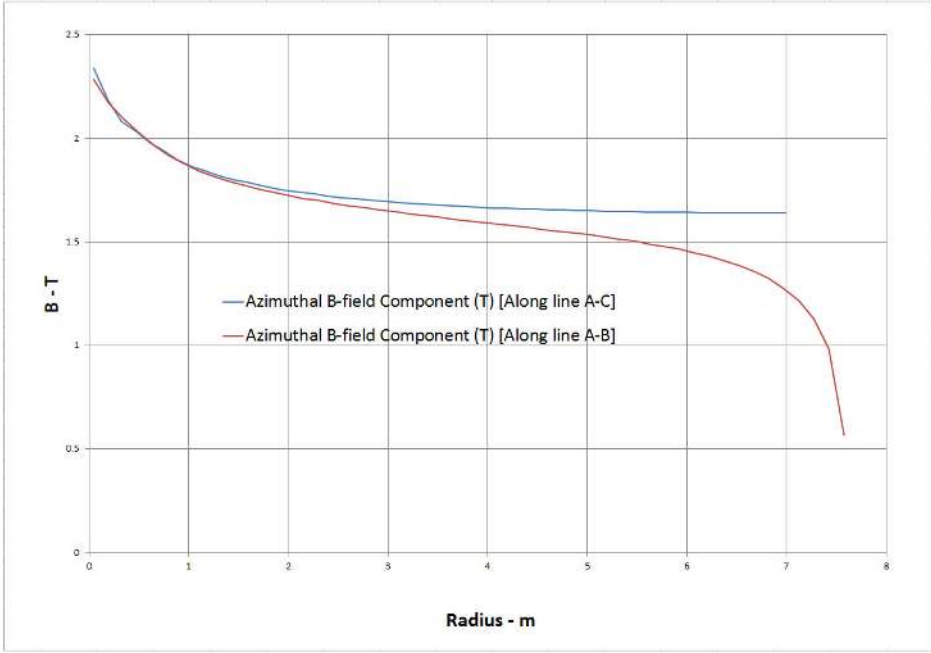

Figure 110. Magnetic field along the lines A-B and A-C in figure 109

3.2.2.5. Detector planes

Scintillator

Particle detection using extruded scintillator and optical fibres is a mature technology. MINOS has shown that co-extruded solid scintillator with embedded wavelength shifting (WLS) fibres and PMT readout produces adequate light for MIP tracking and that it can be manufactured with excellent quality control and uniformity in an industrial setting. Many experiments use this same technology for the active elements of their detectors, such as the K2K Scibar [327], the T2K INGRID, the T2K P0D, the T2K ECAL [328] and the Double-Chooz detectors [329].

Our initial concept for the readout planes for MIND is to have both an x and a y view between each plate. The simulations done to date have assumed a scintillator extrusion profile that is $3.5 \times 1.0\,\mathrm{cm}^2$. This gives both the required point resolution and light yield. We are also considering an option where we use triangular extrusions similar to those used in Minerva [330].

Rectangular extrusions

The existing MIND simulations have assumed that the readout planes will use a rectangular extrusion that is $3.5 \times 1.0\,\mathrm{cm}^2$, see figure 112. A 1 mm hole down the centre of the extrusion is provided for insertion of the wavelength shifting fibre. This is a relatively simple part to manufacture and has already been fabricated in a similar form for a number of small-scale applications. The scintillator

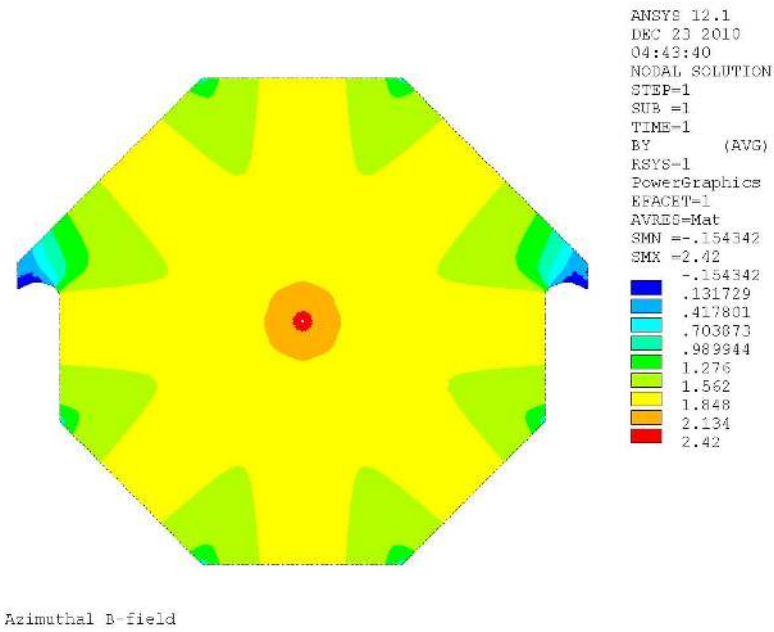

Figure 111. Contours of constant magnetic B-field.

strips will consist of an extruded polystyrene core doped with blue-emitting fluorescent compounds, a co-extruded TiO_2 outer layer for reflectivity, and a hole in the middle for a WLS fibre. Dow Styron 665 W polystyrene pellets are doped with PPO (1% by weight) and POPOP (0.03% by weight). The strips have a white, co-extruded, 0.25 mm thick TiO_2 reflective coating. This layer is introduced in a single step as part of a co-extrusion process. The composition of this capstocking is 15% TiO_2 (rutile) in polystyrene. In addition to its reflectivity properties, the layer facilitates the assembly of the scintillator strips into modules. The ruggedness of this coating enables the direct gluing of the strips to each other and to the module skins which results in labour and time savings for the experiment. This process has now been used in a number of experiments.

Figure 112. Schematic of rectangular scintillator extrusion.

Minerva extrusions

We are also considering using the Minerva extrusion (see figure 113) for MIND. The triangle has a 3.3-cm base and a 1.7-cm height, and a 2.6 mm hole for a WLS fibre (figure 114).

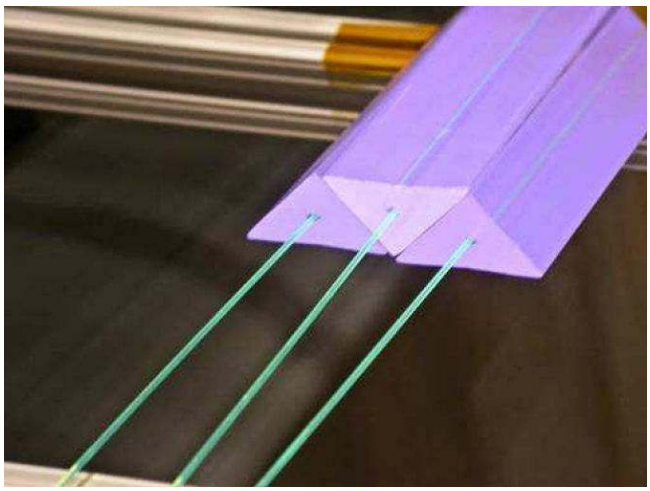

Figure 113. Minerva extrusions showing partial readout plane and wavelength shifting fibres.

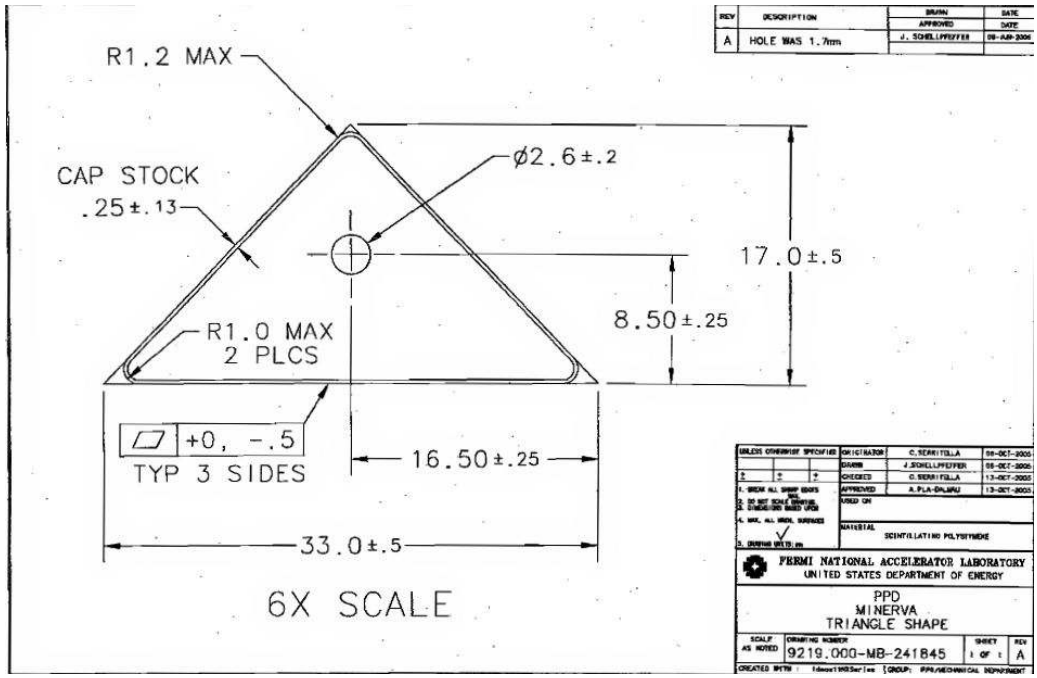

Figure 114. Minerva extrusion engineering drawing.

Photo-detector

Given the rapid development in recent years of solid-state photo-detectors based on Geiger mode operation of silicon avalanche photodiodes, we have chosen this technology for MIND. Although various names are used for this technology, we will use silicon photomultiplier or SiPM.

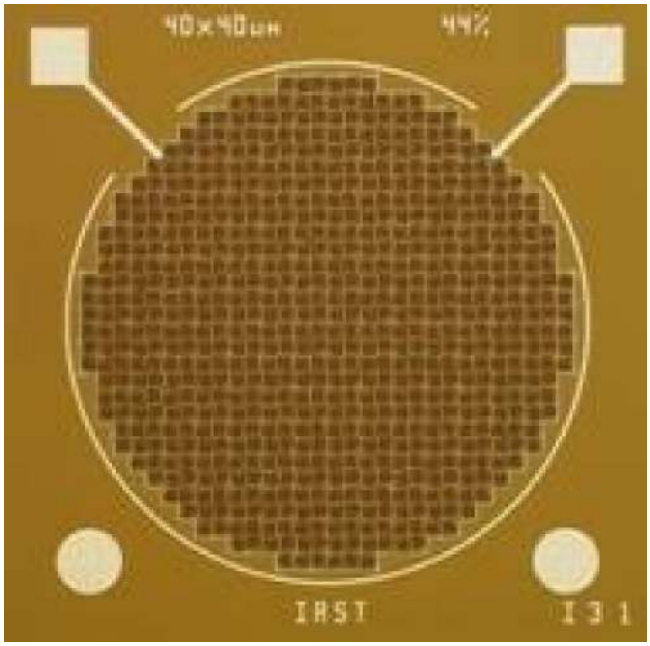

Figure 115. Photograph of SiPM

SiPM Overview

SiPM is the often-used name for a type of photo detector formed by combining many small avalanche photodiodes operated in the Geiger mode to form a single detector [331, 332]. Detailed information and basic principles of operation of these "multi-pixel" photodiodes can be found in a recent review paper and the references therein [333]. The first generation of these detectors use a polysilicon resistor connected to each avalanche photodiode forming a pixel. Pixels usually vary in size from 10 $\times 10\,\mu\text{m}^2$ to 100 $\times 100\,\mu\text{m}^2$ (see figure 115). All the diodes are connected to a common electrical point on one side, typically through the substrate, and all the resistors are connected to a common grid with metal traces on the other side to form a two-node device. A typical SiPM will have from 100 to 10 000 of these pixels in a single device, with the total area from 1 to 10 mm^2. Because all the diode and the individual quenching resistors are connected in parallel, the SiPM device as a whole appears as a single diode. In operation, the device appears to act somewhat like a conventional APD, but in detail it is radically different. Because the diodes are operated in the Geiger mode, and because every pixel of the SiPM device is nearly identical, the sum of the fired pixels gives the illusion of an analog signal that is proportional to the incident light, but it is, essentially, a digital device.

SiPMs have a number of advantages over conventional photomultiplier tubes, including very high photon-detection efficiency, complete immunity to magnetic fields, excellent timing characteristics, compact size, and physical robustness. They are particularly well suited to applications with fibres, as the natural size of the SiPM is comparable to that of fibres [334, 335]. But the most important single feature of the SiPM is that it can be manufactured in standard microelectronics facilities using nearly standard CMOS processing. This means that huge numbers of devices can be produced without any manual labour, making the SiPMs very economical. Furthermore, it is possible to integrate the

electronics into the SiPM itself, which reduces cost and improves performance. Initial steps have been taken in this direction, though most current SiPMs are not manufactured in this way. The advantages of the SiPM are that it improves performance, reduces cost and can be tailored to a specific application. As the use of SiPMs spreads, so will the use of custom SiPMs with integrated electronics, just as ASICs have superseded standard logic in electronics.

The photon-detection efficiency (PDE) of a SiPM is the product of 3 factors:

$$\text{PDE} = QE \cdot \varepsilon_{Geiger} \cdot \varepsilon_{pixel}\,; \tag{39}$$

where QE is the wavelength-dependent quantum efficiency, ε_{Geiger}, is the probability to initiate the Geiger discharge by a photo-electron, and ε_{pixel} is the fraction of the total photodiode area occupied by sensitive pixels. The bias voltage affects one parameter in the expression 39, ε_{Geiger}. The geometrical factor ε_{pixel} is completely determined by the photodiode topology, and is in the range 50-70%. The PDE of a device manufactured by Hamamatsu [336] (Hamamatsu uses the name multi-pixel photon counter, MPPC) as function of the wavelength of the detected light is shown in figure 116.

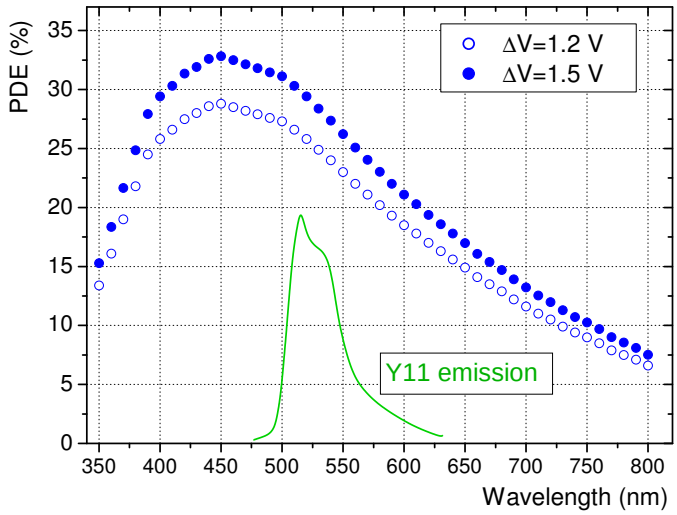

Figure 116. Photon detection efficiency of a Hamamatsu MPPC as a function of wavelength of the detected light at ΔV of 1.2 and 1.5 V at 25°C. The Y11(150 ppm) Kuraray fibre emission spectrum (in a. u.) for fibre length of 150 cm (from Kuraray specification) is also shown.

Implementation for a very large system

Although SiPMs with integrated electronics are in their infancy, we can say quite a bit about what such a device might look like in the case of instrumenting a very large system of extruded scintillator with wavelength shifting fibre readout, with a channel count of many million channels. In a system of

that size, there is no question that an application specific approach, which can reduce the unit costs by factors of five to ten, will easily justify the additional non-refundable expense inherent in a custom development. In this application, the SiPM would have an area of about one square mm, with about 100 pixels and electronics around the periphery of the device. Each cell would have a few transistors along one of the sides to provide active quenching—this differs from first-generation SiPMs, which use a passive resistor as the quenching element. In the case of active quenching, each pixel has essentially a digital latch associated with it. When a pixel fires, the latch is set, until an external reset signal arms the latch once again. This mechanism should not be confused with devices such as vertex pixel detectors. In this case, because the pixel capacitance is very small, the signal voltage is typically between 1 V and 2 V. Unlike vertex detectors, there is no amplification needed, and therefore, there is almost no standing current required in the transistors and the power dissipation is very small. It is only slightly larger than in the case of passive SiPMs and, in any case, much smaller than in vertex detectors. Active quenching has many advantages over passive quenching. For the application we are considering here, one of the main advantages is being able to control precisely when the pixels of the SiPM are re-armed. This greatly improves the dynamic range available for a given number of pixels because each pixel can fire only once during the signal-collection period and therefore it is simple to correct for the probability that some pixels were hit more than once. In the passive quenching case, the pixels will start recharging while there are still signal photons arriving, allowing some pixels to fire when the pixel is not fully charged, violating the rule that every pixel gives the same signal. This makes saturation correction complicated and unreliable, as it depends on many details of the signal and the SiPM. For the application we are considering here, an active quenching SiPM with 100 pixels gives about the same resolution as a passively quenched SiPM with 250 pixels. The smaller number of pixels reduces the ratio of the active area to the area lost to routing, resistors, and optical isolation trenches between the pixels and makes up for the added dead area associated with the active-quench circuitry.

Readout Electronics

On the periphery of the chip there is circuitry that latches the number of fired pixels in a FIFO, adds a time stamp and issues periodic latch resets to the quenching circuits. The communication with the chip is serial, with an input, an output and a clock, all of which are differential signals. SiPM bias and ground complete the connections for a total of eight. The power for the digital circuitry on the chip is extracted from the clock lines. A number of chips would be connected with flex cables, in a ring topology, to a data-concentrator module which would service a large number of SiPMs. A reasonable bandwidth available on differential lines over a flex cable for distances up to a few meters is between 10 Mbps and 100 Mbps. Depending on the rate of signals in the detector, and including things such as protocol overhead and data redundancy, a reasonable estimate of the number of SiPM chips that can be serviced by a single data-concentrator is a few thousand. We expect that in this application, the number of SiPMs in a module associated with a single data-concentrator would be limited by mechanical and operational considerations to something like 250 to 500. From the data concentrator, the data travel over optical links to higher-level data collectors.

3.2.3. Options for Far Detectors

The Magnetised Iron Neutrino Detector described above is the baseline for the distant neutrino detectors. Alternatives to the MIND which, though currently less mature, may offer advantages, are under consideration and will be discussed briefly below.

3.2.3.1. Totally Active Scintillating Detector (TASD)

One alternative for the MIND for the Neutrino Factory detector is to build a totally active scintillator detector (TASD). Although one could consider using TASD for the baseline Neutrino Factory with 25 GeV muon storage rings, TASD has been primarily studied as an option for a machine of lower energy (4 GeV to 5 GeV). For this scenario, the detector must have excellent neutrino event-detection efficiency down to event energies of roughly 500 MeV. Recently, new ideas have made plausible large, cost-effective detectors [114, 115] for lower muon energy, and initial studies of the corresponding physics reach suggest that an experiment with a 4 GeV to 5 GeV Neutrino Factory would provide an impressive sensitivity to the oscillation parameters. Furthermore, compared with high-energy facilities, a low-energy Neutrino Factory would require a less expensive acceleration scheme and a cheaper storage ring that presents fewer underground-engineering issues.

3.2.3.1.1. Overview

The Neutrino Factory TASD being considered consists of plastic scintillator bars with a triangular cross-section arranged in planes which make x and y measurements. Optimisation of the cell cross section still needs further study, but for now we have chosen the MINERνA extrusion design [330]. The scintillator bars have a length of 15 m and the triangular cross-section has a base of 3 cm and a height of 1.5 cm.

Magnetising the large detector volume presents a significant technical challenge for a Neutrino Factory TASD. Conventional room temperature magnets are ruled out due to their prohibitive power consumption, and conventional superconducting magnets are too expensive, due to the cost of the enormous cryostats needed in a conventional superconducting magnet design. In order to eliminate the cryostat, we have investigated a concept based on the superconducting transmission line (STL), the technology chosen for field excitation in MIND. The solenoid windings now consist of this superconducting cable which is confined in its own cryostat (figure 108). Each solenoid (10 are required for the full detector) consists of 150 turns and requires 7 500 m of STL. There is no large vacuum vessel and thus none of the large vacuum loads which make the cryostats for large conventional superconducting magnets so expensive. The 10 solenoids forming what we have called a "Magnetic Cavern" is shown in figure 117.

The Neutrino Factory TASD basic response has been simulated with GEANT4 version 8.1. The GEANT4 model (figure 118) of the detector included each of the individual scintillator bars, but did not include edge effects on light collection or the effects of a central wavelength-shifting fibre. A uniform 0.5 Tesla magnetic field was simulated.

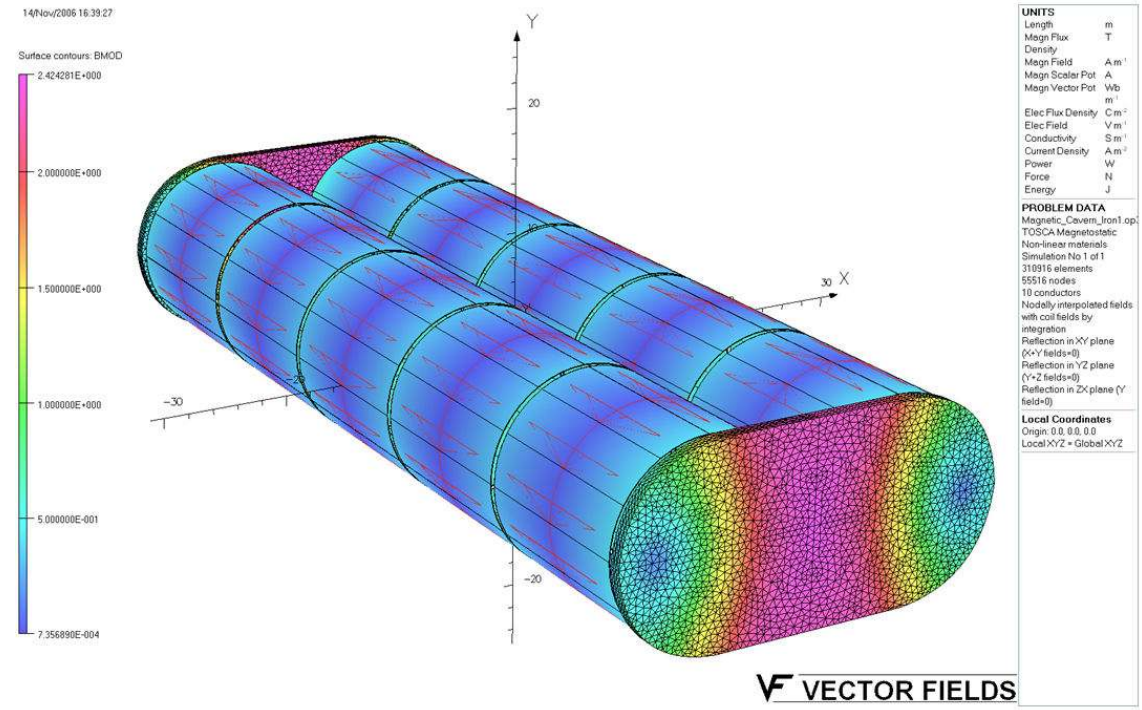

Figure 117. Schematic of the Magnetic Cavern concept.

Samples of isolated muons in the momentum range between 100 MeV/c and 15 GeV/c were simulated to allow for the determination of the detector's momentum resolution and charge identification capabilities. The NUANCE [312] event generator was used to simulate 1 million ν_e and 1 million ν_μ interactions. Events were generated in 50 mono-energetic neutrino-energy bins between 100 MeV and 5 GeV. The results that follow only have one thousand events processed through the full GEANT4 simulation and reconstruction.

The detector response was simulated assuming a light yield consistent with MINERνA measurements and current photo-detector performance [337]. In addition, a 2 photo-electron energy resolution was added through Gaussian smearing. Since a complete pattern recognition algorithm was beyond the scope of this initial study, the Monte Carlo information was used to aid in pattern recognition. All digitised hits from a given simulated particle, where the reconstructed signal was above 0.5 photo electrons, were collected. When using the isolated particles, hits in neighbouring x and y planes were used to determine the 3 dimensional position of the particle. The position resolution was found to be approximately 4.5 mm RMS with a central Gaussian of width 2.5 mm. These space points were then passed to the RecPack Kalman track-fitting package [309].

For each collection of points, the track fit was performed with an assumed positive and negative charge. The momentum resolution and charge misidentification rates were determined by studying the fitted track in each case which had the better χ^2 per degree of freedom. Figure 119 shows the momentum resolution as a function of muon momentum.

As a tracker, TASD achieves a resolution of better than 10% over the momentum range studied. Figure 120 (left) shows the efficiency for reconstructing positive muons as a function of the initial muon momentum. The detector becomes fully efficient above 400 MeV. The charge mis-identification rate was determined by counting the rate at which the track fit with the incorrect charge had a better

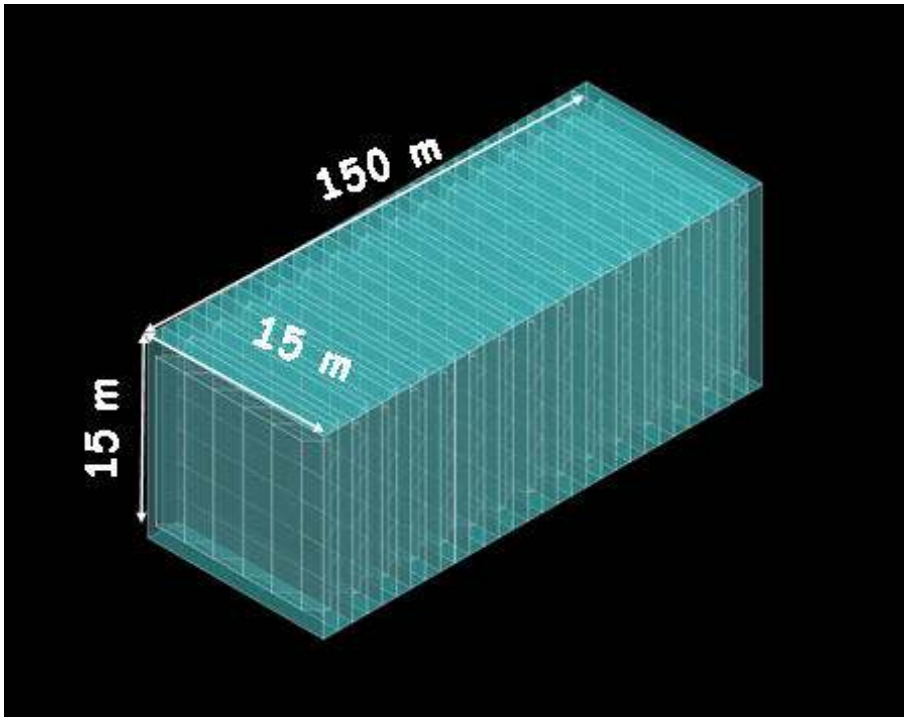

Figure 118. Schematic of the Totally Active Scintillator Detector.

χ^2 per degree of freedom than that with the correct charge. Figure 120 (right) shows the charge mis-identification rate as a function of the initial muon momentum.

Based on these initial studies, TASD meets the required muon charge mis-identification rate criterion needed for physics at a Neutrino Factory and exhibits exceptional tracking and momentum resolution. In order to understand fully the potential performance of TASD at a Neutrino Factory, a Monte Carlo study with full pattern recognition reconstruction and full neutrino event reconstruction must be performed, as has been done for MIND. This will allow for a detailed and quantitative understanding of backgrounds and thus present a realistic estimate of the detector's full potential at a Neutrino Factory.

3.2.3.1.2. Performance

In this section we will show the sensitivity to the neutrino oscillation parameters which can be obtained by a 20 kton Totally Active Scintillating Detector (TASD) used in conjunction with a low-energy Neutrino Factory. This setup was originally considered in references [114, 115] and later in references [116, 117, 122], in which full details can be found. As explained in the main text, we considered the possibility of the addition of the platinum channels ($\nu_\mu \to \nu_e$ and $\bar{\nu}_\mu \to \bar{\nu}_e$) in addition to the usual golden channels ($\nu_e \to \nu_\mu$ and $\bar{\nu}_e \to \bar{\nu}_\mu$). The main assumptions used to simulate the TASD are as follows: we assume an energy threshold of 0.5 GeV with a detection efficiency of 94% above 1 GeV and 74% below 1 GeV for ν_μ and $\bar{\nu}_\mu$ with a background of 10^{-3}. For ν_e and $\bar{\nu}_e$ we assume an efficiency of 47% above 1 GeV and 37% below 1 GeV with a background of 10^{-2}. The main sources of background

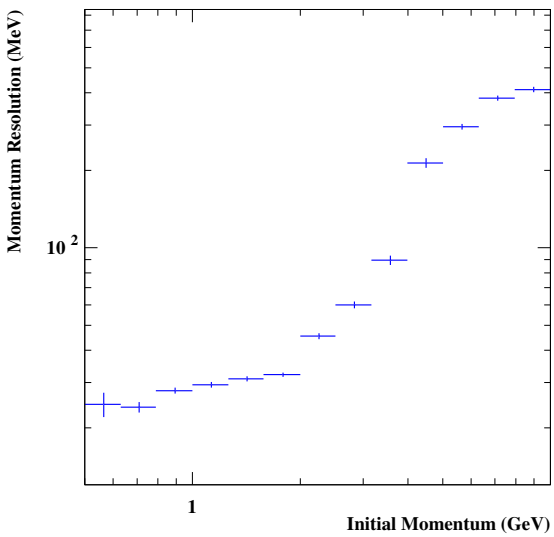

Figure 119. TASD momentum resolution as a function of the muon momentum.

are assumed to arise from charge mis-identification and neutral-current events. The energy resolution is assumed to be 10% for all channels. A 100 kton liquid argon (LAr) detector was also simulated, with the assumptions used to simulate the optimistic performance being the same as for the TASD, so that the optimistic performance of a 100 kton LAr detector coincides roughly with that of a 100 kton TASD.

In figure 121 we show the performance of the 20 kton TASD to standard oscillation parameters when used with a low-energy Neutrino Factory with a single baseline of 1 300 km and assuming a muon flux of 1.4×10^{21} useful muon decays per year per polarity, running for 5 years per polarity. The 3σ θ_{13} discovery potential, CP discovery potential and sensitivity to the mass hierarchy as a function of $\sin^2 2\theta_{13}$ in terms of the CP fraction are shown, for the low-energy Neutrino Factory with a 20 kton TASD (red line), the low-energy Neutrino Factory with a 100 kton LAr detector (blue band - the left-hand edge corresponds to the optimistic assumptions and the right-hand edge to the conservative assumptions), and other experiments - the ISS baseline Neutrino Factory [118] (black line), various β-beams (green [338], orange [339, 340], blue [341] lines), T2HK [118] (yellow line) and the wide-band beam [342] (purple line). In these simulations we used the same oscillation parameters as in reference [343], and have assumed a normal hierarchy.

It can be seen that a low-energy Neutrino Factory with TASD has sensitivity to CP violation which is roughly equal to that of the pessimistic performance of the 100 kton LAr detector. The sensitivity to θ_{13} is also very good and again is roughly equal to that of the pessimistic LAr detector, whilst the sensitivity to the mass hierarchy is better than that of the pessimistic LAr detector.

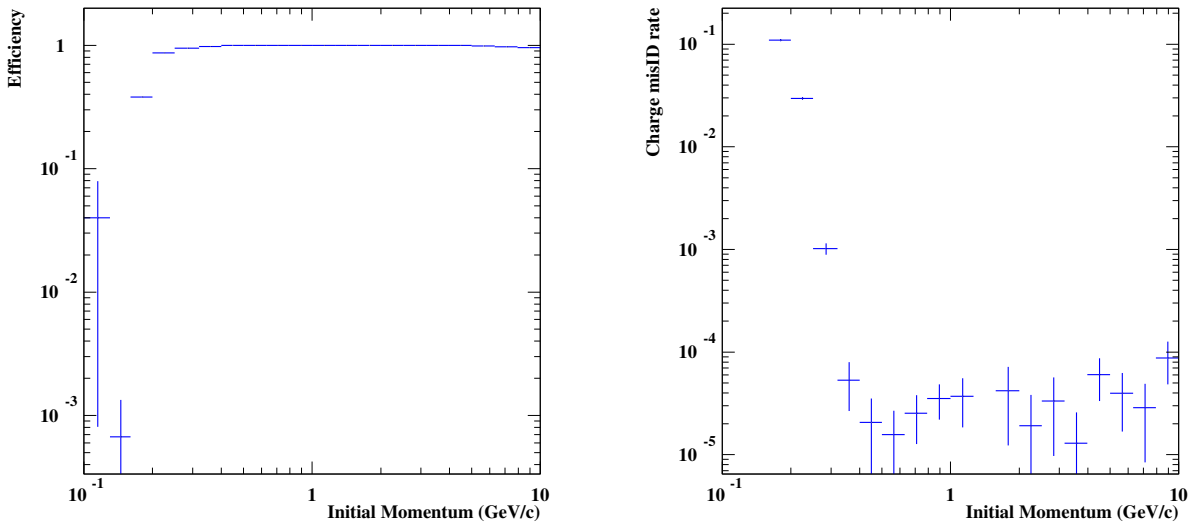

Figure 120. Left: Efficiency for reconstructing positive muons. Right: Muon charge mis-identification rate as a function of the initial muon momentum.

3.2.3.2. Liquid Argon Detectors

Overview

The Liquid Argon Time Projection Chamber (LArTPC) offers the possibility of truly isotropic tracking and calorimetry with fine sampling at the level of a few-percent of a radiation length. Pioneered by the ICARUS project [344], extensive studies and R&D projects have proven the potential of the LArTPC to provide a clean identification of ν_μ, ν_e charged-current events with the efficient rejection of neutral-current backgrounds, excellent energy resolution and sensitivity over a wide energy band including down to very low momentum thresholds. These properties make the LArTPC an interesting candidate for a large-scale far detector for a Neutrino Factory and a number of groups worldwide are actively pursuing LArTPC concept development. Fully contained neutrino interactions have recently been reported by ICARUS illuminated by the CNGS beam (see figure 122(left)) and from the ARGONEUT collaboration situated in the NUMI beam at FNAL (see figure 122(right)).

The largest LArTPC constructed to date is the 2×300 ton ICARUS T600 detector which has a maximum drift length of 1.5 m. R&D programmes underway in Europe, USA and Japan are focused on the issues surrounding scaling up the LArTPC technology to the multi-kiloton scales demanded by a Neutrino Factory in addition to next generation projects for particle astrophysics and proton decay.

Several design concepts have emerged for large scale LArTPC detectors up to ~ 100 kt scale [345–350]. These designs achieve the large mass scale by being made up either of a number of smaller identical modules or by using a single volume based on Liquid Natural Gas (LNG) cryogenic tank

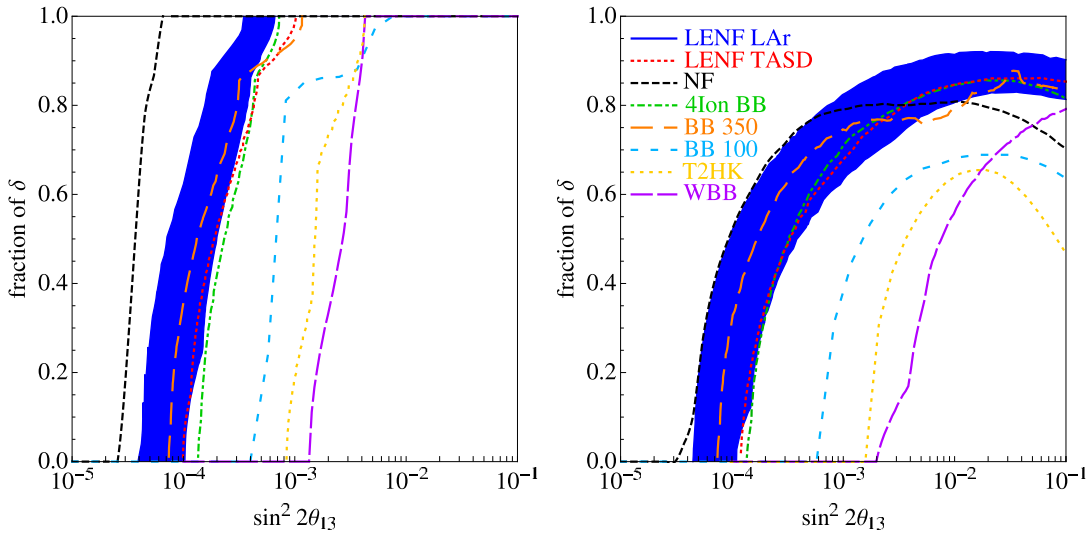

(a) θ_{13} discovery potential.

(b) CP discovery potential.

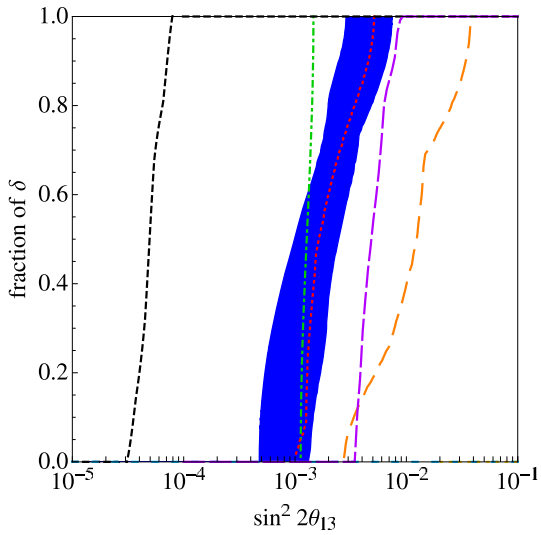

(c) Hierarchy sensitivity.

Figure 121. 3σ allowed contours for the LENF with 20 kton TASD (red line) and 100 kton LAr detector (blue band), the HENF (black line), T2HK (yellow line), the wide-band beam (purple line) and three β-beams (green, orange, light blue lines) for a) θ_{13} discovery potential, b) CP discovery potential and c) hierarchy sensitivity. From reference [116].

technology. Examples of projects from Europe, Japan and the US are shown in figure 123. GLACIER and the JPARC-to-Okinoshima project are both based on a single 100 kton LNG tank with an electron drift distance of up to 20m whereas the DUSEL design achieves large mass scales by stacking 20 kton modules thereby keeping the drift distance down to 2.5 m.

With all of these large scale proposals, there are three main technical areas where R&D solutions need to be found:

- Engineering issues related to constructing large LAr volumes with very low thermal losses,

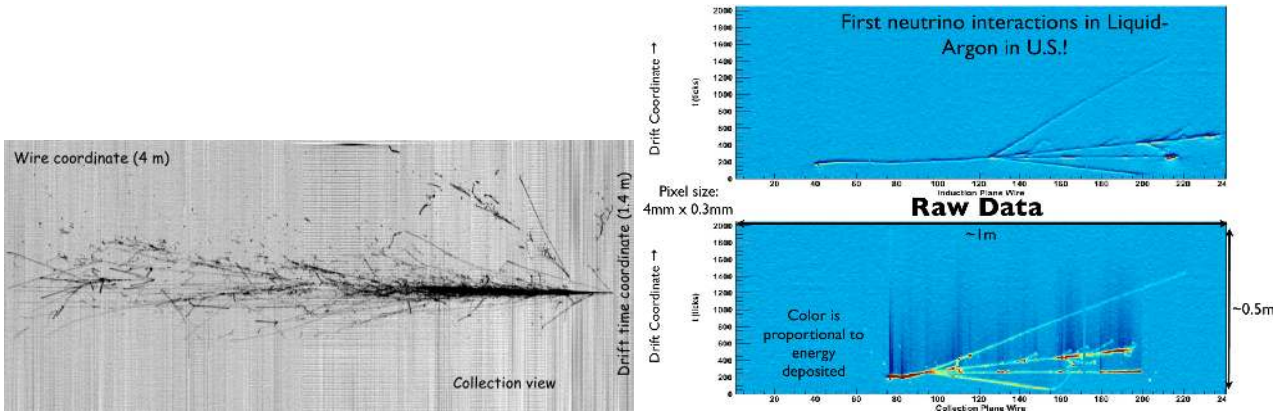

Figure 122. Neutrino interactions as seen in the (left) ICARUS (A. Guglielmi, Neutrino'10) and (right) ArgoNeut detectors (M. Soderberg, Neutrino'10)

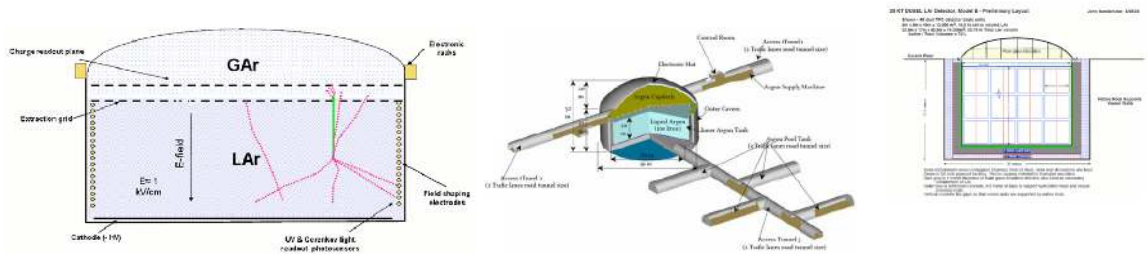

Figure 123. (left) GLACIER, (middle) JPARC-to-Okinoshima 100 kt concept and (right) 20 kt detector for DUSEL.

preferably in an underground location and operation over many years in a safe and stable environment;

- Drift lengths of more than 10 times the 1.5 m ICARUS T600 drift length will only be achievable if drift fields of $0.5-1$ kV/cm can be applied and if the level of electro-negative impurities, which degrade the released ionisation charge, can be controlled at the level of a few tens of parts per trillion (ppt); and
- Reconstructing the $\nu_e \to \nu_\mu$ and $\bar{\nu}_e \to \bar{\nu}_\mu$ 'golden' oscillation channel of the Neutrino Factory requires that the entire LAr volume be magnetised.

R&D Activity

In this section we summarise the status of R&D activity in liquid argon technology.

- **Readout and Electronics:** The 2D reconstruction of charge in ICARUS modules is read out by planes that cannot easily scale in size, due to their large capacitance. An alternative proposal

for single volume designs with drift distances > 10 m (e.g. GLACIER) is to operate in double-phase liquid and gaseous Ar; ionisation charge amplification occurring in the gas phase. A 3 litre double-phase TPC with thick GEM readout (macroscopic hole multipliers fabricated in standard PCBs) [351, 352] has been successfully operated at CERN. More recent developments involve the production of an $X-Y$ 2D projective anode for a Japanese 250 litre prototype, studies with bulk-micromegas [353] and imaging the secondary scintillation light in a single phase LAr volume [354]. ASIC developments using cold electronics (preamplifiers, digitisers and multiplexers) that work inside the cryostat are under development both in Europe [355] and the USA [350];

- **Liquid-argon vessels:** LAr storage vessels are based on a stainless steel vacuum-insulated Dewar. One of the large-scale designs [347] scales this technology by installing support structures within the LAr volume. Studies of the suitability of industrial Liquid Natural Gas (LNG) technology for large-scale LAr storage (up to $2 \times 10^5\,\mathrm{m}^3$) [356] have concluded that, with only passive insulation, boil-off losses of only 0.04%/day for a 100 kton vessel are expected. A stainless steel/Invar membrane is also being considered for the DUSEL 20 kton design [350]. Issues surrounding the feasibility of constructing and running safely such detectors, particularly in underground sites has been studied as part of the LAGUNA design study [357];
- **High Voltage Systems:** The drift time of ionisation electrons over a distance of $\sim 10\,\mathrm{m}$ is around 10 ms for a drift velocity of $1\,\mathrm{mm}/\mu\mathrm{s}$. It is desirable for the drift velocity to be as high as possible, so drift fields in the region of a few kV/cm are needed (in the MV-range for 10 m). The ArDM experiment [358] are generating the high voltages required inside the LAr volume via a submerged Cockcroft-Walton voltage multiplier. Drift fields of ~ 1 kV/cm have already been demonstrated over a 1.2 m drift distance [359].
- **Liquid-argon purity:** Attaining and maintaining sufficient purity of LAr is a challenge given that electronegative impurities (mainly O_2) must be kept at a level of a few tens of ppt in order to ensure electron lifetimes of the order of 10 ms. Proof-of-principle tests for purging with argon gas before filling with LAr have been performed at FNAL [360], KEK [361], and CERN [359] (a $6\,\mathrm{m}^3$ volume achieved 3 ppm O_2 contamination after purging). A closed gaseous Ar purification stage (via cartridges) in addition to a LAr purification stage has been used in ICARUS. Options for purification cartridges are being studied as part of the ArDM project at FNAL [362]. Direct measurements of long electron drifts are underway at CERN (5 m horizontal drift [363]) and at the University of Bern (ARGONTUBE: 5m vertical drift);
- **Magnetisation:** The magnetisation of a multi-kiloton LAr volume is one of the key issues surrounding the evaluation of a LAr TPC as a potential Neutrino Factory detector. Small-scale prototype LAr TPC's have been operated in magnetic fields; e.g. a 10 lt, 150 mm maximum drift length volume in a field of 0.55 T [364], with no significant degradation of the imaging properties. Conceptual studies of magnetising a multi-kiloton LAr volume have concluded that conventional warm coils would dissipate MW's of heat [365], so more recent ideas include immersing a superconducting solenoid directly into the LAr volume [366], or using superconducting transmission lines [367]. Studies are on-going regarding magnetisation issues or the potential of a 'hybrid' detector consisting of a LAr TPC in close proximity to a magnetised MIND-type module or measuring $\nu/\bar{\nu}$ QE CC reactions with nuclei on a statistical basis [368] in the context of a low energy Neutrino Factory;

- **Algorithmic reconstruction:** With the increased interaction rates associated with neutrino beam intensity upgrades, it is essential that automatic reconstruction algorithms for neutrino interaction events in LAr are developed. Studies in Europe [369] and via the LArSoft collaboration in the USA [370] are actively developing algorithms to reconstruct hit clusters, tracks, event vertex points and shower objects. The resulting 'toolbox' of algorithms will be used to validate the performance assumptions for LAr detectors in common use for neutrino oscillation physics studies (see e.g. [180, 371]). These tools will also be useful in estimating reliably the feasibility of non magnetic field solutions to $\nu - \bar{\nu}$ separation in the golden channel discussed above; and
- **Roadmaps:** The R&D programmes in Europe and Japan for future large-scale LAr detectors are closely coordinated. Work is ongoing in delivering the large electron multiplier (LEM) readout technologies, demonstration of long drift lengths (5 m), culminating with the construction of a 1 kton device, which is widely accepted to be the largest possible affordable detector that will allow reliable extrapolations to 100 kton. The roadmap in the USA includes the exploitation of the ArgoNeuT in a neutrino beam, the construction of the 0.1 kton MicroBooNE detector and delivering a 20 kton detector for DUSEL.

3.2.3.3. Large-volume liquid scintillator detectors

Large-volume liquid scintillator detectors (Borexino[372], KamLAND [373]) are presently used for low-energy neutrino physics. Even larger scintillator detectors have been proposed, such as the 50 kton LENA [374]–[384] detector or the 10 kton HanoHano[385, 386] detector. Although these are totally-active scintillator detectors (TASD), these single-volume detectors are conceptually different from segmented scintillator detectors.

The performance of a conventional large volume liquid scintillator detector for high-energy neutrinos (1–5 GeV) has been studied recently [387–390] and a more detailed study is in preparation [391]. It was found that, if the detector, particularly the read-out electronics, is well designed, one can reconstruct the simplest events using photon-arrival times in phototubes. The lepton-flavour identification was determined to be almost perfect and the energy resolution was found to be better than 5%. Hence a large-volume liquid-scintillator detector can be used in conventional neutrino beam experiments [392] and high-energy beta beam [393] experiments, as well as in atmospheric neutrino experiments. If it can be magnetised, it could be also be considered for the detector at a Neutrino Factory [394].

Here we consider a magnetised single-volume liquid scintillator detector of approximately 100 kton. A phenylxylylethane (PXE) scintillator [395–398] doped with PPO (up to 10 g PPO/1 kg PXE) is able to produce fast scintillation decay times, essential for high energy applications (such as the Neutrino Factory). Additionally, we may not need a separate tank and water shielding or buffer as in LENA, but can use rock walls with a suitable liner, thus reducing the cost and optimising the detector volume.

The required shape and volume could be achieved with a horizontal cavern of 30 m diameter and a length of 150 m. The diameter is mostly limited by the transparency of the liquid, typical attenuation lengths being of the order of 15 m [397, 398]. Previous studies performed for LENA hint that at least 30 m width is accessible without excessive cost [399].

It is assumed that photomultiplier tubes are installed in all sides of the detector volume, including the bottom, the surface and both ends. Photomultiplier tubes (PMT) designed to work in magnetic fields, possibly embedded in μ-metal shields and aligned relative to the field with mirrors for light

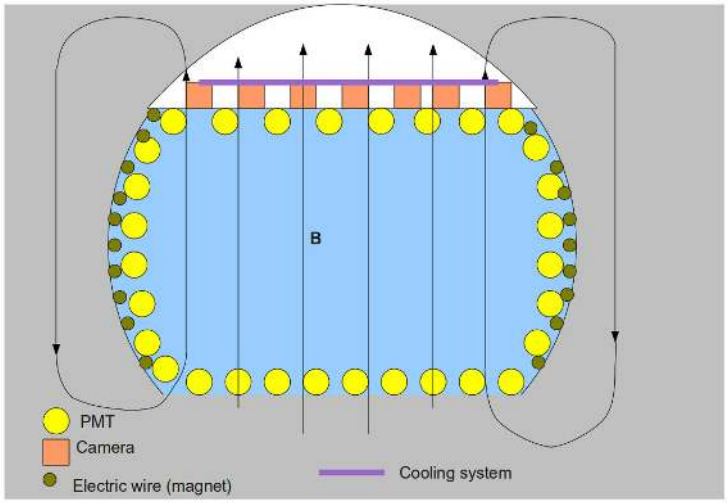

Figure 124. A possible layout of the detector. This shows the transverse cross section. Photomultipliers (yellow circles) are located at all sides of the detector and cameras at the upper surface. In this case the vertical magnetic field is generated by longitudinal wires.

collection, will be required. As an alternative, semiconductor-based (or hybrid) photo-sensors are also under study. They may be faster and immune to magnetic fields, but may suffer from noise and are currently expensive.

Previous studies [391] suggest that a 3% photo-cathode coverage is sufficient for high-energy events. The devices should be able to record multiple photons reliably, with a time resolution in the ns scale, to be achieved by 16 bit Flash ADCs. We may optionally install an array of one-photon capable cameras on the upper surface, when such technology is available and affordable (see e.g. [387]). The liquid-air interface can be used as a lens (objective), because of the high refractive index (1.6 - 1.8) of the oil used as the scintillator. To measure the very faint scintillation light we need single-photon capable pixelized photo-sensors. Potential devices exist based on a number of different technologies such as: ICCD (CCD with image intensifier), EMCCD (Electron multiplier CCD), SPADA (Single photon avalanche diode array) or MCP (micro-channel plate) varieties with binary pixel readout.

A severe problem with all semiconductor photodetectors is their very high noise rate. A typical noise rate is 100 kHz per pixel at room temperature. With cooling, we may expect 10 kHz per pixel at 0° C, and no less than 1 kHz at the freezing point of the liquid, but somewhat lower at liquid nitrogen temperatures. Because of the noise, the camera readout must be externally triggered with the PMT coincidence. A local rolling memory for at least 100 ns, or the full readout time window, is required. The analysis of the PMT data determines the vertex and the end of the muon track with a precision of 20 cm.

It is reasonable to assume 50% quantum efficiency and 70% geometric efficiency. If we also assume 90% transmission through the lens, this then gives a total photo-efficiency of 30%. Assuming a photocell composed of 64×64 pixels (4096 channels), a lens with a 15 cm diameter and an aperture of 0.30, we obtain a mean resolution of 10 cm at 15 m distance. With a lens diameter of 15 cm and 10%

coverage of the upper surface area, we will measure about 10 photons for a 10 cm path-length along the trajectory of a muon (assuming a typical photon yield of 10^4 photons/MeV and 20% transparency at a distance of 15 m).

The detector performance with PMT time signals was simulated with the prototype code "Scinderella". The code simulates the passage of muons and scintillation light emission, individual hadrons and electromagnetic showers and tries to make a fit to a test event using the simulated recorded data of the photo-sensors. For a more quantitative picture, a more detailed simulation applying GEANT4 and physical event generators should be used. Here we considered only the bending of muon tracks. Much more detail about the tracking capability is given elsewhere [391].

It was found that the muon charge was reliably measured using the time profile information of the photo-sensors. The simulations indicate that a magnetic field strength between 0.02 T for ideal electronics and 0.05 T for current standard technology might be sufficient. Older technology designed only for low-energy events, like that used in Borexino [372], is not sufficient. The decay time of the scintillator affected the performance. For high-energy events, the lower transparency of higher-doped scintillators is adequate, if we are not aiming for performance at low energies.

Using the additional camera setup reduces the 20 cm resolution achieved by the PMTs down to a statistical accuracy for an individual track to better than 5 cm. With this resolution, the charge of the muon can be identified for $B > 0.02$ T and a 10 MeV energy resolution can be achieved. The camera setup, in particular, improves the capability to distinguish multiple tracks, such as charged pions and recoil protons. The identification of 10–80 cm long tracks is enhanced with the addition of the cameras when compared to a PMT only setup. The camera setup also makes recoil neutron tracks visible. The neutrons scatter from free protons, giving the proton recoil energies up to half of the neutron energy, within a radius of ~ 1 m. Moreover, the neutron may cause the spallation of additional neutrons that are absorbed giving gammas of a few MeV. The combination of the camera and the PMT measurement may help to identify the absorption signals.

The camera readout will improve the measurement of the energy of the hadron showers produced in multi-GeV neutrino interaction. Electrons and photons causing electromagnetic showers can be identified by observing the gap between the vertex and the shower, which is 42 cm on average. This is important for rejection of neutral-current background events (and also for proton decay $p \to e^+\pi^0$).

Identifying a pion (from a muon) is important for neutral current background rejection. The pion decays with a mean life-time at rest of 26 ns. The resulting muon (4 MeV for a decay at rest) has a path-length of about 2 cm. In the case of decay in flight, the decay is recognised by an energy bump in the time profile and a sharp change in the direction of the path. To see the angle, we need a timing resolution better than 1 ns. Negative pions may be absorbed before decaying (giving photons).

We can summarise that a liquid scintillator detector setup with a magnetic field $B > 0.02$ T, good PMTs and adequate electronics is sufficient to determine the muon charge. Combining PMT readout with a camera system gives additional tracking capability, with very good event identification and background rejection. Further studies to quantify these effects at a neutrino beam will be carried out in the future.

3.3. Near detectors

3.3.1. Introduction

As mentioned in section 3.1.2, the baseline is to have four near detectors, one at the end of each of the four straights of the two storage rings. This allows the measurement of the neutrino flux of each neutrino beam and reduces the systematic error in the oscillation parameters [129]. Apart from the flux measurement, the near detector will also be able to perform precision measurements of neutrino-nucleon, neutrino-electron, and charm-production cross-sections. Each of these measurements is necessary to reduce the systematic errors of the neutrino oscillation analysis. Additionally, the near detector will embark on an extended programme of precision neutrino physics and searches for Non Standard Interactions (NSI).

Section 3.3.2 describes the performance required of a near detector at a Neutrino Factory. It includes an analysis using neutrino-electron scattering to extract the neutrino flux with a near detector, a description of how the near detector flux measurement can be used to extrapolate to the far detector to constrain the parameters of the neutrino oscillation signal, a description of the neutrino scattering physics that can be achieved with a near detector (including cross-sections, QCD and other electroweak physics topics) and finally a section on the measurement of charm production from neutrino interactions (one of the dominant backgrounds in the oscillation signal in the far detector) and the tau search, which can be used to constrain NSI.

Section 3.3.3 describes the requirements of the near detector to achieve the above physics goals, including two possible options that are being considered, one with a scintillating fibre tracker and the other using a high resolution straw-tube tracker. In addition, two other options will be considered to perform charm and tau measurements; one of which includes an emulsion detector, the other a silicon vertex detector.

3.3.2. Performance requirements

3.3.2.1. Neutrino flux measurement; inverse muon decay

Introduction

In order to perform measurements of neutrino oscillations at a neutrino facility, it is necessary to establish the rate of neutrino interactions. The aim of the near detector of the Neutrino Factory is to measure precisely the absolute neutrino flux, the neutrino cross sections, and to estimate the backgrounds in the far detector. Hence, careful design of a near detector is crucial for the reduction of systematic uncertainties in the long-baseline neutrino-oscillation experiment. The paragraphs which follow demonstrate that quasi-elastic neutrino-electron scattering can be used to measure the neutrino flux coming from the Neutrino Factory storage ring with a systematic uncertainty of $\sim 1\%$.

Quasi-Elastic scattering off electrons in the near detector

Quasi-elastic neutrino-electron scattering is suitable for the measurement of the neutrino flux because its absolute cross-section can be calculated theoretically with confidence. The two process of interest for neutrinos from μ^- decays are:

$$\nu_\mu + e^- \rightarrow \nu_e + \mu^- \,; \text{and} \tag{40}$$

$$\bar{\nu_e} + e^- \rightarrow \bar{\nu_\mu} + \mu^- \,. \tag{41}$$

For the processes in equation 40, also known as inverse muon decay, the differential cross section is isotropic in the centre-of-mass system. The total cross section is given by:

$$\sigma = \frac{G_F^2}{\pi} \frac{(s - m_\mu^2)^2}{s} \,. \tag{42}$$

For the process in equation 41, also known as muon production through annihilation, the differential cross section in the centre-of-mass system is given by:

$$\frac{d\sigma}{dcos\theta} = \frac{G_F^2}{\pi} \frac{(s - m_\mu^2)^2}{s} \times \left(1 + \frac{s - m_\mu^2}{s + m_\mu^2} cos\theta\right) \left(1 + \frac{s - m_e^2}{s + m_e^2} cos\theta\right) \,; \tag{43}$$

and the total cross section is:

$$\sigma = \frac{G_F^2}{\pi} \frac{(s - m_\mu^2)^2}{s^2} (E_e E_\mu + \frac{1}{3} E_{\nu 1} E_{\nu 2}) \,; \tag{44}$$

where $E_{\nu 1}$ and $E_{\nu 2}$ are the energies of the neutrinos. $E_{\nu 1}$ and $E_{\nu 2}$ depend, in turn, only on s. Both processes have a threshold at ~ 11 GeV.

Simulation of the near detector

A Monte Carlo simulation of muon decay in flight along the length of the 600 m straight section of the decay ring has been developed. The two leptonic processes in equations 40 and 41 have been simulated in order to determine the detector requirements and to select the best criteria for the suppression of the background. After this, the GENIE [400] event generator and the GEANT4 simulation tool were used to simulate the entire spectrum of neutrino interactions and the response of the detector.

Near detector requirements

If we want to measure the neutrino flux by using the quasi-elastic neutrino-electron scattering for earlier measurements of these processes see [401, 402]), the detector has to be able to distinguish between the leptonic events and inclusive charged current (CC) neutrino-nucleon scattering:

$$\nu_\mu + N \rightarrow \mu^- + X \,; \tag{45}$$

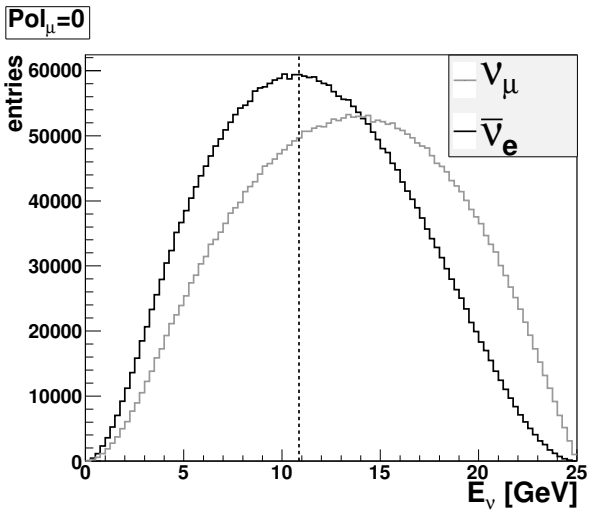

Figure 125. Distributions over the neutrino energy on the plane perpendicular to the straight section and 100 m away from its end. Dotted lines indicate the threshold for the process of quasi-elastic scattering off electrons.

which has a cross section a few orders of magnitude larger. Some of the events from the charged-current processes (equation 45) can mimic leptonic events from quasi-elastic neutrino-electron scattering, but instead of a single muon in the final state there will be also a hadronic system X. The measured recoil energy of this hadronic system can be used as a good criterion for the suppression of the background.

The energy spectrum of the beam of neutrinos 100 m from the end of the straight section are shown in figure 125; the thresholds for the two processes of interest are also shown.

Figure 126 shows the distributions over the energy and the polar angle of the muons from quasi-elastic neutrino-electron scattering at that plane. One can see that all these muons have very small polar angles $\theta_\mu < 5$ mrad. This angular spread comes mainly from the muon beam divergence as the intrinsic scattering angle in processes 40 and 41 is much smaller. We use this as another criterion for suppression of the background.

The properties of the quasi-elastic scattering off electrons described above impose specific requirements on the near detector. The detector has to provide an interaction rate sufficient for the measurement despite the very small cross sections of the leptonic processes, $\sim 4 \times 10^{-41}$ cm^2 at 15 GeV (for comparison, the total $\nu_\mu N$ CC cross section is $\sim 10^{-37}$ cm^2 at this energy). This requires a solid detector. Also, the detector must be able to reconstruct the polar angle of the scattered muon with maximum precision. This requires a low-Z tracker. At the same time, the near detector has to be able to measure the hadronic-recoil energy in the background events down to values of several MeV. This requires a precise calorimeter.

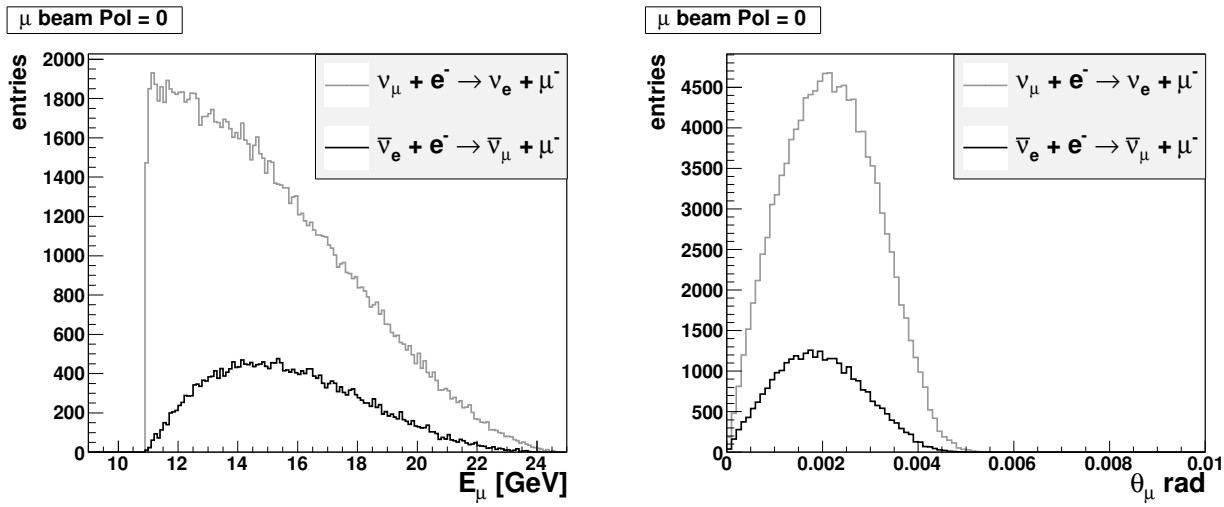

Figure 126. The energy distributions (left) and the polar angle distributions (right) of the muons generated in the detector by the reactions $\nu_\mu + e^- \to \nu_e + \mu^-$ and $\bar{\nu}_e + e^- \to \bar{\nu}_\mu + \mu^-$.

Neutrino event generation

In order to test different criteria for the suppression of the background from CC reactions and to determine the strict requirements for the near detector we make use of the neutrino event generator GENIE [403, 404] to simulate the interactions of the neutrinos with a detector made of polystyrene ($\rho = 1.032$ g/cm^3). The GENIE simulation uses as an input the neutrino flux created by the simulation of muon decay in flight.

The following neutrino interaction processes are included in the GENIE event generator:

- Quasi-elastic scattering;
- Elastic NC scattering;
- Baryon resonance production in charged and neutral current interactions;
- Coherent neutrino-nucleus scattering;
- Non-resonant deep inelastic scattering (DIS);
- Quasi-elastic charm production;
- Deep-inelastic charm production;
- Neutrino-electron elastic scattering; and
- Inverse muon decay.

The process $\bar{\nu}_e + e^- \to \bar{\nu}_\mu + \mu^-$ is not included in GENIE. This is not crucial for our simulation since, for unpolarised muons, it has a rate that is ~ 10 times less than that of inverse muon decay.

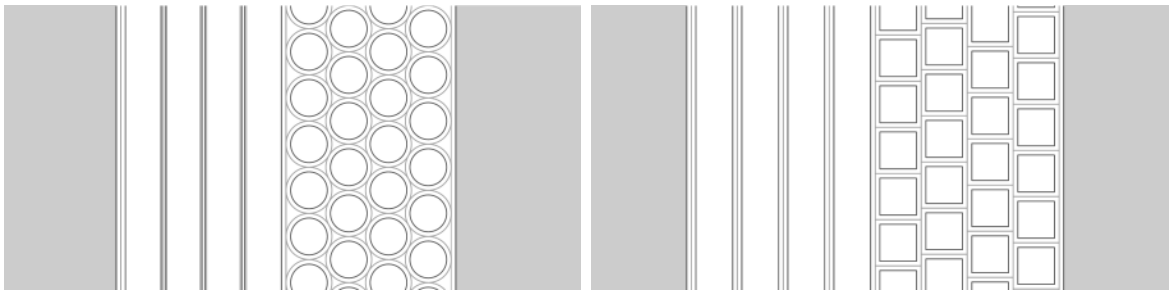

Figure 127. Schematic drawing of a fibre station made of cylindrical (left) and squared (right) fibres.

GEANT4 simulation of the near detector

In the GENIE data files all final state particles are recorded using the GHEP library. These particles are then read through an interface by the GEANT4 simulation and treated as primary particles for tracking through the volume of the detector.

The detector that has been simulated is a low-Z, high-resolution scintillating-fibre tracker. It consists of consecutive modules placed perpendicular to the beam axis. Each module consists of five planes made of plastic-scintillator slabs 1 cm thick and a fibre station. The scintillator slabs serve to absorb and measure the energy of recoil particles in the interaction. The fibre station consists of four layers of fibres with horizontal orientation and four layers with vertical orientation. Signals from individual fibres are used to construct space points (hits) from charged particles crossing the station.

Three different fibre-station conceptual designs have been simulated. The first option is a station made of cylindrical fibres with radius of 0.5 mm. For this design, the position of the fibre centres in a given layer is shifted by 0.25 mm with respect to centres of the fibres in the neighbouring layer (figure 127 - left). The other two options consider a station made of square fibres with 0.5 mm side and displacement between the neighbouring layers of 0.25 mm and 0.125 mm, respectively (figure 127, right panel). In each design the station thickness is 4 mm.

The overall dimensions of the detector are $1.5 \times 1.5 \times 1.08$ m^3 which corresponds to a mass of ~ 2.5 Ton. A sketch of the detector with a $\nu_\mu N$ interaction in its second module is shown in figure 128.

Digitisation

The fibre signal is taken to be proportional to the energy deposition in the corresponding fibre. It is then corrected for the attenuation of the light in its path between the hit and the fibre end. The signal is then smeared with a Gaussian with $\sigma/E = 25\%$. A simplified parametrisation is used for the absorber blocks. The signal in a given slab is taken to be proportional to the total energy deposition and is smeared with a Gaussian with $\sigma/E = 5\%$.

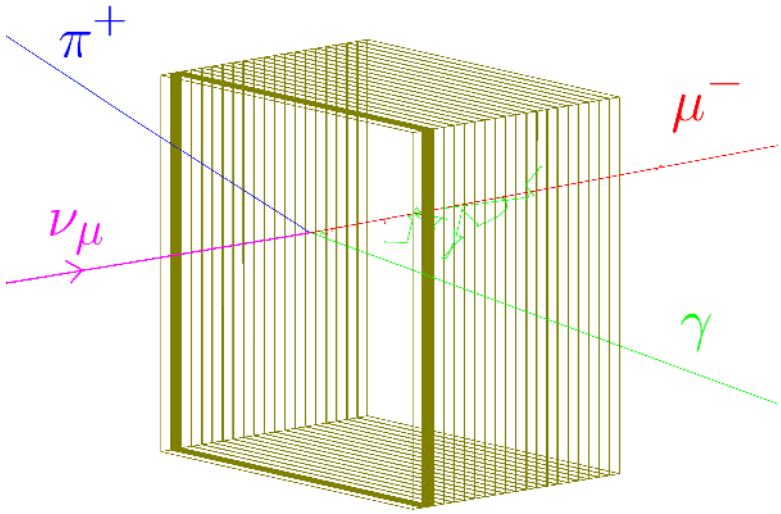

Figure 128. Schematic drawing of the detector with a $\nu_\mu N$ interaction in its second module.

Reconstruction and analysis

Reconstruction of the muon track:
For the purpose of these studies a simplified reconstruction of the events has been used. No pattern recognition is implemented and we simply use hits in the fibres belonging to the muon track. A space point measurement is then created for each fibre station. Its x and y coordinates are calculated independently as the weighted average of the coordinates of the centres of the hit fibres. The weights are proportional to the digitised signals. The space points obtained this way are used to reconstruct the muon track via the Kalman filter (e.g. taking multiple scattering into account).

The difference between the reconstructed polar angle of the muon and its true value from the simulation is used to measure the resolution. Figure 129 shows the distributions over this difference for the three different conceptual designs of the fibre stations. It is seen that the resolution is ~ 0.5 mrad in all three cases.

Background rejection exploiting energy deposition in the absorber blocks
We propose to use the total energy deposition in the first illuminated detector module as a first tool to reject background events. Figure 130 shows the energy deposition in the first illuminated detector module plotted as a function of the reconstructed-muon scattering angle. It is seen that the leptonic events and the CC background are well separated. Figure 131 shows the distributions of the outgoing muons over the reconstructed polar angle θ_μ and the variable $\theta_\mu^2 \times E$. The variable $\theta_\mu^2 \times E$ is proportional to the event inelasticity $1 - y = E_{had}/E_\nu$. Only events with a total energy deposition in the first illuminated absorber block less than 15 MeV are selected. A linear extrapolation of the CC background toward $\theta_\mu = 0$ is used to evaluate the number of background events under the leptonic peak.

The results obtained exploiting both suppression variables are summarised in Table XXXVI. It

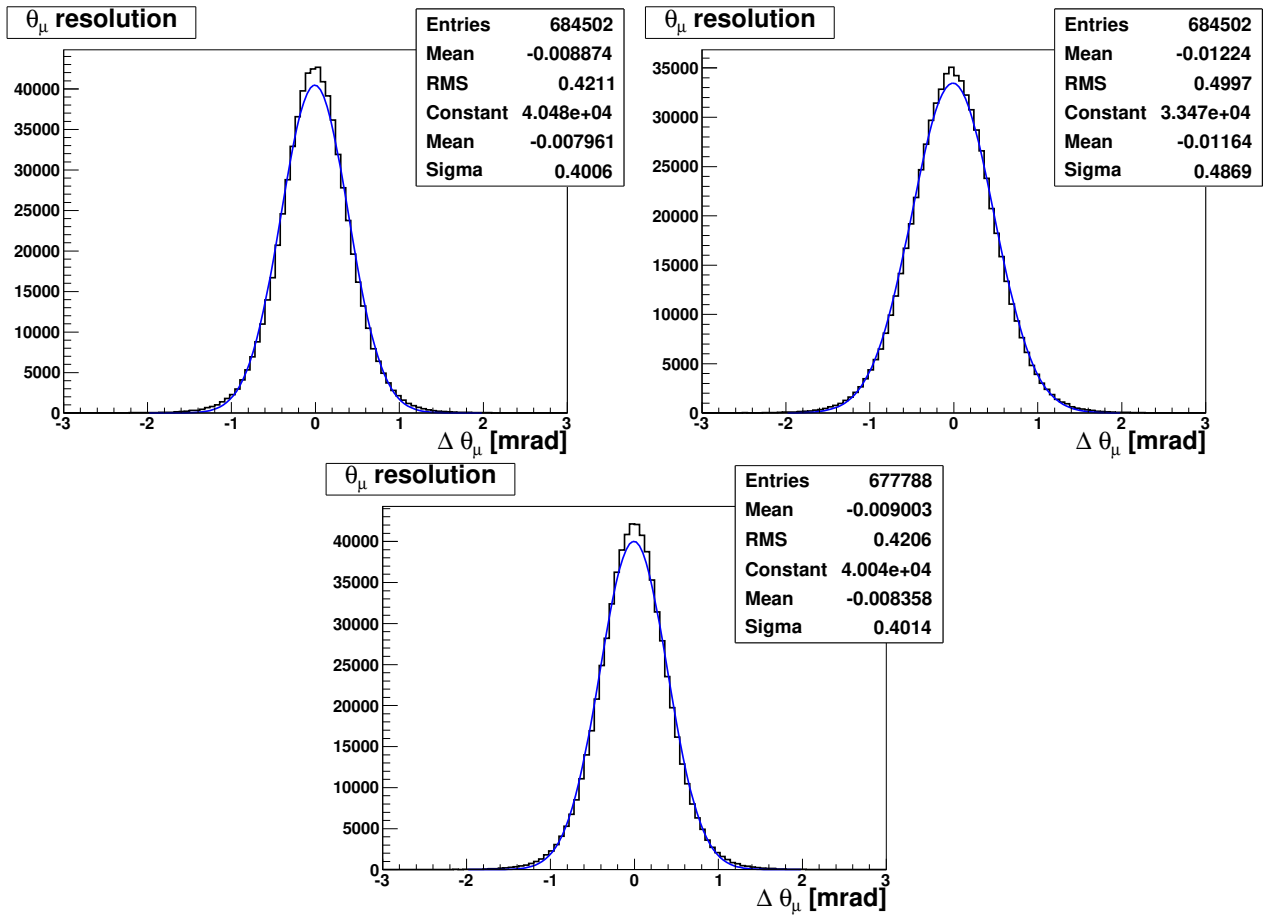

Figure 129. The difference between the reconstructed polar angle of the muons and its true value from the simulation for a fibre station made of cylindrical staggered fibres (top left), squared fibres staggered by 0.25 mm (top right) and squared fibres staggered by 0.125 mm (bottom). Gaussians are fitted to all distributions.

is seen that by imposing a suitable cut on the recoil energy and subtracting the fitted inclusive background with a muon in the final state under the leptonic peak, it is possible to evaluate statistically the number of events due to pure leptonic scattering with a precision of $\sim 1\%$. Both variables θ_μ and $\theta_\mu^2 \times E$ may be used for this task.

Conclusions

The quasi-elastic neutrino-electron scattering can be used to measure the neutrino flux coming from the Neutrino Factory storage ring. The angle θ_μ and the *inelasticity* $1 - y \sim \theta_\mu^2 \times E$ have similar discriminating power. The latter variable seems to have a flatter distribution when $\theta_\mu \to 0$.

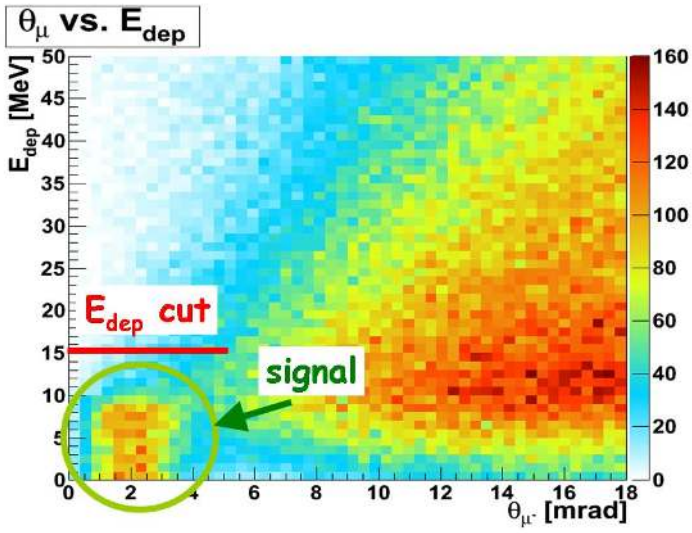

Figure 130. Energy deposition in the first illuminated scintillating slab compared to the reconstructed muon scattering angle.

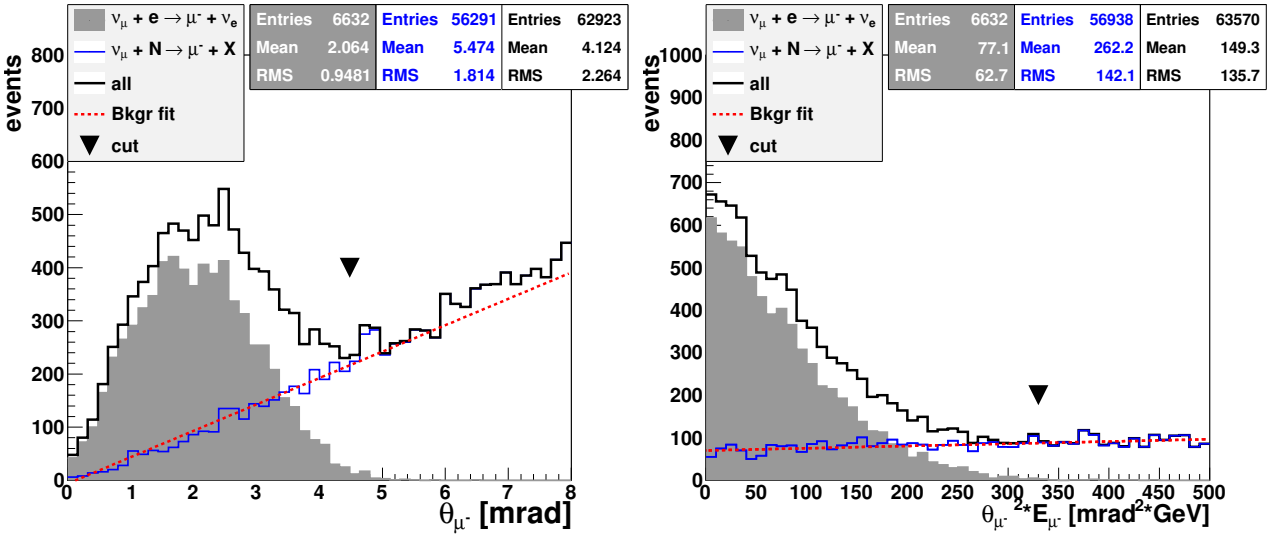

Figure 131. Distributions over the reconstructed polar angle θ_μ (left) and the *inelasticity* $\theta_\mu^2 E$ (right) of the outgoing muons. The leptonic events are filled with grey, the hadronic events are plotted in blue and the total spectrum is in black. The cut value is denoted by a black inverted triangle. The red lines indicate the background extrapolation.

Table XXXVI. Results for background extrapolation exploiting two different suppression variables. The true number of leptonic events is 6632.

Cut on	**All events below the cut**	**Bkgr events below the cut**	**Bkgr events from the fit**	**Simulated leptonic events**	**Leptonic events from the fit**
θ_μ	9450	2860	2865 ± 57	6632	6585 ± 57
$\theta_\mu^2 \times E$	9284	2666	2596 ± 74	6632	6688 ± 74

3.3.2.2. Neutrino flux measurement; neutral current elastic neutrino-electron scattering

The experimental determination of the absolute neutrino flux below 11 GeV will rely upon the measurement of neutral current elastic scattering off electrons: $\nu e^- \to \nu e^-$. The total cross section for NC elastic scattering off electrons is given by [405]:

$$\sigma(\nu_l e \to \nu_l e) = \frac{G_\mu^2 m_e E_\nu}{2\pi}\left[1 - 4\sin^2\theta_W + \frac{16}{3}\sin^4\theta_W\right] \quad (46)$$

$$\sigma(\bar{\nu}_l e \to \bar{\nu}_l e) = \frac{G_\mu^2 m_e E_\nu}{2\pi}\left[\frac{1}{3} - \frac{4}{3}\sin^2\theta_W + \frac{16}{3}\sin^4\theta_W\right] \quad (47)$$

where θ_W is the weak mixing angle. For $\sin^2\theta_W \simeq 0.23$ the cross sections are very small $\sim 10^{-42}(E_\nu/\,\mathrm{GeV})\,\mathrm{cm}^2$. Neutral current elastic scattering off electrons can be used to determine the absolute flux normalisation since the cross sections only depend upon the the knowledge of $\sin^2\theta_W$. The value of $\sin^2\theta_W$ at the average momentum transfer expected at Neutrino Factory near detector $Q \sim 0.07\,\mathrm{GeV}$ can be extrapolated down from the LEP/SLC measurements with a precision of $\sim 0.2\%$ within the Standard Model (SM). However, in order to take into account potential deviations from the SM predictions, in the flux extraction we must initially consider a theoretical uncertainty $\leq 1\%$, obtained from direct measurements of $\sin^2\theta_W$ at momentum scales comparable those that will pertain at the Neutrino Factory near detector. As discussed in Section 3.3.2.5, precision electroweak measurements with the near-detector data at a Neutrino Factory can determine the value of $\sin^2\theta_W$ to better than 0.3%. The theoretical uncertainty on the absolute flux normalisation can therefore be improved substantially by a combined analysis with the electroweak measurements.

The signature of the process $\nu_l(\bar{\nu}_l)e \to \nu_l(\bar{\nu}_l)e$ is a single electron in the final state, emitted almost collinearly with the beam direction ($\theta \sim$ mrad). The dominant backgrounds are given by NC π^0 production and single photon production in which one photon fakes a single electron. A smaller background contribution is given by ν_e quasi-elastic scattering events in which the proton is not visible. This measurement requires a detector which can distinguish between photons and electrons efficiently. The low density magnetised tracker proposed for the Neutrino Factory near detector can identify electrons and positrons and reconstruct the corresponding track parameters, allowing a background rejection $\leq 10^{-6}$. Figure 132 shows the distributions of kinematic variables for signal and background. It is thus possible to select a sample of NC elastic scattering events off electrons with

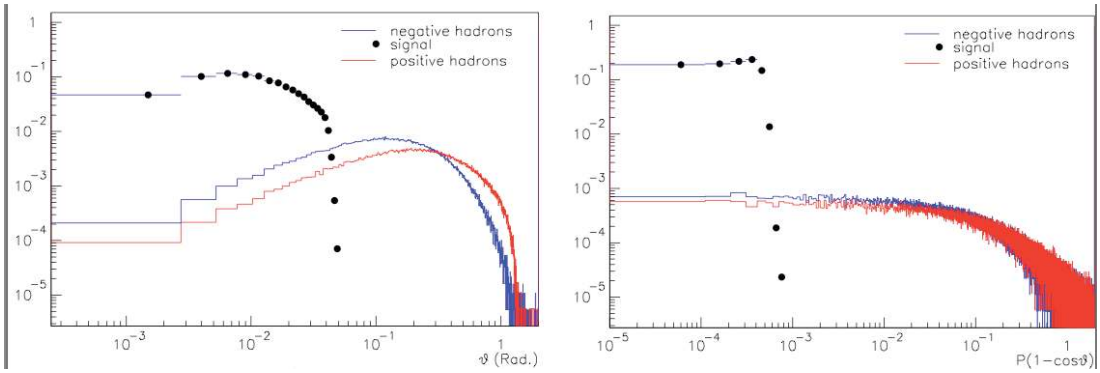

Figure 132. Distributions of the angle of the electron with respect to the beam direction (left) and of the discriminating variable $P(1-\cos\theta)$ (right) for NC elastic scattering off electrons and for the corresponding backgrounds in the near detector.

small background in the Neutrino Factory near detector. The main limitation of such a measurement is the statistics of the selected sample, which, for the Neutrino Factory near detector will not be a problem. It must be noted that in a low density magnetised design the background originates from asymmetric γ conversions in which the positron is not reconstructed. This type of background is expected to be charge-symmetric and this fact gives a powerful tool to calibrate the π^0/γ background in-situ.

3.3.2.3. Effects of High Δm^2 Oscillations on the Flux Extraction

The results described in the previous sections were obtained under the assumption that the events observed in the near detector originate from the same (anti)-neutrino flux produced by the decay of the parent muons. The recent results from the MiniBooNE experiment might suggest the possibility of relatively high Δm^2 anti-neutrino oscillations consistent with the LSND signal. This effect, if confirmed, seems to indicate a different behaviour between neutrinos and anti-neutrinos, which would imply CP or CPT violation. The MINOS experiment also reported different oscillation parameters between ν_μ and $\bar{\nu}_\mu$ from the disappearance analysis, although this result is as yet not statistically compelling.

The presence of high Δm^2 oscillations with characteristic oscillation length comparable to the near detector baseline at the Neutrino Factory energies, would imply that the spectra observed in the near detector could be already distorted by neutrino oscillations. The main effect expected on the flux extraction from a MiniBooNE/LSND oscillation is that a deficit is induced in the $\bar{\nu}_\mu$ CC spectrum from a significant disappearance rate. Any in situ determination of the fluxes would then require the unfolding of the oscillation effect from the measured spectra. The measurement strategy in the near detector should necessarily include a combined oscillation and flux analysis. Since the near detector cannot be easily moved, different complementary measurements are needed.

Several follow-up experiments have been proposed to investigate the MiniBooNE/LSND effects: move MiniBooNE to a near detector location, OscSNS at the ORNL neutron spallation source or a two-detector LAr experiment at the CERN PS. Each experiment is expected to cover the region

in the oscillation parameter space consistent with MiniBooNE/LSND data, so that, by the time the Neutrino Factory experiments will take data, the high Δm^2 oscillation hypothesis may be confirmed or disproved. However, the precision which will ultimately be achieved in the determination of the fluxes at the Neutrino Factory near detector is directly connected to the high Δm^2 oscillation parameters. If the oscillation is confirmed, we will then need dedicated precision measurements in the near detector at the Neutrino Factory.

3.3.2.4. Influence of near detector flux data on far detector sensitivities

Any neutrino near-detector facility will have many possible functions. Among these will be the measurement of the absolute flux in the direction of the far detectors. There is the possibility that this measurement could be used, in addition to the determination of the absolute normalisation, to project a non-oscillation flux prediction to the far detector site to be used in the determination of the oscillation parameters. This would require the reconstruction of the whole flux spectrum at the near detector so that the projection could be carried out reliably. The initial studies of the power of a technique for the projection of the near detector flux spectrum as a means of extracting oscillation parameters are described in the paragraphs which follow.

Flux measurement

Comparison of the neutrino flux at the near and far sites is problematic for various reasons. A detector within ∼1 km of the beam pipe subtends a far greater solid angle than a large scale detector positioned thousands of kilometres from the source. In addition, the solid angle subtended by the near detector as seen from different parts of the decay pipe varies considerably. Considering a 1 m radius near detector placed 100 m from the end of a 600 m long straight decay length and the 14×14 m^2 cross section MIND at 4 000 km from the same decay pipe it can be seen that the solid angle of the near detector as seen from the two ends of the decay pipe ranges from 6.4×10^{-6} sr to 3.1×10^{-4} sr, a range of two orders of magnitude, whereas for the far detector the solid angle ranges between 1.22×10^{-11} sr to 1.23×10^{-11} sr, up to 7 orders of magnitude smaller and varying by only 1% of the larger value. As can be seen in figure 133, this results in a different energy spectrum for near detector distances up to a distance of ∼1 km. Due to the steep angle of the beam direction, positioning the near detector facility at 1 km would be restrictively expensive, as well as problematic from an engineering standpoint. Therefore, one of the main focuses of this study must be to determine whether it is still possible to extract a prediction for the far detector flux, even if the near detector flux differs considerably from the far detector spectrum, when the near detector is positioned close to the end of the decay straight.

Direct comparison of the expected fluxes at the two sites allows for a clear determination of the change in the energy spectrum. This technique would require any near detector to have excellent energy resolution to reduce the errors in the determination of the near detector flux before projection. However, the proximity of the detector to the beam source means that a large mass is not a requirement from a statistical point of view and hence a high resolution detector constructed of multiple

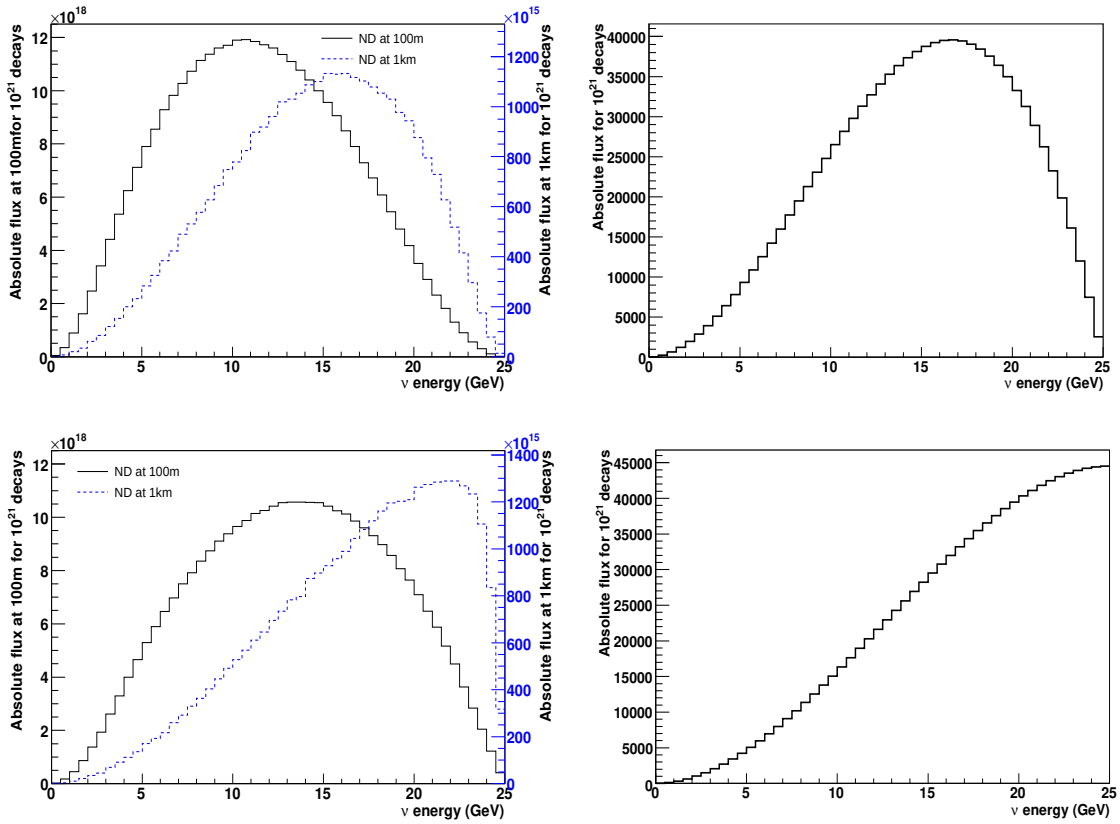

Figure 133. Difference in expected fluxes at near and far sites: (top) ν_e flux through a 1 m radius detector 100 m and 1 km from a 600 m decay straight (left) and at a 7 m radius detector 4000 km from the Neutrino Factory; (bottom) ν_μ flux for the same detectors (using unpolarised muon expectation).

sub-detectors could be built with designs based on upgrades to the NOMAD [406] or Minerva [407] detectors as possible candidates. The studies described below focus on the determination of oscillation parameters via the Neutrino Factory golden channel using a matrix representation of all aspects of the set-up and is inspired by the technique used by the MINOS collaboration [408].

Flux projection for non-oscillation prediction

The technique essentially involves three matrices describing the set-up: near detector response, flux projection and far detector response; in addition to cross-section matrices for the relevant processes and a parametrisation of the oscillation probability which is ultimately used in the determination of the sensitivity to oscillation parameters. Through purely mathematical arguments one can prove that the oscillation probability is related to the two observed signals via the relationship:

$$P_{osc} = M_{FD}^{-1} M_{dat} M_{ND} M_{nOsc}^{-1}; \tag{48}$$

where M_{FD} and M_{ND} are matrices representing the combination of cross-section and response for ν_μ ($\overline{\nu}_\mu$) at the far detector and ν_e ($\overline{\nu}_e$) at the near detector respectively, M_{nOsc} relates the expected far detector ν_e ($\overline{\nu}_e$) flux without oscillations to the expected ν_e ($\overline{\nu}_e$) flux at the near detector and M_{dat} is the ratio of the observed ν_μ ($\overline{\nu}_\mu$) interaction spectrum at the far detector to the observed ν_e ($\overline{\nu}_e$) interaction spectrum at the near detector. The extracted function would then be fit to the oscillation probability formulæto find the best fit values of the θ_{13} and δ. This technique formed the basis of the first study of the matrix method which was presented in [409].

There are, however, a number of problems with this direct method. The finite resolution of both detectors would mean the direct ratio of observed signals could not be used without some correction but, more importantly, fitting such a complex function as the oscillation formula, particularly in the low energy region, can be problematic. Inversion of the response of a detector, particularly a coarse grained calorimeter like the far detector can lead to statistical instabilities or bias in the prediction of the true energy interactions (see [410] for a more detailed discussion of this inverse problem). For these reasons the next step in the study involved a re-definition of the fitted quantity.

This updated method attempts to fit the observed far detector spectrum directly by using the projection of the observed near detector spectrum. That is, the predicted spectrum for a given grid point on the (θ_{13},δ) plane is calculated as:

$$N_{FD} = M_{FD} P_{osc}(\theta_{13}, \delta) M_{nOsc} M_{ND}^{-1} N_{ND}\,; \tag{49}$$

where N_{FD} and N_{ND} are the observed far and near detector spectra respectively, with other symbols defined as in equation 48. In this way only the higher resolution near-detector response needs to be inverted. The prediction here would, however, use binned data as opposed to using the integration of the flux calculations, so the binning used at the near detector would have to be optimised for the projection. Calculation of the expected appearance spectrum from the no-oscillation flux spectrum is aided by fine binning, however, statistical significance and detector resolution limit how fine the binning can be. An initial study using the golden-channel oscillation without backgrounds was performed and presented in [411] using a near detector with ν_e ($\overline{\nu}_e$) detection threshold of 5 GeV and energy resolution of $35\%/\sqrt{E}$.

In order to predict the interaction spectra at the far detector, the near detector would be required to measure both the ν_μ ($\overline{\nu}_\mu$) and $\overline{\nu}_e$ (ν_e) interaction spectra. The only background to the ν_μ ($\overline{\nu}_\mu$) measurement is likely to be from neutral current interactions. Using a combination of missing p_T and vertex reconstruction, both of which should be measured with high resolution at a near detector, this could be suppressed to at least the level in the far detector. The $\overline{\nu}_e$ (ν_e) measurement would require a more sophisticated analysis to achieve a pure sample. Both channels could benefit from the study of low-rate background processes such as electron scattering but these processes are limited by statistics and take place often in restricted energy ranges and as such could not be used alone to perform this analysis. Any final analysis is likely to use a combination of channels and analyses to maximise statistics and purity.

Projection of the predicted flux is carried out using scaling matrices calculated using a comparison of the true fluxes at the near and far sites. The ultimate analysis would benefit from the use of a Monte Carlo study either to quantify the additional neutrinos expected in the beam from neutral current interactions and the corrections required to take into account the near-detector resolution or to construct a probability matrix relating directly near-detector interactions to unoscillated far-detector

interactions, which is the method favoured in the MINOS analysis [408]. However, a simple scaling argument allows for the understanding of the near detector effects and can be directly compared to existing studies which do not yet take into account the effect of additional neutrinos scattered into the beam by interactions.

Comparison of near detector projection to standard fit method

An initial study of the power of this technique has been carried out assuming a 100 kg cylindrical detector of 1 m radius placed 100 m from the end of a 600 m straight decay section. The flux expected at the near detector site is predicted by generating muon decays randomly along a straight line with an appropriate beam divergence and calculating the expected spectrum from the detector acceptance as calculated for each decay position. The detector is modelled using a conservative estimate of the $\overline{\nu}_e$ (ν_e) energy resolution of $35\%/\sqrt{E}$(GeV) with efficiency rising linearly from 0% at 0 GeV up to 70% above 4 GeV. The ν_μ ($\overline{\nu}_\mu$) resolution is set at $20\%/\sqrt{E}$(GeV), with efficiency of 80% for $\overline{\nu}_\mu$ and 60% for ν_μ above 4 GeV (similar to the far detector). A full detector simulation is not yet available to test the validity of these assumptions or to estimate the background levels, as such the current study assumes the two signals are separated without background.

A smear is performed on the calculated interactions at the near detector and the flux and correlation matrices for each channel and the far detector are then projected to the appropriate far detector in bins of width 0.5 GeV. The total integrated interaction spectra expected at a near detector over a data taking run of 5 years allows the flux through the detector to be predicted to a high level of accuracy using the inversion of the response matrices (see figure 134). Only slight oscillation of the predicted values is visible at higher energies. However, the quality of the prediction is likely to be worse if the technique were to be used for a limited data-set, or if the efficiencies or energy resolutions were reduced. In the future a more sophisticated unfolding will be developed.

The far detector spectra are calculated with the non-oscillation predictions from the near detector. The far-detector spectra obtained are then used to perform a fit using the function:

$$\chi^2 = \sum_i \sum_j (N_{i,j} - n_{i,j}) V_{i,j}^{-1} (N_{i,j} - n_{i,j})^T ; \tag{50}$$

where i is the detector baseline, j the polarity, N the predicted spectrum, n the data spectrum and V the correlation matrix, composed of the projected matrix of the prediction and the expected errors on the far detector measurement. Figure 135 shows the results of fits to a range of θ_{13} and δ values using this technique (left) compared to similar fits performed in which the neutrino flux is allowed to be part of the fit (right), rather than be constrained by the near-detector data. As can be seen, the resolution of θ_{13} is as good or better using the projection technique. Resolution of δ is generally better for large θ_{13} but reduces to a similar level for $\theta_{13} \leq 1^\circ$.

This tendency is illustrated in figure 136 for a set of true values of $\theta_{13} = 1^\circ$ and $\delta = 45^\circ$ where the minimum χ^2 is projected onto each axis in turn. At the 1σ level ($\chi^2 - \chi^2_{min} = 1$) the fit to θ_{13} is very similar for both methods, however, the near-far projection is already better at the 3σ level ($\chi^2 - \chi^2_{min} = 9$). The projection onto the δ axis for both methods is very similar, although for this example case the true value is a better fit in the case of the near-far-projection method.

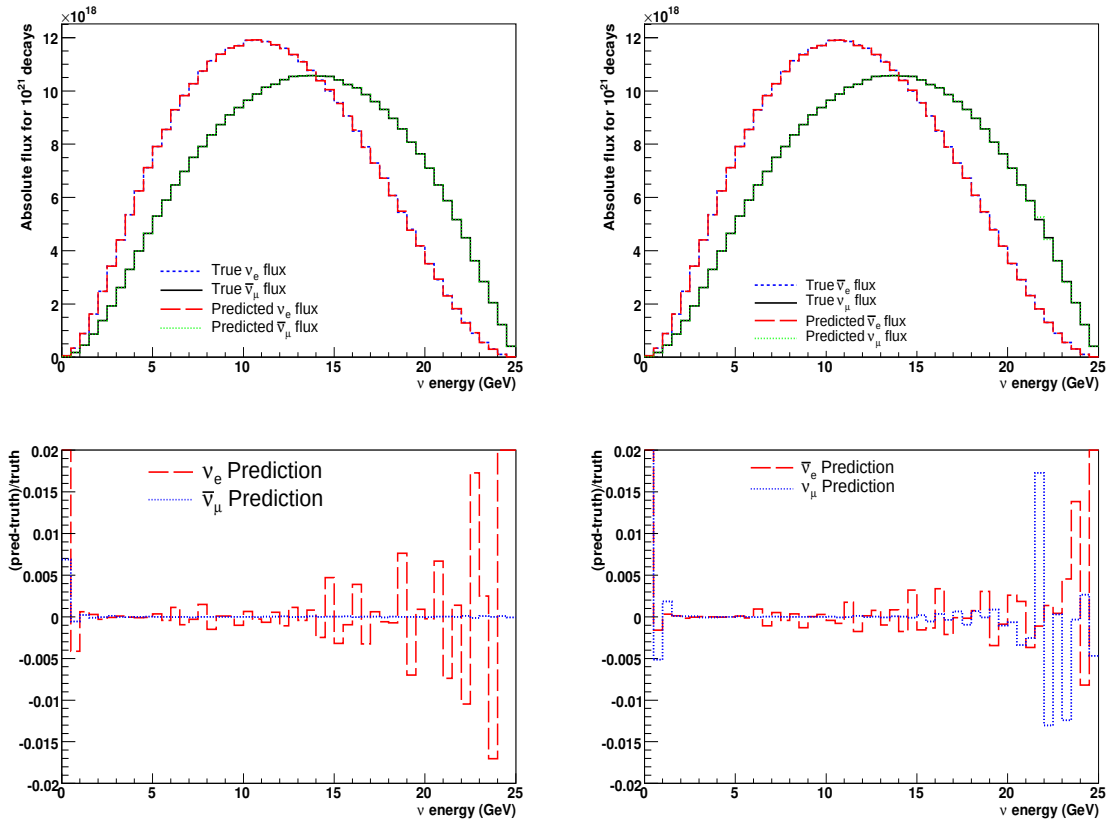

Figure 134. Comparison of predicted to true flux through the near detector for stored μ^+ (left) and stored μ^-(right). (top) Actual spectra and (bottom) fractional residuals.

Figure 137 shows the trend for the measurement of the oscillation parameters for both the near-far projection method and the fitted-flux method. In both cases, 1σ errors are garnered from the projection of the minimum χ^2 onto the appropriate axis and θ_{13} is determined very precisely, with the true value being the best fit value in most cases. Determination of δ is not as precise, with the precision of the near-far projection method being somewhat better. Considering the deviation of the best fit delta value from the true value, it can be seen that the mean difference for the standard method is $\sim 0.9\sigma$ whereas for the projection method it is $\sim 0.6\sigma$.

Conclusions

A basic method for the projection of the observed near detector spectrum at the Neutrino Factory to the far-detector sites has been developed. Under the assumption of pure near detector signals it has been shown that this projection can be used to predict accurately the far detector spectrum in the absence of oscillations. While in its current form this method has no clear advantage at the 1σ

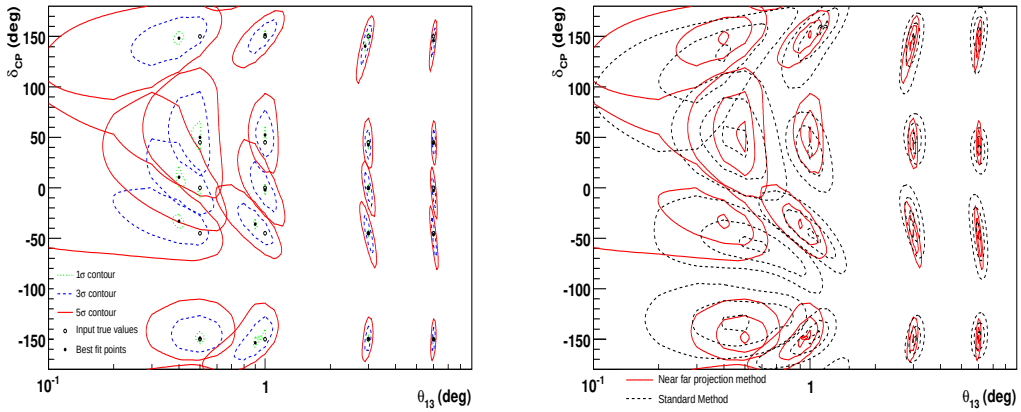

Figure 135. Fits to simulated data using the near-far prediction (left) and compared to equivalent fits performed allowing the flux to be determined as part of the fit (right). All fits assume normal hierarchy.

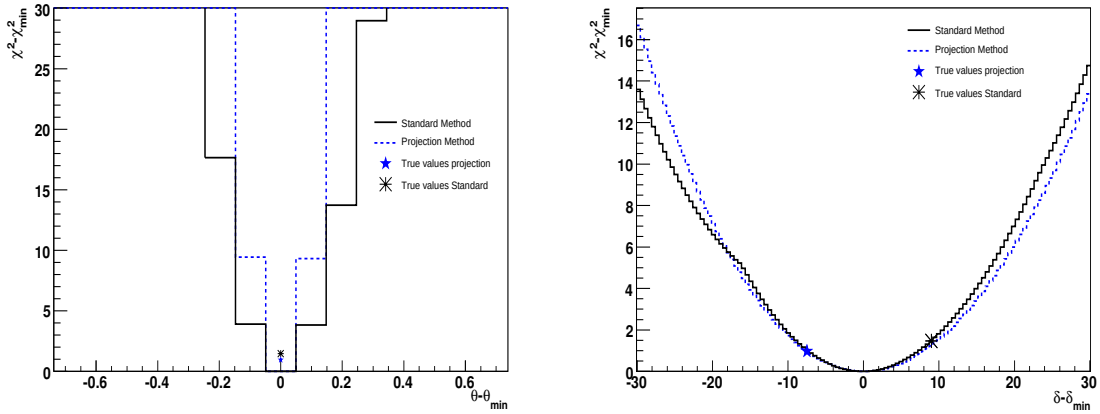

Figure 136. Projection of the minimum χ^2 onto the θ_{13} axis (left) and the δ axis (right) for $\theta_{13} = 1°$ and $\delta = 45°$.

level over a method in which the flux is extracted from the fit directly, there seems to be evidence of improved sensitivity at 3σ. These preliminary results show the potential for a high-resolution near detector to improve the precision with which the oscillation parameters can be measured.

3.3.2.5. Study of neutrino interactions

The unprecedented neutrino fluxes available for the Neutrino Factory program will allow the collection of a large number of inclusive neutrino charged current (CC) interactions. As discussed above, the

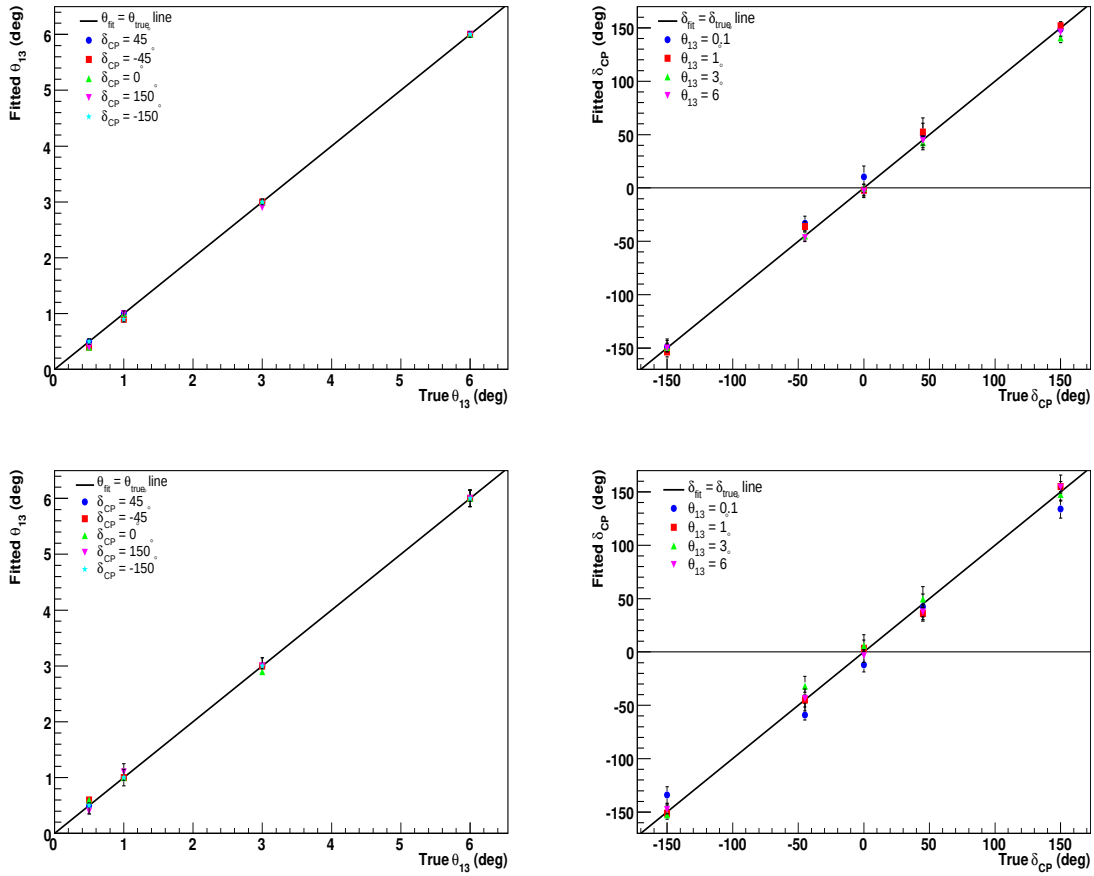

Figure 137. Quality of fit to θ_{13} (left) and δ (right) for a range of values. Using the near-far projection method (top) and a method in which the neutrino flux is part of the fit (bottom).

reduction of systematic uncertainties for the neutrino oscillation program requires a highly segmented near detector, thus providing excellent resolution in the reconstruction of neutrino events. The combination of this substantial flux with a finely segmented near detector offers a unique opportunity to produce a range of neutrino scattering physics measurements, in addition to those needed by the long base line oscillation program. The combined statistics and precision expected in the near detector will allow precise tests of fundamental interactions and better understanding of the structure of matter. Given the broad energy range of the beam, a diverse range of physics measurements is possible in the Neutrino Factory near detector. To provide a flavour for the outstanding physics potential, we give a short description of the studies that can be performed at a Neutrino Factory near detector for a few selected topics. A more detailed and complete discussion of the short baseline physics potential will appear in a separate physics working group paper and in subsequent Neutrino Factory reports.

Electroweak Physics

Neutrinos are a natural probe for the investigation of electroweak physics. Interest in a precise determination of the weak mixing angle ($\sin^2\theta_W$) at Neutrino Factory energies via neutrino scattering is twofold: a) it provides a direct measurement of neutrino couplings to the Z boson and b) it probes a different scale of momentum transfer than LEP by virtue of not being on the Z pole. The weak mixing angle can be extracted experimentally from three main NC physics processes:

1. Deep inelastic scattering off quarks inside nucleons: $\nu N \to \nu X$;
2. Elastic scattering off electrons: $\nu e^- \to \nu e^-$; and
3. Elastic scattering off protons: $\nu p \to \nu p$.

The most precise measurement of $\sin^2\theta_W$ in neutrino deep inelastic scattering (DIS) comes from the NuTeV experiment, which reported a value that is 3σ from the Standard Model [412]. The Neutrino Factory near detector can perform a similar analysis in the DIS channel by measuring the ratio of NC and CC interactions induced by neutrinos:

$$\mathcal{R}^\nu \equiv \frac{\sigma^\nu_{\rm NC}}{\sigma^\nu_{\rm CC}} \simeq \rho^2 \left(\frac{1}{2} - \sin^2\theta_W + \frac{5}{9}(1+r)\sin^4\theta_W \right) \tag{51}$$

where ρ is the relative coupling strength of the neutral to charged current interactions ($\rho = 1$ at tree level in the Standard Model) and r is the ratio of anti-neutrino to neutrino cross section ($r \sim 0.5$).

The measurement of $\sin^2\theta_W$ from DIS interactions can be performed with a low density magnetised tracker since an accurate reconstruction of the NC event kinematics and of the ν_e CC interactions are crucial to keep the systematic uncertainties on the event selection under control. The analysis selects events in the near detector after imposing a cut on the visible hadronic energy of $E_{\rm had} > 3$ GeV, as in the NOMAD $\sin^2\theta_W$ analysis (the CHARM analysis had $E_{\rm had} > 4$ GeV).

The use of a low density magnetised tracker can substantially reduce systematic uncertainties with respect to a massive calorimeter. The largest experimental systematic uncertainty in NuTeV is related to the subtraction of the ν_e CC contamination from the NC sample. Since the low density tracker at the Neutrino Factory can efficiently reconstruct the electron tracks, the ν_e CC interactions can be identified on an event-by-event basis, reducing the corresponding uncertainty to a negligible level. Similarly, uncertainties related to the location of the interaction vertex, noise, counter efficiency etc. are removed by the higher resolution and by the different analysis selection.

A second independent measurement of $\sin^2\theta_W$ can be obtained from NC $\nu_\mu e$ elastic scattering. This channel has lower systematic uncertainties since it does not depend upon the knowledge of the structure of nuclei, but has limited statistics due to its very low cross section. The value of $\sin^2\theta_W$ can be extracted from the ratio of neutrino to anti-neutrino interactions [405]:

$$\mathcal{R}_{\nu e}(Q^2) \equiv \frac{\sigma(\bar\nu_\mu e \to \bar\nu_\mu e)}{\sigma(\nu_\mu e \to \nu_\mu e)}(Q^2) \simeq \frac{1 - 4\sin^2\theta_W + 16\sin^4\theta_W}{3 - 12\sin^2\theta_W + 16\sin^4\theta_W} \tag{52}$$

in which systematic uncertainties related to the selection and electron identification cancel out.

The extraction of the weak mixing angle is dominated by the systematic uncertainty on the $\bar\nu_\mu/\nu_\mu$ flux ratio, which enters equation 52. At a Neutrino Factory this systematic uncertainty will be considerably reduced over conventional beam facilities used for previous studies. Together, the DIS and the NC elastic scattering channels involve substantially different scales of momentum transfer,

providing a tool to test the running of $\sin^2\theta_W$ in a single experiment. To this end, the study of NC elastic scattering off protons can provide additional information since it occurs at a momentum scale which is intermediate between the two other processes. Furthermore, in the two NC elastic processes off electrons and protons it is possible to reconstruct the Q^2 on an event-by-event basis, providing additional sensitivity.

Strange Content of the Nucleon

The role of the strange quark in the proton remains a central investigation in hadronic physics. The interesting question is to what extent the strange quarks contribute substantially to the nucleon vector and axial-vector currents. A large observed value of the strange quark contribution to the nucleon spin (axial current), Δs, would require further theoretical speculations with respect to present assumptions. The nucleon spin structure also affects the couplings of axions and supersymmetric particles to dark matter. To better understand this, experiments at MIT/Bates, Mainz, and Jefferson Lab probed and continue to probe the contribution of strange quarks to the electromagnetic (vector) current. However, the only reliable measurement of Δs can be obtained from the detection of neutrino-proton NC elastic scattering, $\nu p \to \nu p$. In the limit $Q^2 \to 0$, the differential cross section is proportional to the square of the iso-vector axial-vector form factor plus/minus the strange axial form factor, $(G_A \pm G_s)^2$, where $G_s^2(Q^2 = 0) = \Delta s$. Unfortunately, previous neutrino scattering experiments have not been precise enough to provide a definitive statement on the contribution of the strange sea to either the axial or vector form factor. The Neutrino Factory near detector neutrino beam will be sufficiently intense that a measurement of NC elastic scattering can provide a definitive statement on the contribution of the strange sea to either the axial or vector form factor. Systematic uncertainties can be reduced by measuring the NC/CC ratios for both neutrinos and anti-neutrinos as a function of Q^2:

$$\mathcal{R}_{\nu p}(Q^2) \equiv \frac{\sigma(\nu_\mu p \to \nu_\mu p)}{\sigma(\nu_\mu n \to \mu^- p)}(Q^2); \qquad \mathcal{R}_{\bar{\nu} p}(Q^2) \equiv \frac{\sigma(\bar{\nu}_\mu p \to \bar{\nu}_\mu p)}{\sigma(\bar{\nu}_\mu p \to \mu^+ n)}(Q^2) \tag{53}$$

Structure of the Nucleon

The following have been identified as important physics topics to address the structure of the nucleon at a near detector of a Neutrino Factory:

- Measurement of form factors and structure functions;
- QCD analysis of parton distribution functions;
- d/u parton distribution functions at large Bjorken-x;
- GLS sum rule and α_s;
- Non-perturbative contributions and higher twists;
- Quark-hadron duality; and
- Generalised parton distributions.

Parton Distribution Functions

A QCD analysis of the near detector data in the framework of global fits to extract parton distribution functions is a crucial step to constrain systematic uncertainties on the electroweak measurements. In addition, precision measurements of (anti)-neutrino structure functions and differential cross sections would directly affect the long-baseline oscillation searches, providing an estimate of all background processes which are dependent upon the angular distribution of the outgoing particles in the far detector.

For quantitative studies of inclusive deep-inelastic lepton-nucleon scattering, it is vital to have precise F_3 structure functions, which can only be measured with neutrino and antineutrino beams, as input into global PDF fits. Because it depends on weak axial quark charges, the F_3 structure function is unique in its ability to differentiate between the quark and antiquark content of the nucleon. On a proton target, for instance, the neutrino and antineutrino F_3 structure functions (at leading order in α_s) are given by:

$$xF_3^{\nu p}(x) \;=\; 2x\left(d(x) - \bar{u}(x) + \bar{s}(x) + \cdots\right) ; \text{and} \tag{54}$$

$$xF_3^{\bar{\nu} p}(x) \;=\; 2x\left(u(x) - \bar{d}(x) - \bar{s}(x) + \cdots\right) . \tag{55}$$

In contrast, electromagnetic probes are sensitive only to a sum of quark and antiquark PDFs. Unfortunately, the neutrino scattering cross sections have considerably larger uncertainties than the electromagnetic inclusive cross sections at present. The high intensity Neutrino Factory facility offers the promise to reduce the gap between the uncertainties on the weak and electromagnetic structure functions, and would have a major impact on global PDF analyses. In addition to data in the DIS region, there is considerable interest in obtaining data at low Q^2 (down to $Q^2 \sim 1$ GeV^2) and low W ($W < 2$ GeV).

Global PDF fits show that at large values of (Bjorken) x ($x > 0.5 - 0.6$) the d quark distribution (or the d/u ratio) is very poorly determined. The main reason for this is the absence of free neutron targets. Because the electric charge on the u quark is larger than that on the d, the electromagnetic proton F_2 structure function data provide strong constraints on the u quark distribution, but are relatively insensitive to the d quark distribution. To constrain the d quark distribution as a function of the hadronic four-momentum transfer squared, t, a precise knowledge of the corresponding neutron F_2^n structure functions is required, which in practice is extracted from inclusive deuterium F_2 data. At large values of x the nuclear corrections in deuterium become large and, more importantly, strongly model dependent, leading to large uncertainties on the resulting d quark distribution.

Perhaps the cleanest and most direct method to determine the d/u ratio at large x is from neutrino and antineutrino DIS on hydrogen. Should a hydrogen target at the Neutrino Factory near detector become available, a new measurement of neutrino and antineutrino DIS from *hydrogen* would offer significantly improved uncertainties and could therefore make an important discovery about the d/u behaviour as $x \to 1$. To be competitive with the proposed JLab 12 GeV experiments, the kinematic reach would need to be up to $x \sim 0.85$ and with as large a Q^2 range as possible to control the higher twist and other sub-leading effects in $1/Q^2$.

3.3.3. Near detector baseline design

3.3.3.1. Option A - scintillating fibre tracker

This option considers a low Z, high resolution scintillating fibre tracker. It is composed of consecutive modules placed perpendicular to the beam axis (figure 138a). Each module (figure 138b) has two volumes: an absorber made of plastic scintillator slabs and a fibre station made of thin scintillating fibres. The recoil hadronic energy is measured in the absorber, while the fibre station reconstructs particle tracks with high angular resolution.

The overall thickness of the absorber is 5 cm. It is subdivided into five layers perpendicular to the beam axis. The light attenuation in the material of the slabs introduces a dependence of the measured signal on the position of the particle hit, which can be eliminated by reading the signal from the absorber scintillator slabs at both edges of a slab.

The fibre station (figure 138c) consists of 4 layers of fibres with horizontal orientation and 4 layers of fibres with vertical orientation. Three different conceptual designs for the fibre station are under consideration. The first one is a station made of cylindrical 0.5 mm thick fibres (figure 138c-bottom). For this design, the position of the fibres in a given layer is shifted by 0.25 mm relative to the fibres in the neighbouring layer. The other two options consider a station made of squared 0.5 mm thick fibres with a displacement between neighbouring layers of 0.25 mm and 0.175 mm respectively (figure 138c-top). In all three options the fibre-station thickness is 4 mm and the station consists of $\sim 12\,000$ fibres. Our baseline option is a detector made of 20 consecutive modules. Thus, the overall detector dimensions are $1.5 \times 1.5 \times 1.08\,\mathrm{m}^3$ that corresponds to a total mass of ~ 2.5 Ton.

In order to achieve maximal resolution on the muon scattering angle the detector volume should be free of magnetic field. Such a choice implies an additional magnetised detector, placed downstream of the scintillating fibre tracker to measure the sign, momentum and trajectory of the outgoing muons.

3.3.3.2. Option B - High resolution straw tube tracker

We propose here a possible high resolution straw tube tracker inspired by the HiResMν near detector [413] being considered for the LBNE project at Fermilab [414, 415]. In this section we describe the detector being considered for LBNE, which would have identical features to the one at a Neutrino Factory.

Building upon the NOMAD-experience [416], we propose a low-density tracking detector with a fiducial mass of 7.4 Ton as a neutrino target. The active-target tracker will have a factor of two more sampling points along the z-axis (ν -direction) and a factor of six more sampling points in the plane transverse to the neutrino compared to the NOMAD experiment. The proposed detector will further enhance the resolving power by having an order of magnitude more tracking points and coverage for side-exiting neutrals and muons.

We are proposing straw-tube trackers (STT) for the active neutrino target, similar to the ATLAS Transition Radiation Tracker [417–419] and the COMPASS detector [420]. The tracker will be composed of straw tubes with 1 cm diameter, in the vertical (y) and horizontal (x) directions. In front of each module a plastic radiator made of many thin foils allows the identification of electrons through

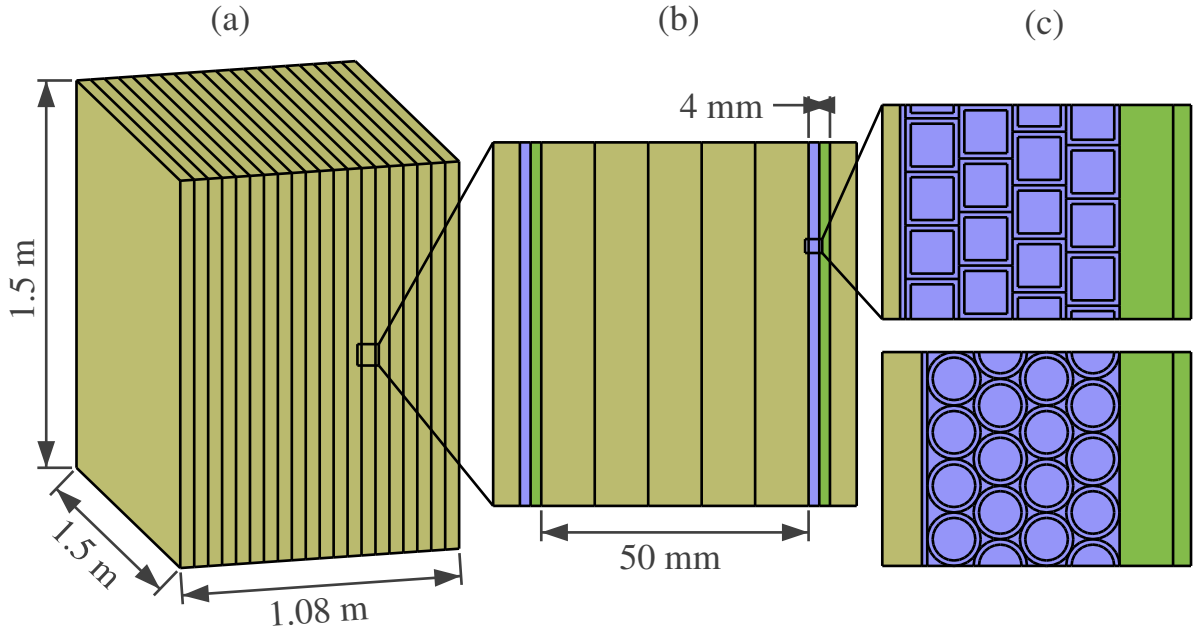

Figure 138. Schematic drawing of the scintillating fibre tracker (a). In each fibre station (b,c) the layers of fibres with horizontal orientation are in blue and the layers with vertical orientation are in green. The absorbers are shown in brown.

their transition radiation. The nominal fiducial volume for CC analysis is: $350 \times 350 \times 600$ cm^3, corresponding to 7.4 tons of mass with an overall density $\rho < 0.1$ g/cm^3.

The STT will be surrounded by an electromagnetic calorimeter (sampling Pb/scintillator) covering the forward and side regions. Both sub-detectors will be installed inside a dipole magnet providing a magnetic field of ~ 0.4 T. An external muon detector based upon Resistive Plate Chambers (RPC) will be placed outside of the magnet (see figure 139).

The neutrino target will be mainly composed of carbon, with a radiation length of about 5 m and space-point resolution around 200 μm. The momentum resolution is dominated by multiple scattering for tracks 1 m long ($\Delta p/p = 0.05$), while the measurement error for $p = 1$ GeV tracks would be $\Delta p/p = 0.006$. The proposed detector will measure track position, dE/dx, and transition radiation (with Xe filling) over the entire instrumented volume. The unconverted photon energy will be measured in the calorimeters with a target energy resolution of $\sim 10\%/\sqrt{E}$. The detector will provide:

- Full reconstruction of charged particles and gammas;
- Identification of electrons, pions, kaons, and protons from dE/dx;
- Electron (positron) identification from transition radiation ($\gamma > 1\,000$);
- Full reconstruction and identification of protons down to momenta of 250 MeV; and
- Reconstruction of electrons down to momenta of 80 MeV from curvature in the B-field.

The proposed near detector will measure the relative abundance, the energy spectrum, and the detailed topologies for ν_μ, $\overline{\nu}_\mu$, ν_e and $\overline{\nu}_e$ induced interactions, including the momentum vectors of

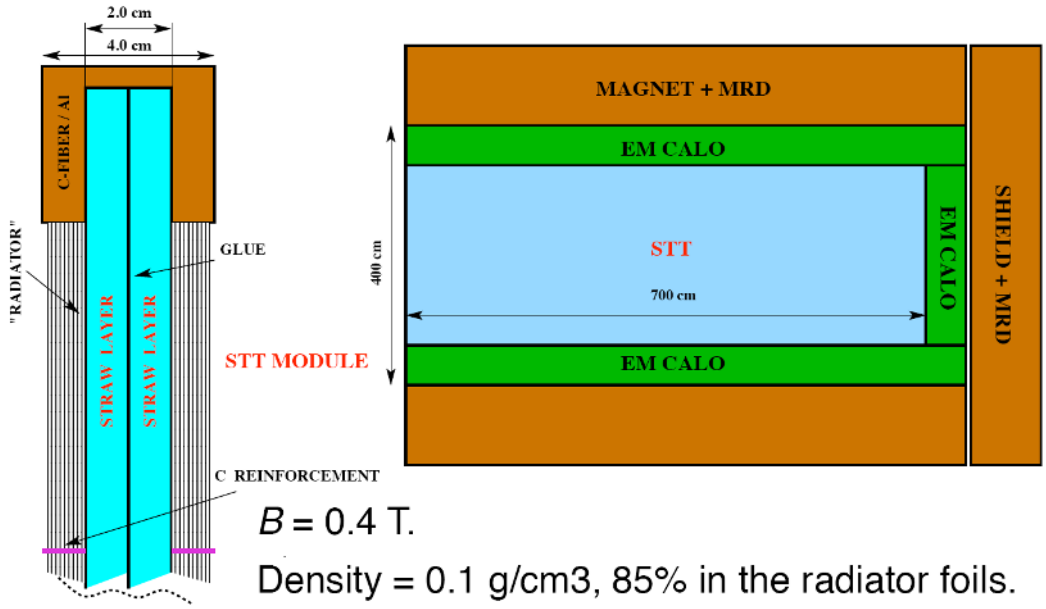

Figure 139. Sketch of the proposed HiRes detector showing the inner straw tube tracker (STT), the electromagnetic calorimeter (EM CALO) and the magnet with the muon range detector (MRD). Also shown is one module of the proposed straw tube tracker (STT). Two planes of straw tubes are glued together and held by an aluminium frame.

negative, positive and neutral (π^0, K_s^0, Λ and $\overline{\Lambda}$) particles composing the hadronic system. A NC event candidate in NOMAD, shown in figure 140, gives an idea of the precision with which the charged-particles and the forward gammas were measured. Detailed simulations of this detector have been carried out in the context of the LBNE proposals [421]. These simulations will be adapted to the neutrino spectra at a Neutrino Factory to derive the performance parameters of this detector in this context. We expect to present such performance parameters in the Reference Design Report.

3.3.3.3. Charm and Tau Detector

A near detector at a Neutrino Factory must measure the charm cross-section to validate the size of the charm background in the far detector, since this is the main background to the wrong-sign muon signature (see section 3.2.1). The charm cross-section and branching fractions are poorly known, especially close to threshold, so a near detector would need to be able to detect charm particles. Data available for charm cross-sections from neutrino interactions result from dimuon events in large mass neutrino experiments or from high resolution emulsion detectors operating at neutrino beams (for a comprehensive review see [422] and references therein). Recent results come from the dimuon data in the CHORUS [423] (8 910 neutrino induced and 430 antineutrino induced dimuon events) and NOMAD [424] experiments ($\sim$ 15 000 dimuon events). The theoretical uncertainty in the charm cross-section arises from the errors in the strange sea content of the nucleon, the semi-leptonic charm

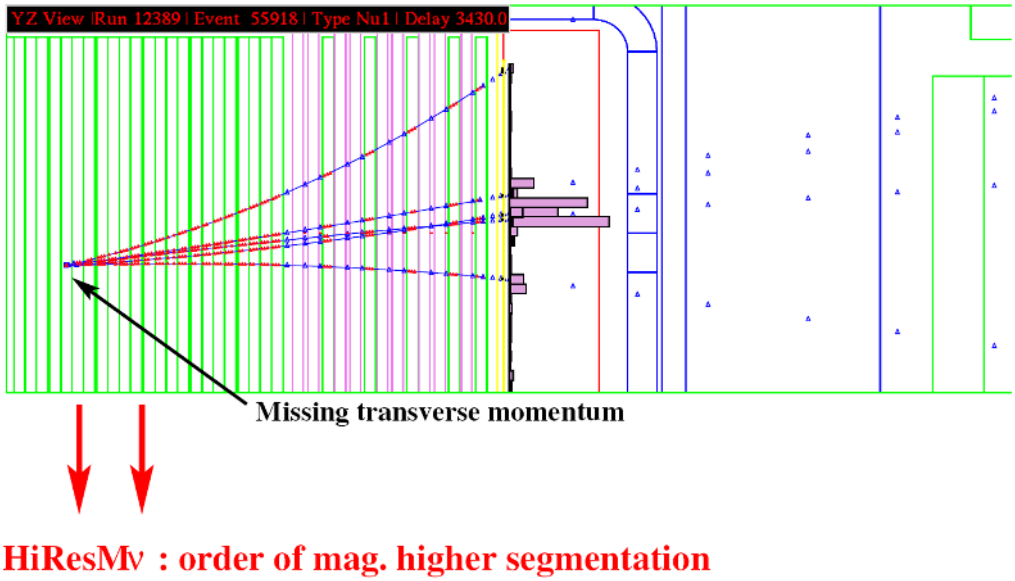

Figure 140. Candidate NC Event in NOMAD. Tracking charged particles in the HiRes detector will provide a factor of two higher segmentation along z-axis and a factor of six higher segmentation in the transverse-plane compared to NOMAD.

to muon branching fraction (with a 10% relative error) and the longitudinal structure function (F_L) and higher-twist effects. For this reason, it is paramount to make an independent near detector measurement of the charm cross-section with of order 10^6 charm events and make the error in the charm cross-section negligible in the estimation of the neutrino oscillation background.

Since tau events have a similar signature to charm events, any detector that can measure charm should be able to measure taus as well. This is important to explore couplings of Non Standard Interactions (NSI) at source $\epsilon^s_{\tau\mu}$, $\epsilon^s_{\tau e}$ or detection $\epsilon^d_{\tau\mu}$, $\epsilon^d_{\tau e}$(see section 1.6 for a comprehensive treatment). Either an emulsion based detector or a semiconductor vertex detector for charm and tau detection could be used for this purpose.

A near detector at about 100 m from the muon decay ring needs to operate in a high intensity environment ($\sim 10^9$ ν_μ CC events per year in a detector of mass 1 ton). The ideal detector to identify the decay topologies of tau leptons and charmed hadrons should be able to cope with the neutrino event rate and any background from the facility. While in principle, the muons are bound inside the storage ring, a calculation of the expected muon escape probability has not been performed yet and would likely be due to rare processes (for example, stray muons either escaping early in one of the arcs or the early part of the straight section and end up scattered towards the near detector). Should this be a problem, active shielding with magnetised iron toroids to sweep away stray muons could be used. Another background problem will be due to photons. Passive shielding, for example, for example using 30–50 X_0 of high-Z material, will be required to remove electromagetic radiation arising from radiative muon decay (1.4%) and radiation from the decay electrons. However, this shielding will in turn cause "neutrino radiation" from neutrino interactions in the shielding itself to create a large muon flux upstream of the near detector. The shielding could be made active and could be used as

a beam profile monitor and, if sufficiently segmented, could be used to measure the beam divergence. A solution to shielding in the near detector has not been found yet and will be studied in time for the Reference Design Report.

Notwithstanding the above mentioned considerations for background shielding, the near detector is required to:

- Have high resolution to identify the short-lived charm hadrons and tau leptons;
- Measure the momentum and the charge of decay particles; and
- Perform a complete and accurate kinematic reconstruction of neutrino events.

In the next two sections we identify two different ways of achieving these goals, one with an emulsion-based detector and the other with a silicon vertex detector.

Emulsion Detector

Nuclear emulsions are a very well proven technology operating on neutrino and charged-particle beams since the 1950s. Emulsion technology, pure nuclear emulsion and Emulsion Cloud Chamber (ECC) targets, has already demonstrated that it is a superb technique for the study of decay topologies [425–431]. A discussion of the performance that has been achieved in previous emulsion-based experiments is beyond the scope of this section. We recall only the outstanding accuracy of this technology in detecting short-lived particles with an excellent signal to background ratio. For details we refer to [432, 433] and references therein.

So far the largest emulsion film production for a high-energy physics experiment is the one for the OPERA detector [434]. Therefore, in the following we consider the emulsion films used for the OPERA target [435]. Each film has transverse dimensions $10 \times 13\,\mathrm{cm}^2$ and consists of a $44\,\mu$m thick emulsion layer on both sides of a $205\,\mu$m thick triacetyl cellulose (TAC) base. The radiation length of the nuclear emulsions is 5.5 cm and of the TAC base 31 cm, while the density is $2.84\,\mathrm{g/cm}^3$ and $1.35\,\mathrm{g/cm}^3$ respectively.

The possibility of exploiting the emulsion technology for a near detector has been already discussed in [6]. It was stressed that the main issue is whether it can cope with the high rate that will be observed at a Neutrino Factory. Here we estimate the practical limits and the performance that could be envisaged for a detector based on the emulsion technology in a very intense neutrino beam. We consider a pure emulsion target, followed by a magnetic spectrometer, exploiting nuclear emulsions as a high-precision (sub-micron) tracker.

The target proposed consists of a sequence of 150 films for a total length of about 4.6 cm. Therefore, the proposed target weight is 1 kg and has a thickness of about $0.2\,X_0$. An important issue is the number of interactions that can be stored in the target whilst preserving the capability of connecting them unambiguously with the hits recorded by the electronic detectors. Experience with OPERA bricks exposed to a neutrino beam, and integrating over thousands of interactions, shows that up to 10 neutrino interactions per cm^3 can be stored [436]. Therefore, in a target (about 500 cm^3 of nuclear emulsions) we can collect up to 5 000 neutrino interactions.

Downstream of the target, we consider a spectrometer: consisting of a sandwich of nuclear emulsions and very light material that we call a "spacer". This material provides a long lever arm between two consecutive emulsions (tracking devices) with a stable mechanical structure. A Rohacell plate, a few centimetres thick, fulfils this requirement. The trajectory measured with the emulsions which precede

and follow the spacer provides the measurement of the charge and momentum of the particle. The total length of the target plus spectrometer is of the order of 10 cm.

Emulsion spectrometers have also been exposed to charged particle beams of 0.5, 1.0 and 2.0 GeV [437]. The spectrometer was composed of three emulsion sheets interleaved with two spacers, each of which produces an air gap of 15 mm, and immersed in a dipole magnetic field of 1.06 T. The measured momentum resolution in the range 0.5 to 2.0 GeV is $13.3 \pm 0.3\%$.

Monte Carlo simulations have been performed in order to compute the momentum resolution and the charge identification efficiency of the spectrometer. Depending on the magnetic field, on the relative alignment of the emulsion plates in the spectrometer and on the spectrometer geometry, the momentum resolution for a 10 GeV muon is better than 25%, with a charge misidentification better than 0.2%. As far as the electrons are concerned, the momentum resolution is as good as in the muon case, while the charge misidentification is much worse due to showering. Very preliminary results show that the electron charge misidentification is of the order of 40%. However, further studies are needed before we can draw firm quantitative conclusions on the electron charge misidentification.

Although it is not the goal of this study, it is worth noting that downstream of the spectrometer we have to place an electronic detector with the aim of providing the time stamp for the events. We plan to perform the scanning of the events without any electronic detector prediction. Therefore, time information is essential in order to match the emulsion information to that of the electronic detector to allow separation of the charged-current and neutral-current events. Furthermore, this electronic detector is also needed to identify primary electrons. Given the expected event density in the target and its dimension, the electronic detector will be able to provide the time stamp only if it has a position accuracy of the order of 50 μm. Therefore, one could imagine synergy between the emulsion detector and an electronic detector (either a silicon or scintillating fibre detector) operating on the same beam-line.

The final question that needs to be addressed is whether an emulsion based detector can operate close to the storage ring of a Neutrino Factory. A dedicated study to answer this question will be carried out in time for the Reference Design Report.

Silicon vertex detector

The second possible detector capable of identifying short lived particles at a near detector of a Neutrino Factory is a silicon vertex tracker. The advantage of this type of detector is that it is able to operate at a high event rate and still have very good spatial resolution. This is necessary to distinguish the primary neutrino interaction vertex from the secondary vertex due to the short lived charm hadron or the tau lepton. Downstream of the vertex detector, we need a tracking detector capable of distinguishing electrons from muons in a magnetic field. So, a possible configuration could consist of a silicon strip or pixel detector, followed by either the scintillating fibre tracker or the straw tube tracker mentioned in the previous section.

Such a vertex detector could be similar to the NOMAD–STAR detector that was installed upstream of the first drift chamber of the NOMAD neutrino oscillation experiment [416] (see figure 141). The main aim of this detector was to test the capabilities of silicon detectors for short-baseline neutrino oscillation searches [438, 439]. However, this set-up can mimic a possible design for a near detector at

a Neutrino Factory [440]. It was used to measure the impact parameter and double-vertex resolution to determine the charm-detection efficiency.

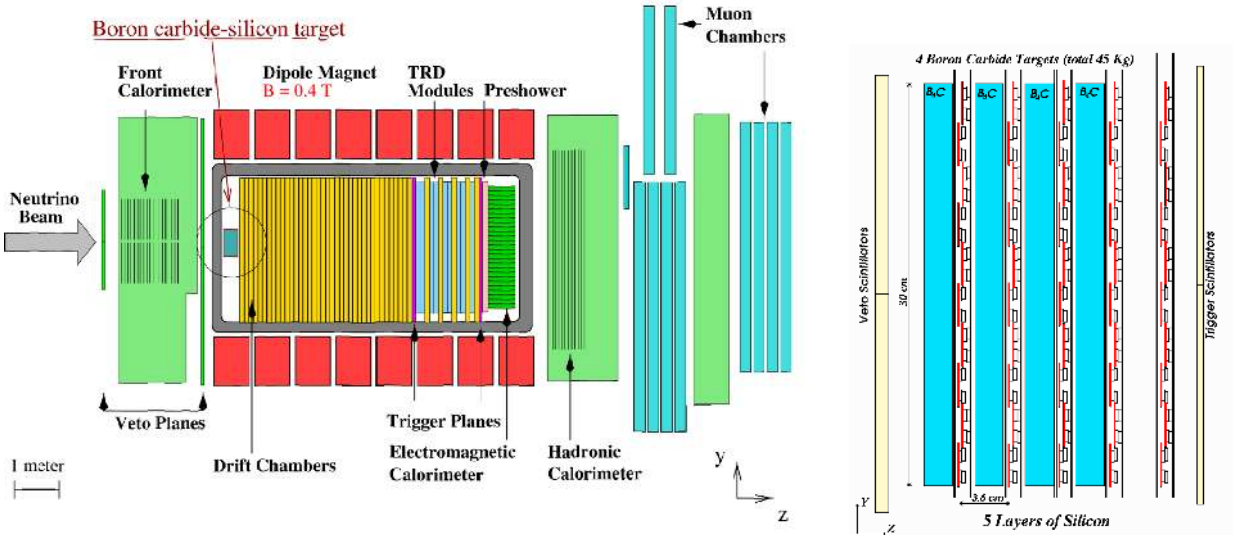

Figure 141. Left: The NOMAD detector with the Silicon TARget (NOMAD–STAR).Right: Side view of NOMAD-STAR.

The flux of neutrinos at a near detector 80 m downstream of a muon storage ring [129] will produce $2.3 \times 10^8 \nu_\mu$ CC events per year in a detector of similar mass as NOMAD–STAR (50 kg). With the measured efficiencies from the NOMAD-STAR analysis, this would correspond to about 7×10^5 charm events reconstructed per year. This would allow a sensitive measurement of the charm cross-section close to the charm threshold.

The reconstruction of taus from an impact parameter signature with a dedicated silicon vertex detector was studied in the NAUSICAA proposal [438]. A silicon vertex detector with a B_4C target was proposed as an ideal medium to identify taus. Standard ν_μ CC interactions have an impact parameter resolution of 28 μm, while tau decays have an impact parameter resolution of 62 μm. By performing a cut on the impact parameter significance (σ_{IP}/IP) one can separate one prong decays of the tau from the background. For three prong decays of the tau, a double-vertex signature is used to separate signal from background. The total net efficiency of the tau signal in NAUSICAA was found to be 12%. With this efficiency, one could have a sensitivity of $P_{\mu\tau} < 3 \times 10^{-6}$ at 90% C.L. on the $\mu - \tau$ conversion probability.

Another idea proposed in 1996 was to use a hybrid detector emulsion-silicon tracking to improve the tau-detection efficiency [439]. A Letter of Intent (called TOSCA) was submitted to the CERN SPSC in 1997 [441] with a detector based around this idea. Tau detection efficiencies of 42%, 10.6% and 27% were determined for the muon, electron and one charged hadron decays of the tau, yielding a net probability of $P_{\mu\tau} < 0.75 \times 10^{-5}$ for the CERN SPS beam at 350 GeV.

Assuming 12% efficiency from the NAUSICAA proposal, and assuming that charm production is about 4% of the ν_μ CC rate between 10 and 30 GeV (CHORUS measured $6.4 \pm 1.0\%$ at 27 GeV)

[422], would imply a signal of 1.2×10^8 tau events and 4×10^7 charm events. Charm events from anti-neutrinos (for example $\overline{\nu}_e$) mimic the potential signal. The identification of the positron can reduce the background, but electron and positron identification normally has a lower efficiency than muon identification. It is very important to have a light detector (i.e., a scintillating fibre tracker) behind the vertex detector inside a magnetic field to identify the positron with high efficiency (in the best scenarios $\sim 80\%$ would be the maximum achievable). A further way to separate the charm background from signal is to use the kinematic techniques of NOMAD. Assuming the NOMAD net efficiency yields a $P_{\mu\tau} < 2 \times 10^{-6}$. These considerations are preliminary and a full study needs to be carried out to validate these assumptions.

4. Towards the Reference Design Report and R&D requirements

The IDS-NF baseline Neutrino Factory (2010/2.0) has been presented in this Interim Design Report. An internationally coordinated R&D programme designed to address the key technological issues that underpin the Neutrino Factory has been underway for a number of years. The details of this programme will not be repeated here. However, the studies that have been carried out to prepare the material presented in this report have led to the identification of a number of issues that must be addressed through an R&D programme. In addition, the conceptual-design and engineering tasks that must be carried out before the Reference Design Report (RDR) can be prepared have also been identified. The paragraphs which follow summarise the R&D programme that is required to reduce the technical risks that the Neutrino Factory project presents and the steps that the IDS-NF collaboration plans to take to deliver the RDR.

In parallel to the programme outlined below, work will continue on the evaluation of alternatives to some of the systems that are presently included in the baseline specification. Examples of such considerations include the possibility that an FFAG may be a cost-effective replacement for one or more of the RLAs. The IDS-NF has established a "change control" process [205] by which a baseline change will be considered if the proposed alternative can be demonstrated to have substantially reduced technical risk or give a performance, or a cost, advantage. The work required to develop such alternatives to systems that are presently included in the baseline is not presented in the paragraphs that follow.

4.1. Accelerator systems

4.1.1. R & D tasks

In this section, an outline of the the R&D programme required to reduce the technical risks that the Neutrino Factory project presents is given. Since detailed descriptions of the R&D programme are available elsewhere, the R&D programme will be presented as a concise list of the tasks that must be accomplished. In the paragraphs which follow, important design and R&D topics are identified, a number of which are printed in boldfaced type to indicate that their completion is essential to the production of the RDR.

4.1.1.1. Proton driver

The IDS-NF will not have a specific proton driver in its baseline design. Instead, multiple laboratories will describe how they could construct a proton driver that meets our specifications. R&D that will be important to the Neutrino Factory project will have two goals: to demonstrate that the facility in question can meet our requirements, and to provide an estimate of the cost, over and above existing or planned facilities, of constructing an proton driver for a Neutrino Factory. Particular challenges of a Neutrino Factory proton driver are the high power and consequently high currents required, the very short bunches that must be delivered, and injecting such an intense beam into the various rings that are needed.

4.1.1.2. Target

The principal R&D tasks that must be carried out to complete the specification of the Neutrino Factory target are:

- **Re-design of the solenoid capture system and its shielding:**
  Two areas of concern necessitate this:
  - *Cryogenic thermal loads:*
    The heat load on the superconducting magnets is too high in the current design. Specifications must be defined for the heat load per proton-driver pulse (temperature rise on each pulse), the local maximum, time-averaged heat load (required local cryogen flow rate), and the total time-averaged heat load (thermal capacity of cryogenic system). The shielding system must be re-designed to meet these requirements;
  - *Mechanical forces:*
    The forces on the solenoids are extremely high. Specifications for acceptable forces need to be defined, and the shielding re-design must be constrained to meet these specifications;
- Coolant flow in the internal shield:
  A system needs to be designed and simulated to ensure adequate coolant flow everywhere. It would be prudent to test the coolant flow patterns in a full size mock-up, for which inexpensive low-Z beads will suffice;
- **Definition of the full infrastructure for a target station**.
  This must include the outer shielding and containment, the remote handling systems, and the mercury loop. These need to be defined to sufficient detail that a cost estimate can be made and any significant technical issues identified;
- Nozzle design and tests:
  The performance of the 1 cm diameter nozzle for the mercury jet in the MERIT experiment was poorer than desired at jet velocities of 15–20 m/s. A program of simulation and design is under way with the goal of developing a better nozzle. This issue should not, however, be left only to design, but should be addressed in laboratory tests once a revised design is developed, on the time scale of 2 years;
- **The beam dump:**
  A complete design of the beam dump must be produced. This must allow for the possibility of a failure of the mercury flow, in which case the entire proton beam would be incident on the dump. Since the beam dump would contain mercury, the hydrodynamics of the jet and the beam hitting this pool must be understood, and systems to mitigate the effects of the splash must be designed and simulated. It would also be useful to conduct a laboratory test of the system in the presence of the mercury jet;
- Pion-yield calculations and measurements:
  Different particle production simulation codes have produced results that, while in broad agreement, sometimes disagree in detail for predicting quantities that are important to the design of a Neutrino Factory [442]. Studies must continue to compare the results from different codes, compare their results with experimental data, and assess the uncertainty in our predictions. Collecting additional experimental data to improve the models in the codes, as proposed in [443] would also be desirable; and

- Beam window designs:
  Complete designs of the windows must be performed.

4.1.1.3. Muon front-end

The R&D tasks required to complete the specification of the muon front-end are:

- RF cavities in magnetic fields:
  Our understanding of the limitations on RF gradients caused by magnet fields must be improved through experiments such as MuCool. As the limitations are better understood, lattice designs will need to be revised accordingly, either by modifying the baseline design or switching to one of the alternative designs;
- **Particle losses:**
  A system for managing particle losses needs to be defined. Three items have been identified for investigation: a proton absorber to remove low momentum protons; a chicane to remove high-momentum protons; and transverse collimators to remove high-amplitude particles. A Wien filter has also been suggested as a method to filter off-momentum particles. Energy deposition in various systems, in particular superconducting magnets, must be computed. Appropriate shielding will need to be designed;
- **A full engineering design:**
  Designs for superconducting magnets, RF cavities, and their associated services are required. Heat deposition in lithium hydride absorbers need to be studied, and an active cooling system needs to be designed if it is needed;
- Further optimisation of lattice optics:
  In particular, between the phase rotation and ionisation cooling sections, there is a longitudinal mismatch, and the transverse matching can also be improved; and
- Ionisation cooling experiments:
  In particular, the results from MICE are critical.

4.1.1.4. Linac and RLAs

To complete the specification of the linac and RLA systems, the following tasks must be completed:

- **Full lattice design:**
  While the lattice design is nearly complete, there are a few sections (such as matching sections in the arcs and the second injection chicane) which still need to be designed;
- **Magnet designs:**
  First-pass designs of all magnets need to be made;
- **Physical layout:**
  In particular this is necessary around injection chicanes, separators, and arc crossings, to ensure that the theoretical lattice design can be constructed; and
- **Full particle tracking:**
  Particles need to be tracked through the entire system. This needs to include realistic magnet designs. Matching sections designs need to be adjusted to reduce losses.

4.1.1.5. FFAG

The principal R&D tasks required to complete the specification of the muon FFAG are:

- **Determine the optimal amount of, and method for, the chromaticity correction;**
- **Compute the matched beam in longitudinal phase space:**
  Computing the optimal phase-space shape for the longitudinal distribution is complex [444]. This needs to be done for this design, taking into account the asymmetric dependence of time-of-flight on energy and the dependence of time-of-flight on transverse amplitude;
- **Design matching to other systems:**
  In particular for longitudinal phase space.
- **6-D tracking through the system;**
- **Determine error tolerances;**
- **Perform approximate cost comparison of FFAG design for an RLA replacement;**
- **Produce single-layer combined-function designs for main ring magnets;** and
- **Hardware studies of kicker magnets and their power supplies.**

4.1.1.6. Decay ring

To complete the specification of the decay ring, the following issues must be addressed:

- **Design injection system;**
- **Decide on inclusion of sextupoles;**
- **Polarimeter design;**
- Design of OTR system for angular divergence measurement;
- **Decide on optimal system for measuring or computing neutrino flux spectrum going to far the detectors;** and
- Compute particle spectrum based on storage ring tracking:
  An accurate neutrino spectrum is needed to simulate the far detectors' performance. The spectrum and trajectories of lost muons, electrons, and synchrotron radiation photons are needed to compute heat loads in the storage ring and undesired particles in the near detector.

4.1.2. Plan to produce the RDR

Our primary goals for the accelerator portion of the RDR are to have:

- A complete design for a Neutrino Factory accelerator facility that we believe is technologically feasible and would have the required performance;
- An estimate of the cost of such a facility. This will require designs of the system components at a sufficiently detailed level to produced such a cost estimate; and
- A complete end-to-end tracking result for a realistic particle distribution through the system to verify that the system works as expected.

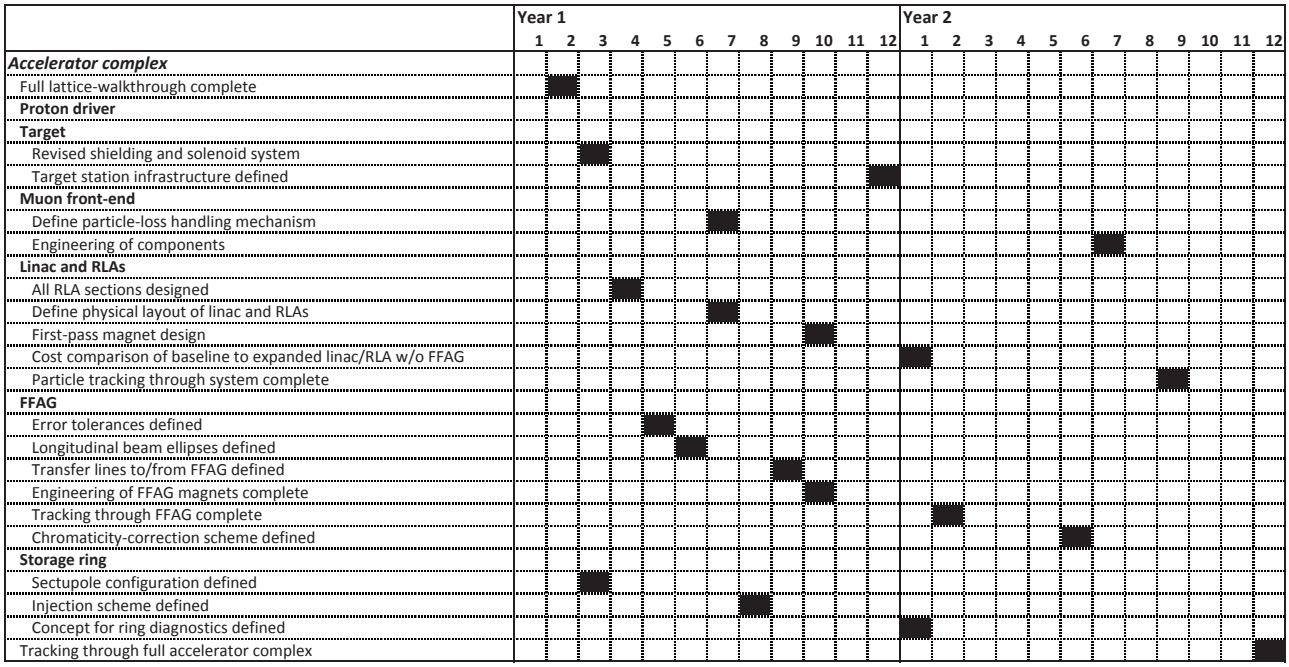

Figure 142. Approximate time-line for completing important tasks needed for the RDR.

An approximate time-line for completing these tasks is shown in figure 142. These tasks give the required input for attaining the primary goals for the RDR. The time-line does not include common tasks such as supplying component designs and making cost estimates, except when they are emphasised because, for instance, component designs are more ambiguous than usual.

4.2. Detector Systems

4.2.1. Simulation and Analysis Work towards RDR

While there has been considerable progress in the definition of a baseline detector configuration, including an improved analysis of MIND and defining the specifications of the near detector, there is still a significant amount of work that needs to be performed before the performance of the near and far detectors at the Neutrino Factory can be finalised for the Reference Design Report (RDR).

The efficiency of identification of ν_μ and $\overline{\nu}_\mu$ CC interactions, along with the associated backgrounds, has been studied for MIND. All efficiencies and backgrounds have been calculated using full pattern recognition and reconstruction of neutrino events, that now include QEL and RES events, in addition to DIS events. As a consequence, the efficiencies obtained demonstrate an extension of the performance of MIND at low energies that allows the oscillation maximum to be within the efficiency plateau, while maintaining backgrounds at the 10^{-4} level. The systematic error on the signal efficiencies obtained is about $\sim 1\%$ over the whole neutrino-energy range. However, there are still a number of simplifications that have been carried out in the MIND simulations that need to be addressed before we can quote a final sensitivity for the RDR.

Similarly, the requirements of the near detector have been identified, but we have yet to perform

a full near detector simulation and analysis to determine the realistic prospects to measure the flux over the full energy range, to measure cross-sections, to measure the divergence of the neutrino beam, to measure charm production and to search for NSI from tau events. We will itemise the next steps needed to complete these and other studies in time for the RDR in the following sections.

4.2.1.1. Steps towards RDR for MIND analysis

Multi-variate likelihood analysis

A number of additional steps will be required to fully benchmark the performance of MIND. This section presents some possible improvements to the analysis which have not yet been fully exploited. As mentioned in section 3.2.1.4, two energy-deposit based parameters used by MINOS were studied but not included in the analysis presented here. The extra parameters include the total energy in the candidate and the mean deposit per plane of the candidate. The distributions of these variables for a test set of neutral-current and charged-current events were used to form PDFs, named l_{frac} and l_{mean} respectively, shown in figure 143. Samples are taken from the NC and CC PDFs to form the four log-likelihood rejection parameters:

$$\mathcal{L}_1 = \log\left(\frac{l_{hit}^{CC}}{l_{hit}^{NC}}\right) \tag{56}$$

$$\mathcal{L}_2 = \log\left(\frac{l_{hit}^{CC} \times l_{frac}^{CC}}{l_{hit}^{NC} \times l_{frac}^{NC}}\right) \tag{57}$$

$$\mathcal{L}_3 = \log\left(\frac{l_{hit}^{CC} \times l_{mean}^{CC}}{l_{hit}^{NC} \times l_{mean}^{NC}}\right) \tag{58}$$

$$\mathcal{L}_4 = \log\left(\frac{l_{hit}^{CC} \times l_{frac}^{CC} \times l_{mean}^{CC}}{l_{hit}^{NC} \times l_{frac}^{NC} \times l_{mean}^{NC}}\right) \tag{59}$$

An analysis using the likelihood functions described in equations 56 – 59 was implemented but no improvement in performance was obtained with respect to using $\mathcal{L}_1$. Distributions of these functions for a test statistic are shown in figure 144. There is significant correlation between these parameters. Development of a multivariate analysis or neural net based on these variables, which take their correlations into account, will be studied for future analyses.

Muon momentum measurement by range

Measurement of the muon momentum using the range of the candidate in the detector was shown to improve resolution, particularly at low momenta, by MINOS [445]. An independent measure of the momentum could aid in the MIND analysis. The cuts currently implemented via equations 31 and 32 are highly correlated with the range of the muon and their power to remove background is likely to be improved with the inclusion of the muon range measurement.

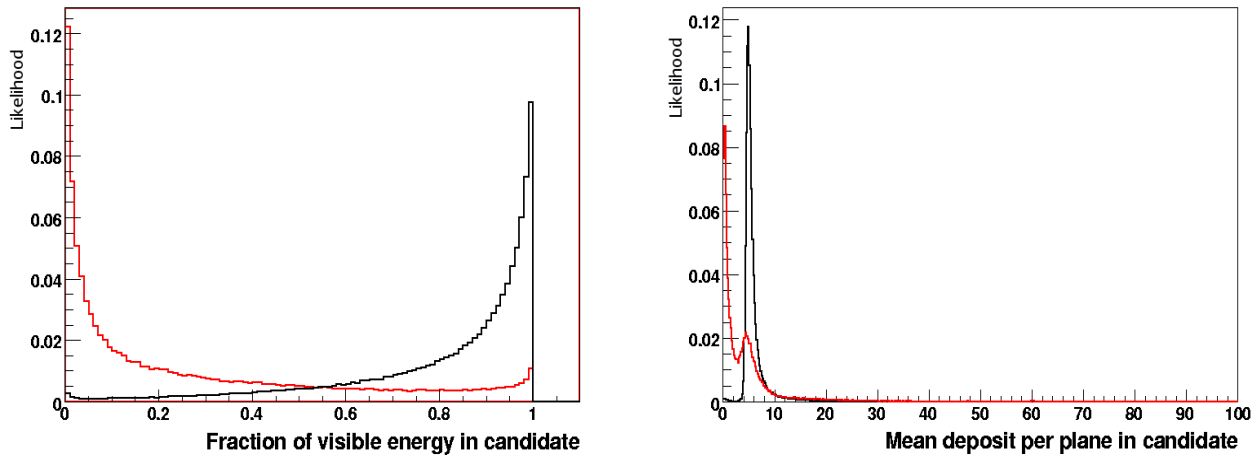

Figure 143. Additional PDFs for the NC rejection parameters. (left) fraction of visible energy in candidate and (right) candidate mean deposit per plane. CC in black and NC in red.

Hadronic reconstruction

The studies presented use parameterisations based on results presented by Monolith and MINOS to estimate the quality of reconstruction of the hadronic energy and direction. These parameters are important both for the reconstruction of neutrino energy and for the formation of the kinematic cuts. In the ultimate analysis, reconstruction will be performed on an event-by-event basis using deposited charge and distribution information from that part of the event not associated to the candidate muon.

A dedicated study will be required to understand fully the best method to perform the hadronic reconstruction. Using the observable quantities from the event, we could form a seed for a jet fitting algorithm which could reconstruct both the energy and momentum of the hadronic shower. Using the known structure of neutrino interactions, we can also use the combination of the muon momentum and hadronic energy to calibrate the total energy of the neutrino interaction.

Cosmic backgrounds

The background from cosmic rays and cosmic neutrinos has not been studied yet. This will be important to determine the final detector design and its location, either in an underground laboratory or in a green field site on the surface with minimal overburden. While understanding the timing of the accelerator system and directional arguments will enable the rejection of many of these events it is clear that some level of rock overburden or active vetoing will be required, especially when considering the surface area of a 50–100 kTon MIND. The expected Neutrino Factory duty cycle—the proportional time window when beam related interactions are possible—of ∼10% will need to be taken into account to determine the level of overburden that will be required.

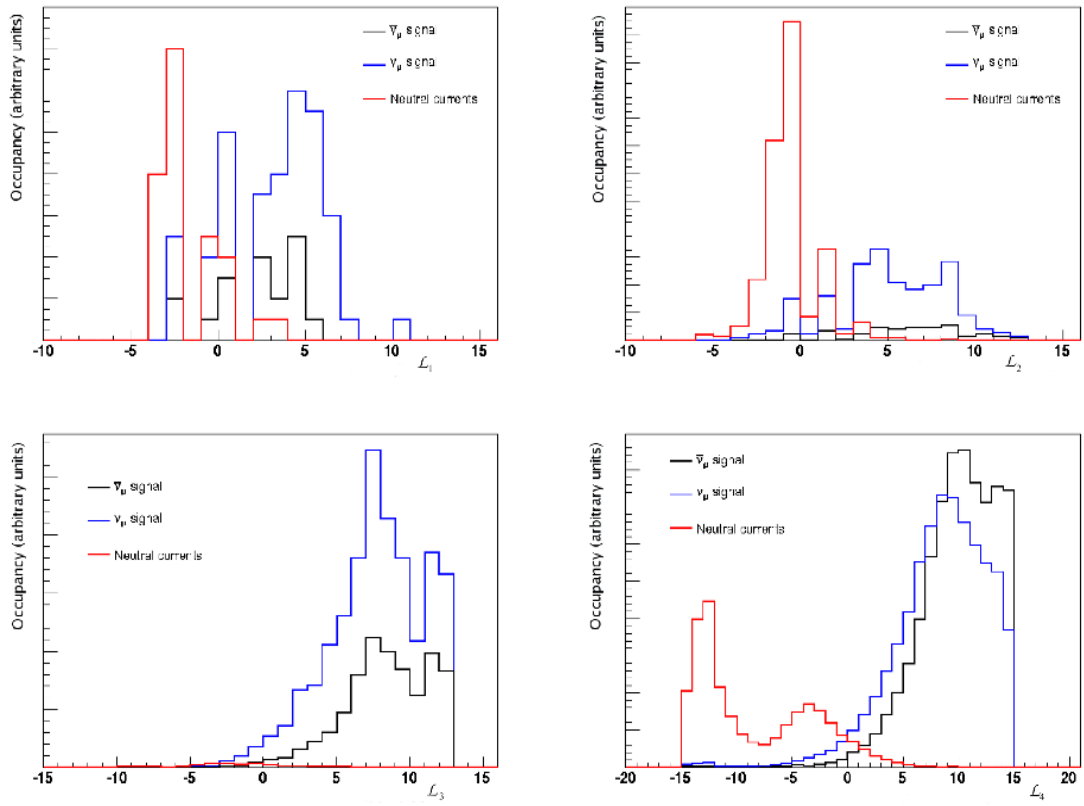

Figure 144. Log likelihood distributions for the four possible scenarios. (top left) $\mathcal{L}_1$, (top right) $\mathcal{L}_2$, (bottom left) $\mathcal{L}_3$ and (bottom right) $\mathcal{L}_4$

Tau background

Another important study that is required is the determination of the contribution to the reconstructed spectrum from $\nu_e \to \nu_\tau$ ($\overline{\nu}_e \to \overline{\nu}_\tau$) interactions. This oscillation channel would be expected to produce a similar absolute flux of ν_τ ($\overline{\nu}_\tau$) to that produced by the golden channel ν_μ ($\overline{\nu}_\mu$) oscillation [137]. While the high interaction threshold for these species means that fewer interactions will take place in the detector, tau interactions become significant above $\sim$8 GeV. Since the τ produced in CC interactions will decay promptly and has a branching fraction for μ containing channels of $(17.36 \pm 0.05)\%$ [315] it is possible that a significant fraction of these events may survive the analysis. However, understanding this background, if treated with care, can contribute information to the fit instead of detracting from it [139]. The distortion caused is highly sensitive to the oscillation parameters so fitting for this distortion could help in the removal of ambiguities in the determination of θ_{13} and δ_{CP}. To include this study in the full simulation of MIND, we will need to migrate from NUANCE to GENIE, as NUANCE does not contain tau production and decays. Migration of the full simulation to GENIE has already commenced.

Realistic MIND Geometry with Toroidal Magnetic Field Map

The MIND simulation described in section 3.2.1 includes an idealised geometry with square iron plates 14 m×14 m and 3 cm thick, with two layers of scintillator, each of 1 cm thickness. The magnetic field assumed was a simple uniform dipole field of 1 T. However, a design that can be realised in practice, with achievable engineering constraints consisting of octagonal plates of 14 m×14 m and with a toroidal field map between 1 T and 2.2 T, was presented in 3.2.2. While we do not expect that the change in geometry will affect the MIND performance significantly, it is necessary to perform a new simulation with these new parameters. These changes will be carried out for the RDR.

4.2.1.2. Steps towards RDR for Near Detector

We have two options for the near detector baseline: one with a scintillating-fibre tracker and the other with a straw-tube tracker. These detectors need to be immersed in a magnetic field to be able to take full advantage of the detector resolution to measure the momentum of the particles produced in the neutrino interaction. Either option would have to be followed by a muon spectrometer, which could be a smaller version of MIND. We need to benchmark both of these options and determine which of the detectors provides better performance. Additionally, upstream of the near detector, we would place a high resolution charm and tau detector. We need to establish whether an emulsion detector is feasible at a Neutrino Factory or whether the only way we can measure charm and tau events is using a silicon vertex detector.

We also need to determine for the RDR whether we need four near detectors or whether two detectors will suffice (for example, this could be achieved if the near detector were on rails, and it could be moved to either of the straight sections of the storage ring, depending on the charge of the muon). Moreover, we need to determine the optimum distance from the near detector to the end of the decay straight and what shielding is required. All of these considerations need to be resolved through detailed simulations before the publication of the RDR. Full response matrices, similar to those that have been prepared for the MIND (see Appendix H), for signal and background at the final near detector configuration, will also need to be determined so that the physics performance may be quantified.

To achieve these goals, the following simulations still need to be carried out:

- Neutrino electron scattering: Simulations for Inverse Muon Decay (IMD) have already been produced as a way of calibrating the neutrino flux (section 3.3.2). However, IMD has a threshold of 11 GeV, and we need a method of determining the flux at lower energies as well. Neutrino-electron $\nu_e e^- \to \nu_e e^-$ and $\overline{\nu}_e e^- \to \overline{\nu}_e e^-$ elastic scattering can provide such a flux measurement over the whole neutrino energy range and can be used to cross-check the IMD results;
- Flux extrapolation from near to far detector: Preliminary results on the flux extrapolation method have been presented in section 3.3.2. A method to deduce and take into account the systematic errors from the near detector data storage must be developed;
- Tau and charm analysis: A full simulation with a silicon vertex detector and an emulsion detector needs to be carried out to determine the tau and charm detection efficiency and relevant backgrounds of the tau/charm detector at a neutrino factory;
- Near detector shielding: This is an important topic that needs to be addressed at the interface between the storage ring and the near detector. From the accelerator end, we need to understand

potential muon losses in the storage ring and photon contamination from radiative decays. From the near detector point of view, we need to ascertain the impact of these backgrounds and what type of shielding can be tolerated. The flux of neutrino induced muons from the shielding itself will also need to be calculated; and

- Performance of near detector for neutrino scattering physics topics: Once the near detector facility has been defined, the performance of a near detector to determine neutrino cross-sections, parton distribution functions and other topics in neutrino scattering physics will be carried out.

4.2.2. Detector R&D Plan

4.2.2.1. Magnetisation

4.2.2.1.1. STL optimisation for MIND

Since the STL implementation we envision for MIND is essentially identical to that planned for the VLHC and what was actually prototyped during the R&D program for the VLHC, there is a relatively small amount of work that needs to be done prior to developing the engineering design document for MIND. The one area of investigation would be to use multiple superconductor loops within the STL cryostat. The overall size of the STL would remain the same, the total amount of the superconductor would remain the same, the forces would be essentially the same, but now the external excitation current would be reduced from 90-100kA to that number divided by the number of separate circuits in the STL. Configurations with between 5 and 10 circuits will be investigated. This makes the external power supply and the room temperature current leads much more straightforward.

4.2.2.2. Photo-detectors

Given the enormous amount of R&D currently underway in Europe, the United States, Russia and Japan on various Geiger-mode, multi-pixel avalanche photo-diodes (and the rapid progress on performance and cost), we do not plan to initiate any separate R&D in this area. We will monitor the progress on these types of devices world wide and stay abreast of advances by communicating with our colleagues actively working in the field and by staying current with the literature on the devices.

4.2.2.3. Scintillator

Extruded scintillator is an advanced and mature technology. There are a number of areas that we will devote R&D to, however. These are summarised below.

Specify final extrusion profile through simulation (square or triangle)

Simulation studies will advise us on the relative merits of square versus triangle cross-section extrusions. These studies will lead to a final choice regarding the scintillator cross section and dimensions.

Once the extrusion profile design is finalised, we will initiate discussions with extrusion die manufacturers to optimise the die design for:

- Part uniformity;
- Production speed; and
- Tooling lifetime.

Engineer detector plane mechanics

The iron plate design currently is quite mature. R&D will be needed to integrate the detector planes with the steel. We will start with the concepts that were used by MINOS and then extend them to address the larger cross section of the MIND and the fact that the photo-detectors will be mounted directly on the scintillator extrusions, thus eliminating the need for fibre manifolds. This simplifies the detector plane tremendously and also allows for the additional bolts needed for the iron plate support. The work will include 2D and 3D modelling with associated ANSYS analyses.

Investigate the possibility of co-extruding the fibre with the scintillator.

Possibly the most manpower-intensive step in the detector plane fabrication is the insertion (and gluing) of the WLS fibre into the scintillator extrusion. Preliminary investigations have been done at Fermilab to develop extrusion die tooling that would allow commercial WLS fibre (from Kuraray most likely) to be co-extruded with the scintillator (inserted into the hot melt zone and pulled along with the polymer flow). Although this is a very tricky process, initial studies were successful with post-cladding Kuraray WLS fibre with various thin (few hundred micron) layers of polyethylene, Kapton and Kynar. Industrial experts in this field have been contacted and believe it is possible to develop the process tooling to accomplish this. We will work with the Fermilab Scintillator Detector group and outside vendors to develop process die tooling for this application.

Alternate detector plane possibility

Although we believe that solid scintillator is the optimum choice for the detection planes, we will monitor the progress the INO collaboration is making with RPC R&D and production for their detector. INO is a candidate far detector for a Neutrino Factory located in Europe or Japan.

4.2.2.4. Fibre

Although we do not feel that R&D is needed to improve the performance of the best available wavelength shifting (WLS) fibre that is currently available, this product only comes from a single-source supplier, Kuraray. We will investigate with university groups versed in polymer science and optical-fibre fabrication to see if an alternate technology base can be developed that could be transferred to industry in order to present experimenters with a choice of vendors. This could also have a positive impact on cost.

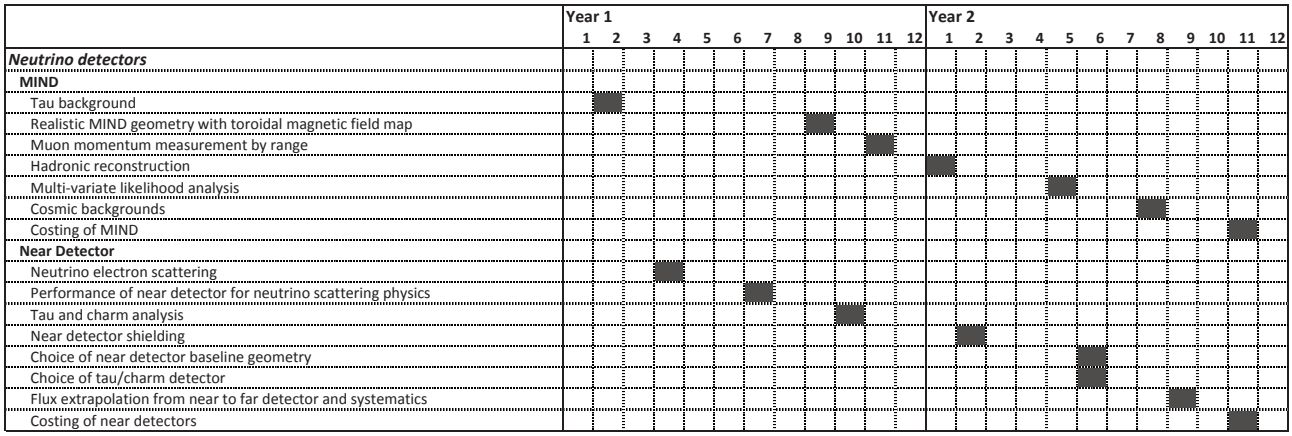

Figure 145. Approximate time-line for completing important near and far detector tasks needed for the RDR.

4.2.2.5. Prototyping

Prototyping a scale version of MIND will allow the technical feasibility of the MIND design, including the use of extruded scintillator and SiPM readout options. There will be an added benefit that this prototype can be exposed to a test beam to validate the performance of the detector under realistic conditions.

AIDA (Advanced European Infrastructures for Detectors at Accelerators) [446] is a European project to develop infrastructures for particle physics detector R&D. As part of this project, a MIND prototype will be assembled and placed at the end of the H8 beam-line by a consortium of European institutions. The main purpose will be to benchmark and validate simulations to determine the muon charge identification performance, but also to measure hadron energy reconstruction and test different reconstruction algorithms. After studying its performance the module will be available as a muon spectrometer for future users of the beam. Also, as part of AIDA, a small Totally Active Scintillating Detector (TASD) will be constructed and placed inside the Morpurgo magnet of the H8 beam line. The device will be used to measure the electron charge identification efficiency in a test beam with a realistic detector.

4.2.2.6. Detailed Costing and time-line for the RDR

For the RDR, we will provide a detailed costing for MIND. We will start with the WBS structure for MINOS and then develop our own costing model based on the MIND components, fabrication techniques and siting issues. At present, we do not see any big unknowns that would result in large cost uncertainties. An approximate time-line for the completion of the near and far detector tasks that are required to deliver the RDR is shown in figure 145.

4.3. Estimation of the cost of the facility

The cost of providing the accelerator complex and the neutrino detectors must be evaluated and presented in the Reference Design Report (RDR) to allow the value of the outstanding physics reach to be evaluated. The RDR will contain an estimate of the capital cost of the proposed accelerator complex and neutrino detectors together with an evaluation of the uncertainty on the costing. The estimation will need to identify items such as expenses related to the final design, installation and commissioning. Consideration needs to be given to items such as:

- The cost of a programme of R&D that will address the remaining technical issues and mitigate the various risks. This programme will include the construction and test of prototypes;
- The cost that will be incurred in the design and manufacture of specialised tooling;
- The construction of the facility, including materials, equipment, and labour. In addition, the cost of installation and the field-supervision of the construction will be estimated;
- The cost of inspection, commissioning, and testing of components and systems; and
- The cost implications that arise in the development of designs that meet safety and radiation requirements.

The estimation of the cost of the facility as complex of the Neutrino Factory is challenging, requires a significant engineering effort, and must be carefully organised to ensure consistency of approach across the systems that make up the facility. The costing methodology that has been adopted by the IDS-NF collaboration is outlined in the paragraphs which follow.

The cost estimate to be presented in the RDR will be based on a Project Breakdown Structure (PBS) for the accelerator complex and the neutrino detectors. The PBS is a hierarchical breakdown of the elements of the accelerator complex and detector systems. The top level of the PBS is shown in table XXXVII. The Neutrino Factory facility is broken down into the accelerator complex and the neutrino detectors at level 2. At level 3, the principal systems are identified. The breakdown then continues until a level of detail is reached at which a cost can be determined for the component or sub-system. The costing tool developed at CERN [447] will be used for the management of the PBS and the costing data. The tool allows the costs relating to each component to be entered and provides full functionality for indexation and reporting at various levels and in various formats and currencies.

The tool allows data related to different options to be entered as parallel sub-PBS structures, and provides an easy way to combine such options in a project report. This functionality is particularly interesting as for some sub-systems, for example the proton driver, a number of options will be carried to the RDR. The tool also has facilities to take various financial factors, for example indexation, price escalation, and costs that relate to the specific example site under consideration, to be taken into account. Finally the tool provides "version management", archive functionality, cost monitoring for each element or sub-system so that the evolution of the cost can be followed over the lifetime of the project. Example sites (CERN, FNAL, and RAL) have been chosen to allow site-specific aspects of various choices to be evaluated.

Preparing an estimate of the cost for a large project such as the Neutrino Factory is a collective effort. Each sub-system (PBS level 3) will have an individual responsible for the collection of the cost estimates for all sub-nodes in the PBS and for entering and maintaining the information in the costing tool. A costing panel composed of the sub-system conveners and the individuals responsible

Table XXXVII. Top-level Project Breakdown Structure for the Neutrino Factory that will be elaborated to prepare the cost estimate to be presented in the RDR.

Level 1	**Level 2**	**Level 3**
Neutrino Factory	Accelerator complex	Proton driver
		Target
		Muon front-end
		Linac and RLAs
		FFAG
		Storage ring
	Neutrino Detectors	Near detector
		Intermediate baseline detector
		Magic baseline detector

for coordinating the cost data, will be convened to ensure that a coherent and uniform approach is maintained across all the subsystems. At the component or sub-system level a pragmatic approach will be taken to determine the contribution to the overall cost. In some cases it may be possible to provide an analytical approach to determine the cost of the element from manufacturers, while in other cases costing formulæor scaling from previous experience will be applied. In each case an "assumption data sheet" will be prepared in which the list of components will be specified together with the technical and economic assumptions that have been made to derive the cost. The assumption data sheets will also contain a change record and be stored in the costing tool.

The complexity of the Neutrino Factory facility is such that the implementation of a number of the sub-systems carry known technical risks. Examples of such sub-systems include the muon front-end, where the reduction in the break-down potential of cavities in the presence of magnetic field may lead to the need to revise the design as discussed in Appendix D. Such cases will be dealt with by developing a "risk register" in which such risks are identified and the cost of mitigation is presented. A "risk score" will be assigned to each element of the risk table. The risk score is defined as the product of the probability that the risk will occur and the impact on the Neutrino Factory project should the un-mitigated risk occur. The risk score will be used to inform the definition of the R&D programme that must be carried out as the first phase of the Neutrino Factory project. The cost of the R&D programme will also be evaluated and presented as part of the total cost of the Neutrino Factory project.

The Neutrino Factory project will be carried out by a large, international collaboration funded by a variety of stakeholders. The cost of the facility that will be presented in the RDR must therefore be accessible to all the different stakeholders. While it is recognised that the costing presented in the RDR must address the issues of the different costing models that have been adopted by the various stakeholders in a clear and concise manner, the details of the paradigm that will be adopted have yet to be defined.

Acknowledgements

During the course of the IDS-NF to date, we have been welcomed at a number of laboratories across the world and therefore thank the CERN, FNAL, and RAL laboratories and the Tata Institute of Fundamental Research for hosting the IDS-NF plenary meetings. The authors acknowledge the support of the European Community under the European Commission Framework Programme 7 Design Study: EUROnu, Project Number 212372. The authors acknowledge the support of Grants-in-Aid for Scientific Research, Japan Society for the Promotion of Science and the World Premier International Research Center Initiative (WPI Initiative), MEXT, Japan. The work was supported by the Science and Technology Facilities Council under grant numbers PP/E003192/1, ST/H001735/1, ST/H003142/1 and through SLAs with STFC supported laboratories. This research was partially supported by the Director, Office of Science, Office of High Energy Physics, of the U.S. Department of Energy, under contract numbers DE-AC02-07CH11359, DE-AC02-05CH11231, DE-AC02-98CH10886, DE-AC05-06OR23177, and DE-AC05-00OR22725.

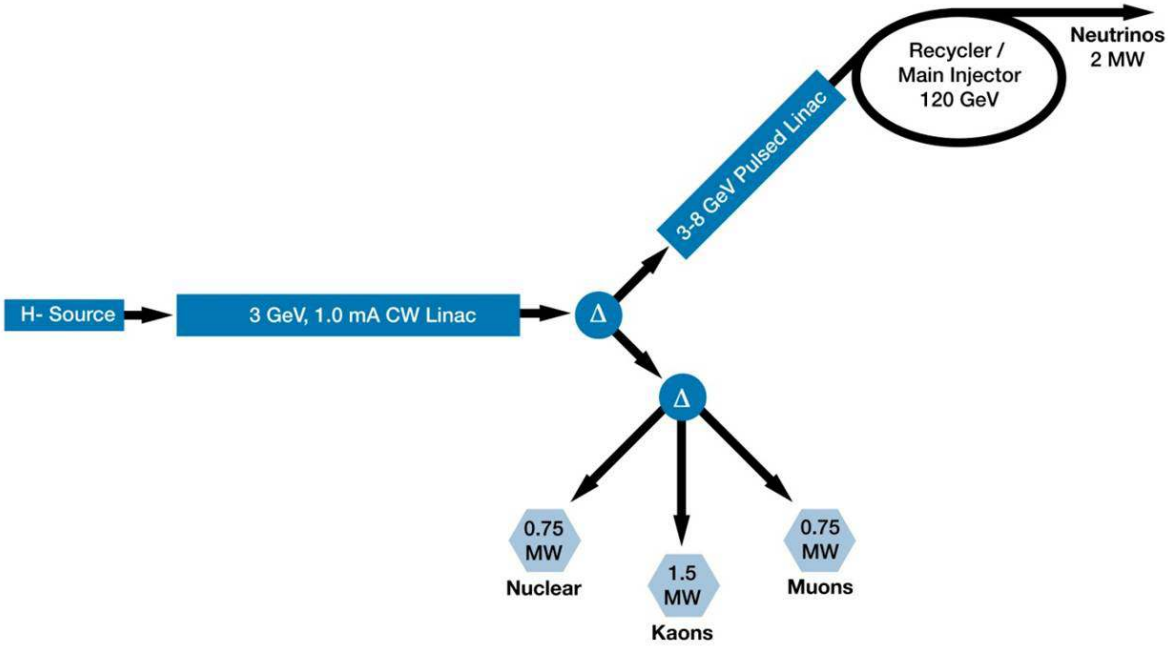

Figure 146. Schematic of FNAL Project X. 3 to 8 GeV acceleration will be done using a pulsed linac.

Appendices

A. FNAL Proton Driver

FNAL proposes to build Project X [448] as a new high intensity proton source. Project X has three physics goals:

1. To provide neutrino beams for long baseline neutrino oscillation experiments;
2. To provide intense kaon and muon beams for precision experiments; and
3. To develop a path toward a muon source for a possible Neutrino Factory

The third goal provides the beam needed for a Neutrino Factory but additional accelerator rings will be needed to provide the correct time structure for the beam. A schematic layout of the Project X reference design is shown in figure 146.

Project X will accelerate H^- ions in two linacs. The first linac will be CW and accelerate beam to ≈3 GeV. The beam will then be directed either to a switchyard area to perform precision experiments or to the second linac. A pulsed linac will accelerate the beam from the CW linac to ≈8 GeV, the injection energy of the Recycler Ring. After converting the H^- beam, protons are accumulated in the Recycler Ring before transfer to the Main Injector where the beam is accelerated for the long baseline neutrino program.

The beam originates from a 1—10 mA DC H^- source. The beam is bunched and accelerated by a CW normal-conducting RFQ to 2.5 MeV. The RFQ is followed by a Medium Energy Beam Transport (MEBT) section, which includes a chopper following a pre-programmed time-line formatting the bunch

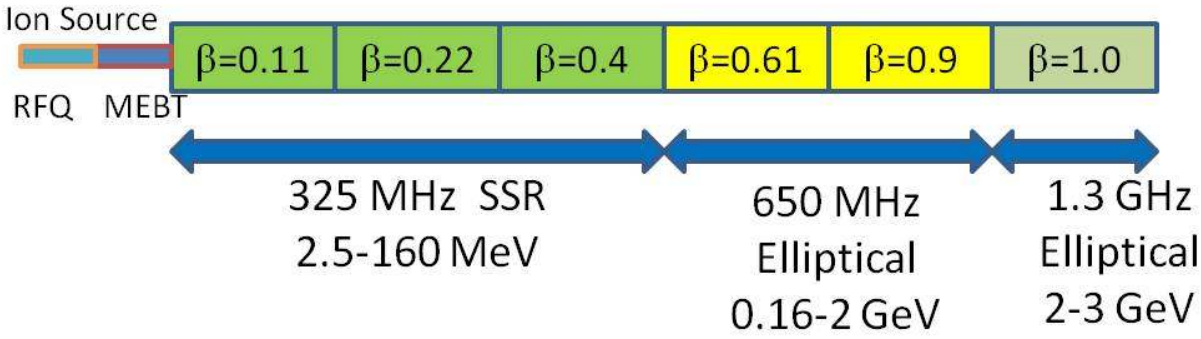

Figure 147. Front-end and CW linac where the energy range and geometrical phase velocity are shown for each section.

pattern. Since the linac average beam current is 1 mA and the beam current at the ion source can be as high as 10 mA, up to 90% of the beam has to be removed by a chopper in the MEBT section. The bunch spacing will be 3.1 ns with a maximum intensity of 1.9×10^8 protons per bunch exiting the front end. However, the CW linac will have an average beam current of 1 mA (averaged over 1 μs).

The CW linac will use several types of superconducting RF cavities. Three types of single-spoke cavities operating at 325 MHz will be used to accelerate beam from 2.5 MeV to 160 MeV. To increase the energy to 2 GeV, two types of 650 MHz elliptical cavities will be used. 1300 MHz elliptical cavities complete the CW linac with a final energy of 3 GeV. Figure 147 shows a schematic of the front end and CW linac. Table XXXVIII contains the CW linac cavity parameters. Cavities and focusing elements are grouped within cryomodules. In the 325 MHz section of the linac focusing is provided by solenoids. In the 650 MHz section a standard focusing/defocusing (FD) quadrupole doublet lattice is used, followed by a FODO lattice in the 1300 MHz section. All magnets are superconducting with built-in dipole correctors for beam steering.

The CW linac accelerates H^- ions having the base bunch frequency of 325 MHz set by the RFQ. The beam may be steered toward the high-energy linac (pulsed linac), to the experimental area, or to the linac dump. The injection to the pulsed linac is controlled by a pulsed switching-magnet. If the switch magnet is off, then the beam encounters another selection dipole magnet to steer it to the 3 GeV experimental area or the dump. In the experimental area, an RF beam separator is used to split the beam.

The 3–8 GeV pulsed linac is also a superconducting linac. Six 2.2 ms pulses of beam are provided at a rate of 10 Hz. These pulses of beam are accelerated in the pulsed linac and transferred to the Recycler/Main Injector in support of the long-baseline neutrino program. The pulsed linac will deliver 26 mA-ms of charge in less than 0.75 s to the Recycler Ring; Project X will deliver 345 kW at 8 GeV. The pulsed linac is based on 1.3 GHz, 9-cell cavities optimised for $\beta = 1$ and International Linear Collider (ILC) type cryomodules, providing a FODO focusing structure. A cavity gradient of 25 MV/m, which is readily achieved with current superconducting RF technology, means that 224 cavities are needed to accelerate the H^- beam from 3 to 8 GeV.

The two linacs fit comfortably within FNAL's Tevatron Ring. The basic idea is that, after upgrading Project X, an accumulation ring will be put at the end of the second linac. The accumulated protons

Table XXXVIII. Accelerating cavity specifications for the CW linac. β_G is cavity geometrical phase velocity. The type of accelerating structure used in the various sections of the linac are noted on the figure: SSR refers to single spoke resonators; the 650 MHz elliptical cavities are optimised for two geometrical phase velocities in the low energy (LE) and high energy (HE) sections of the linac; and the 1.3 GHz elliptical cavities are referred to as "ILC" cavities.

Section	β_G	**Freq** (MHz)	**Cavity type**	**Number of cavities**	**Gradient** (MV/m)	$\mathbf{Q_0}$ (10^{10})	**Energy** (MeV)
SSR0	0.114	325	Single Spoke	26	6	0.6	2.5—10
SSR1	0.215	325	Single Spoke	18	7	1.1	10—32
SSR2	0.42	325	Single Spoke	44	9	1.3	32—160
LE650	0.61	650	Elliptic	42	16	1.7	160—500
HE650	0.9	650	Elliptic	96	19	1.7	500—2000
ILC	1	1300	Elliptic	72	17	1.5	2000—3000

would then be transferred to a separate bunch compression ring. From that ring, beam will be sent to the Neutrino Factory target station. The target station and ensuing muon collection, acceleration and decay ring will fit within the Tevatron Ring as well. Figure 148 shows a possible layout of the additional rings and target station.

To achieve 4 MW at 8 GeV, the pulsed linac will need to deliver 10 mA-ms of charge in less than 20 ms (50 Hz). With the initial 1 mA average CW linac current, half of the CW linac beam would have to be accelerated by the pulse linac to achieve 4 MW. This would mean that the high energy linac would have to pulse 50% of the time. Instead of converting the pulsed linac to CW, the average injection current can be raised. Provisions are being designed into Project X to support an upgrade of the CW linac to deliver a current of 4–5 mA.

The transfer line from the pulsed linac to the accumulator ring will have the same characteristics as the Project X transfer line to the Recycler that is being designed to avoid loss of the H^- ions due to Lorentz stripping, black-body radiation stripping, and stripping through collisions with residual gas in the beam pipe. Dipole fields will be limited to 0.05 T to prevent stripping of the weakly bound second electron. The vacuum of the transfer line will be required to be $\sim 5 \times 10^{-9}$ Torr. To mitigate black-body-radiation stripping, a liquid-nitrogen cryogenic shield will surround the beam pipe. The transport line will include a transverse collimation scheme for capturing large amplitude particles, a momentum-collimation system for the protection of off-energy particles, and a passive phase-rotator cavity to compensate for energy jitter.

The preliminary design for the accumulator ring has a circumference of ≈ 250 m. Injection will incorporate a stripping system to convert H^--ions to protons. Foil or laser stripping of electrons from a beam of such power will need to be developed. The stripping processes are quantum mechanical which could leave $\sim 1\%$ of the H^- ions unaffected. The non-stripped beam results in a need for a ≈ 50 kW beam dump integrated into the proton accumulation ring.

The major concern with a foil stripping system is the survival of the foil. Current systems rely upon short H^- beam pulses. Pulses much longer than 1 ms will deposit enough energy to melt/damage

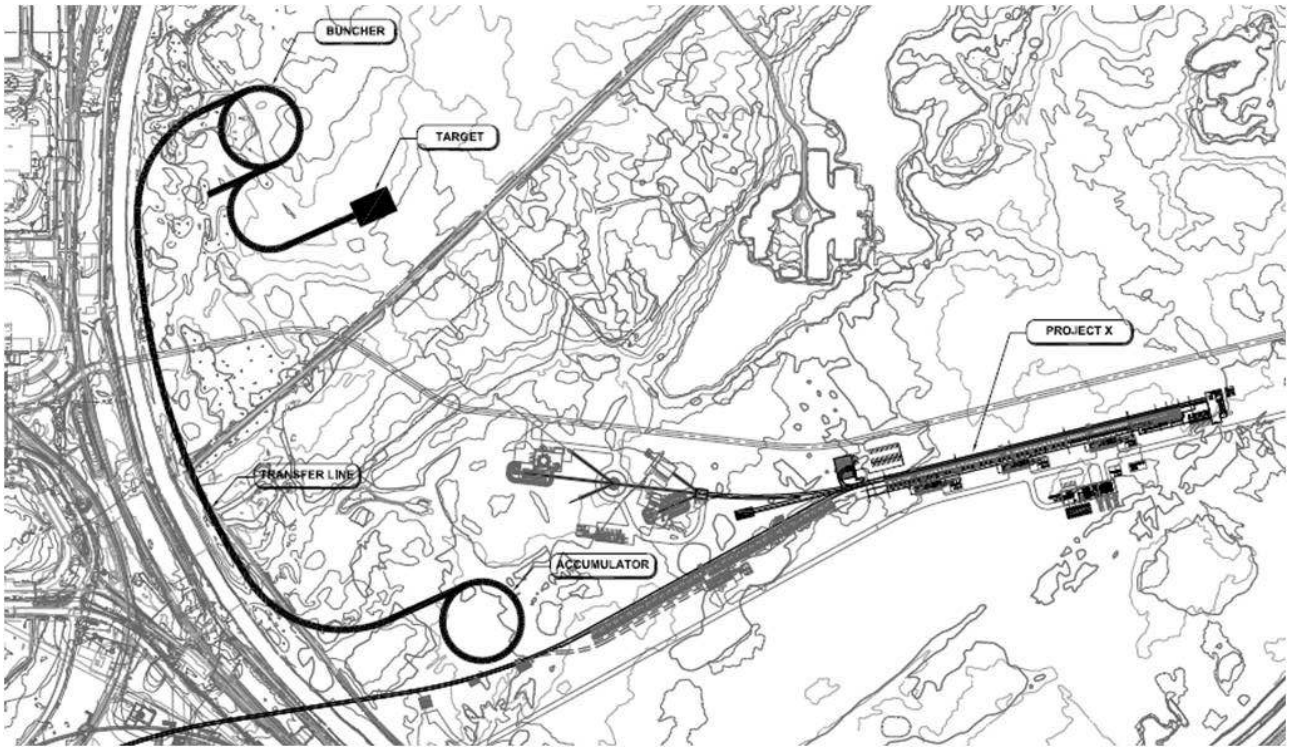

Figure 148. Project X siting within the Tevatron ring and possible locations of accumulator and proton ring to form a proton driver for a Neutrino Factory

the foil. The foil stripping-injection process will have to employ transverse/longitudinal phase-space painting to spread the energy deposition over the foil. There must be enough time between pulses ($\approx$ 10 ms) such that the foil can radiate. The bulk of the energy deposited in the foil comes from multiple passes of protons. To reduce the number of proton hits, the circulating beam is moved away from the foil when there is no beam being injected into the linac. Development of cooled foils or a rotating foil may also increase the stripping foil survivability.

A demonstration of high efficiency laser stripping system is needed. A laser based stripping system depends upon two abrupt magnetic fields and a bright-broad laser intersecting the beam. The H^- beam is subjected to an abrupt exposure to a high-field dipole magnet where an electron will immediately Lorentz strip. After the dipole, the hydrogen beam is exposed to a laser that excites the remaining electron. A second high-field dipole magnet Lorentz strips the excited electron. The laser beam is divergent and at an angle with respect to the hydrogen beam so that the spread of Lorentz transformed photon energies matches the spread in hydrogen-beam energies. The laser must be bright enough to ensure a high efficiency for exciting the hydrogen. The laser could be high-powered, pulsing synchronously with the beam. A moderate-power laser with a resonant cavity across the beam could also be used. Either arrangement needs development to survive in the radiation area of an accelerator enclosure.

The CW linac front-end will be programmed to give short bursts, injecting beam repeatedly into the same RF buckets of the proton accumulator ring. When 2×10^{13} protons have been loaded into each

of three RF buckets, the RF voltage is increased to shorten the bunch lengths. The proton beam is then transferred to the bunching ring. A preliminary design for both rings has been developed; beam instabilities remain to be studied. Space charge, as well as other conditions, will influence the high intensity bunches. The bunching ring will accept the proton bunches and immediately perform bunch rotation of the beam to the final bunch length. The beam is then extracted within 240 μs; extractions are separated by 120 μs. The extracted beam is then directed to the target. The last transfer line magnet element will be outside the target station shielding and equipment; the last focusing and steering elements will be at least 3 m from the target.

B. RAL proton driver

1. Introduction

The Rutherford Appleton Laboratory (RAL) is home to ISIS, the world's most productive spallation neutron source. ISIS has two neutron producing target stations (TS-1 and TS-2), driven at 40 Hz and 10 Hz respectively by a 50 Hz, 800 MeV proton beam from a rapid cycling synchrotron (RCS), which is fed by a 70 MeV H^- drift tube linac (DTL) [449]. The schematic layout of the ISIS facility is shown in figure 149.

Potential upgrades of the ISIS accelerators to provide beam powers of 2–5 MW in the few GeV energy range could be envisaged as the starting point for a proton driver shared between a short-pulse spallation neutron source and the Neutrino Factory [450]. The concept of sharing a proton driver between other facilities and the Neutrino Factory is an attractive, cost-effective solution which is already being studied in site-specific cases at CERN [238] and FNAL [451]. Although in the RAL case the requirements for the Neutrino Factory baseline proton energy and time structure are different from those for a spallation neutron source, an additional RCS or FFAG booster bridging the gap in proton energy and performing appropriate bunch compression seems feasible.

2. ISIS megawatt upgrades

A detailed comparison of reasonable upgrade routes for ISIS that will provide a major boost in beam power has been carried out in order to identify optimal upgrades. Designs are to be developed primarily for an optimised neutron facility, and will include the provision of an appropriate proton beam to the existing TS-2 target station. This forms part of the ongoing research programme into high intensity proton beams at ISIS [452, 453], based on understanding, optimising and upgrading both the existing ISIS RCS and putative new upgrade synchrotrons at ISIS. Development and experimental testing of simulation codes is under way using the SNS code ORBIT [237] and also with the in-house code SET [454]. The latter is presently being expanded to cover 3-D particle motion, exploiting the parallel computing facilities available at RAL. The aim is to adapt models being verified on the present ISIS synchrotron to proposed new running regimes.

The recommended first stage of the upgrade path is to replace parts or all of the 70 MeV H^- injector. Replacement with a new or partly new linac of the same energy could address obsolescence issues with the present linac, and ensure reliable operation for the foreseeable future. The more exciting, but more

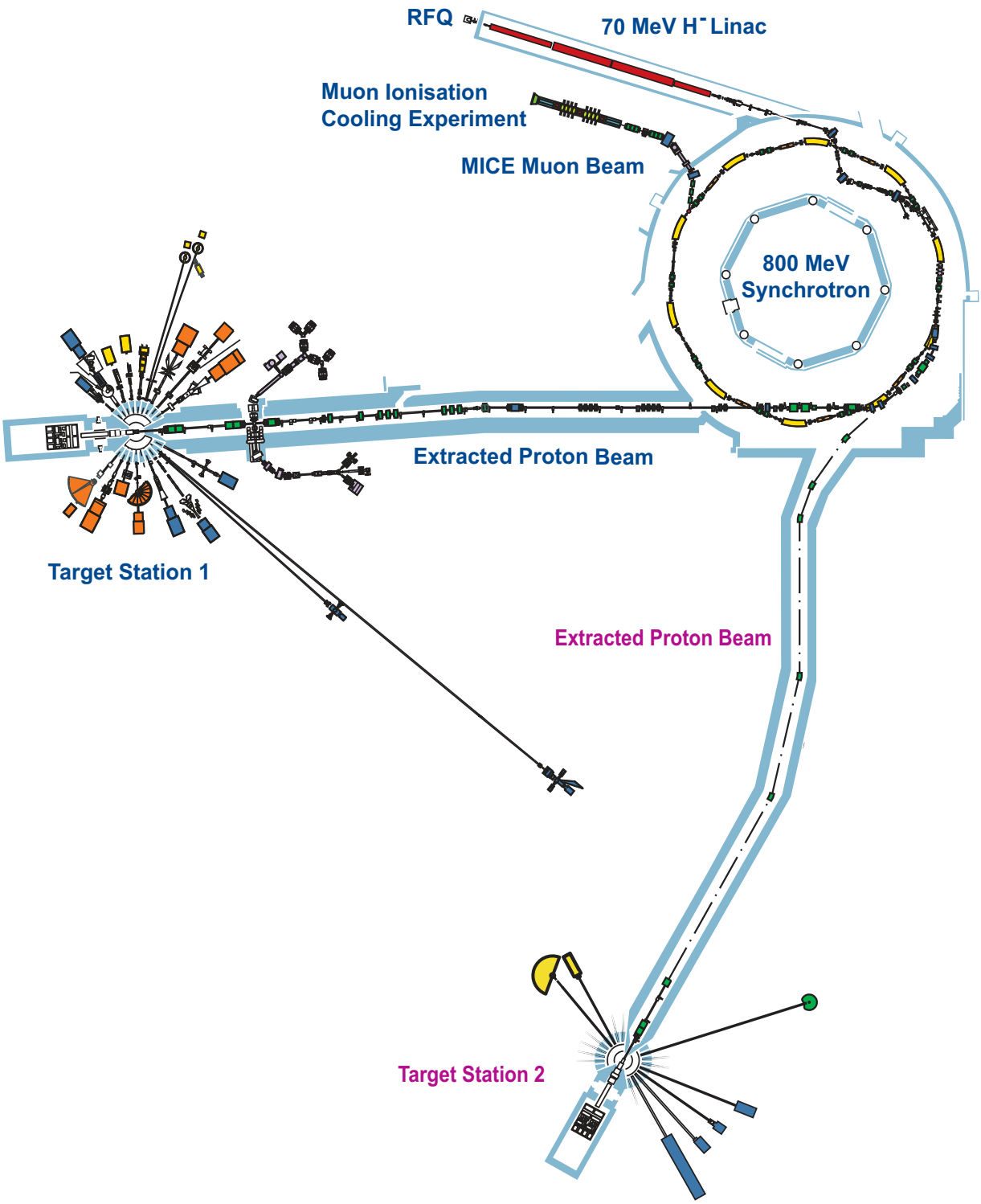

Figure 149. ISIS schematic layout.

challenging, option is to install a higher energy linac (up to ≈ 180 MeV), with a new optimised injection system into the present ring. This could give a substantial increase in beam power (up to a factor of 2), but there are numerous issues to be considered, and these are currently being studied [455]. Until the study is complete, it will not be possible to confirm the viability of such an upgrade. However, the calculations, simulation models and experimental comparisons with the existing machine required in the course of the work will form an essential baseline for any further ISIS upgrades.

The next stage is a new ≈ 3.2 GeV RCS that can be employed to increase the energy of the existing ISIS beam to provide powers of ≈ 1 MW. This new RCS would require a new building, along with a new ≈ 1 MW target station. The new RCS could be built with minimal interruptions to ISIS operations, would give predictable increases in power at reasonable estimated costs, and would have well-defined upgrade routes. RCS designs will include the features required for fast injection directly from the existing ISIS RCS, together with the option for optimised multi-turn injection from a new 800 MeV H^- linac.

The final upgrade stage is to accumulate and accelerate beam in the ≈ 3.2 GeV RCS from a new 800 MeV linac for 2–5 MW beams. It should be noted that a significant collimation section or achromat would be required after the linac to provide a suitably stable beam for injection into the RCS. The new RCS and 800 MeV linac would need to be located some distance from the present accelerators. A schematic layout of these upgrades to the ISIS facility is shown in figure 150.

Studies and simulations will assess the key loss mechanisms that will impose intensity limitations. Important factors include injection, RF systems, instabilities, loss control and longitudinal and transverse space charge.

a. ≈ 3.2 GeV RCS studies

There are a number of possible candidates for the ≈ 3.2 GeV, 50 Hz RCS, but studies are presently focused on a 3.2 GeV doublet-triplet design with five super-periods (5SP) and a 3.2 GeV triplet design with four super-periods (4SP) [456], as shown in figure 151.

The 5SP ring has a mean radius (R) of 58.5 m ($R/R_0 = 9/4$, where $R_0 = 26.0$ m is the mean radius of the ISIS 800 MeV synchrotron) and RF cavities running at harmonic number $h = 9$, i.e. at nine times the ring revolution frequency (6.18–7.15 MHz). This ring is optimised to give small dipole apertures and therefore to minimise the magnet power supply requirements. Meanwhile, the 4SP ring has a mean radius of 65.0 m ($R/R_0 = 5/2$) and RF cavities running at harmonic number $h = 5$, i.e. at five times the ring revolution frequency (3.09—3.57 MHz). This ring is optimised to make fast injection from ISIS easier, but has larger apertures. Both of these ring designs (and appropriate variations) will be studied in detail in order to assess their suitability for the recommended upgrades. Initial work, however, has concentrated mostly on the 5SP design.

Work is now under way to study the key issues for the ≈ 3.2 GeV ring designs, underpinned by extensive development of the relevant codes and benchmarking during machine physics studies on ISIS. The main topics include space charge, injection, provision for RF, beam stability and the requirement to keep beam losses below about 0.01%.

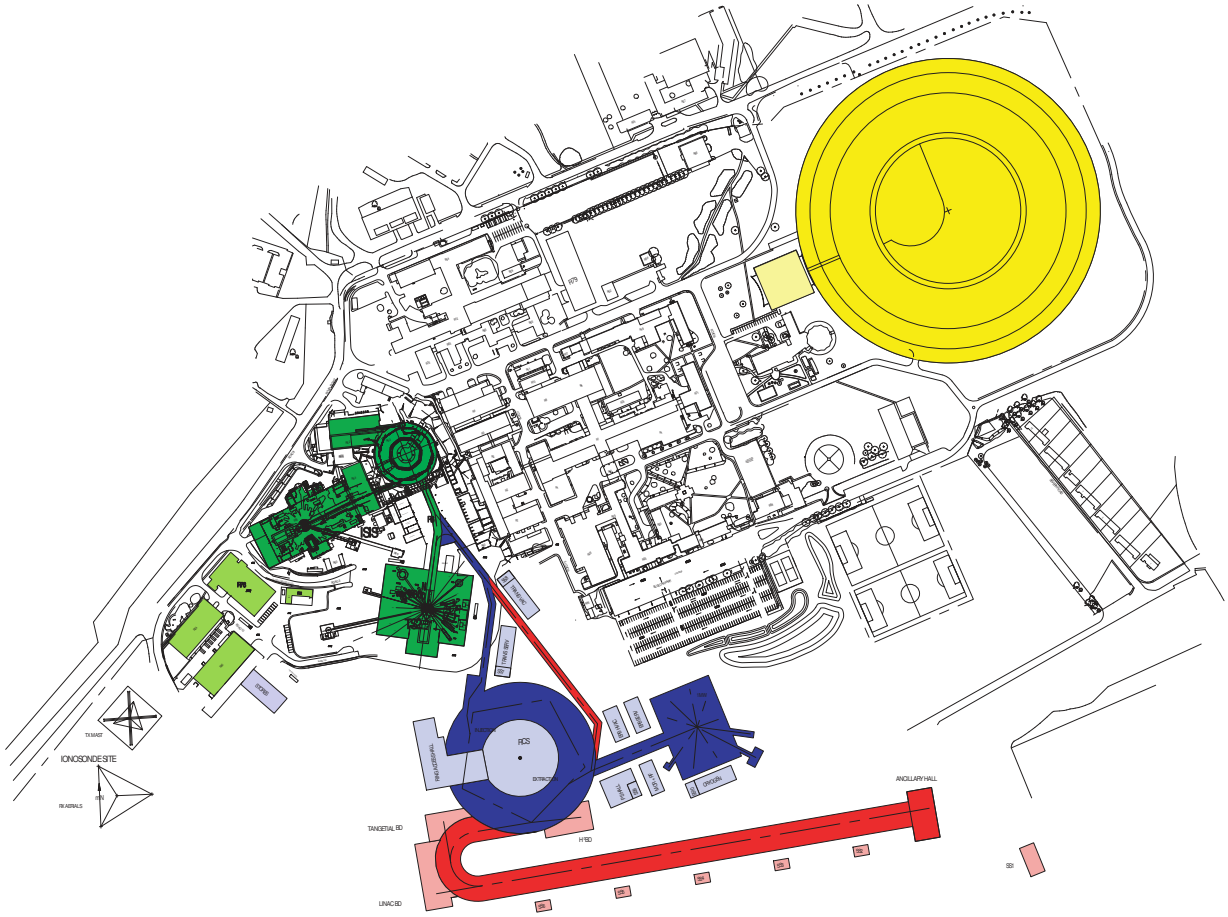

Figure 150. Schematic showing the RAL site with ISIS (dark green), the Diamond light source (yellow), ≈3.2 GeV RCS (blue) and 800 MeV linac (red). The light green shading indicates the workshop and other ancillary buildings.

b. 800 MeV linac studies

An 800 MeV H^- linac design has been produced [457], following the designs of the SNS [458] and European Spallation Source (ESS) [459] linacs. The initial 74.8 MeV stage is based around the 324 MHz frequency of the 2.5 MW peak power Toshiba klystron used in the J-PARC linac [460]. The design includes an ion source, low energy beam transport (LEBT), 3 MeV radio frequency quadrupole (RFQ) and medium energy beam transport (MEBT), all based on the Front End Test Stand (FETS) at RAL [461], followed by a 74.8 MeV DTL. An intermediate energy beam transport (IEBT) collimation section follows the DTL.

Three options have been considered for acceleration from 74.8 to ≈200 MeV: a room temperature coupled cavity linac (CCL) at 648 MHz, and superconducting cavity linacs at 648 MHz (ScL1) or 324 MHz (ScLa), both with geometric β_G values of 0.45. The first two options require a high power klystron development at 648 MHz, but are preferred to the 324 MHz ScLa option for reasons of practicality and beam dynamics. The CCL design option could also be adopted for the ≈180 MeV

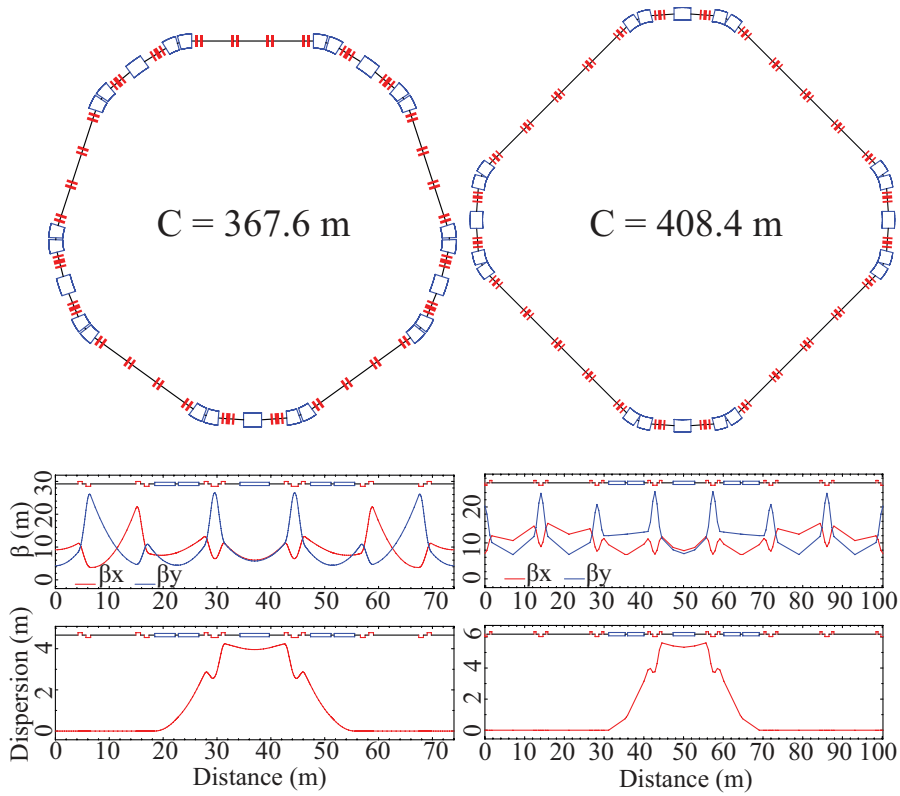

Figure 151. Schematic layouts for 5SP (left) and 4SP (right) RCS designs, with their respective beta and dispersion functions (below).

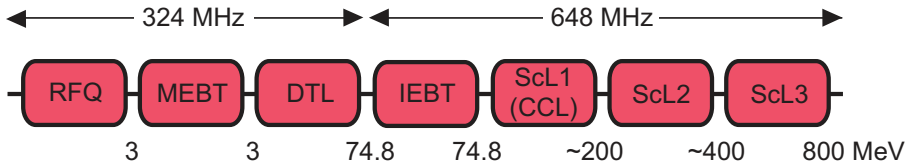

Figure 152. Schematic arrangement for the 800 MeV linac, showing the option of ScL1 or CCL.

linac to replace the ISIS 70 MeV H^- injector, although in this instance the IEBT would not be required.

In the 800 MeV linac after ≈200 MeV, new superconducting structures are used with a β_G value of 0.62 at energies up to ≈400 MeV and a β_G value of 0.76 for ≈400 to 800 MeV. The preferred options continue to use 648 MHz cavities, first in ScL2 stage to ≈400 MeV and then in ScL3 to 800 MeV. The schematic arrangement for the 800 MeV linac is shown in figure 152.

Beam transport lines between the linacs and rings need achromatic bending sections and also added cavities to ramp the output energy of the beam and to control the beam momentum spread for H^- charge-exchange injection into the new ≈3.2 GeV RCS.

Table XXXIX. Scenarios for bunch sharing between an upgraded ISIS neutron source and a Neutrino Factory, assuming bunches will be transferred from the ≈3.2 GeV RCS at 50 Hz with a total power of 4–5 MW and that 4 MW is required for the Neutrino Factory target.

≈3.2 GeV RCS design	**Power at 3.2 GeV** (MW)	**Total number of bunches**	**Bunch spacing** (ns)	**Protons per bunch** ($\times 10^{13}$)	**Number of bunches to ISIS**	**Power to ISIS** (MW)	**Number of bunches to NF**	**NF booster energy** (GeV)
4SP	5	5	280	3.9	2	2	3	4.3
4SP	5	5	280	3.9	3	3	2	6.4
5SP	5	9	140	2.2	6	3.33	3	7.7
5SP	4	9	140	1.76	6	2.66	3	9.6

3. Common proton driver

In a common proton driver for a neutron source and the Neutrino Factory, based on a 2–5 MW ISIS upgrade with an 800 MeV linac and a ≈3.2 GeV RCS, both facilities have the same ion source, RFQ, MEBT, linac, H^- injection, accumulation and acceleration to ≈3.2 GeV. Bunches of protons are shared between the two facilities at ≈3.2 GeV, and a dedicated RCS or FFAG booster must then accelerate the Neutrino Factory bunches to meet the requirements for the Neutrino Factory baseline (4 MW and 5–15 GeV). Taking the optimistic case of a total power of 4–5 MW at ≈3.2 GeV, some possible bunch sharing scenarios are outlined in table XXXIX.

Assuming that at least half of the power at ≈3.2 GeV should be delivered to the neutron source, both the 4SP and 5SP ≈3.2 GeV RCS designs could meet the power and energy needs of the Neutrino Factory (although for the 4SP design only two bunches are delivered rather than the Neutrino Factory baseline of three). It would appear that the 5SP design is most suitable, as it meets all the requirements of the Neutrino Factory baseline and provides more beam power to the neutron source, but its merits need to be established by thorough beam dynamics studies. In order to give some flexibility in case the total power at ≈3.2 GeV is somewhat less than 5 MW, 6.4–10.3 GeV RCS and FFAG booster designs will be considered. Figure 153 shows the conceptual layout of the common proton driver.

a. Dedicated Neutrino Factory booster

Based on the time structure and longitudinal dynamics of the ISIS upgrade ≈3.2 GeV RCS, a further RCS or an FFAG can be considered as a booster ring to reach the required Neutrino Factory baseline. Preliminary RCS designs [450] have concentrated on achieving the necessary acceleration and bunch compression with present-day, cost-effective RCS technology, e.g., dipole magnets with a maximum field of 1.2 T, an RF system similar to that used at ISIS [462] and long straight sections for injection, extraction, RF and collimation. An RCS design based on injection from the 5SP 3.2 GeV booster with harmonic number 9 and 4 MW total beam power (the last entry in Table XXXIX) has been investigated. This case dictates a rather large final proton energy of 9.6 GeV, but allows delivery of the required beam parameters to both facilities with minimal impact on the neutron source performance.

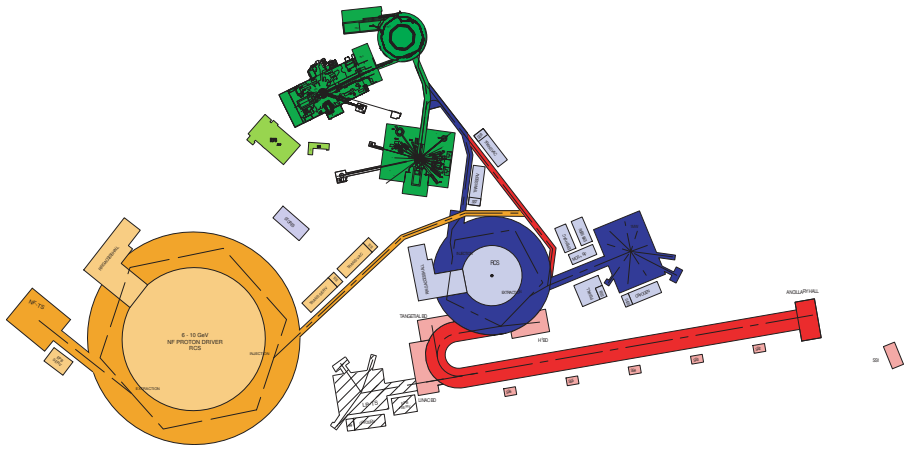

Figure 153. Conceptual layout of the Neutrino Factory proton driver, with the dedicated Neutrino Factory booster shown in orange.

Table XL. Parameters of the dedicated Neutrino Factory booster RCS ring for 3.2–9.6 GeV.

Parameter	**Value**
Number of super-periods	6
Circumference (m)	694.352
Harmonic number	17
RF frequency (MHz)	7.149–7.311
Injection energy (GeV)	3.2
Extraction energy (GeV)	9.6
Maximum dipole field (T)	1.2
Tune	8.72 (h), 7.82 (v)
Long straight section length (m)	14 m
Gamma transition	13.37 (flexible)
RF voltage per turn (MV)	≈ 3.7

The RCS has six super-periods with six FDF triplet cells each, uses only three quadrupole families and allows for a flexible choice of gamma transition. The main RCS parameters for this design are summarised in Table XL and the optical functions are shown in figure 154. Although the preliminary lattice design has been produced, a great deal of work remains to be done to produce a full conceptual scenario.

FFAG options are yet to be explored, and would be based on technology which remains to be fully tested, but in principle would offer the advantage of allowing all the bunches to be extracted to the Neutrino Factory target with the same energy (unlike the RCS where the 120 μs sequential extraction delay required by the Neutrino Factory baseline would give time for the main magnet field to vary between bunches).

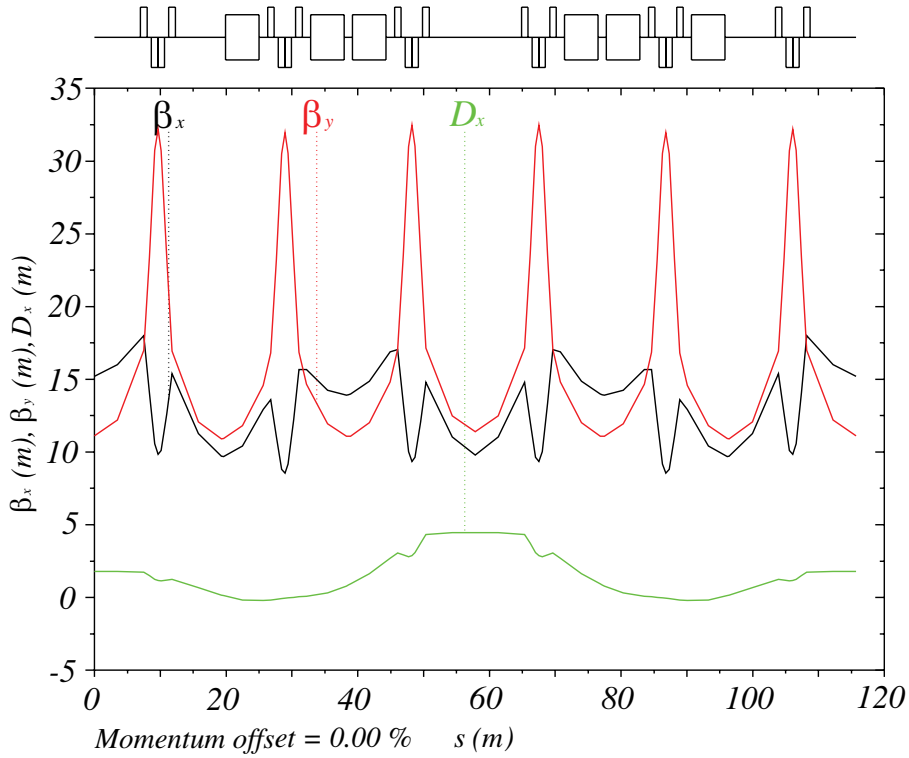

Figure 154. Optical functions in the dedicated Neutrino Factory booster RCS ring for 3.2–9.6 GeV.

b. Neutrino Factory bunch compression

Optimised longitudinal muon capture in the muon front end of the Neutrino Factory requires compression of the proton bunch length from the ≈ 100 ns for the neutron source to 1–3 ns at the Neutrino Factory target. Several methods have been proposed in order to reach this goal [463], based on either adiabatic compression during acceleration or fast phase rotation at the end of acceleration (or in an additional dedicated compressor ring).

Adiabatic compression during acceleration requires relatively high RF voltage (V) because the bunch length scales as $V^{-1/4}$. Variations of this method apply higher harmonic RF systems or lattices just below transition at the end of compression. Compression by fast phase rotation allows a lower RF gradient, but requires earlier bunch stretching to reduce the momentum spread just before the rotation and does not allow the compressed bunches to be held for many turns. Manipulations close to transition may also be applied in this scheme. Fast phase rotation in an additional dedicated compressor ring, possibly based on the CERN design [238], could provide an alternative solution if RF manipulation in the booster itself proves impractical.

Bunch compression is clearly of vital importance to the success of a common proton driver and future studies must address the longitudinal dynamics and the space charge forces in detail.

Table XLI. Baseline proton beam parameters at the Neutrino Factory pion-production target compared with expected parameters from a proton driver based on an ISIS MW upgrade at RAL.

Parameter	**Baseline**	**RAL**
Beam power (MW)	4	4
Pulse repetition frequency (Hz)	50	50
Proton kinetic energy (GeV)	5–15	6.4–10.3
Proton rms bunch length (ns)	1–3	1–3
Number of proton bunches per pulse	3	2 or 3
Sequential extraction delay (μs)	120	120
RMS transverse bunch size (rms bunch radius) at target (mm)	1.2	
Geometric transverse emittance at target (μm)	< 5	
β^* of proton beam at target (cm)	≥ 30	

4. Summary

A common proton driver for neutrons and neutrinos compatible with an ISIS upgrade is an attractive solution to create a cost-effective, multi-user facility, but careful attention must be given to potential sharing conflicts between the neutron and neutrino communities. A conceptual design has been produced, in which it appears to be feasible that the Neutrino Factory baseline can be met, as shown in Table XLI, although a lot of the detailed beam dynamics remains to be done and no consideration has yet been given to beam transport to the pion-production target.

The site-specific design at RAL is clearly at a preliminary stage, and will require extensive effort on beam dynamics and accelerator engineering (and strategic research and development in a number of key areas) before it can be regarded as viable. The common proton driver could fit onto the RAL site, on land already set aside for large facilities and research expansion, but the complete Neutrino Factory would require the use of part of the Harwell Science and Innovation Campus (HSIC), where some former UK Atomic Energy Authority (UKAEA) land would need to be decommissioned before any building or tunnelling work could begin. A possible schematic layout of the Neutrino Factory on the HSIC site is shown in figure 155.

C. Alternative Target Materials

1. Powder Jet

A fluidised tungsten-powder target is being developed at Rutherford Appleton Laboratory [464] as an alternative to the baseline mercury jet. The motivation for studying a flowing-powder target is to investigate whether such a technology can combine some of the advantages of a solid target with those of a liquid while avoiding some of the disadvantages of either. The configuration of such a target in a neutrino factory would be similar to that for the mercury jet, i.e., it is broadly compatible with the baseline solenoid arrangement. As for the mercury jet, a return path for the tungsten powder would need to be devised, possibly by engineering a longitudinal gap between the coils, although other

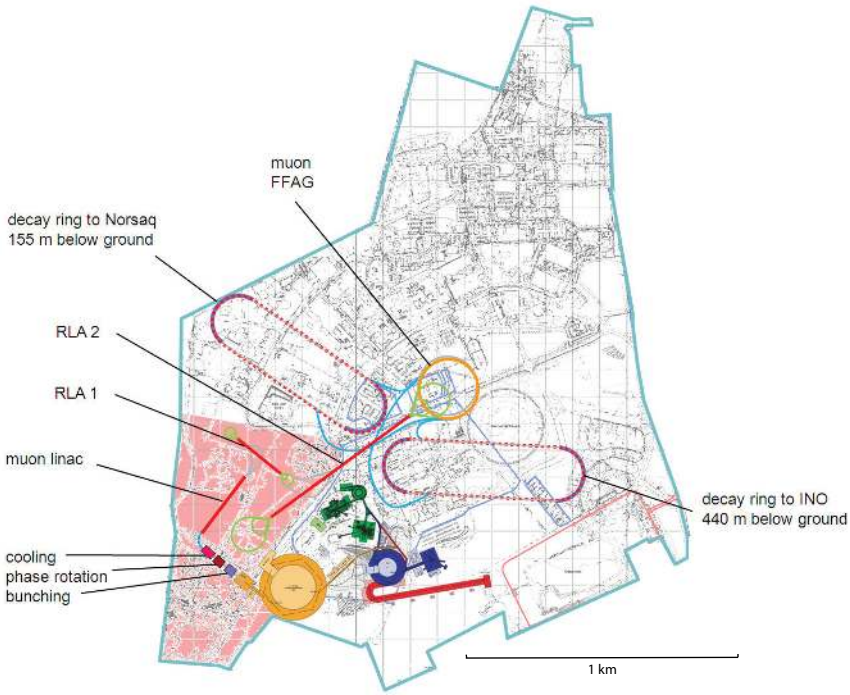

Figure 155. Schematic layout of the Neutrino Factory on the HSIC site. The components of the proton driver are shown in blue, red and orange as in figures 150 and 153, and the HSIC site boundary is shown in light blue. The area shown in pink is former UKAEA land which would need to be decommissioned. Norsaq (in Greenland) and the Indian Neutrino Observatory (INO) are possible far detector sites.

configurations may be possible. A tungsten powder target of 50% material fraction has been computed to deliver the same meson production performance as the mercury jet, by increasing the length to compensate for the reduced material fraction.

The potential attractions of such a scheme include: intrinsic resilience of grains to beam induced stress waves and radiation damage; no propagation of stress waves to pipe walls; possibility to re-circulate material in an external cooling loop; continual reforming of target-material geometry; short conduction path and consequently good heat transfer characteristics; no cavitation or associated phenomena; and negligible interaction with magnetic fields. Some potential issues that would need to be addressed for a fluidised powder target system are expected to include: erosion of pipe and container walls, particularly for recirculation at high velocity in a lean phase; secondary heating and radiation damage of a pipe wall for the preferred geometry of a contained flowing powder rather than a free jet; and integration of a powder-recirculation system within the confines of the target station and solenoid system.

Most of these issues can be studied in an off-line experimental programme, which has already begun [464]. The RAL test rig is shown in figure 156. The test programme has demonstrated the feasibility of generating a stable flow regime of tungsten powder at around 40–45% material fraction in both contained and open jet configurations. The long dimension of the target is horizontal, suitable for a neutrino factory. An example of an open, 2 cm diameter, tungsten powder jet with a velocity of 3.7 m/s generated by the rig operating at a 2 bar driving pressure is shown in figure 157. A vertical lift

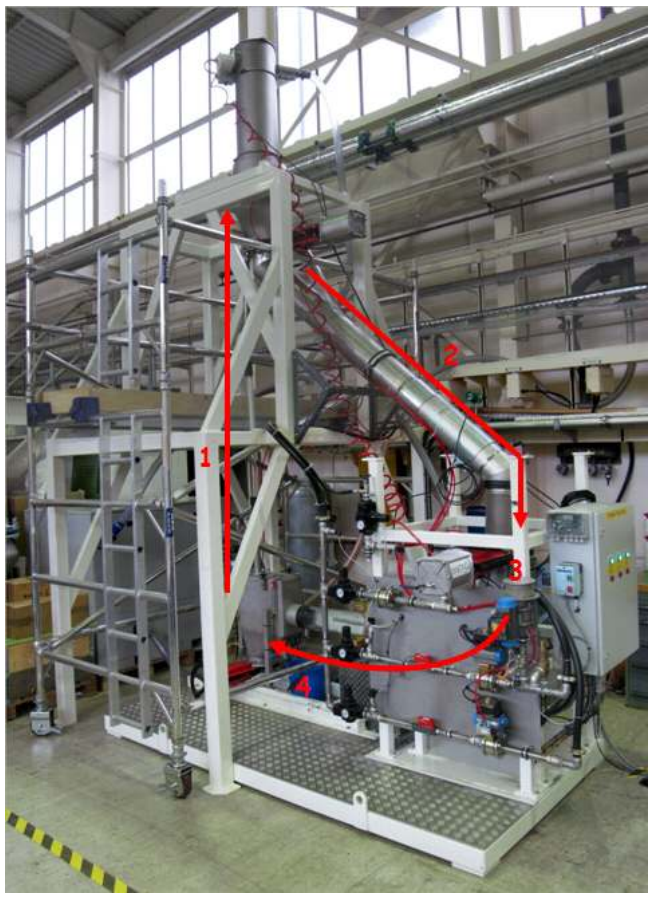

Figure 156. Fluidised powder test rig showing (1) Suction/lift, (2) Chute to hopper, (3) Pressurised hopper and (4) Powder ejection to receiver hopper.

vacuum recirculation system has lifted the powder at the rate required for the rig to be able to operate in CW mode for the optimised target radius of 0.47 cm. In a neutrino factory, this arrangement would require a longitudinal gap between the solenoid elements to accommodate the vertical lift pipe. It may be possible to devise a recirculation path that is closer to that proposed for the mercury loop, at the cost of increased complexity.

A free jet requires an even higher velocity flow than the mercury jet to generate the necessary target interaction length. This high velocity generates concerns over erosion of the downstream components. Consequently, the preferred configuration is for low velocity (2–3 m/s) flow within a contained pipe, which should be tolerant to multiple beam pulses interacting with the same material as it traverses the discharge pipe. This configuration has received the focus of the test effort to date. No erosion has been observed in the pipes used for experiments so far, although this has only been for about 30 minutes of integrated operation. The main concern with this configuration is with secondary heating and radiation damage of the pipe walls; external cooling of the pipe wall, possibly by high pressure helium, is expected to be necessary. The design of such a circuit should permit rapid replacement of such pipework.

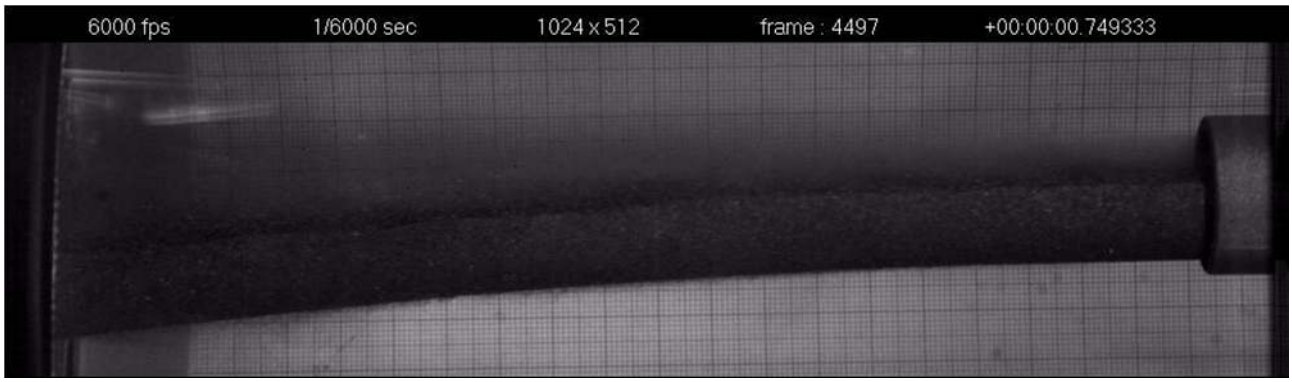

Figure 157. Free tungsten powder jet demonstrating stable dense flow at 3.7 m/s and 40-45% material fraction.

2. Solid Target

A solid-target option is also being studied for a Neutrino Factory. This is motivated by the many years of experience in the use of high atomic-number materials as targets, for example at ISIS, and the clear benefits for radio-protection. Two materials have been investigated, tantalum and tungsten, and initial studies have focused on their lifetime under the thermal shock created by the high-energy-density proton beam. A test facility (see figure 158) employing a current pulse of up to 8 mA and with a rise time of 100 ns has been used to emulate in wires, ranging from 0.35 mm to 1 mm in diameter, the thermal shock in the target. Some results of this work are shown in figure 159. At the working temperature of the target ($\sim 1\,200$ °C), tantalum is not strong enough. However, it has been demonstrated that the lifetime of tungsten is more than sufficient [465]. To verify this outcome, it is planned to test real tungsten targets in a proton beam of high energy density at CERN in 2011. During this work, the Young's modulus of tantalum and tungsten at temperatures and strain-rates much larger than measurements presented in the existing literature have been made. This work on tantalum and tungsten outlined above is being published in appropriate journals.

After shock, the second most important issue for solid targets is the heat generated by the beam. The only practical solution to this is to change the target between beam pulses. This must be done in a way that minimises the impact on useful pion production and the heat load to the superconducting capture coils. Various schemes, employing 200—500 targets, are being considered and detailed engineering studies of this are now starting. In addition, we must also worry about the effect of radiation on the targets. With 200 target bars, the activation rate is already slower than a single ISIS target. Several ISIS targets have been used and, while they have not been examined in detail, there are no visible signs of the expected effects of radiation damage. Further, earlier studies of irradiated tungsten indicate that it remains strong enough for use after significant neutron irradiation. Nevertheless, we are investigating making detailed measurements of an ISIS target that has been irradiated to verify these observations. Finally, MARS simulations show that the pion yield is comparable to the yields from the mercury-jet system [466].

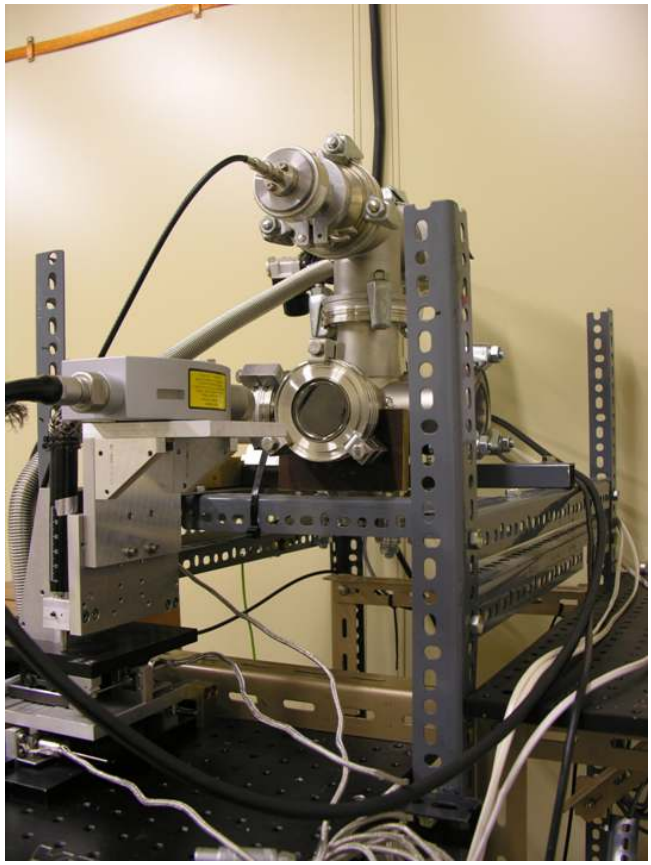

Figure 158. The solid target test rig. The cable from the pulsed power supply enters from the left. The test wire can be viewed through a number of windows. The head of the Doppler laser vibrometer used to measure the shock waves for comparison with modelling can be seen in the foreground.

D. Alternative lattices for the muon front-end

The presence of magnetic fields overlapping RF cavities has been identified as a technical risk that may reduce the capture efficiency of the muon front-end due to a reduction in the peak gradient that can be achieved in the RF cavities [273, 274]. Three alternative lattices have been proposed for the cooling section to mitigate this risk. A schematic of the three lattices and the number of muons accepted as a function of distance along the channel is shown in figure 160 and 161 [226]. The principal characteristics of the three alternative lattices are:

1. RF cavities filled with high pressure (HP) gas have been demonstrated to operate without degradation even in the presence of strong magnetic fields. A study of a hybrid system using high pressure gas has shown that the baseline performance can be achieved even in the presence of strong magnetic fields [223]. The cavities will be tested in the presence of beam and the gas-ionisation effect on RF breakdown will be studied in the near future;
2. Magnetically insulated cavities are designed such that magnetic field lines are parallel to the RF cavity surface, so that field emission electrons are redirected onto the RF cavity surface before they are accelerated by the RF field. It is hoped that this may prevent breakdown [224]; and

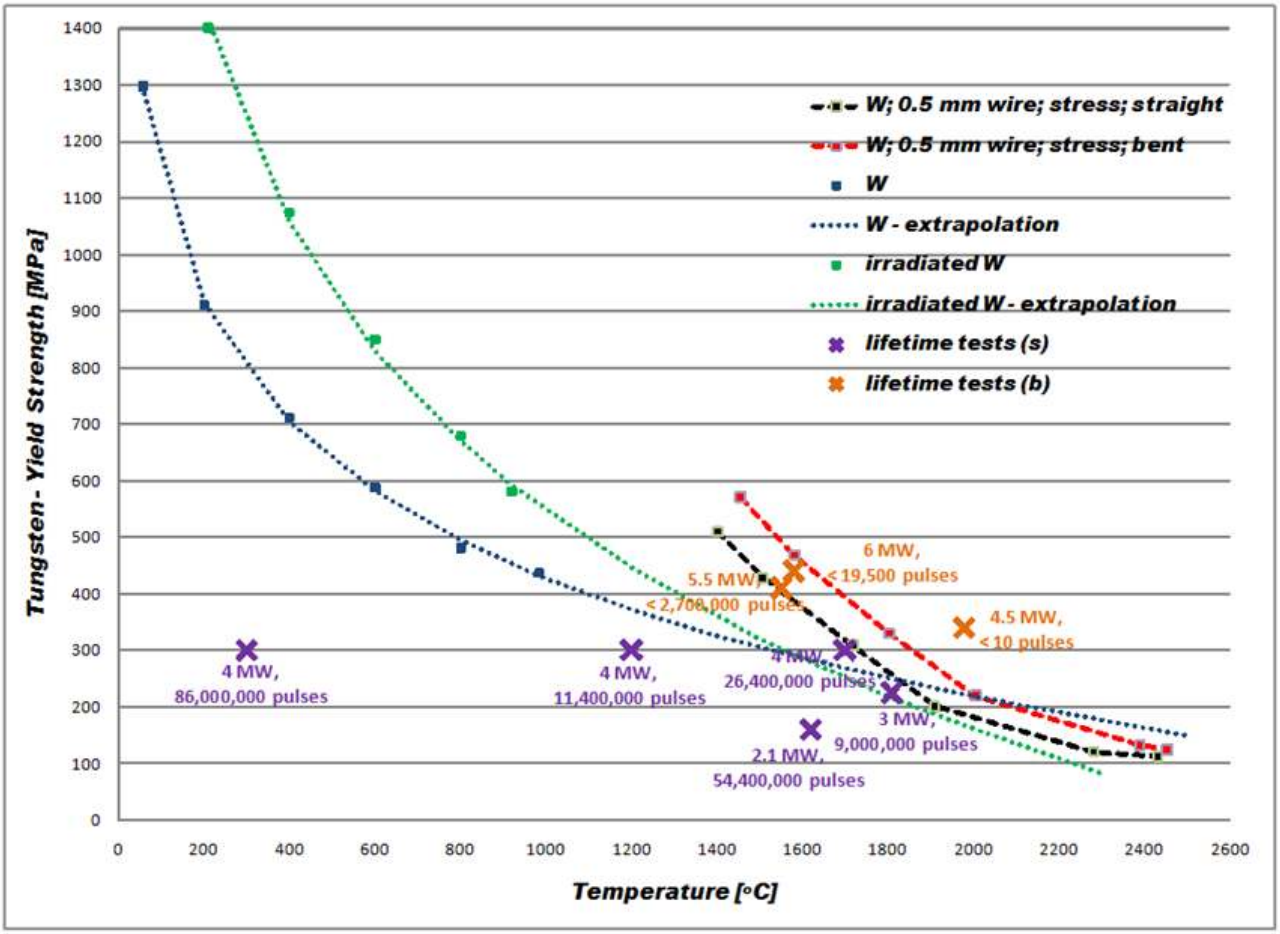

Figure 159. The measured yield strength of tungsten. The square points show earlier measurements of the yield strength of tungsten as a function of temperature both before and after irradiation. The dotted lines are a fit to these points, used to extrapolate them. The dashed lines are measurements made by us, which constrain the yield strength to lie between them. Note that there is a difference at lower temperature because the strain rate we use is much larger than in the existing measurements. The crosses show measured lifetimes for the targets. For yellow crosses, the target broke, for purple it did not. The working temperature for a Neutrino Factory target will be less than 1 500 °C and one year's operation corresponds to 1.25M pulses with 400 bars.

3. In the shielded lattice, the magnetic field on the RF cavities is reduced by stretching the lattice and adding shielding around the coils. This reduces the acceptance and performance of the system but much of the performance can be recovered by reducing the geometric emittance of the beam by means of an initial acceleration after the phase rotation system [225].

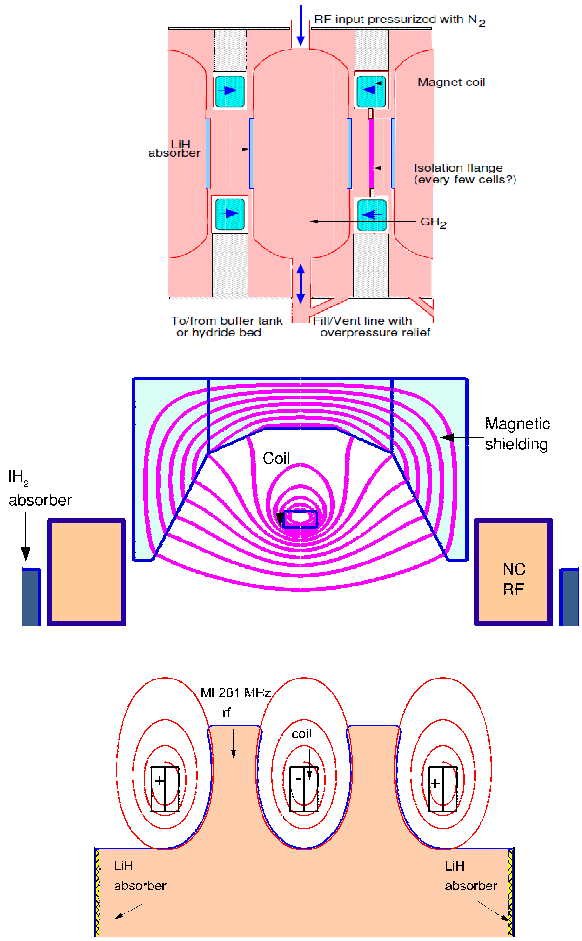

Figure 160. Schematic drawings of the proposed alternative lattices: (top) high pressure gas-filled hybrid lattice; (middle) shielded RF cavities; (bottom) magnetically insulated lattice.

E. Replacement of the RLA arcs by a compact FFAG lattice

We developed a complete linear optics for a 4-pass muon dog-bone RLA consisting of a single linac and two droplet-shaped return arcs at each end of the linac. In order to reduce the number of required return arcs, we employ the non-scaling fixed-field alternating-gradient (NS-FFAG) arc lattice design, which allows transport of two consecutive passes with very different energies through the same string of arc magnets. As illustrated in figure 162, each droplet arc consists of a 60° outward bend, a 300° inward bend and another 60° outward bend so that the net bend is 180°. Such an arc geometry has the advantage that the outward and inward bends are made up of similar cells and the geometry automatically closes without the need for any additional straight sections, thus making it simpler and more compact. In the scheme presently under consideration, a 0.9 GeV/c muon beam is injected at the middle of a linac with 0.6 GeV energy gain per pass. Therefore, with a four-pass scheme, there are 1.2 and 2.4 GeV/c passes through one arc and 1.8 and 3.0 GeV/c passes through the other. In addition to accommodating the appropriate momenta, each arc must satisfy the following requirements: (a)

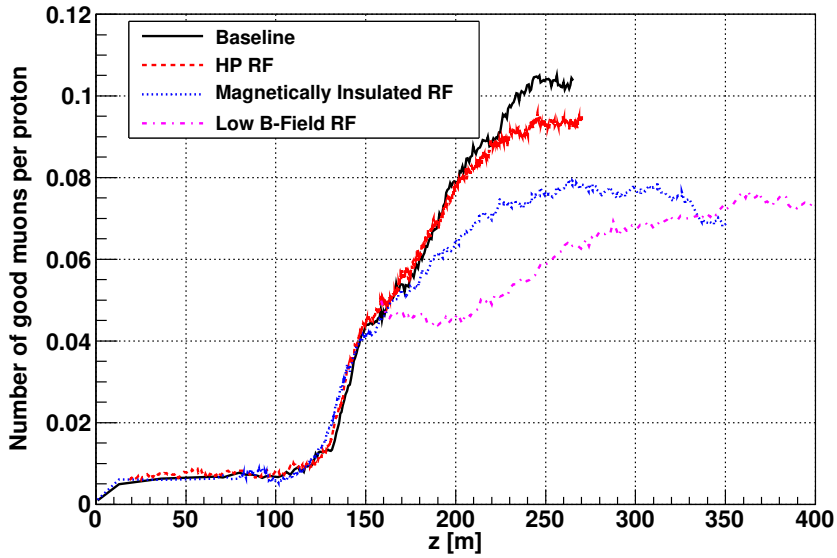

Figure 161. Comparison of muon capture performance of the proposed alternative lattices and the baseline outlined above. A 'good' muon is one that falls within a momentum range of ± 100 MeV/c of the nominal momentum, that has longitudinal amplitude $A_L^2 < 0.15$ m and has transverse amplitude squared $A_\perp^2 < 0.030$ m.

for each momentum transported, the offset of the periodic orbit must be zero at the entrance and the exit to the arc to ensure that the beam goes through the centre of the linac; (b) the arc must be achromatic for each momentum to guarantee matching to the linac; (c) the arc must be mirror symmetric, so that μ^+ and μ^- can pass through the same lattice in opposite directions; (d) the arc must be nearly isochronous for both energies to ensure the proper phasing with the linac RF; and (e) the size of the orbit offsets, beta functions, and dispersion should be small enough to keep the aperture size reasonable.

We used a ns-FFAG triplet magnet arrangement as the basic cell of the arc design. The inward-bending triplet cell has an outward-bending combined-function magnet with positive gradient (horizontally focusing) at the centre and two inward-bending magnets located on either side with equal negative gradients. The outward-bending triplet-cell has the same structure but reversed dipole fields. The cell symmetry ensures that their periodic solutions have $\alpha_x = \alpha_y = 0$ and $D'_x = 0$ at the beginning and the end. Since perturbative-method codes are not suitable for large-momentum-offset cases, we studied the NS-FFAG optics using the Polymorphic Tracking Code (PTC) module of the MAD-X program [467], which allows symplectic integration through all elements with user control over the precision (with the full or expanded Hamiltonian).

Since the two arc designs are very similar, we focus on the details of the optics of the 1.2 GeV/c and the 2.4 GeV/c arcs. We choose the lower 1.2 GeV/c momentum as the nominal momentum going through the magnet centres. The constraint that the lower-energy periodic orbit must have zero offset coming in and out of the cell is then automatically satisfied. Besides, once the 1.2 GeV/c linear optics is adjusted using quadrupole gradients, introduction of the sextupole and octupole magnetic

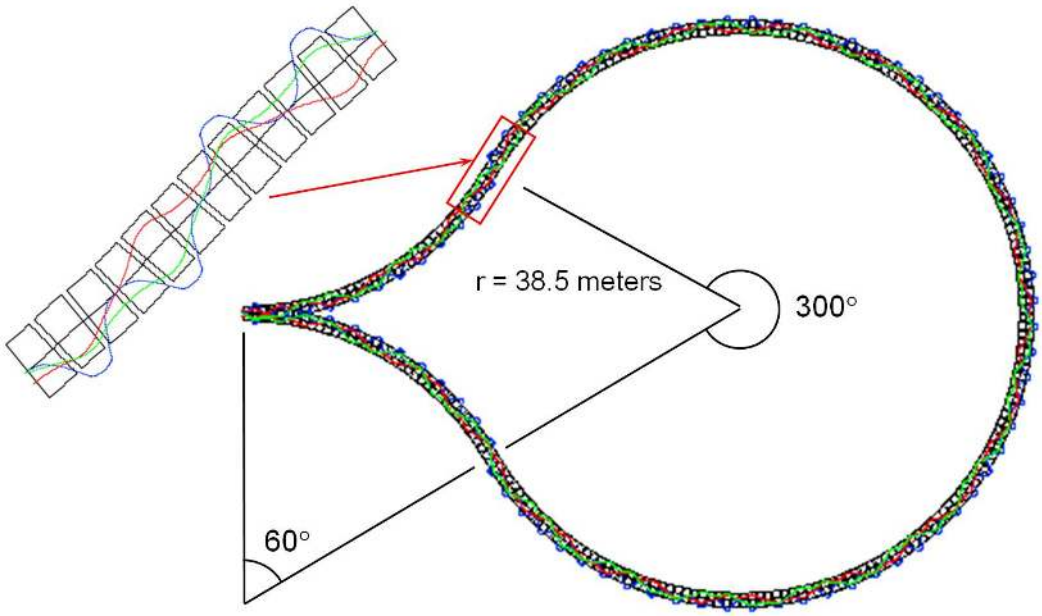

Figure 162. Layout and building-block-cell of a droplet-shaped return arc based on ns-FFAG optics.

field components required for accommodating the 2.4 GeV/c momentum does not change it. This decouples the 1.2 GeV/c linear optics from the 2.4 GeV/c optics and ensures that, once the $D_x = 0$ and $D'_x = 0$ conditions are met for 1.2 GeV/c, they are not affected by the tuning of the 2.4 GeV/c optics.

The triplet is composed of 1 m long magnets separated by 20 cm gaps with each magnet's bending angle being 5°. The quadrupole gradients are adjusted to make the cell achromatic. Figure 163a shows the 1.2 GeV/c periodic orbit and dispersion, as well as the beta functions for the inward- outward-bending cells. In this case, the Bogacz-Lebedev β_{11} and β_{22} are equal to the usual horizontal and vertical beta-functions, respectively. The outward-bending cell has the same beta functions but its dispersion has opposite sign. With a single triplet, one is not able to satisfy, at the same time, the zero orbit-offset and achromatic conditions for 2.4 GeV/c optics. Therefore, three triplet cells are combined into a "super-cell". Sextupole and octupole field components are introduced in the middle magnets of the triplets while maintaining the super-cell's overall mirror symmetry. By tuning the sextupole components, we simultaneously satisfy the conditions of the super-cell being achromatic and having zero incoming and outgoing periodic-orbit offsets. The octupole components are adjusted, keeping their strengths the same until transverse stability is reached in both dimensions. Figure 163b shows the 2.4 GeV/c periodic orbit, dispersion, and the beta functions for the inward- and outward-bending super-cells. In the outward-bending super-cell, the dipole and sextupole fields are reversed. The beta functions in the outward-bending super-cell remain the same while the periodic orbit and dispersion change sign. Since both the inward and outward-bending super-cells are achromatic and have zero incoming and outgoing periodic orbit offsets, it is clear that the super-cells are automatically matched at both energies. Since the net bend of each super-cell is 15°, they can be combined easily to form the 60° outward and 300° inward bends of the droplet arc.

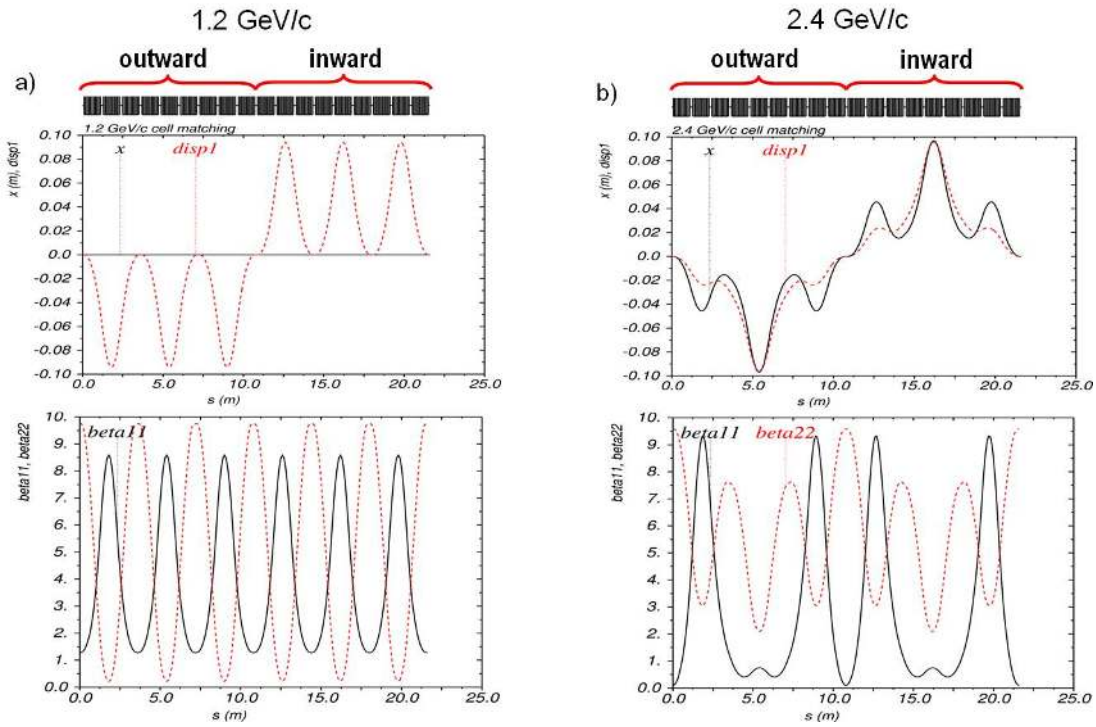

Figure 163. Periodic orbit, dispersion, and beta functions for the inward-outward bending super-cell transition at 1.2 GeV/c and 2.4 GeV/c, the two momenta of interest.

Finally, the linac optics needs to be matched to both arcs for all passes simultaneously by adjusting the strengths of the linac fixed-field quadrupoles. The new solution was obtained by modifying the bi-sected linac profile where the quadrupole strengths increase linearly from the linac's centre toward the ends. Investigation of the complete non-linear dynamics aiming to optimise the RLA's dynamic aperture is under study, as well as phase control to maintain RF synchronisation.

F. Scaling FFAG replacing the final RLA stage

The possibility of using the scaling type of FFAG ring for muon acceleration has already been proposed [468], but it was done assuming very low RF frequencies, incompatible with a frequency of the order of 200 MHz or higher. Here we present a scheme based on stationary-bucket acceleration [469] to accelerate muon beams in a scaling FFAG ring with an RF frequency of 200 MHz.

1. Muon Beam Acceleration

The example of a 3.6 GeV to 12.6 GeV ring with parameters given in table XLII is considered. It is assumed that scaling FFAG magnets with a maximum field of about 4 T are used. This is a reasonable assumption once superconducting magnets with a left-right asymmetric coil distribution

Table XLII. Ring parameters.

Lattice type	scaling FFAG FDF triplet
Injection energy	3.6 GeV
Extraction energy	12.6 GeV
RF frequency	200 MHz
Mean radius	$\sim$ 160.9 m
Synchronous energy (kinetic)	8.04 GeV
Harmonic number h	675
Number of cells	225
Field index k	1 390
RF peak voltage (per turn)	1.8 GV
Number of turns	6
B_{max} (at 12.6 GeV)	3.9 T
Drift length	$\sim$ 1.5 m
Horizontal phase advance per cell	85.86 deg.
Vertical phase advance per cell	33.81 deg.
Excursion	14.3 cm

[470] are employed to realise the scaling-field law. In order to allow the simultaneous acceleration of μ^+ and μ^- beams, the path length per cell of the synchronous particle is adjusted to be a multiple of $\frac{1}{2}\beta_s\lambda_{RF}$, with β_s the ratio of the synchronous particle velocity to the speed of light, and λ_{RF} the RF wavelength.

We use stepwise particle-tracking in a geometrical field model with Enge-type fringe field [471] to study the beam dynamics. Results of single-particle tracking at fixed energy show a normalised transverse acceptance larger than 30 π.mm.rad for both horizontal and vertical planes.

a. 6D Simulation of a Whole Acceleration Cycle

At the beginning of 6D tracking, the bunch of particles is prepared as follows: 1 000 particles are uniformly distributed inside a transverse, 4D ellipsoid (Water-bag distribution) and uniformly inside an ellipse in the longitudinal plane. The initial normalised bunch emittances are 30 π.mm.rad in both horizontal and vertical planes and 150 mm in the longitudinal plane.

Tracking results show no beam lost during the acceleration cycle. No significant emittance blow-up is observed in either the longitudinal (see figure 164) or the transverse planes (see figure 165).

Tracking introducing random alignment errors in the lattice has been performed. No beam loss has been observed with an rms alignment error smaller than 1 mm.

2. Summary

A scheme to accelerate muon beams inside the stationary RF bucket of scaling FFAG rings using 200 MHz RF cavities has been proposed. The ring can accelerate both μ^+ and μ^- beams simultaneously. Acceleration is performed within 6 turns, the RF is used in an efficient manner. A detailed

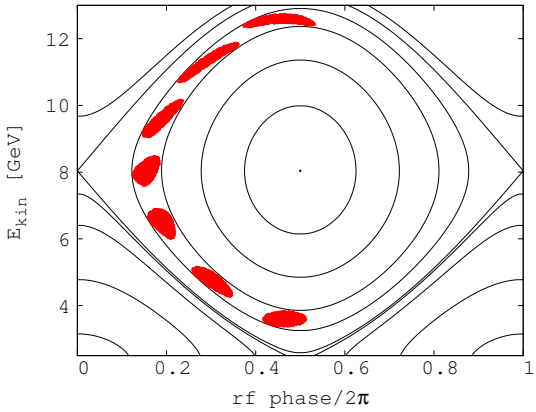

Figure 164. 6-turn acceleration cycle plotted in the longitudinal phase space. Hamiltonian contours are superimposed.

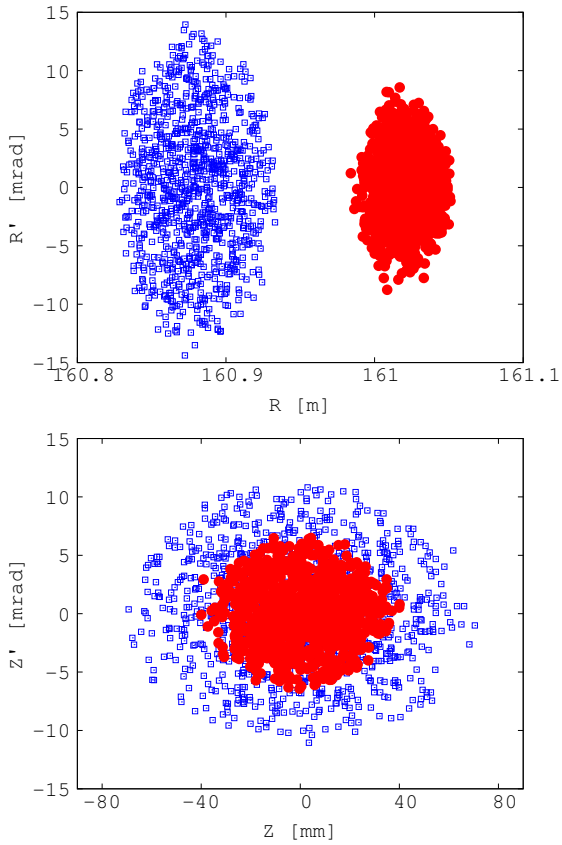

Figure 165. Initial (blue squares) and final (red dots) particle positions plotted in the horizontal (left figure) and vertical (right figure) phase spaces.

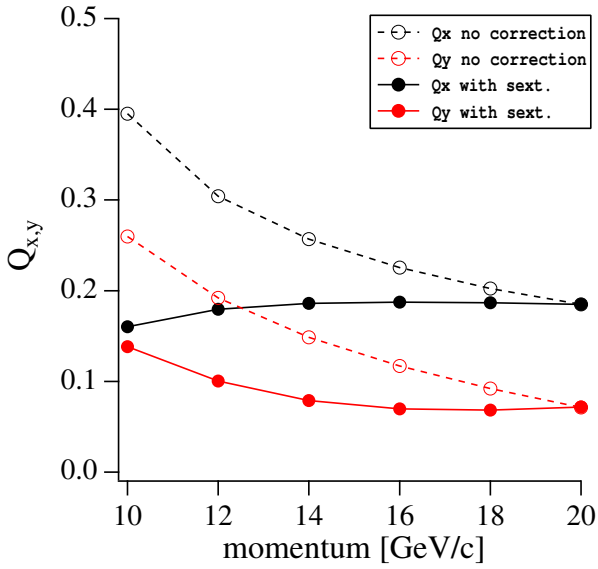

Figure 166. Tune as a function of momentum for a ns-FFAG without (dashed lines/open circles) and with (solid lines/filled circles) sextupole components to correct chromaticity.

tracking-study of the example of a 3.6 GeV to 12.6 GeV muon ring has been presented. 6D particle tracking in a soft-edge-field model shows that the acceptance of this scheme is larger than 30 π.mm.rad in both horizontal and vertical planes, and larger than 150 mm in the longitudinal plane. No beam loss and no significant emittance blow-up was observed in neither the transverse nor the longitudinal planes. This scheme also shows a good tolerance to errors.

G. Chromaticity correction for the linear non-scaling FFAG

A particle with large betatron amplitude has a different time-of-flight because the path length is longer. The effect exists in any ring accelerator, but turns out to be the crucial issue in a muon FFAG for the following reasons. Firstly, the transverse emittance of a muon beam is huge, even after ionisation cooling. Secondly, a muon FFAG accelerates the beam outside the RF bucket with an almost isochronous lattice. Energy gain is sensitive to the RF phase at each turn since there are no synchrotron oscillations which average the different energy gains at each turn. As a result, the longitudinal emittance blows up significantly after acceleration in a linear, ns-FFAG [295]. Furthermore, a scheme to use an FFAG cascade to boost the muon energy is not possible.

It was found that chromaticity correction mitigates the problem [296]. Sextupole fields introduce amplitude-dependent revolution orbits, which cancel the increase of time-of-flight experienced by large amplitude oscillations. In a chromaticity-corrected lattice as shown in figure 166, longitudinal-emittance blowup can be eliminated as shown in figure 167.

On the other hand, there is a price to be paid. In the chromaticity corrected lattice, the orbit shift due to acceleration is large, as shown in figure 168. This directly increases the magnet aperture and the cost. Another side-effect is the asymmetry of the time-of-flight curve shown in figure 168. This implies

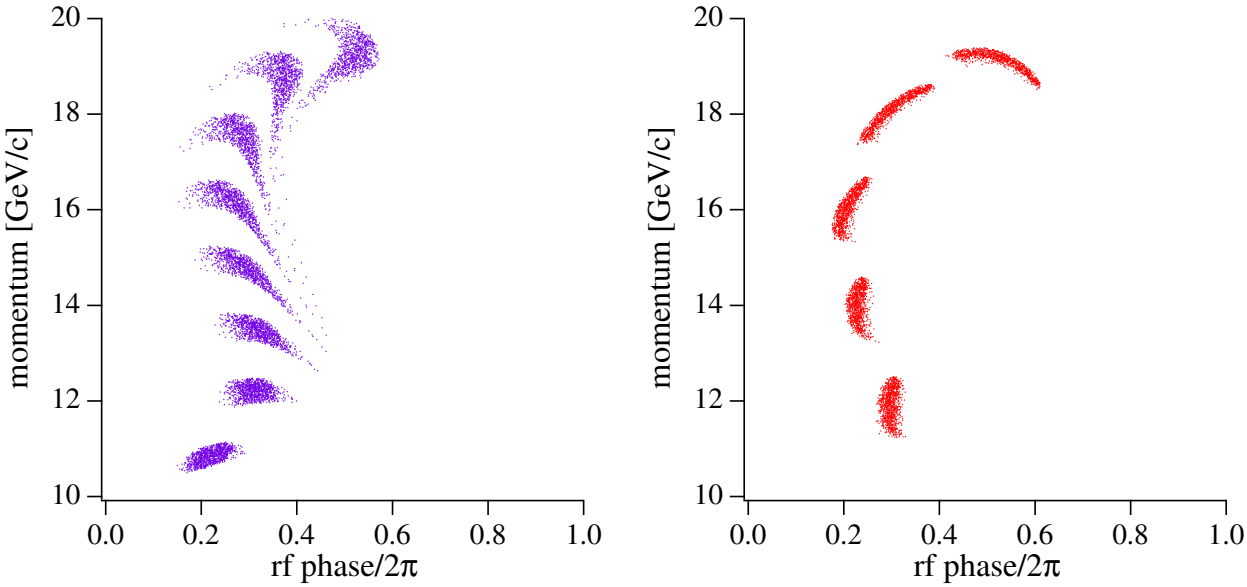

Figure 167. Longitudinal phase space on successive turns with (left) and without (right) chromaticity correction.

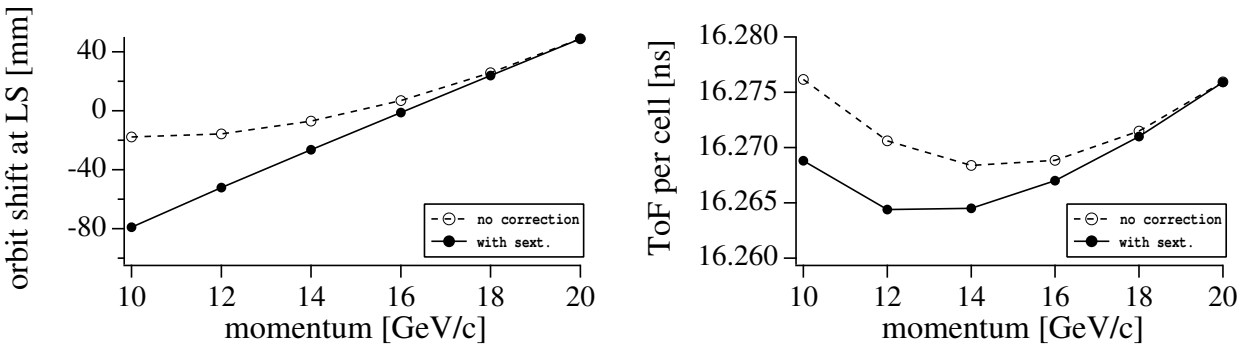

Figure 168. Left: closed position in the long straight (LS) versus momentum without (dashed lines, open circles) and with (solid lines, filled circles) chromaticity correction. Right: time of flight as a function of momentum without and with chromaticity correction.

an increase of total RF voltage. Finally, the most significant impact of the chromaticity correction is the reduction of the dynamic aperture. Non-linearity introduced to correct chromaticity makes the dynamic aperture smaller than 30 mm (dynamic aperture is defined the maximum transverse amplitude which can survive during acceleration). As a result of these adverse effects, chromaticity corrections are not included in the present muon FFAG lattice.

H. Response Matrices for MIND analysis

This appendix summarises the response matrices of signal (wrong sign ν_μ and $\overline{\nu}_\mu$ appearance) and all backgrounds ($\overline{\nu}_\mu$, ν_μ CC, $\overline{\nu}_e$, ν_e CC and NC) in bins of true and reconstructed neutrino energy, relevant to an oscillation analysis. Each entry in the table is the survival probability for each species. In all tables, columns represent the true neutrino energy in GeV and rows the reconstructed energy, also in GeV. The overflow bin in reconstructed energy represents all events with a reconstructed energy greater than the known maximum.

ν_μ appearance

Signal Efficiency

Table XLIII. ν_μ appearance detection efficiency. All values $\times 10^{-4}$.

	0-2.0	2.0-3.0	3.0-4.0	4.0-5.0	5.0-6.0	6.0-8.0	8.0-10.0	10.0-12.5	12.5-15.0	15.0-20.0	20.0-25.0
0-2.0	211.8	331.0	48.55	13.92	5.73	2.371	0.790	0.377	0.142	0.076	0.039
2.0-3.0	154.4	1379	522.0	118.0	42.03	15.18	4.903	1.916	1.049	0.572	0.156
3.0-4.0	45.17	906.6	1408	554.5	145.6	41.82	13.36	4.334	2.211	0.934	0.429
4.0-5.0	17.93	422.1	1377	1352	544.5	105.4	26.26	8.951	3.288	1.449	0.722
5.0-6.0	7.509	155.6	744.7	1476	1233	318.5	49.26	14.82	4.535	2.307	0.761
6.0-8.0	2.017	70.17	421.2	1469	2729	2010	447.4	71.04	18.31	7.302	3.025
8.0-10.0	0.112	7.406	46.89	230.1	850.6	2371	1823	380.8	56.63	13.65	5.212
10.05-12.5	0	2.134	12.61	37.15	134.9	963.9	2756	2011	416.5	48.96	11.50
12.5-15.0	0	0.126	2.739	11.20	27.05	127.4	886.8	2519	1788	242.5	22.84
15.0-20.0	0	0.126	0.498	2.346	7.930	36.72	173.2	1207	3621	2840	340.5
20.0-25.0	0	0	0.083	0.076	0.088	1.186	11.52	61.27	380.2	2665	2562
overflow	0	0	0	0	0	0.514	0.757	5.685	31.86	477.2	3338

$\overline{\nu}_\mu$ CC background

	0-2.0	2.0-3.0	3.0-4.0	4.0-5.0	5.0-6.0	6.0-8.0	8.0-10.0	10.0-12.5	12.5-15.0	15.0-20.0	20.0-25.0
0-2.0	0	0	0.096	0	0	0.041	0	0	0	0	0
2.0-3.0	0.346	0.546	0	0.083	0	0	0	0	0	0.039	0.020
3.0-4.0	0.173	0.273	0.096	0	0	0.084	0	0.065	0.029	0.077	0.020
4.0-5.0	0.173	0.546	0.192	0.166	0	0.042	0.068	0.065	0	0	0.020
5.0-6.0	0	0.273	0.384	0.083	0.187	0.042	0.034	0	0.029	0.039	0.039
6.0-8.0	0	0.273	0.288	0.249	0.468	0.209	0.068	0.097	0.115	0.096	0.039
8.0-10.0	0	0	0.096	0	0	0.084	0.137	0.129	0.086	0.116	0.020
10.0-12.5	0	0	0	0	0.094	0.042	0.205	0.032	0.086	0.019	0.138
12.5-15.0	0	0	0	0.083	0.094	0	0.102	0	0.058	0.058	0.079
15.0-20.0	0	0	0	0	0	0.084	0.068	0.065	0.029	0.116	0.079
20.0-25.0	0	0	0	0	0	0.042	0	0.032	0.086	0.058	0.059
overflow	0	0	0	0	0	0	0	0	0	0.019	0.098

Table XLIV. $\overline{\nu}_\mu$ *CC background. All values* $\times 10^{-4}$.

ν_e CC background

	0-2.0	2.0-3.0	3.0-4.0	4.0-5.0	5.0-6.0	6.0-8.0	8.0-10.0	10.0-12.5	12.5-15.0	15.0-20.0	20.0-25.0
0-2.0	0	0	0	0	0	0	0	0	0.020	0.013	0
2.0-3.0	0	0	0	0	0	0	0.023	0.045	0.040	0	0
3.0-4.0	0	0	0	0	0	0	0	0	0	0.013	0.055
4.0-5.0	0	0	0	0	0	0.028	0	0	0	0	0.014
5.0-6.0	0	0	0	0	0	0	0	0	0	0	0.014
6.0-8.0	0	0	0	0	0	0	0	0	0.020	0	0
8.0-10.0	0	0	0	0	0	0	0	0	0	0	0
10.0-12.5	0	0	0	0.054	0	0	0	0	0	0	0
12.5-15.0	0	0	0	0	0	0	0	0	0	0	0
15.0-20.0	0	0	0	0	0	0	0	0.022	0.020	0	0
20.0-25.0	0	0	0	0	0	0	0	0	0	0	0
overflow	0	0	0	0	0	0	0	0	0	0	0

Table XLV. ν_e *CC background. All values* $\times 10^{-4}$.

NC background

	0-2.0	2.0-3.0	3.0-4.0	4.0-5.0	5.0-6.0	6.0-8.0	8.0-10.0	10.0-12.5	12.5-15.0	15.0-20.0	20.0-25.0
0-2.0	0	0	0	0	0.035	0	0.026	0.050	0.022	0.015	0
2.0-3.0	0	0	0.034	0.061	0.070	0.016	0.052	0.050	0.034	0.030	0.039
3.0-4.0	0	0	0	0.061	0.070	0	0.052	0.076	0.056	0.068	0.055
4.0-5.0	0	0	0.034	0.030	0.106	0.157	0.210	0.088	0.146	0.106	0.086
5.0-6.0	0	0	0	0.030	0.035	0.031	0.026	0.076	0.067	0.030	0.023
6.0-8.0	0	0	0	0	0	0.094	0.105	0.113	0.067	0.046	0.047
8.0-10.0	0	0	0	0	0.035	0.047	0.026	0.088	0.011	0.015	0.023
10.0-12.5	0	0	0	0	0	0	0.013	0.025	0.034	0.046	0.055
12.5-15.0	0	0	0	0	0	0	0	0	0.034	0.015	0.008
15.0-20.0	0	0	0	0	0	0	0	0.013	0.011	0.030	0.016
20.0-25.0	0	0	0	0	0	0	0	0	0	0	0.008
overflow	0	0	0	0	0	0	0	0	0	0	0

Table XLVI. *NC background. All values* $\times 10^{-4}$.

$\overline{\nu}_\mu$ appearance

Signal Efficiency

	0-2.0	2.0-3.0	3.0-4.0	4.0-5.0	5.0-6.0	6.0-8.0	8.0-10.0	10.0-12.5	12.5-15.0	15.0-20.0	20.0-25.0
0-2.0	169.5	228.4	47.07	9.966	3.558	1.170	0.648	0.485	0.173	0.077	0
2.0-3.0	378.0	1007	392.8	103.1	24.72	7.939	2.594	1.260	0.490	0.270	0.157
3.0-4.0	310.3	1762	1234	435.1	115.1	22.06	4.983	2.197	0.951	0.481	0.216
4.0-5.0	97.66	1271	2188	1306	448.7	79.27	12.66	3.521	1.729	0.828	0.452
5.0-6.0	24.41	419.5	1627	2009	1188	258.6	30.55	8.561	2.825	1.367	0.748
6.0-8.0	6.926	146.9	895.2	2620	3790	2173	386.3	51.72	12.80	4.622	2.715
8.0-10.0	0.346	12.01	87.04	400.3	1451	3242	2012	354.2	48.22	12.81	5.371
10.0-12.5	0.173	3.274	25.27	70.34	224.4	1460	3617	2256	393.9	49.64	15.19
12.5-15.0	0	0.136	5.283	26.99	55.52	199.2	1243	3171	1971	249.2	29.33
15.0-20.0	0	0.136	0.384	2.907	14.79	68.24	273.2	1634	4485	3151	357.7
20.0-25.0	0	0	0	0	0.281	1.713	19.83	95.11	528.3	3212	2766
overflow	0	0	0	0	0	0.209	1.058	7.980	44.73	631.9	3982

Table XLVII. $\overline{\nu}_\mu$ *appearance detection efficiency. All values* $\times 10^{-4}$

ν_μ CC background

	0-2.0	2.0-3.0	3.0-4.0	4.0-5.0	5.0-6.0	6.0-8.0	8.0-10.0	10.0-12.5	12.5-15.0	15.0-20.0	20.0-25.0
0-2.0	0	0.251	0	0	0	0	0	0	0	0	0
2.0-3.0	0.112	0.251	0	0	0	0	0	0	0	0	0.039
3.0-4.0	0.224	0.126	0	0.076	0	0	0	0	0	0	0.020
4.0-5.0	0	0.628	0.249	0.076	0.176	0.079	0	0	0	0	0
5.0-6.0	0	0	0.166	0.378	0.088	0.040	0.033	0	0.028	0	0
6.0-8.0	0	0.251	0.249	0.605	0.529	0.119	0.329	0.126	0.057	0.095	0.098
8.0-10.0	0	0.126	0	0.151	0.176	0.316	0.099	0.063	0.028	0.057	0.078
10.0-12.5	0	0	0	0.076	0.088	0.277	0.066	0.063	0.142	0.076	0.098
12.5-15.0	0	0	0	0	0.088	0.119	0.197	0.126	0.113	0.057	0.098
15.0-20.0	0	0	0	0	0	0	0.033	0.063	0.085	0.038	0.078
20.0-25.0	0	0	0	0	0	0	0	0.031	0.028	0.057	0.059
overflow	0	0	0	0	0	0	0	0	0.057	0.038	0.078

Table XLVIII. $\overline{\nu}_\mu$ *CC background. All values* $\times 10^{-4}$.

$\overline{\nu}_e$ CC background

	0-2.0	2.0-3.0	3.0-4.0	4.0-5.0	5.0-6.0	6.0-8.0	8.0-10.0	10.0-12.5	12.5-15.0	15.0-20.0	20.0-25.0
0-2.0	0	0	0	0	0	0	0.030	0	0	0.017	0.018
2.0-3.0	0	0	0	0	0	0.037	0	0.029	0	0	0.053
3.0-4.0	0	0	0	0	0	0	0	0	0	0	0
4.0-5.0	0	0	0	0	0	0	0	0	0	0.035	0
5.0-6.0	0	0	0	0	0	0	0	0	0.026	0	0.018
6.0-8.0	0	0	0	0	0	0	0	0	0	0	0
8.0-10.0	0	0	0	0	0	0	0	0	0	0.017	0
10.0-12.5	0	0	0	0	0	0.037	0	0	0	0	0
12.5-15.0	0	0	0	0	0	0	0	0	0	0	0
15.0-20.0	0	0	0	0	0	0	0	0	0	0	0
20.0-25.0	0	0	0	0	0	0	0	0	0	0	0
overflow	0	0	0	0	0	0	0	0	0	0	0

Table XLIX. *$\overline{\nu}_e$ CC background. All values* $\times 10^{-4}$.

NC background

	0-2.0	2.0-3.0	3.0-4.0	4.0-5.0	5.0-6.0	6.0-8.0	8.0-10.0	10.0-12.5	12.5-15.0	15.0-20.0	20.0-25.0
0-2.0	0	0	0	0	0.070	0.016	0.013	0.038	0.056	0.023	0.055
2.0-3.0	0	0	0.068	0.030	0.070	0.094	0.026	0.038	0.079	0.061	0.063
3.0-4.0	0	0	0.137	0.091	0.106	0.110	0.092	0.088	0.213	0.129	0.117
4.0-5.0	0	0	0.068	0.122	0.317	0.268	0.275	0.189	0.213	0.236	0.250
5.0-6.0	0	0	0	0.030	0	0.063	0.079	0.101	0.067	0.084	0.055
6.0-8.0	0	0	0	0	0.070	0.094	0.171	0.076	0.180	0.137	0.156
8.0-10.0	0	0	0	0	0	0.016	0.105	0.076	0.101	0.084	0.117
10.0-12.5	0	0	0	0	0	0	0.039	0.06	0.056	0.053	0.055
12.5-15.0	0	0	0	0	0	0	0	0.025	0.011	0.053	0.031
15.0-20.0	0	0	0	0	0	0	0	0	0.011	0.023	0.047
20.0-25.0	0	0	0	0	0	0	0	0	0	0	0.008
overflow	0	0	0	0	0	0	0	0	0	0	0.008

Table L. *NC background. All values* $\times 10^{-4}$.

[1] **IDS-NF** Collaboration, "The International Design Study for the Neutrino Factory.". https://www.ids-nf.org/wiki/FrontPage.

[2] "Ninth International Workshop on Neutrino Factories, super-beams, and beta-beams.". http://fphy.hep.okayama-u.ac.jp/nufact07/.

[3] **IDS-NF** Collaboration, The Steering Group on behalf of the collaboration, "Principal objectives.". https://www.ids-nf.org/wiki/FrontPage/Documentation?action=AttachFile&do=get&target=IDS-NF-001-v1.0.pdf.

[4] **ISS Physics Working Group** Collaboration, A. Bandyopadhyay *et al.*, "Physics at a future Neutrino Factory and super-beam facility," *Rept. Prog. Phys.* **72** (2009) 106201, arXiv:0710.4947 [hep-ph].

[5] **ISS Accelerator Working Group** Collaboration, M. Apollonio *et al.*, "Accelerator Design Concept for Future Neutrino Factories," *JINST* **4** (2009) P07001.

[6] **ISS Detector Working Group** Collaboration, T. Abe *et al.*, "Detectors and flux instrumentation for future neutrino facilities," *JINST* **4** (2009) T05001, arXiv:0712.4129 [physics.ins-det].

[7] **Particle Data Group** Collaboration, C. Amsler *et al.*, "Review of particle physics," *Phys. Lett. B* **667** (2008) 1–6.

[8] B. Pontecorvo, "Mesonium and antimesonium," *Sov. Phys. JETP* **6** (1957) 429.

[9] B. Pontecorvo, "Inverse beta processes and nonconservation of lepton charge," *Sov. Phys. JETP* **7** (1958) 172–173.

[10] Z. Maki, M. Nakagawa, and S. Sakata, "Remarks on the unified model of elementary particles," *Prog. Theor. Phys.* **28** (1962) 870–880.

[11] S. M. Bilenky, S. Pascoli, and S. T. Petcov, "Majorana neutrinos, neutrino mass spectrum, CP-violation and neutrinoless double beta-decay. I: The three-neutrino mixing case," *Phys. Rev. D* **64** (2001) 053010, arXiv:0102265 [hep-ph].

[12] J. Kopp, M. Lindner, and T. Ota, "Discovery reach for non-standard interactions in a neutrino factory," *Phys. Rev. D* **76** (2007) 013001, arXiv:0702269 [hep-ph].

[13] A. Cervera, A. Laing, J. Martin-Albo, and F. J. P. Soler, "Performance of the MIND detector at a Neutrino Factory using realistic muon reconstruction," *Nucl. Instrum. Meth. A* **624** (2010) 601–614, arXiv:1004.0358 [hep-ex].

[14] M. M. Alsharo'a *et al.*, "Recent progress in neutrino factory and muon collider research within the muon collaboration," *Phys. Rev. ST Accel. Beams* **6** (2003) 081001.

[15] R. B. Palmer, "Muon collider progress," in *Proceedings of the 23rd Particle Accelerator Conference* [474], pp. 652–656.

[16] M. C. Gonzalez-Garcia and M. Maltoni, "Phenomenology with Massive Neutrinos," *Phys. Rept.* **460** (2008) 1–129, arXiv:0704.1800 [hep-ph].

[17] R. N. Mohapatra *et al.*, "Theory of neutrinos: A white paper," *Rept. Prog. Phys.* **70** (2007) 1757–1867, arXiv:0510213 [hep-ph].

[18] **Particle Data Group** Collaboration, K. Nakamura *et al.*, "Review of particle physics," *J. Phys. G* **37** (2010) 075021.

[19] M. C. Gonzalez-Garcia, M. Maltoni, and J. Salvado, "Updated global fit to three neutrino mixing: status of the hints of $\theta_{13} > 0$," *JHEP* **04** (2010) 056, arXiv:1001.4524 [hep-ph].

[20] M. Mezzetto and T. Schwetz, "θ_{13}: Phenomenology, present status and prospect," *J.Phys.G* **37** (2010) 103001, arXiv:1003.5800 [hep-ph].

[21] F. Ardellier *et al.*, "Letter of intent for Double-CHOOZ: A search for the mixing angle θ_{13}," arXiv:0405032 [hep-ex].

[22] **RENO** Collaboration, J. K. Ahn *et al.*, "RENO: An Experiment for Neutrino Oscillation Parameter θ_{13} Using Reactor Neutrinos at Yonggwang," arXiv:1003.1391 [hep-ex].

[23] **Daya-Bay** Collaboration, X. Guo *et al.*, "A precision measurement of the neutrino mixing angle θ_{13} using reactor antineutrinos at Daya Bay," arXiv:0701029 [hep-ex].
[24] Y. Itow *et al.*, "The JHF-Kamioka neutrino project," *Nucl. Phys. Proc. Suppl.* **111** (2001) 146–151, arXiv:0106019 [hep-ex].
[25] **NOvA** Collaboration, D. S. Ayres *et al.*, "NOvA proposal to build a 30-kiloton off-axis detector to study neutrino oscillations in the Fermilab NuMI beamline," arXiv:0503053 [hep-ex].
[26] G. Altarelli and F. Feruglio, "Models of neutrino masses and mixings," *New J. Phys.* **6** (2004) 106, arXiv:0405048 [hep-ph].
[27] C. H. Albright and M.-C. Chen, "Model predictions for neutrino oscillation parameters," *Phys. Rev. D* **74** (2006) 113006, arXiv:0608137 [hep-ex].
[28] P. F. Harrison, D. H. Perkins, and W. G. Scott, "Tri-bimaximal mixing and the neutrino oscillation data," *Phys. Lett. B* **530** (2002) 167, arXiv:0202074 [hep-ph].
[29] A. de Gouvêa, "Deviation of atmospheric mixing from maximal and structure in the leptonic flavor sector," *Phys.Rev. D* **69** (2004) 093007, arXiv:0401220 [hep-ph].
[30] M. Fukugita and T. Yanagida, "Baryogenesis Without Grand Unification," *Phys. Lett. B* **174** (1986) 45.
[31] S. Davidson, E. Nardi, and Y. Nir, "Leptogenesis," *Phys. Rept.* **466** (2008) 105–177, arXiv:0802.2962 [hep-ph].
[32] M. R. Buckley and H. Murayama, "How can we test seesaw experimentally?," *Phys. Rev. Lett.* **97** (2006) 231801, arXiv:0606088 [hep-ph].
[33] M. L. Mangano *et al.*, "Physics at the front end of a neutrino factory: A Quantitative appraisal," arXiv:0105155 [hep-ph]. Report of the nuDIS Working Group for the ECFA-CERN Neutrino-Factory study.
[34] A. de Gouvêa and J. Jenkins, "What can we learn from neutrino electron scattering?," *Phys. Rev. D* **74** (2006) 033004, arXiv:0603036 [hep-ph].
[35] J. Aysto *et al.*, "Physics with low-energy muons at a neutrino factory complex," arXiv:0109217 [hep-ph]. Report of the Stopped Muons Working Group for the ECFA - CERN study on Neutrino Factory and Muon Storage Rings at CERN.
[36] T. Schwetz, M. A. Tortola, and J. W. F. Valle, "Three-flavour neutrino oscillation update," *New J. Phys.* **10** (2008) 113011, arXiv:0808.2016 [hep-ph].
[37] G. Fogli *et al.*, "Observables sensitive to absolute neutrino masses. II.," *Phys. Rev. D* **78** (2008) 033010, arXiv:0805.2517 [hep-ph].
[38] G. L. Fogli, E. Lisi, A. Marrone, A. Palazzo, and A. M. Rotunno, "SNO, KamLAND and neutrino oscillations: θ_{13}," arXiv:0905.3549 [hep-ph].
[39] **KamLAND** Collaboration, S. Abe *et al.*, "Precision Measurement of Neutrino Oscillation Parameters with KamLAND," *Phys. Rev. Lett.* **100** (2008) 221803, arXiv:0801.4589 [hep-ex].
[40] **KamLAND** Collaboration, A. Gando *et al.*, "Constraints on θ_{13} from A Three-Flavor Oscillation Analysis of Reactor Antineutrinos at KamLAND," arXiv:1009.4771 [hep-ex].
[41] **SNO** Collaboration, B. Aharmim *et al.*, "Combined Analysis of all Three Phases of Solar Neutrino Data from the Sudbury Neutrino Observatory," arXiv:1109.0763 [nucl-ex].
[42] **SNO** Collaboration, B. Aharmim *et al.*, "An Independent Measurement of the Total Active ^{8}B Solar Neutrino Flux Using an Array of ^{3}He Proportional Counters at the Sudbury Neutrino Observatory," *Phys. Rev. Lett.* **101** (2008) 111301, arXiv:0806.0989 [nucl-ex].
[43] **SNO** Collaboration, B. Aharmim *et al.*, "Low Energy Threshold Analysis of the Phase I and Phase II Data Sets of the Sudbury Neutrino Observatory," *Phys. Rev. C* **81** (2010) 055504, arXiv:0910.2984 [nucl-ex].
[44] B. T. Cleveland *et al.*, "Measurement of the solar electron neutrino flux with the Homestake chlorine detector," *Astrophys. J.* **496** (1998) 505–526.
[45] **GNO** Collaboration, M. Altmann *et al.*, "Complete results for five years of GNO solar neutrino observations," *Phys. Lett. B* **616** (2005) 174–190, arXiv:0504037 [hep-ex].

[46] **Super-Kamkiokande** Collaboration, J. Hosaka *et al.*, "Solar neutrino measurements in Super-Kamiokande-I," *Phys. Rev. D* **73** (2006) 112001, arXiv:0508053 [hep-ex].

[47] **SAGE** Collaboration, J. N. Abdurashitov *et al.*, "Measurement of the solar neutrino capture rate with gallium metal. III: Results for the 2002–2007 data-taking period," *Phys. Rev. C* **80** (2009) 015807, arXiv:0901.2200 [nucl-ex].

[48] F. Kaether, W. Hampel, G. Heusser, J. Kiko, and T. Kirsten, "Reanalysis of the GALLEX solar neutrino flux and source experiments," *Phys. Lett. B* **685** (2010) 47–54, arXiv:1001.2731 [hep-ex].

[49] **Borexino** Collaboration, C. Arpesella *et al.*, "Direct Measurement of the ^7Be Solar Neutrino Flux with 192 Days of Borexino Data," *Phys. Rev. Lett.* **101** (2008) 091302, arXiv:0805.3843 [astro-ph].

[50] **MINOS** Collaboration, P. Adamson *et al.*, "Measurement of neutrino oscillations with the MINOS detectors in the NuMI beam," *Phys. Rev. Lett.* **101** (2008) 131802, arXiv:0806.2237 [hep-ex].

[51] P. Vahle [Minos Collaboration], Talk at the Neutrino 2010 Conference, Athens, 2010.

[52] M. Maltoni and T. Schwetz, "Testing the statistical compatibility of independent data sets," *Phys. Rev. D* **68** (2003) 033020, arXiv:0304176 [hep-ph].

[53] **K2K** Collaboration, E. Aliu *et al.*, "Evidence for muon neutrino oscillation in an accelerator-based experiment," *Phys. Rev. Lett.* **94** (2005) 081802, arXiv:0411038 [hep-ex].

[54] **Super-Kamiokande** Collaboration, R. Wendell *et al.*, "Atmospheric neutrino oscillation analysis with sub-leading effects in Super-Kamiokande I, II, and III," *Phys. Rev. D* **81** (2010) 092004, arXiv:1002.3471 [hep-ex].

[55] G. L. Fogli, E. Lisi, A. Marrone, and A. Palazzo, "Global analysis of three-flavor neutrino masses and mixings," *Prog. Part. Nucl. Phys.* **57** (2006) 742–795, arXiv:0506083 [hep-ph].

[56] T. Schwetz, "Global fits to neutrino oscillation data," *Phys. Scripta T* **127** (2006) 1–5, arXiv:0606060 [hep-ph].

[57] **CHOOZ** Collaboration, M. Apollonio *et al.*, "Search for neutrino oscillations on a long base-line at the CHOOZ nuclear power station," *Eur. Phys. J. C* **27** (2003) 331–374, arXiv:0301017 [hep-ex].

[58] G. L. Fogli, E. Lisi, A. Marrone, A. Palazzo, and A. M. Rotunno, "Hints of $\theta_{13} > 0$ from global neutrino data analysis," *Phys. Rev. Lett.* **101** (2008) 141801, arXiv:0806.2649 [hep-ph].

[59] M. Maltoni and T. Schwetz, "Three-flavour neutrino oscillation update and comments on possible hints for a non-zero θ_{13}," *Proc. of Science IDM* (2008) 072, arXiv:0812.3161 [hep-ph].

[60] **MINOS** Collaboration, P. Adamson *et al.*, "New constraints on muon-neutrino to electron-neutrino transitions in MINOS," *Phys. Rev. D* **82** (2010) 051102, arXiv:1006.0996 [hep-ex].

[61] **MINOS** Collaboration, P. Adamson *et al.*, "Search for muon-neutrino to electron-neutrino transitions in MINOS," *Phys. Rev. Lett.* **103** (2009) 261802, arXiv:0909.4996 [hep-ex].

[62] M. Maltoni, T. Schwetz, M. A. Tortola, and J. W. F. Valle, "Status of global fits to neutrino oscillations," *New J. Phys.* **6** (2004) 122, arXiv:0405172 [hep-ph]. Updated results in hep-ph/0450172 (v6).

[63] S. Goswami and A. Y. Smirnov, "Solar neutrinos and 1-3 leptonic mixing," *Phys. Rev. D* **72** (2005) 053011, arXiv:0411359 [hep-ph].

[64] A. Balantekin and D. Yilmaz, "Contrasting solar and reactor neutrinos with a non-zero value of θ_{13}," *J. Phys. G* **35** (2008) 075007, arXiv:0804.3345 [hep-ph].

[65] M. Maltoni, T. Schwetz, M. A. Tortola, and J. W. F. Valle, "Status of three-neutrino oscillations after the SNO-salt data," *Phys. Rev. D* **68** (2003) 113010, arXiv:0309130 [hep-ph].

[66] **MiniBooNE** Collaboration, A. A. Aguilar-Arevalo *et al.*, "Observed event excess in the MiniBooNE search for $\bar{\nu}_\mu \to \bar{\nu}_e$ oscillations," arXiv:1007.1150 [hep-ex].

[67] **LSND** Collaboration, A. Aguilar *et al.*, "Evidence for neutrino oscillations from the observation of $\bar{\nu}_e$ appearance in a $\bar{\nu}_\mu$ beam," *Phys. Rev. D* **64** (2001) 112007, arXiv:0104049 [hep-ex].

[68] **MiniBooNE** Collaboration, A. A. Aguilar-Arevalo *et al.*, "A search for electron neutrino appearance at the $\Delta m^2 \sim 1$ eV^2 scale," *Phys. Rev. Lett.* **98** (2007) 231801, arXiv:0704.1500 [hep-ex].

[69] Y. Declais *et al.*, "Search for neutrino oscillations at 15-meters, 40-meters, and 95-meters from a nuclear

power reactor at bugey," *Nucl. Phys. B* **434** (1995) 503–534.
[70] F. Dydak *et al.*, "A Search for Muon-neutrino Oscillations in the Δm^2 Range 0.3-eV^2 to 90-eV^2," *Phys. Lett. B* **134** (1984) 281.
[71] **MiniBooNE** Collaboration, A. A. Aguilar-Arevalo *et al.*, "A search for muon neutrino and antineutrino disappearance in MiniBooNE," *Phys. Rev. Lett.* **103** (2009) 061802, arXiv:0903.2465 [hep-ex].
[72] **MINOS** Collaboration, P. Adamson *et al.*, "Search for sterile neutrino mixing in the MINOS long-baseline experiment," (2010) , arXiv:1001.0336 [hep-ex].
[73] S. M. Bilenky, C. Giunti, W. Grimus, and T. Schwetz, "Four-neutrino mass spectra and the Super-Kamiokande atmospheric up-down asymmetry," *Phys. Rev. D* **60** (1999) 073007, arXiv:9903454 [hep-ph].
[74] M. Maltoni, T. Schwetz, M. A. Tortola, and J. W. F. Valle, "Ruling out four-neutrino oscillation interpretations of the LSND anomaly?," *Nucl. Phys. B* **643** (2002) 321–338, arXiv:0207157 [hep-ph].
[75] E. Akhmedov and T. Schwetz, "MiniBooNE and LSND data: non-standard neutrino interactions in a (3+1) scheme versus (3+2) oscillations," arXiv:1007.4171 [hep-ph].
[76] O. L. G. Peres and A. Y. Smirnov, "(3+1) spectrum of neutrino masses: A chance for LSND?," *Nucl. Phys. B* **599** (2001) 3, arXiv:0011054 [hep-ph].
[77] M. Sorel, J. M. Conrad, and M. Shaevitz, "A combined analysis of short-baseline neutrino experiments in the (3+1) and (3+2) sterile neutrino oscillation hypotheses," *Phys. Rev. D* **70** (2004) 073004, arXiv:0305255 [hep-ph].
[78] G. Karagiorgi *et al.*, "Leptonic CP violation studies at MiniBooNE in the (3+2) sterile neutrino oscillation hypothesis," *Phys. Rev. D* **75** (2007) 013011, arXiv:0609177 [hep-ph].
[79] M. Maltoni and T. Schwetz, "Sterile neutrino oscillations after first MiniBooNE results," *Phys. Rev. D* **76** (2007) 093005, arXiv:0705.0107 [hep-ph].
[80] G. Karagiorgi, Z. Djurcic, J. M. Conrad, M. H. Shaevitz, and M. Sorel, "Viability of $\Delta m^2 \sim 1$ eV^2 sterile neutrino mixing models in light of MiniBooNE electron neutrino and antineutrino data from the Booster and NuMI beamlines," *Phys. Rev. D* **80** (2009) 073001, arXiv:0906.1997 [hep-ph].
[81] E. Ma, G. Rajasekaran, and I. Stancu, "Hierarchical four-neutrino oscillations with a decay option," *Phys. Rev. D* **61** (2000) 071302, arXiv:9908489 [hep-ph].
[82] S. Palomares-Ruiz, S. Pascoli, and T. Schwetz, "Explaining LSND by a decaying sterile neutrino," *JHEP* **09** (2005) 048, arXiv:0505216 [hep-ph].
[83] S. Gninenko, "A resolution of puzzles from the LSND, KARMEN, and MiniBooNE experiments," arXiv:1009.5536 [hep-ph].
[84] H. Murayama and T. Yanagida, "LSND, SN1987A, and CPT violation," *Phys. Lett. B* **520** (2001) 263–268, arXiv:0010178 [hep-ph].
[85] G. Barenboim, L. Borissov, and J. D. Lykken, "CPT violating neutrinos in the light of KamLAND," arXiv:0212116 [hep-ph].
[86] M. C. Gonzalez-Garcia, M. Maltoni, and T. Schwetz, "Status of the CPT violating interpretations of the LSND signal," *Phys. Rev. D* **68** (2003) 053007, arXiv:0306226 [hep-ph].
[87] V. Barger, D. Marfatia, and K. Whisnant, "LSND anomaly from CPT violation in four-neutrino models," *Phys. Lett. B* **576** (2003) 303–308, arXiv:0308299 [hep-ph].
[88] V. A. Kostelecky and M. Mewes, "Lorentz violation and short-baseline neutrino experiments," *Phys. Rev. D* **70** (2004) 076002, arXiv:0406255 [hep-ph].
[89] A. de Gouvêa and Y. Grossman, "A three-flavor, Lorentz-violating solution to the LSND anomaly," *Phys. Rev. D* **74** (2006) 093008, arXiv:0602237 [hep-ph].
[90] T. Katori, V. A. Kostelecky, and R. Tayloe, "Global three-parameter model for neutrino oscillations using Lorentz violation," *Phys. Rev.D* **74** (2006) 105009, arXiv:0606154 [hep-ph].
[91] G. Barenboim and N. E. Mavromatos, "CPT violating decoherence and LSND: A possible window to Planck scale physics," *JHEP* **01** (2005) 034, arXiv:0404014 [hep-ph].
[92] Y. Farzan, T. Schwetz, and A. Y. Smirnov, "Reconciling results of LSND, MiniBooNE and other

experiments with soft decoherence," *JHEP* **07** (2008) 067, arXiv:0805.2098 [hep-ph].

[93] D. B. Kaplan, A. E. Nelson, and N. Weiner, "Neutrino oscillations as a probe of dark energy," *Phys. Rev. Lett.* **93** (2004) 091801, arXiv:0401099 [hep-ph].

[94] V. Barger, D. Marfatia, and K. Whisnant, "Confronting mass-varying neutrinos with MiniBooNE," *Phys. Rev. D* **73** (2006) 013005, arXiv:0509163 [hep-ph].

[95] H. Pas, S. Pakvasa, and T. J. Weiler, "Sterile - active neutrino oscillations and shortcuts in the extra dimension," *Phys. Rev. D* **72** (2005) 095017, arXiv:0504096 [hep-ph].

[96] T. Schwetz, "LSND versus MiniBooNE: Sterile neutrinos with energy dependent masses and mixing?," *JHEP* **02** (2008) 011, arXiv:0710.2985 [hep-ph].

[97] A. E. Nelson, "Effects of CP Violation from Neutral Heavy Fermions on Neutrino Oscillations, and the LSND/MiniBooNE Anomalies," arXiv:1010.3970 [hep-ph].

[98] P. Huber, M. Lindner, T. Schwetz, and W. Winter, "First hint for CP violation in neutrino oscillations from upcoming superbeam and reactor experiments," *JHEP* **11** (2009) 044, arXiv:0907.1896 [hep-ph].

[99] M. Bishai *et al.*, "Physics report of LBNE," (2011) .

[100] J. Tang and W. Winter, "Neutrino factory in stages: Low energy, high energy, off-axis," *Phys. Rev. D* **81** (2010) 033005, arXiv:0911.5052 [hep-ph].

[101] V. Barger, S. Geer, and K. Whisnant, "Long baseline neutrino physics with a muon storage ring neutrino source," *Phys. Rev. D* **61** (2000) 053004, arXiv:9906487 [hep-ph].

[102] A. Cervera *et al.*, "Golden measurements at a neutrino factory," *Nucl. Phys.* **B579** (2000) 17–55, arXiv:hep-ph/0002108.

[103] J. Burguet-Castell, M. B. Gavela, J. J. Gomez-Cadenas, P. Hernandez, and O. Mena, "On the measurement of leptonic CP violation," *Nucl. Phys. B* **608** (2001) 301–318, arXiv:0103258 [hep-ph].

[104] M. Freund, P. Huber, and M. Lindner, "Systematic exploration of the neutrino factory parameter space including errors and correlations," *Nucl. Phys.* **B615** (2001) 331–357, hep-ph/0105071.

[105] P. Huber and W. Winter, "Neutrino factories and the 'magic' baseline," *Phys. Rev.* **D68** (2003) 037301, arXiv:hep-ph/0301257.

[106] A. Donini, E. Fernandez-Martinez, D. Meloni, and S. Rigolin, "nu/mu disappearance at the SPL, T2K-I, NOnuA and the neutrino factory," *Nucl. Phys.* **B743** (2006) 41–73, arXiv:hep-ph/0512038.

[107] P. Huber, M. Lindner, M. Rolinec, and W. Winter, "Optimization of a neutrino factory oscillation experiment," *Phys. Rev.* **D74** (2006) 073003, arXiv:hep-ph/0606119.

[108] R. Gandhi and W. Winter, "Physics with a very long neutrino factory baseline," *Phys. Rev.* **D75** (2007) 053002, arXiv:hep-ph/0612158.

[109] J. Kopp, T. Ota, and W. Winter, "Neutrino factory optimization for non-standard interactions," *Phys. Rev.* **D78** (2008) 053007, arXiv:0804.2261 [hep-ph].

[110] S. K. Agarwalla, P. Huber, J. Tang, and W. Walter, "Optimization of the neutrino factory, revisited," (2010) , arXiv:1012.1872 [hep-ph].

[111] P. Huber, M. Lindner, and W. Winter, "Simulation of long-baseline neutrino oscillation experiments with GLoBES," *Comput. Phys. Commun.* **167** (2005) 195, hep-ph/0407333. http://www.mpi-hd.mpg.de/~globes.

[112] P. Huber, J. Kopp, M. Lindner, M. Rolinec, and W. Winter, "New features in the simulation of neutrino oscillation experiments with GLoBES 3.0," *Comput. Phys. Commun.* **177** (2007) 432–438, hep-ph/0701187. http://www.mpi-hd.mpg.de/~globes.

[113] A. Y. Smirnov, "Neutrino oscillations: What is magic about the 'magic' baseline?," hep-ph/0610198.

[114] S. Geer, O. Mena, and S. Pascoli, "A Low energy neutrino factory for large θ_{13}," *Phys. Rev.* **D75** (2007) 093001, arXiv:hep-ph/0701258.

[115] A. D. Bross, M. Ellis, S. Geer, O. Mena, and S. Pascoli, "A Neutrino factory for both large and small θ_{13}," *Phys. Rev.* **D77** (2008) 093012, arXiv:0709.3889 [hep-ph].

[116] E. Fernández Martínez, T. Li, S. Pascoli, and O. Mena, "Improvement of the low energy neutrino

factory," *Phys. Rev.* **D81** (2010) 073010, arXiv:0911.3776 [Unknown].

[117] T. Li, *Phenomenology of a low-energy neutrino factory and related experiments*. PhD thesis, Durham University, 2010.

[118] **ISS Physics Working Group** Collaboration, A. Bandyopadhyay *et al.*, "Physics at a future Neutrino Factory and super-beam facility," *Rept. Prog. Phys.* **72** (2009) 106201, arXiv:0710.4947 [hep-ph].

[119] C. Rubbia, "The Liquid Argon Time Projection Chamber: A New Concept for Neutrino Detectors," *CERN-EP-INT-77-08* (1977) .

[120] P. Huber and T. Schwetz, "A low energy neutrino factory with non-magnetic detectors," *Phys. Lett.* **B669** (2008) 294–300, arXiv:0805.2019 [hep-ph].

[121] J. Peltoniemi, "Simulations of neutrino oscillations for a low-energy neutrino factory with a magnetized large-volume liquid scintillator at 2288 km baseline," arXiv:0912.2611 [hep-ph].

[122] E. Fernández Martínez, T. Li, S. Pascoli, and O. Mena, "in preparation,".

[123] E. Fernández Martínez, T. Li, S. Pascoli, and O. Mena, "Improvement of the low energy neutrino factory," *Phys. Rev. D* **81** no. 7, (Apr, 2010) 073010.

[124] A. D. Bross, M. Ellis, S. Geer, O. Mena, and S. Pascoli, "A Neutrino factory for both large and small θ_{13}," *Phys. Rev.* **D77** (2008) 093012, arXiv:0709.3889 [hep-ph].

[125] N. C. Ribeiro, H. Minakata, H. Nunokawa, S. Uchinami, and R. Zukanovich-Funchal, "Probing Non-Standard Neutrino Interactions with Neutrino Factories," *JHEP* **12** (2007) 002, arXiv:0709.1980 [hep-ph].

[126] V. Barger, D. Marfatia, and K. Whisnant, "Breaking eight-fold degeneracies in neutrino CP violation, mixing, and mass hierarchy," *Phys. Rev. D* **65** (2002) 073023, arXiv:0112119 [hep-ph].

[127] P. Huber, M. Lindner, and W. Winter, "Superbeams versus neutrino factories," *Nucl. Phys.* **B645** (2002) 3–48, hep-ph/0204352.

[128] T. Ohlsson and W. Winter, "The role of matter density uncertainties in the analysis of future neutrino factory experiments," *Phys. Rev.* **D68** (2003) 073007, hep-ph/0307178.

[129] J. Tang and W. Winter, "Physics with near detectors at a neutrino factory," *Phys. Rev. D* **80** (2009) 053001, arXiv:0903.3039 [hep-ph].

[130] P. Huber, M. Lindner, and W. Winter, "From parameter space constraints to the precision determination of the leptonic dirac cp phase," *JHEP* **05** (2005) 020, hep-ph/0412199.

[131] A. de Gouvêa and W. Winter, "What would it take to determine the neutrino mass hierarchy if $theta_{13}$ were too small?," *Phys. Rev. D* **73** (2006) 033003, arXiv:0509359 [hep-ph].

[132] S. Antusch, P. Huber, J. Kersten, T. Schwetz, and W. Winter, "Is there maximal mixing in the lepton sector?," *Phys. Rev. D* **70** (2004) 097302, arXiv:0404268 [hep-ph].

[133] W. Winter, "Direct test of the MSW effect by the solar appearance term in beam experiments," *Phys. Lett.* **B613** (2005) 67–73, arXiv:hep-ph/0411309.

[134] W. Winter, "Probing the absolute density of the earth's core using a vertical neutrino beam," *Phys. Rev.* **D72** (2005) 037302, hep-ph/0502097.

[135] H. Minakata and S. Uchinami, "On in situ determination of earth matter density in neutrino factory," *Phys. Rev.* **D75** (2007) 073013, hep-ph/0612002.

[136] A. de Gouvêa, J. Jenkins, and B. Kayser, "Neutrino mass hierarchy, vacuum oscillations, and vanishing $|U_{e3}|$," *Phys. Rev. D* **71** (2005) 113009, arXiv:0503079 [hep-ph].

[137] D. Indumathi and N. Sinha, "Effect of tau neutrino contribution to muon signals at neutrino factories," *Phys. Rev.* **D80** (2009) 113012, arXiv:0910.2020 [hep-ph].

[138] A. Cervera, F. Dydak, and J. Gomez Cadenas, "A large magnetic detector for the neutrino factory," *Nucl. Instrum. Meth.* **A451** (2000) 123–130.

[139] A. Donini, J. J. Gomez Cadenas, and D. Meloni, "The τ-contamination of the golden muon sample at the Neutrino Factory," *JHEP* **02** (2011) 95, arXiv:1005.2275 [hep-ph].

[140] C. Densham, M. Dracos, A. Longhin, and M. Zito, "Baseline scenario for the euronu super beam studies," Tech. Rep. EUROnu WP2 Note 09-05, 2009.

[141] J. E. Campagne and A. Cazes, "The θ_{13} and δ_{CP} sensitivities of the SPL-Frejus project revisited," *Eur. Phys. J.* **C45** (2006) 643–657, hep-ex/0411062.
[142] J.-E. Campagne, M. Maltoni, M. Mezzetto, and T. Schwetz, "Physics potential of the CERN-MEMPHYS neutrino oscillation project," *JHEP* **04** (2007) 003, arXiv:hep-ph/0603172.
[143] P. Huber and J. Kopp, "Two experiments for the price of one? – The role of the second oscillation maximum in long baseline neutrino experiments," *JHEP* **03** (2011) 013, arXiv:1010.3706 [hep-ph].
[144] P. Zucchelli, "A novel concept for a $\overline{\nu}_e/\nu_e$ neutrino factory: The beta beam," *Phys. Lett.* **B532** (2002) 166–172.
[145] "Eurisol design report," Tech. Rep. European Commission Contract No. 515768 RIDS.
[146] E. Wildner, "Beta Beams," *Acta Phys. Polon.* **B41** (2010) 1525–1538.
[147] J. Bernabeu *et al.*, "EURONU WP6 2009 yearly report: Update of the physics potential of Nufact, superbeams and betabeams," arXiv:1005.3146 [hep-ph].
[148] J. Burguet-Castell, D. Casper, J. J. Gomez-Cadenas, P. Hernandez, and F. Sanchez, "Neutrino oscillation physics with a higher gamma beta-beam," *Nucl. Phys.* **B695** (2004) 217–240, arXiv:hep-ph/0312068.
[149] J. Burguet-Castell, D. Casper, E. Couce, J. J. Gomez-Cadenas, and P. Hernandez, "Optimal beta-beam at the CERN-SPS," *Nucl. Phys.* **B725** (2005) 306–326, arXiv:hep-ph/0503021.
[150] S. K. Agarwalla, A. Raychaudhuri, and A. Samanta, "Exploration prospects of a long baseline beta beam neutrino experiment with an iron calorimeter detector," hep-ph/0505015.
[151] P. Huber, M. Lindner, M. Rolinec, and W. Winter, "Physics and optimization of beta-beams: From low to very high gamma," *Phys. Rev.* **D73** (2006) 053002, hep-ph/0506237.
[152] A. Donini *et al.*, "A beta beam complex based on the machine upgrades of the LHC," *Eur. Phys. J.* **C48** (2006) 787–796, arXiv:hep-ph/0604229.
[153] S. K. Agarwalla, S. Choubey, and A. Raychaudhuri, "Neutrino mass hierarchy and θ_{13} with a magic baseline beta-beam experiment," *Nucl. Phys. B* **771** (2007) 1–27, arXiv:hep-ph/0610333.
[154] S. K. Agarwalla, S. Choubey, and A. Raychaudhuri, "Exceptional sensitivity to neutrino parameters with a two baseline beta-beam set-up," *Nucl. Phys. B* **805** (2008) 305–325, arXiv:0804.3007 [hep-ph].
[155] S. K. Agarwalla, S. Choubey, A. Raychaudhuri, and W. Winter, "Optimizing the greenfield beta-beam," *JHEP* **06** (2008) 090, arXiv:0802.3621 [hep-ex].
[156] P. Coloma, A. Donini, P. Migliozzi, L. S. Lavina, and F. Terranova, "A minimal Beta Beam with high-Q ions to address CP violation in the leptonic sector," arXiv:1004.3773 [hep-ph].
[157] L. Wolfenstein, "Neutrino oscillations in matter," *Phys. Rev.* **D17** (1978) 2369–2374.
[158] Y. Grossman, "Nonstandard neutrino interactions and neutrino oscillation experiments," *Phys. Lett.* **B359** (1995) 141–147, hep-ph/9507344.
[159] N. Fornengo, M. Maltoni, R. T. Bayo, and J. W. F. Valle, "Probing neutrino non-standard interactions with atmospheric neutrino data," *Phys. Rev.* **D65** (2001) 013010, hep-ph/0108043.
[160] S. Davidson, C. Pena-Garay, N. Rius, and A. Santamaria, "Present and future bounds on non-standard neutrino interactions," *JHEP* **03** (2003) 011, arXiv:0302093 [hep-ph].
[161] C. Biggio, M. Blennow, and E. Fernandez-Martinez, "Loop bounds on non-standard neutrino interactions," *JHEP* **03** (2009) 139, arXiv:0902.0607 [hep-ph].
[162] C. Biggio, M. Blennow, and E. Fernandez-Martinez, "General bounds on non-standard neutrino interactions," *JHEP* **08** (2009) 090, arXiv:0907.0097 [hep-ph].
[163] S. Antusch, J. P. Baumann, and E. Fernandez-Martinez, "Non-Standard Neutrino Interactions with Matter from Physics Beyond the Standard Model," *Nucl. Phys.* **B810** (2009) 369–388, arXiv:0807.1003 [hep-ph].
[164] M. B. Gavela, D. Hernandez, T. Ota, and W. Winter, "Large gauge invariant non-standard neutrino interactions," *Phys. Rev.* **D79** (2009) 013007, arXiv:0809.3451 [hep-ph].
[165] A. L. Fitzpatrick, D. Hooper, and K. M. Zurek, "Implications of CoGeNT and DAMA for Light WIMP Dark Matter," arXiv:1003.0014 [hep-ph].

[166] D. Hooper, J. Collar, J. Hall, and D. McKinsey, "A Consistent Dark Matter Interpretation For CoGeNT and DAMA/LIBRA," *Phys. Rev. D* **82** (2010) 123509, arXiv:1007.1005 [hep-ph].
[167] C. Arina and M. H. G. Tytgat, "Constraints on a Light WIMP from the Isotropic Diffuse Gamma-Ray Emission," arXiv:1007.2765 [astro-ph.CO].
[168] J. Lavalle, "10 GeV dark matter candidates and cosmic-ray antiprotons," *Phys. Rev.* **D82** (2010) 081302, arXiv:1007.5253 [astro-ph.HE].
[169] D. T. Cumberbatch, J. A. Guzik, J. Silk, L. S. Watson, and S. M. West, "Light WIMPs in the Sun: Constraints from Helioseismology," *Phyd. Rev. D* **82** (2010) 103503, arXiv:1005.5102 [astro-ph.SR].
[170] E. Kuflik, A. Pierce, and K. M. Zurek, "Light Neutralinos with Large Scattering Cross Sections in the Minimal Supersymmetric Standard Model," *Phys. Rev.* **D81** (2010) 111701, arXiv:1003.0682 [hep-ph].
[171] A. S. Joshipura and S. Mohanty, "Constraints on flavour-dependent long-range forces from atmospheric neutrino observations at Super-Kamiokande," *Phys. Lett.* **B584** (2004) 103–108, arXiv:hep-ph/0310210.
[172] J. A. Grifols and E. Masso, "Neutrino oscillations in the sun probe long-range leptonic forces," *Phys. Lett.* **B579** (2004) 123–126, arXiv:hep-ph/0311141.
[173] M. C. Gonzalez-Garcia, P. C. de Holanda, E. Masso, and R. Zukanovich Funchal, "Probing long-range leptonic forces with solar and reactor neutrinos," *JCAP* **0701** (2007) 005, arXiv:0609094 [hep-ph].
[174] A. Bandyopadhyay, A. Dighe, and A. S. Joshipura, "Constraints on flavor-dependent long range forces from solar neutrinos and KamLAND," *Phys. Rev.* **D75** (2007) 093005, arXiv:hep-ph/0610263.
[175] A. Samanta, "Long range forces, oscillation parameters and mass hierarchy with atmospheric neutrinos at a magnetized muon detector," arXiv:1001.5344 [hep-ph].
[176] J. Heeck and W. Rodejohann, "Gauged L_μ - L_τ and different Muon Neutrino and Anti- Neutrino Oscillations: MINOS and beyond," arXiv:1007.2655 [hep-ph].
[177] S. Antusch, M. Blennow, E. Fernandez-Martinez, and J. Lopez-Pavon, "Probing non-unitary mixing and CP-violation at a Neutrino Factory," *Phys. Rev.* **D80** (2009) 033002, arXiv:0903.3986 [hep-ph].
[178] D. Meloni, T. Ohlsson, W. Winter, and H. Zhang, "Non-standard interactions versus non-unitary lepton flavor mixing at a neutrino factory," *JHEP* **04** (2010) 041, arXiv:0912.2735 [hep-ph].
[179] R. Alonso *et al.*, "Summary report of MINSIS workshop in Madrid," arXiv:1009.0476 [hep-ph]. MINSIS workshop in Madrid:https://www.ft.uam.es/workshops/neutrino/default.html.
[180] E. Fernandez Martinez, T. Li, S. Pascoli, and O. Mena, "Improvement of the low energy neutrino factory," *Phys. Rev.* **D81** (2010) 073010.
[181] M. Blennow and E. Fernandez-Martinez, "Neutrino oscillation parameter sampling with MonteCUBES," *Comput. Phys. Commun.* **181** (2010) 227–231, arXiv:0903.3985 [hep-ph].
[182] M. Blennow and E. Fernandez-Martinez, "MonteCUBES homepage." HTTP://WWWTH.MPPMU.MPG.DE/MEMBERS/BLENNOW/MONTECUBES/, 2009.
[183] P. Langacker and D. London, "Mixing Between Ordinary and Exotic Fermions," *Phys.Rev.* **D38** (1988) 886.
[184] A. Broncano, M. Gavela, and E. E. Jenkins, "The Effective Lagrangian for the seesaw model of neutrino mass and leptogenesis," *Phys.Lett.* **B552** (2003) 177–184, arXiv:hep-ph/0210271 [hep-ph].
[185] A. Broncano, M. Gavela, and E. E. Jenkins, "Neutrino physics in the seesaw model," *Nucl.Phys.* **B672** (2003) 163–198, arXiv:hep-ph/0307058 [hep-ph].
[186] S. Antusch, S. Blanchet, M. Blennow, and E. Fernandez-Martinez, "Non-unitary Leptonic Mixing and Leptogenesis," arXiv:arXiv:0910.5957 [hep-ph].
[187] M. B. Gavela, T. Hambye, D. Hernandez, and P. Hernandez, "Minimal Flavour Seesaw Models," *JHEP* **09** (2009) 038, arXiv:0906.1461 [hep-ph].
[188] T. Ohlsson, C. Popa, and H. Zhang, "Non-unitarity of the leptonic mixing matrix in the TeV- scale type-I seesaw model," arXiv:1007.0106 [hep-ph].
[189] E. Fernandez-Martinez, M. B. Gavela, J. Lopez-Pavon, and O. Yasuda, "CP-violation from non-unitary

leptonic mixing," *Phys. Lett.* **B649** (2007) 427–435, arXiv:hep-ph/0703098.

[190] E. Nardi, E. Roulet, and D. Tommasini, "Limits on neutrino mixing with new heavy particles," *Phys. Lett.* **B327** (1994) 319–326, hep-ph/9402224.

[191] D. Tommasini, G. Barenboim, J. Bernabeu, and C. Jarlskog, "Nondecoupling of heavy neutrinos and lepton flavor violation," *Nucl.Phys.* **B444** (1995) 451–467, arXiv:hep-ph/9503228 [hep-ph].

[192] S. Antusch, C. Biggio, E. Fernandez-Martinez, M. B. Gavela, and J. Lopez-Pavon, "Unitarity of the Leptonic Mixing Matrix," *JHEP* **10** (2006) 084, arXiv:0607020 [hep-ph].

[193] J. Holeczek, J. Kisiel, J. Syska, and M. Zralek, "Searching for new physics in future neutrino factory experiments," *Eur.Phys.J.* **C52** (2007) 905–917, arXiv:arXiv:0706.1442 [hep-ph].

[194] S. Goswami and T. Ota, "Testing non-unitarity of neutrino mixing matrices at neutrino factories," *Phys. Rev. D* **78** (2008) 033012, arXiv:0802.1434 [hep-ph].

[195] A. Donini, K.-i. Fuki, J. Lopez-Pavon, D. Meloni, and O. Yasuda, "The discovery channel at the Neutrino Factory: $\nu_\mu \to \nu_\tau$ pointing to sterile neutrinos," *JHEP* **08** (2009) 041, arXiv:0812.3703 [hep-ph].

[196] D. Meloni, J. Tang, and W. Winter, "Sterile neutrinos beyond LSND at the Neutrino Factory," arXiv:1007.2419 [hep-ph].

[197] A. Donini, M. Gavela, P. Hernandez, and S. Rigolin, "Neutrino mixing and CP violation," *Nucl.Phys.* **B574** (2000) 23–42, arXiv:hep-ph/9909254 [hep-ph].

[198] A. Kalliomaki, J. Maalampi, and M. Tanimoto, "Search for CP violation at a neutrino factory in a four neutrino model," *Phys.Lett.* **B469** (1999) 179–187, arXiv:hep-ph/9909301 [hep-ph].

[199] A. Donini, M. Lusignoli, and D. Meloni, "Telling three from four neutrinos at the neutrino factory," *Nucl. Phys.* **B624** (2002) 405–422, arXiv:hep-ph/0107231.

[200] A. Donini and D. Meloni, "The 2+2 and 3+1 four-family neutrino mixing at the neutrino factory," *Eur. Phys. J.* **C22** (2001) 179–186, arXiv:hep-ph/0105089.

[201] A. Dighe and S. Ray, "Signatures of heavy sterile neutrinos at long baseline experiments," *Phys. Rev.* **D76** (2007) 113001, arXiv:0709.0383 [hep-ph].

[202] C. Giunti, M. Laveder, and W. Winter, "Short-Baseline Electron Neutrino Disappearance at a Neutrino Factory," *Phys. Rev.* **D80** (2009) 073005, arXiv:0907.5487 [hep-ph].

[203] O. Yasuda, "Sensitivity to sterile neutrino mixings and the discovery channel at a neutrino factory," arXiv:1004.2388 [hep-ph].

[204] C. Crisan and S. Geer, "How well do we need to know the beam properties at a neutrino factory," Tech. Rep. FERMILAB-TM-2101, Fermilab, Batavia, IL, February, 2000.

[205] **The International Design Study for the Neutrino Factory** Collaboration, T. I.-N. S. Group, "Neutrino factory: specification of baseline.". https://www.ids-nf.org/wiki/FrontPage/Documentation?action=AttachFile&do=get&target=IDS-NF-002-v1.1.pdf.

[206] **The International Design Study for the Neutrino Factory** Collaboration, The IDS-NF Steering Group, "Specification of the baseline for the Neutrino Factory accelerator facility, neutrino detectors, and instrumentation.". in preparation.

[207] K. T. McDonald *et al.*, "The MERIT high-power target experiment at the CERN PS," in *Proceedings of the 23rd Particle Accelerator Conference* [474], p. 795.

[208] X. Ding, D. Cline, H. Kirk, and J. S. Berg, "Optimized parameters for a mercury jet target," in *Proceedings of the 23rd Particle Accelerator Conference* [474], p. 2748.

[209] X. Ding, D. Cline, H. Kirk, and J. S. Berg, "A pion production and capture system for a 4 MW target station," in *Proceedings of IPAC'10, Kyoto, Japan* [472], p. 4272.

[210] N. V. Mokhov, "The mars code system user's guide," Tech. Rep. Fermilab-FN-628, Fermilab, 1995.

[211] N. V. Mokhov and O. E. Krivosheev, "MARS code status," in *Advanced Monte Carlo for Radiation Physics, Particle Transport Simulation and Applications*, A. King, F. J. C. Barao, M. Nakagawa, L. Tavora, and P. Vaz, eds., p. 943. Springer, 2001. FERMILAB-Conf-00/181.

[212] N. V. Mokhov, "Status of MARS code," in *Shielding Aspects of Accelerators, Targets and Irradiation Facilities — SATIF 6*. OECD Publishing, 2004. FERMILAB-Conf-03/053.

[213] N. V. Mokhov *et al.*, "Recent enhancements to the MARS15 code," *Radiat. Prot. Dosim.* **116** (2005) 99–103. FERMILAB-Conf-04/053-AD.

[214] `http://www-ap.fnal.gov/MARS/`.

[215] G. Battistoni *et al.*, "The FLUKA code: Description and benchmarking," in *Proceedings of the Hadronic Shower Simulation Workshop 2006*, M. Albrow and R. Raja, eds., vol. 896 of *AIP Conference Proceedings*, pp. 31–49. AIP, 2007.

[216] A. Fasso, A. Ferrari, J. Ranft, and P. R. Sala, "Fluka: a multi-particle transport code," Tech. Rep. CERN-2005-10 and SLAC-R-773, 2005.

[217] J. Back, "Update on fluka–mars comparison." `http://www.hep.princeton.edu/mumu/target/Back/FlukaMarsYields.pdf`, 2010.

[218] J. Back, "Status and consequences of heat and radiation dissipation simulations." Presentation at the 6th IDS-NF Plenary Meeting, RAL, September 22–25, 2010, September, 2010. `https://www.ids-nf.org/wiki/RAL-2010-09-22/Agenda/Accelerator`.

[219] C. Ankenbrandt *et al.*, "Low-energy neutrino factory design," *Phys. Rev. ST Accel. Beams* **12** (2009) 070101.

[220] D. Neuffer *et al.*, "Muon capture in the front end of the IDS neutrino factory," in *Proceedings of IPAC'10, Kyoto, Japan* [472], pp. 3500–3502.

[221] D. Huang *et al.*, "RF studies at fermilab MuCool test area," in *Proceedings of the 23rd Particle Accelerator Conference* [474], p. 888.

[222] A. Alekou, "MICE status," in *Proceedings of IPAC'10, Kyoto, Japan* [472], pp. 3443–3445.

[223] J. C. Gallardo and M. S. Zisman, "A possible hybrid cooling channel for a neutrino factory," in *Proceedings of IPAC'10, Kyoto, Japan* [472], pp. 3515–3517.

[224] D. Stratakis, J. C. Gallardo, and R. B. Palmer, "Magneticall insulated high-gradient accelerating strucvtures for muon acceleration," *J. Phys. G* **37** (2010) 105011.

[225] C. T. Rogers, "Design for a Muon Front End with Magnetically Shielded RF Cavities," in Goodman *et. al.* [475], pp. 298–302.

[226] A. Alekou *et al.*, "Alternative muon front-end for the international design study (IDS)," in *Proceedings of IPAC'10, Kyoto, Japan* [472], pp. 3455–3457.

[227] D. Neuffer, "Varying gradients and magnetic fields and muon capture for a neutrino factory," Tech. Rep. NFMCC-doc-540-v1, Neutrino Factory/Muon Collider, September, 2009. `http://nfmcc-docdb.fnal.gov/`.

[228] S. A. Bogacz, "Recirculating linac acceleration—end-to-end simulation," in Goodman *et. al.* [475], pp. 363–367.

[229] J. S. Berg and S. Machida, "FFAG designs for the International Design Study for the Neutrino Factory," in *Proceedings of the 23rd Particle Accelerator Conference* [474], pp. 657–659.

[230] J. Pasternak *et al.*, "Injection/extraction system of the muon FFAG for the neutrino factory," in *Proceedings of IPAC'10, Kyoto, Japan* [472], pp. 3476–3478.

[231] M. Apollonio, D. J. Kelliher, and A. Blondel, "Muon polarimeter in a neutrino factory decay ring," in *Proceedings of IPAC'10, Kyoto, Japan* [472], pp. 3464–3466.

[232] R. Piteira, "Conception et simulation d'un système optique mesurant la divergence d'un faisceau de muons de 50 gev." Report of "stage de recherche,", magistère interuniversitaire de physique, ecole normale supérieure, paris, 2001.

[233] F. Gerigk *et al.*, "Conceptual design of the SPL II: A high-power superconducting h^- linac at CERN," Tech. Rep. CERN-2006-006, CERN, Geneva, Switzerland, July, 2006.

[234] R. Garoby, "SPL at CERN," in *Proceedings SRF 2009, 14th International Conference on RF Superconductivity, DBB Forum, Berlin September 20–25, 2009*, pp. 930–933. Helmholtz-Zentrum Berlin, Berlin, 2009.

[235] F. Gerigk *et al.*, "Layout and machine optimisation for the SPL at CERN," Tech. Rep. CERN-ATS-2010-208, CERN, Geneva, Switzerland, 2010.

[236] E. Benedetto, "Beam stability in the SPL proton driver accumulator for a Neutrino Factory at CERN.". Published in the proceedings of the 11$^{\text{th}}$ International Workshop on Neutrino Factories, Superbeams and Beta Beams, July 20–25, 2009, Illinois Institute of Technology, Chicago.

[237] J. D. Galambos, J. A. Holmes, and D. K. Olsen, "ORBIT user manual, version 1.10," Tech. Rep. SNS/ORNL/AP Technical Note 011 Rev. 1, Oak Ridge National Laboratory, Oak Ridge, TN, 1999. `http://neutrons.ornl.gov/APGroup/Codes/orbit.htm`.

[238] R. Garoby, E. Benedetto, M. Aiba, and M. Meddahi, "Linac-based Proton Driver for a Neutrino Factory," Tech. Rep. CERN-NEUTRINO-FACTORY-NOTE-157, CERN, Geneva, Switzerland, December, 2009.

[239] L. Arnaudon *et al.*, "Linac4 technical design report," Tech. Rep. CERN-AB-2006-084 ABP/RF and CARE-Note-2006-022-HIPPI, CERN, Geneva, Switzerland, December, 2006.

[240] M. Vretenar, "Status of Linac4 construction at CERN," Tech. Rep. CERN-ATS-2010-227, CERN, Geneva, Switzerland, 2010.

[241] R. C. Fernow, "Recent developments on the muon-facility design-code ICOOL," in *Proceedings of 2005 Particle Accelerator Conference, Knoxville, Tennessee*, pp. 2651–2653. IEEE, Piscataway, NJ, 2005.

[242] J. C. Gallardo, "Note on the calculation of meson (π,k) production distributions for different proton bunch length," Tech. Rep. NFMCC-doc-340, Neutrino Factory/Muon Collider, 2006. `http://nfmcc-docdb.fnal.gov/`.

[243] N. Simos *et al.*, "Irradiation damage studies of high power accelerator materials," *J. Nucl. Mater.* **377** (2008) 41–51.

[244] J. R. J. Bennett *et al.*, "Studies of a Target System for a 4-MW, 24-GeV Proton Beam," Tech. Rep. CERN-INTC-2004-016, CERN, Geneva, Switzerland, April, 2004.

[245] S. Ozaki, R. B. Palmer, M. S. Zisman, and J. C. Gallardo, "Feasibility Study-II of a Muon-Based Neutrino Source," Tech. Rep. BNL-52623, Brookhaven National Laboratory, Upton, NY, 2001.

[246] N. Souchlas, "Shielding studies for the muon collider target." Presentation at the solenoid capture workshop, 29–30 november 2010, brookhanve national laboratory, `http://www.cap.bnl.gov/mumu/conf/solenoidcapture-101129/`, November, 2010.

[247] P. Loveridge, "Technical challenges of the neutrino-factory/muon-collider capture system." Presentation at the solenoid capture workshop, 29–30 november 2010, brookhanve national laboratory, `http://www.cap.bnl.gov/mumu/conf/solenoidcapture-101129/`, November, 2010.

[248] NHMFL, "45 T Hybrid.". `http://www.magnet.fsu.edu/mediacenter/features/meetthemagnets/hybrid.html`.

[249] GHMFL, "Magnet M8.". `http://ghmfl.grenoble.cnrs.fr/spip.php?rubrique77&lang=en`.

[250] A. Fabich, *High Power Proton Beam Shocks and Magnetohydrodynamics in a Mercury Jet Target for a Neutrino Factory*. PhD thesis, University of Vienna, November, 2002. CERN-THESIS-2002-038.

[251] X. Ding, "Energy Deposition of 4-MW Beam Power in a Mercury Jet Target." `http://www.hep.princeton.edu/~mcdonald/mumu/target/Ding/ding_020910.pdf`, 2010.

[252] K. T. McDonald *et al.*, "The MERIT high-power target experiment at the CERN PS," in *Proceedings of IPAC'10, Kyoto, Japan* [472], p. 3527.

[253] M. Rooney, "The current T2K beam window design and upgrade potential." Presentation at the 2nd Oxford-Princeton High-Power Target Workshop, November 6–7, 2008, `http://www.physics.princeton.edu/~bridges/targetworkshop2/`, November, 2008.

[254] N. Li *et al.*, "Irradiation effects in tungsten and tantalum." Presentation at the Third High-Power Targetry Workshop, September 10–14, 2007, Bad Zurzach, Switzerland, `http://asq.web.psi.ch/hptrgts/`, 2007.

[255] C. Song, P. Wang, and H. A. Makse, "A phase diagram for jammed matter," *Nature* **453** (2008) 629.

[256] R. B. Palmer, D. V. Neuffer, and J. Gallardo, "A Practical High-Energy High-Luminosity μ^+-μ^-

Collider," in *The Sixth Advanced Accelerator Concepts Workshop*, P. Schoessow, ed., vol. 335 of *AIP Conference Proceedings*, pp. 635–645. AIP, 1995.

[257] R. B. Palmer *et al.*, "Muon colliders," in *The 9th Advanced ICFA Beam Dynamics Workshop: Beam Dynamics and Technology Issues for $\mu^+\mu^-$ Colliders* [477], pp. 3–30.

[258] M. A. Green, "Some options for the muon collider capture and decay solenoids," in *The 9th Advanced ICFA Beam Dynamics Workshop: Beam Dynamics and Technology Issues for $\mu^+\mu^-$ Colliders* [477], pp. 100–107.

[259] N. V. Mokhov, R. J. Noble, and A. V. Ginneken, "Target and collection optimization for muon colliders," in *The 9th Advanced ICFA Beam Dynamics Workshop: Beam Dynamics and Technology Issues for $\mu^+\mu^-$ Colliders* [477], pp. 61–86.

[260] R. C. Gupta. Private communication, August, 2010.

[261] R. Gupta, G. Greene, W. Sampson, and Y. Shiroyanagi, "HTS for magnets in high radiation environments." Presentation at CIMTEC 2010, montecatini term, italy, 5th forum on new material, `http://www.bnl.gov/magnets/Staff/Gupta/Talks/cimtec/cimtec2010-\%20FK-7.pdf`, June, 2010.

[262] F. Soler, "Pion production for neutrino factory — challenges," in *Proceedings of NuFACT'10*. AIP, 2010. to appear.

[263] T. J. Roberts *et al.*, "G4Beamline particle tracking in matter-dominated beam lines," in *Proceedings of EPAC08, Genoa, Italy* [478].

[264] R. C. Fernow, "Physics analysis performed by ECALC9," Tech. Rep. NFMCC-doc-280, Neutrino Factory/Muon Collider, 2003. `http://nfmcc-docdb.fnal.gov/`.

[265] J. Strait, N. V. Mokhov, and S. I. Striganov, "Towards the optimal energy of the proton driver for a neutrino factory and muon collider," *Phys. Rev. ST Accel. Beams* **13** (2010) 111001.

[266] **HARP** Collaboration, M. G. Catanesi, "Large-angle production of charged pions with 3–12.9 GeV/c incident protons on nuclear targets," *Phys. Rev. C* **77** (2008) 055207.

[267] A. Bolshakova *et al.*, "Cross sections of large-angle hadron production in proton- and pion-nucleus interactions III: tantalum nuclei and beam momenta from $\pm$3 GeV/c to $\pm$15 GeV/c," *Eur. Phys. J. C* **63** (2009) 549–609.

[268] **Neutrino Factory/Muon Collider** Collaboration, C. Albright *et al.*, "The neutrino factory and beta beam experiments and development," (2004) , `physics/0411123`.

[269] G. Penn and J. S. Wurtele, "Beam envelope equations for cooling of muons in solenoid fields," *Phys. Rev. Lett.* **85** (2000) 764.

[270] S. Agostinelli *et al.*, "GEANT4—a simulation toolkit," *Nucl. Instrum. Methods A* **506** (2003) 250–303.

[271] R. C. Fernow, "Modeling solenoids using coil, sheet and block conductors," Tech. Rep. NFMCC-doc-281, Neutrino Factory/Muon Collider, 2003. `http://nfmcc-docdb.fnal.gov/`.

[272] C. T. Rogers, "Modelling of the neutrino factory muon front end in ICOOL 3.10 and 3.20," Tech. Rep. UK Neutrino Factory Note 57, UK Neutrino Factory, 2010. `http://hepunx.rl.ac.uk/uknf/wp1/`.

[273] A. Moretti *et al.*, "Effects of high solenoidal magnetic fields on rf accelerating cavities," *Phys. Rev. ST Accel. Beams* **8** (2005) 072001.

[274] R. B. Palmer *et al.*, "RF breakdown with external magnetic fields in 201 and 805 MHz cavities," *Phys. Rev. ST Accel. Beams* **12** (2009) 031002.

[275] S. A. Bogacz, "Maximizing number of passes in muon RLA," in *Neutrino Factories, Superbeams and Betabeams: 9th International Workshop on Neutrino Factories, Superbeams, and Betabeams - NuFact 07*, O. Yasuda, N. Mondal, and C. Ohmori, eds., vol. 981 of *AIP Conference Proceedings*, pp. 324–326. AIP, 2008.

[276] S. A. Bogacz, "Beam Dynamics of Muon Acceleration for Neutrino Factory," *J. Phys. G: Nucl. Part. Phys* **29** (2003) 1723.

[277] S. A. Bogacz, "Low Energy Stages - 'Dogbone' Muon RLA," *Nucl. Phys. B Proc. Suppl.* **149** (2005) 309–312.

[278] J. S. Berg *et al.*, "Cost-effective design for a neutrino factory," *Phys. Rev. ST Accel. Beams* **9** (2006)

011001.
[279] M. Borland, "Elegant: A Flexible SDDS-Compliant Code for Accelerator Simulation," Light Source Note LS-287, Argonne National Laboratory, Argonne, IL, 2000. http://www.aps.anl.gov/Science/Publications/lsnotes/.
[280] M. Borland, "Elegant." HTTP://WWW.APS.ANL.GOV/ACCELERATOR_SYSTEMS_DIVISION/OPERATIONS_ANALYSIS/OAGPACKAGES.SHTML.
[281] V. Lebedev, "Optim." HTTP://WWW-BDNEW.FNAL.GOV/PBAR/ORGANIZATIONALCHART/LEBEDEV/OPTIM/OPTIM.HTM.
[282] "Mad-x." HTTP://MAD.HOME.CERN.CH/MAD/.
[283] "Poisson superfish." HTTP://LAACG1.LANL.GOV/LAACG/SERVICES/DOWNLOAD_SF.PHTML.
[284] K. Halbach and R. F. Holsinger, "SUPERFISH - a computer program for evaluation of RF cavities with cylindrical symmetry," *Part. Accel.* **7** (1976) 213–222.
[285] "CST Microwave Studio." HTTP://WWW.CST.COM.
[286] HTTP://WWW.COMSOL.COM/.
[287] S. B. van der Geer and M. J. de Loos, "General Particle Tracer." HTTP://WWW.PULSAR.NL/GPT/.
[288] J. S. Berg and R. B. Palmer, "Cost optimization of non-scaling FFAG lattices for muon acceleration," in *Proceedings of EPAC 2004, Lucerne, Switzerland*, pp. 902–904, EPAC. European Physical Society Accelerators Group, CERN, 2004.
[289] T. Ogitsu *et al.*, "Status of superconducting magnet system for the J-PARC neutrino beam line," *IEEE Trans. Appl. Supercond.* **19** no. 3, (June, 2009) 1081–1086.
[290] e2v technologies, *CX1925, CX1925X: Liquid Cooled, Hollow Anode, Three-Gap Metal/Ceramic Thyratrons*, November, 2004.
[291] FERROXCUBE, *8C11 Material Specification*, September, 2004.
[292] Vacuumschmelze, *Soft Magnetic Cobalt-Iron-Alloys: VACOFLUX 48, VACOFLUX 50, VACODUR 50, VACOFLUX 17*, 2001.
[293] B. Auchmann, J. Chambrillon, and S. Russenschuck, "The ROXIE program." HTTPS://ESPACE.CERN.CH/ROXIE.
[294] O. Brüning *et al.*, "Lhc design report volume I: The LHC main ring," Tech. Rep. CERN-2004-003-V-1, CERN, Geneva, Switzerland, June, 2004.
[295] S. Machida, "Longitudinal emittance blowup in fixed field alternating gradient muon accelerators," *Phys. Rev. ST Accel. Beams* **9** (2006) 104002.
[296] J. S. Berg, "Amplitude dependence of time of flight and its connection to chromaticity," *Nucl. Instrum. Methods A* **570** no. 1, (2007) 15–21.
[297] C. R. Prior, "Muon storage rings for a neutrino factory," in *Proceedings of the 23rd Particle Accelerator Conference* [474], p. 2739.
[298] A. Blondel, "Muon polarisation in the neutrino factory," *Nucl. Instrum. Methods A* **451** no. 1, (August, 2000) 131–137.
[299] R. Raja and A. Tollestrup, "Calibrating the energy of a 50×50 gev muon collider using spin precession," in *Physics Potential and Development of mu-mu Colliders: Fourth International Conference*, D. B. Cline, ed., vol. 441 of *AIP Conference Proceedings*, pp. 228–241. American Institute of Physics, 1998.
[300] B. Autin, A. Blondel, and J. Ellis, "Prospective study of muon storage rings at CERN," Tech. Rep. CERN 99-02, CERN, Geneva, Switzerland, April, 1999.
[301] X. Z. Qiu, X. Wang, and I. Ben-Zvi, "Proposal for using optical transition radiation for electron beam alignment and emittance measurement for the free electron laser experiments at ATF," Tech. Rep. BNL-60999, Brookhaven National Laboratory, Upton, NY, 1994.
[302] X. Z. Qiu, X. J. Wang, K. Batchelor, and I. Ben-Zvi, "Transition radiation electron beam diagnostic study at ATF," in *Proceedings of the 1995 Particle Accelerator Conference and International Conference on High-Energy Accelerators*, L. Gennari, ed., vol. 3, pp. 2530–2532. IEEE, Piscataway, NJ, 1996.
[303] R. B. Fiorito and D. W. Rule, "Optical transition radiation beam emittance diagnostics," in *Beam*

Instrumentation Workshop, R. E. Shafer, ed., vol. 319 of *AIP Conference Proceedings*, pp. 21–37. AIP, 1994.

[304] J.-C. Denard, P. Piot, K. Capek, and E. Feldl, "High power beam profile monitor with optical transition radiation," in *Proceedings of the 1997 Particle Accelerator Conference*, M. Comyn, M. K. Craddock, M. Reiser, and J. Thomson, eds., vol. 2, pp. 2198–2200. IEEE, Piscataway, NJ, 1998.

[305] A. Cervera-Villanueva, "MIND performance and prototyping," *AIP Conf. Proc.* **981** (2008) 178–180.

[306] A. De Rujula, M. B. Gavela, and P. Hernandez, "Neutrino oscillation physics with a neutrino factory," *Nucl. Phys.* **B547** (1999) 21–38, arXiv:hep-ph/9811390.

[307] G. Ingelman, A. Edin, and J. Rathsman, "LEPTO 6.5 - A Monte Carlo generator for deep inelastic lepton-nucleon scattering," *Computer Physics Communications* **101** (1997) 108–134(27).

[308] "Geant 3.21 CERN Program Library.". CERN Long write up W5013. http://wwwasdoc.web.cern.ch/wwwasdoc/pdfdir/geant.pdf.

[309] A. Cervera-Villanueva, J. J. Gomez-Cadenas, and J. A. Hernando, "'RecPack' a reconstruction toolkit," *Nucl. Instrum. Meth.* **A534** (2004) 180–183.

[310] D. Emeliyanov, I. Gorbounov, and I. Kisel, "OTR/ITR-CATS: Tracking Based on Cellular Automaton and Kalman Filter," 2001. {http://www-linux.gsi.de/\~{}ikisel/reco/HERA-B/cats_main.pdf}. HERA-B note 01-137.

[311] A. Cervera and A. Laing, "Status of MIND," *PoS* **Nufact08** (2008) 042.

[312] D. Casper, "The Nuance neutrino physics simulation, and the future," *Nucl. Phys. Proc. Suppl.* **112** (2002) 161–170, arXiv:hep-ph/0208030.

[313] **Geant4** Collaboration, J. Apostolakis and D. H. Wright, "An overview of the GEANT4 toolkit," *AIP Conf. Proc.* **896** (2007) 1–10.

[314] G. P. Zeller, "Low energy neutrino cross sections from K2K, MiniBooNE, SciBooNE, and MINERvA," *J. Phys. Conf. Ser.* **136** (2008) 022028.

[315] C. Amsler *et al.*, "Review of particle physics," *Physics Letters B* **667** no. 1-5, (2008) 1–6. http://pdg.lbl.gov. and 2009 partial update for 2010 edition.

[316] "Geant4 Physics Reference Manual.". http://cern.ch/geant4/UserDocumentation/UsersGuides/PhysicsReferenceManual/html/.

[317] **MINERvA** Collaboration, A. Pla-Dalmau, A. D. Bross, V. V. Rykalin, and B. M. Wood, "Extruded plastic scintillator for MINERvA.". Proceedings of 2005 IEEE Nuclear Science Symposium and Medical Imaging Conference, El Conquistador Resort, Puerto Rico, 23-29 Oct 2005.

[318] **MINOS** Collaboration, D. G. Michael *et al.*, "The Magnetized steel and scintillator calorimeters of the MINOS experiment," *Nucl. Instrum. Meth.* **A596** (2008) 190–228, arXiv:0805.3170 [physics.ins-det].

[319] A. Blondel, M. Campanelli, and M. Fechner, "Energy reconstruction in quasi-elastic events unfolding physics and detector effects," *Nucl. Instrum. Meth.* **A535** (2004) 665–673.

[320] A. Cervera-Villanueva, "Review of large magnetic calorimeters for a neutrino factory," *Nucl. Phys. Proc. Suppl.* **149** (2005) 201–202.

[321] K. Zuber, *Neutrino physics*. IOP, 2003.

[322] **NOMAD** Collaboration, V. Lyubushkin *et al.*, "A study of quasi-elastic muon neutrino and antineutrino scattering in the NOMAD experiment," *Eur. Phys. J.* **C63** (2009) 355–381, arXiv:0812.4543 [hep-ex].

[323] **MiniBooNE** Collaboration, A. A. Aguilar-Arevalo *et al.*, "First measurement of the muon neutrino charged current quasielastic double differential cross section," *Phys. Rev. D* **81** (2010) 092005, arXiv:1002.2680 [hep-ex].

[324] **K2K** Collaboration, A. Rodriguez *et al.*, "Measurement of single charged pion production in the charged-current interactions of neutrinos in a 1.3 gev wide band beam," *Phys. Rev. D* **78** (2008) 032003, arXiv:0805.0186 [hep-ex].

[325] **MINOS** Collaboration, K. Lang, "MINOS detectors for neutrino interactions," *Nucl. Instrum. Meth.*

A461 (2001) 290–292.

[326] **VLHC Design Study Group** Collaboration, G. Ambrosio *et al.*, "Design study for a staged very large hadron collider,". SLAC-R-591; FERMILAB-TM-2149.

[327] A. Y. Rodriguez Marrero, "Measurement of the exclusive ($\nu_\mu p \to \mu^- p \pi^+$) and inclusive ($\nu_\mu N \to \mu^- N' \pi^+$) single pion ν interaction cross section in a carbon target using the SciBar ,".

[328] **T2K** Collaboration, Y. Kudenko, "The near neutrino detector for the T2K experiment," *Nucl. Instrum. Meth.* **A598** (2009) 289–295, arXiv:0805.0411 [physics.ins-det].

[329] D. Greiner, T. Lachenmaier, J. Jochum, and A. Cabrera, "Double Chooz detectors design," *Nucl. Instrum. Meth.* **A581** (2007) 139–142.

[330] **MINERvA** Collaboration, K. S. McFarland, "MINERvA: A dedicated neutrino scattering experiment at NuMI," *Nucl. Phys. Proc. Suppl.* **159** (2006) 107–112, arXiv:physics/0605088.

[331] Z. Sadygov, 1996. Russian patent No. 2102820.

[332] N. Bacchetta *et al.*, "New type of metal-resistive layer-silicon avalanche detectors for visible and UV light detection," *Nucl. Instrum. Meth.* **A383** (1996) 263–265.

[333] D. Renker and E. Lorenz, "Advances in solid state photon detectors," *JINST* **4** (2009) P04004.

[334] V. Balagura *et al.*, "Study of scintillator strip with wavelength shifting fiber and silicon photomultiplier," *Nucl. Instrum. Meth.* **A564** (2006) 590–596, arXiv:physics/0504194.

[335] M. Yokoyama *et al.*, "Performance of Multi-Pixel Photon Counters for the T2K near detectors," *Nucl. Instrum. Meth.* **A622** (2010) 567–573, arXiv:1007.2712 [physics.ins-det].

[336] "Hamamatsu Photonics.". http://www.hamamatsu.com/.

[337] **NOvA** Collaboration, J. M. Paley, "NOvA detector research and development," *AIP Conf. Proc.* **981** (2008) 160–162.

[338] P. Zucchelli, "A novel concept for a anti-ν_e / ν_e neutrino factory: The beta beam," *Phys. Lett.* **B532** (2002) 166–172.

[339] J. Burguet-Castell, D. Casper, E. Couce, J. J. Gomez-Cadenas, and P. Hernandez, "Optimal beta-beam at the CERN-SPS," *Nucl. Phys.* **B725** (2005) 306–326, arXiv:hep-ph/0503021.

[340] J. Burguet-Castell, D. Casper, J. J. Gomez-Cadenas, P. Hernandez, and F. Sanchez, "Neutrino oscillation physics with a higher gamma beta- beam," *Nucl. Phys.* **B695** (2004) 217–240, arXiv:hep-ph/0312068.

[341] S. Choubey, P. Coloma, A. Donini, and E. Fernandez-Martinez, "Optimized two-baseline beta-beam experiment," *JHEP* **12** (2009) 020, arXiv:0907.2379 [hep-ph].

[342] V. Barger *et al.*, "Report of the US long baseline neutrino experiment study," arXiv:0705.4396 [hep-ph].

[343] "Neutrino Factory: specification of baseline for the accelerator complex and detector systems," *IDS-NF Steering Group, IDS-NF-Baseline-2007/1.0* (2008) .

[344] **ICARUS** Collaboration, S. Amerio *et al.*, "Design, construction and tests of the ICARUS T600 detector," *Nucl. Instrum. Meth. A* **A527** (2004) 329–410.

[345] A. Rubbia, "Underground Neutrino Detectors for Particle and Astroparticle Science: the Giant Liquid Argon Charge Imaging ExpeRiment (GLACIER)," *J. Phys. Conf. Ser.* **171** (2009) 012020, arXiv:0908.1286 [hep-ph].

[346] L. Bartoszek *et al.*, "FLARE: Fermilab liquid argon experiments," arXiv:hep-ex/0408121.

[347] D. B. Cline, F. Raffaelli, and F. Sergiampietri, "LANNDD: A line of liquid argon TPC detectors scalable in mass from 200-tons to 100-ktons," *JINST* **1** (2006) T09001, arXiv:astro-ph/0604548.

[348] D. Angeli *et al.*, "Towards a new Liquid Argon Imaging Chamber for the MODULAr project," *JINST* **4** (2009) P02003.

[349] T. Nakano, "Development towards a giant liquid argon observatory in Japan.". Talk at Neutrino 2010, June 2010, Athens, Greece.

[350] B. Fleming, "Liquid Ar R&D in the US.". Talk at NNN09, October 2009.

[351] A. Badertscher, "Construction and operation of a Double Phase LAr Large Electron Multiplier Time

Projection Chamber.". Proc. 2008 IEEE Nuclear Science Symposium, Dresden, Germany, arXiv:0811:3384.
[352] A. Badertscher, "Operation of a double-phase pure argon Large Electron Multiplier Time Projection Chamber: comparison of single and double phase operation.". Talk given at the 11th Pisa meeting on advanced detectors - Isola d'Elba 26 May 2009, arXiv:0907.2944.
[353] A. Rubbia, "Liquid argon projects in Europe and Japan.". Talk given at NNN10, Toyama, Japan (2010).
[354] P. K. Lightfoot, G. J. Barker, K. Mavrokoridis, Y. A. Ramachers, and N. J. C. Spooner, "Optical readout of secondary scintillation from liquid argon generated by a thick gas electron multiplier," *J. Phys. Conf. Ser.* **179** (2009) 012014.
[355] S. Centro, "Cost effective electronics for LAr and photodetectors readout.". CERN-2010-003 (2010).
[356] T. I. Ltd., "Large underground argon storage tank study report.". December, 2004, (commissioned by ETH Zurich.
[357] **LAGUNA** Collaboration, A. Rubbia, "The LAGUNA design study: Towards giant liquid based underground detectors for neutrino physics and astrophysics and proton decay searches," *Acta Phys. Polon.* **B41** (2010) 1727–1732.
[358] L. Kaufmann and A. Rubbia, "The ArDM project: A direct detection experiment, based on liquid argon, for the search of dark matter," *Nucl. Phys. Proc. Suppl.* **173** (2007) 141–143.
[359] A. Rubbia, "R&D towards a giant LAr charge imaging experiment (GALCIER).". Talk at EuroNU week, Strasbourg, June 2010.
[360] W. Jaskierny, H. Jostlein, S. H. Pordes, P. A. Rapidis, and T. Tope, "Test of purging a small tank with argon,". FERMILAB-TM-2384-E.
[361] T. Maruyama, "Liquid Ar R&D in Japan.". Talk at NNN09, October 2009.
[362] R. Andrews *et al.*, "A system to test the effects of materials on the electron drift lifetime in liquid argon and observations on the effect of water," *Nucl. Instrum. Meth. A* **608** (2009) 251–258.
[363] D. Cline, "New experiments at the new underground laboratories.". Talk at NNN09, October 2009.
[364] A. Badertscher, M. Laffranchi, A. Meregaglia, A. Muller, and A. Rubbia, "First results from a liquid argon time projection chamber in a magnetic field," *Nucl. Instrum. Meth.* **A555** (2005) 294–309, `physics/0505151`.
[365] D. B. Cline, F. Sergiampietri, J. G. Learned, and K. McDonald, "LANNDD: A massive liquid argon detector for proton decay, supernova and solar neutrino studies, and a neutrino factory detector," *Nucl. Instrum. Meth.* **A503** (2003) 136–140, `arXiv:astro-ph/0105442`.
[366] A. Ereditato and A. Rubbia, "Conceptual design of a scalable multi-kton superconducting magnetized liquid argon tpc," *Nucl. Phys. Proc. Suppl.* **155** (2006) 233–236, `hep-ph/0510131`.
[367] A. Bross, "Applications for large solid scintillator detectors in neutrino and particle astrophysics.". Talk at Neutrino 2010, June 2010, Athens, Greece.
[368] P. Huber and T. Schwetz, "A low energy neutrino factory with non-magnetic detectors," *Phys. Lett.* **B669** (2008) 294–300, `arXiv:0805.2019 [hep-ph]`.
[369] G. J. Barker, "Neutrino event reconstruction in a liquid argon TPC.". Proceedings of GLA2010, March 2010.
[370] J. Spitz, "ArgoNeuT and the Neutrino-Argon Charged Current Quasi-Elastic Cross Section.". Talk presented at the International Nuclear Physics Conference, Vancouver, Canada, July 4-9, 2010, arXiv:1009.2515.
[371] V. Barger, P. Huber, D. Marfatia, and W. Winter, "Which long-baseline neutrino experiments are preferable?," *Phys. Rev. D* **76** (2007) 053005, `arXiv:0703029 [hep-ph]`.
[372] **Borexino Collaboration** Collaboration, G. Alimonti *et al.*, "The Borexino detector at the Laboratori Nazionali del Gran Sasso," *Nucl.Instrum.Meth.* **A600** (2009) 568–593, `arXiv:0806.2400 [physics.ins-det]`.
[373] F. Suekane, T. Iwamoto, H. Ogawa, O. Tajima, H. Watanabe, *et al.*, "An overview of the kamland 1-kiloton liquid scintillator," `arXiv:physics/0404071 [physics]`.

[374] M. Wurm *et al.*, "Detection potential for the diffuse supernova neutrino background in the large liquid-scintillator detector LENA," *Phys. Rev.* **D75** (2007) 023007, arXiv:astro-ph/0701305.
[375] L. Oberauer *et al.*, "LENA,". Prepared for 3rd International Workshop on NO-VE: Neutrino Oscillations in Venice: 50 Years after the Neutrino Experimental Discovery, Venice, Italy, 7-10 Feb 2006.
[376] K. A. Hochmuth *et al.*, "Probing the Earth's interior with the LENA detector," *Earth Moon Planets* **99** (2006) 253–264, arXiv:hep-ph/0610048.
[377] T. Marrodan Undagoitia *et al.*, "Low energy neutrino astronomy with the large liquid- scintillation detector LENA," *J. Phys. Conf. Ser.* **39** (2006) 287–290.
[378] T. Marrodan Undagoitia *et al.*, "Proton decay in the large liquid scintillator detector LENA: Study of the background," *J. Phys. Conf. Ser.* **39** (2006) 269–271.
[379] T. Marrodan Undagoitia *et al.*, "Simulation of the proton decay in the LENA detector," *Prog. Part. Nucl. Phys.* **57** (2006) 290–292.
[380] T. Marrodan Undagoitia *et al.*, "Low energy neutrino astronomy with the large liquid scintillation detector LENA," *Prog. Part. Nucl. Phys.* **57** (2006) 283–289, arXiv:hep-ph/0605229.
[381] T. Marrodan Undagoitia *et al.*, "Search for the proton decay p –¿ K+ anti-nu in the large liquid scintillator low energy neutrino astronomy detector LENA," *Phys. Rev.* **D72** (2005) 075014, arXiv:hep-ph/0511230.
[382] D. Autiero *et al.*, "Large underground, liquid based detectors for astro- particle physics in Europe: scientific case and prospects," *JCAP* **0711** (2007) 011, arXiv:0705.0116 [hep-ph].
[383] M. Wurm *et al.*, "The Physics Potential of the LENA Detector," *Acta Phys. Polon.* **B41** (2010) 1749–1764, arXiv:1004.3474 [physics.ins-det].
[384] T. Lachenmaier *et al.*, "Physics with the large liquid-scintillator detector LENA," *Prog. Part. Nucl. Phys.* **64** (2010) 381–383.
[385] M. Batygov *et al.*, "Hanohano:A Deep Ocean Antineutrino Observatory," *J. Phys. Conf. Ser.* **136** (2008) 042002, arXiv:0810.0564 [hep-ex].
[386] J. G. Learned, S. T. Dye, and S. Pakvasa, "Hanohano: A Deep ocean anti-neutrino detector for unique neutrino physics and geophysics studies," arXiv:0810.4975 [hep-ex].
[387] J. G. Learned, "High Energy Neutrino Physics with Liquid Scintillation Detectors," arXiv:0902.4009 [hep-ex].
[388] J. Peltoniemi, "Liquid scintillator as tracking detector for high-energy events," arXiv:0909.4974 [physics.ins-det].
[389] S. N. Smith and J. G. Learned, "Liquid scintillation detectors for high energy neutrinos," *AIP Conf. Proc.* **1222** (2010) 127–130.
[390] R. Möllenberg, F. von Feilitzsch, M. Göger-Neff, D. Hellgartner, T. Lewke, Q. Meindl, L. Oberauer, J. Peltoniemi, W. Potzel, M. Tippmann, J. Winter, and M. Wurm, "Reconstruction of gev neutrino events in lena," in *Proceedings of nuFact2010*. 2010.
[391] LENA group, "Reconstruction of neutrino events at GeV energies in the large liquid-scintillator detector LENA." 2010.
[392] J. Peltoniemi, "Simulations of neutrino oscillations for a wide band beam from CERN to LENA," arXiv:0911.4876 [hep-ex].
[393] J. Peltoniemi, "Simulations of neutrino oscillations with a high-energy beta beam from CERN to LENA at Pyhasalmi Mine," arXiv:0911.5234 [hep-ph].
[394] J. Peltoniemi, "Simulations of neutrino oscillations for a low-energy neutrino factory with a magnetized large-volume liquid scintillator at 2288 km baseline," arXiv:0912.2611 [hep-ph].
[395] **Borexino Collaboration** Collaboration, H. Back *et al.*, "Phenylxylylethane (PXE): A High-density, high-flashpoint organic liquid scintillator for applications in low-energy particle and astrophysics experiments," *Nucl.Instrum.Meth.A* (2004) , arXiv:physics/0408032 [physics].
[396] S. E. Quirk, "Purification of Liquid Scintillator and Monte Carlo Simulations of Relevant Internal Backgrounds in SNO+," PhD Thesis, Queen's University Kingston, Canada, 2008.

[397] T. Marrodan Undagoitia *et al.*, "Fluorescence decay-time constants in organic liquid scintillators," *Rev. Sci. Instr.* **80** (2009) 043301, arXiv:0904.4602 [physics.ins-det].

[398] M. Wurm, F. von Feilitzsch, M. Goeger-Neff, M. Hofmann, T. Lachenmaier, *et al.*, "Optical Scattering Lengths in Large Liquid-Scintillator Neutrino Detectors," *Rev.Sci.Instrum.* **81** (2010) 053301, arXiv:1004.0811 [physics.ins-det].

[399] G. Nuijten *et al.*, "Laguna design study deliverable 2.1," deliverable deliverable 2.1, LAGUNA design study, 2010.

[400] **GENIE** Collaboration, C. Andreopoulos, "The GENIE neutrino Monte Carlo generator," *Acta Phys. Polon.* **B40** (2009) 2461–2475.

[401] **CHARM-II** Collaboration, P. Vilain *et al.*, "A Precise measurement of the cross-section of the inverse muon decay muon-neutrino + e- → mu- + electron- neutrino," *Phys. Lett.* **B364** (1995) 121–126.

[402] S. R. Mishra *et al.*, "INVERSE MUON DECAY, muon-neutrino e → mu- electron- neutrino, AT THE FERMILAB TEVATRON," *Phys. Lett.* **B252** (1990) 170–176.

[403] "GENIE web site." http://www.genie-mc.org.

[404] C. Andreopoulos *et al.*, "The GENIE Neutrino Monte Carlo Generator," *Nucl. Instrum. Meth. A* **614** (2010) 87–104, arXiv:0905.2517 [hep-ph].

[405] W. J. Marciano and Z. Parsa, "Neutrino-Electron Scattering Theory," *J. Phys.* **G29** (2003) 2629–2645, arXiv:hep-ph/0403168.

[406] G. Barichello *et al.*, "Performance of the NOMAD-STAR detector," *Nucl. Instrum. Meth.* **A506** (2003) 217–237.

[407] **MINERvA** Collaboration, T. Kafka and V. Paolone, "Prospects and status of the MINERvA experiment at FNAL," *Prog. Part. Nucl. Phys.* **64** (2010) 181–183.

[408] **MINOS** Collaboration, D. G. Michael *et al.*, "Observation of muon neutrino disappearance with the minos detectors and the numi neutrino beam," *Phys. Rev. Lett.* **97** (2006) 191801, hep-ex/0607088.

[409] A. Laing and F. J. P. Soler, "Flux measurement at a neutrino factory near detector for neutrino oscillations," *AIP Conf. Proc.* **981** (2008) 166–168.

[410] G. Cowan, *Statistical data analysis*. Oxford University Press, UK: Clarendon, 1998.

[411] A. Laing and F. J. P. Soler, "Oscillation probability fits using near detector data at a neutrino factory," *PoS* **NUFACT08** (2008) 129.

[412] **NuTeV** Collaboration, G. P. Zeller *et al.*, "A precise determination of electroweak parameters in neutrino nucleon scattering," *Phys. Rev. Lett.* **88** (2002) 091802, hep-ex/0110059.

[413] S. R. Mishra, R. Petti, and C. Rosenfeld, "A High Resolution Neutrino Experiment in a Magnetic Field for Project-X at Fermilab," *PoS* **NUFACT08** (2008) 069, arXiv:0812.4527 [hep-ex].

[414] "Preparation for p5 meetings on physics with a high intensity proton source," 2007. http://www.fnal.gov/directorate/Longrange/Steering_Public/P5.html.

[415] "Fermilab steering group report," 2007. http://www.fnal.gov/pub/directorate/steering/pdfs/SGR_2007.pdf.

[416] **NOMAD** Collaboration, J. Altegoer *et al.*, "The NOMAD experiment at the CERN SPS," *Nucl. Instrum. Meth. A* **404** (1998) 96–128.

[417] **ATLAS TRT** Collaboration, T. Akesson *et al.*, "Status of design and construction of the Transition Radiation Tracker (TRT) for the ATLAS experiment at the LHC," *Nucl. Instrum. Meth.* **A522** (2004) 131–145.

[418] **ATLAS TRT** Collaboration, T. Akesson *et al.*, "ATLAS Transition Radiation Tracker test-beam results," *Nucl. Instrum. Meth.* **A522** (2004) 50–55.

[419] **ATLAS TRT** Collaboration, E. Abat *et al.*, "The ATLAS Transition Radiation Tracker (TRT) proportional drift tube: Design and performance," *JINST* **3** (2008) P02013.

[420] V. N. Bychkov *et al.*, "Construction and manufacture of large size straw-chambers of the COMPASS spectrometer tracking system," *Part. Nucl. Lett.* **111** (2002) 64–73.

[421] "Long baseline neutrino experiment," 2010. http://lbne.fnal.gov/.

[422] G. D. Lellis, P. Migliozzi, and P. Santorelli, "Charm physics with neutrinos," *Phys. Rept.* **399** (2004) 227–320.

[423] **CHORUS** Collaboration, A. Kayis-Topaksu *et al.*, "Leading order analysis of neutrino induced dimuon events in the chorus experiment," *Nucl. Phys. B* **798** (2008) 1–16, arXiv:0804.1869 [hep-ex].

[424] R. Petti *et al.*, "A precise measurement of Charm Dimuon production in neutrino interactions from the NOMAD experiment," *PoS* **DIS 2010** (2010) 170.

[425] K. Niu, E. Mikumo, and Y. Maeda, "A Possible decay in flight of a new type particle," *Prog. Theor. Phys.* **46** (1971) 1644–1646.

[426] N. Ushida *et al.*, "Measurement of the D0 Lifetime," *Phys. Rev. Lett.* **45** (1980) 1049–1052.

[427] N. Ushida *et al.*, "Measurement of the D+, F+, and Lambda(c)+ Charmed Particle Lifetimes," *Phys. Rev. Lett.* **45** (1980) 1053–1056.

[428] J. P. Albanese *et al.*, "Direct observation of the decay of beauty particles into charm particles," *Phys. Lett. B* **158** (1985) 186.

[429] **CHORUS** Collaboration, A. Kayis-Topaksu *et al.*, "Associated charm production in neutrino-nucleus interactions," *Eur. Phys. J. C* **52** (2007) 543–552, arXiv:0708.2820 [hep-ex].

[430] **DONUT** Collaboration, K. Kodama *et al.*, "Observation of tau-neutrino interactions," *Phys. Lett.* **B504** (2001) 218–224, arXiv:hep-ex/0012035.

[431] **OPERA** Collaboration, N. Agafonova *et al.*, "Observation of a first ν_τ candidate in the OPERA experiment in the CNGS beam," *Phys. Lett. B* **691** (2010) 138–145, arXiv:1006.1623 [hep-ex].

[432] L. Camilleri, *Principles and Methods: Subvolume B: Detectors for Particles and Radiation - Volume 21: Elementary Particles - Group I: Elementary Particles, Nuclei and Atoms*. Springer, 2011. %%http://www.amazon.com/Principles-Methods-Subvolume-Detectors-Elementary/dp/3642036058%3FSubscriptionId%3D0JYN1NVW651KCA56C102%26tag%3Dtechkie-20%26linkCode%3Dxm2%26camp%3D2025%26creative%3D165953%26creativeASIN%3D3642036058%%.

[433] L. Arrabito *et al.*, "Track reconstruction in the emulsion-lead target of the OPERA experiment using the ESS microscope," *JINST* **2** (2007) P05004, arXiv:0705.3102 [physics.ins-det].

[434] T. Nakamura *et al.*, "The OPERA film: New nuclear emulsion for large-scale, high-precision experiments," *Nucl. Instrum. Meth.* **A556** (2006) 80–86.

[435] R. Acquafredda *et al.*, "The OPERA experiment in the CERN to Gran Sasso neutrino beam," *JINST* **4** (2009) P04018.

[436] S. Aoki *et al.*, "Measurement of low-energy neutrino cross-sections with the PEANUT experiment," *New J. Phys.* **12** (2010) 113028.

[437] C. Fukushima *et al.*, "A thin emulsion spectrometer using a compact permanent magnet," *Nucl. Instrum. Meth.* **A592** (2008) 56–62.

[438] J. J. Gomez-Cadenas, J. A. Hernando, and A. Bueno, "A Neutrino apparatus with improved capabilities for a short baseline muon-neutrino (electron-neutrino) $\rightarrow$ tau- neutrino search," *Nucl. Instrum. Meth.* **A378** (1996) 196–220.

[439] J. J. Gomez-Cadenas and J. A. Hernando, "Search for nu/mu (nu/e) $\rightarrow$ nu/tau oscillations with a detector based on a emulsion-silicon target," *Nucl. Instrum. Meth.* **A381** (1996) 223–235.

[440] M. Ellis and F. J. P. Soler, "Near detector at a neutrino factory," *Nucl. Instrum. Meth.* **A569** (2006) 127–131.

[441] A. Ayan and others (TOSCA Collaboration), "A High Sensitivity Short Baseline Experiment to search for $\nu_\mu \rightarrow \nu_\tau$," 1997. TOSCA Letter of Intent, CERN-SPSC/97-5, SPSC I213, http://tosca.web.cern.ch/TOSCA/Public/LetterOfIntent/.

[442] J. Strait, "HARP Data and $E_{\min}$ for Proton Driver." Presentation at the 11th international workshop on neutrino factories, superbeams and beta beams, http://nufact09.iit.edu, 2009.

[443] M. Sadler *et al.*, "Proposal to upgrade the MIPP experiment," Tech. Rep. Fermilab Proposal P-960, Fermilab, 2010.

[444] J. S. Berg, "Minimizing longitudinal distortion in a nearly isochronous linear nonscaling fixed-field

alternating gradient accelerator," *Phys. Rev. ST Accel. Beams* **9** (2006) 034001.
[445] **MINOS** Collaboration, P. Adamson *et al.*, "A Study of Muon Neutrino Disappearance Using the Fermilab Main Injector Neutrino Beam," *Phys. Rev. D* **77** (2008) 072002, arXiv:0711.0769 [hep-ex].
[446] "AIDA: Advanced european infrastructures for detectors at accelerators," 2010. http://cern.ch/aida.
[447] J. Bonnal, P. De Jonghe *et al.*, "CERN tool for project costing," 2010. http://indico.cern.ch/getFile.py/access?contribId=11&sessionId=2&resId=1&materialId=slides&confId=85004.
[448] S. D. Holmes, "Project X—reference design report," Tech. Rep. Project-X-doc-776, Fermilab, November, 2010. https://projectx-docdb.fnal.gov:440/cgi-bin/DocumentDatabase.
[449] D. J. S. Findlay, "ISIS, pulsed neutron and muon source," in *Proceedings of PAC07, Albuquerque, New Mexico, USA* [476], p. 695.
[450] J. Pasternak, M. Aslaninejad, K. Long, and J. Pozimski, "Feasibility of a common proton driver for a neutron spallation source and a neutrino factory," in *Proceedings of the 23rd Particle Accelerator Conference* [474], p. 1433.
[451] S. D. Holmes, "Project X: a multi-MW proton source at Fermilab," in *Proceedings of IPAC'10, Kyoto, Japan* [472], p. 1299.
[452] C. M. Warsop *et al.*, "Space charge and high intensity studies on ISIS," in *Proceedings of Hadron Beam 2008, Nashville, Tennessee, USA* [479], p. 143.
[453] C. M. Warsop *et al.*, "High intensity studies on the ISIS synchrotron, including key factors for upgrades and the effects of half integer resonance.," in *Proceedings of HB2010, Morschach, Switzerland*. 2010. to appear.
[454] B. G. Pine and C. M. Warsop, "Image simulations on the ISIS synchrotron," in *Proceedings of EPAC08, Genoa, Italy* [478], p. 3215.
[455] J. W. G. Thomason *et al.*, "Injection upgrades for the ISIS synchrotron," in *Proceedings of IPAC'10, Kyoto, Japan* [472], p. 705.
[456] J. W. G. Thomason *et al.*, "Megawatt upgrades for the ISIS facility," in *Proceedings of Hadron Beam 2008, Nashville, Tennessee, USA* [479], p. 434.
[457] G. H. Rees, "Linac, beam line and ring studies for an upgrading of ISIS," Tech. Rep. Research note GHR1, ASTeC, 2009.
[458] I. E. Campisi *et al.*, "Status and Performance of the Spallation Neutron Source Superconducting Linac," in *Proceedings of PAC07, Albuquerque, New Mexico, USA* [476], p. 2502.
[459] ESS Council, "The ESS project, volume III: Technical report," tech. rep., ESS Council, Jülich, Germany, 2002. http://neutron.neutron-eu.net/n_documentation/n_reports/n_ess_reports_and_more.
[460] Accelerator Group, JAERI/KEK Joint Project Team, "Accelerator technical design report for J-PARC," KEK Report 2002-13, JAERI/KEK, 2003.
[461] A. Letchford *et al.*, "Status of the RAL Front End Test Stand ," in *Proceedings of IPAC'10, Kyoto, Japan* [472], p. 642.
[462] A. Seville *et al.*, "Progress on dual harmonic acceleration on the ISIS synchrotron," in *Proceedings of EPAC08, Genoa, Italy* [478], p. 349.
[463] C. R. Prior, "Neutrino factory proton Driver: preferred scenarios and remaining issues," in *10th International Workshop on Neutrino Factories, Super beams and Beta beams* [473], p. PoS(Nufact08)070.
[464] C. Densham, O. Caretta, and P. Loveridge, "The Development of Fluidised Powder Target Technology for a Neutrino Factory, Muon Collider or Superbeam." Presentation at NuFact10, the 12th International Workshop on Neutrino Factories, Superbeams and Beta Beams, October, 2010.
[465] J. R. J. Bennett *et al.*, "Thermal shock measurements and modelling for solid high-power targets at high temperatures," *J. Nucl. Mater.* **377** no. 1, (2008) 285–289.
[466] J. Back, "Pion and muon yields from a 10 GeV proton beam on various targets," in *10th International Workshop on Neutrino Factories, Super beams and Beta beams* [473], p. PoS(Nufact08)084.
[467] F. Schmidt, "Mad-x a worthy successor for mad8?," *Nucl. Instrum. Meth.* **A 558** (2006) 47.
[468] Y. Kuno *et al.*, "A feasibility study of a neutrino factory in japan."

HTTP://WWW-PRISM.KEK.JP/NUFACTJ/, May, 2001.
[469] Y. Mori, "FFAG accelerators and their applications," in *Proceedings of EPAC 2006, Edinburgh, Scotland*, pp. 950–954, EPAC. European Physical Society Accelerator Group, 2006.
[470] T. Nakamoto *et al.*, "Design of superconducting combined function magnets for the 50 GeV proton beam line for the J-PARC neutrino experiment," *IEEE Trans. Appl. Supercond.* **14** no. 2, (June, 2004) 616–619.
[471] H. A. Enge, "Deflecting magnets," in *Focusing of Charged Particles*, A. L. Septier, ed., vol. 2. Academic Press, New York, 1967.
[472] *Proceedings of IPAC'10, Kyoto, Japan*. IPAC'10 and Asian Committee for Future Accelerators, 2010.
[473] *10th International Workshop on Neutrino Factories, Super beams and Beta beams*. Proceedings of Science, 2008.
[474] *Proceedings of the 23rd Particle Accelerator Conference*. 2010.
[475] M. C. Goodman, D. M. Kaplan, and Z. Sullivan, eds., *Neutrino Factories, Superbeams and Beta Beams: 11th International Workshop on Neutrino Factories, Superbeams and Beta Beams—NuFact09*, vol. 1222 of *AIP Conference Proceedings*. American Institute of Physics, Melville, NY, 2010.
[476] *Proceedings of PAC07, Albuquerque, New Mexico, USA*. IEEE, 2007.
[477] *The 9th Advanced ICFA Beam Dynamics Workshop: Beam Dynamics and Technology Issues for $\mu^+\mu^-$ Colliders*, vol. 372 of *AIP Conference Proceedings*. AIP, 1996.
[478] EPAC, *Proceedings of EPAC08, Genoa, Italy*. European Physical Society Accelerator Group, 2008.
[479] *Proceedings of Hadron Beam 2008, Nashville, Tennessee, USA*. 2008.